

# Investigation into Flow-induced Vibrations of Piano Key Weirs

by

Frank Joris Maria Denys



*Dissertation presented for the degree of  
Doctor of Philosophy in Civil Engineering  
in the Faculty of Engineering  
at Stellenbosch University*

Supervisors:

Prof GR Basson  
Dr JAvB Strasheim

April 2019

This page is intentionally left blank.

## Declaration

By submitting this dissertation electronically, I declare that the entirety of the work contained therein is my own, original work, that I am the sole author thereof (save to the extent explicitly otherwise stated), that reproduction and publication thereof by Stellenbosch University will not infringe any third party rights and that I have not previously in its entirety or in part submitted it for obtaining any qualification.

Date: ..... April 2019 .....

Copyright © 2019 Stellenbosch University  
All rights reserved.

This page is intentionally left blank.



UNIVERSITEIT • STELLENBOSCH • UNIVERSITY  
jou kennisvennoot • your knowledge partner

### Plagiaatverklaring / Plagiarism Declaration

- 1 Plagiaat is die oorneem en gebruik van die idees, materiaal en ander intellektuele eiendom van ander persone asof dit jou eie werk is.  
*Plagiarism is the use of ideas, material and other intellectual property of another's work and to present it as my own.*
- 2 Ek erken dat die pleeg van plagiaat 'n strafbare oortreding is aangesien dit 'n vorm van diefstal is.  
*I agree that plagiarism is a punishable offence because it constitutes theft.*
- 3 Ek verstaan ook dat direkte vertalings plagiaat is.  
*I also understand that direct translations are plagiarism.*
- 4 Dienooreenkomstig is alle aanhalings en bydraes vanuit enige bron (ingesluit die internet) volledig verwys (erken). Ek erken dat die woordelike aanhaal van teks sonder aanhalingstekens (selfs al word die bron volledig erken) plagiaat is.  
*Accordingly all quotations and contributions from any source whatsoever (including the internet) have been cited fully. I understand that the reproduction of text without quotation marks (even when the source is cited) is plagiarism.*
- 5 Ek verklaar dat die werk in hierdie skryfstuk vervat, behalwe waar anders aangedui, my eie oorspronklike werk is en dat ek dit nie vantevore in die geheel of gedeeltelik ingehandig het vir bepunting in hierdie module/werkstuk of 'n ander module/werkstuk nie.  
*I declare that the work contained in this assignment, except where otherwise stated, is my original work and that I have not previously (in its entirety or in part) submitted it for grading in this module/assignment or another module/assignment.*

13455621 <b>Studentenommer / Student number</b>	 <b>Handtekening / Signature</b>
FJM Denys <b>Voorletters en van / Initials and surname</b>	2018/09/20 <b>Datum / Date</b>

This page is intentionally left blank.

# Abstract

## Investigation into Flow-induced Vibrations of Piano Key Weirs

FJM Denys

*Faculty of Engineering  
Department of Civil Engineering,  
Stellenbosch University,  
Private Bag X1, Matieland 7602, South Africa.*

Dissertation: PhD

April 2019

This thesis considers the transient behaviour of piano key weirs (PKW) from a hydrodynamic and structural perspective. Their geometry makes them very rigid structures, however, there are thinner components of a PKW which may be prone to the onset of vibrations, specifically fluid or flow induced vibrations (FIV). Such vibrations, if strong enough and of sufficient duration may induce material fatigue in high stress zones of the structure. This is especially the case in steel PKWs whose slenderness and low mass may make them susceptible to vibration as detailed in this study.

A number of hydrodynamic sources of excitation were found to occur at PKWs. These include the shedding of vortices from a free shear layer which develops at the entrance of the PKW's inlet key; the unstable fluctuation of the air cavity under the overflow nappe; as well as the oscillation of the nappe itself. The vortex shedding, and the pressure fluctuations it causes on the upstream face of the weir, was the focus of the study as it was found to be a very stable flow feature. In contrast to literature, changes in discharge and the width of the inlet key had no effect on the character of these pressure oscillations.

The manner in which these fluctuations manifest on the lateral sidewall of the PKW were examined in light of the modal shapes of the structure. It was found that there was an overlap between the excitation frequencies and the natural frequencies of the structure, thus there is potential for resonance to occur. However, there was a general lack of correlation in the excitations, which reduced their ability to activate any of the mode shapes despite the overlap in frequency. This means that the vibration response of the structure is limited.

The study consisted of two physical models as well as a series of numerical models of the hydrodynamic (CFD) and structural (FEM) environment. These separate numerical models were calibrated against their physical counterparts and then combined in a staggered coupled fluid structure interaction (FSI) model. This integrated numerical model was able to emulate many of the vibration features observed in the physical model, including the effect of added mass and damping.

Analysis of the generated stress and strain data revealed that, although fluid induced vibrations do occur at the PKW's sidewall, the magnitude of the structural response is limited in

most cases and is thus unlikely to lead to material fatigue. Nevertheless, alternative construction materials such as stainless steel or PVC may still experience such problems and would thus need to account for them in their design.

The findings from this dissertation reveal that Piano Key Weirs are indeed prone to fluid induced vibrations due to their geometry and their thin nature. However, good design should be able to limit the negative effect these vibrations have on the operations and longevity of the structure.

# Uittreksel

## Ondersoek na Vloeigedrewe Vibrasies van Klavierklawer Keerwalle

*("Investigation into Flow-induced Vibrations  
of Piano Key Weirs")*

FJM Denys

*Fakulteit Ingenieurswese  
Departement Siviele Ingenieurswese,  
Stellenbosch Universiteit,  
Privaatsak X1, Matieland 7602, Suid Afrika.*

Proefskrif: PhD

April 2019

Hierdie proefskrif beskou die varierende gedrag van klavierklawer keerwalle (KKK) vanuit 'n hidrodinamiese en strukturele oogpunt. Hul vorm maak hulle baie rigied, maar daar is dunner dele van 'n KKK wat moontlik vatbaar is vir die ontstaan van vibrasies, meer spesifiek vloeigedrewe vibrasies. Sodanige vibrasies, indien sterk genoeg en van voldoende tydsduur, kan lei tot die ontwikkeling van materiële vermoeidheid in hoë spanningsones van die struktuur. Dit is veral die geval in staal KKKs waarvan die slankheid en lae massa dit vatbaar maak vir vibrasie soos in hierdie studie uiteengesit.

'n Aantal hidrodinamiese bronne van opwekking is gevind by KKKs. Dit sluit in die afwerp van werwels vanaf 'n vrye afskuiflaag wat by die ingang van die KKK se inlaat klawer ontwikkel; die onstabiele fluktuasie van die lugholte onder die oorloopnappe; sowel as die ossillasie van die nappe self. Die werwelafwerping, en die drukvariasies wat dit op die stroomopkant van die keerwal veroorsaak, was die fokus van die studie aangesien dit gevind is dat dit 'n baie stabiele vloeiverskynsel is. In teenstelling met literatuur het veranderinge in die deurstroming en die inlaatklawerwydte geen invloed gehad op die eienskappe van hierdie drukossillasies nie.

Die wyse waarop hierdie drukvariasies op die laterale sypuur van die KKK verskyn, is ondersoek in die lig van die modale vorms van die struktuur. Daar is bevind dat daar 'n oorvleueling was tussen die toepassingsfrekwensies en die natuurlike frekwensies van die struktuur, dus bestaan daar 'n moontlikheid vir resonansie om plaas te vind. Daar was egter 'n algemene gebrek aan korrelasie in die toepassings, wat hul vermoë om enige van die modusse te aktiveer verminder het ten spyte van die oorvleueling in frekwensie. Dit beteken dat die vibrasie reaksie van die struktuur beperk is.

Die studie is uitgevoer met twee fisiese modelle sowel as 'n reeks numeriese modelle van die hidrodinamiese en strukturele omgewing. Hierdie afsonderlike numeriese modelle is gekalibreer teen hul fisiese eweknieë en is dan gekombineer in 'n gekoppelde vloeistruktuur-

interaksie model. Hierdie geïntegreerde numeriese model was in staat om baie van die vibrasie-eienskappe wat in die fisiese model waargeneem is, te simuleer, insluitend die invloed van toegevoegde massa en demping.

Ontleding van die gegenereerde stres- en spanningdata het getoon dat, hoewel vloeigedrewe vibrasies by die KKK se symuur voorkom, die grootte van die strukturele reaksie in die meeste gevalle beperk is en dit dus onwaarskynlik sal lei tot materiële vermoeidheid. Nietemin, alternatiewe konstruksiemateriale soos vlekvrystaal of PVC kan nog steeds sulke probleme ervaar wat dus in ag geneem moet word in hul ontwerp.

Die bevindings van hierdie proefskrif toon dat klavierklawer keerwalle wel geneig is tot vloeigedrewe vibrasies as gevolg van hul vorm en hul dun aard. Goeie ontwerp kan egter die negatiewe invloed van hierdie vibrasies op die bedryf en duursaamheid van die struktuur beperk.

## Preface

The research and findings from this thesis were presented to the professional and academic community at a number of conferences and workshops and published in a number of specialist journals. The research findings have been incorporated into the following journal papers and conference proceedings:

- Denys FJM and Basson GR (2018). Transient Hydrodynamics of Piano Key Weirs. *7th IAHR International Symposium on Hydraulic Structures*, Aachen, Germany, 15-18 May.
- Denys FJM, Basson GR, Strasheim JAvB (2017). Fluid Structure Interaction of Piano Key Weirs. *Proceedings of the 3rd International Workshop on Labyrinth and Piano Key Weirs (PKW 2017)*, Qui Nhon, Vietnam, 22-24 February.
- Denys FJM (2017). Piano Key Weir Spillway Standard Design Principles and Flow Induced Vibrations. *Stellenbosch University Short Course: Design, construction, operation and maintenance of dams in Africa* 16-19 May.
- Denys FJM, Basson GR, Strasheim JAvB (2016). Investigation into the Fluid and Structural Behaviour of Piano Key Weirs. *84th ICOLD Annual Meeting and Symposium*, Johannesburg, South Africa, 15-20 May.
- Denys FJM (2015). Design of an Economic Spillway Alternative: Piano Key Weirs. *SAN-COLD Annual Conference: Dam safety, maintenance & rehabilitation of dams in Southern Africa*, Cape Town, South Africa, 1-3 September.

This page is intentionally left blank.

## Acknowledgements

I would like to express my sincere gratitude to the following people and organisations for their support, assistance, guidance, patience and advice:

- The South African National Committee on Large Dams (SANCOLD) for their award of a post-graduate scholarship to partially fund this study
- My supervisors Professor GR Basson and Dr JAvB Strasheim
- The capable and ever ready lab team, Johann Nieuwoudt, Iliyaaz Williams and Ning Ma
- Megan Laker and Jaretha Lombaard for their assistance with the lab work

Special thanks are due to Odon and Wicus for meticulously proofreading the dissertation, my friends, family and especially André for keeping me sane.

This page is intentionally left blank.

## Dedications

*This dissertation is dedicated to  
you as a reader  
and  
to the continual development and understanding  
of Piano Key Weirs.*

This page is intentionally left blank.

# Contents

<b>Declaration</b>	<b>iii</b>
<b>Abstract</b>	<b>vii</b>
<b>Uittreksel</b>	<b>ix</b>
<b>Preface</b>	<b>xi</b>
<b>Acknowledgements</b>	<b>xiii</b>
<b>Contents</b>	<b>xvii</b>
<b>List of Figures</b>	<b>xxiii</b>
<b>List of Tables</b>	<b>xxxi</b>
<b>Nomenclature</b>	<b>xxxiii</b>
<b>1 Background to the research</b>	<b>1</b>
1.1 Introduction . . . . .	1
1.2 Background . . . . .	1
1.3 Research focus . . . . .	1
1.4 Research objectives and scope . . . . .	2
1.5 Research methodology . . . . .	3
1.6 Dissertation outline . . . . .	3
<b>2 Piano key weir hydraulics</b>	<b>5</b>
2.1 Introduction to piano key weirs . . . . .	5
2.2 Unique design aspects . . . . .	6
2.2.1 Reduced structural footprint and stability . . . . .	6
2.2.2 Submergence . . . . .	7
2.2.3 Debris and driftwood . . . . .	7
2.2.4 Modular construction . . . . .	7
2.3 Geometric design . . . . .	8
2.4 Piano key weir hydraulics . . . . .	10
2.4.1 Discharge efficiency . . . . .	10
2.4.2 Flow dynamics . . . . .	12
2.5 Notable design features . . . . .	17
2.5.1 PKW Type . . . . .	17
2.5.2 Inlet key versus outlet key width ratio . . . . .	19

2.5.3	Nose . . . . .	19
2.5.4	Approach flow . . . . .	20
2.5.5	Crest shape . . . . .	21
2.5.6	Additional design aspects . . . . .	21
<b>3</b>	<b>Structural vibration</b>	<b>23</b>
3.1	Introduction . . . . .	23
3.2	Basic overview . . . . .	23
3.2.1	Free vibration . . . . .	24
3.2.2	Forced vibration . . . . .	25
3.2.3	Random vibration . . . . .	26
3.2.4	Vibration in a fluid . . . . .	28
3.3	Modal harmonics . . . . .	29
3.4	Controlling vibration . . . . .	30
<b>4</b>	<b>Flow induced vibration</b>	<b>33</b>
4.1	Introduction . . . . .	33
4.2	General concept . . . . .	33
4.2.1	Extraneously-induced excitation . . . . .	34
4.2.2	Instability-induced excitation . . . . .	36
4.2.3	Movement-induced excitation . . . . .	36
4.3	Flow induced vibration sources at PKWs . . . . .	37
4.3.1	Flow separation and vortex shedding . . . . .	37
4.3.2	Sub-atmospheric pressures . . . . .	45
4.3.3	Nappe oscillation . . . . .	46
4.4	Fluid structure interaction . . . . .	47
<b>5</b>	<b>Experimental investigation of PKW behaviour</b>	<b>49</b>
5.1	Research design . . . . .	49
5.2	Physical modelling . . . . .	50
5.2.1	Hydraulic laboratory . . . . .	50
5.2.2	PKW models . . . . .	52
5.2.3	Instrumentation . . . . .	54
5.2.4	Experiments . . . . .	57
5.2.5	Scale effects . . . . .	62
5.2.6	Limitations . . . . .	67
5.2.7	Data analysis . . . . .	68
5.3	Numerical modelling . . . . .	68
5.3.1	Modelling environment . . . . .	69
5.3.2	Computational Fluid Dynamic models . . . . .	76
5.3.3	Fluid structure interaction . . . . .	77
5.3.4	Computational hardware . . . . .	78
5.3.5	Experiments . . . . .	79

5.3.6	Data analysis . . . . .	80
5.3.7	Limitations . . . . .	80
<b>6</b>	<b>Analysis of the structural behaviour of a PKW</b>	<b>83</b>
6.1	Introduction . . . . .	83
6.2	Stress state . . . . .	83
6.3	Natural frequencies in the physical model . . . . .	84
6.4	Mode shape calibration . . . . .	89
6.5	PKW modal characteristics . . . . .	92
6.5.1	Wall height and thickness . . . . .	92
6.5.2	Construction material . . . . .	92
6.6	Discussion . . . . .	93
<b>7</b>	<b>Analysis of the hydraulic behaviour of a PKW</b>	<b>95</b>
7.1	Introduction . . . . .	95
7.2	Calibration . . . . .	95
7.3	Steady state behaviour . . . . .	97
7.3.1	Discharge coefficient . . . . .	97
7.3.2	Flow lines . . . . .	99
7.3.3	Velocities . . . . .	103
7.3.4	Separation bubble . . . . .	107
7.3.5	Nappe profiles . . . . .	110
7.3.6	Mean wall pressure . . . . .	114
7.4	Transient hydrodynamic behaviour . . . . .	116
7.4.1	Velocity and turbulence . . . . .	116
7.4.2	Vorticity . . . . .	121
7.4.3	Wall pressures . . . . .	123
7.4.4	Nappe undulations . . . . .	129
7.4.5	Nappe cavity apex . . . . .	131
7.4.6	Nappe oscillations . . . . .	136
7.5	Observations and results . . . . .	140
7.5.1	Discharge effect on velocity and turbulence . . . . .	140
7.5.2	Discharge effect on vortices . . . . .	141
7.5.3	Discharge effect on pressure . . . . .	145
7.5.4	Discharge effect on nappe trajectory . . . . .	146
7.5.5	Scale . . . . .	148
7.5.6	Inlet key width . . . . .	149
7.5.7	PKW nose . . . . .	152
7.5.8	PKW type . . . . .	155
7.5.9	Other observations . . . . .	155
7.6	Discussion . . . . .	157

<b>8</b>	<b>PKW behaviour: Vibration analysis</b>	<b>159</b>
8.1	Introduction . . . . .	159
8.2	Excitation . . . . .	160
8.3	Vibration response: Physical model . . . . .	163
8.4	Vibration response: Numerical model . . . . .	166
8.5	Fluid structure interaction . . . . .	168
8.6	Fatigue . . . . .	171
8.7	Discussion . . . . .	173
<b>9</b>	<b>Validation and verification</b>	<b>175</b>
9.1	Introduction . . . . .	175
9.2	Physical model . . . . .	175
9.3	Numerical model . . . . .	176
9.4	External validation . . . . .	178
<b>10</b>	<b>Design guidelines</b>	<b>179</b>
<b>11</b>	<b>Conclusions</b>	<b>181</b>
11.1	Overview . . . . .	181
11.2	Findings . . . . .	181
11.2.1	Structural analysis . . . . .	181
11.2.2	Hydraulic analysis . . . . .	183
11.2.3	Vibration . . . . .	188
11.3	Contributions to engineering science . . . . .	190
11.4	Further research . . . . .	191
11.5	Closing comments . . . . .	191
	<b>Bibliography</b>	<b>193</b>
<b>A</b>	<b>Piano Key Weir discharge methodologies</b>	<b>202</b>
A.1	Standard reference design . . . . .	202
A.2	Kabiri-Samani and Javaheri 2012 . . . . .	202
A.3	Leite Ribeiro et al. 2012 . . . . .	203
A.4	Machiels 2012 . . . . .	204
A.5	Comparison . . . . .	205
<b>B</b>	<b>Experimental details</b>	<b>207</b>
B.1	Laboratory flume photos . . . . .	207
B.2	Model A . . . . .	208
B.2.1	Testing procedures . . . . .	208
B.2.2	Model A schematics . . . . .	208
B.2.3	Model A photos . . . . .	214
B.2.4	Model A scaling . . . . .	217
B.3	Model B . . . . .	217

B.3.1	Testing procedures . . . . .	217
B.3.2	Model B scaling . . . . .	219
B.3.3	Model B schematics . . . . .	220
B.3.4	Model B photos . . . . .	223
B.4	Instrumentation . . . . .	225
B.4.1	Instrument accuracies . . . . .	225
B.4.2	Acoustic Doppler Velocimeter . . . . .	225
B.4.3	Pressure transmitters . . . . .	227
B.4.4	Accelerometers . . . . .	228
B.4.5	Strain gauge . . . . .	228
B.4.6	Instrumentation photos . . . . .	229
B.5	Statistics and data processing . . . . .	230
<b>C</b>	<b>Structural behaviour data</b>	<b>231</b>
C.1	Accelerometer results . . . . .	231
C.2	Numerical model mode shapes . . . . .	238
<b>D</b>	<b>Hydraulic behaviour data</b>	<b>239</b>
D.1	Numerical calibration results . . . . .	239
D.1.1	Model A, Discharge 400 l/s, H/P = 0.36 . . . . .	240
D.1.2	Model A, Discharge 200 l/s, H/P = 0.19 . . . . .	246
D.2	Vector and turbulence graphs . . . . .	252
D.3	Pressure spectrum graphs . . . . .	257
D.4	Physical model discharge data . . . . .	262

This page is intentionally left blank.

## List of Figures

2.1	PKW schematic diagram . . . . .	5
2.2	Typical PKW cross sections . . . . .	5
2.3	L'Etroit Dam PKW . . . . .	6
2.4	Malarce Dam PKW . . . . .	6
2.5	Fundamental parameters of a PKW - 3D view . . . . .	8
2.6	Fundamental parameters of a PKW - plan view . . . . .	9
2.7	Reference design of a Type A PKW . . . . .	10
2.8	Discharge coefficients, $C_{dW}$ , for various weir types . . . . .	12
2.9	Comparison of PKW and Labyrinth discharge coefficients . . . . .	12
2.10	Discharge coefficients, $C_{dL}$ , for PKWs with various width ratios . . . . .	13
2.11	Discharge enhancement ratio for PKWs of varying magnification ratios . . . . .	13
2.12	Flowlines at various locations around a PKW . . . . .	14
2.13	Horizontal flowlines at various elevations around a PKW . . . . .	14
2.14	Vertical flowlines approaching the outlet key . . . . .	15
2.15	Velocity contour plot on horizontal plane at middle depth . . . . .	15
2.16	Free surface profiles for low and high heads . . . . .	16
2.17	PKW types . . . . .	18
2.18	PKW nose at Gloriettes Dam . . . . .	19
2.19	PKW nose at Goulours Dam . . . . .	19
2.20	Nose shape . . . . .	20
2.21	Nose shape and its effect on discharge . . . . .	20
3.1	Simple undamped oscillator . . . . .	24
3.2	Forced vibration oscillator . . . . .	25
3.3	Forced vibration response . . . . .	26
3.4	Evaluation of a random response in the frequency domain . . . . .	27
3.5	Typical example of fatigue S-N diagram . . . . .	32
4.1	Time-mean separation bubble with flow lines and velocity contours . . . . .	38
4.2	Instantaneous snapshot of the flow field of a separation bubble . . . . .	38
4.3	Time-mean longitudinal velocity at a separation bubble . . . . .	39
4.4	RMS of longitudinal velocity at a separation bubble . . . . .	39
4.5	Pressure spectra at $x/x_R = 1$ . . . . .	41
4.6	Snapshot of a vortex sheet showing breakup of a separation bubble . . . . .	42
4.7	Pressure-reduced velocity modes . . . . .	43
4.8	Sloshing of water body behind vibrating weir . . . . .	48
5.1	Diagram of experimental flume: side and top view . . . . .	51

5.2	Overall view of flume . . . . .	51
5.3	Upstream view of flume . . . . .	51
5.4	Model A - rectangular nose . . . . .	53
5.5	Model A showing pressure ports . . . . .	53
5.6	Model A - circular nose . . . . .	54
5.7	Model A - triangular nose . . . . .	54
5.8	Model B with accelerometers . . . . .	55
5.9	Model B with flow guides . . . . .	55
5.10	Model A - Pressure point positions . . . . .	56
5.11	Model B - Accelerometer and strain gauge positions . . . . .	57
5.12	Fluent model mesh . . . . .	71
5.13	Mechanical model mesh . . . . .	74
6.1	Isometric view of PKW unit showing sidewall deflection . . . . .	85
6.2	Side view of PKW showing sidewall deflection . . . . .	85
6.3	Isometric view of PKW unit showing sidewall stresses . . . . .	85
6.4	Side view of PKW showing sidewall stresses . . . . .	85
6.5	Accelerometer FRF showing natural frequencies . . . . .	87
6.6	Strain gauge FRF showing natural frequencies . . . . .	87
6.7	Calibration of numerical model mode shapes with physical model results . . . . .	89
6.8	Mode shapes of PKW walls and overhangs . . . . .	90
6.9	Mode shapes of PKW sidewall only . . . . .	91
6.10	Variation in PKW behaviour with $P$ and $T_s$ . . . . .	93
6.11	First mode frequencies at a range of wall thicknesses and materials . . . . .	94
7.1	Head-discharge data . . . . .	98
7.2	$H/P$ and Discharge coefficient . . . . .	98
7.3	Head-discharge data for different nose types . . . . .	98
7.4	$H/P$ and Discharge coefficient for nose types . . . . .	98
7.5	Flowlines approaching a PKW - oblique view . . . . .	100
7.6	Flowlines approaching a PKW - side view . . . . .	100
7.7	Flowlines approaching a PKW - plan view . . . . .	101
7.8	Flowlines approaching a PKW - upstream view . . . . .	101
7.9	Local flowlines near the upstream edge of the inlet key . . . . .	103
7.10	Location of cross sections in inlet key . . . . .	104
7.11	Isometric view of average longitudinal velocity on three horizontal planes . . . . .	104
7.12	Average velocity contour plots on plane J2 . . . . .	105
7.13	Velocity magnitude along inlet key sidewall . . . . .	106
7.14	Cartesian velocity vector components along inlet key sidewall . . . . .	106
7.15	Rotated velocity vector components along inlet key sidewall . . . . .	106
7.16	Velocity at planes across and along the inlet key . . . . .	108
7.17	Separation bubble for two flow scenarios . . . . .	109
7.18	Non-dimensionalized bubble dimensions over a range of $H/P$ values . . . . .	110

7.19	Non-dimensionalized bubble dimensions over a range of $P$ values . . . . .	110
7.20	View of overflow nappe at low flow . . . . .	111
7.21	Nappe in outlet key showing relevant flow features . . . . .	111
7.22	Bulking of flow under downstream overhang . . . . .	112
7.23	Concave shape of the nappe downstream of the corners . . . . .	112
7.24	Isometric view of numerical model nappe in outlet key . . . . .	113
7.25	Side view of numerical nappe in outlet key . . . . .	113
7.26	Side view of the underside of the numerical model nappe . . . . .	113
7.27	Side cross section view of nappe . . . . .	113
7.28	Plan view of horizontal cross section through nappe in outlet key . . . . .	114
7.29	Transverse cross sections through nappe in outlet key . . . . .	114
7.30	Mean pressures on upstream face of sidewall . . . . .	115
7.31	Mean pressures on downstream face of sidewall . . . . .	117
7.32	Isometric view of instantaneous longitudinal velocity on three horizontal planes . . . . .	118
7.33	Instantaneous velocity contour plots on plane J2 . . . . .	118
7.34	Instantaneous velocity magnitude on plane L along the inlet key . . . . .	119
7.35	Longitudinal velocity time sequence and spectrum . . . . .	120
7.36	Velocity and turbulence parameters along inlet key - top level . . . . .	121
7.37	Velocity and turbulence parameters along inlet key - base level . . . . .	121
7.38	Vorticity on plane L along the inlet key . . . . .	122
7.39	Q-criterion at 3 horizontal levels . . . . .	122
7.40	Q-criterion at plane J along inlet key . . . . .	122
7.41	Q-criterion vortices . . . . .	124
7.42	Near inlet key wall horizontal flow field generating pressure fluctuations . . . . .	125
7.43	Instantaneous pressure fluctuations on upstream face of sidewall . . . . .	126
7.44	RMS of pressure fluctuations on upstream sidewall . . . . .	127
7.45	Pressure fluctuations in the time and frequency space . . . . .	128
7.46	Pressure PSD calibration results between physical and numerical data . . . . .	129
7.47	Sequence of crest undulations - Model B . . . . .	130
7.48	Sequence of crest undulations - Model A . . . . .	131
7.49	Side view of surface undulation on crest . . . . .	132
7.50	Attached and detached nappe cavity apexes . . . . .	133
7.51	Balance between water pressure and air velocity under the nappe . . . . .	134
7.52	Nappe cavity apexes at different discharges . . . . .	134
7.53	Oscillation time sequence of air cavity over pressure sensors . . . . .	135
7.54	Sequence of photos of vibrating nappe at a range of discharges . . . . .	137
7.55	Frequency PSD plots of vibrating nappe at various discharges . . . . .	138
7.56	Nappe vibration change with discharge and hysteresis . . . . .	139
7.57	Velocity vector magnitudes at horizontal X-lines at various discharges . . . . .	141
7.58	Turbulence properties at horizontal X-lines at various discharges . . . . .	142
7.59	Velocity vector magnitudes at horizontal Y-lines at various discharges . . . . .	142
7.60	Velocity vector magnitudes at vertical Z-lines at various discharges . . . . .	143

7.61	Variation in velocity magnitude on a horizontal plane over a range of discharges . . . . .	143
7.62	Variation in velocity magnitude on a longitudinal plane over a range of discharges . . . . .	144
7.63	Plan view of inlet key vortices over range of discharges . . . . .	144
7.64	Side view of inlet key vortices over range of discharges . . . . .	145
7.65	Physical model pressure spectra over a range of discharges . . . . .	147
7.66	Water level profiles under aerated and unaerated conditions . . . . .	148
7.67	Frequency PSD at various scales . . . . .	149
7.68	Side view of inlet key vortices over range of weir heights . . . . .	150
7.69	Frequency PSD at point A5 with a variety of key width ratios . . . . .	151
7.70	Separation bubble size metric for a range of inlet key width ratios . . . . .	151
7.71	Plan view of longitudinal velocity in inlet key as inlet key width reduces . . . . .	151
7.72	Plan view of vortices in inlet key as inlet key width reduces . . . . .	152
7.73	Horizontal view of longitudinal velocity at three nose types . . . . .	153
7.74	Side view of the vortices emanating from three nose types . . . . .	154
7.75	Frequency content of pressure fluctuations with two nose types . . . . .	154
7.76	Side view of vortices for different types of PKW . . . . .	155
8.1	Weighting procedure for fluctuating pressure . . . . .	162
8.2	Resultant weighted wall forces . . . . .	162
8.3	Weighted fluctuation pressures for each of the modes . . . . .	163
8.4	Photos of flows for physical model B . . . . .	164
8.5	Power Spectral Density of model B sidewall vibration . . . . .	165
8.6	Power Spectral Density of model B sidewall vibration ( $H/P = 0.1$ ) . . . . .	167
8.7	Power Spectral Density of model B sidewall vibration ( $H/P = 0.2$ ) . . . . .	167
8.8	Crest point deflection PSD showing numerical and physical results . . . . .	168
8.9	Time sequence of maximum stress . . . . .	169
8.10	Maximum stress spectral density . . . . .	169
8.11	Upstream wall pressure PSD ( $H/P = 0.1$ ) . . . . .	170
8.12	Correlation between pressure in inlet key and wall movement ( $H/P = 0.2$ ) . . . . .	171
8.13	Nappe adjustment due to wall movement of 1mm ( $H/P = 0.1$ ) . . . . .	172
8.14	Stress variation rainfall counting results . . . . .	172
11.1	Structural response to hydrostatic load . . . . .	182
11.2	Mode shapes of sidewall . . . . .	182
11.3	Strain gauge FRF showing natural frequencies for four scenarios . . . . .	183
11.4	Instantaneous velocity magnitude on plane L along the inlet key . . . . .	184
11.5	Side view of Q-criterion vortices with water level . . . . .	184
11.6	Pressure spectra at point A2 . . . . .	185
11.7	Physical model frequencies . . . . .	189
11.8	Numerical model frequencies . . . . .	189
A.1	Reference design of a Type A PKW . . . . .	203
A.2	Comparison of rating curves for PKW . . . . .	206

B.1	Empty flume looking upstream . . . . .	207
B.2	View of flume with model A . . . . .	207
B.3	Upstream stilling basin . . . . .	207
B.4	Flume looking downstream . . . . .	207
B.5	Model A construction 1 . . . . .	214
B.6	Model A construction 2 . . . . .	214
B.7	Model A construction 3 . . . . .	214
B.8	Model A construction 4 . . . . .	214
B.9	Model A with no upstream nose . . . . .	215
B.10	Model A with circular nose . . . . .	215
B.11	Model A with triangular nose . . . . .	215
B.12	Model A circular nose . . . . .	216
B.13	Model A triangular nose . . . . .	216
B.14	Model A with aeration pipes . . . . .	216
B.15	Model B with crest parapet . . . . .	223
B.16	Model B with guide walls . . . . .	223
B.17	Model B crest detail . . . . .	223
B.18	Model B at low flow with closed air vent . . . . .	223
B.19	ADV grid . . . . .	226
B.20	4-pronged down looking ADV sensor head . . . . .	229
B.21	ADV body mounted on trolley with extendible arm . . . . .	229
B.22	Pressure pipes exiting the flume wall . . . . .	229
B.23	Pressure gauge with T-piece attachment . . . . .	229
C.1	Model B - Accelerometer and strain gauge positions . . . . .	231
C.2	Model B - Accelerometer point 1 Frequency Response Functions . . . . .	232
C.3	Model B - Accelerometer point 2 Frequency Response Functions . . . . .	232
C.4	Model B - Accelerometer point 3 Frequency Response Functions . . . . .	233
C.5	Model B - Accelerometer point 4 Frequency Response Functions . . . . .	233
C.6	Model B - Accelerometer point 5 Frequency Response Functions . . . . .	234
C.7	Model B - Accelerometer point 6 Frequency Response Functions . . . . .	234
C.8	Model B - Accelerometer point 7 Frequency Response Functions . . . . .	235
C.9	Model B - Accelerometer FRF with natural frequencies - Dry scenario . . . . .	236
C.10	Model B - Accelerometer FRF with natural frequencies - Full scenario . . . . .	237
C.11	Model B - numerical mode shapes . . . . .	238
D.1	Horizontal physical and numerical velocity magnitude at elevation of $0.54P$ , $4001/s$ . . . . .	240
D.2	Horizontal physical and numerical velocity vectors at elevation of $0.54P$ , $4001/s$ . . . . .	240
D.3	Horizontal physical and numerical velocity magnitude at elevation of $0.79P$ , $4001/s$ . . . . .	240
D.4	Horizontal physical and numerical velocity vectors at elevation of $0.79P$ , $4001/s$ . . . . .	241
D.5	Velocity vector magnitudes along the inlet key at elevation of $0.54P$ , $4001/s$ . . . . .	241
D.6	Velocity vector magnitudes along the inlet key at elevation of $0.79P$ , $4001/s$ . . . . .	241
D.7	Velocity vector magnitudes across the inlet key at elevation of $0.54P$ , $4001/s$ . . . . .	241

D.8	Velocity vector magnitudes across the inlet key at elevation of 0.79P, 4001/s . . . .	241
D.9	Horizontal physical and numerical kinetic energy at elevation of 0.54P, 4001/s . .	242
D.10	Horizontal physical and numerical kinetic energy at elevation of 0.79P, 4001/s . .	242
D.11	Velocity RMS values along the inlet key at elevation of 0.54P, 4001/s . . . . .	242
D.12	Turbulence properties along the inlet key at elevation of 0.54P, 4001/s . . . . .	242
D.13	Longitudinal physical and numerical velocity magnitude), 4001/s . . . . .	243
D.14	Longitudinal physical and numerical velocity vectors), 4001/s . . . . .	243
D.15	Longitudinal physical and numerical kinetic energy), 4001/s . . . . .	244
D.16	Transverse physical and numerical velocity vectors, 4001/s . . . . .	244
D.17	Transverse physical and numerical velocity magnitude, 4001/s . . . . .	245
D.18	Transverse physical and numerical kinetic energy, 4001/s . . . . .	245
D.19	Horizontal physical and numerical velocity magnitude at elevation of 0.54P, 2001/s	246
D.20	Horizontal physical and numerical velocity vectors at elevation of 0.54P, 2001/s .	246
D.21	Horizontal physical and numerical velocity magnitude at elevation of 0.79P, 2001/s	246
D.22	Horizontal physical and numerical velocity vectors at elevation of 0.79P, 2001/s .	247
D.23	Velocity vector magnitudes along the inlet key at elevation of 0.54P, 2001/s . . . .	247
D.24	Velocity vector magnitudes along the inlet key at elevation of 0.79P, 2001/s . . . .	247
D.25	Velocity vector magnitudes across the inlet key at elevation of 0.54P, 2001/s . . . .	247
D.26	Velocity vector magnitudes across the inlet key at elevation of 0.79P, 2001/s . . . .	247
D.27	Horizontal physical and numerical kinetic energy at elevation of 0.54P, 2001/s . .	248
D.28	Horizontal physical and numerical kinetic energy at elevation of 0.79P, 2001/s . .	248
D.29	Velocity RMS values along the inlet key at elevation of 0.54P, 2001/s . . . . .	248
D.30	Turbulence properties along the inlet key at elevation of 0.54P, 2001/s . . . . .	248
D.31	Longitudinal physical and numerical velocity magnitude), 2001/s . . . . .	249
D.32	Longitudinal physical and numerical velocity vectors), 2001/s . . . . .	249
D.33	Longitudinal physical and numerical kinetic energy), 2001/s . . . . .	250
D.34	Transverse physical and numerical velocity vectors, 2001/s . . . . .	250
D.35	Transverse physical and numerical velocity magnitude, 2001/s . . . . .	251
D.36	Transverse physical and numerical kinetic energy, 2001/s . . . . .	251
D.37	X-axis vectors, base level . . . . .	252
D.38	X-axis U-vector, base level . . . . .	252
D.39	X-axis V-vector, base level . . . . .	253
D.40	X-axis W-vector, base level . . . . .	253
D.41	X-axis RMS, base level . . . . .	253
D.42	X-axis turbulence, base level . . . . .	253
D.43	X-axis vectors, top level . . . . .	253
D.44	X-axis U-vector, top level . . . . .	253
D.45	X-axis V-vector, top level . . . . .	254
D.46	X-axis W-vector, top level . . . . .	254
D.47	X-axis RMS, top level . . . . .	254
D.48	X-axis turbulence, top level . . . . .	254
D.49	Y-axis vectors, A2 . . . . .	254

D.50	Y-axis U-vector, A2 . . . . .	254
D.51	Y-axis V-vector, A2 . . . . .	255
D.52	Y-axis W-vector, A2 . . . . .	255
D.53	Y-axis vectors, A5 . . . . .	255
D.54	Y-axis U-vector, A5 . . . . .	255
D.55	Y-axis V-vector, A5 . . . . .	255
D.56	Y-axis W-vector, A5 . . . . .	255
D.57	Z-axis vectors, A2-A7 . . . . .	256
D.58	Z-axis U-vector, A2-A7 . . . . .	256
D.59	Z-axis V-vector, A2-A7 . . . . .	256
D.60	Z-axis W-vector, A2-A7 . . . . .	256
D.61	Pressure spectrum calibration - 1001/s . . . . .	257
D.62	Pressure spectrum calibration - 2001/s . . . . .	257
D.63	Pressure spectrum calibration - 3001/s . . . . .	258
D.64	Pressure spectrum calibration - 4001/s . . . . .	258
D.65	Pressure spectrum calibration - 5001/s . . . . .	259
D.66	Pressure spectrum calibration - 6001/s . . . . .	259
D.67	Physical model pressure spectra over a range of discharges with circular nose . . .	260
D.68	Physical model pressure spectra over a range of discharges with triangular nose .	261

This page is intentionally left blank.

## List of Tables

2.1	Fundamental parameter nomenclature . . . . .	9
5.1	Physical model parameters . . . . .	52
5.2	Dimensionless force ratios . . . . .	63
5.3	Model A scaling ratios and dimensions . . . . .	64
5.4	Model B scaling ratios and dimensions . . . . .	65
5.5	Fluent modelling parameters . . . . .	72
5.6	Fluent boundary conditions . . . . .	73
5.7	Mechanical material properties used in FEM model . . . . .	74
6.1	Natural frequencies measured from physical model . . . . .	86
6.2	Natural frequencies measured from numerical model . . . . .	88
6.3	Idealised sidewall frequency calibration . . . . .	91
7.1	Numerical model discharge . . . . .	99
7.2	Frequency and signal strength of nappe vibration . . . . .	138
7.3	Overflow ratios and discharge at model A scale . . . . .	141
7.4	Peak vortex frequencies at each pressure point for a range of discharges . . . . .	146
7.5	Numerical model discharge with changing PKW scales . . . . .	148
7.6	Numerical model frequency with changing PKW scales . . . . .	149
7.7	Numerical model discharge with changing inlet key widths . . . . .	150
8.1	Recorded strain gauge vibration frequency peaks at various discharges . . . . .	166
A.1	Application limits for the Type-A PKW capacity equations . . . . .	202
B.1	Model A scaling ratios and dimensions . . . . .	218
B.2	Model A scenarios and their force ratios . . . . .	219
B.3	Model B scaling ratios and dimensions . . . . .	224
B.4	Physical model instrument accuracies . . . . .	225

This page is intentionally left blank.

## Nomenclature

### Constants

$$g = 9.81 \text{ m/s}^2$$

$$\rho_{air} = 1.225 \text{ kg/m}^3$$

$$\rho_{water} = 998.2 \text{ kg/m}^3$$

$$\nu = 1 \times 10^{-6} \text{ m}^2/\text{s}$$

$$\text{Surface Tension, } \sigma = 0.072 \text{ N/m}$$

### Variables

$\zeta$	Damping ratio	[–]
$\lambda$	Natural frequency, eigenvalue	[–]
$\lambda$	Scaling factor	[–]
$\zeta_i$	Mode shape amplitude	[–]
$\rho$	Density	[kg/m <sup>3</sup> ]
$\sigma$	Surface tension	[N/m]
$\phi$	Mode shape vector, eigenvector	[–]
$\phi\sigma_{ult}$	Ultimate limit state	[–]
$\varphi$	Phase	[radians]
$\chi_m$	Mechanical admittance	[–]
$\omega$	Circular frequency	[radians/s]
$\omega_d$	Damping circular frequency	[radians/s]
$\omega_n$	Natural circular frequency	[radians/s]
$\omega_s$	Forcing circular frequency	[radians/s]
$A'$	Added mass coefficient	[–]
$B$	Damping coefficient	[–]
$B'$	Added damping coefficient	[–]
$B_b$	Weir base length	[m]
$B_i$	Overhang length of inlet key	[m]
$B_o$	Overhang length of outlet key	[m]
$C$	Stiffness factor	[–]
$C'$	Added stiffness factor	[–]
$C_d$	Discharge coefficient	[–]
$C_{dL}$	Discharge coefficient related to weir length	[–]
$C_{dW}$	Discharge coefficient related to weir width	[–]
$Ch$	Cauchy number	[–]
$E$	Young's modulus	[GPa]
$Eu$	Euler number	[–]
$f$	Frequency	[Hz]
$f_n$	Natural frequency	[Hz]

$F$	Force	[N]
$F'$	Force fluctuation	[N]
$F_o$	Force amplitude	[N]
$H$	Blockage width	[m]
$H$	Overflow depth	[m]
$H_d$	Design upstream water head	[m]
$H_t$	Total upstream water head	[m]
$H/P$	Overflow depth ratio	[–]
$I$	Moment of inertia	[10 <sup>6</sup> m <sup>4</sup> ]
$k$	Turbulent kinetic energy	[m <sup>2</sup> /s <sup>2</sup> ]
$l$	Reattachment length	[m]
$L$	Weir length (along crest)	[m]
$L$	Characteristic length	[m]
$L_x$	Vortex eddy size	[m]
$L/\delta$	Serviceability limit state	[–]
$m$	Mass	[kg]
$M$	Mass matrix	[kg]
$Ma$	Mach number	[–]
$n$	Developed length ratio	[–]
$N$	Degrees of freedom	[–]
$N_u$	Number of PKW units	[–]
$p$	Pressure	[Pa]
$P$	Weir height	[m]
$q$	Specific Discharge	[m <sup>3</sup> /(ms)]
$Q$	Discharge	[m <sup>3</sup> /s]
$Q_P$	Piano key weir discharge	[m <sup>3</sup> /s]
$Q_s$	Linear (sharp crested) weir discharge	[m <sup>3</sup> /s]
$r$	Discharge enhancement ratio	[–]
$Re$	Reynolds number	[–]
$S_F$	Force spectra	[–]
$S_x$	Displacement spectra	[–]
$St$	Strouhal number	[–]
$t$	Time	[s]
$T_u$	Turbulent intensity in longitudinal velocity vector (u)	[%]
$T_s$	Wall thickness	[m]
$TI$	Turbulence intensity	[%]
$TKE$	Turbulent kinetic energy	[m <sup>2</sup> /s <sup>2</sup> ]
$u$	Longitudinal velocity	[m/s]
$u'$	Longitudinal velocity fluctuation	[m/s]
$\bar{u}$	Mean longitudinal velocity	[m/s]
$u_0$	Longitudinal free stream velocity	[m/s]
$u_c$	Longitudinal convection velocity, phase velocity	[m/s]

$v$	Transverse velocity	[ m/s ]
$v'$	Transverse velocity fluctuation	[ m/s ]
$V$	Characteristic velocity	[ m/s ]
$w$	Vertical velocity	[ m/s ]
$w'$	Vertical velocity fluctuation	[ m/s ]
$W$	Linear weir width	[ m ]
$W_i$	Width of inlet key	[ m ]
$W_o$	Width of outlet key	[ m ]
$We$	Weber number	[ – ]
$x$	Displacement	[ m ]
$\{x\}$	Displacement vector	[ m ]
$x'$	Displacement fluctuation	[ m ]
$x_o$	Vibration amplitude	[ m ]
$\dot{x}$	Velocity	[ m/s ]
$\ddot{x}$	Acceleration	[ m/s <sup>2</sup> ]
$x_R$	Reattachment length	[ m ]
$X$	Longitudinal coordinate	[ m ]
$y_c$	Mean shear layer centre	[ m ]
$y_\delta$	Mean shear layer edge	[ m ]
$Y$	Transverse coordinate	[ m ]
$Z$	Vertical coordinate	[ m ]

### Subscripts

$c$	Convection
$F$	Force
$i$	Inlet
$o$	Outlet
$P$	Piano Key Weir
$t$	Total
$u$	Unit
$x$	Displacement response

### Abbreviations

2D	Two Dimensional
3D	Three Dimensional
ADV	Acoustic Doppler Velocimeter
CHPC	Centre for High Performance Computing
CFD	Computational Fluid Dynamics
CSIR	Council for Scientific and Industrial Research
DES	Detached Eddy Simulation
DNS	Direct Numerical Simulation
DWS	Department of Water and Sanitation

EIE	Extraneously Induced Excitation
FEM	Finite Element Modelling
FFT	Fast Fourier Transform
FIV	Fluid Induced Vibration
FRF	Frequency Response Function
FSI	Fluid Structure Interaction
HDPE	High-density polyethylene
HECE	Hydraulics in Environmental and Civil Engineering
IIE	Instability Induced Excitation
KH	Kelvin-Helmholtz
LCH	Laboratoire de Constructions Hydrauliques
LES	Large Eddy Simulation
MIE	Movement Induced Excitation
PKW	Piano Key Weir
POD	Proper Orthogonal Decomposition
PSD	Power Spectral Density
PVC	Polyvinyl Chloride
RANS	Reynolds Averaged Navier-Stokes
RMS	Root Mean Square
SANCOLD	South African National Commission on Large Dams
SRS	Scale Resolving Simulation
TS	Tollmien-Schlichting
VIV	Vortex Induced Vibration
VOF	Volume of Fluid

# 1 Background to the research

## 1.1 Introduction

This research study is submitted in reference to Frank Denys' registration as a PhD student at the Department of Civil Engineering of the University of Stellenbosch and in accordance with the requirements of the doctoral programme of the University.

## 1.2 Background

Piano Key Weirs (often shortened to PKW or PK weir) are a relatively recent development in the field of spillway hydraulics. A significant volume of research investigating the hydraulic behaviour of piano key weirs has been undertaken in the recent past. They have also been successfully implemented at a number of dams worldwide. Three workshops (in 2011, 2013 and 2017) were convened to discuss and collate current knowledge regarding these structures as well as to propose further research into the field. One research gap that was identified is: *"aeration and specifically research exploring what pressure and structural stability changes take place at the outlets"* [1; 2]. Put differently, this statement refers to the possible occurrence of negative pressures underneath the overflow nappe, how these could affect the weir itself and how potential problems could be alleviated by, for example, aerating this nappe.

Another occurrence that could affect structural stability, is the presence of oscillating pressure variations on the upstream side of the narrow crested weir. This transient pressure behaviour stems from the periodic shedding of vortices generated by the separated shear layer as flow enters the inlet key of the weir.

This research thus aims to address some of the deficiencies in the knowledge on the behaviour and design of these weirs, particularly aspects relating to how the flow over the weir affects the structural vibrations and longevity of the hydraulic structure.

## 1.3 Research focus

The hydraulic behaviour of piano key weirs, and the large number of variables which affect it, is reasonably well understood despite its complex nature [3]. The interaction between the flow and the thin-walled structure have, however, not received much research focus. The intent of the research project is thus to experimentally explore and numerically model piano key weirs, specifically how the structure interacts with, and reacts to, the forces imposed on it by the overflowing water. The corollary of how the response of the structure affects the flow is also relevant.

One of the main concerns is how the flow induced vibrations affect the structure from the perspective of increased stresses, material fatigue, undesirable motion and noise [4]. The possi-

bility of resonance behaviour in the thin concrete walls of the weir together with the possibility of material fatigue, has been raised previously [5] and although it is generally disregarded, it should be investigated in greater detail. The reason for this disregard is that most PKWs are ordinarily built from reinforced concrete which are sufficiently stiff to resist this behaviour. Some projects have also considered steel as an alternative construction material, which is far more susceptible to vibrations and thus warrants the need for this investigation.

The focus of the research is on the identification of possible sources of excitations at the weir which may induce it to vibrate and exploring their sensitivity to various forms of control. Particular aspects that were investigated included the development of vortex induced pressure fluctuations on the sidewall, negative pressures underneath the overflow nappe as well as the occurrence of nappe vibrations. It is noted that several of these phenomena are the most pronounced where the weakest structural components of the weir are most sensitive to them.

The prime goal of the broad field of PKW research would be to determine the most optimal geometry of the weir considering various factors such as total discharge, cost, operational risk, energy dissipation, nappe aeration, structural stability and foundation conditions among others. It is likely that no single optimal solution exists for every scenario and that each solution would depend on a unique set of input parameters. The proposed research will assist in identifying and defining these parameters further.

## 1.4 Research objectives and scope

The general aim of this investigation is to conduct a scientific assessment of the fluid induced vibrations which occur at PKWs. The main goal is to develop an improvement in the understanding of their behaviour by defining and quantifying the vibration phenomenon. This entails a study of the hydrodynamic sources of the excitation forces, a study of the vibration characteristics of the PKW and a study of how the excitation forces activate the vibrations of the PKW and to what degree.

There are three main objectives for this study. They all concern or relate to the characterisation of vibrations at Piano Key Weirs.

- Characterise the source of fluid induced excitation which occur at a PKW
- Characterise the natural frequencies and modal parameters of a thin-walled PKW
- Quantify the structural response of a thin-walled PKW to fluid induced vibrations

Additional secondary objectives include:

- Proposing guidelines for the design of thin-walled PKWs in light of their vibration potential
- Highlight possible future research tasks
- Disseminate the learned knowledge to the professional and academic community

The scope of the study is limited to describing the vibration behaviour and highlighting the potential for its occurrence. The study does not aim to be an exhaustive assessment of the phenomena nor result in a prescriptive characterisation of all potential PKW vibrations.

Furthermore, the study is limited to type A PKWs, although other types are briefly examined.

## 1.5 Research methodology

The study will explore the various vibration inducing phenomena by observing them in a sequence of scaled physical models in an hydraulics laboratory. Suitable data will be collected to allow for the calibration of a numerical model. This model will then be used to emulate the observed behaviour across a range of scenarios and test its sensitivity to a number of potential control parameters.

## 1.6 Dissertation outline

The dissertation begins by describing the concept of Piano Key Weirs in Chapter 2. It explains their intended purpose and emphasizes some of their more interesting features. It then goes on to cover some of the relevant literature regarding structural vibration, in Chapter 3, and specifically fluid induced vibrations in Chapter 4. The research design and methodology are dealt with in Chapter 5, which also discusses the scope of the physical and numerical models. Chapter 6 presents the results of the structural and modal analysis of the PKW, whereas Chapter 7 does the same for the hydrodynamic analysis. These two chapters form the core of the thesis and describe the various observed phenomena in detail. The results from the previous two chapters are combined into a single coupled model which can emulate the vibration behaviour, as outlined in Chapter 8. The verification and validation of the various models is discussed in Chapter 9 and a set of design guidelines and proposals for future research are highlighted in Chapter 10 and section 11.4. The research is summarised in Chapter 11.

This page is intentionally left blank.

## 2 Piano key weir hydraulics

### 2.1 Introduction to piano key weirs

Piano key weirs are a relatively recent development in the field of spillway hydraulics. They were first developed in the late 1990's and early 2000's as part of an investigation by Hydrocoop (France) and the University of Biskra (Algeria), among several others, into improvements for the well-known labyrinth weir [6]. A typical labyrinth weir has a folded, zig-zag, layout in plan so that its total overflow length is longer than that of a linear weir spanning the same width. In so doing, a labyrinth weir is capable of discharging higher volumes of flow when compared to linear weirs [7].

Piano key weirs can be considered a sub-type of the broad scope of labyrinth weirs, as they also attempt to increase the total overflow length to increase the discharge capacity. Instead of the folded zig-zag, a PKW has an alternating rectangular plan layout. Furthermore, these rectangular keys have sloping bases which guide flow over and away from the crest of the weir, thus increasing the discharge capacity for a given overflow head. Incidentally, the repeating staggered overhangs resemble piano keys, hence their name. Schematic diagrams of a typical Type-A piano key weir, with its symmetrical overhangs, are shown in Figures 2.1 and 2.2.

Motivations for their use are varied but mainly revolve around their large specific discharge. As a result, they are ideal for dam safety improvement programmes (in terms of inadequate spillway capacity) as well as the rehabilitation of, or upgrades to, existing water resource schemes (i.e. the raising of dams to increase their storage capacity). There are several technologies that have been developed which are capable of raising or altering an existing spillway without increasing the risk of overtopping. However, many of these involve mechanical gates, which are susceptible to failure if not maintained or operated correctly, and are thus not favoured by many dam experts. Gate management is also of concern throughout Africa, so much so that avoidance of their use is being recommended by many dam specialists [10]. Piano key weirs, on the other hand, are permanent structures that are able to safely, efficiently

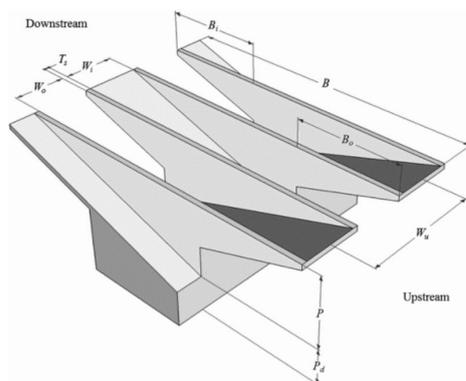


Figure 2.1: PKW schematic diagram [8]

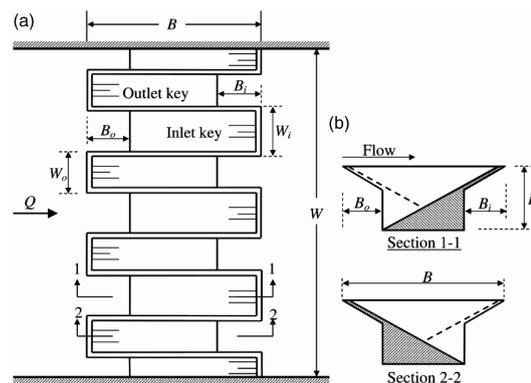


Figure 2.2: Typical PKW cross sections [9]



Figure 2.3: L'Étroit Dam PKW, France [13]



Figure 2.4: Malarce Dam PKW, France [1]

and economically achieve an increase in the full supply level of a reservoir or the discharge capacity of a spillway without the need to raise the dam wall as a whole.

Several PK weir projects have been implemented worldwide despite historic shortcomings in a comprehensive understanding of their behaviour. Countries where they have been successfully implemented include France, India, Australia, Sri Lanka, Vietnam, Switzerland and Algeria. Representative prototypes are shown in Figures 2.3 and 2.4. In most instances where they have been previously deployed, the designers made use of scaled physical models and generalised performance curves to predict their behaviour [11]. In South Africa, the raising of the Hazelmere Dam using a PKW, currently under construction and nearing completion, was iteratively tested using scaled physical models in the Department of Water Affairs and Sanitation (DWS) hydraulics laboratory. It is likely that the design of the raising of the Tzaneen Dam using PKWs will undergo a similar process [12]. Other, smaller, dam sites have also been investigated as possible candidates where PKWs could play a beneficial role.

## 2.2 Unique design aspects

PK weirs have several unique design aspects which enable them to provide effective solutions for both dam and riverine applications.

### 2.2.1 Reduced structural footprint and stability

One of the main advantages of a PK weir is its relatively narrow footprint when compared to normal labyrinth weirs. This is not only beneficial from a cost perspective (with its much-reduced volumes of concrete) but also allows these structures to be placed on the narrow crests of gravity dams where labyrinth weirs are not viable due to their large base widths. A cost comparative exercise conducted by Paxson *et al.* [14], which compared PK weirs, labyrinth weirs and gated spillways, concluded that PKWs are an ideal and unique solution for increasing the spillway capacities of existing dams.

The PKW also has internal slopes in each of the keys which reduces the height of the lateral

sidewalls which then leads to a reduction in the hydrostatic forces acting on these walls. This can lead to savings in the structural costs. However, a typical PKW is generally designed with more reinforcement steel, when compared to classic structural loads, in order to withstand the appreciable thermal loads which can develop in the structure [15].

### 2.2.2 Submergence

Due to the unique flow patterns at a PKW (see Section 2.4.2), it is able to operate under submerged conditions at a higher efficiency (i.e. a lower upstream head for a given discharge) than other weir types. This is despite the fact that, at such large heads, the discharge efficiency of the PKW is not much different to that of a normal linear weir [16; 17]. This characteristic makes PK weirs effective in riparian conditions where developments upstream of the weir may place limits on the water elevations in the river.

It is surmised that the high downstream water level only directly affects the most downstream portion of the crest of the weir. The upper portions (i.e. the lateral and upstream crests) may possibly be less affected since there is sufficient flow momentum in the outlet key to "push" the high downstream water level further downstream, thus allowing these portions of the crest to operate under more ideal conditions. This supposition has, however, not been proven.

### 2.2.3 Debris and driftwood

The sensitivity of a PK weir to debris and driftwood has been investigated and found to be relatively small. Although the presence of debris on the PK weir does marginally reduce the discharge efficiency of the weir [18], laboratory studies found that at larger flows, most debris would be washed downstream. Should such debris not wash away, the PKW still retains approximately 75 to 80% of its discharge capacity. This is probably because of the unique flow dynamics of the structure which draws flow from below the surface of the upstream water level, thus bypassing any debris that may be stuck at the upstream crest of the outlet key [19; 15]. As noted in Section 2.4.2, the vast majority of the flow enters the inlet key (also see Figures 2.12 and 2.13)

PK weirs are thus generally safe to use in afforested catchments although the potential of blockages occurring should still be incorporated into their design.

### 2.2.4 Modular construction

Due to its thin and repetitive nature, it is possible to construct a typical PKW off site in pre-cast modular units which are then assembled on site as was done at the Black Esk Reservoir, UK [20]. This not only allows for the easier construction of the thin-section concrete members but also allows for better quality control resulting in a more accurate and level crest profile. Pre-production also leads to cost savings and possibly shorter construction periods. This is especially relevant in locations with very short available time windows for construction (e.g. due to the regular occurrence of floods), where most of the components of the PKW can be constructed off site and stockpiled prior to their installation.

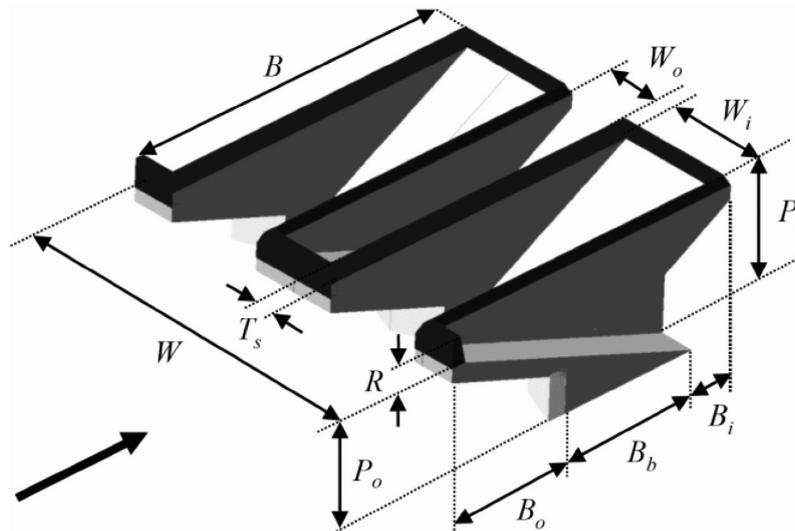


Figure 2.5: Fundamental parameters of a PKW - 3D view [21]

This manufacture methodology also allows for the use of construction materials other than concrete. The effect these differing construction materials have on the behaviour of the PKW is unknown, although it is not expected that the discharge capacity would be altered in any meaningful way. However, the dynamic behaviour of the structure itself could drastically change in comparison to a concrete PKW. Structural vibration is one such behavioural aspect which is being addressed in the current research.

### 2.3 Geometric design

Prior to describing the features of a PK weir, it is beneficial to be familiar with the terminology and parameters used in defining its design and behaviour. Unlike a standard sharp crested weir, there are a large number of geometrical parameters which have an influence on the discharge behaviour of a PK weir. In order to assist in research efforts and prevent confusion, a standardised terminology to describe these was proposed in Pralong *et al.* [21]. The terminology is comprehensive, thus, for brevity, only a summary of the relevant details has been provided here. The key parameters relating to physical dimensions are depicted in Figures 2.5 and 2.6. These figures indicate most of the influential geometrical parameters that dictate PK weir behaviour. The subscript “*i*” refers to an aspect of the inlet key and “*o*” the outlet key. Some of the key parameters and related ratios are further described in Table 2.1.

A great deal of research has been conducted into how these various parameters affect the discharge capability of the Piano Key Weir (see Section 2.4). It has been shown that by knowing four dominant geometrical parameters, namely the crest length  $L$ , the overflow head  $H_t$ , the upstream weir height  $P_i$ , and the total weir (channel) width  $W$ , (encapsulated into the dimensionless ratios,  $L/W$  and  $H_t/P_i$ ) the discharge can be empirically determined with a maximum error of only  $\sim 17\%$  [22]. The additional parameters also play a role but their individual effect on discharge is generally limited to less than  $5\%$  [23]. Additional parameters which have been determined to boost the discharge efficiency are expanded upon in Section 2.5.

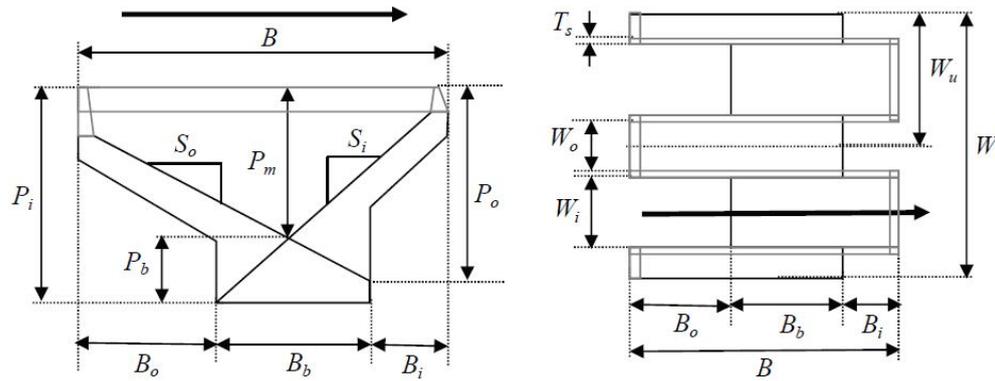


Figure 2.6: Fundamental parameters of a PKW - plan view (right) and cross section (left) (dark arrows show flow direction) [21]

Table 2.1: Fundamental parameter nomenclature [21]

Parameter	Definition
$B$	Upstream-downstream length of PKW, $B = B_b + B_i + B_o$
$B_b$	Base length of PKW footing
$B_i, B_o$	Downstream (inlet key) / Upstream (outlet key) overhang length
$C_{dW}$	Discharge coefficient related to total width, where $Q = C_{dW} W \sqrt{2gH^3}$
$H_t$	Total head over crest upstream of weir, $H_t = h + V^2/2g$
$L$	Total developed length along overflowing crest axis
$L_u$	Developed length of one PKW unit, $L_u = W_i + W_o + 2T_s + 2B_h$
$n$	Developed length ratio, aka magnification ratio, $n = L/W$
$N_u$	Number of PKW units
$P_i, P_o$	Height of the inlet entrance / outlet exit measured from PKW crest
$Q$	Discharge ( $\text{m}^3/\text{s}$ )
$q$	Specific discharge ( $\text{m}^3/\text{s}/\text{m}$ )
$R_o$	Outlet key parapet wall height
$S_i, S_o$	Slope of the inlet/outlet key apron
$T_s$	Sidewall thickness
$W$	Total width of the PKW
$W_i, W_o$	Width of the inlet/outlet key (wall to wall)
$W_u$	Width of a PKW unit (one inlet + two half outlets), $W_u = W_i + W_o + 2T_s$

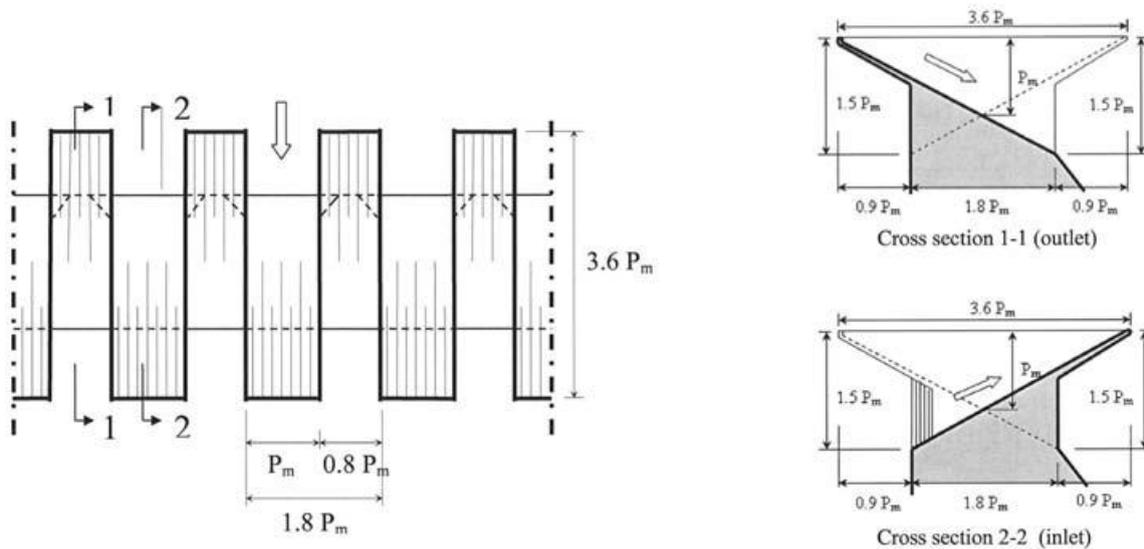


Figure 2.7: Reference design of a Type A PKW (arrows show flow direction) [26]

Published research have indicated that the geometric design which has the highest discharge capacity is not necessarily the most economic to construct. A balance must thus be struck between the discharge capability and the implementation cost of the structure. A clear balance between the two has not been defined, as this optimum design is often dictated by site specific conditions [24]. Despite this, a “near optimal” reference design was proposed in ICOLD Bulletin 144 [25], to serve as a preliminary base for future testing and site specific optimisation. This default design is shown in Figure 2.7. Due to the lack of site-specific data in the present research project, this standardised design (for Type A PKWs, see Section 2.5) forms the initial basis of the investigation into flow induced vibrations at PKWs.

## 2.4 Piano key weir hydraulics

The discharge capabilities of a PKW are a result of the unique flow patterns that it induces in its vicinity. This capability and the manner in which it is achieved are described below:

### 2.4.1 Discharge efficiency

The typical PKW design aims to provide a much longer overflow length than normal linear weirs, much the same as a labyrinth weir. In so doing, an increased specific discharge can be achieved for a given upstream head when compared to such linear weirs. At their peak efficiency these structures can allow specific discharges of up to  $100 \text{ m}^3/(\text{s m})$ , although in practice they are usually in the order of 20 to  $40 \text{ m}^3/(\text{s m})$  [6]. This is typically between two to four times higher than that for a linear weir at a similar hydraulic head. It is notable, however, that this high specific discharge can only be attained at relatively low overflow heads, as is demonstrated in Figures 2.8 to 2.11.

A number of quantitative methodologies have been developed to describe the discharge behaviour of a PK weir. They are all broadly based on the approach that the discharge over a

PKW, like all free surface overflows, is proportional to the upstream head,  $H_t$ , in the form of:

$$Q \propto \sqrt{2gH_t^3} \quad (2.4.1)$$

The proportionality factor dictating this relationship can be based on either the developed crest length,  $L$ , or the linear width of the weir,  $W$ , together with their respective discharge coefficients,  $C_{dL}$  and  $C_{dW}$  [27; 28]. The equation can thus be written as :

$$Q_P = C_{dW}W\sqrt{2gH_t^3} \quad (2.4.2)$$

or

$$Q_P = C_{dL}L\sqrt{2gH_t^3} \quad (2.4.3)$$

depending on which technique is followed.

Using the above basic framework, different parametric studies have used different methodologies to arithmetically define PKW discharge behaviour. The study by Machiels [24] focussed on the changes in the developed length of the overflow in combination with the discharge coefficient as in Equation (2.4.3). Kabiri-Samani and Javaheri [9] and Ribeiro, Pfister, Schleiss and Boillat [29] assumed a fixed physical parameter,  $W$ , and incorporated the variable behaviour (including the much longer overflow length,  $L$ ) in the  $C_{dW}$  coefficient. Often, studies preferred to refer to a mathematical construct called the discharge increase or enhancement ratio [27; 30]. This ratio is defined as the PKW overflow relative to the overflow over an ogee or a sharp crested weir at the same overflow head, as shown in Equation (2.4.4). When using this ratio, care must be taken when interpreting the results which reference weir was used.

$$r = \frac{Q_P}{Q_S} = \frac{C_{dW}W\sqrt{2gH_t^3}}{C_dW\sqrt{2gH_t^3}} = \frac{C_{dW}}{C_d} \quad (2.4.4)$$

In the case of a sharp crested weir,  $C_d$  is typically assumed as a constant value of 0.42, which is referenced to Hager and Schleiss [31] [29; 3]. For ogee shaped overflows, the  $C_d$  value is allowed to change in accordance with the water level's deviation from the design head [27].

Whichever technique was selected in the study, the premise of each study was to estimate the relevant coefficient or ratio from the physically measured, or numerically modelled, discharge [3]. The discussion of the arithmetic formulas which have been developed to date is beyond the scope of this text. However, as their input parameters do shed light on the behaviour of PKWs, a summary of these equations has been included in Appendix A.

An indication of typical discharge coefficients and discharge increase ratios of different PKWs, labyrinth weirs and a linear ogee overflow are shown in Figures 2.8 to 2.11. Figure 2.8 shows that, in terms of  $C_{dW}$  (Equation (2.4.2)) there is a marked increase in efficiency when comparing non-linear weirs to their linear counterparts. However, this behaviour only holds true for low upstream water heads. As the water level increases, proportionate to the weir's height, the relative benefit reduces asymptotically. This is why PKWs should be designed to operate only at lower heads. Although PKWs have been tested at a range of upstream heads

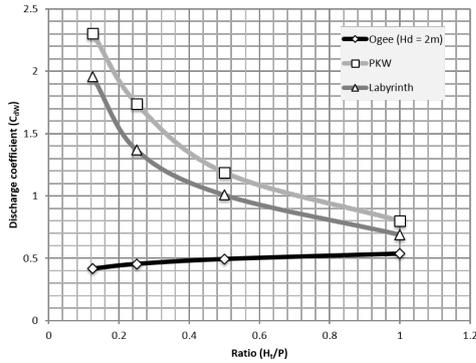


Figure 2.8: Discharge coefficients,  $C_{dW}$ , for various weir types [32]

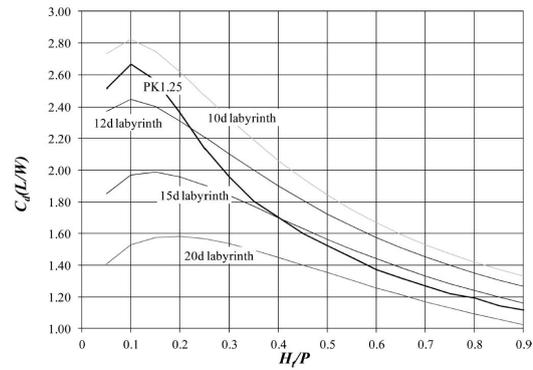


Figure 2.9: Comparison of PKW and Labyrinth discharge coefficients ( $C_{dW}$ ) [14]

( $0 < H_t/P < 3$ ), none have been built to operate at larger than  $H_t/P = 0.66$ . Most prototypes are designed to discharge their maximum flows at around  $H_t/P = 0.3$  [22].

It should be noted that, under certain conditions, a labyrinth weir is capable of achieving a higher discharge than a PKW at a lower cost, as illustrated in Figure 2.9. Therefore, each spillway type (linear, labyrinth and PKW) should be assessed on its merits during the options analysis and preliminary design process. The figure shows that, in the instance under consideration, the efficiency of a PKW (with a  $W_i/W_o$  ratio of 1.25) is comparable to that of a labyrinth weir with a sidewall angle of  $15^\circ$  at an  $H_t/P$  value greater than 0.4.

Figure 2.10 again illustrates the high discharge efficiency of the PKW, in this instance, in terms of  $C_{dL}$  (Equation (2.4.3)). The coefficient thus reflects a more physical representation of a discharge coefficient. The reduction in the efficiency as  $H_t/P$  increases shows how the overflow length is effectively reduced as the various factors which influence PKW discharge behaviour take effect (see Section 2.4.2). The graph also shows how the variation in width ratios,  $W_i/W_o$ , which range from 0.67 to 1.5, affect the discharge. It is clear that this ratio has an influence, with a higher ratio leading to higher discharge efficiencies, but that its role is marginal.

The graph in Figure 2.11 illustrates similar behaviour in terms of the discharge enhancement ratio, (Equation (2.4.4)). Here the magnification ratio,  $L/W$ , is examined [28]. It concludes that  $L/W$  is a key parameter but only for low  $H_t/P$  values.

The physical processes, which are influenced by the various PKW parameters mentioned above, are described in the next section.

## 2.4.2 Flow dynamics

The flow regime as it approaches, interacts with and then departs the piano key weir is unique and three-dimensional. The dynamics of this interaction are key to an understanding of many of the behavioural trends and inherent efficiencies that these structures exhibit.

In general, the majority of the flow lines follow the same basic path over a PK weir (see Figure 2.12). Flow approaching the outlet key would divert underneath the upstream overhang to one of the inlet keys on either side of it. Flow approaching the inlet key would converge with this flow and enter the inlet key directly. Once inside the inlet key, the upward sloping base

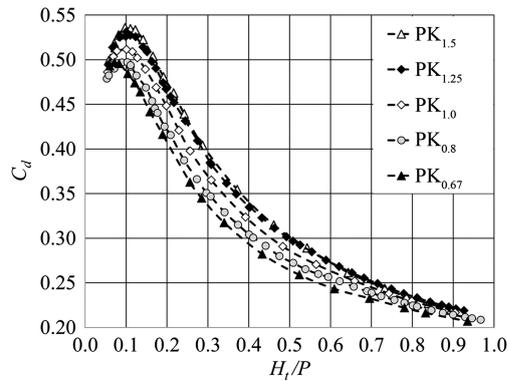


Figure 2.10: Discharge coefficients,  $C_{dL}$ , for PKWs with various width ratios ( $W_i/W_o$ ) [33]

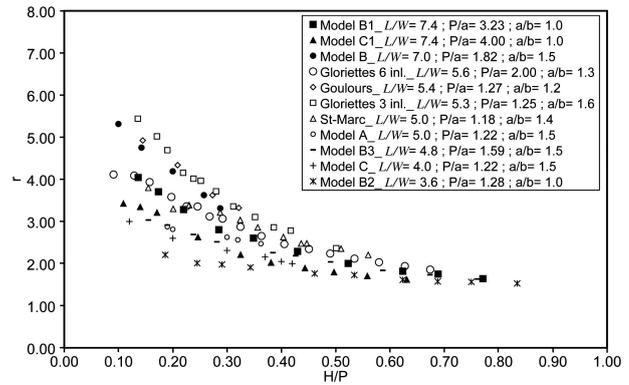


Figure 2.11: Discharge enhancement ratio for PKWs of varying magnification ratios ( $L/W$ ) [28]

forces flow upward toward the crest where it is discharged mainly over the lateral sidewall crest. Depending on the overflow depth, flow over this crest would fall free as a continuous curtain or nappe and collect at the base of the outlet key. The downward sloping base of this key guides flow to its exit at supercritical velocities. If there is sufficient tail water depth, a hydraulic jump forms either in the outlet key or shortly downstream of it.

The highest discharge efficiencies are achieved at low overflow depths. This is because, at these depths, the approach velocity vector magnitude, and thus its momentum, is low enough to allow it to readily change direction. As a result, flow can overtop the upstream crest, the downstream crest and the sidewall crest perpendicularly, which maximises their efficiency. At these low depths, the weir effectively acts like a very long linear weir, meaning that, the longer the magnification ratio, the greater the discharge [24].

At marginally higher flow depths, the increased longitudinal velocity and momentum cause the overtopping trajectory to begin deviating from this normal vector, reducing the discharge efficiency.

At even higher depths the dynamics of the inlet and outlet keys start to play a role. This is explored in greater detail in the following sections, but the basic premise is that the flow lines approaching the weir diverge away from the outlet key and converge into the inlet key. The converging nature of the flow and the limited flow area lead to higher flow velocities and higher energy losses which lead to reductions in discharge efficiency [24].

A wide inlet key is thus desirable to limit these impacts. However, a wider inlet key entails a narrower outlet key. At very high heads, the total discharge over the weir becomes a function of the ability of the outlet key to remove flow from the weir. As explained below, the hydraulics which dictate this relate to the occurrence of local submergence in the key as portions of the outlet become overfull.

There is thus a balance that must be achieved between these two opposing effects. This balance has been a focus of numerous parametric design studies as described in Section 2.5. It has also led to the development of trapezoidal piano key weirs, which widen the entrance to the inlet key as well as the exit of the outlet key but keep many of the other beneficial features of traditional piano key weirs [34; 35; 36].

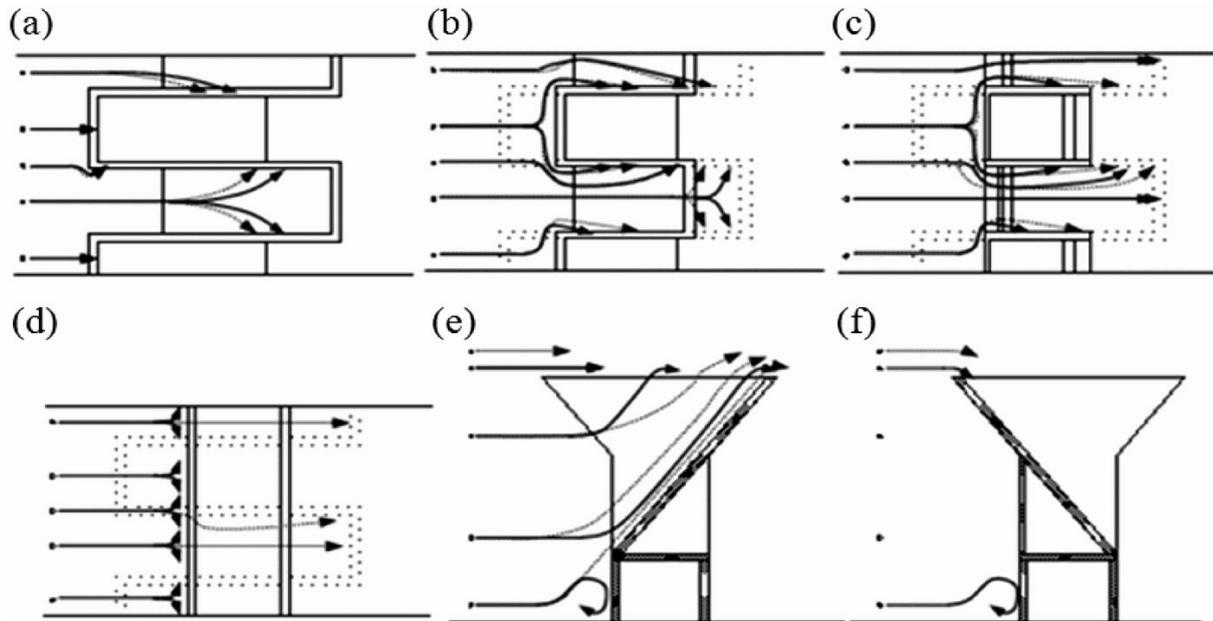


Figure 2.12: Flowlines at various locations around a PKW [37]

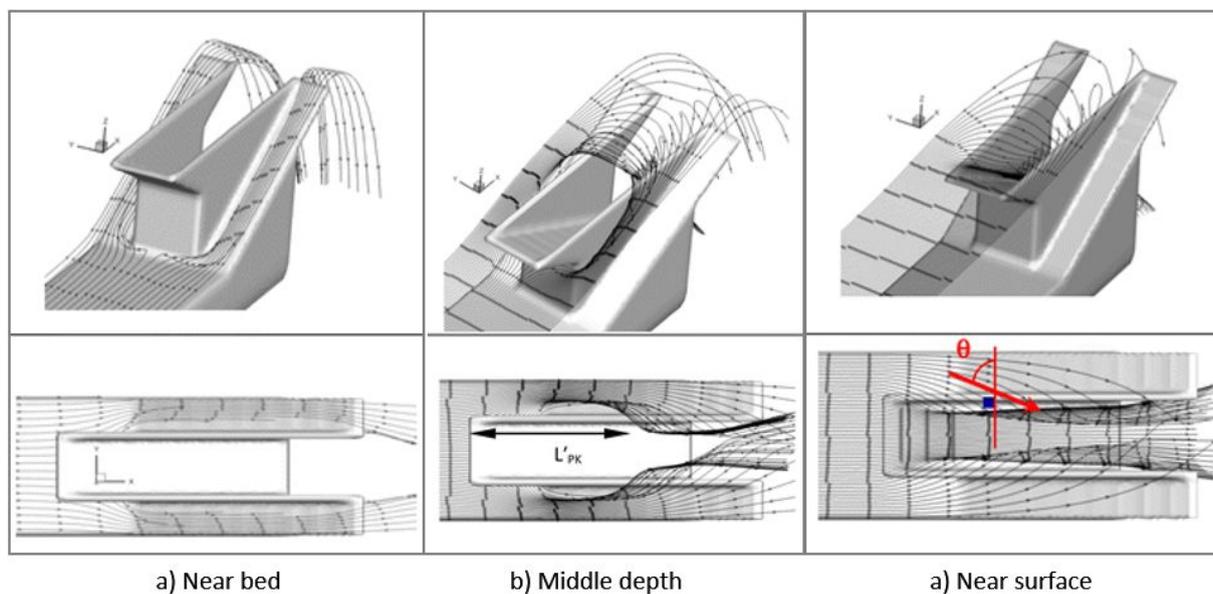


Figure 2.13: Horizontal flowlines at various elevations around a PKW [36]

### Flow dynamics of the inlet key

Observing the flow lines in the inlet key gives an indication of the processes which dictate the behaviour of the key. It also provides insight into the sources of instabilities which could potentially affect the weir.

Indicative flow lines at various depths and locations as they approach a PKW are shown in Figure 2.12. More detailed flow lines, as determined numerically, which depict a number of horizontal sheets of flow as it approaches and overtops the PKW are shown in Figure 2.13. Vertical approach flow lines and velocity profiles are also presented in Figures 2.14 and 2.15.

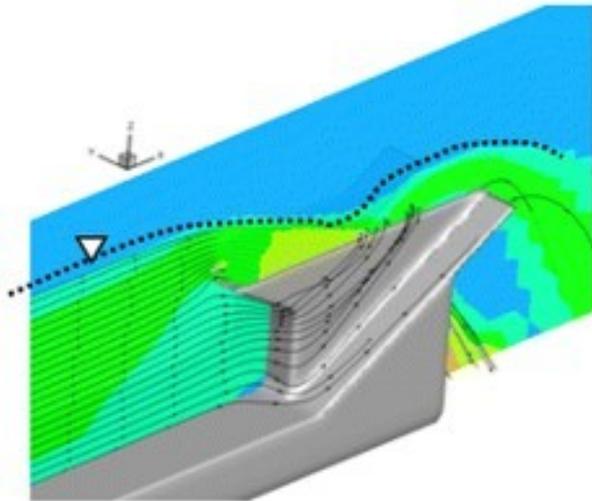


Figure 2.14: Vertical flowlines approaching the outlet key [36]

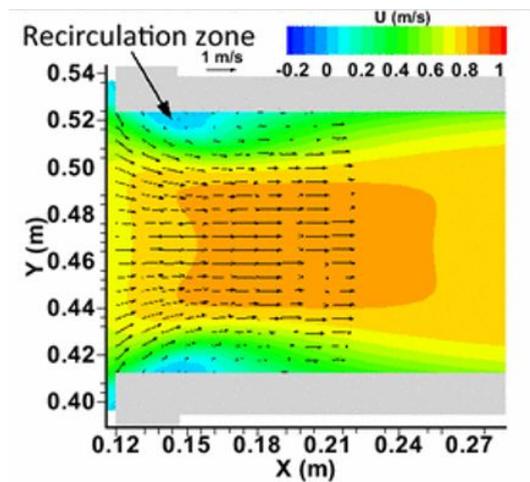


Figure 2.15: Velocity contour plot on horizontal plane at middle depth [36]

The flow lines presented in these figures showcase a number of relevant flow patterns:

- There is only a small portion of the total flow which discharges over the upstream crest of the outlet key. Only flow approaching the outlet key which flows near the surface does so. All remaining flow is diverted into the inlet key. Previous studies have estimated that more than 92 % of the total flow, enters the inlet key in this way [32; 38; 39].
- The convergence of flow in the inlet leads to higher flow velocities. These lead to lower local water levels in the key which has a direct impact on the discharge volumes over the sidewall and downstream crests. At high discharge a point is reached when portions of the flow in the inlet key exceed critical velocity. The control section of the weir then moves from the crest to the new control section at the critical depth, which effectively reduces the overflow length of the weir leading to further reductions in discharge efficiency [37]. This is depicted in Figure 2.16.
- The height at which flow approaches the weir determines, to a large degree, over which section of the weir it will overtop the crest:
  - The lowest flow lines diverge around the outlet key, converge into the inlet key, where they get forced upward by the sloping base. They mainly discharge at the downstream end of the crest.
  - The middle flow sheet follows the same pattern as the one below it and reaches the crest roughly halfway along its length.
  - The uppermost flow sheet discharges over the upstream sections of the lateral crest and is the only flow to discharge directly into the outlet key.
- Flow approaching the outlet key is diverted away from the stagnation pressure zone which forms against and underneath the overhang. This flow must make a sharp transition as it comes around the corner of the inlet key. The transverse momentum of the flow

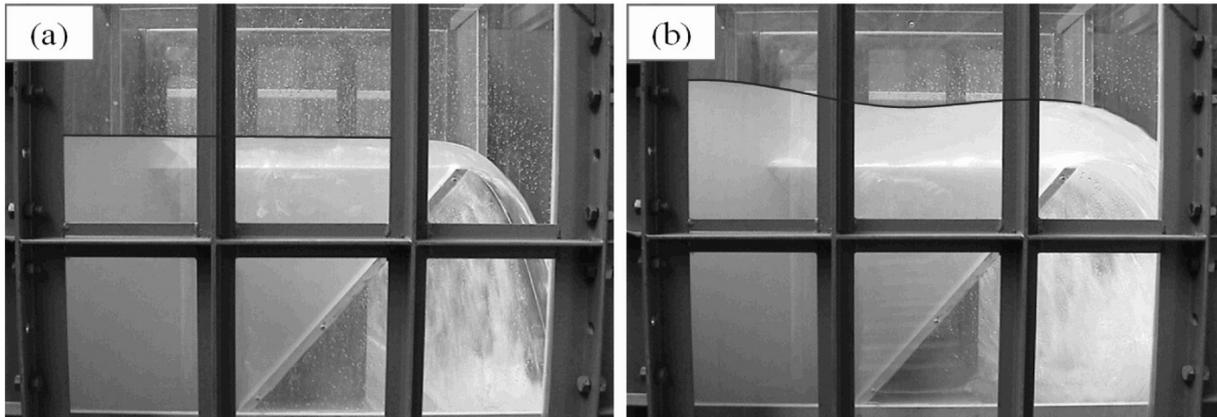


Figure 2.16: Free surface profiles for low and high heads [37]

as it enters the inlet key creates a separated shear boundary layer starting at the corner. A swirling or recirculation zone, also known as a separation bubble, forms behind this layer which is the cause of the negative longitudinal velocities which have been noted by other studies [24; 36; 5]. In this zone the flow is dynamically unstable and results in vortex shedding which is one cause of fluid vibrations at a PKW. This separation bubble and its dynamics are explored further in Chapter 7 and Section 4.3.1. It is noted that the slanted (zig-zag) nature of typical labyrinth weirs do not exhibit this behaviour allowing them to achieve higher discharge coefficients per unit length [33].

### Flow dynamics of the outlet key

The discharge capacity of the weir as a whole at high water levels is mainly determined by the ability of the outlet to remove flow which enters it. The width of the key, the slope of its base and its overall volume, determine the local water level and should this level exceed that of the crest at that point, local submergence effects may limit the discharge there. At low heads, local submergence is limited to the corners of the outlet key's upstream crest, where two orthogonal flows collide. At larger heads, this zone grows until the entire upstream portion of the outlet key crest is subjected to submergence effects resulting in a lower discharge when compared to the free overflow discharge over the weir. Increasing the volume of the outlet key by, for example, including a parapet wall on the upstream crest, or decreasing the wall thickness, can limit the onset of this local submergence [40]. It should be noted that this local submergence is separate of but linked to the downstream submergence mentioned in Section 2.2.2.

Observing the flow lines in an outlet key showcase a number of relevant flow patterns:

- Flow at the upstream crest is longitudinal so enters the key directly, although it may develop a small zone of low or negative pressure at the crest due to the vertical momentum of the flow. At the corners, this flow encounters flow from lateral crest, creating a small standing wave.
- Flow at the lateral crest has both longitudinal and transverse momentum meaning that the free-fall overflow nappe which develops has a three dimensional component. This

implies that the PKW's nappe does not extend as far as a normal free-fall nappe.

- The fall height of the nappe differs depending on its location along the lateral crest. This not only determines how far from the wall the nappe falls, but also affects its thickness. The nappes from opposite sides of the key may collide and interact. This frontal interaction has been found to have little effect on the discharge capacity of the weir so long as the interaction zone does not exceed the upstream water surface elevation under free flow conditions [24].
- The nappe forms a continuous curtain of water which encloses an air pocket underneath it. Air entrainment, from friction or the nappe interaction is expected to have an effect on the dynamics of this air cavity.
- The nappe has been shown to exhibit three types of behaviour [41; 37]. All three of these can occur under a single flow condition depending on the location along the lateral crest.
  - At low heads or low velocities, the nappe clings to the crest and the downstream wall, which is known as *clinging* flow.
  - At higher heads, the nappe pulls away from the wall but remains in contact with the crest's downstream end, known as *leaping* flow.
  - At even higher heads *springing* flow develops where the nappe detaches from the upstream corner of the crest.
  - As with labyrinth weirs, the profile shape of the crest has an effect on this nappe behaviour and can be used to marginally boost the discharge capacity of the weir (see Section 2.5.5).

## 2.5 Notable design features

As stated in Section 2.3, the discharge over a PKW is largely defined by the  $L/W$  and  $H_t/P_i$  dimensionless geometric ratios. There are additional features which can be implemented to increase the discharge efficiency. Despite the fact that their net benefit in terms of discharge is marginal, their inclusion in the design of a PKW should be considered as they have other advantages. A number of these features are highlighted below:

### 2.5.1 PKW Type

As alluded to above, there are several types of PK weirs. The four main types differ according to the presence of upstream and/or downstream overhangs, as described below and shown in Figure 2.17:

- **Type A:** This is the general shape of the “*typical*” PKW which has both upstream and downstream overhangs. These need not be symmetrical, although from a structural stability perspective, symmetry is preferred to ensure that, in the static force analysis, the force resultant is located within the base of the structure thus making it safe against overturning.

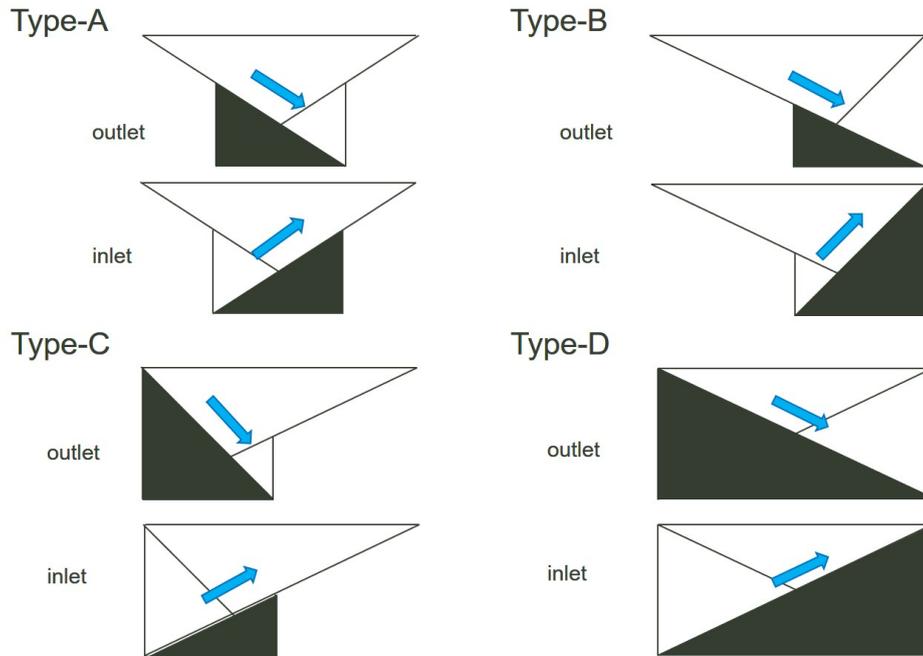


Figure 2.17: Cross sectional sketches of PKW types (flow is from left to right)

- Type B:** A type B PKW only has upstream overhangs. It has been shown to have a marginally larger discharge capacity (by  $\sim 3\%$ ) than the type A geometry [39; 27]. This is because the longer upstream overhangs (with the same overflow length) allow for slightly lower energy losses in both the approach flow and the inlet key. This benefit is minimal and the use of a type B PK weir does present additional structural challenges which are not encountered by a type A PK weir [39]. This is because the structure is unbalanced when considering its overturning moment and must thus be fully incorporated into the main dam superstructure or its foundations. For this reason, type B PKWs are generally only considered during new projects, where the additional support mechanisms can be incorporated into the initial design, and not on spillway rehabilitation projects where the necessary anchors, dowels or cables are more difficult to put in place.
- Type C:** Type C PKWs only have downstream overhangs. They have shown no benefit from a discharge efficiency perspective, however, their use may be warranted depending on site specific conditions.
- Type D, E:** These are additional types which have been defined to have no overhangs on either the upstream or downstream sides. They have either full sloping bases or partially filled in spaces within the keys which differentiates them from a rectangularly shaped labyrinth weir. Since these types of PK weirs lose the benefit of a reduced footprint they are useful where their wider footprint is a necessity. A good example of this is in alluvial rivers where foundation conditions may not be able to support a reduced foundation footprint. They have other benefits such as being easier to construct and having a lower steel reinforcement requirement [15].

Note that the present research study focusses mostly on type A PKWs.



Figure 2.18: PKW nose at Gloriettes Dam [43] Figure 2.19: PKW nose at Goulours Dam [15]

### 2.5.2 Inlet key versus outlet key width ratio

Numerous physical and numerical experiments have determined that an inlet key that is wider than the outlet key is generally beneficial to discharge efficiency [3; 34; 39; 42; 24; 29; 41]. These studies state that this is primarily due to the fact that a wide inlet key leads to lower energy losses. This then increases discharge efficiency. This width cannot be too large, however, as a point is reached where local submergence in the ever narrower outlet key becomes the limiting factor.

The energy losses being referred to are partially linked to the necessity for up to  $\sim 92\%$  [38] of the flow needing to enter the inlet key even though it typically only comprises approximately 50% of the upstream flow area. Entrance losses, linked to turbulence and the formation of separation bubbles (see Section 7.3.4), play a large role in the passage of this flow. There are additional influences such as the increasing flow velocities as flow moves down the inlet key and the potential for supercritical flow to develop as a result [24]. The effect of the ratio on discharge can be seen in Figure 2.10.

The optimum value for this dimensionless ratio ( $W_i/W_o$ ) is not fixed, as it is dependent on other factors. There is broad agreement that the ratio's value is equal to or larger than 1.0, i.e. an inlet key equal in width or wider than the outlet key. Studies have examined ranges from 0.2 to 2.2 and have determined that the optimal value for this ratio changes with the upstream head [24; 27]. However, for most practical applications the ratio should lie somewhere between 1.3 to 1.6. The optimal  $W_i/W_o$  value for the reference design (see Section 2.3) is equal to 1.25.

### 2.5.3 Nose

The clear preference for an inlet / outlet key width ratio greater than unity alludes to the energy losses as flow enters the inlet key (Section 2.5.2). Another method, besides widening the inlet, which has been found to also reduce the magnitude of these losses is to streamline the entrance [5]. This can be done by the provision of a so-called "nose" upstream of, and underneath, the outlet key. Some typical examples can be seen in Figures 2.18 and 2.19.

Its presence leads to smoother flow lines into the inlet key, lower head losses and less vortex

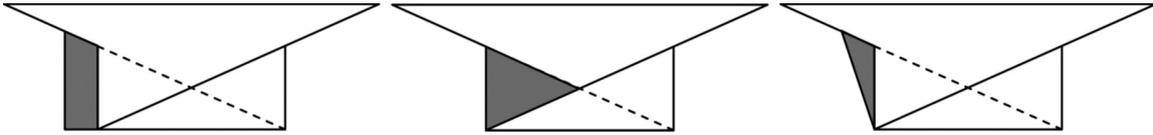


Figure 2.20: Nose shapes: triangular or circular (left), extruded triangular (centre), tapered triangular (right) [23]

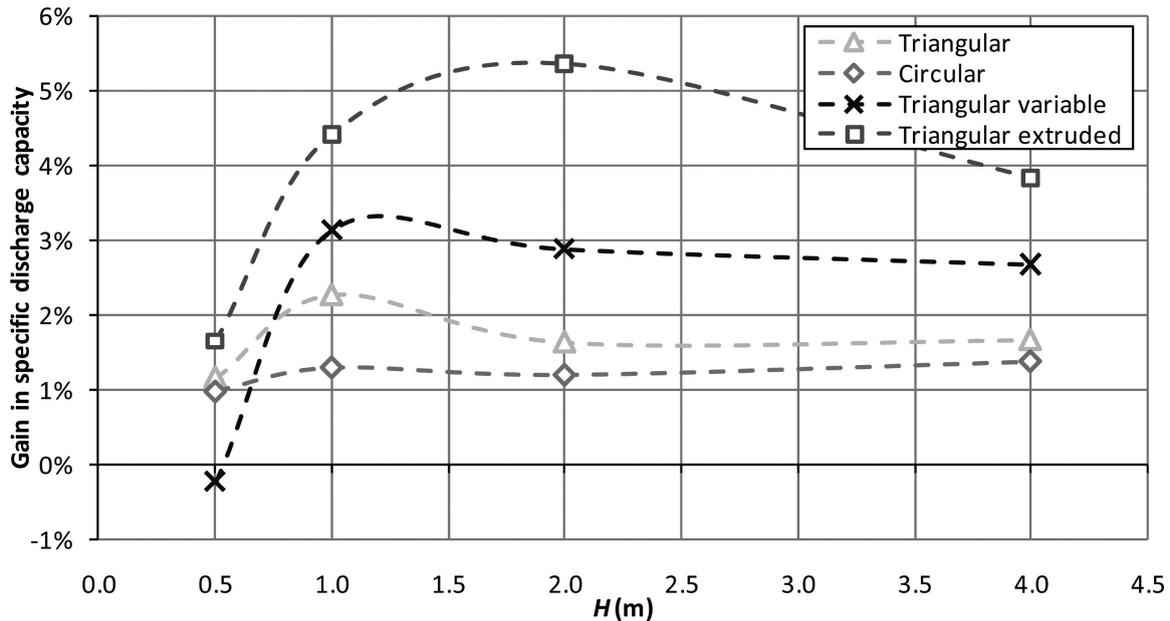


Figure 2.21: Nose shape and its effect on discharge [23]

shedding from the bluff edge of the entrance. This then leads to increases in the discharge efficiency of the PK weir. The quantitative impact a nose has on PKW behaviour has been investigated but has, to date, not been incorporated in the design equations in Section 2.4.1. Their use is generally recommended but their quantified effect can only be determined by physical or numerical modelling.

The nose can be any shape or size so long as it serves the purpose of deflecting the flow underneath the outlet key toward the inlet keys on either side. Its size is dictated by  $B_n$  which stipulates the horizontal length of the nose from the vertical base of the outlet key. Ideally their shape would be such that no wake, or separation bubble, is generated at the leading edge of the inlet key, i.e. a semi-elliptical shape [44]. Such shapes are more difficult to construct than more geometric shapes, thus, to date only triangular and circular noses have been implemented [15]. The possibility of extruding the triangular profile out of the mass concrete body underneath the outlet key or of tapering the nose has been investigated and found to be promising (see Figure 2.21) [23].

#### 2.5.4 Approach flow

As with most other dam spillways, whether they have uncontrolled linear overflows or gated structures, the dynamic patterns of the approach flow can have a marked effect on their efficiency. Contracting flow or uneven, non-normal velocities effectively cause a reduction in the

overflow length which reduces the discharge efficiency [45]. Should a PKW be located on or near an abutment, or if a non-normal approach is suspected, the effect of the approach flow patterns should be investigated via a numerical or physical model [46].

Furthermore, the use of the PKW in either a dam or a channel application has a marked influence on its behaviour. Physical experiments have determined that PKWs in channel applications (with a straight approach channel) have a noticeably higher discharge than PKWs which have wide approach channels (where the channel is wider than the overflow) [47]. Wide channels have transverse flows approaching the overflow in addition to longitudinal flows. It is interesting to note that the influence of this lateral flow may override the effect of one of the main determinants in the spillway discharge, namely the upstream channel depth,  $P$ . This means that the same spillway with a shallow but narrow and straight approach flow will result in a larger discharge capacity than one with a deep but wide channel. Naturally, a deep, narrow and straight approach would be the most ideal. Alternatively, shaped abutments can significantly limit the effects of lateral flow separation.

### 2.5.5 Crest shape

The shape of the crest has a fairly significant role to play on the efficiency of any spillway, especially at low water levels. Their effect on a PKW is decisive at low  $H/P$  values, but this effect reduces significantly as  $H/P > 0.3$ . Scaled physical models have been used to investigate the effect and determined that a half-round or quarter round crest on the lateral (sidewall) crest had the largest impact when compared to a flat topped crest [48].

It was also found that the crest shape on the upstream and downstream portions had little influence, probably due to their short length. Nonetheless, in order to achieve smoother flow lines, it was recommended that the upstream crest be rounded (quarter round on its upstream side) and the downstream crest be sharp crested. Radii of curvature generally range from  $0.5 T_s$  to  $1.0 T_s$ , where  $T_s$  is the wall thickness.

### 2.5.6 Additional design aspects

Certain additional aspects which have bearings on the design of a PK weir but don't have a direct influence on the present study are listed below.

- **Parapet wall:** Parapet walls refer to a relatively short vertical wall positioned on the crest of the PKW. Their presence has been shown to be beneficial under certain conditions as they increase the volume of the individual keys in addition to giving the weir greater height. It has been found that there is only a marginal benefit to a parapet on the downstream crest of the inlet key, but that there is a marked benefit to placing one on the upstream crest of the outlet key [40]. This is because, with its greater volume, the outlet key is able to operate under undrowned conditions for longer than would otherwise be the case, allowing the side crest to operate at its free-flowing efficiency for longer.
- **Energy dissipation:** Due to their high discharge efficiency, energy dissipation downstream of the weir is of concern. Special attention should be given to the design of energy

dissipation structures downstream of a PKW to prevent undesirable aspects such as scour and cavitation [49]. The unstable nature of this flow may also lead to possible vibrations in the main structure especially if there is a high downstream water level, although it is expected that this can only be determined on a site specific basis.

- **Economics:** A PKW can be designed with a high hydraulic efficiency. As alluded to previously (see Section 2.3), such a solution is often not economic and thus an optimum balance between efficiency and cost needs to be found. The cost criterion upon which such an analysis is based can be linked to a simple metric such as the total concrete volume. An evaluation of design alternatives can be carried out to compare the cost-benefit ratio of a PKW versus that of a labyrinth or even a gated spillway.

Indicative cost optimisation studies have determined that PKWs are most cost-effective and a technically efficient solution when they are implemented at existing dams, but that the use of labyrinth spillways can often offer a more ideal solution at new dams based on local site conditions and existing operational restraints [14; 33].

- **Constructability:** The constructability of a PKW plays a significant role in its design. In many existing prototypes, limitations on the extent of the overhang lengths were imposed due to practicality, construction equipment capability limits, site access and occupational health and safety factors [15; 50].

Furthermore, the angular edges of a PKW, which present themselves as leading edges (see Section 2.4.2) may lead to the formation of a separated shear layer and the consequent shedding of vortices. The smoothing of these edges can significantly reduce this phenomenon as evidenced by the inclusion of noses under the outlet key (see Section 2.5.3). These smoother profiles are, however, much more complex to construct as the necessary concrete formwork becomes more difficult to design and install. The possibility of manufacturing the components of the PKW as pre-cast elements at an off-site factory does allow custom made moulds to be prepared, which could incorporate such smoothed or contoured features. Naturally, the size of the individual elements has a role to play as they need to be transported to the site using regular roads.

An additional constructability issue is that of timing. The occurrence of periodic or seasonal flooding can limit access to a particular construction site. Again, modular construction (see Section 2.2.4) can assist in this regards by shortening the amount of time needed for installation.

## 3 Structural vibration

### 3.1 Introduction

Vibration can be broadly defined as a periodic response of a body when it is initially displaced from its position at rest or loaded by an instantaneous, periodic or random force. There is thus a transfer of energy from the unbalanced force to the oscillatory body which is then converted to other forms of energy (e.g. motion), transferred onward to other components in the system, or dissipated as dictated by the dynamic characteristics. The vibration of a structure is of primary engineering concern due to the fatigue related issues that large or long-duration oscillations may have [51]. Other areas of concern are the generation of sound waves as noise and the inefficient use of energy.

This chapter will cover the basic principles of vibration and highlight aspects which are relevant to the dynamic behaviour of piano key weirs.

### 3.2 Basic overview

Vibration is inherently time variant thus, when assessed in the time domain, a complex wave or signal can be considered as a superposition of any number of sinusoidal components. The most basic vibration is a motion of the form presented in Equation (3.2.1) and Figure 3.1:

$$x = x_0 \cos(\omega t) \quad \text{with} \quad \omega = 2\pi f \quad (3.2.1)$$

where  $x$  is the displacement from equilibrium,  $x_0$  is the vibration amplitude,  $\omega$  is the circular frequency,  $t$  is time and  $f$  is the frequency in Hertz, Hz. As presented in Figure 3.1(a), this equation represents a discrete, undamped, single degree-of-freedom oscillator, i.e. a system consisting of a mass with a spring but no damper element. The inertia of the mass and the restoring force due to the spring act on the mass when it is deflected from its equilibrium position. Equation (3.2.1) describes the displacement from equilibrium over time and is the idealized solution to the system's equation of motion, as shown by Equation (3.2.2). This more general equation is defined by Figure 3.2 where the simple system described above is also acted upon by a damping force and an applied force.

$$m\ddot{x} + B\dot{x} + Cx = F(t) \quad (3.2.2)$$

The three terms of the left hand side of Equation (3.2.2) represent the inertial force, the damping force and the restoring force, respectively, which together equal the applied force. The inertial force is the product of the body's mass,  $m$ , and its acceleration,  $\ddot{x}$ , and represents the kinetic energy of the system. The damping force is the damping coefficient,  $B$ , multiplied by the body's velocity,  $\dot{x}$ , and emulates the loss of energy from the system by elements such as

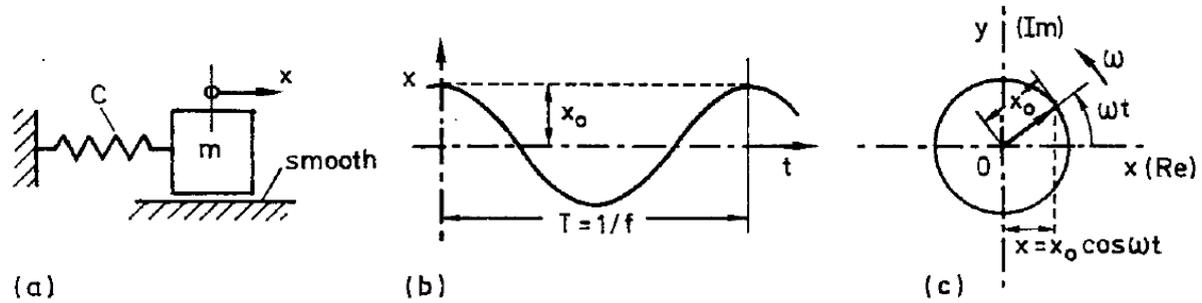


Figure 3.1: (a) Simple undamped oscillator with response shown in (b) graphical and (c) vector representation [52]

friction. The restoring force is the stiffness factor,  $C$ , multiplied by the body's displacement,  $x$ , and represents the ability of the system to store potential energy via distortion or displacement from its position of rest [52; 51]. It should be noted that in the present study, the coefficients in Equation (3.2.2) are linear and parametrically fixed in time. Furthermore, when distributed mass systems are analysed, coupling between the multiple degrees-of-freedom requires that the equations be considered in matrix form [53; 52].

### 3.2.1 Free vibration

When given an initial displacement and allowed to vibrate freely, the energy balance of the system results in it vibrating at one or more of its natural frequencies. Each of these frequencies is associated with its own unique modal shape which can be seen as the deflection shape at which the potential energy contained in the deformed structure is balanced by the kinetic energy of the structure in its undeformed shape and so absorbs all the available energy [51]. This is expanded upon in greater detail in Section 3.3.

For a discrete mass system with no damping, part of the solution to the equation of motion gives the natural frequency, which is equal to:

$$\omega_n = 2\pi f_n = \sqrt{\frac{C}{m}} \quad (3.2.3)$$

This shows that the higher the mass of the system, the lower the natural frequency, and the higher the stiffness, the higher the natural frequency [51]. Temperature changes can also change the system stiffness and thus also change the modal values. When damping is accounted for in free vibration the oscillation frequency at which the body will respond is based on the natural frequency with additional accounting for the amount of damping, as follows:

$$\omega_d = \omega_n \sqrt{1 - \zeta^2} \quad \text{with} \quad \zeta = \frac{B}{B_{cr}} = \frac{B}{2\sqrt{mC}} \quad (3.2.4)$$

The damping ratio,  $\zeta$ , defined as the ratio of damping to the critical damping (above which the response is asymptotic), should be less than 1 for vibration to occur, i.e. under-damped [53]. Using Equations (3.2.3) and (3.2.4) the equation of motion for the free vibration of a single degree-of-freedom system can be rewritten as per Equation (3.2.5):

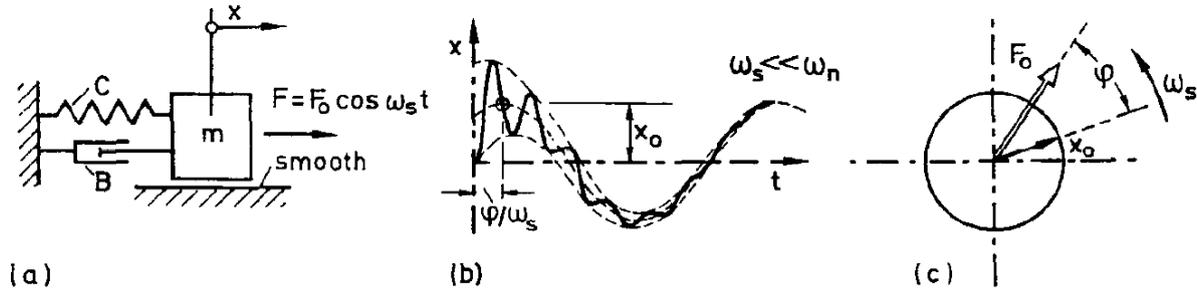


Figure 3.2: Forced vibration oscillator with response shown in (b) graphical and (c) vector representation [52]

$$\ddot{x} + 2\omega_n\zeta\dot{x} + \omega_n^2x = \frac{F(t)}{m} = 0 \quad (3.2.5)$$

### 3.2.2 Forced vibration

When the system is not just disturbed by an initial displacement but acted upon by a periodic or random force, the resultant vibrations are said to be forced. In the same idealized, discrete, one dimension-of-freedom environment as in the previous section, the equation of motion is the same as presented in Equation (3.2.2). If the applied force is periodic and oscillates at the forcing frequency,  $\omega_s$ , the force takes the form:

$$F(t) = F_0 \cos(\omega_s t) \quad (3.2.6)$$

and the response, which lags behind the applied force by the phase,  $\phi$ , becomes:

$$x(t) = x_0 \cos(\omega_s t - \phi) \quad (3.2.7)$$

This shows that an oscillating force will cause the system to respond with a vibration with the same frequency as is shown in Figure 3.2 [51]. The magnitude of the response that develops in this simple system depends on the ratio of the forcing frequency to the system's undamped natural frequency,  $\omega_s/\omega_n$  as well as the amount of damping,  $\zeta$ , that is present. The effect these two factors have is presented in Figure 3.3.

The ratio between the maximum deflection of the vibration,  $x_0$ , and the deflection caused by the force if it were statically applied,  $F_0/C$ , is known as the magnification factor [52]. Figure 3.3(a) shows that this factor can get very large (i.e. much larger deflections compared to the static case) when the forcing frequency is close to the natural frequency of the system. This phenomenon is known as resonance [51]. Even with relatively high damping ( $\zeta \approx 0.5$ ), or small applied forces resonant conditions can generate a large amplitude response [53]. When the forcing frequency is very high, however, the vibration deflections are lower than for the static case. In terms of the phase of the response, Figure 3.3(b) shows that when the forcing frequency,  $\omega_s$ , is very small compared to  $\omega_n$ , the deflection response is nearly synchronous to that of the forcing frequency. When  $\omega_s$  is close to the natural frequency, this phase difference

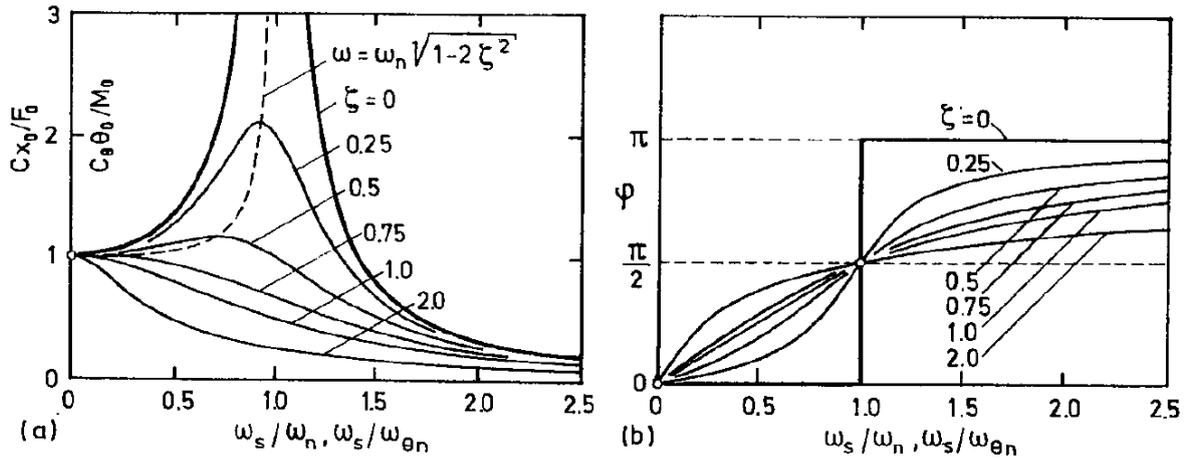


Figure 3.3: Forced vibration response (a) amplitude (b) phase [52]

tends toward  $\frac{\pi}{2}$  and then continues to increase asymptotically to  $\pi$  as the forcing frequency increases further.

The graphs in Figure 3.3 show that damping has no (or very little) effect on the natural or resonant frequency, hence damping is generally disregarded in determining the natural frequencies of a system. The graphs also show that altering a system to increase its natural frequency or its damping can be an effective strategy to limit excessive vibrations [51].

Another valuable descriptor of vibration is the concept of mechanical admittance. In mathematical terms, it is simply a transfer function defined as the ratio of the response to the applied force, as follows:

$$\chi_m(\omega) = \frac{\text{Body displacement}}{\text{Exciting force}} = \frac{x(t)}{F(t)} \quad (3.2.8)$$

In a straightforward, discrete, linear and lightly damped system, the mechanical admittance can be given as follows:

$$|\chi_m(f)| = \frac{1}{2\pi m f_n} \left[ \left( 1 - \left( \frac{f}{f_n} \right)^2 \right)^2 + \left( 2\zeta \frac{f}{f_n} \right)^2 \right]^{-\frac{1}{2}} \quad (3.2.9)$$

Equation (3.2.9) shows that the admittance of a mechanical system is mainly influenced by its mass and damping components, the natural frequency as well as the frequency of the applied exciting forcing function [52]. Having information of the mechanical admittance of a system allows one to predict the magnitude of the response of that system to an exciting force. This is useful in testing the response to a range or spectrum of possible forces as is expanded upon in the next section.

### 3.2.3 Random vibration

Instead of a single periodic force being applied, as per the previous section, a random fluctuating force such as turbulence is applied. Due to the chaotic and non-repetitive nature, no

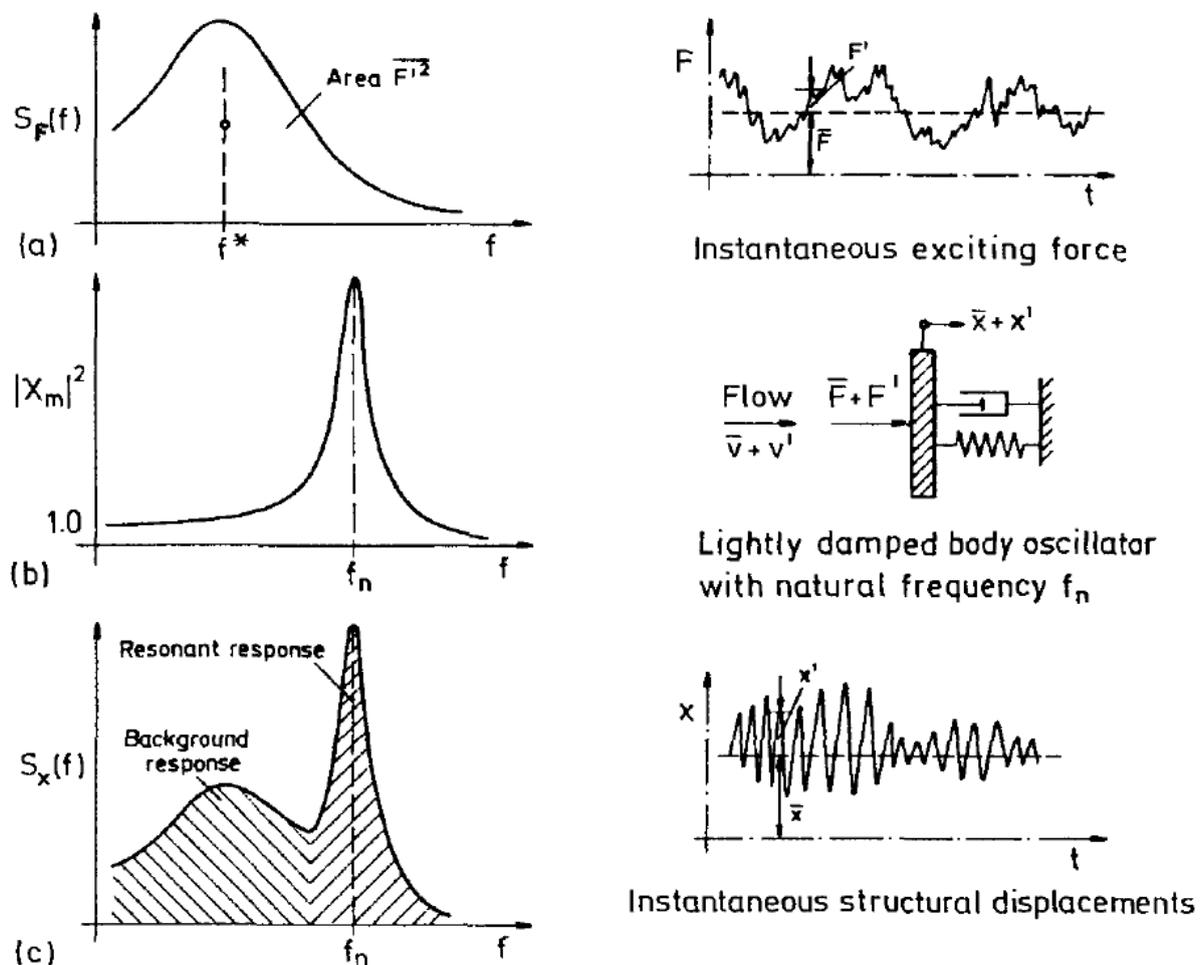


Figure 3.4: Evaluation of a random response in the frequency domain [52]

exact deterministic solutions can be found. However, if the force is statistically stationary and ergodic, probability density functions of the response can be determined [53].

The time-variant force fluctuations can be broken down by Fourier analysis into an infinite series of sinusoidal component signals. In doing so the signal in time-domain gets converted to frequency-domain in the form of a *power spectral density* (PSD) function. In mathematical terms the original signal is first broken up into its mean and fluctuating components, and then the mean square values of these fluctuations are further decomposed using the Fast Fourier Transform (FFT) [52; 51]. The spectra of the force and the response can thus be defined as shown in Equation (3.2.10) and depicted in Figure 3.4.

$$S_F(f) = \frac{\overline{F_f'^2}}{df} \quad \text{and} \quad S_x(f) = \frac{\overline{x_f'^2}}{df} \quad (3.2.10)$$

The resulting PSD function, when summed over its entire spectrum is such that it is equal to the square of the statistically useful *RMS* (root-mean-square) value.

$$x'_{RMS} = \sqrt{\overline{x'^2}} = \left[ \int_0^\infty S_x(f) df \right]^{\frac{1}{2}} \quad (3.2.11)$$

The PSD summarises the amplitude and the frequency of the original time-domain signal although it discards the phase differences between the various component signals. Bear in mind that the “height” of the PSD is generally meaningless and it is the area under the graph, representing the power or strength of the signal at that frequency, which is of interest. PSDs generated from experimental data often exhibit a noise floor which appears as a horizontal band at the base of the graph. It represents the contribution of random or unwanted background fluctuations and interference recorded by the measurement instrument [54].

Figure 3.4 indicates that the mechanical admittance,  $\chi_m$ , can be used as a base to transfer between the PSD of the exciting force and that of the response in the form of Equation (3.2.12). In the example presented in the figure it is clear that the strongest frequency in the forcing spectra does not coincide with that of the natural frequency. Despite this, due to the very weak damping in the system, the low strength forces which do operate at the natural frequency are able to generate a much larger response compared to the response for the strongest forces which recede into the background.

$$S_x(f) = |\chi_m(f)|^2 S_F(f) \quad \text{where} \quad f = \frac{\omega}{2\pi} \quad (3.2.12)$$

### 3.2.4 Vibration in a fluid

When a body vibrates in a fluid, the body induces movement in the fluid which is directly adjacent to it, meaning that the body transfers energy to the fluid which thus needs to be accounted for in the equation of motion. This transfer of energy and the forces which are associated with them can be described in terms of the displacement, speed and acceleration of the body [52]. In the same form as Equation (3.2.2), the equation of motion for a simple discrete oscillator becomes:

$$(m + A')\ddot{x} + (B + B')\dot{x} + (C + C')x = F(t) \quad (3.2.13)$$

where  $A'$  is known as the added mass,  $B'$  the added damping and  $C'$  the added stiffness. As described above, the mass, damping and stiffness of a body fundamentally defines how that body responds to an external force, hence these added quantities alter the way in which the body behaves. For example, Equation (3.2.3) which defines the natural frequency is altered such that:

$$(f_n)_{fluid} = \frac{1}{2\pi} \sqrt{\frac{C + C'}{m + A'}} \quad (3.2.14)$$

In practice the added stiffness coefficient is difficult to estimate on its own since its displacement operator,  $x$ , oscillates in phase with that of the acceleration. The added mass and added stiffness can thus not be separated from each other without developing a fundamental theoretical model of their interaction. In lieu of this, the effect of the added stiffness is usually lumped together with that of the added mass [52]. The natural frequency of the body in fluid can then be estimated relative to its natural frequency in a vacuum.

$$\frac{(f_n)_{fluid}}{f_n} = \sqrt{\frac{1}{1 + A'/m}} \quad (3.2.15)$$

The added mass and the fluid damping are functions of a number of variables, a few of which are listed below [52]:

- **Geometry:** The shape and size of the oscillating body has a decisive impact on  $A'$  and  $B'$ . Furthermore, cross-coupling between these two factors as well as the structural mass and damping often requires complex configurations. The presence of a nearby boundary or free-surface also increases added mass.
- **Viscosity:** As viscosity of the fluid increases, so too do the values of added mass and added damping.
- **Mean flow:** When the fluid around the oscillator is not static, the mean flow in the fluid can be a source of additional energy for the oscillator. The influence of this added energy on the added mass and damping depends on the direction of the flow and the movement of the system.
- **Two-phase flow:** Although no general statements can be made, there appears to be a trend that the more air is present in a two-phase flow, the less added mass there is but the more added damping.

### 3.3 Modal harmonics

As alluded to in the above sections, there are certain frequencies at which a body may vibrate with large amplitudes, due to an inherent balance between the kinetic and potential energies encapsulated in its stiffness and its mass [51]. Each one of these frequencies has its own unique modal shape such that, in physical energy terms, at the maximum deflection the kinetic energy is zero (velocity is zero) but the potential elastic energy is at its maximum, and at its un-deformed shape, in the middle of the stroke (i.e. deflection is zero) velocity is at maximum and kinetic energy is at its peak [52].

In mathematical terms, the natural or resonant frequency is the eigenvalue and the modal shape the eigenvector solution of the eigenvalue problem balancing the mass and stiffness of the system. This is briefly expanded upon below.

The equation of motion in matrix form is identical to Equation (3.2.2). As shown in Section 3.2.2, damping can generally be disregarded in determining the modes of a system. Thus, when the undamped system is assessed in free vibration the equation of motion, in matrix form, becomes:

$$[M]\{\ddot{x}\} + [C]\{x\} = 0 \quad (3.3.1)$$

where  $[M]$  is the mass matrix and  $[C]$  the stiffness matrix. If a harmonic solution is assumed (i.e. the structural response has a basic shape which does not change, only its amplitude changes) which is differentiated and then substituted back into Equation (3.3.1), one obtains:

$$([C] - \omega^2[M])\{\phi\} = 0 \quad (3.3.2)$$

where  $\omega$  is a natural frequency of the system and  $\phi$  a vector defining the mode shape. This equation has the same structure as a typical eigenvalue problem. When substituting  $\lambda = \omega^2$  it becomes the eigenvalue and  $\phi$  the eigenvector. In order for the solution to be non-trivial (i.e.  $\{\phi\} \neq 0$ ):

$$|C - \lambda M| = 0 \quad (3.3.3)$$

Generally, for  $N$  degrees of freedom there are  $N$  independent eigenvalues. Equation (3.3.3) thus represents an  $N^{\text{th}}$  polynomial in  $\lambda$  whose roots are the  $N$  eigenvalues. For each  $\lambda_i$  ( $i = 1, 2, \dots, N$ ) there is a non-trivial solution  $\phi_i$  which are its eigenvectors [53].

The benefit of having the eigenvectors (modal shapes) and eigenvalues (natural frequencies) of a system is that they can be used to describe the response of any linear elastic structure in free or forced vibration. At any given time, the deflection profile of a structure can be given by superimposing the mode shapes multiplied by their amplitude and accounting for their frequency and phase [52] in the form of:

$$[x] = \sum_i \{\phi_i\} \zeta_i \quad (3.3.4)$$

where  $x$  is the vector of displacements,  $\phi_i$  is the  $i^{\text{th}}$  mode shape and  $\zeta_i$  is the amplitude of the  $i^{\text{th}}$  mode shape. Bear in mind that this equation only reflects the oscillating portion of the response. Should there be a static force being applied, its static response must be added to determine the total displacement.

Previous sections have shown that if a forcing frequency, whether a discrete frequency or part of a spectrum, is close to the natural frequency, then the amplitudes associated with that frequency's mode shape can be very large if damping is relatively low. The relevant mode in Equation (3.3.4) would then have a large amplitude value attributed to it.

### 3.4 Controlling vibration

Excessive vibration could lead to problems when it leads to large amplitude displacements and stresses, high frequency sound or mechanical wear and tear. An additional problem is that of material fatigue, where even small amplitude vibrations may cause material failure if they occur for long enough periods of time.

The probability of fatigue or the determination of the lifespan of a structural element exposed to cyclic forces can be assessed using the S-N curve, which describes the number of cycles at a given amplitude a material can withstand. A typical, statistically averaged and idealized example is presented in Figure 3.5. The lower the stress oscillation in relation to the yield stress of the material the more cycles are needed to induce fatigue failure. However, a stress point is reached, known as the fatigue or endurance limit, below which an infinite (or suitably large) number of cycles will not lead to failure. This limit differs depending on the material

that the structure is made of. Steel typically has an endurance limit equal to roughly half its yield strength whereas in other alloys this ratio can be as low as 0.4 [51]. Although concrete does have a theoretical fatigue limit, concrete failure due to fatigue is rare.

A brief scoping level assessment of the possibility of fatigue at a PKW was conducted to determine the potential for its occurrence. The methodology that was used in this assessment was the rainflow counting procedure, as defined in ASTM E1049-85 [55], together with the Palmgren-Miner's Linear Damage Rule and the S-N curve (see Figure 3.5), which estimates the stress-life of the structure under the specified loading [56]. The Linear Damage Rule is a damage accumulation model that sums up the damage done by a number of cycles of a particular stress range as a ratio to the number of cycles needed to cause failure at that stress range. The model can be summarised as in Equation (3.4.1).

$$D = \sum_i^m \frac{n_i}{N_i} \quad (3.4.1)$$

where  $D$  is the total damage, with a maximum value of 1 for failure to occur,  $m$  is the number of stress ranges,  $n$  is the number of cycles at a particular stress range as determined in the rainflow counting technique, and  $N$  is the number of cycles needed to induce failure at the same stress range as determined from the S-N curve.

This process was conducted using an automated tool called STOFLO [57]. The tool pre-processes the data to reduce the time series to only peaks and valleys. It then conducts the rainflow counting procedure and provides some post-processing tools for closer analysis. A number of life estimates are provided and the one selected for the current analysis bases the endurance limit of the material on the Morrow limiting criteria which in turn is based on the fracture strength of the material. The Morrow criteria is the preferred criteria for steel [58]. The STOFLO tool allows for the mean stress state and its influence on the fatigue damage to be corrected.

It should be noted that there are several factors which can influence the endurance limit of a material including the mean stress state and how the cyclical load is applied [59]. The higher the mean of the fluctuating stress or force, the lower the endurance limit becomes. Given that standard design is usually based on the yield strength, accounting for relevant factors of safety, this leads to relatively high mean stress states. These lead to a much lower limit on the amplitude of any vibrations that may occur in order to prevent fatigue damage or failure [51].

Design approaches to prevent fatigue failure thus revolve around limiting the mean stress state on a structure or limiting the vibration amplitudes that do occur. Limiting the mean stress state may lead to overdesign hence targeting vibration amplitudes is preferable. This can be achieved via either limiting the vibration amplitudes during resonance or adjusting the resonance frequency such that resonance is less likely to occur. Vibration amplitude can be controlled by increasing the damping of the system and the frequency can be adjusted by increasing the stiffness of the structure or reducing its mass (see Equation (3.2.3)). Generally, the most cost effective method of controlling vibration caused by broad-spectrum forces is to increase the stiffness of the structure, using struts or braces, or making small changes to its geometry. In so doing the natural frequencies are increased to a range beyond the forcing

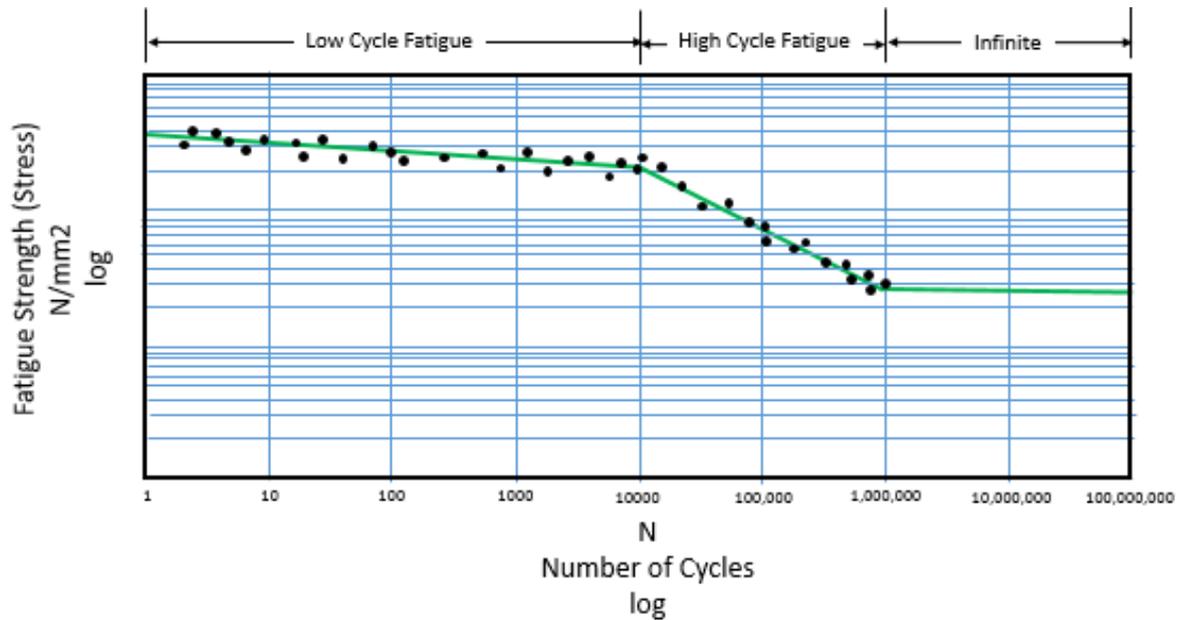


Figure 3.5: Typical example of fatigue S-N diagram [59]

frequency or certain weak modal shapes are removed entirely [52]. Increasing the stiffness also limits the amplitude of the vibration.

Other approaches which could be utilised should fatigue failure be of concern is the selection of an alternative construction material or alternative treatments of a selected material. Fatigue damage occurs through the initiation and propagation of cracks. If crack initiation can be hindered through surface strengthening the onset of fatigue may be delayed.

## 4 Flow induced vibration

### 4.1 Introduction

Flow- or fluid-induced vibrations (FIVs) are a known concern in the design of many overflow and other hydraulic structures [53]. As implied by the name, the behaviour describes the transfer of energy from fluctuating pressures in a fluid to a structure or system, whose damping and feedback defines its response as dictated by the equation of motion.

Where the mass or stiffness of the structure in question is large enough to provide sufficient inertia to resist large deflections, FIVs are ordinarily not addressed in the hydraulic design process. Generic examples of where such mass or stiffness is sometimes absent, and where significant FIV excitations could be present, is at gated or thin plate overflows and flow through trash racks [60; 61]. Other examples where oscillation of the fluid body itself needs to be addressed are free-fall overflow nappes and standing waves or sloshing in stilling basins [62; 52].

The mass and stiffness of a hydraulic structure, or any structural element, are inversely proportional to its damping ratio as described in Chapter 3. These properties also have an effect on the natural frequencies of the structure as well as on the amplitude of the resultant vibration. Designing a structure to be resistant to vibrations must thus strike a balance between these aspects and should incorporate all available information regarding its natural modes as well as the characteristics of the excitations activating these modes [52]. Thus, should FIV be of concern, its nature or source should be closely assessed to identify alternative methods of controlling undesirable vibrations. The present chapter aims to highlight FIV concepts relevant to PK weirs.

### 4.2 General concept

In general terms fluid-induced vibration requires three elements: an oscillating body, an oscillating fluid and a source of energy or excitation [52]. Oscillations occur when either a fluid or a solid body is acted upon by a restoring force when it is deflected from its equilibrium state. Considering the source of the excitation, three broad categories of FIV have been described [52]:

- **Extraneously-induced excitation (EIE):** Random or periodic external excitations, which are independent of any instability originating from the system in vibration, cause the oscillator to vibrate (e.g. in-stream turbulence from an upstream water body causing the body to respond)
- **Instability-induced excitation (IIE):** Excitation caused by an instability which is caused by the flow system itself, and which is inherent to the flow created by the structure under consideration (e.g. the undulating zone of negative pressure, generated by the shedding of vortices as flow passes around a cylinder, which cause the cylinder to oscillate)

- **Movement-induced excitation (MIE):** Fluctuating forces which arise from the movements of the oscillating body, meaning an initial disturbance in the body instigates a flow field around the disturbed body which then increases or exacerbates the disturbance (e.g. aerofoil flutter or galloping)

The above broad terminology can be used to identify and begin to assess the sources of FIV in a particular system. Once the excitation sources are known, and what flow control conditions are present in order for oscillation to lead to instabilities, corrective measures can be implemented [63]. Generally, most instances of FIV may combine all three excitation sources to some degree, in which case the dominant excitation needs to be identified.

#### 4.2.1 Extraneously-induced excitation

Extraneously-induced excitation, EIE, in engineering flows is usually associated with turbulence [52]. However, vibrations caused by two-phase flows, waves, machine vibrations and earthquakes also fall under this category.

Hinze (1959) defined turbulence in a fluid as “an irregular condition of flow in which the various quantities show a random variation with time and space coordinates, so that statistically distinct average values can be discerned.” [64]. In mathematical terms this means that the three velocity vector components, or the pressure, of any stationary flow can be separated into its mean and its fluctuating portions, as follows:

$$u(t) = \bar{u} + u'(t) \quad (4.2.1)$$

One of the more important characteristics of turbulence is its intensity [65]. The root mean square (RMS) value of the fluctuating component describes the average magnitude of the fluctuations about the mean. The relative turbulent intensity is then obtained by comparing it to the mean flow magnitude as shown in Equation (4.2.2). Typical relative turbulence intensities for rivers range from 5 to 20 % and are generally higher closer to the boundary layer at the base of the channel [65].

$$T_u = \frac{u'_{RMS}}{\bar{u}} = \frac{\sqrt{\overline{u'^2}}}{\bar{u}} \quad (4.2.2)$$

The fluctuating flow values can also be used to determine the turbulent kinetic energy of the flow as follows:

$$k = \frac{1}{2} \left( \overline{u'^2} + \overline{v'^2} + \overline{w'^2} \right) \quad (4.2.3)$$

where  $u$ ,  $v$  and  $w$  are the three velocity vector components in the streamwise, transverse and vertical directions respectively.

Another measure of turbulence is its integral time scale, which describes the size of the eddies which make up an instantaneous flow field [52]. In mathematical terms, it is determined from the autocorrelation function of the time variant velocity signal. Transverse length scales can also be determined by the cross-correlation of two signals some distance apart. At the

mean eddy convection or phase velocity,  $\overline{u_c}$ , an eddy with a size  $L_x$ , will generate fluctuations in velocity and pressure at a frequency equal to:

$$f = \frac{\overline{u_c}}{L_x} \quad (4.2.4)$$

This means that with a range of eddy sizes, the fluctuating flows operate across a spectrum of frequencies. The power spectrum distribution (PSD) or energy spectrum of a flow variable thus describes which frequencies, or which eddy sizes, are the most energetic in a given flow scenario, in much the same way as described in Figure 3.4.

There are certain flow scenarios which result in a large portion of energy being focussed in a narrow band of frequencies. A characteristic frequency can then be identified which is often non-dimensionalised into the so-called *Strouhal* number, as defined in Equation (4.2.5). The Strouhal number can be regarded as the ratio of the speed of the oscillation versus the mean speed of the flow [66].

$$St = \frac{fl}{u_0} \quad (4.2.5)$$

where  $f$  is the frequency in Hz,  $l$  is the reattachment length, and  $u_0$  the free stream velocity. A particular frequency, as reported in literature, is typically presented in the form of  $f = St u_0 / l$ .

The use of the Strouhal number is a valuable analysis tool however it requires the identification of a relevant, and preferably correlated, characteristic length and velocity. These are not always immediately evident as is shown in Section 7.5.3.

The manner in which turbulence, and the pressure forces generated by it, interacts with a structure is highly dependent on the flow scenario, hence no generalised statements regarding the vibration it may cause can be made. However, based on the scenario of a bluff body being buffeted by a turbulent flow, the body will experience drag or inertial forces in a similar fashion to Equation (4.2.1). The magnitude of the fluctuating load is related to the size of the significant eddies and their strength as per their PSD. A fluid-dynamic admittance, or transfer function, thus exists between the fluid velocity and the fluid load on the structure. The larger the turbulent eddy the larger the correlation between the pressure forces at two different locations on the body, and thus the larger the instantaneous resultant loading. The smaller the eddies, the lower the probability that the fluctuating loads at two different locations will correlate [52].

The modal shapes of the structure in relation to the eddy sizes also play a role in turbulence buffeting. Eddies of different sizes may excite different modes and inhibit other modes [52]. This is explored in the case of PKWs in Section 8.2.

In terms of turbulent intensity and kinetic energy, highly energetic flows have been shown to have a limiting influence on the formation of vortices around bluff structures [52]. This is especially relevant to lift forces and to the generation of vortices as described in the next section.

### 4.2.2 Instability-induced excitation

Instability-induced excitations, IIE, in engineering flows are generally related to the presence of free shear layers, phase interfaces or swirling flows. In each of these cases the instability is caused by the fluid system as it flows around or past a structure or obstruction. Key to IIE is the amount and type of control that is exercised on the instability and the presence of any amplification or feedback mechanisms which limit or dictate the oscillations that occur. These mechanisms can be grouped into the following categories [67]:

- **Fluid-dynamic:** The excitation force is a function of the dynamics of the flow only
- **Fluid-elastic:** The excitation force is a function of the flow conditions as well as an elastic resonating structure
- **Fluid-resonant:** The excitation force is a function of the dynamics of the flow as well as a resonating fluid body

In each of these cases there is a transfer of energy from the flow to the instability which then transfers energy back via a feedback loop to the flow. The latter two of the above involve a resonant response in the feedback loop which can lead to a *lock in* of the frequency of the excitation with that of the resonator [52]. When locked-in the feedback loop takes control of the flow field by altering its phase velocity. The resonator dictates the eddy frequency (as per Equation (4.2.4)) which directly affects the excitation forces which then go on to induce a resonant response which in turn controls the flow field, thus closing the feedback loop.

The control or prevention of IIE vibrations is best achieved by alterations to the geometry of the system, its flow dynamics, or both. By changing the geometry, the resultant resonant frequencies should lie outside the range of the excitation frequencies by a limit of at least 40 % [52]. Altering the flow conditions can be done using flow disturbances (e.g. flow splitters), instability inhibitors (e.g. shear layer reattachment in the form of flow guides), among other alternatives. Should neither of these be feasible, positive damping should be added to the system to reduce the amplitudes of vibration.

The phenomena of vortex shedding and phase interface instability are two IIE vibrations which are relevant to Piano Key Weirs. They are expanded upon in Sections 4.3.1 to 4.3.3.

### 4.2.3 Movement-induced excitation

Whereas both EIE and IIE can occur with stationary bodies, movement-induced excitation, MIE, is inherently linked to the movement of a body [52]. It occurs when the acceleration of a body through a fluid changes the fluid state such that its forces on the body result in a transfer of energy to the body (negative damping), thus inducing self-excited vibration.

It is considered unlikely that MIE, or negative damping can occur at PKWs hence, they are not discussed further.

### 4.3 Flow induced vibration sources at PKWs

The main portions of the typical PKW which are potentially susceptible to flow-induced vibrations are the transverse sidewall between the keys as well as the sloping overhangs of the inlet and outlet keys. The slenderness of each of these structural elements exposes them to FIV because of their relative lack of geometric stiffness, mass and damping to perpendicular movement. These weak zones are reflected in the mode shapes that a PKW exhibits (see Section 6.4). The largest amplitudes in the mode shapes occur at the crest centre of the transverse wall as well as the middle of the overhang crests. The spectrum of fluctuating pressures that occur at these locations are thus of interest as these may be able to activate vibrations here.

Three potential sources for flow-induced pressure oscillations and subsequent structural vibration have been identified. Each of these is expanded upon in the sections below. They are:

- Vortex shedding from the separation shear layer which forms as flow enters the inlet key
- The dynamics and sub-atmospheric pressures of the air cavity under the nappe in the outlet key
- The occurrence of oscillations in the overflow nappe

#### 4.3.1 Flow separation and vortex shedding

##### Separation bubble

The standard Type-A PKW shape as originally proposed by Lempérière and Ouamane [6] consists of repeating rectangular keys (see Figure 2.2). The rectangular outlet key acts as a bluff blockage that directs approaching flow toward the inlet key which involves a transition around a sharp 90° corner. As reported in Section 2.4.2, hydraulic studies have determined that some 90% of the flow approaching the PKW enters the inlet key.

Flow around bluff geometric bodies, regardless of its velocity, Reynolds number, or level of turbulence, will cause a transfer of transverse momentum which leads to the formation of a free shear boundary at the edge of the body. Such separated boundary layers do eventually re-attach themselves to a nearby wall some distance downstream. The zone bounded by this free shear layer is known as a separation bubble and consists of a volume of relatively low-velocity and recirculating flow [68].

The phenomenon of massive and local separated flows has been the focus of numerous design studies as well as general academic research for many years. It is of crucial importance in the field of aerodynamics including the engineering design of aerofoils, vehicles and large buildings. They play a key role in the determination of the dynamic forces which are applied to a structure [69]. The complex physical processes which dictate the phenomena are fairly well understood with most behaviours having been described [70]. A thorough understanding of many of these aspects is not required in the present study involving PK weirs, however, a brief review of relevant aspects is described below.

Under turbulent conditions, a typical separation bubble is a highly dynamic and three dimensional phenomenon, however a static, two-dimensional, time-mean depiction is a useful

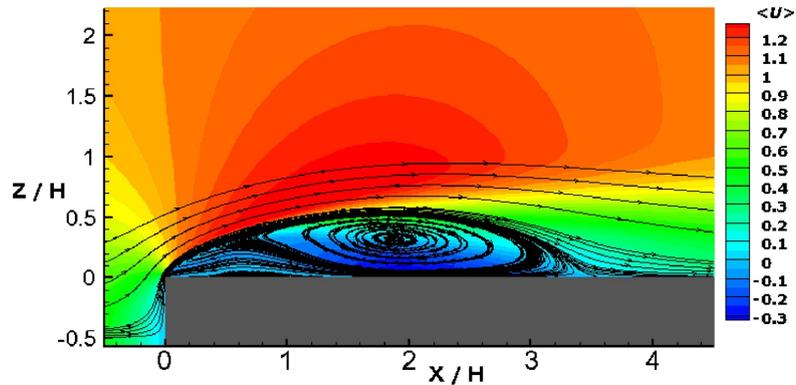


Figure 4.1: Time-mean separation bubble with flow lines and velocity contours [69]

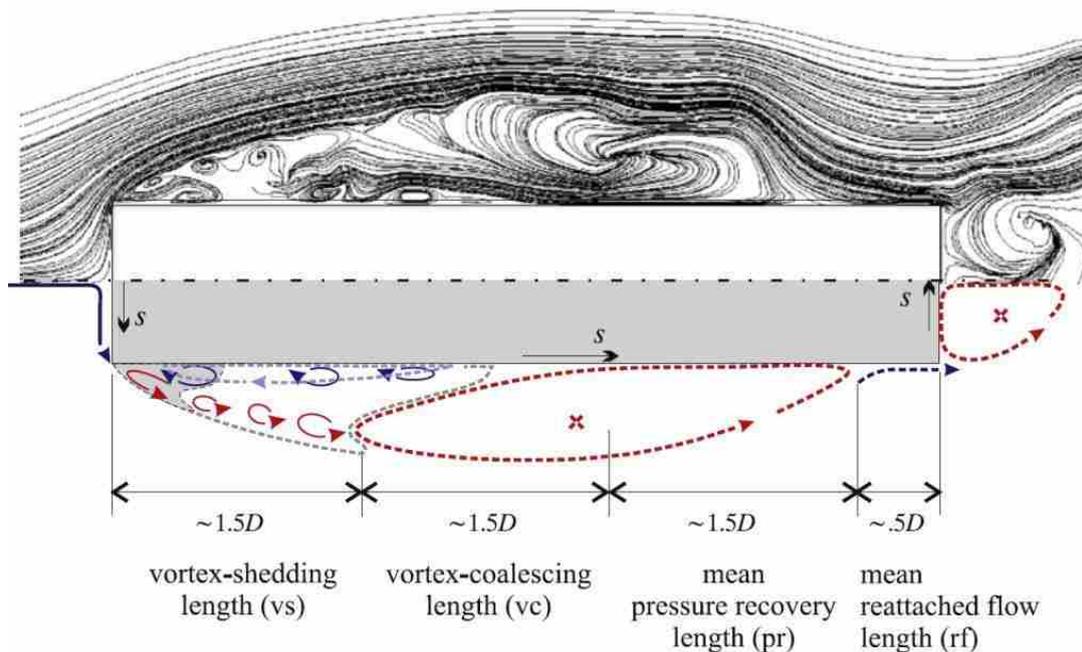


Figure 4.2: Instantaneous snapshot of the flow field showing typical flow structures [71]

descriptor of its properties. Such a 2D time-mean bubble is shown in Figure 4.1 and a snapshot of an instantaneous flow-field of a bubble with indicative flow structures is shown in Figure 4.2.

The basic premise is that the bubble consists of a zone of low-velocity, higher pressure flow which is in contrast to the high-velocity, lower pressure characteristics of the main flow. There exists a relatively narrow boundary between these two zones which has a high velocity- and adverse pressure-gradient across it (see Figure 4.3). This high shear zone, which is also known as a vortex sheet or mixing layer, is typically laminar at or near the point of separation but over time and distance from the separation point, instabilities build up in the boundary leading to its eventual transition to turbulent flow.

The nature of these instabilities depends on the free stream turbulence among other factors. If the free stream turbulence is relatively low ( $<2\%$ ) then the boundary layer breakup is initiated by the Kelvin-Helmholtz (KH) instability. At higher levels of turbulence, buffeting of the main flow begins to destabilise the boundary layer before the KH instability can take effect.

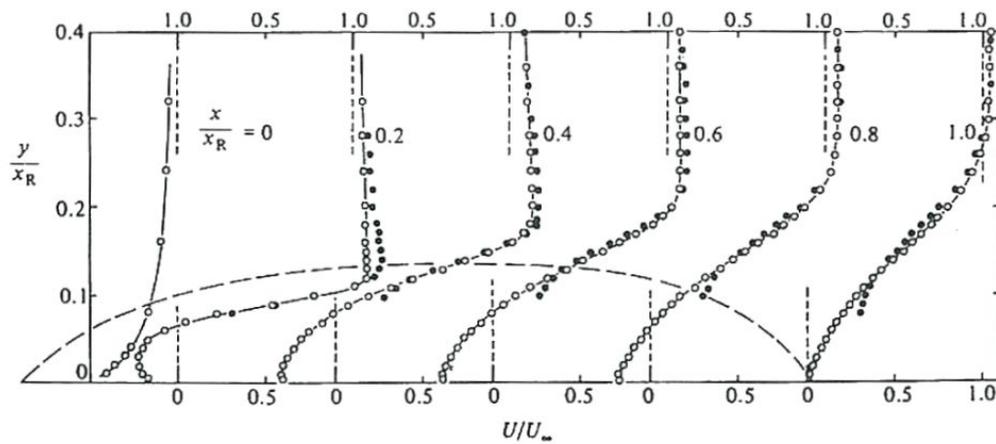


Figure 4.3: Time-mean longitudinal velocity at regular sections in a separation bubble (dashed line shows dividing streamline) [72]

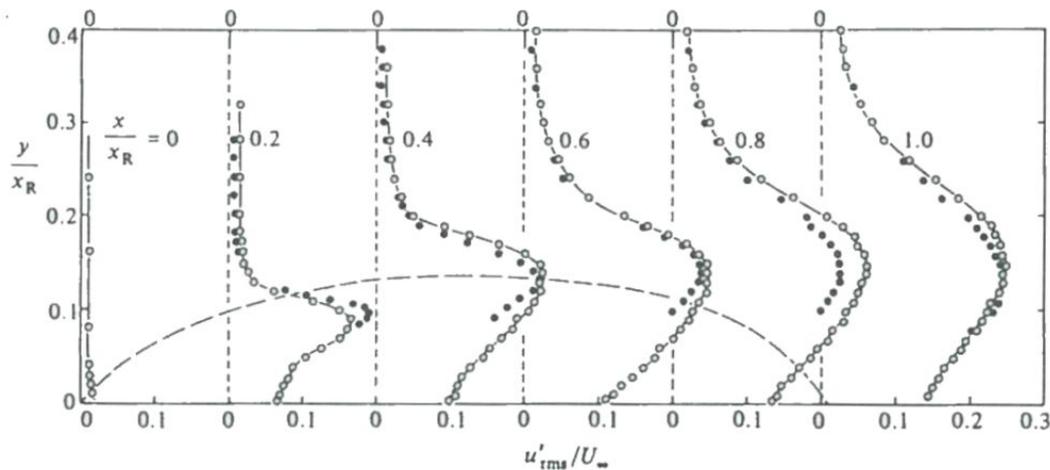


Figure 4.4: RMS of longitudinal velocity at regular sections in a separation bubble (dashed line shows dividing streamline) [72]

The Kelvin-Helmholtz instability occurs when there is a velocity difference between two zones of flow. The intermediate zone between the two is inherently unstable such that any small disturbance or perturbation is amplified by the high velocity gradient. The Tollmien-Schlichting (TS) instability has also been surmised to occur in the destabilisation of boundary layers although this is generally only present in viscous boundary layers attached to or near boundary walls [72; 73].

The breakup of the shear layer occurs when the initial instabilities grow in amplitude. These then begin to distort as they are convected downstream and eventually roll up to form vortices. These are zones of flow which have a rotating structure with a low pressure core. These are shed from the bubble and depending on the nature of the initial instability will form lambda or horseshoe shaped vortices in the zone downstream of the bubble. 3D interaction between these and other disturbances causes the flow to break down into a large number of eddies eventually leading to a fully turbulent flow regime [73].

Research studies report that the size of the bubble plays a role in the size and regularity of these vortices. The main component typically used to specify the bubble size is its reattachment length,  $x_R$  (also denoted as  $l$  in some studies). This is defined differently in various studies, but each definition does result in a similar result. It can be defined as the time-mean location on the wall or boundary where the reverse flow intermittency is equal to 0.5; where the longitudinal velocity is zero or where the shear stress along the wall is zero. Other metrics of the bubble include the time-mean centre of the shear layer,  $y_c$ , defined as the location where  $u'_{RMS}$  is at a local maximum (see Figure 4.4) as well as the time-mean edge of the shear layer,  $y_\delta$ , defined as the location where the local velocity amounts to 99% of the main flow velocity [72].

The reattachment length, as determined by numerous physical and numerical studies, varies around a mean value of  $x_R = 5H$ , where  $H$  is the blockage width. This value is however, dependent on a number of flow parameters such as turbulence intensity and blockage ratio [74; 75; 69]. The reattachment length is typically the characteristic length parameter used to non-dimensionalize the frequency of the vortex shedding in the form of the Strouhal number (see Section 4.2.1).

It is known that flows encountering blunt geometry and that have well-defined separation points, have oscillations at Strouhal numbers that are effectively constant over a large range of turbulence values. In essence this means that the  $St$  value of a particular flow is largely independent of the Reynolds number and that as the free stream velocity increases, so too does the oscillation frequency, since the bubble length decreases with higher turbulence. Only at very small or very large  $Re$  numbers does  $St$  begin to deviate from its normal value [66; 4]. Interestingly, this is not observed in the present study (see Section 7.3.4).

Numerous physical and numerical studies of separated flows in wind tunnels have determined that there is a dominant vortex shedding frequency located at  $0.6 - 0.8 u_0/l$  [70; 72; 76; 77; 78; 79; 80; 81]. The ubiquity of this result has led to it being characterised as an inherent feature of turbulent bubbles. An example of typical wall pressure spectra highlighting this dominant frequency is shown in Figure 4.5. Certain of these studies, though not all, have also identified a lower frequency oscillation at  $0.12 - 0.2 u_0/l$ . This has been termed as a low frequency flapping motion of the shear layer. Its occurrence as well as its cause are still not well understood, although it has been surmised that they only occur when the upstream flow is in the turbulent regime ( $\gg 2\%$ ). It has been described as a gradual growth of the bubble as it absorbs vorticity from the surrounding flow as well as adjacent portions of the bubble alongside. When it has become too large this vorticity is shed as a large vortex leading to the sudden collapse in size of the bubble.

Other studies involving wall boundary flows have implicated the stagnation bubble that can form upstream of the blunt edge [82]. These also grow over time, especially when an ephemeral zone of marginally lower velocity flow approaches the blunt geometry from the upstream water body. When this is then followed by a zone of higher velocity the bubble collapses and causes the stagnant flow to spill over the edge, merging with the separation bubble there, also causing it to collapse. The flapping motion is thus linked to the turbulent motion of the approaching flow.

The level of turbulence has also been implicated in the type of vortices which are shed

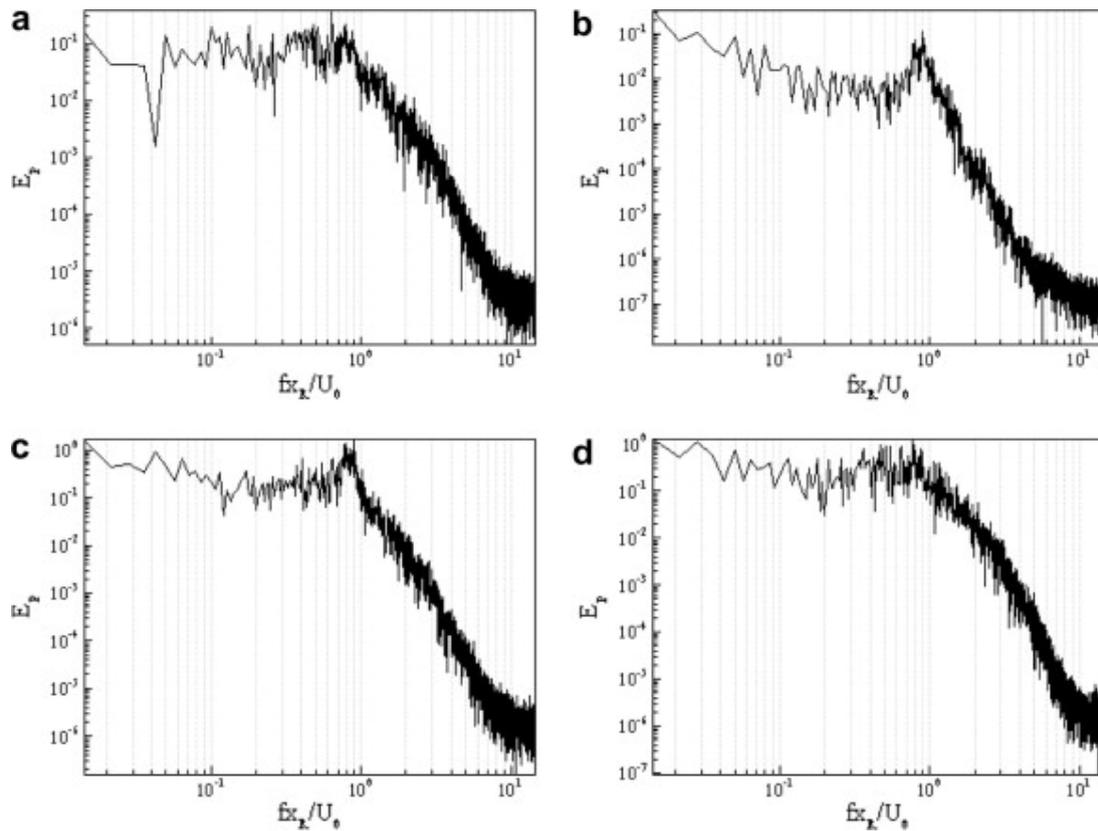


Figure 4.5: Pressure spectra at  $x/x_R = 1$ , (a)  $y = y/x_R = 0.01$ , (b)  $y = y/x_R = 0.05$ . (c)  $y = y/x_R = 0.13$ , (d)  $y = y/x_R = 0.2$  [80]

from the bubble. In cases where there is a lack of turbulence, the KH instability is active in the transition process which breaks up the vortex sheet. As the largely two-dimensional KH vortex rolls move downstream they can evolve into  $\Lambda$ - and horseshoe-shaped vortices among other shapes. In more turbulent flow regimes, the KH instability is bypassed by the turbulence's perturbations. The vortex sheet decays into a much more chaotic three dimensional set of vortices. A typical vortex breakup in the turbulent regime is shown in Figure 4.6.

An additional impact of higher intensity turbulence is that it causes an earlier breakup of the shear layer thereby creating a smaller separation bubble. It is notable that the turbulence length scale appears not to have an effect on bubble size [74; 75]. The turbulent intensity has a direct impact on the distance, away from the wall, that the shear layer can attain, which affects the size of the vortices that are generated by it. The length scale of these vortices is thus reduced.

Another factor which has a significant effect on the size, shape and strength of the bubble (and thus the vortices which get shed from it) is the shape of the leading edge. Most studies into separated shear layers focus on sharp ( $90^\circ$ ) leading edges as these provide a defined separation point. Decreasing the angle of separation at the leading edge by incorporating triangular or rounded profiles results in smaller, shorter separation bubbles. However, the vortex shedding frequency increased for these smoother profiles. This has been shown to be caused by the higher mean velocities outside of the recirculation region which are associated with smaller bubbles [44]. The fluctuations are however less energetic with smaller bubbles [83].

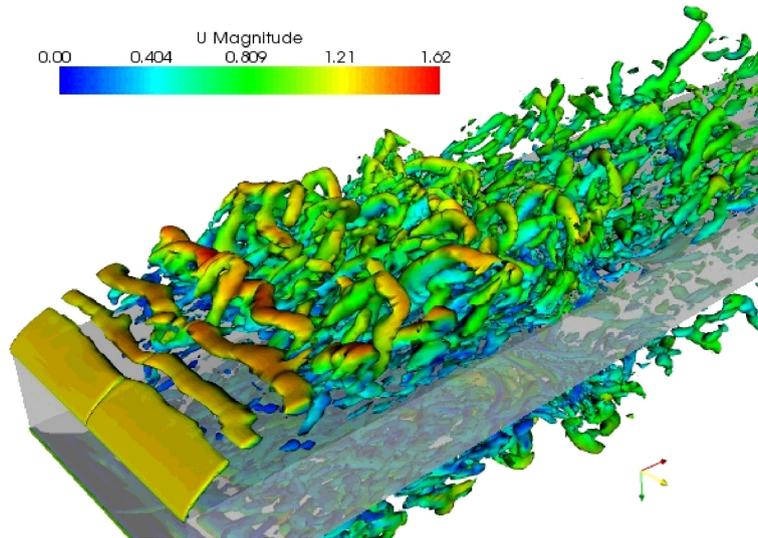


Figure 4.6: Snapshot of a vortex sheet showing breakup of a separation bubble [69]

### Pressure undulations

There is a direct link between the presence of a vortex in the vicinity of a point on a boundary wall and the pressure experienced at that point. Although pressure is not a local quantity as it is influenced by the entire flow field, far-field contributions reduce rapidly as the distance to them increases. Several physical studies have determined that there is a coherent link between the two flow quantities in the region around a separation bubble [84].

Initial studies, focussing on the problem in a two-dimensional framework, determined that large scale vortices, both within the bubble and downstream of it, are associated with localised pressure minimums on the boundary wall. Pressure maximums tend to occur between the passage of two vortices. It was surmised that negative pressures occurred when fluid was pulled away from the wall and positive pressure occurred when fluid flowed toward it [72; 84].

The shed vortices continue to exert an influence on the wall for long distances downstream. Even though the flow downstream of the reattachment point rapidly (within  $3x_R$ ) develops into a new turbulent boundary layer, it remains distinctly different to normal *canonical* boundary layer flows due to these shed vortices. The downstream boundary layer exhibits the expected log-law velocity profile, however, the large scale vortices shed by the free mixing layer continue to alter the turbulence structure for long distances downstream of reattachment ( $> 20x_R$ ) [85].

Physical studies determined that vortices and the pressures they induce are a transient three-dimensional phenomenon. A prime example of this is typical hairpin (or horseshoe) vortices which have two legs of counter-rotating flow that pull flow away from the wall. This creates a localised zone of negative pressure, which follows the vortex as it is convected downstream [84]. The speed at which vortices move downstream, their convection velocity, has been estimated at  $u_c \approx 0.7u_0$  or lower [86; 87]. Although  $u_c$  is largely constant in the region directly behind the separated region, it does exhibit a small decreasing tendency as the velocity profile of the boundary reestablishes itself. The gradual decrease in the peak frequency of the pressure spectra as the distance from the reattachment point increases, has been ascribed to this [86].

Numerical models have enabled vortex behaviour to be studied in much greater detail.

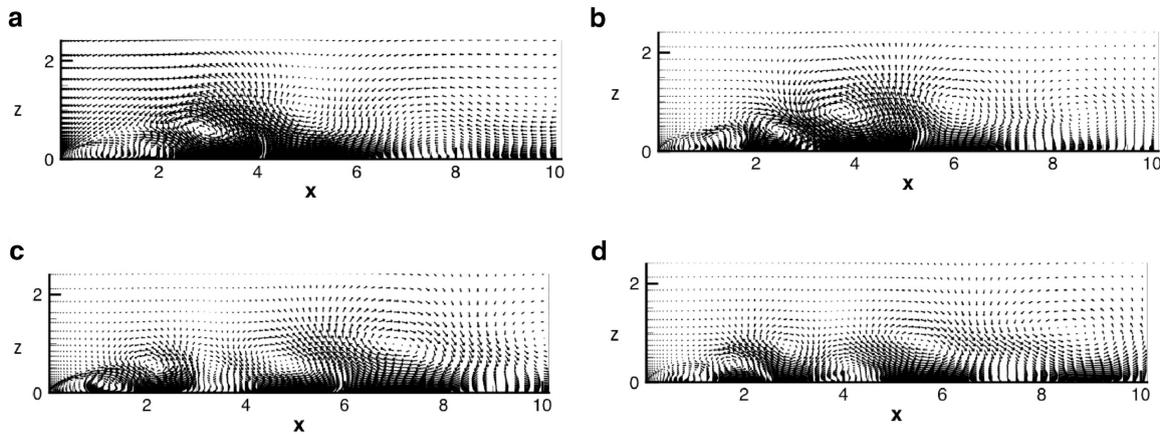


Figure 4.7: Pressure-duced velocity modes [69]

This has advanced to the degree that the flow field buffeting a wall can be mathematically derived from wall-pressure measurements with a fair level of accuracy. The main flow structure components contributing to the pressure undulations can thus be identified. These data have supported previous findings that the largest pressure undulations on the wall are experienced just upstream of the mean reattachment point, and that these are typically caused by hairpin shaped structures [88; 81].

A technique called Proper Orthogonal Decomposition (POD) has also been applied to the phenomenon. It allows a time variant flow field, with any number of its parameters (including velocity and pressure) to be decomposed into dominant modes in much the same way that a structural vibration is decomposed into its component modal shapes (see Section 3.3). Figure 4.7 shows the results of such an analysis on a separated shear layer. It depicts the first four extended POD modes of the wall-pressure-duced velocities which represent those velocity modes that were identified by the POD technique as being dominant in their correlation (and thus possibly their causation) to the pressures being experienced at the wall.

A number of aspects can be noted from Figure 4.7 [69]

- The first two modes (a and b) are nearly identical as are the subsequent pair (c and d). This is because both of these modes are transient and a pair of modes is required to describe their transient nature.
- The dominant first pair of modes show a strong vortex above the reattachment point at  $x = 3$ . This vortex grows in size as it is convected downstream as indicated by the interplay between modes (a) and (b). This pair of modes has been correlated with the vortex shedding behaviour of the bubble.
- The second pair of modes show a vortex inside the recirculating region as well as another just downstream of it. These also grow as they convect downstream. This pair of modes has been correlated with the flapping behaviour of the separated shear layer.
- Both sets of vortices occur at an elevation of approximately  $0.5H$  above the boundary wall (where  $H$  is the width of the blunt obstruction). Other vortices occur at higher eleva-

tions, but since these have a more limited influence on the wall pressures, these are only encapsulated in higher order, less influential, modes (not shown here).

It has thus been surmised that the smaller vortices presented in Figure 4.7, i.e. those that dominate the pressure fluctuations, are not the large-scale vortices which make up the separation bubble. This is because these large vortices carry a relatively low proportion of the total flow energy, despite their size. The fluctuating velocities and the pressures they cause are dominated by smaller scale 3D structures which obtain their kinetic energy via transfers from the larger vortices [81]. It is these smaller 3D vortices that are visible in the first few modes in Figure 4.7. That said, the large scale shed vortices still have a correlated influence on the wall pressures downstream of the reattachment point, albeit to a lesser degree than other sources [86].

The large vortices shed from the bubble lose their intensity as they transfer their energy to the smaller vortices. As they move farther downstream of the separation region, they grow in size while steadily moving farther away from the wall boundary and so increasing their convection velocity until eventually they decay entirely into free stream turbulence [81]. The three dimensional nature of the flow field around a PKW, however, does not allow these large vortices to decay in this fashion. Instead of continuing downstream the streamlines direct flow, and the large vortices inside it, toward the sidewall crest. Being in the near-field vicinity of the wall, the large vortices can once again influence the wall-pressures. This is described in greater detail in Section 7.4.3.

In addition to the above behavioural description, the following relevant trends have also been noted in literature:

- Free stream turbulence in the approach flow has an effect on the pressure fluctuations in the separation bubble. High turbulence intensity leads to a reduced reattachment length with a lower mean pressure. Pressure fluctuations, however, increase with increased turbulence. Other periodic velocity perturbations, such as sound, also have similar effects [87; 89; 69].
- The turbulent length scale of the approaching flow has little influence on the reattachment length or mean pressure. Larger length scales do, however, lead to larger pressure fluctuations [87].
- A larger blockage ratio has an increasing effect on both the mean and the fluctuating pressures in the separation bubble [87].

The nature in which these pressure fluctuations can lead to structural vibrations is expanded upon in the next section.

### **Fluid induced vibration**

Fluid induced vibration (FIV) in the case of the excitations imposed on the upstream face of a PKW amount to vortex induced vibration (VIV). This is where a structure is receiving energy from a system of vortices which are caused by the movement of the fluid past the structure.

The transfer of energy takes the form of an alternating pressure field which induces both lift and drag forces [53]. The force which is most of concern at PKWs is the lift force since the slenderness of the sidewall exposes it to such forces. The drag force on the other hand is readily resisted by the rigid and stiff nature of the structure.

The lift force arises out of the oscillating pressure field which in turn stems from the velocity field in the near vicinity of the wall. The manner in which the structure responds to the forces depends on the surface distribution of the pressure force, its magnitude, its frequency and its spatial relation with other pressure forces on the wall. The correlation between these aspects determines if any of the modes of the structure would be excited. The forces may occur at one of the natural frequencies of the structure but if their spatial extent is such that they prevent or resist the mode shape at that frequency from moving, the resultant response will be limited.

Any force, at any frequency will cause a structure to respond. The magnitude of this response will be dictated by the natural frequencies and modal shapes of the structure. Should the vortex shedding frequency, or that of the pressure fluctuations they cause, approach one of the natural frequencies of the structure, there is the potential for synchronisation to take place. This is where the forces generated by the flow operate at a frequency at which the structure is at its weakest causing it to respond with large amplitude vibrations. There is also the phenomenon of *lock-in* to consider, where the excitation frequency does not need to match the modal frequency of the structure exactly. Should the excitation frequency get within a certain range of a natural mode, the movements of the structure in this mode will interact with the excitation pressures and induce the excitation to meet this frequency, again leading to large amplitude vibrations [53].

It is noted that the excitation forces are likely to occur along a broad range of frequencies instead of a focussed band. Should one of the modes of the structure lie in this range then the vibration response at this frequency will be a great deal higher than those in the remainder of the spectrum as was described in Figure 3.4. That said, if the excitation is of low magnitude at this frequency, so too will the response. It will then stand out as a low peak above the remainder of the vibration signal.

Another factor that will dictate the amplitude of the fluid induced vibration response is the amount of damping or added mass that the fluid imposes on the structure. The damping will reduce the amplitudes of the vibration response and the added mass will adjust the frequencies. In addition to the influence of damping and added mass, the mass ratio between the structure and the fluid (or more precisely, the mass of the volume of fluid displaced by the vibration) is also of key importance. This effect occurs over and above the damping effect. The lower the mass ratio the larger the vibration response [53]. The current study focussed on steel as a construction material but it would be interesting to note the vibration response of other materials, such as PVC, HDPE or wood.

### 4.3.2 Sub-atmospheric pressures

The development of sub-atmospheric pressures underneath an overflow nappe is known to occur at a number of hydraulic structures including flap gates and labyrinth weirs [7]. These may

lead to the depression of the overflow nappe sometimes inducing it to cling to the downstream side of the wall and potentially causing it to beat or oscillate.

At labyrinth weirs specifically, the aeration characteristics of the underside of the nappe under large flow conditions can result in large spatial and temporal fluctuations of the nappe cavity [90]. As a result, they can affect the discharge capacity of the weir and lead to nappe instabilities which can cause changes to the static and dynamic forces on the wall [7]. Artificial aeration of the nappe does reportedly assist in minimising nappe instability but does not prevent them altogether [91].

It has been found that the flow over PKWs is self-aerating to a large degree and that the air demand under the nappe is lower than that at other hydraulic structures such as flap gates [92]. That said, almost all PKWs that have been built to date have some form of artificial aeration network. Despite this aeration however, at high flow the nappe cavity underneath the nappe does become unstable and moves away downstream which would affect the pressures on the downstream side of the wall in unique ways [35].

### 4.3.3 Nappe oscillation

Nappe oscillation refers to the phenomenon where the shape of the overflow nappe becomes unstable and starts to oscillate [93; 62]. There are several potential causes for this phenomenon, some of which are related to the pressure differential between the air pocket underneath the nappe and the atmosphere above it, surface tension effects, or boundary layer development at the crest [94]. It appears that a feedback mechanism related to the aeration of the nappe as mentioned in the previous section can drive this effect. However, there are instances where nappe instabilities have been noted at fully aerated nappes [62; 95; 94], which is why it has been listed as a separate vibration source. Recent studies have confirmed that the presence of confined air behind the nappe does not alter the onset of nappe vibration but that it does act as an amplification and stabilising factor [94].

It should be noted that the main region interest or influence on the oscillations of the nappe is not the impact of these oscillations on the downstream water body but rather the oscillations themselves and their interaction with the surrounding air. The fluctuating interaction creates sound waves which are then able to transfer their energy to, and possibly induce vibrations in, structures which are distant from the source. Crookston *et al.* [62] noted an interesting case where nappe vibrations at a recently constructed labyrinth weir caused vibrations in a nearby residence some 50 m distant.

It is known from recent characteristic studies of these oscillations that they are related to the number of wavelengths present in the length of the falling nappe [94]. The occurrence of nappe oscillation is thus dependent on the fall height of the nappe. Given that the fall height at a PKW changes depending on the location in the outlet key, it may occur that different sections of the outlet key nappe become exposed to different wavelengths or frequencies depending on its fall height. It is feasible that this may induce a range of frequencies which could be wide enough to encompass at least one natural frequency of the sidewall. This possibility is noted but has been excluded from the present study but is recommended for future investigation.

## 4.4 Fluid structure interaction

Fluid structure interaction (FSI) is where the movement of a structure within a fluid has an effect on the behaviour of the fluid which in turn has an effect on the movement of the structure. There is an exchange of mechanical energy between the two systems. The deformations of a structure would modify the boundary conditions of the flow, which would alter the flow such that it induces a change in the forces that act on the structure causing it to change its deformations, thus closing the interaction loop [96; 97].

It should be noted that the coupling between fluid flow and structural motion does not need to be an active process. The concept of added mass is a good example where the natural modes of vibration of a structure is resisted by the volume of fluid around it. The interaction between the stagnant body of water and the structure results in lowering the natural frequency. This system would be classified as weakly coupled since the effect of one of the systems dominates the other.

This dominance can be predicted by examining the *Mass* and *Cauchy* numbers as well as the *Reduced Velocity*. The *Mass number* is defined as the proportion of the density of the fluid to that of the structure. The heavier the fluid, the larger the *Mass number* and the larger the inertial effects of the fluid on the interaction. The *Cauchy number* relates the dynamic pressure of the flow to the elasticity of the structure (see Table 5.2). It reveals how susceptible the structure is to the fluid forces upon it. Very small *Cauchy numbers* indicate very stiff structures resulting in small deformations such that they may be ignored in the analysis altogether. The *Reduced Velocity* refers to the ratio of the characteristic flow velocity of the fluid and the velocity of wave propagation in the structure. A large *Reduced Velocity* value implies that the fluid dominates the system and that the time dynamics of the structure are not important [96].

Simple systems where one medium is clearly more important than the other, or where there is a limited exchange of energy between the two, allows analytical, acoustic or decoupled models to be used in their analysis. Strongly coupled systems however require the system integration to be coupled [96; 97]. When the system comprises a moving fluid and thin structural members susceptible to deformation, as is the case for PKWs, then both the fluid and structural systems need to be assessed in a coupled fashion. The nature of this coupling is discussed in more detail in Section 5.3.3.

Coupling of the unsteady fluid flow and structural motion of the PKW can manifest in a number of FSI behaviours. The phenomenon of added mass and damping, mentioned above, is a form of FSI. The vibration movement of a PKW sidewall will also have a dynamic effect on the shape of the nappe which may lead to pressure fluctuations in the air cavity under the nappe which in turn may affect the vibration of the wall. Another potential FSI aspect, mentioned previously, is the possibility of lock-in where the fluid induced vibrations of the wall lead to changes in the vortex formation and transmission process and alter the frequencies of the vortices closer to one of the natural modes of the structure. The precise FSI mechanism of such a lock-in is not immediately evident, hence its occurrence is considered unlikely. That said, it is known that acoustic pressure signals are able to influence the rate at which vortices are shed from a separated shear layer thus its occurrence cannot be discounted altogether [98].

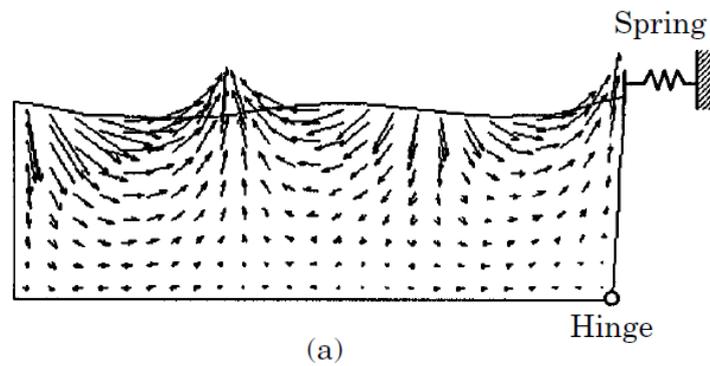


Figure 4.8: Sloshing of water body behind vibrating weir [99]

The pressures induced in the inlet key water body by the vibrating sidewall and their wave-type propagation away from the wall infers that sloshing and bulging may occur under the right conditions. The potential for this is emulated in Figure 4.8. In this system there is a body of water held back by a fixed plate weir with a hinge allowing it to oscillate. The arrows show the velocity vectors in the flow field which indicate a system of waves emanating from the oscillating wall. In this system these waves strike the opposite wall and reflect back. In the case of a PKW inlet key however, there is another oscillating weir which is being vibrated by a similar set of excitations. It is unclear how the opposite wall will react to being excited by these waves nor how the waves from each wall will react with each other.

## 5 Experimental investigation of PKW behaviour

### 5.1 Research design

The behaviour being investigated experimentally involves possible, flow-induced, vibrations in the sidewall of a PKW. The focus of the research programme that was established was thus placed on the sources of these vibrations within the fluid body and then how these sources translate into the oscillating forces which act on the wall. As described in the previous section, these sources include vortices which are periodically shed from the upstream flow boundary separation, the unstable movement of the nappe bubble's apex as well as oscillations of the nappe itself.

The study of this complex behaviour was approached from an experimental perspective, incorporating both physical and numerical modelling. This approach is supported by general practice recommendations, which state that even though the developed PKW design equations are useful conceptual design tools (also see Appendix A), they are only applicable within the parameters within which they were validated [100; 30]. Proposed applications outside of these parameters should thus be investigated in greater detail using physical or numerical models, or preferably both [3; 101; 102]. To date, almost all large scale PKW installations have been validated and optimized with physical models [102].

A series of scaled physical models was designed and constructed to enable the capture of appropriate experimental data with which to calibrate a numerical model. The flexible nature of the calibrated numerical model enables it to then be used to extrapolate or extend the behavioural trends observed in the physical model as well as establish other trends which could not explicitly be studied in the physical model. Details of each of the models, their design and construction, the data capture and analysis methodology as well as notable limitations in the experiment design are given in the sections below.

The main variables which need to be measured in the experiments are the velocity vector field of the flow, the static and dynamic pressures both in the fluid body and those acting on the sidewall, as well as the movement response of the wall itself. Furthermore, additional parameters such as depth, discharge and water surface profiles were also noted for calibration purposes. It is worthwhile noting that each of these variables are directly dependent upon each other and that, as a consequence, the synchronous collection of the different streams of data also plays a key role.

Special cognisance was taken of experimental error, especially in regards to extraneous background noise which could affect or conceal observed phenomena. This was chiefly addressed via the repetition of experiments at different times and the careful recording of observed background events while data capturing was taking place. Inherent errors in the data capturing instruments themselves, via the physics of their operation, was taken note of and incorporated in the interpretation of the data.

Due to their inherent structural stability, their repetitive geometry and the fact that the majority of the PKW prototypes implemented to date incorporate both upstream and downstream overhangs [43; 15], the present research study has focussed solely on type-A PKWs. Certain of the research findings are applicable to all PKW types (i.e. the flow dynamics of the inlet key) but other aspects (such as the modal shapes) are only applicable to type-A PKWs.

## 5.2 Physical modelling

Physical modelling of hydraulic structures allows for the scaled reproduction of hydrodynamic flow fields incorporating almost every complexity present in their prototypes. This is especially important where the coupling of multiple unknown factors may be at play [4]. In a controlled environment it enables both qualitative as well as quantitative analyses to be made [102]. The scaled nature of the models does present unique challenges but their ability to model all aspects of the physics of a flow (especially those which are too difficult or too time consuming to model numerically) makes them invaluable.

Due to the nature of the phenomena under study, a hydroelastic model approach was followed. Two models were built, with the first focussing on the hydrodynamics and the second on the fully hydroelastic behaviour of the PKW. The first model is rigid such that structural motion will not affect the hydrodynamic forces and thus examines the phenomena from an external (EIE) and an instability (IIE) excitation perspective (see Chapter 4). The second model is continuously elastic such that the potential for coupling between the hydrodynamic forces and the structural vibrations can be examined [4]. The aim is thus to check how the lowest resonance frequencies in the structure relate to the dominant turbulent flow frequencies [103].

### 5.2.1 Hydraulic laboratory

The physical modelling for the study was undertaken at the Hydraulics Laboratory of the Department of Civil Engineering at the Stellenbosch University, South Africa. A 20 m long, 1.5 m wide flume, fed by a 600 mm diameter inflow pipe was dedicated to the study. Flows up to a maximum of 750 l/s were discharged into the upstream stilling basin, passed through a set of flow stabilizers and further steadied by the length of the flume up to the scaled model which was installed near the downstream end of the flume. Downstream of the model weir, flow was discharged into a sub-floor sump leading to the laboratory's pump set for return to the upstream end of the flume.

The flume length was selected to ensure that the flow patterns approaching the model were fully established and contained no latent effects of the inlet arrangement. The approach and the model's location on the floor of the flume represents the PKW as an in-channel application as opposed to an in-reservoir application. The brick walls are mortar lined and the floor is concrete.

The flume, its layout, and the location of the model within it are shown in Figure 5.1. Photos of the flume are shown in Figures 5.2 and 5.3. More detailed photographs of the flume are presented in Appendix B.

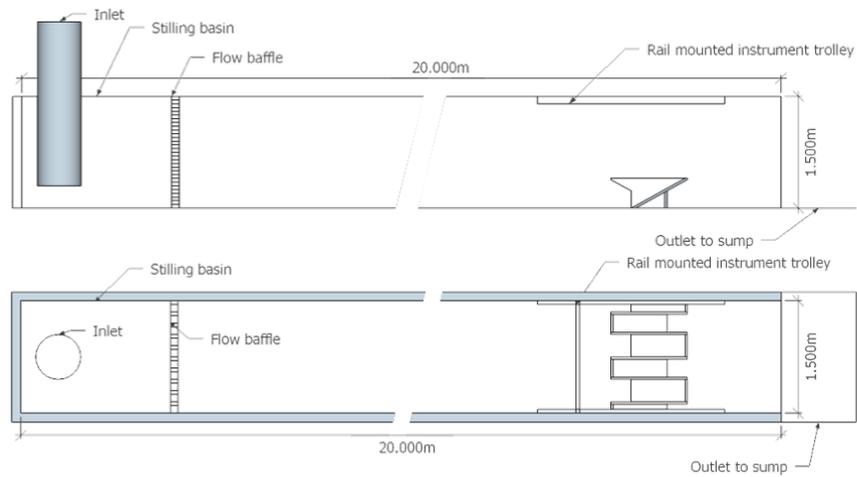


Figure 5.1: Diagram of experimental flume: side and top view



Figure 5.2: Overall view of flume



Figure 5.3: Upstream view of flume

### 5.2.2 PKW models

The two physical models were designed and in turn installed in the flume. Both represent a standard Type A PKW (Section 2.5.1) with the main dimension proportions adhering to those proposed by ICOLD [25]. Some of the dimensions, notably around the crest as well as the inlet and outlet key width deviated from these dimension proportions (see Section 2.3) so as to make them more convenient for installation inside the 1.5 m flume width. The main difference between the two models are their scale as well as their construction material. Note that the two models represent slightly different though broadly similar prototypes. Relevant parameters of each model are summarised in Table 5.1 and expanded upon in the sections below.

Table 5.1: Physical model parameters

Parameter	Model A	Model B
Model scale	7.50	2.73
Material	Wood (pine)	Structural steel
Weir height, $P_i, P_o$ [m]	0.40	1.10
Inlet key width, $W_i$ [m]	0.30	0.72
Outlet key width, $W_o$ [m]	0.24	0.72
Key width ratio, $W_i/W_o$ [–]	1.25	1.00
Crest thickness, $T_s$ [m]	0.03	0.006
Base length, $B_b$ [m]	0.48	1.32
Overhang length, $B_i, B_o$ [m]	0.27	0.66
Units, $\frac{1}{2}$ cycle [ $No$ ]	5	2

#### Model A

Model A was designed to investigate the hydrodynamic processes that occur in the vicinity of a PKW, in particular the patterns of turbulence around the structure. It was thus built from 30 mm thick wood panels (coated with alkali and acid resistant paint) which can be considered sufficiently rigid such that any vibrations that do occur in the structure would not affect the hydrodynamics of the flow. The design schematics are shown in Appendix B.2.

The scale of the model was selected such that a sufficient band of frequencies can be generated by the model fluid, but still be practical from a measurement and construction perspective. It is known that scaled versions of prototypes may have a limited ability to generate certain high frequency oscillations [5; 4]. This means that the scale should be as large as possible if high frequency oscillations are of concern. However, the reach of certain of the instruments is limited (see Section 5.2.3), hence, in order for them to be able to observe the whole flow field, a realistic limit had to be placed on the depth of the water column upstream of the scaled PKW. This resulted in a weir height of 0.4 m with an overflow depth in the order of 0.3 m at the maximum discharge.



Figure 5.4: Model A - rectangular nose



Figure 5.5: Model A showing pressure ports

At the selected scale and dimensions, the model has 5 units comprising of two whole inlet and outlet keys and one half inlet and outlet key at either side. By focussing the majority of the readings on the central inlet and outlet key, any effects the walls of the flume have on the flow regime are minimized.

The main measurements in Model A included the recording of :

- time variant water pressure on the sidewall and sloping base of the PKW
- time variant and average velocity vectors in the inlet key
- time variant air and water pressures in the outlet key
- water surface elevations both upstream of and at the PKW

Details of the testing procedures are presented in Appendix B.

In addition to the default PKW, two alternative scenarios were tested where the blunt rectangular face of the underside of the outlet key was replaced by a triangular or a circular protrusion or nose. The presence of a nose smooths the transition of flow around the inlet key entrance and these two scenarios examine to what degree this is beneficial. Photos of model A together with the two upstream nose alternatives are shown in Figures 5.4 to 5.7

Further to the above scenarios the model was reinstalled into the flume after experiments using model B were completed. This was done to repeat certain of the experiments but also to allow for the inclusion of a set of aeration pipes inside the PKW. These air pipes required the model to be installed at a slightly higher elevation than the previous one (12 cm off the floor of the flume instead of 7 cm for the previous one). Photos and further details are provided in Appendix B.

### Model B

Model B consisted of a thin walled steel PKW with the aim to investigate the vibrations in the sidewall. It is expected that typical concrete PKWs would have sufficient stiffness values to resist significant vibrations. However, steel PKWs, due to their limited thickness may be prone to such vibrations.



Figure 5.6: Model A - circular nose



Figure 5.7: Model A - triangular nose

The model was scaled to be as large as possible to allow for the elastic behaviour of the material to mimic the prototype behaviour as much as possible, but still fit inside the laboratory flume. The selected scale, 2.73, resulted in a model with one full inlet key and one full outlet key of equal width and a weir height of 1.1 m. It was decided to construct a full inlet and outlet key such that the bending behaviour exhibited by the central sidewall would not be influenced by the attachment arrangement at the flume walls. Had only a half inlet and half outlet key been installed, these end points would have had to be braced thus limiting their degree of freedom in vibration. This would have led to the movement of the sidewall being affected, making it appear stiffer than it should be. Refer to Sections 6.4 and 6.5.

The configuration of the model has the consequence that the outermost sidewalls are in contact with the walls of the flume and thus cannot pass flow. This would then result in an incorrect head-discharge relationship which was corrected by limiting all flow to the central portion of the flume. This was achieved via the installation of flow guides in the flume which limited flow to the central halves of the inlet and outlet keys. This can be seen in Figures 5.8 and 5.9.

The main measurements in model B included the recording of:

- the modal shapes and frequencies of the sidewall when empty, half full, full and overfull
- the time variant vibrations of the sidewall under flow
- time variant and average velocity vectors in the inlet key
- time variant air pressures in the outlet key
- water surface elevations both upstream of and at the PKW

### 5.2.3 Instrumentation

The physical models were utilized to make recordings of the following data:

- **Flow rate:** A range of flows was utilized and its effect on the other variables noted. A SAFMAG electromagnetic flow meter fitted on the main 600 mm diameter inlet pipe was used for this purpose. The flow rate was controlled via a 600 mm diameter gate valve.

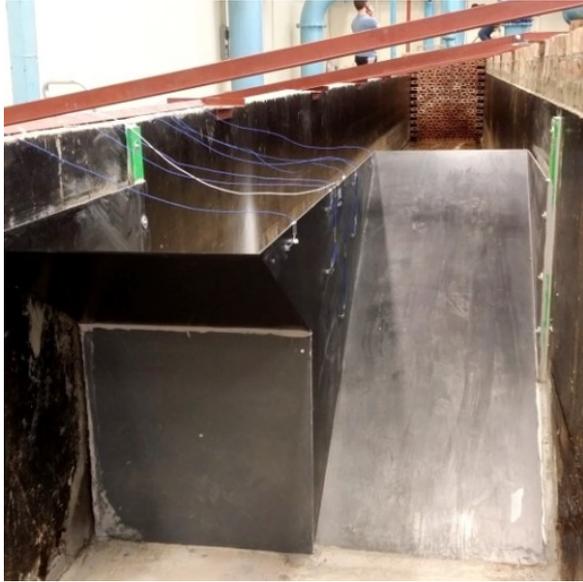


Figure 5.8: Model B with accelerometers



Figure 5.9: Model B with flow guides

- Water level:** Water surface elevations a short distance upstream of the weir as well as halfway along the flume were logged for each discharge. This was achieved using a trolley mounted vertically suspended point gauge. An estimate of the velocity head was also made via the installation of a 20 mm diameter pitot tube on the floor of the flume facing in the upstream direction. This pipe, which extended to the outside of the flume, allowed for direct comparison of the water levels measured by the point gauge midway along the flume.
- Velocity vectors:** Instantaneous three-dimensional velocity vectors were measured using a trolley mounted Nortek Vectrino Acoustic Doppler Velocimeter (ADV). Data were logged at a rate of 200 Hz using a down looking probe with 4 sensor heads arranged equidistantly around a central acoustic emitter. Readings were taken in a pre-set grid pattern covering horizontal, vertical and transverse cross sections of the inlet key. The maximum depth at which readings could be taken was 250 mm, since the instrument housing was not sufficiently waterproof to allow deeper measurements. The minimum distance to the sidewall was 25 mm due to the dimensions of the sensor head. Data were cleaned, despiked and processed using the procedure described in Appendix B. No simultaneous measurements could be taken, however, recording and subsequent analysis of the time variant signals allowed for the estimation of averaged flow descriptors of the flow field as a whole. These include turbulence intensity, kinetic energy, Reynolds stresses and intermittency, among others. These are expanded upon in Chapter 7.
- Pressure:** Water and air pressures were recorded at a fixed set of 18 points using pre-installed tubes or conduits in the wooden walls of the model (internal diameter of 5 mm). Their installation can be seen in Appendix B. The locations of these on the inlet key sidewall are shown in Figure 5.10. Each of these tubes was primed before data capturing to form a pneumatic circuit and their ends fitted with a WIKA S-10 pressure transmitter

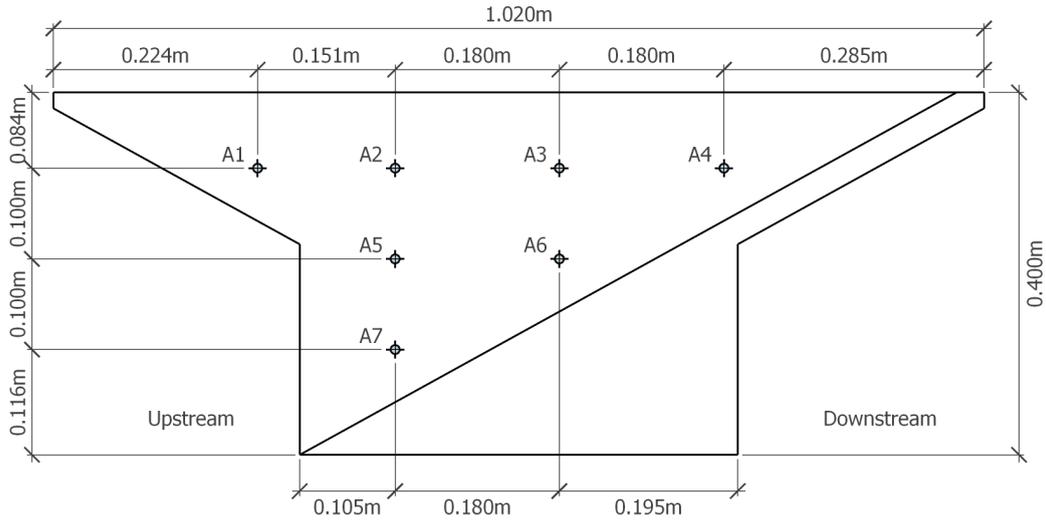


Figure 5.10: Model A - Pressure point positions

which logged the pressure in the pipe at a frequency of 1000 Hz.

Simultaneous measurements were taken to determine how low and high pressure zones moved downstream in the inlet key. Data were statistically analysed to reflect the behaviour of the vortices which cause the pressure oscillations.

The steel model was not fitted with pressure sensors. The small pressure conduits would have been excessively prone to external disturbances if they had been installed. Furthermore, the recorded pressures would have been tainted by the movement of the wall and would not reflect the true hydrodynamic pressures.

- **Vibrations:** Structural vibrations were measured on the steel model B first using a grid of 7 PCB 333B32 accelerometers and by a half-bridge strain gauge. The accelerometers were used to determine the modal shape of the structure and its natural frequencies but could not be used under flow conditions as the sensors could not be rendered waterproof. The strain gauge, located in the middle and top of the PKW sidewall, was used to monitor vibrations in the wall under full flow conditions. The sensor locations are shown in Figure 5.11 and further details of these configurations are provided in Appendix B. No vibrations were logged on model A due to its stiff nature.

Careful cognisance had to be taken of the location of each of the individual readings of the various sensors such that they could be correlated to one another. In addition to this, the orientation of these sensor coordinates was key to defining aspects such as vector direction and rotation. The convention used in this research study follows the right hand rule where:

- flow downstream is positive
- flow upward is positive
- flow to the left (looking downstream) is positive
- in each of these directions, clockwise rotation is positive

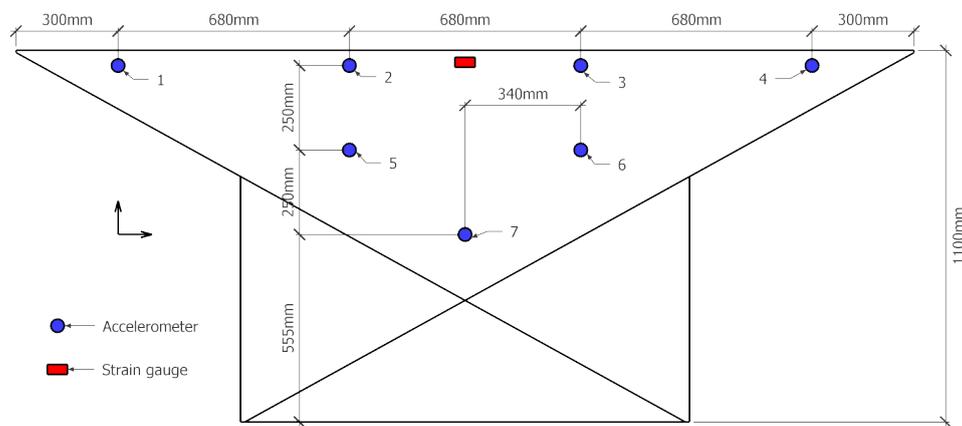


Figure 5.11: Model B - Accelerometer and strain gauge positions

The longitudinal direction is denoted by  $X$  and velocity vectors along this axis are denoted as  $U$ . The transverse direction is  $Y$  and its vector is  $V$ . The vertical direction is  $Z$  and its vector is  $W$ . The origin of the coordinate system is at the farthest upstream edge of the PKW crest (longitudinally), at floor level (vertically), and on a plane equal to the upstream face of the sidewall (transversely).

It should be noted that ANSYS Fluent, used for the numerical modelling, uses a different coordinate system in which the axes are rotated twice ( $Z$  is longitudinal,  $X$  is transverse and  $Y$  is vertical). It should also be borne in mind that in certain cases it is advantageous to represent distance as a directionless scalar value instead of as a vector. This is clearly stated where this occurs.

## 5.2.4 Experiments

A number of experiments were performed on the two physical models, with selected scenarios used in each experiment. The aim of each of these is described in the sections below.

### Water levels and discharge

The relationship between the discharge in the flume and the total head over the weir was established for both model A and model B. This was done so as to be certain that the models were operating as expected when compared to data and equations from previous published studies. The total head was estimated using the static head, as measured by the point gauge, together with the dynamic head. The dynamic head was measured from the pitot tube (the level difference between it and the point gauge at the same location) and also estimated arithmetically from the flow area and the measured discharge.

The results of these experiments are presented in Chapter 7.

### Velocity field

The average velocity vectors were measured at several points arranged in a grid pattern inside the inlet key of model A. The most central inlet key was selected as it would be least affected by the sidewall of the flume. Furthermore, the grid only extended across half of the inlet as the average velocity field is mirrored on the other half. The grid consisted of a number of cross sections in all three cardinal directions: one vertical plane in the longitudinal direction (parallel and near to the PKW sidewall), one vertical in the transverse direction across the flow, and two horizontal planes at different elevations. The intersections between the planes coincide with the pressure measurement point locations (see next section). These planes, and the grid spacings across them are shown in Appendix B. The spacing is closer in areas of interest and wider where flow is more stable and uniform. The grid was limited in scope, in terms of the maximum depth and the proximity to the wall and floor, as determined by the capabilities of the ADV as well as its dimensions. The total number of grid points is 385.

Data was collected for five discharge scenarios, namely 100 to 500 l/s for each of the three upstream nose profiles (rectangular, triangular and circular). Under each flow scenario the ADV sensor was positioned at each individual grid point and the velocity data logged for a duration of 21 s at a frequency of 200 Hz. This time period was selected due to it being just longer than the required  $2^{12} = 4096$  number of recordings making it convenient for FFT processing. The data was checked for stationarity, despiked using the methodology described in Goring and Nikora [104], and the resultant vector components reoriented as described in Appendix B.

The resultant, time-variant signal of velocity vector components was then processed to provide a number of relevant flow parameters. Each of these could then be compared to the same parameters obtained from the numerical model as part of the calibration of that model. These averaged parameters include:

- flow velocity vector components
- velocity magnitude
- vector heading and pitch
- velocity component root-mean-square (RMS) value
- turbulent intensity of each flow velocity component
- kinetic energy
- normalized normal and Reynolds stresses
- integral turbulent time scale

A set of velocity vector readings was also taken for model B. However, due to the limited depth reach of the ADV instrument, the extent of the velocity data is restricted to the area near the crest of the weir.

The results of these experiments are presented in Chapter 7.

### Pressures

The pre-installed conduits in the wooden walls of model A allowed for the measurement of relative pressures at a fixed set of locations on the walls. These locations, which can be seen in the drawings in Appendix B, can be described as follows:

- 7 pressure sensors in a grid on the inlet key side of the middle-most sidewall of the PKW (see Figure 5.10). The locations allow for the measurement of the separation bubble and the vortices which are shed from it.
- 3 pressure sensors in a line on the outlet key side of the middle-most sidewall of the PKW. The locations allow for the measurement of the air cavity bubble which forms under the nappe.
- 3 pressure sensors on the inlet key side of the sidewall in the adjacent inlet key. Simultaneous recording of these sensors with the 7 in the main inlet key allows for assessing whether or not the pressures on either side of this outlet key are synchronised in any way.
- 4 pressure sensors on the sloping base of the inlet key. These allow for the measurement of the water level as well as any aberrant vortices or turbulent structures which enter the inlet key from upstream.
- 1 pressure sensor on the downstream side of the inlet key underneath the overhang. This sensor can record air pressures under the nappe.

Data was collected for a range of flows from 50 to 750 l/s in 50 l/s increments for each of the three upstream nose profiles (rectangular, triangular and circular). A number of scenarios were also investigated with increased downstream water levels as well as under aerated or unaerated nappe conditions.

The pressures at each of the points was recorded simultaneously such that relevant cross-correlations between them and turbulent length scales could be assessed. Each data sequence was recorded for a duration of at least 130 s at a frequency of 1000 Hz. This duration was selected to record a sufficient number of cyclical pressure fluctuations. The data were controlled for stationarity during data capturing such that the raw data did not have to be detrended. The raw signal data was then converted to pressure data and then processed by FFT (see Appendix B).

The peak in the resultant PSD was the main calibration target in the numerical model. It was aimed to achieve both the strength of the peak as well as the frequency of the peak, with the frequency portion being the more important of the two.

The results of these experiments are presented in Chapter 7.

### Modal parameters

The modal shapes and their associated natural frequencies were measured using the accelerometers and strain gauge that were installed on the outlet key side of sidewall of model B. The grid of 7 accelerometers was laid out to determine the first four mode shapes of the sidewall. The

grid layout can be seen in Figure 5.11. The accelerometer points consisted of a 4-2-1 pattern, with points 1-4 installed near the crest, points 5 and 6 midway, and point 7 nearer the base. The strain gauge was installed in the middle of the sidewall near the crest. Although this grid layout could only define the first few mode shapes, numerous additional mode frequencies could be detected due to the high sensitivity and frequency of the accelerometers. The shapes of these higher-order modes could not be defined however.

It should be noted that the sensors were only placed on the sidewall of the PKW and not on the upstream or downstream overhangs. Although it is expected that the mode shape of the PKW as a whole would incorporate deflections at both the sidewall and the overhangs, it was surmised that only the sidewall could be excited by the fluctuating hydrodynamic forces present in the inlet and outlet keys. It is feasible that other fluctuating forces are present that would excite the two overhangs, but these were excluded from the present study.

In each test the sidewall was subjected to an instantaneous force (impact hammer) in a set location. The selected impact site was near to accelerometer 2 as an impact at this location would be able to activate the largest number of modes. The response from each of the 7 accelerometers was recorded for a series of hammer strikes. A time domain window of the high frequency response data of each strike and the subsequent damping period was processed using the Fast Fourier Transform (FFT) to obtain the frequency response functions (FRF) with their associated coherence functions. The test was repeated 3 times and the strongest FRF processed further to extract the relevant modal parameters. These included the real and imaginary component of the signal in frequency space as well as the signal's coherence. These could then be used to calculate the amplitude of the signal as well as its phase which then highlighted the likely natural frequencies present in the data. Once these were identified, the modal shapes could be estimated from the imaginary component of the signal at those frequencies together with the relative locations of the sensors.

Model B was specifically constructed such that the sidewall could vibrate freely without being influenced by the attachment details of the model to the flume walls. The high geometric stiffness of the PKW's edges and corners means that deflection of one portion of the PKW, such as the sidewall, would incur deflections in another portion of the PKW, such as the overhang. It was surmised that, in order for the sidewall to vibrate freely, the overhangs would need to be unbraced. The model therefore needed to consist of a complete inlet and outlet key with their associated overhangs. This meant that, when installed in the flume, the model would be attached to the flume wall via the two adjacent sidewalls.

The steel model was thus expected to vibrate correctly but consequently did not exhibit the correct hydraulic behaviour (seeing as the adjacent sidewalls are effectively blocked by the flume wall). To counter this, two false walls were installed in the centre of the inlet and outlet keys to once again approximate the correct discharge to head relationship. The joint between the false wall and the overhangs were made as wide as possible and filled with a flexible putty such that their effect on the mode shape would be minimised.

The modal parameters of the steel PKW (model B) were determined for four scenarios which each incorporated different water levels behind the weir. The aim was to explore the effect of the added mass of the water body on the mode shapes and frequencies. The first three

scenarios are *empty*, *half-full* and *full*. A fourth scenario, termed *overflow*, was tested to see the effect of a water level above the crest of the weir. In other words, to determine if the modes of the PKW when it is being overtopped by flow differ from those when no overtopping is taking place. The *overflow* case was achieved via the installation of a 200 mm tall sheet of PVC along the entire crest of the PKW, thus forming a loose parapet wall. The presence of this PVC wall could feasibly alter the modes, hence the first three water level tests were repeated with the PVC wall.

The accelerometers could not remain installed during the flow tests as they could not be suitably rendered waterproof. As an alternative, a half-bridge strain gauge was installed in the top middle of the sidewall. Several tests were thus repeated to provide a link between the accelerometer and strain gauge results.

The mode shapes and frequencies were used to calibrate the numerical model. The results of this calibration and these experiments are presented in Chapter 6.

### **Sidewall vibrations**

The above-mentioned strain gauge was the main sensor used in measuring the vibrations of the PKW sidewall under flow conditions. Vibrations were measured on model B under a range of flow scenarios ranging from 50 to 400 l/s at 50 l/s increments. It should be reiterated that, since only a single strain gauge was used, it was not possible to obtain any information regarding the shape of the modes. Only the frequency of the modes could be detected.

The results of these experiments are presented in Chapter 8.

### **Nappe oscillation**

Nappe oscillations generally occur at very low overflow depths and large fall heights [94; 95; 105]. A range of very low flows was then discharged over model B to test for this behaviour. Flow discharges ranged from 1 to 20 l/s in 1 l/s intervals.

The flow behaviour was carefully observed and any nappe vibrations noted. The frequency of any vibration was recorded via a pressure sensor located underneath the overhang. The pressure sensor, exposed to air, thus picked up the sound generated by the oscillations.

Various ways of breaking or disturbing the nappe were experimented with to ascertain their effect on the nappe oscillation. This also highlighted further behavioural characteristics of the oscillation.

The results of these experiments are presented in Chapter 8.

### **Aeration**

An additional scenario in several of the above experiments was the inclusion or exclusion of the provision of air into the cavity underneath the nappe. In each case, in either model A or B, an aeration pipe of a specified diameter allowed the air pocket under the nappe to make direct contact with atmospheric pressure. The data allowed the effect this aeration had on the hydraulics or the vibration to be determined. Air flow velocities in the pipe were also

measured, however these are outside the scope of the present study but will be presented in Lombaard [106].

The results of these experiments are presented in Chapter 7.

### 5.2.5 Scale effects

The issue of scaling and similitude is of crucial importance when scaled physical modelling is undertaken [4]. When the effect or measurement being studied is up-scaled to prototype values, there will be discrepancies between it and real world values which need to be explicitly addressed [107]. There are several possible reasons for these discrepancies which range from the incorrect reproduction of the geometry in the model to scale effects which are caused by the inability of the model to precisely replicate a physical force [107].

In most hydraulic models the discrepancy is largely attributable to the magnitude of the influence that the inertia, viscosity or surface tension of the water has at different scales. In the present study, the elastic behaviour of the material the model is made of also needs to be accounted for. It is usually not possible to attain complete mechanical similarity between a model and its prototype with geometric (its dimensions), kinematic (its motion; time, velocity) and dynamic (its forces) similitude being achieved [107]. When the same fluid or material is used in the scaled model as in the prototype only one of the relevant force ratios can be made equivalent. The dynamic force ratio that plays the most dominant role in the phenomenon being studied is then selected and the effects of the other ratios being unequal is minimized.

#### Fluid scaling

The main force ratios which play a role in typical hydrodynamic models are as shown in Table 5.2. Froude similitude was selected for the present physical tests as is usual for open channel hydraulics [107]. It is noted that vorticity and air entrainment in the model is affected because the turbulence of the flow, as represented by the Reynolds number,  $Re$ , is underestimated. Furthermore, surface tension, in the form of the Weber number,  $We$ , is overestimated, which may affect the behaviour of the overflow nappe as well as the amount of air entrainment that occurs underneath the nappe [108; 4]. Another aspect affecting the behaviour of air under the nappe is its compressibility, encapsulated in the Cauchy,  $Ch$ , or Mach number,  $Ma$ . Air becomes less compressible or hard, at small model scale ratios [107]. It is noted that vibrations, in the form of the Strouhal number,  $St$ , and pressure, in the Euler number,  $Eu$ , have similitude by default, by their relation to the Froude number.

The scale effects can be minimized if limitations in terms of the disjoint in the model and prototype values of  $Re$  and  $We$  are respected. Pfister and Chanson [108] recommend either  $We^{0.5} > 140$  or  $Re > 2 - 3 \times 10^{-5}$  for high-velocity air-water two-phase flows using Froude similitude. The Weber number and Reynolds number are co-dependent and so limiting the one implicates the other [108], thus allowing only a single target for limiting scale effects to be specified. Nonetheless, even if the disjoint in these two numbers is large, errors can be minimized by keeping the model  $We$  and  $Re$  numbers as large as possible.

In terms of the present study, the Reynolds number is the most relevant target variable since

viscosity has a direct influence on the shedding of vortices [109], which are the focal point for the physical model. That being said, the Weber number is arguably easier to measure since, when assuming temperature is kept constant, nappe behaviour at the crest is solely a function of the upstream overflow head,  $H$  [110]. Previous physical models on PKWs have specified a limiting value of the Weber number of  $We > 54$  above which surface tension scale effects can be deemed negligible. This equates to an overflow head of 0.03 m [110; 111]. Predictive studies of the discharge coefficient generally adhere to this guideline, although a recent study into scale effects has determined that smaller overflow values can still generate useful data (with error margins in the order of 10 %) [112]. Only when  $H/P < 0.022$  (which equates to 0.009 m in model A) do significant underestimation errors in the discharge coefficient realise. In terms of the Cauchy number, air compressibility is usually only of concern when velocities approach the wave celerity (i.e. the speed of sound) or when shockwaves are present. Although neither of these are expected to be present in the study, a scale factor smaller than 20 is recommended [113].

The majority of the flow scenarios examined in the physical models exceed the 0.03 m height guideline, thus the depth to discharge relationship and the general flow profile which generates it can be considered to be representative. Tables 5.3 and 5.4 reflects some relevant scale ratios and other dimensions as they pertain to the two models based on the assumption that the prototype fluid is the same as the model fluid, i.e. water. A more comprehensive list is included in Table B.2 in Appendix B. The tables show how all the hydraulically relevant forces and their ratios were scaled in the models and how Froude similitude resulted in a disjoint in the Reynolds and Weber numbers. Despite a mismatch in these numbers, their values generally remain large enough to limit excessive scaling errors.

The range of flows that were tested on model A is detailed in Table B.2 (see Appendix B). The Reynolds number of the upstream water body remains in the fully turbulent range for all the flows considered and the model behaviour thus remains representative of the phenomena under study. The Weber number at the overflow crest does marginally drop below the suggested limit at the lower flows thus some errors related to higher relative surface tension and the relative compressibility of air can be expected. That said, the main nappe behaviour of con-

Table 5.2: Dimensionless force ratios [4]

Dimensionless number	Force ratio	Formulation
Froude	$Fr = \sqrt{\frac{\text{Inertial Force}}{\text{Gravitational Force}}}$	$Fr = \frac{V}{\sqrt{gL}}$
Reynolds	$Re = \frac{\text{Inertial Force}}{\text{Viscous Force}}$	$Re = \frac{LV}{\nu}$
Weber	$We = \sqrt{\frac{\text{Inertial Force}}{\text{Surface Tension Force}}}$	$We = \frac{\rho V^2 L}{\sigma}$
Cauchy	$Ch = \frac{\text{Inertial Force}}{\text{Elastic Force}}$	$Ch = \frac{\rho V^2}{E}$
Euler	$Eu = \frac{\text{Pressure Force}}{\text{Inertial Force}}$	$Eu = \frac{p}{\rho V^2}$
Strouhal	$St = \frac{\text{Inertial Force due to flow unsteadiness}}{\text{Inertial Force due to velocity gradient}}$	$St = \frac{fL}{V}$

Table 5.3: Model A scaling ratios and dimensions

Dimension / Ratio	Sym-bol	Scaling ratio	Unit	Proto-type	Model (as scaled)	Model (as built)
Scale	$\lambda$	$\frac{\text{prototype}}{\text{model}}$	-	1	7.5	7.5
Height	$P$	$\lambda$	m	3.000	0.400	0.400
Discharge	$Q$	$\lambda^{5/3}$	m <sup>3</sup> /s	77.0	0.500	0.500
Pressure	$p$	$\lambda$	Pa	75.0	10.0	10.0
Frequency	$\omega$	$\frac{1}{\sqrt{\lambda}}$	Hz	1.826	5.00	5.00
Plate mass	$m$	$\lambda^3$	kg	4050.0	9.60	2.20
Material density	$\rho$	1	kg/m <sup>3</sup>	2400	2400	550
Froude number	$Fr$	<i>gravity</i>	—	0.442	0.442	0.442
Reynolds number	$Re$	<i>viscosity</i>	—	$2.1 \times 10^6$	$1.0 \times 10^5$	$1.0 \times 10^5$
Weber number	$We$	<i>surface tension</i>	—	103 170	1834	1834
Strouhal number	$St$	<i>frequency</i>	—	1.51	1.51	1.51
Cauchy number	$Ch$	<i>volumetric elasticity</i>		302.5	302.5	16.8
Euler number	$Eu$	<i>pressure</i>	—	0.030	0.030	0.030

cern is linked to the aeration of the underside of the nappe and the possible sub-atmospheric conditions that may develop as a result. This behaviour, fortunately, only manifests at the higher flows when higher levels of turbulence in the outlet key lead to greater air entrainment. The low Weber number at low flows is thus not expected to be problematic.

Besides surface tension, another aspect which has an influence on air entrainment in a scaled model is bubble size. If the same fluid is used in the model as in the prototype, the physics of the flow does not change and thus bubble size cannot be scaled. Previous model studies into drop structures have specified that these effects are overcome when the critical fall velocity of 6 m/s is exceeded [113]. Unfortunately, neither of the models exceed this threshold. Nonetheless, the highly turbulent nature of the outlet key is expected to keep these scaling errors to a minimum.

The main flows used in model B were fairly large with overflow depths of  $H/P > 0.1$ . These tests can thus be considered to be free of large scale scaling effects caused by the disjoint in their Reynolds and Weber numbers. Some much smaller flows were also tested, however, all of which fall well below the recommended limits of overflow depth. These tests specifically examined the behaviour of the nappe under these almost laminar conditions. As such, the Reynold number is not of relevance, but the Weber number is of crucial importance. The only way to reconcile the very low Weber number is to consider model B as a full-scale prototype

Table 5.4: Model B scaling ratios and dimensions

Dimension / Ratio	Sym- bol	Scaling ratio	Unit	Proto- type	Model (as scaled)	Model (as built)
Scale	$\lambda$	$\frac{\text{prototype}}{\text{model}}$	-	1	2.72	2.72
Height	$P$	$\lambda$	m	3.000	1.100	1.100
Thickness	$T_s$	$\lambda$	m	0.025	0.009	0.006
Discharge	$Q$	$\lambda^{5/3}$	m <sup>3</sup> /s	3.68	0.300	0.300
Pressure	$p$	$\lambda$	Pa	27.3	10.0	10.0
Frequency	$\omega$	$\frac{1}{\sqrt{\lambda}}$	Hz	3.03	5.00	5.00
Plate mass	$m$	$\lambda^3$	kg	1413.0	69.7	45.6
Material density	$\rho$	1	kg/m <sup>3</sup>	7850	7850	7850
Young's modulus	$E$	$\lambda$	GPa	200	73.3	200
Moment of inertia	$I$	$\lambda^4$	10 <sup>6</sup> m <sup>4</sup>	2.604	0.047	0.013
Flexural rigidity	$EI$	$\lambda^5$	N m <sup>2</sup>	520 833	3454	2640
Froude number	$Fr$	<i>gravity</i>		0.243	0.243	0.243
Reynolds number	$Re$	<i>viscosity</i>		$4.9 \times 10^6$	$1.1 \times 10^6$	$1.1 \times 10^6$
Weber number	$We$	<i>surface tension</i>		12 871	1731	1731
Strouhal number	$St$	<i>frequency</i>		1.0	1.0	1.0
Cauchy number	$Ch$	<i>volumetric elasticity</i>		78.9	78.9	28.9
Euler number	$Eu$	<i>pressure</i>		0.014	0.014	0.014

and assess the low-flow nappe behaviour and the results on that basis.

Although most of the dimensioned aspects of the PKW models can be scaled in accordance with the Froude similitude scaling laws [4], certain dimensionless flow characteristics, such as turbulence intensity, are difficult to scale directly. A data relationship between the two physical models could be considered and, with the assistance of the numerical model (which also has its own inherent errors to account for), some of these parameters could be scaled if so desired.

Lastly, it is worthwhile noting that the selected model scale ratios (1:7.5 and 1:2.72) are much smaller than those usually selected for scaled models, which are typically in the order of 1:10 or larger. The biggest of the two models (model B) is large enough that it can be considered a prototype in its own right.

### Materials scaling

The accurate or representative scaling of the characteristics of a material in a hydroelastic model plays a large role in the accuracy of its results. The model material must be able to represent the stiffness, inertia, density and damping properties of the prototype. The hydrodynamics of the flow can overcome the limits of most of its scaling errors at relatively small scales. Given that the number of suitable, practical and affordable materials are limited the scale of a hydroelastic model has to be fairly large [4]. That said, there is a limit on the maximum size such that the flow still remains suitably turbulent ( $Re > 10^5$ ) at the chosen scale.

The present model is continuous, meaning that it is free to vibrate and is not limited to any particular degree of freedom. This means that the model must adhere to hydroelastic similitude. The main parameters that need to be adhered to are the same as those for Froude similitude but also include the modulus of elasticity, Poisson ratio and density of the material. In so doing the scaled-down pressures should induce a response such that the damping behaviour and damping ratios of the scaled-down frequencies are equal. It is noted that the strength of the model material is not of primary concern so long as the material behaviour remains in its uniform linear elastic range [113].

There are two main ways to achieve hydroelastic similitude. The first is to adhere to the scaling laws of a reduced modulus of elasticity (Young's modulus) but an equal density and Poisson's ratio (assuming the same fluid is used in the model as in the prototype) [4]. Depending on the scale, it is possible to manufacture materials which have such a lower modulus but with an equal density. A composite material such as epoxy, plastic or rubber with suspended lead or barite particles can be used to emulate concrete for example [114].

A second method is to use the same material in the model as in the prototype and make adjustments to the geometry of the structure to reduce its stiffness (in this case bending stiffness or flexural rigidity) to emulate the lower modulus of elasticity [4; 103]. By default, using the same material gives the model an equal density and Poisson's ratio. In the present model the stiffness was reduced by reducing the geometrical thickness of the steel plate used to construct the model.

Reduction in geometrical thickness to get better material similitude has the general disadvantage that this may disrupt the geometry of the flow [103]. This is fortunately not the case in the present model. Although the thickness of the sidewalls does have an effect on the discharge efficiency of a PKW, this effect is minor and is chiefly related to the total volume of the inlet and outlet keys which is reduced with thicker walls. [115].

The reduction in the wall thickness is presented in Table 5.4 (a more comprehensive table is available in Appendix B.3.2). A prototype thickness of 25 mm is reduced by the scaling ratio to 9 mm. Since the same material is used in the model as in the prototype, the model would appear too stiff as it would have the same modulus of elasticity. The model thickness was reduced to 6 mm such that the thinner plate with a modulus of elasticity of  $E = 200$  GPa would have a reduced area moment of inertia,  $I$ , such that their product (which is proportional to flexural rigidity) is near equal to that of the same product of the 9 mm thick plate. Note that exact values of the various scaling ratios could not be attained as the precise model thickness

needed to achieve this is 6.6 mm. Steel plate of this thickness is not generally available, hence the nearest available thickness of 6 mm was selected. The model is thus slightly weaker than it should be. This is explained in greater detail in Appendix B.3.2.

The dimensionless Cauchy number,  $Ch$ , which reflects the behaviour of a structure in terms of volumetric elasticity or compressibility, is related to the modulus of elasticity,  $E$  and not to structural stiffness related to  $EI/L$ . For this reason, there is a difference in this number between the model and the prototype making the model appear stronger than the prototype even though the structure has been made weaker.

Another relevant aspect that needs to be considered in hydroelastic models is the effect of damping. The relative damping effect (i.e. damping effect vs. critical damping effect) should be the same in the model and the prototype. This should also incorporate the apparent increase in mass as the structure is vibrating in a liquid (the added fluid mass). Damping reduces the vibration amplitudes of resonant vibrations as it dissipates the kinetic energy. A hydroelastic model that has a damping value that is equal or lower than the value of its prototype can still emulate resonant conditions [4]. The damping effect can possibly be the same in the prototype and the model if the same materials are used in the model and the prototype, since this coefficient is to a large degree a material constant. However, damping sources such as friction and viscosity may not necessarily be modelled correctly. This is not a concern considering that neither friction (between moving parts) nor viscosity (shear forces between the fluid and the structure) are thought to play a significant role in the vibration behaviour of the PKW.

### 5.2.6 Limitations

Certain limitations are inherent in the methodologies, scales and instrumentation used in the physical models. Some of these are highlighted below.

- The Nortek Vectrino Acoustic Doppler Velocimeter is limited to a data capture rate of 200Hz. This largely limited the frequency range to 100 Hz or lower as per the Nyquist theorem [116]. That said, since the sampling volume is relatively large, a higher frequency would only pick up signal noise as the higher frequency velocities operate at much smaller scales than the sampling volume and so can't be picked up by the instrument. Another limitation of the ADV is that its housing cannot operate underwater. The housing had to remain above water which limited the depth to which the sensor could be placed. The geometry of the sensor head also limited to proximity to the sidewall. Furthermore, readings close to the base of the water column could also not be taken due to echoes from this flow boundary.
- It was noted that the trolley mount above the physical model had a slight misalignment of approximately 4 mm from one side of the flume to the other as well as in the upstream-downstream direction. This would have an effect on some of the water level readings and on the locations of the velocity vector grid. The discrepancy is however small in relation to the size of the grid spacings, and given the general lack of variability in the velocity from one grid point to the next, this discrepancy is deemed acceptable.

- The pressure sensors were located remotely from the locations on the model. This implies that there is a timelag between a pressure change at the end of the conduit and the time the sensor picks up the change. This lag is related to the speed of sound in water, which for the short conduits in question is imperceptibly small. Care was taken to ensure that the conduits from the points to the sensors were of equal length such that the timelag, however small, was equal in all instances.

The pressure sensors and their conduits worked most efficiently when completely submerged in water. The conduit openings on the downstream side of the sidewall, however, were exposed to both water and air as dictated by the flow in the outlet key. This unsteady environment of fluctuating pressure and phase transitions would cause air bubbles to enter the conduit. These not only damped the pressure signal to the sensor but also affected the actual pressure reading. This hampered the identification of negative pressures, as the atmospheric baseline was continually reset by water and air entering and exiting the small conduit. The quality of the data from this set of sensors is thus of poor quality.

- The accelerometers could not be used under flow conditions as they could not be water-proofed. They were thus replaced by a strain gauge. The singular strain gauge can only be used to determine vibration frequency and not the vibration modes.

### 5.2.7 Data analysis

The various data sets that were collected in the experiments were checked for errors and inadequacies, cleaned where necessary and subsequently processed and verified where possible.

Single point measurements like the discharge and water level readings were duplicated several times and compared to ensure that erroneous readings would be rejected.

The time variant data (velocity, pressure, strain) was checked for stationarity and rejected if it was unduly variable or affected by signal or background noise. The ADV velocity data was then cleaned and despiked using a number of methods including that described by Goring and Nikora [104] and Parsheh *et al.* [117]. The pressure and strain data generally did not require such data cleaning. When the signals were converted to the frequency space using the Fast Fourier Transform (FFT), the Welch method was applied to reduce the signal noise level and randomness of the resultant power spectral density estimation [118]. More specific details regarding these techniques is presented in Appendix B.

## 5.3 Numerical modelling

Numerical modelling allows for the simulation of real world phenomena and exploring what factors affect the behaviour of that phenomena. In the field of hydraulic structures, this is also known as Computational Fluid Dynamics (CFD). It should be borne in mind that a numerical model remains a simulation or a representation of real world processes. Although it is possible in CFD to directly model most (relevant) physical processes, this is relatively expensive in computational terms and often deemed unnecessary to answer the questions or test the hypothesis that the model was compiled to resolve. This means that the model environment that is chosen

should be tailored to the problem at hand. This then also allows for simplifications to be made to speed up the development of the solution.

These simplifications may harbour unintended or hidden inadequacies that could affect the final results. Thus, numerical models need to be calibrated against physical data such that their behaviour can be modelled more accurately meaning that more certainty can be ascribed to the results.

This procedure can be a major drawback for the use of numerical models, especially if no such physical data is available. However, one of the main benefits of numerical models is that they are able to generate good quality data at high temporal and spatial scales such that the modelled phenomena can be explored in detail.

As described in the previous sections, the present study investigates fluid induced vibrations. Two models were compiled, one dealing with the hydrodynamic behaviour and another dealing with the structural response. The hydrodynamic model generated pressure or force data which are then applied as a load onto the structural Finite-Element-Model (FEM) which simulates the response. The movement or deflection component of this response can then be fed back into the CFD model which may alter the hydrodynamics of the flow, thus forming a potential feedback loop [119]. This two-way coupling, and other particular details of the models, are described further in the subsections below as well as in Section 5.3.3.

The aim of the numerical modelling exercise was to discover trends in the hydrodynamic and structural behaviour of PKWs and to explore factors which affect, and can thus be used to control, this behaviour. It was also sought to prove that the fluid-induced-vibration phenomena can be modelled by numerical means and to determine whether any feedback loops are present.

### 5.3.1 Modelling environment

The modelling software environment that was selected for the study was ANSYS v.18.1, with its Fluent [120] and Mechanical [121] modules. Fluent conducts the CFD component and Mechanical conducts the structural FEM component of the model. ANSYS Fluent model has a large number of functional components which can be utilised to simulate a wide variety of flow scenarios, from supersonic aerofoils to microscopic multiphase flows. Ansys Mechanical on the other hand is capable of calculating the responses of a 3D solid body ranging from basic structural loads to complex scenarios involving thermodynamics, electromagnetism, and acoustics. The present study aims to build a three-dimensional, transient, two-phase, free-surface, fluid-structure interaction model. The two models were first compiled and calibrated separately and then coupled using the inbuilt System Coupling module which allows the two modules to share data and so interact with each other.

#### Fluent

The Fluent model was compiled using the parameters shown in Table 5.5. The majority of these parameters are based on the type of flow being emulated, namely open-channel turbulent flow with water and air. However, some parameters are specific to the present model and had to be calibrated. These include the selection of the turbulence model as well as the solution methods.

The turbulence model is of particular importance as the calibration showed that many of the transient phenomena observed in the physical model could only be emulated with the Large Eddy Simulation (LES) methodology [120]. This is explained further in Section 5.3.2.

The model space was defined to incorporate one PKW unit, i.e. half of an inlet and half of an outlet as shown in Figure 5.12a. This space was discretized into a grid of hexahedrons using the uniform CutCell Assembly meshing method [120]. The mesh sizing proved to be a sensitive component of the model. In CFD analyses, a mesh refinement exercise is ordinarily conducted to ensure that the mesh is capable of emulating the desired phenomena. The size of the individual mesh cells is reduced until a scenario is reached where a relevant metric does not change by more than a certain percentage. Finer meshes would then not contribute significantly to the result as they would approach an asymptotic value.

In the present instance however, a different tactic had to be used. The chosen turbulence model, LES, as its name implies, simulates the actual eddies where are present in the turbulent flow. It can however only model eddies equal in size to the smallest cell size at any particular location in the mesh. This means that smaller mesh sizes lead to much smaller eddies being simulated. Turbulence scales smaller than the smallest cell size are modelled using a relevant subgrid scale model (see Table 5.5). Applying a mesh refinement analysis results in ever smaller eddies being simulated, which may or may not be of relevance, thus no metric change asymptote can be reached. It was found in the calibration exercise that the large scale metrics, e.g. discharge or average velocity, could be accurately simulated with very large cell sizes. Very small cell sizes resulted in very fine eddies which oscillated with small fluctuations and high frequencies. These contributed a significant level of noise to the extracted pressure signals and were not deemed relevant as they do not have a significant impact on the phenomena being studied. A balance between these two extremes was thus found such that the generated numerical eddies emulated the physically measured ones at similar scales.

The resultant mesh, at the same scale as model A, consisted of a regular grid of between 3 to 5 million cubes each 5 mm to a side. This had to be reduced stepwise to 2 mm and 1 mm at the crest of the PKW and the upstream inlet key edge respectively. This was needed to more accurately define the high pressure and velocity gradients which are present there. The mesh, shown in Figures 5.12b to 5.12d, indicates where these finer mesh areas are and how they transition to the larger mesh areas. The figures also show the starting water level for the model (blue for water and red for air). The mesh sizes for the larger full-scale models were proportionally larger, with an approximate 20 to 30 cells across the width of the half-inlet key.

The boundary conditions that were applied are shown in Table 5.6. The standard operating conditions for air-water flows were applied, including surface tension of 0.072 N/m, gravitational acceleration, standard atmospheric pressure and densities of 1.225 kg/m<sup>3</sup> and 998.2 kg/m<sup>3</sup> for air and water respectively. As in any CFD computation, the more accurately the starting conditions can be specified the quicker convergence will be achieved. The starting conditions were specified as a still standing volume of water in the inlet key and upstream approach channel up to the desired water level, as shown in Figure 5.12a.

The time step used in the analysis is limited by the desired output. The desired frequency range extended up to 100 Hz which means that, as per Nyquist sampling criterion, at least

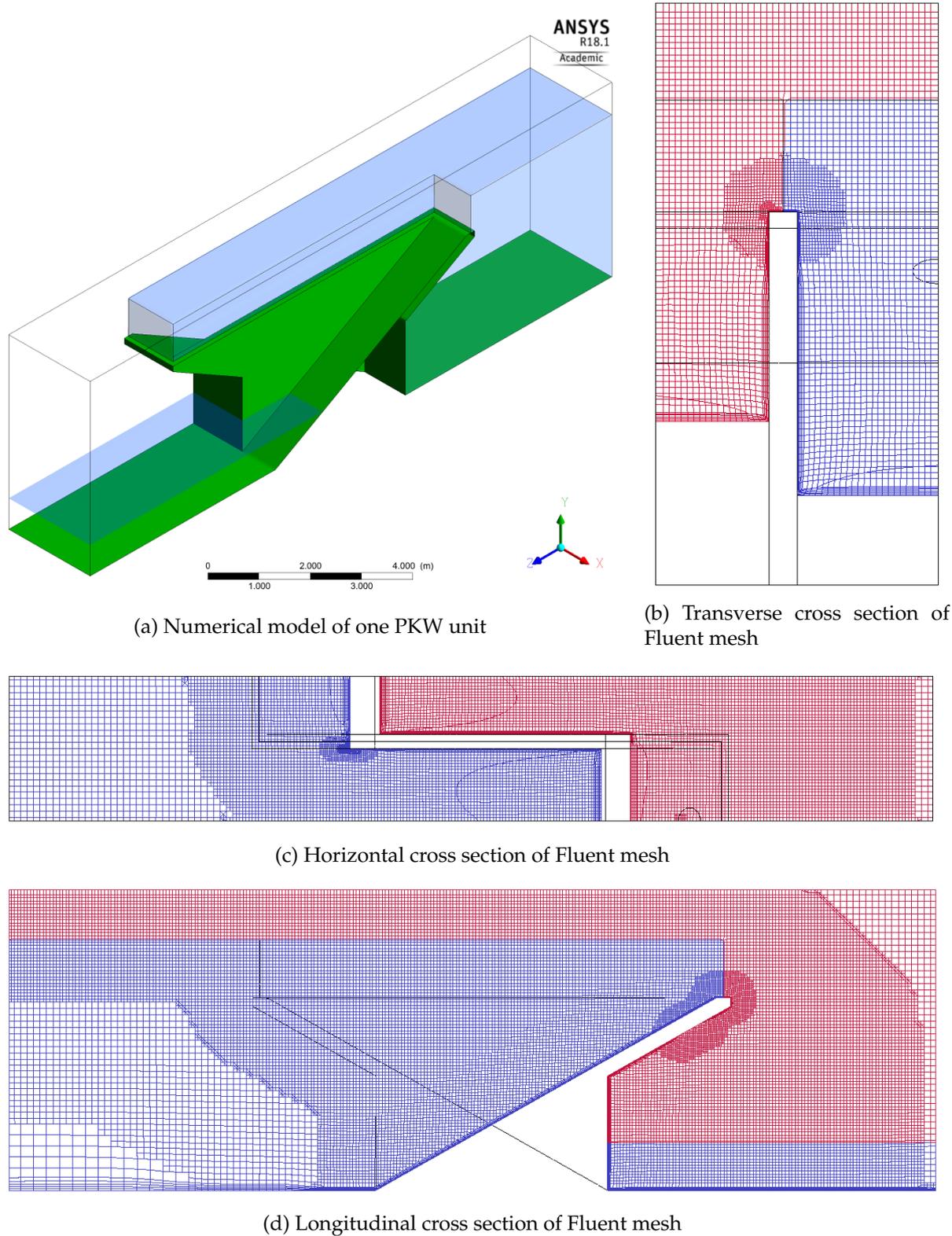


Figure 5.12: Fluent model mesh

Table 5.5: Fluent modelling parameters

Aspect	Parameter	Value
Solver	Type	Pressure-based
Solver	Time	Transient
Flow model	Multiphase	Volume of Fluid (VOF)
Flow model	Viscous flow (turbulence)	Large Eddy Simulation (LES)
Flow Model	Subgrid-Scale model	WMLES S-Omega
Material (Phase)	Fluid	Air
Material (Phase)	Fluid	Water-liquid
Solution method	Pressure-velocity coupling	SIMPLEC
Solution method	Spatial Discretization: Gradient	Least Squares Cell Based
Solution method	Spatial Discretization: Pressure	Body Force Weighted
Solution method	Spatial Discretization: Momentum	Bounded Central Differencing
Solution method	Spatial Discretization: Volume Fraction	Compressive
Solution method	Transient formulation	Second order implicit
Solution controls	Under-relaxation factors	Default
Solution controls	Time step	Constant

200 Hz needs to be sampled. This equates to a fixed time step size of 0.005 s. Almost all the models could successfully run at this time step although those simulations with very thin walls (<10 mm) required time steps as small as 0.0001 s. 20 to 30 iterations per time step were specified to allow the model to overcome the initial convergence difficulties but were scarcely needed later in the transient simulation.

### Mechanical

Since the loads that are being applied to the structure are a function of time, the ANSYS Mechanical Transient Structural module was used to assess structural and FSI behaviour of the PKW. The modal behaviour was assessed using the Modal module.

The majority of the model's parameters were kept at their default values as it was found that the structure could be readily calibrated by making adjustments to the geometry of the structure to more accurately mimic the actual physical structure as it was constructed.

A mesh refinement exercise was undertaken and resulted in the mesh shown in Figure 5.13a. The mesh consists largely of tetrahedrons which are approximately 75 mm in size near the crest and 10 mm near the base of the sidewall where the largest stresses are expected to occur (see Figure 6.4). As detailed further in Section 6.4 the PKW was simplified to just that component which would be directly affected by the fluctuations in the inlet and outlet keys, namely the lateral sidewall. The lower portions of the sidewall are braced by the thick base of the PKW and would thus not undergo noticeable deformations (see Figure 6.2). This means that only the triangular shaped piece was incorporated in the FSI model. Its mesh is shown in Figure 5.13b. This simplified structure was suitably calibrated to mimic the complete structure by using elas-

Table 5.6: Fluent boundary conditions

Boundary condition	Parameter	Value
Upstream	Type	Pressure inlet
Upstream	Phase	Open Channel
Upstream	Flow	Free surface level and velocity
Upstream	Velocity fluctuations	Spectral Synthesizer
Upstream	Turbulence Intensity	10%
Downstream	Type	Pressure outlet
Downstream	Phase	Open Channel
Downstream	Flow	Free surface level
Downstream	Backflow	Total pressure
Air inlet	Type	Pressure inlet
Air inlet	Gauge pressure	1 Pa
Ambient	Type	Pressure outlet
Ambient	Gauge pressure	0 Pa
Flow boundary	Type	Symmetry
Wall	Shear	No slip
Stationary wall	Dynamic mesh	Stationary
Deforming wall	Dynamic mesh	System Coupling
Dynamic mesh	Mesh method	Smoothing: Diffusion
Dynamic mesh	Diffusion function	Boundary-distance, 0.5
Dynamic mesh	Stabilization	Volume based, 0.025

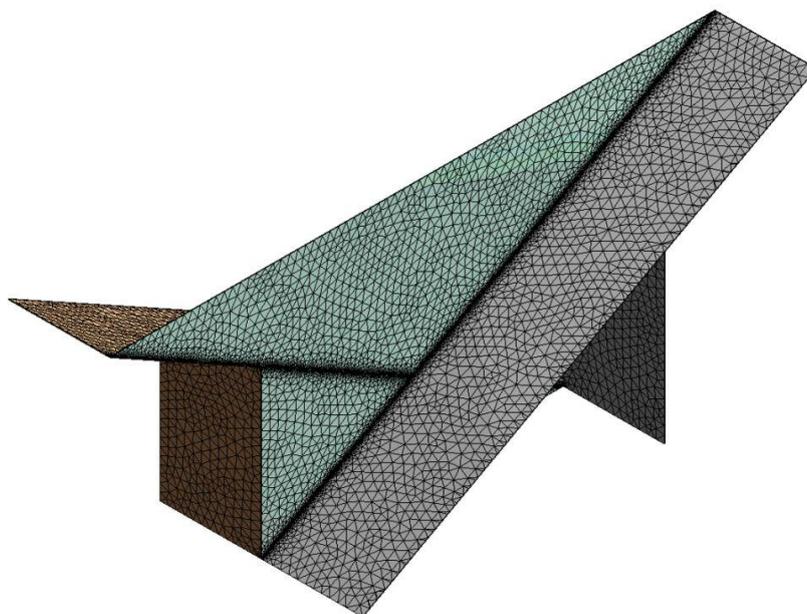
tic supports at the interface with the remainder of the wall.

The boundary conditions that were applied on the mechanical model were as follows: The plane footings of the PKW were assigned fixed supports and could thus not move. The plane edges of the PKW unit, where the symmetry boundary is located in the Fluent model, were assigned frictionless supports. These are able to move freely within the plane of the support but not out of the plane. The sloping bases of the simplified triangular sidewall were assigned as elastic supports such that they could flex and in so doing emulate the missing portions of the PKW. One of their edges was also assigned a fixed support to fix the structure in space.

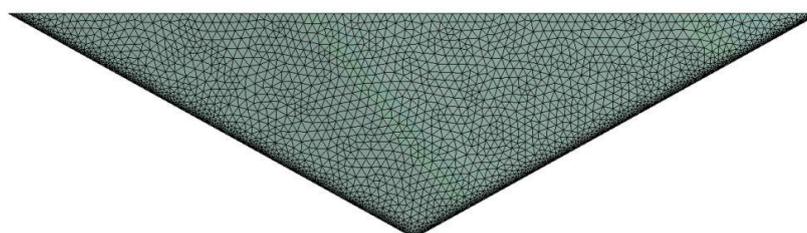
All the models that were run in Mechanical were specified as being constructed of either structural steel or reinforced concrete depending on the scenario being investigated. The material properties listed in the ANSYS materials database, as shown in Table 5.7, were used directly.

### System coupling

The ANSYS System Coupling module is, at first glance, a fairly simple straightforward tool to allow any number of modules to communicate and share data. In this instance, the upstream and downstream faces of the simplified triangular sidewall were connected to identical faces in



(a) Mechanical mesh of model B



(b) Mechanical mesh of sidewall

Figure 5.13: Mechanical model mesh

Table 5.7: Mechanical material properties used in FEM model

Material	Density ( $\text{kg}/\text{m}^3$ )	Young's modulus (GPa)	Poisson's ratio
Structural steel	7850	200	0.30
Concrete	2400	30	0.18
PVC	1360	3	0.40

the Fluent model. These communication channels can be activated as desired. The underlying algorithms are however relatively complex as described in more detail in Section 5.3.3.

In a two-way Fluid-Structure-Interaction (FSI) model, the pressure forces being generated by the Fluent model at a particular time step would be converted to force values which would then be applied to the associated face elements of the Mechanical model. This model would calculate the deflection that the wall would undergo and communicate these nodal displacements to the Fluent model. These displacements amount to the movement of the mesh domain. The Fluent model thus re-calculates the dynamic mesh in the localised region where movement took place in accordance with the specified parameters (see Table 5.6). The Fluent model then recalculates the solution for the updated mesh, including any dynamic forces resulting from the moving mesh, and forwards the updated pressure forces back to the Mechanical model, and so forth. The models repeat this iterative approach until the changes in the forces and the displacement that are calculated in each iteration (known as residuals) converge to a small enough value. Once the Fluent model, the Mechanical model and the force and displacement values have all converged, the model will then proceed to the next time step and repeat the process.

A one-way model is similar, however, the communication is only one way and thus does not account for feedback. The Fluent model sends the generated pressures to the Mechanical model which then calculates the deflections. These deflections are recorded but not sent back to the Fluent model. The mesh in Fluent is thus static. In this way the effect of the pressures of the wall can be determined. However, any potential feedback loops or damping effects would be lost. That said, a one-way FSI model can complete a simulation in a much shorter time period.

The coupling of the two systems does lead to much longer computational run times. Whereas the Fluent model alone could complete a 20 s simulation of the flow around a PKW in approximately 6 hours, a two-way simulation of the flow together with the structural response of the same duration would require 200 hours (8 days). The reason for this large additional time cost is the iterative process to achieve convergence at each step. Furthermore, in order to remain stable, very small time steps (in the order of 0.0002 to 0.0005 s) had to be utilised to prevent the mesh from becoming too distorted. Larger time steps would result in the small mesh cells at the crest of the sidewall (see Figure 5.12b) moving a distance greater than their individual widths resulting in rapid divergence of the solution.

The model was set up to only collect data at four main locations in order to limit the large volumes of data that would otherwise result from such a simulation. These locations included the moving coordinates of three equidistant points located along the crest of the sidewall. These points were situated in the centre and one on either side of it at a distance of one sixth of the sidewall length. The fourth data collection point was the stress state of a range of cells which make up a zone at the base of the sidewall near where the overhang begins. This zone was identified (see Figure 6.4) as the region where the highest equivalent stresses (von Mises) are expected to occur. The time variant signal of these stresses could thus be used to assess the potential for fatigue to develop there.

The Fluent model was run first and allowed to establish the steady state flows around the PKW. The results of the initial Fluent run were then used to start the coupled run. The sidewall

was started off in its vertical position which, when exposed to the hydrostatic pressure of the water body around it, quickly deformed to a shape similar to that shown in Figure 6.1. Since the structural model is transient, this initial deflection caused an oscillation which was damped out by the water body after about 1.5 seconds. This is roughly the same amount of time that it took for the largest deflections from a hammer strike in the physical model to damp out. This highly dynamic start to the simulation entails high velocity and pressure gradients in the CFD model, which may lead to divergence. These large gradients can be brought on more gradually by the inclusion of a volume-based, solution stabilization factor (with a value of 0.025). This factor does not alter the solution but will slow down the speed of the solution somewhat but does insure a greater chance of convergence being achieved. Once the simulation was stable, the first 2 seconds of data from the numerical model, that was needed to allow both the structure and flow to stabilise, was discarded.

### 5.3.2 Computational Fluid Dynamic models

CFD models consist of a variety of numerical simulation techniques to solve flow problems. The assumptions made and the choice of CFD technique plays a significant role in the accuracy of the results. This is especially true of the choice of turbulence model. It is known that Reynolds Averaged Navier-Stokes (RANS) models are capable of accurately modelling steady or pseudo-transient states as has been shown by numerous PKW studies to date [24; 13; 1; 122]. The present study is dynamic and fully-transient and it was confirmed in the numerical model calibration (see Section 7.2) that although the steady state characteristics of the flow could be accurately emulated by a RANS model, no RANS model could mimic the transient behaviour of the physical model [123]. This is because the RANS turbulence models are based on statistical time-averaged representations of turbulence and its fluctuations and are thus not capable of directly emulating vortices. Alternative turbulence models which resolve the turbulent eddies directly were thus explored.

Direct Numerical Simulation (DNS) solves the full unsteady Navier-Stokes equation and thus resolves all turbulent scales of the flow. They therefore require very fine spatial and temporal scales [124] and are computationally expensive to run. They were thus not considered in this study.

The Large Eddy Simulation (LES) is a Scale Resolving Simulation (SRS) that filters out the finer scales smaller than the grid size and only resolves the large scale eddies. The turbulent dissipation at smaller scales is approximated using a suitable subgrid scale turbulence model. The method is inherently unsteady and is thus useful to study transient phenomena [123]. Although they are less computationally costly than DNS, they still require cluster level parallel processing to provide quick turnaround times.

Another SRS alternative is the Detached Eddy Simulation (DES) which attempts to incorporate the advantages of both the LES and RANS methods. The method assigns certain portions of flow (as desired) to be modelled with RANS and others where more detailed transient or turbulence data is needed to be modelled with LES.

Both the DES and LES models were found capable of emulating the physically observed

behaviour. The DES model was chosen to model the hydraulic only simulations. The LES methodology was chosen for the FSI simulation as the DES methodology currently does not allow it to be coupled to ANSYS Mechanical for FSI simulations. The selected subgrid scale turbulence model for the LES method was the WMLES S-Omega. This is an amended form of the Wall-Modelled LES formulation which more accurately simulates separated or free shear boundary flows [120].

Another technique that needs consideration is how the free surface interface of the multi-phase simulation is tracked. Ansys utilises an amended Volume-of-Fluid (VOF) methodology which models the flow equations for both water and the air and tracks the interface between them. This is different from the true VOF technique which does not need to model the air above the water level. In the present instance, however, the ANSYS methodology is advantageous since the interaction between the air and the flow is important to the behaviour of the nappe over the PKW.

### 5.3.3 Fluid structure interaction

Section 4.4 highlighted the potential for the occurrence of fluid structure interaction at PKWs. Not only does the mass of the water body affect the modal characteristics of the sidewall vibration, the vibration also has an effect on the flow which excites it. They form an integrated system of interactions and feedback loops.

The inherently non-linear and transient nature of the behaviour makes its investigation using analytical approaches difficult. The development of suitable mathematical tools, such as computational modelling, to solve this complexity is ongoing [97].

The basic premise is that there is an inter-dependence of the fluid solution and the structural solution. In other words, the fluid solution is affected by the movement of the wall and vice versa. There are thus two sets of different differential equations that need to be satisfied simultaneously. The domains do not overlap, hence this fluid-structure interface needs to be tracked and data transferred across it from one set of equations to the other [97; 96].

The solution of the problem may be tackled in a staggered or monolithic fashion. The monolithic methodology is needed for strongly coupled FSI problems where both the fluid and structural components are solved simultaneously. Both are then contained in a single mesh hence the solver requires an interface capturing method. The monolithic solver is a robust methodology as it ensures that the kinematics and traction at the interface are directly modelled. This does require a very fine mesh to allow the interface to be captured with a suitable degree of accuracy [97; 96].

The alternative, staggered or partitioned, method solves the two systems separately. In this methodology, the two sets of equations are solved sequentially in an uncoupled fashion. During each time step the fluid equation is solved in its spatial domain. Its fluid forces on the interface are then collected and transferred to the corresponding mesh elements of the structural equation. It then computes for the deflections caused by these forces. These deformations result in changes to the spatial domain of the fluid equation. Its domain is thus re-meshed and the solution re-solved[97].

The staggered methodology commonly has convergence problems since the fluid solution, the structural solution, the re-meshing and the data transfer all need to converge to small enough residuals. Additional internal calculation loops can be added to allow more time for all these equations to converge. The staggered method has the benefit that existing fluid and structural modules can be used in the analysis together with their capable suite of solvers [96].

The interface between them is defined by an interface tracking module which determines its location as the mesh of the structure and that of the fluid field moves. As the interface moves to conform with the deflections calculated in the structural model it requires the fluid mesh to be re-meshed. There is thus a third solver that needs to be incorporated into the solution technique, namely the re-meshing module. The re-meshing ensures that the movement of the mesh and its refinement does not distort the individual elements to such a degree that they result in a diverged solution [96]. This usually requires very small time steps however.

The manner in which the data is transferred across the interface is a source of error in the calculation. This is because the meshes on either side do not match (i.e. there is no direct spatial coupling) and are thus open to interpolation errors when one node value is transferred to a nearby node in the opposing mesh. The preferred interpolation method for cases where the quantity of the overall transfer of energy is an important parameter, is the *conservation of profile* method. This checks that the integrals of the force values on both sides of the transfer are equal.

Another solver method which is usually reserved for strongly coupled systems and where the fluid is near stagnant or the structural deflections are limited is the use of *acoustic fluid formulations* [96]. FSI problems are ordinarily solved in a transient fashion, however, acoustic formulations would be solved in the frequency space. Considering the largely steady state nature of the flow around a PKW it is feasible to imagine that the problem could be approached from a frequency domain perspective. By allowing the steady state deformations and flows to interact via small incremental movements represented as frequencies, both the fluid and structure could respond to these frequencies in their own modal shapes and frequencies. It is beyond the scope of this study to consider the feasibility of this methodology although it would be an interesting topic for future research.

### 5.3.4 Computational hardware

The numerical simulations were compiled and tested in ANSYS Workbench Release 18.1 on an 8 core Intel®Core™ i7 CPU 2.93 GHz with 16 GB of RAM.

Once the setup was shown to function it was transferred to the Centre for High Performance Computing (CHPC) of the Council for Scientific and Industrial Research (CSIR) in Cape Town for the actual computations. The research dedicated centre houses a petaFLOP level cluster consisting of 23832 Intel®Xeon® CPU cores each with a clock speed of 2.6 GHz and memory of 148.5 TB. Fair use quotas limit normal research users to 10 nodes, which each consist of 24 cores and 128 GB of memory, and a maximum runtime of 48 hours [125]. The inbuilt parallel processing algorithms of ANSYS allowed the computational time to be reduced by more than an order of magnitude when comparing the two platforms. A typical 3 million element Fluent

run could generate some 30 s of data in approximately 12 hours.

### 5.3.5 Experiments

Once the numerical model was calibrated for a number of flows, a range of scenarios were simulated as described below:

#### Water levels and discharge

The relationship between the discharge in the flume and the total head over the weir that was established for the physical model was compared (and also used for calibration) to that of the numerical model.

Flow entering the upstream inlet boundary was monitored as the simulation progressed and was found to fluctuate slightly. The time mean discharge and total water head values are presented in Chapter 7.

#### Velocity field and pressures

Similar to the velocity field and pressure experiments of the physical model, the numerical CFD model collected a large sample of data for comparison and analysis. Whereas the physical model was limited to a few data collection points which could often not be recorded simultaneously, the numerical model could generate data for every grid point in its mesh at every time step. Such massive volumes of data are however unnecessary and are difficult to process. Data was thus only collected for a chosen set of data points in locations similar to the planes shown in Figure B.19 although at a much greater spatial resolution ( $\sim 2$  cm). Data was collected at time steps of at least 0.005 s which equates to a frequency of 200 Hz.

Data that was collected included the following:

- velocity vectors,  $u, v, w$
- total and dynamic pressures
- density of air and water
- Q-criterion
- vorticity
- Volume-of-Fluid factor

In addition to the resultant data quantities that could be determined from this data as described for the physical data, the present data could also be assessed based on its close spatial and temporal scales. This allowed for the visualisation of the vortices, the overflow nappe and numerous other phenomena as shown in Chapter 7.

Scenarios that were simulated to ascertain their effect on the hydrodynamic behaviour of the PKW are:

- a variable water level and discharge

- a variable inlet key width
- a range of PKW at different scales
- different PKW types: A, B and C
- different nose types: none, triangular and circular

The results of these analyses are presented in Chapter 7.

### Structural parameters

The structural FEM model and its *Static Structural* and *Modal* modules was utilized to run a varied number of PKW configurations to determine its modal characteristics, its deflections as well as the stress and strain state under various hydrostatic loads. The geometries tested mostly emulated the model B dimensions however, larger scales were also examined as were different materials.

### Sidewall vibrations

The system coupling of the calibrated *Fluent* module and the calibrated *Static Structural* module allowed for the fluid-structure interaction of a PKW to be simulated. Only two scenarios could be run due to their high computational cost. These are a discharge of 200 l/s and 400 l/s at the scale of model B, i.e.  $P = 1.1$  m.

### 5.3.6 Data analysis

The numerical data was handled and analysed in much the same manner as the physical data. The only major difference between the two is that the numerical data exhibits much less background noise, if any. This data thus did not have to undergo any cleaning. Care was taken to ensure that those portions of the data recorded when the model solution was still converging or stabilising were discarded.

### 5.3.7 Limitations

All numerical simulations, regardless of their refinement, are limited by their boundary conditions. It should be borne in mind that they are representations of a physical system which has been ring-fenced and simplified in some shape or form to allow it to be emulated. This means that the results of the numerical model may be considered non-physical as they may contain either numerical or modelling errors. On other words, the behaviour witnessed in the numerical model may not be present in a real world representation of the same model.

Numerical errors refer to the way the equations and parameters of the problem are represented and calculated using numerical techniques and include aspects like spatial and temporal discretization errors, poor convergence and rounding-off errors. These can be controlled to a degree by the user by using smaller grid sizes, smaller time steps and better reference values. Modelling errors on the other hand consist of inconsistencies in the assumptions and

approximations used to build the model. Examples include the geometry, boundary conditions, material properties and the choice of the formulation equations of the model [126].

Another aspect that has not been addressed in detail in the numerical analysis is that of sensitivity. Most of the input values used in the simulations have been specified as fixed quantities. It is expected that many of the values will indeed have no or negligible effect on the final results, but there are a few which may have a larger effect. These include the thickness of the sidewall, the material strength properties and the upstream approach depth.

Furthermore, as mentioned previously, only a single PKW unit was simulated in most of the scenarios. This means that if there were interactions between the flow in the opposing sides of the inlet or outlet keys, these would not be modelled. The inlet key was modelled in its entire width in one of the scenarios but this was limited to a CFD simulation only. The potential FSI caused by the pressure waves from the opposing walls of the inlet key has not been modelled.

This page is intentionally left blank.

## 6 Analysis of the structural behaviour of a PKW

### 6.1 Introduction

One of the key advantages of Piano Key Weirs, and one of the main reasons for their development, is their relatively narrow bases in comparison to their labyrinth weir counterparts. These narrow bases allow for their installation on top of existing concrete gravity dams [13]. Like gravity dams, type-A PKWs, are stable structures under most loading conditions.

However, the individual components which make up the PKW, especially the sidewall and overhangs, do require individual structural assessment. This chapter examines relevant aspects of the structural behaviour of some of these components. First the overall stress state of the structure is examined to identify those areas of the structure which experience the highest stresses. The impact that vibration caused by dynamic action on the structure may have on these locations is then considered.

Next, the modal characteristics of the PKW are explored. The mode shapes of the PKW are of interest as they indicate how the structure responds to dynamic loads and where it is most susceptible to vibration. Observing the deflections of a PKW under a hydrostatic load (see Figure 6.1) it is clear that the most susceptible portions of the wall (i.e. those experiencing the largest deflections) are the lateral sidewall between the inlet and outlet key as well as the upstream and downstream overhangs.

Due to its geometric nature, the mode shapes of a PKW can be analysed either from a global perspective or for each of the individual structural components. The sidewall of the structure is exposed to the largest fluctuating forces and is thus the structural component on which this study focusses. Although the vibration of the overhangs could be excited by some of the transient forces acting on the PKW, this component was excluded from the present research and should be studied at a later date.

### 6.2 Stress state

PKWs are considered rigid structures which, due to their numerous edges, corners and limited spans, have a high degree of geometric stiffness [127; 1]. This means that usual, unusual and extreme loading conditions result in only limited stresses in the structure, allowing it to be constructed using reinforced concrete without dense meshes of reinforcement steel. That said, as with all thin walled hydraulic structures, high thermal gradients can develop across these thin members leading to high thermal stresses. These stresses materialise in the structure, especially in the lateral wall, when one side of the wall is exposed to solar radiation and the opposite side remains cool due to its immersion in water. This necessitates at least nominal quantities of steel reinforcement ( $\sim 90 \text{ kg/m}^3$ ) [38].

These reinforcement requirements and the associated concrete cover specifications limit the

minimum thickness of the concrete sidewall to 0.2 to 0.45 m [122] depending on the slenderness of the wall. PKWs constructed from other materials, such as steel, can be much thinner from a few millimetres to a few centimetres again depending on the slenderness of the wall as well as the allowable deflections. In the present structural analysis, it has been assumed that the maximum deflection under unusual loads (a hydrostatic load equal to a water level of  $H/P = 0.2$ ) should be limited to  $L/100$ , with  $L$  being defined as the cantilever (perpendicular) distance from the crest of the sidewall to the base.

Considering the thin-walled steel PKW at prototype scale ( $P = 3.0$  m,  $T_s = 0.025$  m) under a hydrostatic load of  $H/P = 0.2$ , the highest deflections and stresses are caused by the bending moment acting on the cantilever-type sidewall. The highest deflections are located at the centre of the sidewall as shown in Figures 6.1 and 6.2. The highest stresses, here represented by the von-Mises equivalent stress, are located near the base of the sidewall where it meets the sloping base, as shown in Figures 6.3 and 6.4.

The bending stress profile across the sidewall at these high stress locations equate to tension forces on the upstream side of the wall and compression on the downstream side. This implies that, should cracking occur, it would occur on the side that is most susceptible to corrosion. This corrosion may lead to microscopic weaknesses in the region which may lead crack nucleation. Fluctuating tensile forces at these small cracks may then cause them to expand.

Furthermore, as stated in Section 3.4, the tensile stresses on the upstream side marginally reduce the fatigue limit at these locations. This means that small but repetitive vibrations whose amplitudes are ordinarily below the fatigue limit of the material, may now lie above this limit and thus lead to fatigue at these stress locations. The life of the structure may thus be limited as a result.

Figures 6.2 and 6.4 also show that the PKW unit can be idealised in the numerical model by only considering the structural behaviour of the sidewall, excluding the influence of the overhangs. The boundary conditions in the numerical model were calibrated to make certain that this idealised sidewall remains representative of the PKW as a whole. This is detailed in Section 6.4.

### 6.3 Natural frequencies in the physical model

The modal shapes and natural frequencies of a type-A PKW were determined both physically and numerically. The accelerometers installed on physical model B (see Chapter 5) were used to estimate the mode shape and their associated frequencies for the first few mode numbers. Due to the limited number of accelerometers that could be placed on the physical model, higher order mode shapes could not be extracted from the data, however their frequencies could still be estimated. Physical model data was captured for a number of water level elevations to ascertain the effect of the water body on the modal parameters.

The physical data was then utilized to calibrate a numerical model at the same scale. Due to the relatively simple geometry of the structure, the numerical model was able to emulate the physical modal behaviour with almost no calibration. The only adjustments that had to be made were to ensure that the geometry of the physical model was replicated as closely as

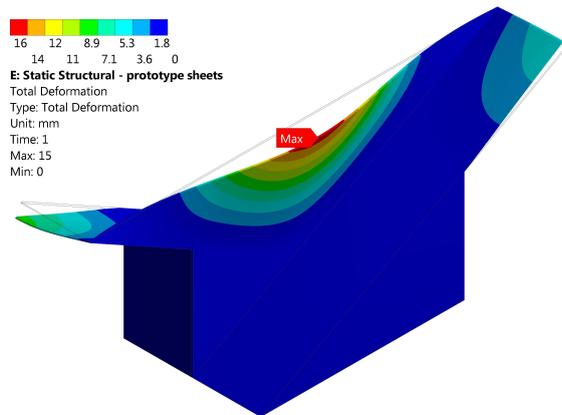


Figure 6.1: Isometric view of PKW showing sidewall deflection at  $H/P = 0.2$

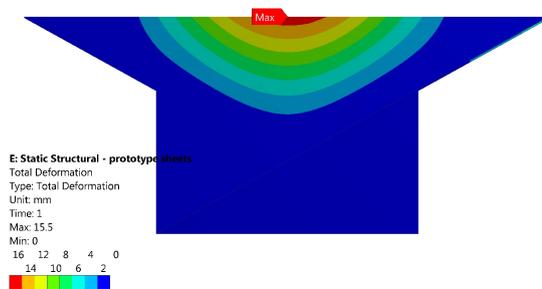


Figure 6.2: Side view of PKW showing sidewall deflection at  $H/P = 0.2$

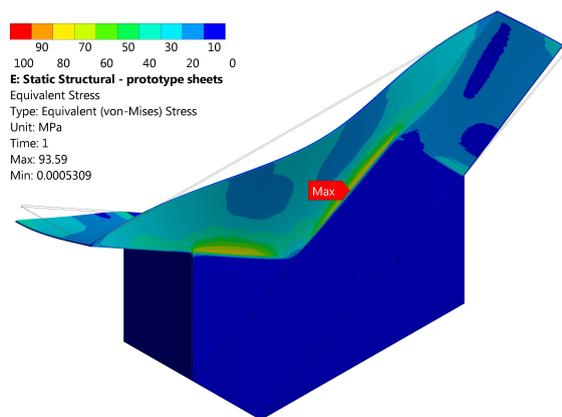


Figure 6.3: Isometric view of PKW showing sidewall stresses at  $H/P = 0.2$

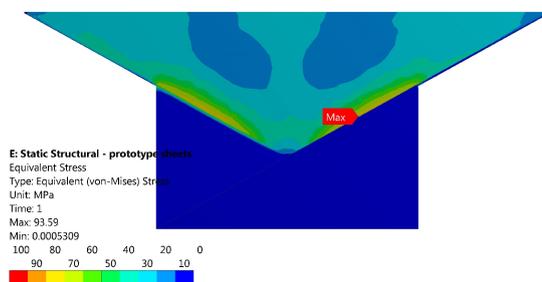


Figure 6.4: Side view of PKW showing sidewall stresses at  $H/P = 0.2$

possible in the numerical model. Considering that the numerical model was able to emulate the physical behaviour with no real calibration it means that the numerical model can be considered validated.

The simple geometry was then simplified even further to only include the sidewall (see Figure 6.9) and recalibrated such that the simplifications would not unduly affect the model behaviour. This simplification was done so as to limit the computational expense of the coupled numerical vibration model (see Chapter 8). Furthermore, analysis of the sidewall-only mode shapes allowed for a much clearer presentation of their behaviour.

It should be noted that only the sidewall was fitted with sensors. This means that the overhangs could not be directly included in the calibration. That said, the frequencies of their vibration are present in the data but their mode shapes could not be directly ascertained.

Furthermore, the physical model test involved the use of an impact hammer which activated the vibration. For consistency, and to activate the most number of modes, for each test the hammer was struck near the top of the sidewall, but off-centre, near to accelerometer number 2 (see Figure C.1). Some of the unscaled data shown below may thus reflect large amplitude deflections of certain modes which happen to be excited by an impact at this location. These large amplitudes should not be seen as indicative of their lack of stiffness or damping.

Table 6.1: Natural frequencies measured from physical model (Hz)

	Accelerometer data			Strain gauge data			
	0.0P	0.5P	1.0P	0.0P	0.5P	1.0P	1.2P
Water level							
Mode-1	20.8	20.2	13.2	20.3	20.3	12.4	7.1
Mode-*	34.3	34.5	29.4	34.2	34.2	27.9	–
Mode-2	41.8	42.1	40.5	41.5	41.6	39.5	32.0
Mode-3	58.0	57.8	57.0	57.4	57.4	56.5	52.0
Mode-4	75.0	75.0	73.5	75.4	75.4	75.4	–
Mode-5	89.6	90.4	–	81.0	80.8	–	–
Mode-6	98.0	97.8	97.5	98.0	98.3	–	91.4

A series of tests were run, with several repetitions of each test to prevent data errors. Nonetheless, it appears that accelerometer point 7 was incorrectly installed as its results could not be reconciled with the other data sets. The data from this point was thus discarded. Fortunately, the numerical model confirmed that the data from this point is not crucial to an understanding of the modal behaviour of the sidewall.

The complete set of the accelerometer data is presented in Appendix C. Relevant results for the various scenarios are described below. Note that only those mode frequencies up to 100 Hz are included in the analysis. The selection of this limit was made as mode shapes above this value can no longer be identified by the limited number of accelerometers.

Table 6.1 presents the frequencies obtained from the physical model. The data shows that, though there is some slight variance, the strain gauge and accelerometers picked up the same frequencies. This means that the much more accurate accelerometers which could not be used under active flow conditions could be suitably replaced by the strain gauge. One shortcoming is that, due to its location in the centre of the wall at a node of several of the mode shapes, the strain gauge has only a very weak capability of sensing these modes. This is reflected by certain missing values in Table 6.1. Analysis of the related data for those particular scenarios suggest the presence of a mode but none could be detected in the data. It is likely that these modes were not activated with sufficient energy during the experiments.

Table 6.1 also shows the effect of the water body behind the model PKW. The values for the *empty* and *half-full* scenarios are identical probably because the water level was not high enough to influence the most flexible portions of the weir which are incorporated in the weakest vibration modes. At a water level equal to the crest of the PKW there is a noted decrease in all the measured natural frequencies as the added mass of the water body takes effect. This trend is seen to continue in the strain gauge data with water levels above the crest (PVC parapet wall scenario). It is possible that the presence of the PVC parapet wall unduly influenced the frequency results but this was shown not to be the case. The results for the *empty*, *half-full* and *full* with and without the PVC parapet wall were identical.

The decreasing trend in the natural frequencies with increasing water levels is evident from the Frequency Response Function (FRF) of both the accelerometer and strain gauge data as

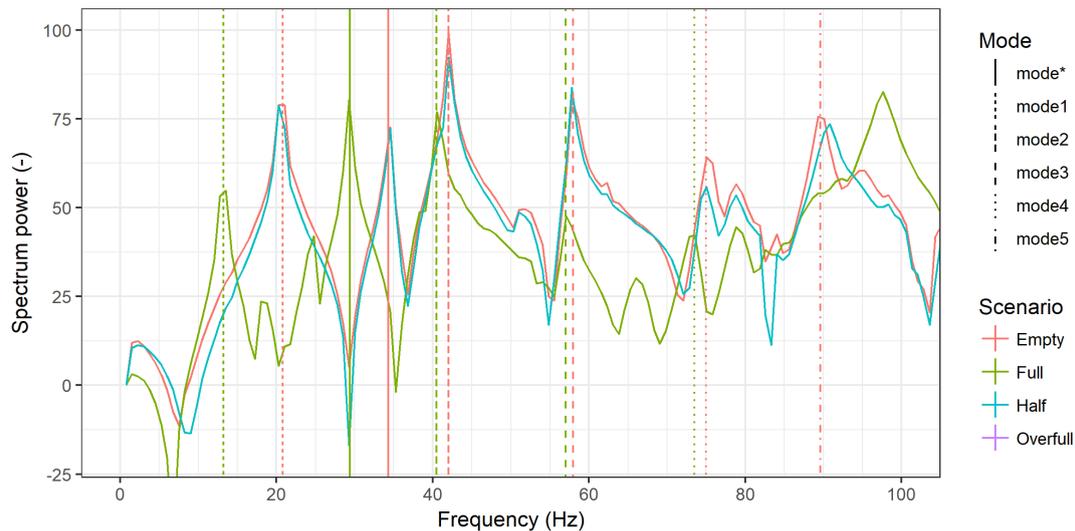


Figure 6.5: Accelerometer FRF showing natural frequencies for three scenarios

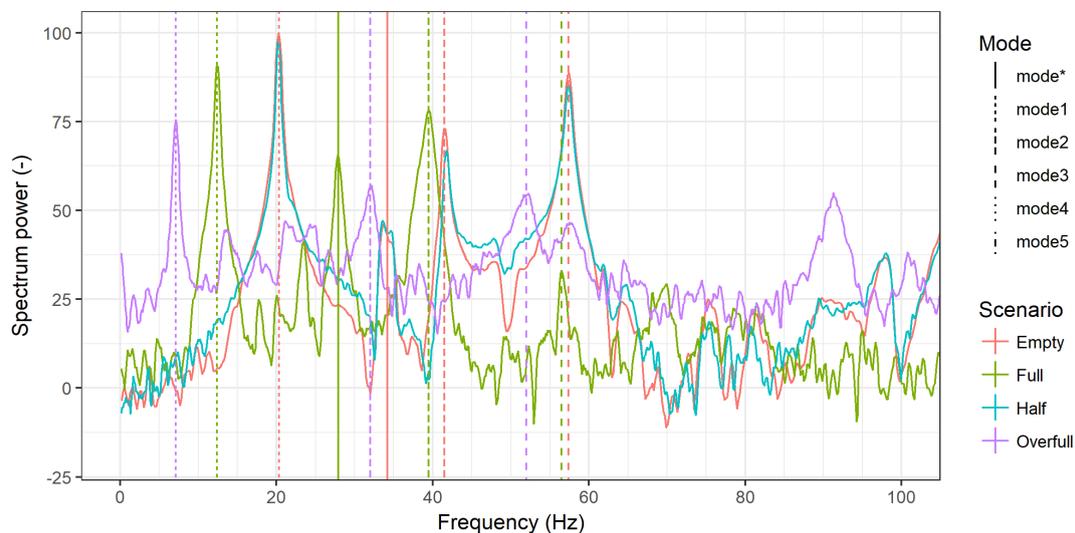


Figure 6.6: Strain gauge FRF showing natural frequencies for four scenarios

presented in Figure 6.5 and Figure 6.6 respectively. Note that these graphs do not show the *half-full* frequencies as these are identical to the *empty* frequencies. The magnitude of the change appears to reduce at higher mode numbers, with only marginal decreases occurring from the third mode onwards. It is surmised that this may be due to the smaller mode shapes of these higher mode numbers, which activate a lower volume (or area) of water during vibrations in that mode. Alternatively, it is possible that some of these higher modes were damped out entirely such that they could no longer be discerned in the data. The mode shapes are discussed in greater detail in Section 6.4.

The natural frequencies which were physically measured could be fairly accurately simulated by the numerical model with little calibration. Geometric adjustments were made to the numerical model to replicate the physical model as closely as possible. The main geometric aspect which was so altered was the thickness of the steel plates. The specified thickness of the steel plate as provided to the manufacturer was 6.0 mm. However, it was found that a value

Table 6.2: Natural frequencies measured from numerical model (Hz)

Mode	Dry scenario			Full scenario		
	Numerical	Physical	Calibration	Numerical	Physical	Calibration
Mode-1	21.1	20.8	1.7%	13.3	13.2	0.6%
Mode-2	41.3	41.8	-1.3%	37.9	40.5	-6.5%
Mode-3	57.7	58.0	-0.6%	56.0	57.0	-1.7%
Mode-4	78.9	75.0	5.1%	80.0	73.5	8.8%
Mode-5	95.0	89.6	6.1%	93.4	—	—%

of up to 6.2 mm was needed to emulate many of the measured natural frequencies. It is noted, however, that a single plate thickness value could not emulate all the modes of interest. It is not unusual to consider that the manufacturer would supply steel plate marginally thicker than the specification and that the thickness of the plate would vary by a value well within the tolerance limits for their manufacture. The effect of changes in thickness on the frequencies of the steel PKW is explored further in Section 6.5.1.

As noted in the next section, the numerical model was capable of picking up several additional modes than were noted in the physical model. This is because the structure as a whole and not just the sidewall was considered for this numerical model, as was done for the physical model. There is thus a disjoint between the two sets of mode frequencies which was reconciled using the shapes of each of the modes. This means that only those modes for which mode shapes could be reliably determined were assessed, i.e. modes 1-5. Furthermore, as explained in the next section, those modes which are dominated by the overhang, floor or any other structural element besides the sidewall were excluded (e.g. Mode-\* in Table 6.1). The numerical model frequencies (at the scale of model B) of relevance are reported in Table 6.2. The entire set of frequencies is presented in Figure C.11. The numerical frequency data show that there is good agreement with the physical results, especially when considering the tolerance limits of the thickness of the steel plate of 0.3 mm = 5%.

The *full* scenario, which reflects the added mass damping of the water body behind the weir, was also simulated. The results, presented in Table 6.2, show good agreement with the physical data. The calibration parameter used in this scenario was however arbitrary as there were several parameters which could be used to emulate the behaviour of the added mass. A simulation, using as calibration parameter a mass-matrix damping multiplier factor of 207, was capable of emulating the natural frequencies of the physical model. This value would however not be applicable to other weir heights. Hence this factor would need to be empirically determined in each case. Fortunately, since the vibration model (see Chapter 8) incorporates the water body and its mass directly there is no need to account for it with an arbitrary factor.

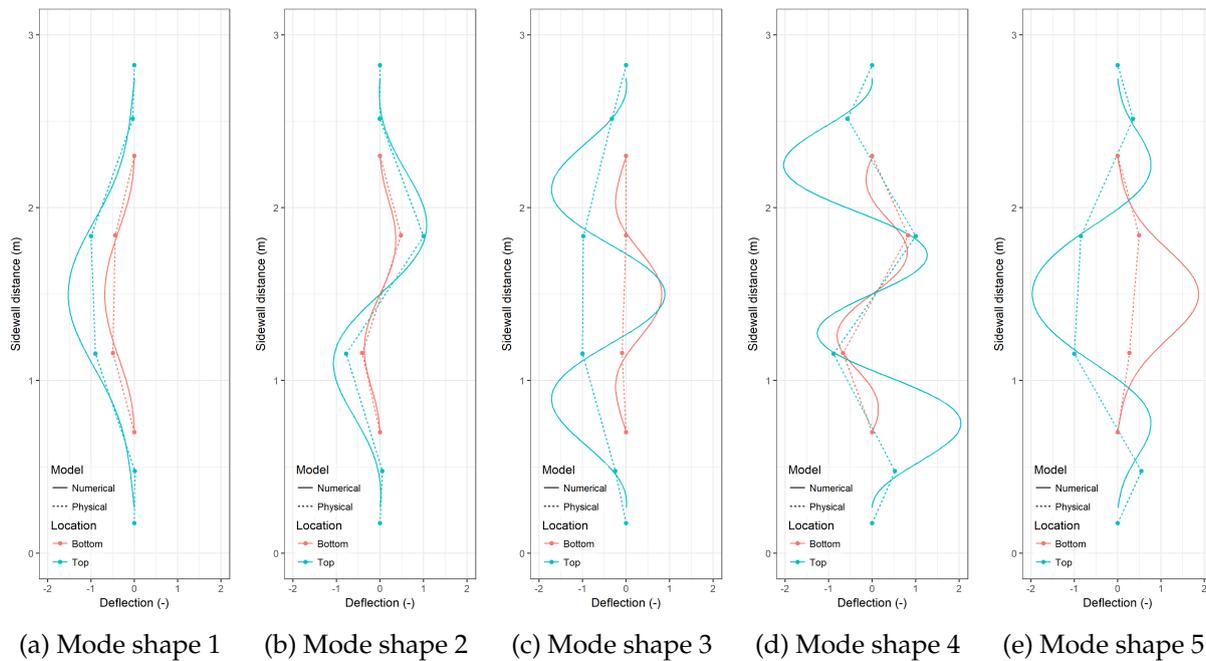


Figure 6.7: Calibration of numerical model mode shapes with physical model results

## 6.4 Mode shape calibration

Analysis of the accelerometer data allowed for the estimation of the mode shapes of the vibrating PKW sidewall. This allowed for the results of the numerical model to be compared to the physical data, and so to be calibrated. As mentioned above, it was found that the numerical model was able to adequately predict both the natural frequencies and the mode shapes with only very minor calibration. The calibration results of the first five mode shapes are shown in Figure 6.7. The *Top* and *Bottom* locations refer to the top (points 1-4) and bottom (points 5-6) lines of accelerometers as shown in Figure 5.11.

The modes shown in the figure emulate the typical vibration modes of a beam fixed at both ends with a number of repetitions of a sinusoidally shaped curve. The lower portion of the wall follows the same pattern as for the top portion of the wall except for the fifth mode. Here, the lower portion of the sidewall follows the opposite trajectory followed by the upper portion. This unusual mode shape can be seen in the ninth mode in Figure 6.8 and in Figure 6.9e. This mode shows that despite the apparent two dimensional nature of many of the modes, they are actually fully three dimensional.

The areas which experience the greatest deflection in each mode are of interest as only certain areas are exposed to fluctuating forces of the PKW under flow. Hence, even if the fluctuating force oscillates at a frequency equal to one of the identified modes, it needs to be active over the area of that mode in order for large amplitude vibrations to form. This is explored further in Chapter 8.

As mentioned in the previous section, the calibrated numerical results showcased a large number of additional modes which were disregarded in the present analysis of the sidewall. The entire sequence of modes is presented in Figure C.11 where the five modes of interest

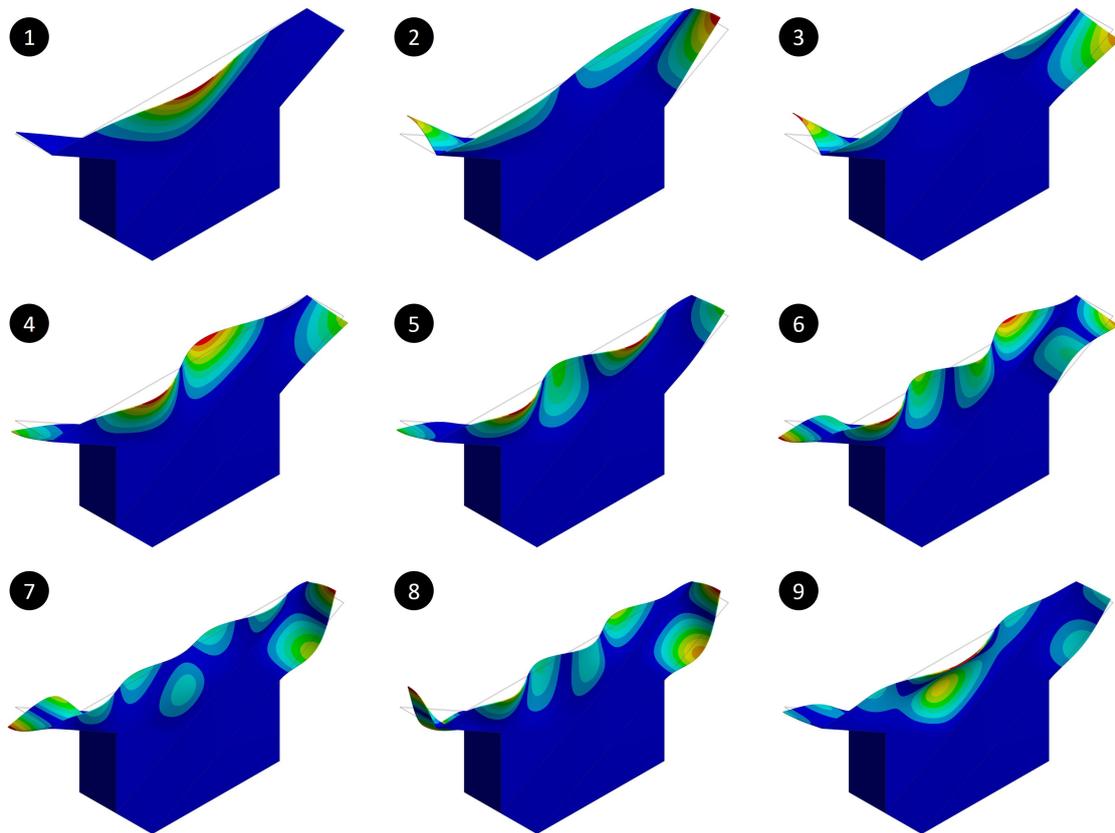


Figure 6.8: Mode shapes of PKW walls and overhangs

have been highlighted. It should be noted that this sequence of modes is only valid for the scaled model which consisted of welded and unsupported sheets of steel. It is highly likely that steel prototypes would have the void under the sloping floor filled for stability, strength and durability reasons. This means that many of the modes involving the floor would fall away as shown in Figure 6.8. This highlights that the infilling of the void under the bases could be used to make the structure stiffer and alter its modal characteristics.

The limited number of modes which involve the sidewall shown in Figure 6.8 as well as the stress state of the PKW (see Section 6.2) allows for the discretization or idealisation of the structure as a whole to just that of the sidewall. This would then permit just this portion of the structure to be incorporated into the numerical vibration model greatly reducing the computational cost of the model. In order for the idealised sidewall to still emulate the PKW as a whole its boundary conditions had to be suitably calibrated. The main parameter that was used in this calibration is the elasticity of the support at the base of the wall. Specifying an elastic foundation stiffness of 800 GPa at the elastic support along the base of the idealised sidewall resulted in the exact emulation of the first six mode shapes as shown in Figure 6.9. The mode frequencies so obtained are presented in Table 6.3 and show good agreement with both the physical and numerical (whole PKW) results.

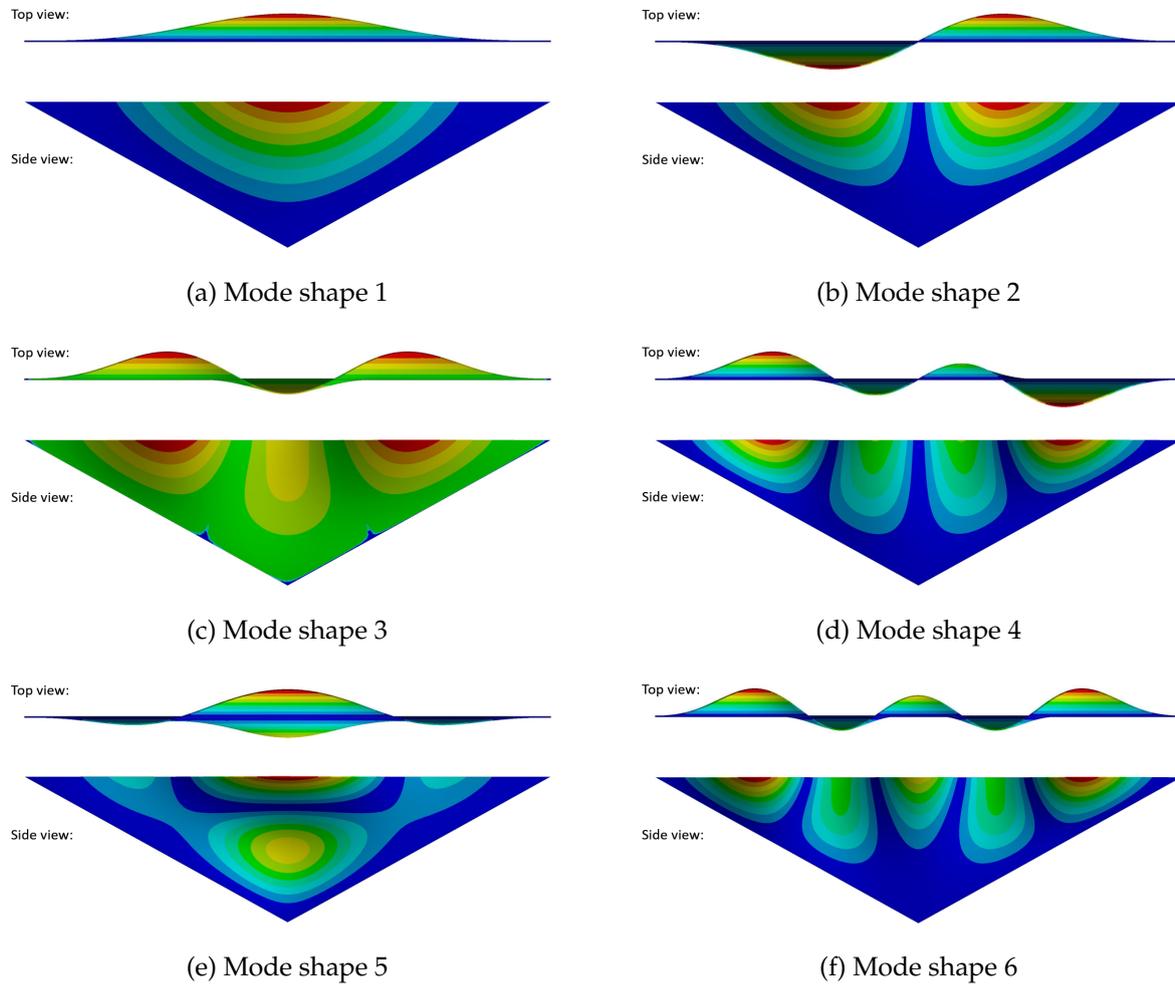


Figure 6.9: Mode shapes of PKW sidewall only

Table 6.3: Idealised sidewall frequency calibration (Hz)

Mode number	Physical (PKW unit)	Numerical (PKW unit)	Numerical (sidewall)	Calibration (to physical)	Calibration (to numerical)
Mode-1	20.8	21.1	20.1	-3.2%	-4.8%
Mode-2	41.8	41.3	38.8	-7.1%	-5.8%
Mode-3	58.0	57.7	58.6	1.0%	1.5%
Mode-4	75.0	78.9	83.7	11.6%	6.2%
Mode-5	89.6	95.0	92.4	3.1%	-2.8%

## 6.5 PKW modal characteristics

Once it was determined that the numerical model was capable of reliably emulating the structural modal behaviour of PKWs, a number of scenarios were examined. The following aspects were explored to ascertain their effect on the modes and also determine how sensitive the modes are to them:

### 6.5.1 Wall height and thickness

Figure 6.10 a) shows the trend in natural frequencies of the first mode of the PKW sidewall over a range of weir height,  $P$ , and wall thickness,  $T_s$ , values. Figures b) and c) likewise show the trends in the deflection and stress in the sidewall respectively under a water head of  $H/P = 0.2$ . The deflection is reported in the form of  $L/\delta$  with  $L$  being the shortest distance from centre of sidewall crest to the sloping base. The stresses shown are the maximum von Mises stresses whose location is similar to that shown in Figure 6.4. The contours of each plot are superimposed in Figure 6.10 d).

These graphs can be used as a design guideline in the sense that for a given pair of  $P$  and  $T_s$  values the serviceability limit state ( $L/\delta$ ), the ultimate limit state ( $\phi\sigma_{ult}$ ) and the first natural mode ( $f_1$ ) can be checked. Bear in mind that the frequencies presented showcase no added damping, hence the frequencies in the presence of water behind the weir will be lower than these values.

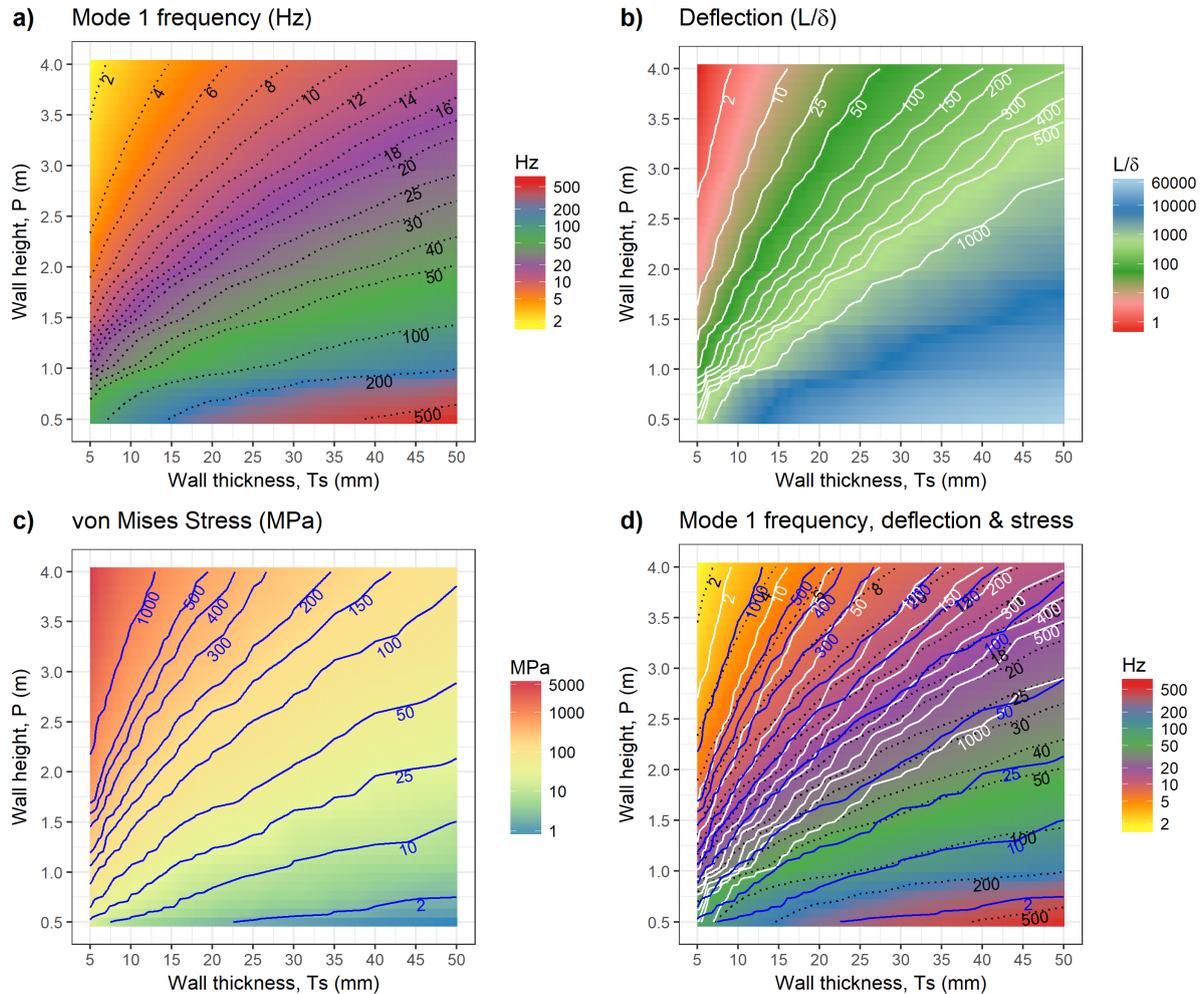
The observed trends in these graphs are as expected with very short and very thick PKWs experiencing very high frequencies and vice versa. The contour gradients in Figure 6.10 a) imply that for very thin weirs (<25 mm), small changes in thickness significantly affect the natural frequency. For very thick weirs (>35 mm), changing the height of the weir has a greater influence. Hence, if exposure to certain frequencies is of concern at a PKW, a thick PKW should be marginally shortened rather than made thicker.

### 6.5.2 Construction material

The material of which the sidewall is constructed has a decisive role on modal behaviour. The three materials which were examined are steel, concrete and PVC, which each have distinct material properties which affect the modes. These are shown in Table 5.7. Steel has a much higher modulus of elasticity and is thus much stiffer than concrete and PVC. It thus exhibits smaller vibration amplitudes. However, it is also more dense, which reduces its damping.

It should be noted that when a PKW is constructed of any of these materials, their properties play a role in the chosen wall thickness. Steel or PVC walls can be constructed from very thin members of a few millimetres or centimetres in width. Reinforced concrete however, with its internal steel mesh requires thicknesses of 200 mm or more.

The first natural frequencies of a PKW sidewall with a  $P$  of 1 m and 3 m over a range of materials and wall thicknesses is shown in Figure 6.11. Note that walls with a large thickness to height ratio will not have their first modes along the sidewall but rather along the overhangs. The graph reveals that steel, being a very stiff material, has the highest frequencies, whereas

Figure 6.10: Variation in PKW behaviour with  $P$  and  $T_s$ 

concrete has marginally lower frequencies. PVC, on the other hand, has very low natural frequencies in its range of realistic values (i.e. values that would be considered for their use). Fluid induced vibrations would certainly need to be accounted for in the design of such a PKW.

## 6.6 Discussion

The modal and structural behaviour of a steel PKW, specifically its thin sidewall, were examined in both a physical and numerical model. Due to the well-defined and relatively simple geometry of PKWs, it was straightforward to emulate the physically observed behaviour in the numerical model. It was found that small incremental changes to the thickness of the steel sidewall (much smaller than normal tolerance limits for their manufacture) were responsible for the small differences in the modal characteristics that were noted between the two models. This implies that these minor adjustments could be used during the design process to combat vibrations should they be of concern. That said, it may be more efficient to reduce the height of the weir instead and reduce the slenderness of the wall that way, seeing as steel comes in standard thicknesses. It also highlights that exceptionally good quality control is needed to

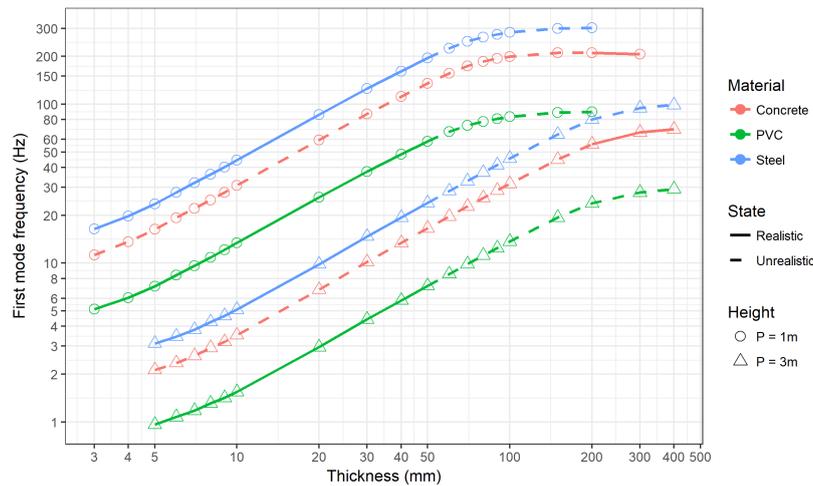


Figure 6.11: First mode frequencies at a range of wall thicknesses and materials

ensure that the steel plate supplied by the manufacturer is indeed thicker than specified since this appears to be such a sensitive parameter to its vibration.

The modal parameters of the PKW were determined in their dry as well as their damped state. There was a clear reduction in the modal frequencies when the PKW was being restricted by the added mass of a water body behind it. Only the lowermost mode numbers experienced this however. The higher mode numbers either did not reduce as much or were damped out to such a degree that they could no longer be discerned from the data.

The stress state in the sidewall was examined on the basis of its equivalent von Mises stress. The highest stresses occurred near the base of the sidewall, where it meets the sloping base, close to the start of the overhangs. The stress is in the form of a bending moment across the wall which manifests as a tension force on the upstream side and compression on the downstream side. It is noted that vibration of the sidewall would induce alternating stresses superimposed on the mean stress state. On the upstream side of the wall this could lead to long term fatigue and cracking in the high stress zone. This area may thus also be susceptible to corrosion ultimately weakening the structure. Corrosion protection could be installed here but this too would need to resist the long term fluctuating forces.

The PKW as a whole was simplified to just that portion where the most deflections were noted, namely the sidewall. Only this portion is included in the numerical vibration model to reduce the computational cost of this model.

It is noted that the study focusses mostly on steel PKWs as it is these that are the most susceptible to vibrations. Reinforced concrete may have its own set of vibration related concerns. Excessive thermal stress as well as concrete ageing could lead to the development of tension cracks on the upstream face of the transverse wall of the PKW. These cracks could lead to a reduction in the stiffness and damping of the transverse wall to perpendicular movement. Thus, despite the inclusion of appreciable quantities of steel reinforcement, if surface cracking is not specifically combated, it could lead to an increased susceptibility of the slender elements of a PKW to FIV. This highlights the possibility that cracking would alter the modal and damping characteristics of a PKW. This should be explored further.

## 7 Analysis of the hydraulic behaviour of a PKW

### 7.1 Introduction

The basic hydraulic behaviour of piano key weirs was explained in Chapter 2. It reviewed the current understanding as reported in literature, which is largely restricted to the steady state condition. This chapter covers this behaviour in more detail and also explores additional transient or temporal features which are present at the weir. It especially focusses on those aspects which are relevant to the generation of fluctuating forces or pressures on the sidewall.

The various flow phenomena were studied from both a physical and numerical perspective, with the data from the physical model used to calibrate and validate the numerical model. Whereas the physical models that were built are capable of emulating the phenomena with only minor discrepancies, capturing qualitative data from these models can be challenging. As described in Chapter 5, the data that was collected in the physical models consisted of time variant velocity, pressure and vibration data at a discrete number of pre-selected locations.

The numerical model, on the other hand, readily allows for capturing large quantities of data at small spatial and temporal scales. However, it suffers from shortcomings where the numerical equations are not always capable of emulating the physical behaviour. Without calibration, there is a risk that the numerical model results are non-physical.

Once the numerical model was successfully calibrated, a parametric analysis was conducted to explore the factors which influence the pressure oscillations on the sidewall. These include the inlet key width, the weir size, the discharge, the PKW type and upstream noses.

### 7.2 Calibration

The calibration process consisted of comparing the results of the numerical model with those of the physical model. In this exercise, both model types used the same scale so as to eliminate the scaling factor as much as possible. The main calibration targets were as follows:

- the sidewall pressure frequency
- the discharge-head relationship
- trends in the average velocity field
- the average turbulence intensity field
- the overall visual appearance and behaviour of the downstream nappe

The many functional components of the ANSYS Fluent software model allow it to simulate a wide variety of flow scenarios. There is fortunately a great deal of documentation and guidance which is provided by ANSYS and CFD forums on which parameters are most of relevance for

which scenario. These parameters were used as a baseline for later incremental adjustments in the calibration exercise.

The majority of the numerical modelling research that has been conducted to date in piano key weir hydraulics has used the Reynolds Averaged Navier-Stokes (RANS) methodology. It quickly became evident in the present numerical modelling that, although the average flow field and discharge behaviour could be accurately emulated, almost no oscillatory data was being generated. The reason for this is that the RANS turbulence models are based on statistical time-averaged representations of turbulence and its fluctuations [123]. They are thus not capable of generating eddies which are the primary cause of the witnessed oscillations. The LES and DES methodologies, which are capable of modelling turbulent eddies, were thus utilized.

The LES model effectively filters out all turbulent eddies which are smaller than the grid cell size and subsequently models these using a subgrid scale turbulence model. Only those eddies which are larger than a group of four cells can be accurately modelled by LES. This means that cell size is an important aspect to examine in the calibration exercise. Other aspects which were iteratively checked and had an effect on the calibration quality are shown in the list below. Some of these were more sensitive than others.

- **Cell size:** A fixed cell size was stipulated for most of the flow region. The sizes had to be refined along the upstream edge of the inlet key as well as all along the crest to allow for the development of high velocity gradients at these locations. It was thought that a higher density of cells along the inlet key sidewall would assist in modelling the turbulent eddies. However, this only resulted in small high frequency eddies which did not contribute to the observed oscillations and added unnecessary noise to the generated pressure signal. At the scale of model A, the overall cell size in the PKW keys was 5 mm with refinements down to 1 mm. For larger scale models the grid size was scaled upward to suit the larger geometry while still keeping the crest and upstream edge relatively fine.
- **Upstream turbulence intensity:** Fluent allows for the inlet boundary to be specified with a turbulent intensity. This is achieved by a Spectral Synthesizer which generates random velocity perturbations in the plane of the upstream boundary. Since the PKW being modelled is in a channel configuration, some channel turbulence is expected. A value of 10 % was found to fit the physical model data. Note that there is also an option to simulate actual vortices at this inlet boundary. This was found to be computationally expensive and did not meaningfully alter the calibration and was thus excluded.
- **Upstream approach length:** Related to the above turbulence inlet boundary condition, increasing the upstream approach length allowed a system of vortices to develop along this length. The effect on the pressure oscillations of these developed vortices was found to be identical to the artificial randomly generated turbulence at the inlet boundary as described above. The latter was thus selected as preferable due to its lower computational cost.
- **Transient formulation:** The *Bounded 2<sup>nd</sup> order implicit* transient formulation was applied to the hydraulic models which were based on DES. This greatly supported the conver-

gence of the solution. This formulation is, however, not available in the FSI Coupling models because of the moving boundary in these simulations. The DES could not achieve satisfactory convergence without this formulation hence LES was used instead for the FSI simulations. These employed the 2<sup>nd</sup> order implicit transient formulation.

- **Pressure-velocity coupling:** There is a choice of handling the pressure-based solvers in a segregated or coupled manner. Full coupling between the pressure correction and momentum equations does improve the results marginally, but it did require a longer run time. The segregated SIMPLEC scheme provided similar results in a faster time. SIMPLEC was selected.
- **Volume of Fluid:** The VOF spatial discretization was conducted using the *Compressive* technique. The *Modified HRIC* is recommended for LES or DES models, however, this technique rapidly diverged the solution.
- **Under relaxation factors:** The URF values were adjusted in an attempt to speed up convergence but were found to have little significant effect. They were thus left at their default values.

The results of the calibration are shown in the sections that follow.

### 7.3 Steady state behaviour

The steady state behaviour of a typical PKW is fairly well understood and is described in Chapter 2 [68]. The primary focus of these previous studies has been on the discharge efficiency that these weirs can attain. Besides the discharge coefficient,  $C_d$ , other steady state aspects which have been covered in literature include general flow patterns, nappe behaviour and water level profiles. This body of knowledge is expanded upon by the observed steady state behaviour of the physical and numerical models of this study.

#### 7.3.1 Discharge coefficient

Although the present study does not aim to maximise the discharge in any way, it is worthwhile verifying the observed discharge efficiency and the computed discharge efficiency with the predictive models that have been compiled from published data. Figures 7.1 and 7.2 describe how the physical model data compares to the numerical data and how these relate to the predictive models. For reference purposes, the numerically determined discharges, overflow depths and discharge coefficients are presented in Table 7.1. The physical data is attached in Appendix D.

The data demonstrate that the numerical model is readily capable of emulating the physical model. In terms of the predictive models, the data fall between the two equations which are applicable. It should be noted that the Kabiri-Samani & Javaheri equation [9] is not applicable since some of the parameters used fall outside the limits of its use (see Appendix A). The study data tends more toward the Leite Ribeiro equation [29] when examining the head-discharge

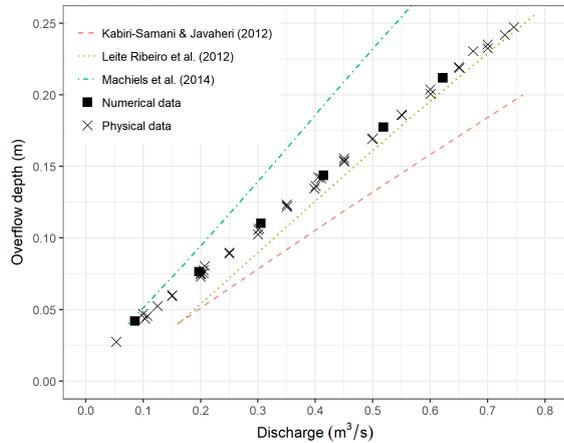


Figure 7.1: Head-discharge data

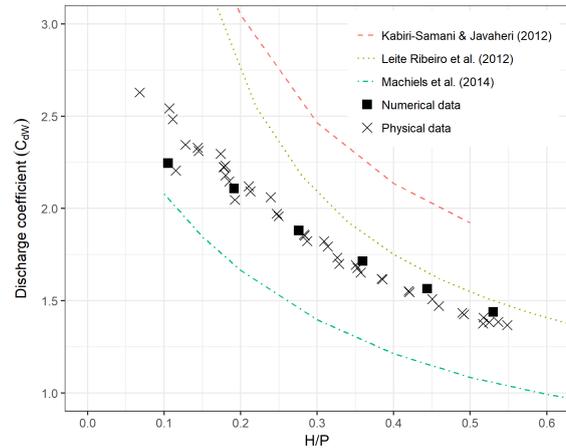
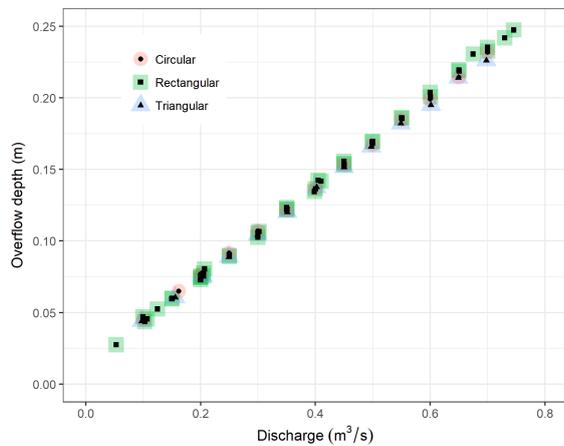
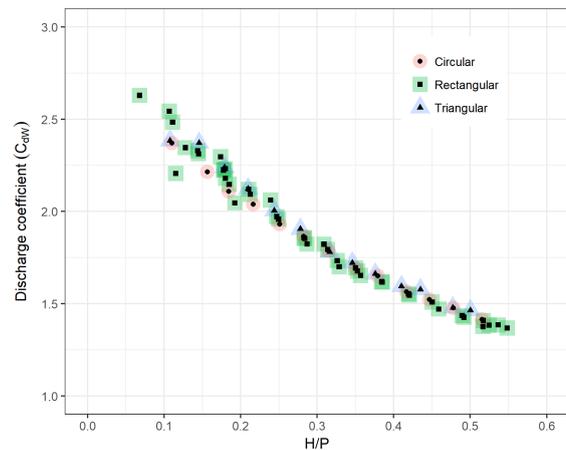
Figure 7.2:  $H/P$  and Discharge coefficient

Figure 7.3: Head-discharge data for different nose types

Figure 7.4:  $H/P$  and Discharge coefficient for nose types

relationship. However, it more closely follows the shape of the Machiels equation [8] when considering the discharge coefficient. This is probably because the very high discharge coefficients predicted by the Leite Ribeiro equation at low overflow depths are related to half-round crests, whereas the present study and that of Machiels involve flat topped crests. The shape of the crest has less of an influence at higher heads.

The changes in the discharge efficiency in the physical model as a result of the different types of upstream noses is set out in Figures 7.3 and 7.4. Although there is a consistent increase in the discharge for both the triangular and circular nose compared to the rectangular profile, this difference is so small that it is of little practical significance. This is supported by Figure 2.21.

The discharge coefficients for the larger model B, with  $P = 1.1$  m, were also estimated. The analysis was limited to very low flows which are further described in Section 7.4.6. These very low flows, the thin nature of the crest and the pseudo-prototype scale resulted in very high discharge coefficients.  $C_{dW}$  values of up to 5.53 were achieved for a discharge of 51/s ( $H/P = 0.005$ ). The entire data set is presented in Appendix D. These discharge coefficients

Table 7.1: Numerical model discharge

$W_i$ [m]	$W_o$ [m]	$W_i/W_o$ [-]	$W_u$ [m]	$P$ [m]	$H$ [m]	$H/P$ [m]	$T_s$ [m]	$Q$ (1unit) [m <sup>3</sup> /s]	$Q$ (5units) [m <sup>3</sup> /s]	$C_{dW}$ [-]
0.3	0.24	1.25	0.3	0.4	0.042	0.105	0.03	0.017	0.086	2.25
0.3	0.24	1.25	0.3	0.4	0.077	0.191	0.03	0.040	0.198	2.11
0.3	0.24	1.25	0.3	0.4	0.110	0.276	0.03	0.061	0.305	1.88
0.3	0.24	1.25	0.3	0.4	0.144	0.360	0.03	0.083	0.414	1.71
0.3	0.24	1.25	0.3	0.4	0.178	0.444	0.03	0.104	0.518	1.57
0.3	0.24	1.25	0.3	0.4	0.212	0.530	0.03	0.124	0.622	1.44

(1unit) - 1 PKW unit with one half inlet key and one half outlet key  
(5unit) - 5 PKW units, equivalent to the physical model

are a great deal higher than those described in the literature. This can be explained by the much smaller model scales that were used in those tests which could not accurately emulate prototype behaviour at such small overflow depths. The current model is large enough that it can be considered as a prototype for the discharge measurements, meaning that no scaling effects need to be considered. Furthermore, the sharp crested nature of the crest encouraged high discharge at low overflow heads.

### 7.3.2 Flow lines

Flow lines approaching and overtopping a type A PKW are described in Section 2.4.2. These are qualitative only and so can only be visually compared to those obtained in the numerical models. The figures below showcase the flowlines as determined in the numerical model. They are described first from a global perspective and then in a closer view of the inlet edge.

#### Global flowlines

Figures 7.5 to 7.8 characterise the flowlines from a global perspective. In each of these figures Figure(a) represents three horizontal sheets of flow as they approach the weir at heights of  $P/3$  (red),  $2P/3$  (yellow) and  $P$  (green). Figure(b) represents two vertical flow sheets, one approaching the outlet key (blue) and the other the inlet key (orange).

The flowlines presented in these figures showcase a number of relevant flow patterns:

- There is only a small portion of the total flow which discharges over the upstream crest of the outlet key. Only flow approaching the outlet key which flows near the surface does so (see blue and green lines). All remaining flow gets diverted into the inlet key.
- The height at which flow approaches the weir determines, to a large degree, over which section of the weir it will overtop the crest:
  - In general there is little mixing that takes place between the flows from the various locations. The flow sheets represented by the red, yellow and green lines remain

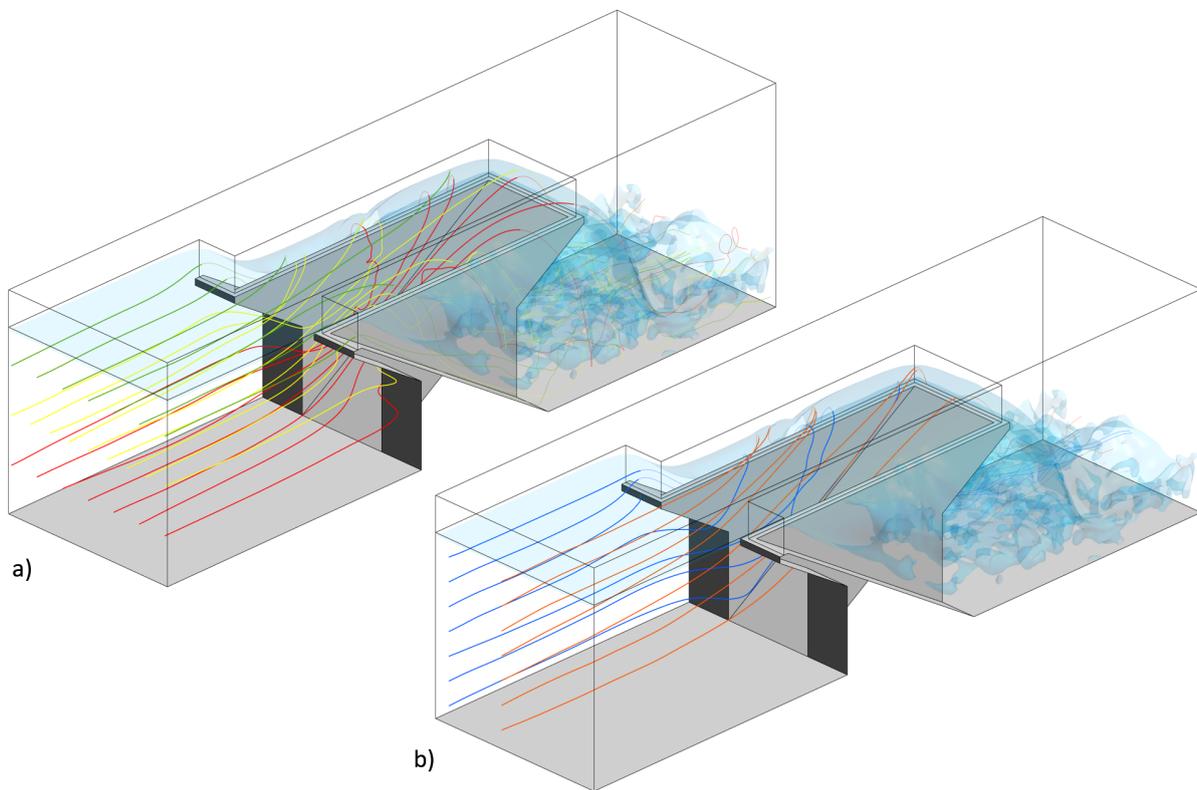


Figure 7.5: Flowlines approaching a PKW - oblique view (flow is up and to the right)

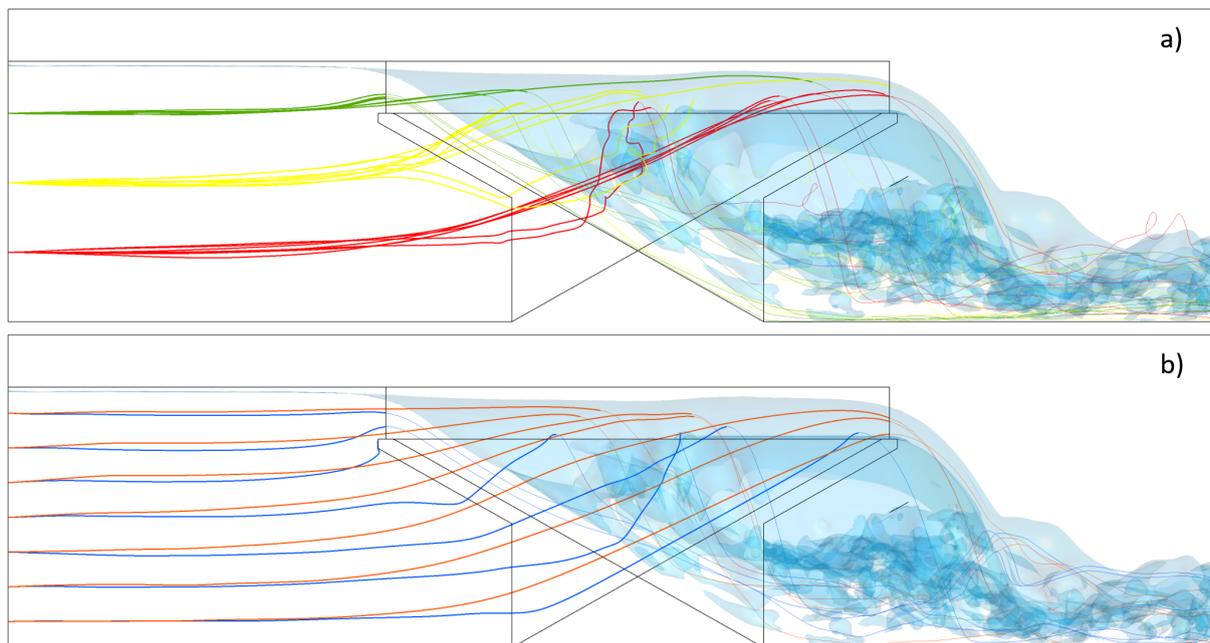


Figure 7.6: Flowlines approaching a PKW - side view (flow is left to right)

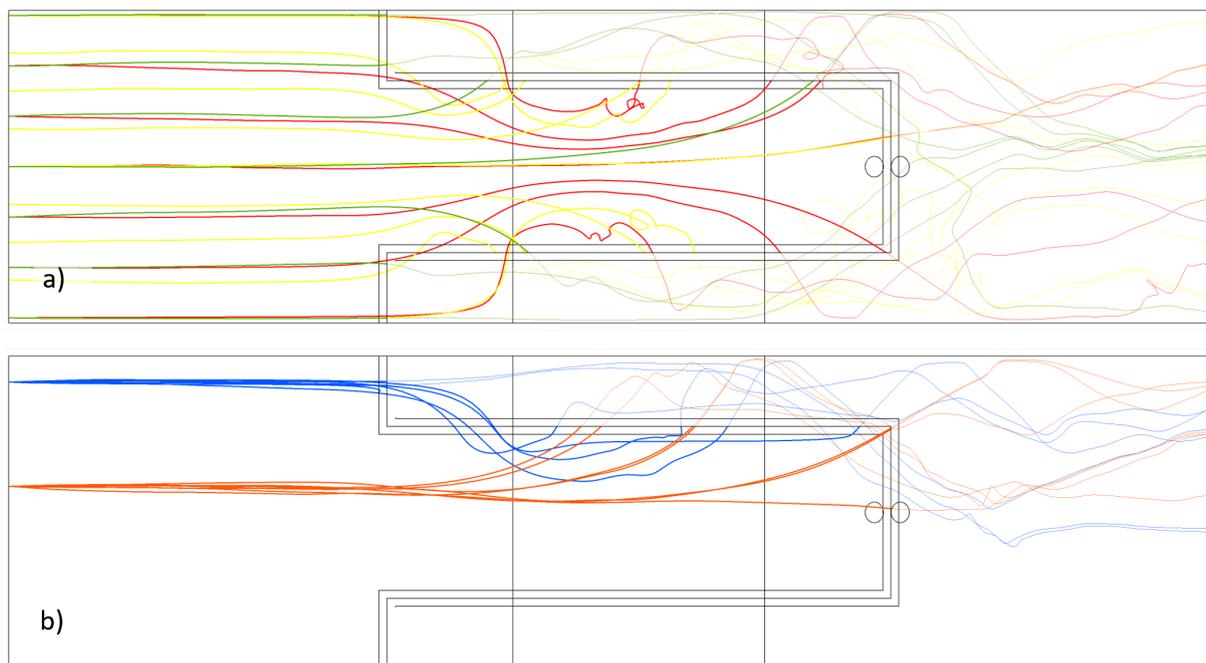


Figure 7.7: Flowlines approaching a PKW - plan view (flow is left to right)

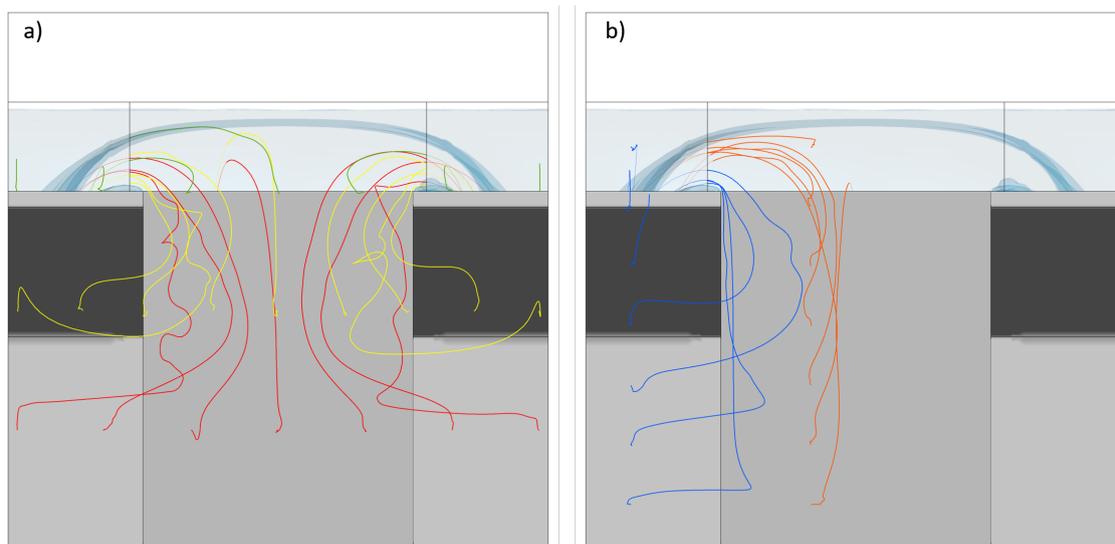
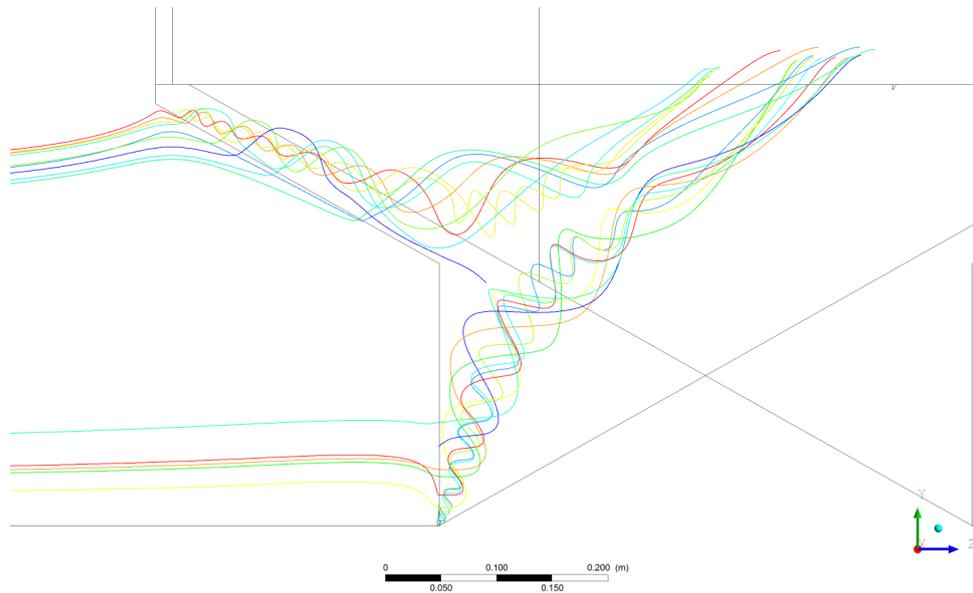


Figure 7.8: Flowlines approaching a PKW - upstream view (flow is into the page)

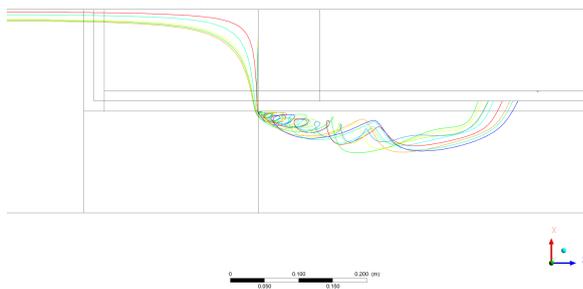
- distinctly separate as they enter and discharge over the crest. Only in the turbulent region downstream of the weir does mixing occur.
- The lowest flow sheet (red) shows converging flowlines as they enter the inlet key where they get forced upward by the sloping base. They mainly discharge at the downstream end of the crest.
  - The middle flow sheet (yellow) follows the same pattern as the red sheet below it and reaches the sidewall crest halfway along its length.
  - The uppermost flow sheet (green) discharges over the upstream sections of the sidewall crest and is also the only flow that can discharge directly into the outlet key.
- Flow approaching the outlet key (blue) is diverted away from the stagnation pressure zone which forms against and underneath the upstream overhang. This flow must make a sharp transition as it comes around the corner of the inlet key. This transverse momentum as flow enters the inlet key, creates a separated shear boundary layer starting at the corner. A swirling or recirculation zone forms behind this layer and is the cause of the negative longitudinal velocities which have been noted by other studies [24; 36]. This zone is highly dynamic and it grows as it absorbs flow from its surroundings and then collapses when it grows too large. As explained in Section 4.3.1 this collapse occurs as vortex shedding and is one cause of fluid vibrations at a PKW. The swirling vortex located here was validated visually in the physical model by the use of coloured dye. The duration with which this dye remained in the vortex is testament to the stagnant nature of the flow in this vortex.
  - Flow approaching the inlet key (orange) enters it directly after merging with the flow diverted from upstream of the outlet key.
  - The approach from upstream of the outlet or inlet key appears to determine where in the water column it overtops the transverse wall crest. The blue flows make up the lowermost portion of the overflow nappe whereas the orange flows make up the topmost portion.

### Local flowlines

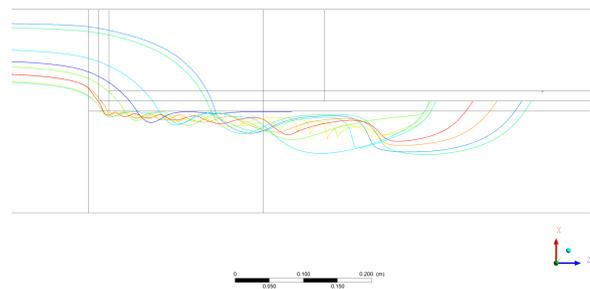
The mean velocity flowlines in the vicinity of the upstream edge of the inlet key are presented in Figure 7.9. It shows that the geometry of the inlet causes two distinct recirculation regions, or separation bubbles, to form, one at the base of the inlet key edge and one along the sloping edge of upstream overhang. Both of these form rotating zones of flow which grow in size as they move downstream and eventually get swept over the crest of the sidewall by the main flow. The two zones of flow move toward each other but do not merge or mix.



(a) Side view of local flowlines



(b) Flowlines near lower edge - plan view



(c) Flowlines near upper edge - plan view

Figure 7.9: Local flowlines near the upstream edge of the inlet key

### 7.3.3 Velocities

#### Inlet key velocities

The regions of flow identified by the flowlines were examined in greater detail by the mean velocity contour plots as presented in Figures 7.11 and 7.12. The cross section in these figures as well as those following are indicated in Figure 7.10. Recall that, as discussed in Chapter 5, only one PKW unit was modelled which comprises half of an inlet key width and half an outlet key width. The figures above and those that follow typically show the inlet key half only with the outlet key portion blanked out.

Examining these figures, especially Figure 7.12a, illustrates that the flow behaviour in the lower separation bubble is in many respects very similar to that observed in two-dimensional boundary separation (see Section 4.3.1). A separation boundary forms at the edge and forms a separation bubble of negative velocity flow directly behind it. The mean flow quickly re-establishes itself downstream of the bubble. The 2D behaviour noted in literature implied that

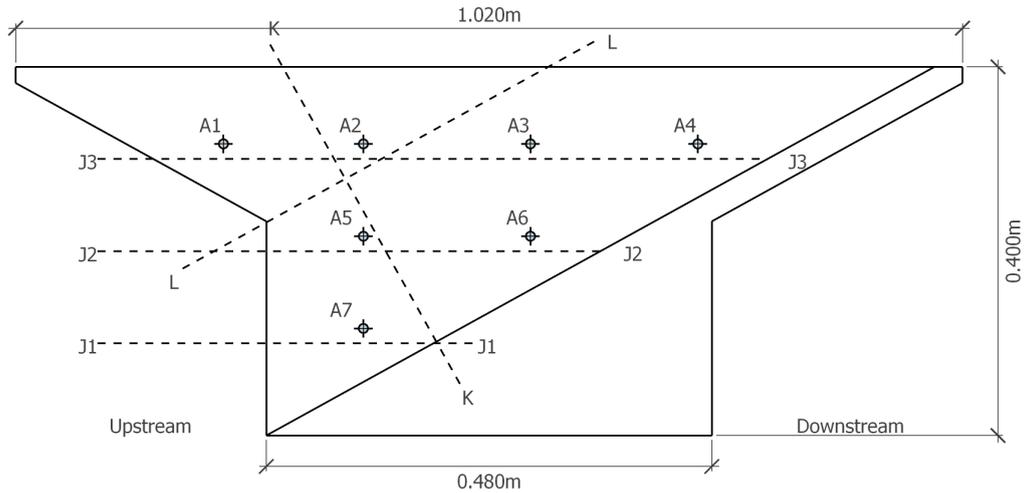


Figure 7.10: Location of cross sections in inlet key

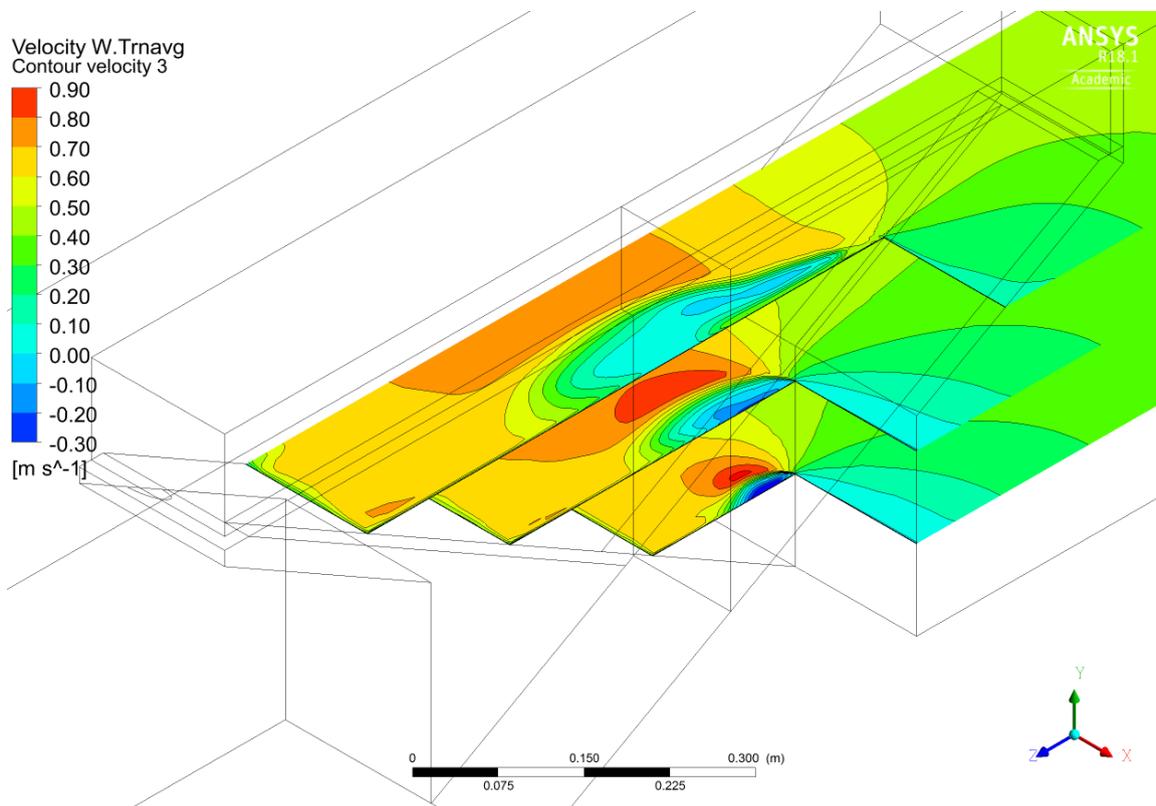


Figure 7.11: Isometric view of average longitudinal velocity on three horizontal planes (J1,J2,J3) (Flow is down and to the left)

there were transient 3D flow patterns present in the separation zone, but that these averaged out to zero over time. PKWs on the other hand exhibit strong 3D qualities [68]. This is reflected in Figure 7.12c, which shows the vertical average velocities through the plane, and demonstrates that there are deviations from this theoretical 2D flow field. This is supported by the flowlines shown in Figure 7.9b which exhibit reverse flows near the wall.

Figure 7.11 depicts the longitudinal velocity at three horizontal planes in the inlet key. It

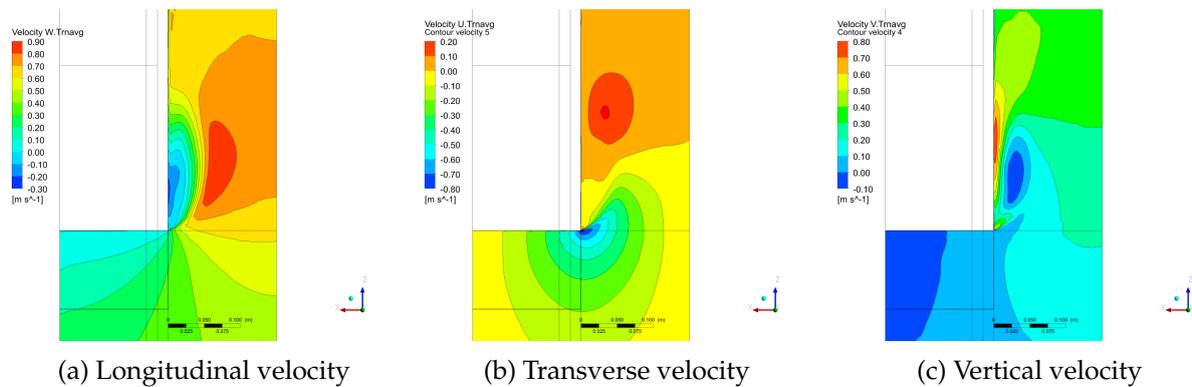


Figure 7.12: Average velocity (m/s) contour plots on plane J2 (flow is upward)

clearly exhibits the negative flows along the lower edge of the inlet. The longitudinal flows along the upstream overhang edge appear to be less affected by the bubble there. This is because, as implied in Figure 7.9c, the vortex that forms here has a semi-longitudinal axis, meaning that rotational flows here would not be negative in the longitudinal direction. If the flow field is rotated from the Cartesian coordinate system to one which runs parallel to the sloping floor of the inlet key (and so also roughly parallel to the bulk of the flow in the key) the reverse flows in the upper separation bubble become evident. The orientation then becomes aligned with planes K and L in Figure 7.10.

### Near wall velocities

The velocity magnitudes along a vertical plane in close proximity to the inlet key sidewall are presented in Figure 7.13. The Cartesian vector components of the velocity are displayed in Figure 7.14 and the rotated vector components are shown in Figure 7.15.

Flow arrows have been presented in each of these figures which give an indication of the direction of flow vector at that point. The colour bands indicate the vector magnitude. The figures in Figures 7.14b and 7.15b appear to be broadly similar in that they both reflect the same zones of flow approaching or flowing away from the sloping base. Near wall flows in the lower bubble exhibit strong upward flow, whereas near wall flows in the upper bubble exhibit strong downward flow. The differences between Figures 7.14a and 7.15a are more marked and demonstrate that there is a zone of reverse flow at both the upper and lower separation bubbles. This variable can thus be used to measure the size of these bubbles as presented in Section 7.3.4.

Figure 7.15a, like its parent Figure 7.13 implies that there is a large near-stagnant zone of flow at the centre of the wall. This means that this area of the key is not efficiently contributing to the total discharge efforts of the piano key weir as a whole. Cross sections through this zone of flow (planes K and L in Figure 7.10) showcase the extent to which this low-velocity zone extends into the inlet key. These are depicted in Figure 7.16 and indicate that in this flow scenario (model A, with a discharge of 4001/s,  $H/P = 0.36$ ), the low-velocity zone extends from the wall to approximately one third of the whole width of the key. This implies that only two thirds of the width of the key is efficiently being utilised to discharge flow. That being

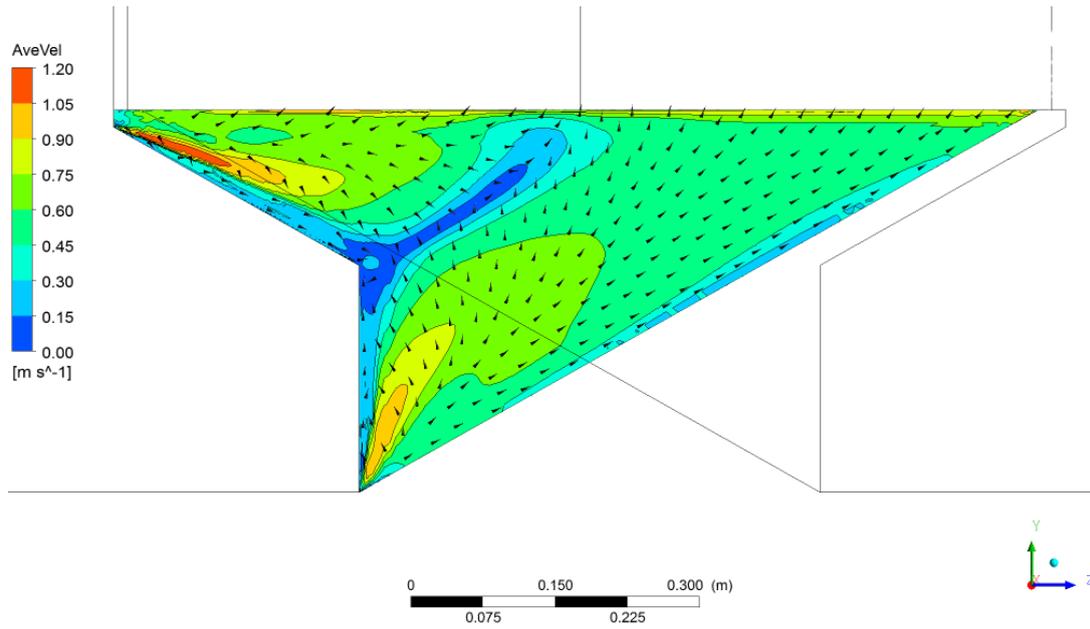
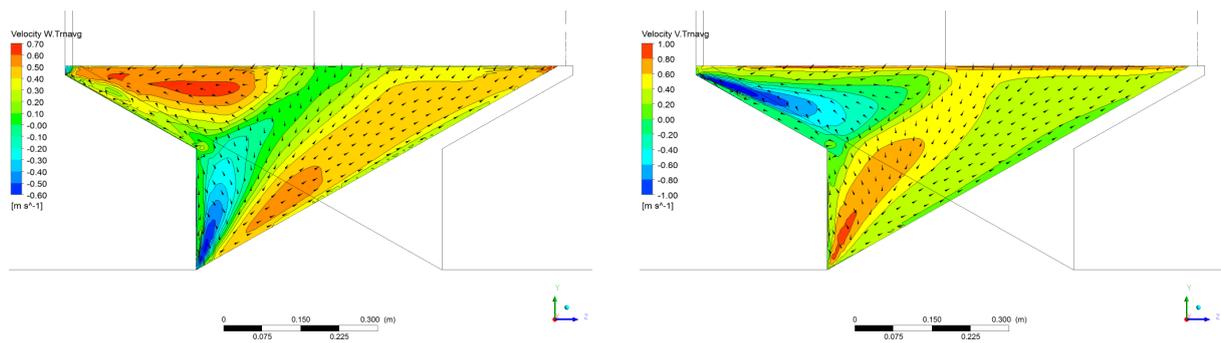


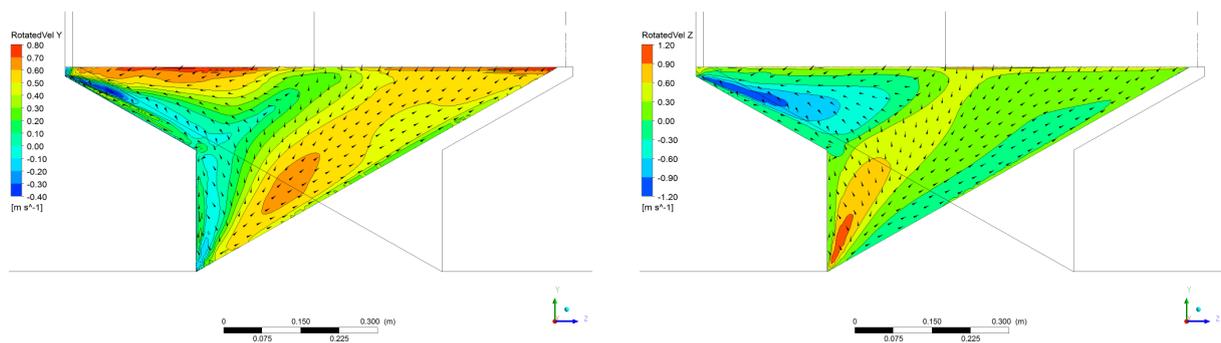
Figure 7.13: Velocity magnitude (m/s) along inlet key sidewall



(a) Longitudinal velocity vector component - Cartesian direction

(b) Vertical velocity vector component - Cartesian direction

Figure 7.14: Cartesian velocity vector components along inlet key sidewall (m/s)



(a) Longitudinal velocity vector component - rotated direction

(b) Vertical velocity vector component - rotated direction

Figure 7.15: Rotated velocity vector components along inlet key sidewall (m/s)

said, although the low-flow zone extends almost to the crest of the sidewall, its cross-flow extent (along plane K) is limited (see Figure 7.16b).

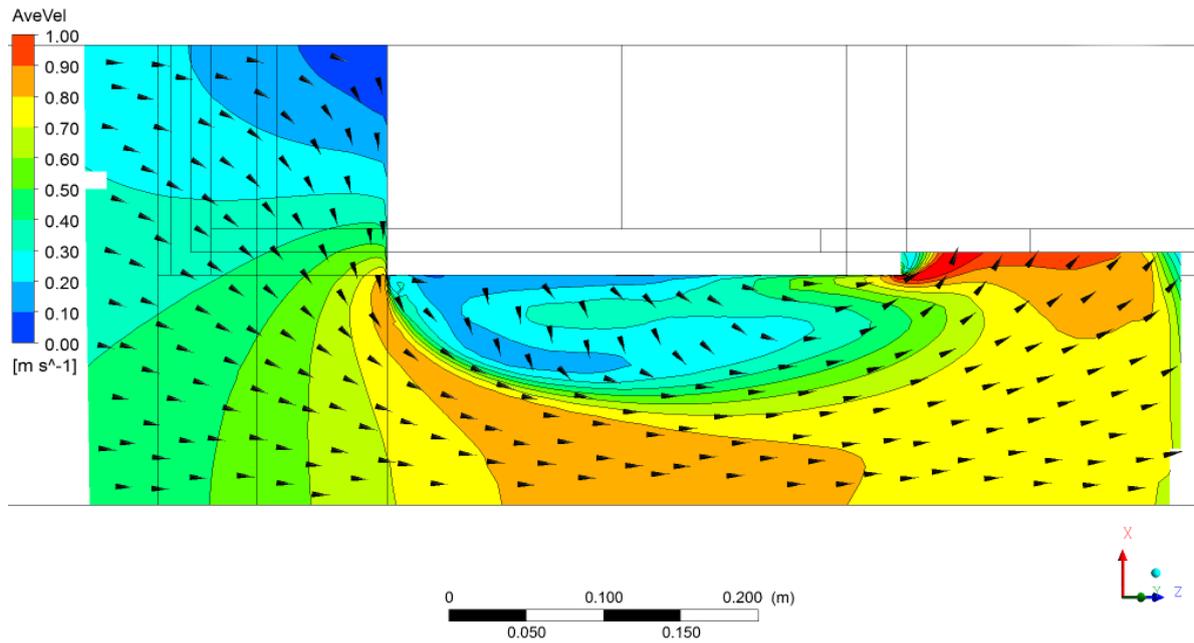
Another interesting aspect is that the average velocity vector arrows on these figures point toward the development of two counter-rotating areas of flow one to either side of the central portion of flow. These rotating zones are the same zones which are reflected in Figure 7.9a. These time-average counter-rotating vortices cause flow to be pulled away from the wall, potentially forming a region of low pressure on the wall. This is emphasised in Figure 7.16c which shows how the near wall flows approach each other (red and blue zones along the wall), converge, and then flow away from the wall.

The behaviour described in this section showcases typical trends and is for a single flow scenario. These trends are expected to alter with changes in discharge, scale, inlet key width, among other aspects. The effects that these aspects have are described in Section 7.5.

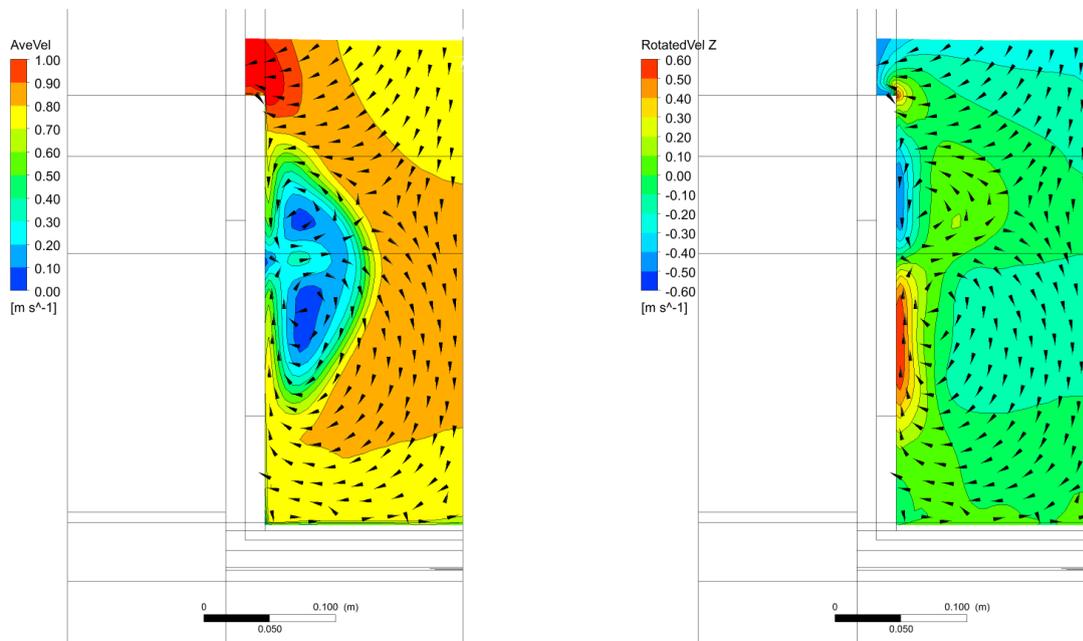
#### 7.3.4 Separation bubble

As surmised above, the transformation of the velocity vectors to reflect the dominant flow in the inlet key (to planes K and L) allows the separation bubble at the inlet key edge to be defined. Research literature describe two dimensional separation bubbles as having both a width and a reattachment length (see Section 4.3.1). Both of these dimensions are however difficult if not impossible to specify in the 3D environment of the PKW. That said, the bubble length and width are merely descriptors of the bubble's size. Thus, if different definitions of the bubble size can be stipulated, the same aim would be met.

The bubble was defined as that region of flow where the time-mean rotated/transformed velocity vector in its longitudinal direction was equal to or less than zero. A number of different metrics of this region of flow were recorded. These included the surface area of this zone, its volume as well as its maximum extent away from and along the sidewall. Each of these dimensions was non-dimensionalized so as to make them comparable across multiple scales. The surface area of the bubble was divided by the area of the opening of the inlet key; the volume was divided by the volume of the inlet key, and the two length dimensions by the weir height,  $P$ .



(a) Average velocity magnitude (m/s) on plane L along the inlet key



(b) Velocity magnitude (m/s) on plane K across the inlet key (flow into the page)

(c) Rotated vertical velocity vector (m/s) on plane K across the inlet key

Figure 7.16: Velocity (m/s) at planes across and along the inlet key

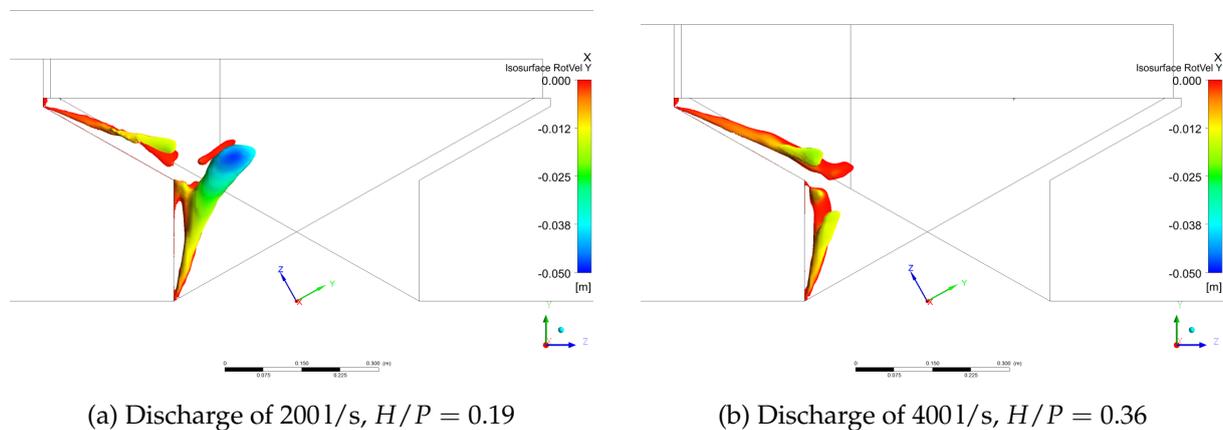


Figure 7.17: Separation bubble for two flow scenarios showing coloured with distance from sidewall

The separation bubble volume for two scenarios ( $H/P = 0.19$  &  $0.36$ ), extracted from the numerical model at same scale as model A, is displayed in Figure 7.17. The colouration of the bubble gives an indication of the orthogonal distance from the sidewall. The figures outline how the two bubbles together extend almost the entire length of the inlet key edge. It also reveals that they grow in extent as they develop: with the lower bubble growing vertically and the upper bubble growing longitudinally.

It is clear that the bubble for the higher discharge scenario appears smaller in size, not only in terms of extent but also distance from the sidewall. This trend is noted graphically in Figure 7.18 which details the various bubble size metrics over a range of  $H/P$  values. All the dimensions reduce as the overflow depth and discharge increases. The largest change occurs at a low  $H/P$  value and then appears to reach an asymptotic value. This implies that, as soon as the approach velocity, which is directly linked to the discharge, reaches some critical value its momentum is able to suppress the formation of a large negative zone of flow at the inlet key entrance. It is possible that the rotational structures associated with these negative velocities are still present at higher discharges but that they are being carried downstream by the average flow field at a rate which converts them to positive flows thus hiding them from view in this analysis.

Figure 7.19 examines the effect of scale on the bubble size. The numerical model was proportionally scaled upward from  $P = 0.4$  m to  $P = 3.0$  m. Even though there is some scatter in the data and some possibly aberrant readings, the results show that the bubble remains the same proportional size for all the metrics considered. This result supports the premise that the physical phenomena observed in the scaled model translates well to larger scales.

The numerical data reveal that the steady state separation bubble forms along the edge and extends only a short perpendicular distance above the sidewall, within a few centimetres. Due to this small distance, the presence of the bubble cannot be substantiated with physical data. The geometry of the ADV sensor was such that it could not record data in such close proximity to the wall. That said, the data that was captured at slightly larger distances from the wall in

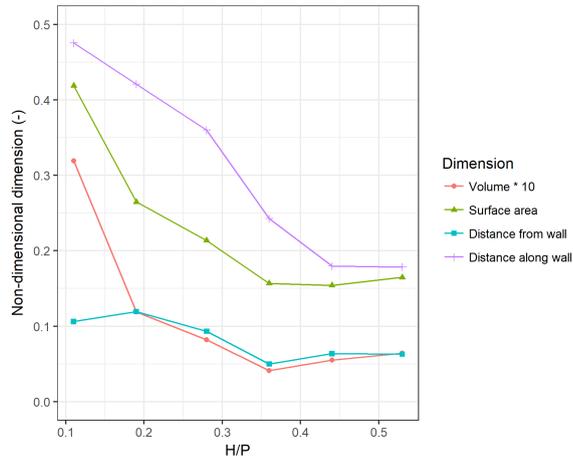


Figure 7.18: Non-dimensionalized bubble dimensions over a range of  $H/P$  values

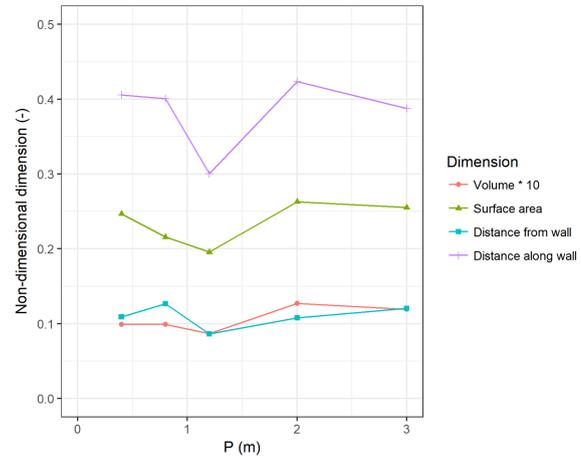


Figure 7.19: Non-dimensionalized bubble dimensions over a range of  $P$  values

the vicinity of the bubble do reflect low, near zero, velocities as expected. This is summarised in Section 7.5.

### 7.3.5 Nappe profiles

The previous sections mostly focussed on flow in the inlet key. The steady state behaviour of the flow in the downstream outlet key, and especially the overflow nappe, are described in this section. Note that due to the highly turbulent and dual-phase nature of the flows in this portion of the PKW very few physical measurements could be taken. Many of the numerical results could thus only be compared visually. However, water level readings were recorded as reported in Section 7.5.4.

The flow as it discharges over the crest directly or collects in the outlet key from the sidewall is shown in the photos in Figure 7.20. They reveal how the nappe forms a closed curtain of water from the crest down to the base enclosing an air cavity. The top surface of the water is fairly smooth and clear allowing observation of the underside of the nappe profile. Its surface is a great deal rougher due to its initial contact with the crest which makes it more visible.

The two nappe profiles on either side of the outlet key collide in its centre creating a small standing wave as shown in the upper section of the outlet key in Figure 7.21. Also visible in this figure is the underside of the nappe and how the apex of this cavity forms a conical shape keeping close to the upstream portion of the sidewall. This is a very stable feature of the flow in the outlet key and was evident in almost all flow scenarios. Only at very high flows ( $H/P > 0.45$ ) did this apex detach and is forced downstream by the momentum of the flow as is pictured in Figure 7.50. This transient feature is discussed further in Sections 7.3.6 and 7.4.5.

Another transient feature which is noteworthy is the undulation at the crest of the sidewall midway along its length (see Figure 7.21). These disturbances periodically reach the surface and are related to the vortices described in Section 7.3.3. They are explored in greater detail in Section 7.4.2. For the purposes of this steady state examination of the outlet key, it is relevant to note that the undulations were found to generally (but not always) form the boundary of



(a) Inlet key

(b) Outlet key

Figure 7.20: View of overflow nappe at low flow (looking upstream)

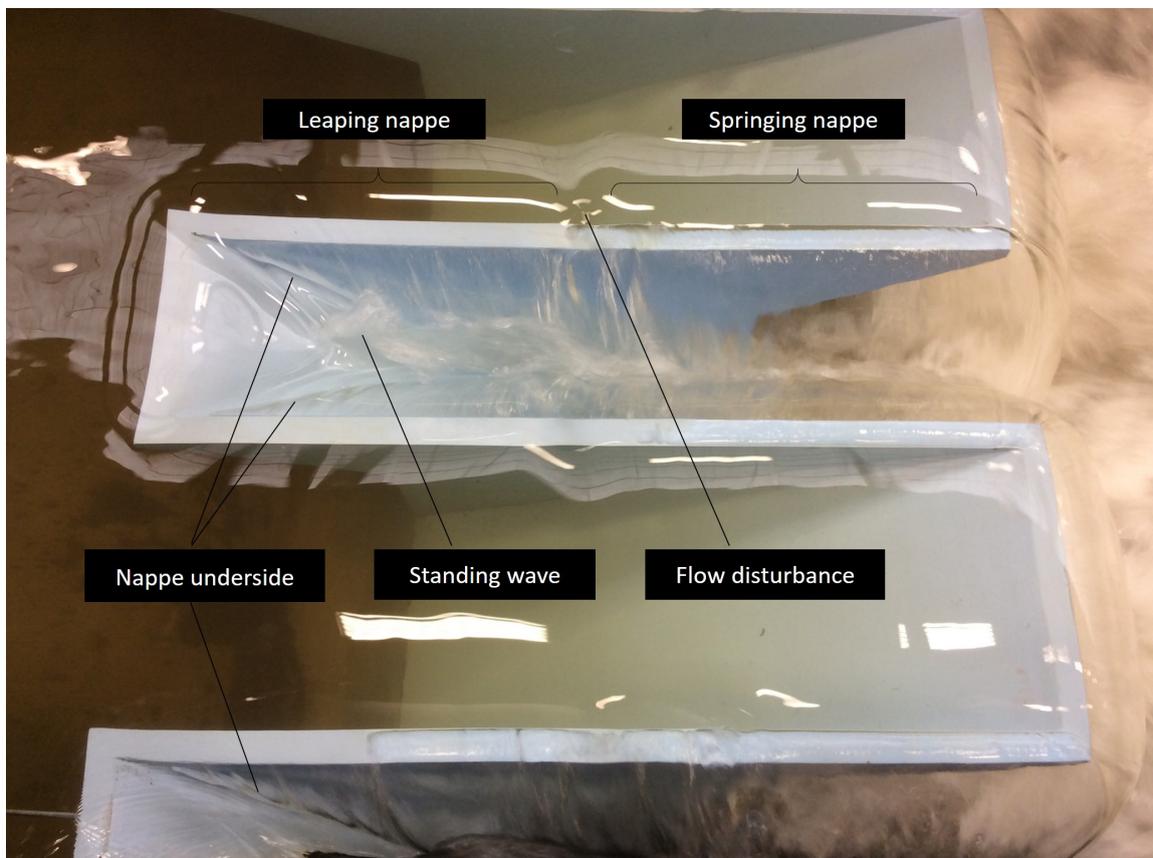


Figure 7.21: Nappe in outlet key showing relevant flow features

where the nappe on the crest transitions from leaping behaviour to springing behaviour [128]. This behaviour is linked to the amount of energy or momentum that the flow contains to detach from the crest and also affects the discharge efficiency of the weir [129; 130].

The discharge that is collected in the outlet key flows down the sloping floor and enters the downstream water body. At low downstream water levels, this highly supercritical flow spreads laterally out as soon as it exits the key. In doing so it collides with the spreading flow



Figure 7.22: Bulking of flow under downstream overhang



Figure 7.23: Concave shape of the nappe downstream of the corners

from the adjacent key and creates an unstable hydraulic jump underneath the nappe directly downstream of the inlet key (see Figure 7.22). There is a great deal of flow bulking in this zone which presumably absorbs air from the cavity and expels it downstream. Furthermore, the falling nappe, when impacting the water level at the base of the key, entrains air from the cavity underneath the nappe. The high longitudinal velocity of this flow then carries this highly aerated flow downstream of the weir. This causes reductions in air volume (and thus air pressure) underneath the nappe. Piano key weirs are reportedly self-aerating [92], hence this removal of air from under the nappe is being balanced by the ingress or entrainment of air from the atmosphere at the colliding nappe curtains. This is discussed further in Sections 7.5.4 and 7.5.9.

Figure 7.23 shows how even a small imbalance in air pressure between the underside of the nappe and the atmosphere can alter the shape of the nappe. The corner edges of the nappe consist of diverging flow and only receive flow from a very narrow portion of the crest. The nappe in this region is thus much thinner than elsewhere, and due to a pressure imbalance may develop the concave shape portrayed in the figure. This feature only manifests at small discharges where the flow momentum of the nappe is small enough to be overcome by air pressure. Although not observed in the smaller wooden physical model, the larger steel model showed that these thin nappe concavities can develop instabilities and start to oscillate. This is explored in more detail in Section 7.4.6.

The ability of the numerical model to simulate the above, physically observed, steady state behaviour in the outlet key is depicted in Figures 7.24 to 7.29. The figures detail the results

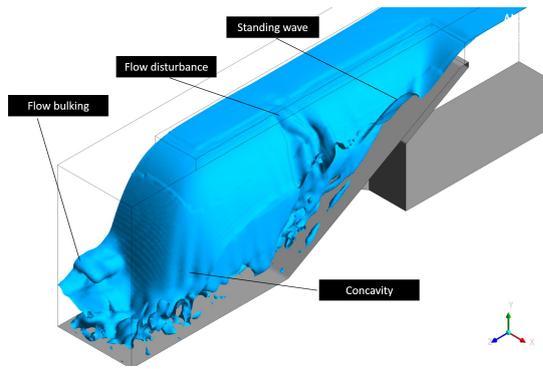


Figure 7.24: Isometric view of numerical model nappe in outlet key

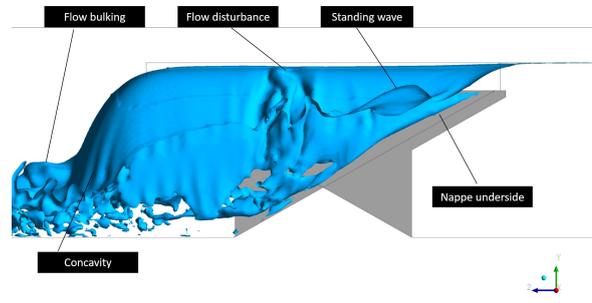


Figure 7.25: Side view of numerical nappe in outlet key

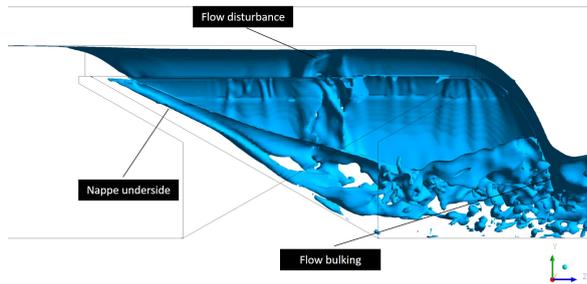


Figure 7.26: Side view of the underside of the numerical model nappe

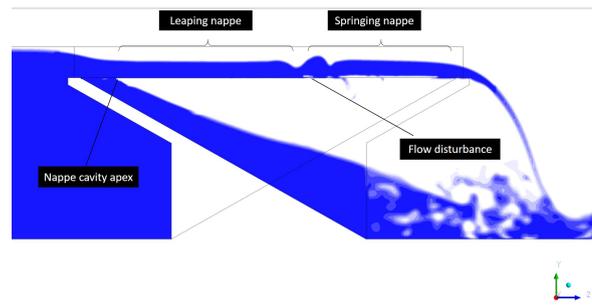


Figure 7.27: Side cross section view of nappe along longitudinal plane just downstream of the sidewall

of a numerical simulation from a variety of perspectives and cross sections. Recall that the numerical model was limited to one PKW unit consisting of half an inlet key and half an outlet key. Flows in the opposite (or missing) half of the keys would be symmetrical as is evidenced by the physical model photos. Despite being qualitative in nature, the figures visually prove that the numerical model successfully emulated the physical model by observing a number of flow features which are directly visible.

Figures 7.24 to 7.26 show the air-water contact which represents the water level in the numerical model. This contact thus not only allows the top surface to be seen but also the air cavity under the nappe. The main features which are visible include the standing wave, the flow disturbance at the crest of the weir, the flow bulking and the underside of the nappe. The concavity is also visible, but to a lesser degree. The very thin nature of the nappe in this region requires a very fine mesh size to emulate it correctly. Since this feature is not crucial to an understanding of the hydraulics of the weir this mesh refinement was not done. Despite this, the model is still able to approximate the concavity in this area.

Figures 7.27 to 7.29 present longitudinal, horizontal and transverse cross sections of the water body as it overtops the weir. These sections clearly define the air cavity under the nappe. The upstream conically shaped apex, the flow disturbance and even the leaping / springing behaviour are well emulated.

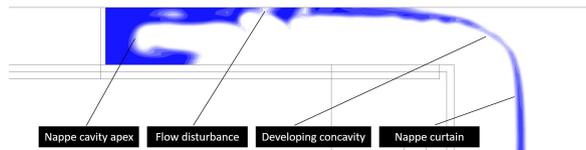


Figure 7.28: Plan view of horizontal cross section through nappe in outlet key

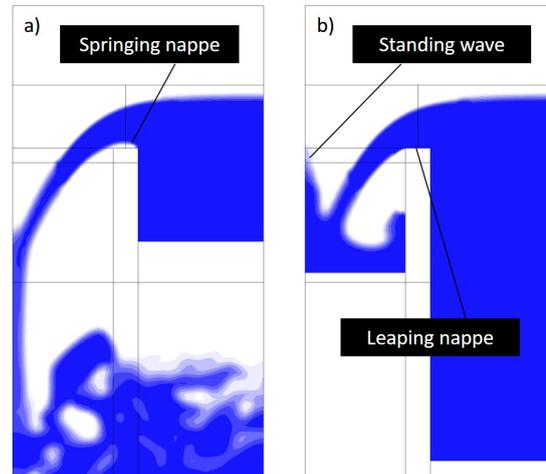


Figure 7.29: Transverse cross sections through nappe in outlet key: a) downstream section, b) upstream section

### 7.3.6 Mean wall pressure

#### Upstream face

The effect that the flow field may have on the pressures on the upstream face of the sidewall was alluded to above. Even under steady state conditions, zones of lower pressure are expected on the upstream face in the vicinity and downstream of the separation bubble. The mean pressures on the upstream face are characterised in Figure 7.30. The numerical model allows the total pressure on the face to be divided up into a static pressure component (i.e. those pressures caused by water head or depth) and a dynamic pressure component (i.e. those pressures caused by the velocity component of the flow in the form of  $v^2/2g$ ). The upstream face will thus experience the forces of the static pressures at all times, but only those dynamic pressures caused by flow vectors which involve flow to or away from the face will manifest as normal forces on the wall. It is these directional pressures which are depicted on the contour plots.

The static pressure field displays a typical hydrostatic pressure profile directly upstream of the PKW. As the flow traverses the weir and the recirculation zone develops at the upstream edges, the static pressure drops but still remains largely hydrostatic in nature. This drop in static pressure is partially replaced by the dynamic pressure, meaning that the drop in total pressure is not as marked. This implies that the static pressure has been converted to kinetic energy at these locations. Despite this, the drop in the total pressure does indicate that there is a loss of pressure or energy at the inlet edge which is not accounted for by either of these pressures. These energy losses are a common occurrence at the inlets of typical hydraulic structures.

The magnitude of the energy lost is visualised in the pressure coefficient detailed in Figure 7.30d. This coefficient represents the relative difference between the total pressure at any point with (and to) the total upstream head available upstream of the weir. Red zones depict almost no loss of energy, but green and blue zones represent higher energy losses. The highest apparent energy loss is approximately 15% of the total available energy upstream of the weir.

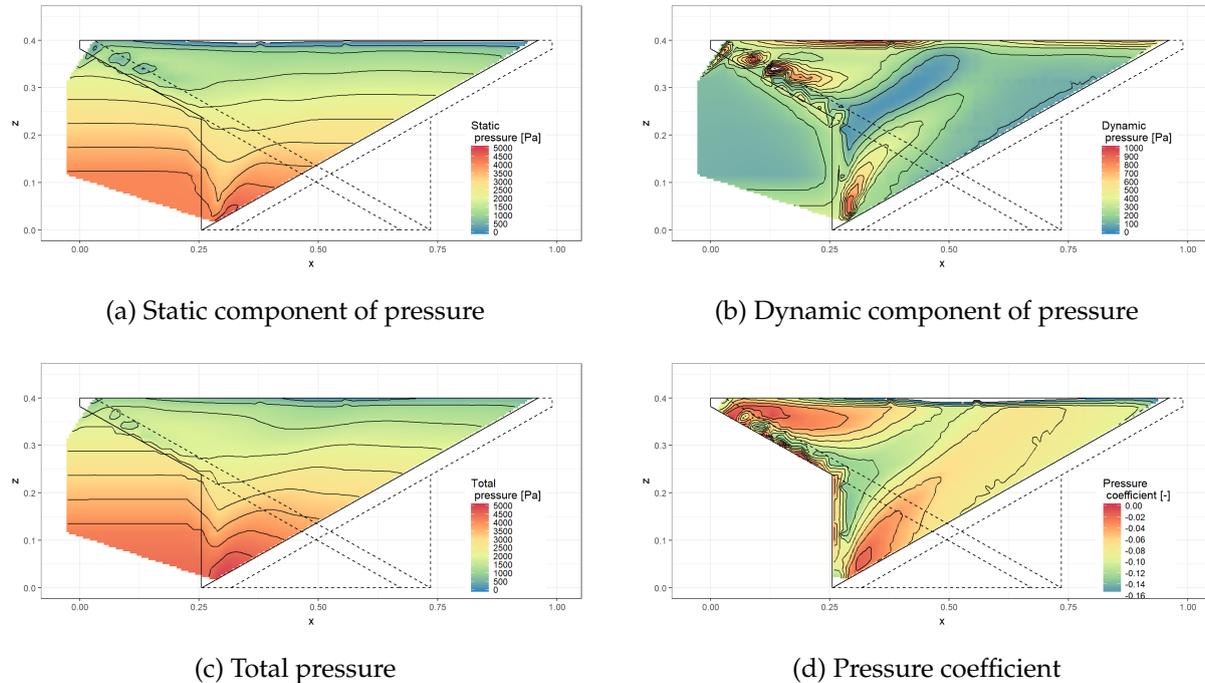


Figure 7.30: Mean pressures on upstream face of sidewall

Bear in mind that not all of this is due to the inlet geometry but is also related to the amount of flow that has already been discharged over the weir crest upstream of this location.

Note that the pressure coefficient plot closely approximates the velocity plots presented in the previous section. The lower pressure zones in the middle of the upstream face are correlated with the lower velocity zones there. Furthermore, the zone of lower pressure extends to the upper middle of the sidewall where the wall is most sensitive to normal forces.

### Downstream face

On the downstream face of the sidewall, the pressures are heavily affected by whether or not the face is inundated. Those areas above the water level may be exposed to sub-atmospheric pressures caused by the dynamics of the overflow nappe, but these are very small in comparison to those pressures caused by the water body. Figure 7.31 illustrates the flow field in the outlet key for two scenarios with different discharges and downstream water levels to illustrate this. On the left of the figure are the water levels, total pressure and static pressures for a scenario with  $H/P = 0.28$ . Under these flow conditions, the air cavity is fully established under the nappe and almost reaches the upstream apex at the upstream overhang crest. The air pressure is slightly sub-atmospheric (by a few Pascal) and the pressures are thus dominated by the water level in the outlet key which slopes downward toward the key's exit. There is a marked difference between the total and static pressures. These are largely made up by the energy contained in the high velocity flow in the outlet key (not shown here). Again, only those vectors which flow toward or away from the wall would contribute to this. The majority of the flow is directed toward the downstream end of the key, hence those vectors would not lead to pressures on the sidewall.

On the right of Figure 7.31 a flow field for  $H/P = 0.36$  with a high downstream water level is depicted. It can be seen that only a small portion of the wall is exposed to the atmosphere, but that it too is only slightly sub-atmospheric. The much higher water level leads to higher total pressures on the downstream face. Once again, and for the same reason, there is an appreciable difference between the total and static pressure fields. The static pressure field does however exhibit a zone of strong negative pressures near to where the water surface would be if it were not drowned. These negative pressures are caused by the overflow nappe in this region pulling flow away from the wall in the transverse direction. These pressures would ordinarily be relieved by the air under the nappe, but it is prevented from doing so by the strong longitudinal flow momentum from the upstream side. There is thus a balance of flow, velocity, momentum and pressure between the transverse flow away from the sidewall which induces the negative pressure, the air under the nappe which would rapidly travel upstream to relieve this pressure and the flow momentum in the downstream longitudinal direction pushing the air away downstream. The figures only present a time-average depiction of this unstable equilibrium which develops. The actual transient flow is highly dynamic, and as each of these three components change with time a new equilibrium is determined. This phenomenon is explored further in Section 7.4.5.

## 7.4 Transient hydrodynamic behaviour

This section presents the transient hydraulic phenomena which occur at PKWs in contrast to the steady state behaviour which is described above. It should be noted that the discharge approaching the weir remains constant throughout, meaning that even though the flow scenario is steady, the noted behaviour is not.

The overall behaviour of many of these phenomena can only be examined using data from the numerical model as simultaneous recordings could often not be made in the physical model. The physical model data was, however, used to substantiate or validate the numerical results where relevant.

### 7.4.1 Velocity and turbulence

The average flow velocities in the inlet key were described in Section 7.3.3. How these change over a range of discharges or  $H/P$  values is described in Section 7.5.1. This section aims to demonstrate the variability that is present in the velocity data obtained from the physical model, and how this is emulated by the numerical model. It then goes on to explore how these transient phenomena are interlinked.

A number of instantaneous velocity contour plots is presented in Figures 7.32 and 7.33. These are the equivalent of Figures 7.11 and 7.12a which summarised the time-mean velocity contours plots in the same locations. Comparing the two sets of figures reveals that although the images are similar, they do show the instantaneous velocities exhibit a large degree of variation between any two points in the inlet key. This implies that the flow is highly turbulent there. The flow approaching the PKW in the two sets of images is nearly identical however,

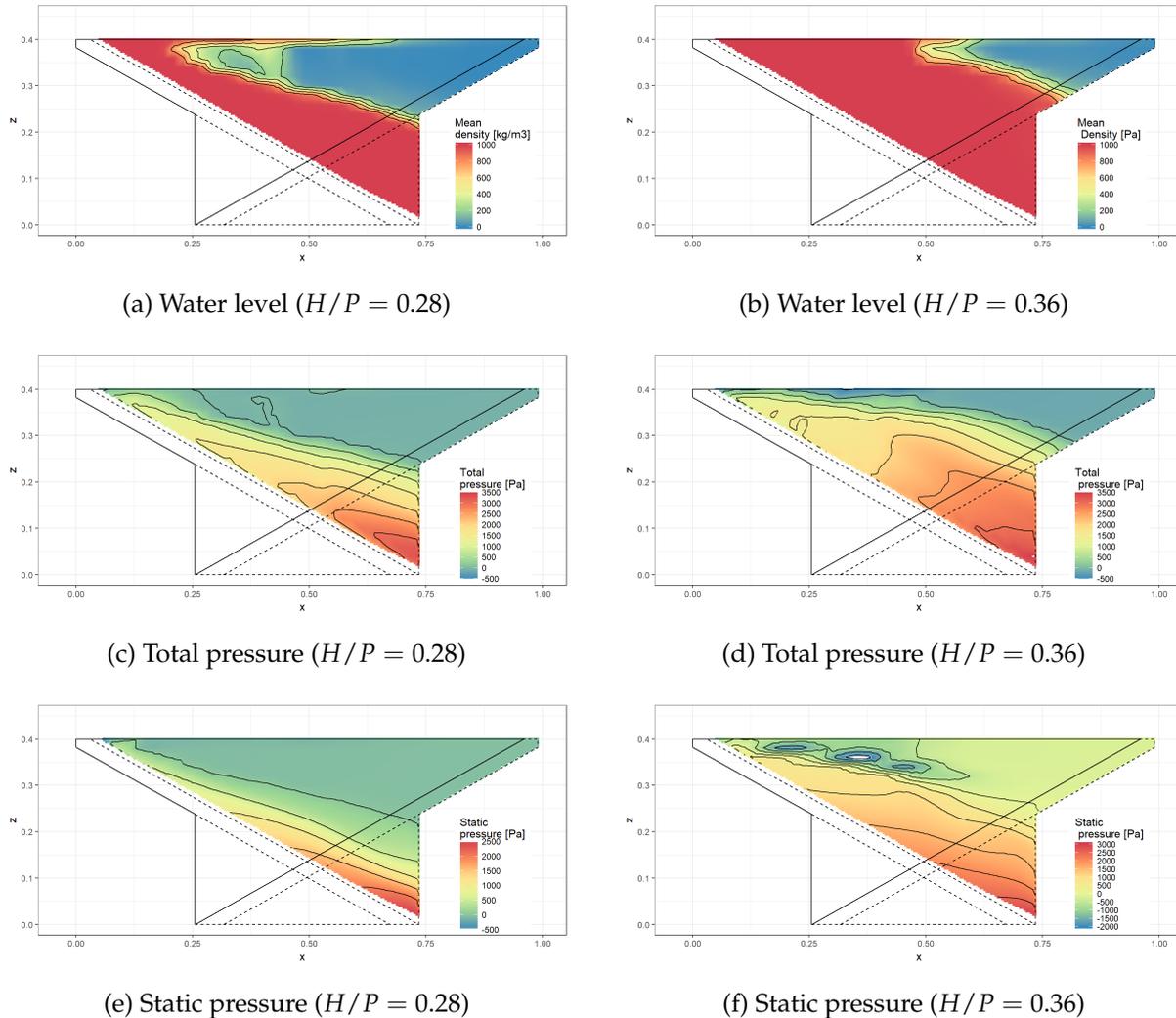


Figure 7.31: Mean pressures on downstream face of sidewall (in outlet key)

suggesting much more stable flow conditions.

This is further supported by Figure 7.34 which shows the contour plot on the section along the inlet key following the general trend of the flowlines (Section L in Figure 7.10). It indicates how the large velocity gradient and shear layer at the entrance of the inlet key is relatively stable at the start of the inlet key. It then starts to decay by developing large scale instabilities or waves. Before the shear layer can fully disintegrate (or reattach to the wall) it is discharged over the crest of the weir. There is thus high shear flow which overtops the sidewall which affects the nappe in interesting ways. This is expanded upon in Section 7.4.4.

The comparison of Figures 7.16a and 7.34 showcases the fact that the concept of the separation bubble is a time-mean phenomenon. Although the rough shape of a separation bubble can be discerned in the instantaneous velocity plot, it is disjointed and its borders difficult to define.

The variability and turbulence of the velocity in the inlet key is depicted in Figure 7.35. The graphs illustrate that there is a great deal of variability in the physical data, even after it was cleaned and despiked. These very fine fluctuations are caused by the small-scale turbulent

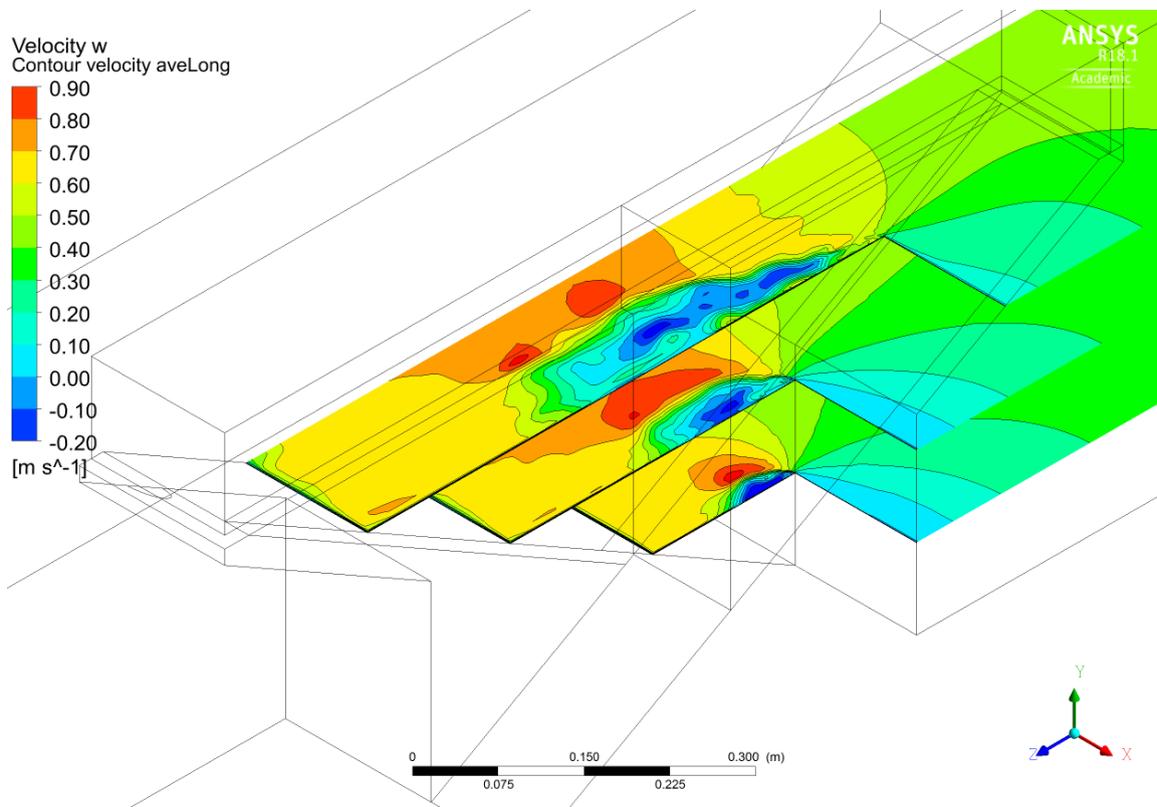


Figure 7.32: Isometric view of instantaneous longitudinal velocity on three horizontal planes (J1,J2,J3) (Flow is downward and to the left)

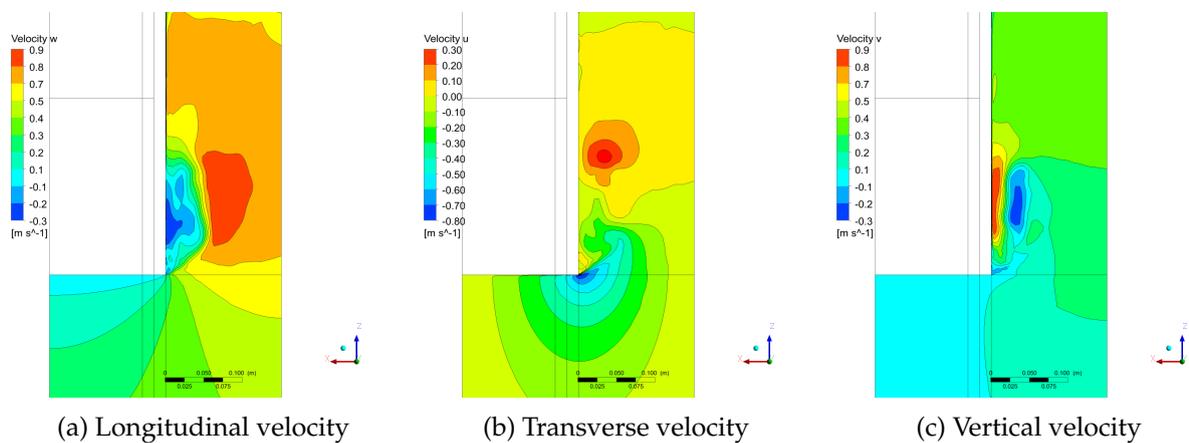


Figure 7.33: Instantaneous velocity (m/s) contour plots on plane J2 (flow is upward)

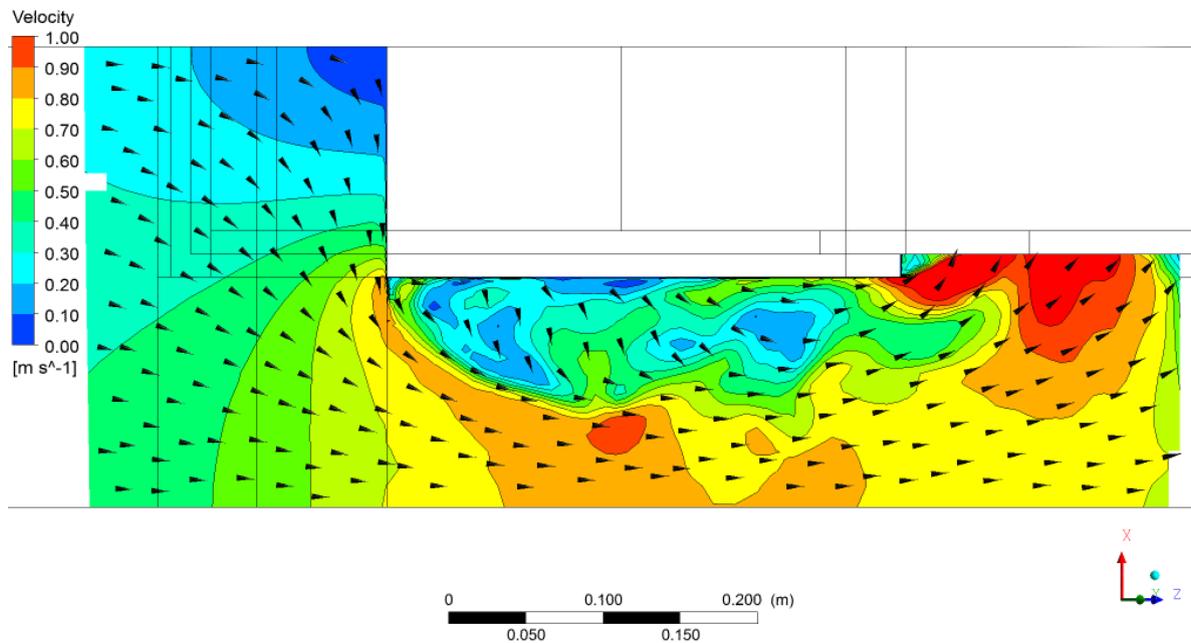


Figure 7.34: Instantaneous velocity magnitude (m/s) on plane L along the inlet key

eddies which are present in the flow. Since the scales of these eddies are much smaller than the grid size of the numerical model they cannot be simulated directly. Their dissipating effect is simulated by the sub-grid scale model but this does not reflect on the resultant time sequence.

The physical data was filtered to remove these small scale, high frequency, fluctuations as demonstrated in the sequence of graphs. The data reveal that, by applying a basic low-pass filter, the physical data closely resembles the numerical simulation both in the time and frequency space. The mean velocity, the number and amplitude of the fluctuations are visually well approximated by the numerical model at locations both near the sidewall as well as near the middle of the inlet key.

Interestingly, the data illustrate that, despite the appearance of regular fluctuations in the time sequence, there are no consistent undulations that appear in the frequency plot. The unfiltered physical data is relatively flat which implies that the data sequence is random to a large degree. This is what would be expected from a turbulent velocity time sequence with roughly equal energies being contained at all frequencies.

The fluctuations in the velocity data can be summarised by computing the *root-mean-square (RMS)* value for each velocity vector. These can then be used to calculate the overall *turbulence intensity (TI)* and *Turbulent kinetic energy (TKE)* contained in the flow. Plots of how these parameters change with their location and relative to each other are displayed in Figures 7.36 and 7.37. The graphs present the data along a longitudinal line at the indicated coordinates. These coordinates are located at the same level as the pressure conduits (see Figure 7.10) at a distance of 0.025 m from the wall (which is the closest that the ADV could record good data). The X-axis coordinates start at the upstream edge of the upstream overhang.

The vector plots (Figures 7.36a and 7.37a) portray the same averaged numerical data as

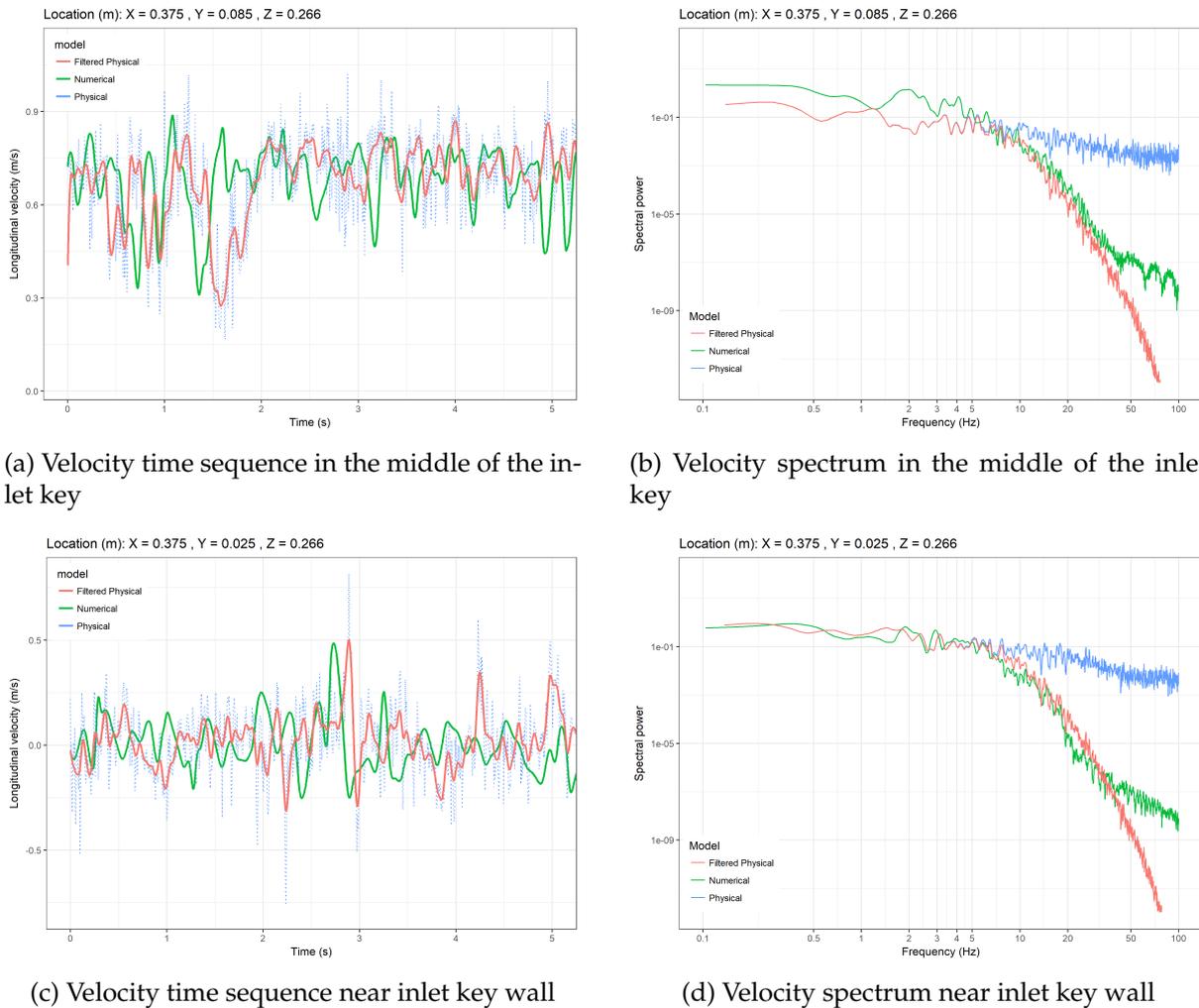


Figure 7.35: Longitudinal velocity (m/s) time sequence and spectrum

that presented in the contour plots in Section 7.3.3. They indicate that the flow increases in velocity along all three vectors as it approaches the upstream edge of the inlet key. The line then enters the separation bubble leading a rapid drop in the velocities thus representing the high velocity gradient there. Subsequent to the bubble, the velocities grow to suit the average flow in the inlet key. The averaged physical data is superimposed to present the accuracy of the calibration. The top line ( $Z=0.316$  m) does not have a good fit (although the general trend is representative), but the base line ( $Z=0.216$  m) has an excellent fit between the two data sets.

The RMS and turbulence graphs show a similar though opposite picture. The low velocity zones are zones of high RMS and turbulence values. The numerical data consistently plots below that of the physical data however. This can be explained by the fact that the physical data turbulence was calculated from the unfiltered data meaning that it contains contributions from small scale eddies which cannot be directly simulated by the numerical model. The numerical model turbulence data was calculated from the velocity time sequence and so does not include the contributions of the sub-grid scale model. Including these contributions would likely make up the shortfall in the difference between the two models.

Similar graphs detailing similar behaviour along lines in the transverse and vertical direc-

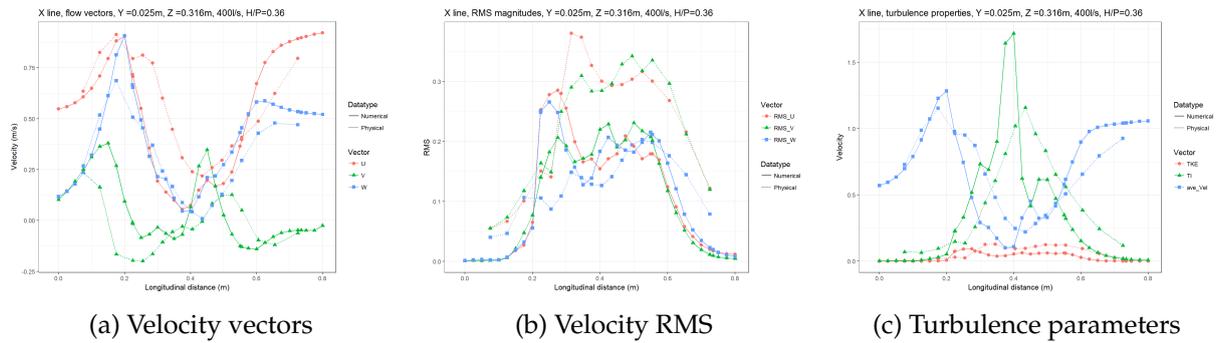


Figure 7.36: Velocity and turbulence parameters along inlet key - top level

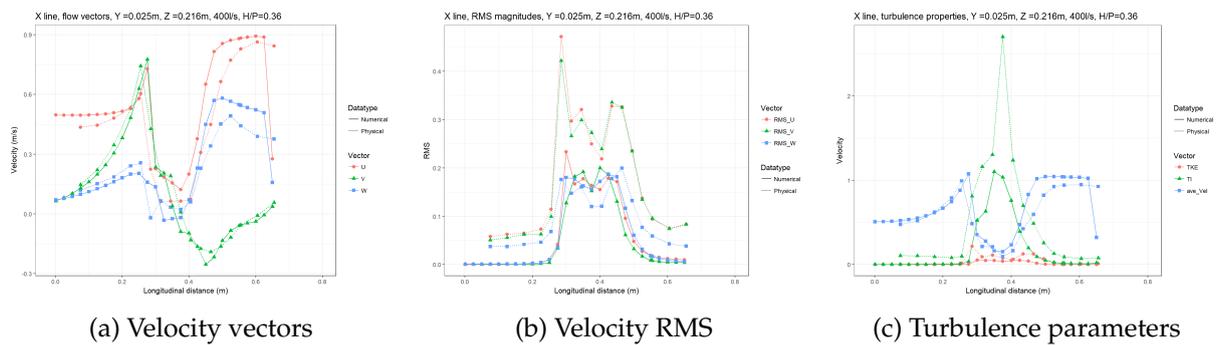


Figure 7.37: Velocity and turbulence parameters along inlet key - base level

tions are included in Appendix D. That set of graphs also includes a comparison between the numerical and physical data sets.

## 7.4.2 Vorticity

The high velocity gradient and the manner in which it collapses, as outlined in Figure 7.34, was described in Section 4.3.1. The shear layer breaks up by developing waves which eventually form rotational structures or vortices. This formation is depicted in Figure 7.38 which displays the vorticity along the inlet key about the vertical axis. Vorticity is a measure of the strength of the shear or velocity gradient in a given direction. Vorticity, in and of itself, does not necessarily involve rotational flow, however when the vorticity along other axes is combined (via the velocity gradient tensor) into the so-called Q-criterion, coherent structures or vortices may be identified [79]. It should be noted that the Q-criterion is only one of many flow visualisation techniques of coherent structures but it was found to work well in the present study.

The Q-criterion flow field at each of the three horizontal planes is presented in Figure 7.39. The figure shows how there is a system of vortices which emanates from the upstream edge, which grow in size as they move downstream but remain in the vicinity of the low-flow region downstream of the separation bubble. There also appears to be no discernible pattern to the vortices until they are observed on the plane running along the inlet key (plane L). This can be seen in Figure 7.40, which reveals that the vortices (red zones) occur at regularly spaced intervals, again supporting the observation that the flow is best viewed in this direction.

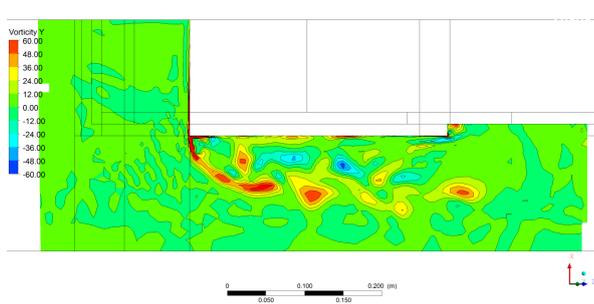


Figure 7.38: Vorticity on plane L along the inlet key

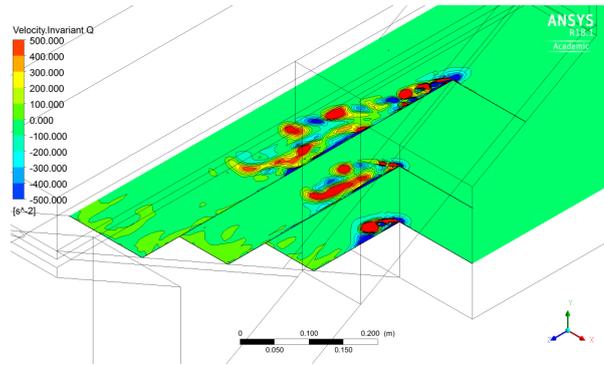


Figure 7.39: Q-criterion at 3 horizontal levels

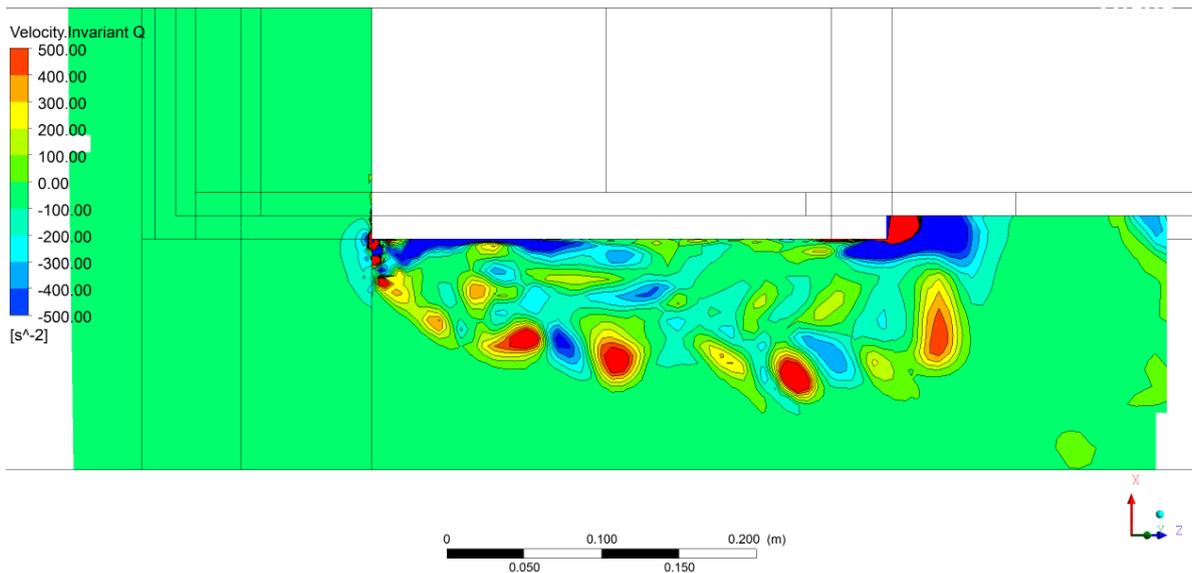


Figure 7.40: Q-criterion at plane J along inlet key

When the high Q-criterion zones are viewed in three dimensional space, the vortices, their scope, size, shape, spacing and velocity become evident. Figure 7.41a depicts the same contour plot of Q-criterion presented in Figure 7.40 in three-dimensional space, together with the *isovolume* of equal Q-criterion over the whole inlet key flow field. The distinct rolls or cores of each individual vortex roll are visible.

This same system of vortices is also portrayed from a side view in Figure 7.41b and a top view in Figure 7.41c. These figures have been coloured with the flow velocity. This reveals that the outermost vortices are the fastest and have an approximate lambda or horseshoe shape, with the crest having an axis roughly perpendicular to the flow. The vortices closer to the wall meanwhile have much lower velocities, being located in the near-stagnant zone downstream of the separation bubble. Those near-wall vortices generated by the upper separation bubble tend to have vertical rotation axes, where as those generated by the lower bubble tend to have horizontal axes. These near wall vortex cores often form the legs of the horseshoe shaped vortices mentioned above.

Figure 7.41b also clearly exhibits the surface of the two separation bubbles or recirculation

zones at the bottom edge of the inlet key and the edge of the upstream overhang. In addition, it details how both of these grow in size as they develop downstream and eventually disintegrate into the system of individual vortices. Another interesting aspect discernible in this figure is the water surface undulations in the outlet key visible in the grey *isosurface*. Notice that they occur in the vicinity of where a vortex is overtopping the crest. This is explored further in Section 7.4.4.

The effect that discharge, scale, PKW type and PKW noses have on this system of vortices is explored in Section 7.5.

### 7.4.3 Wall pressures

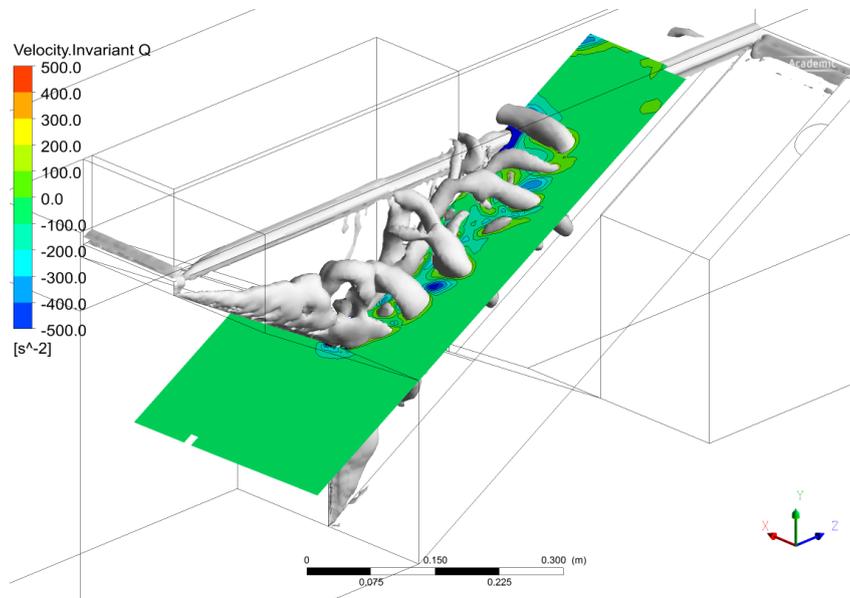
#### Pressure fluctuations

The mean pressure on the wall on both its upstream and downstream faces was described in Section 7.3.6. It detailed how the pressure on the wall was a function of not only the static head but also the flow dynamics toward and away from the wall. In other words, although the pressure field is a macroscopic quantity it can be affected by localised fluctuations. These local fluctuations are of key importance as they will impose oscillatory forces on the sidewall and thus cause it to vibrate.

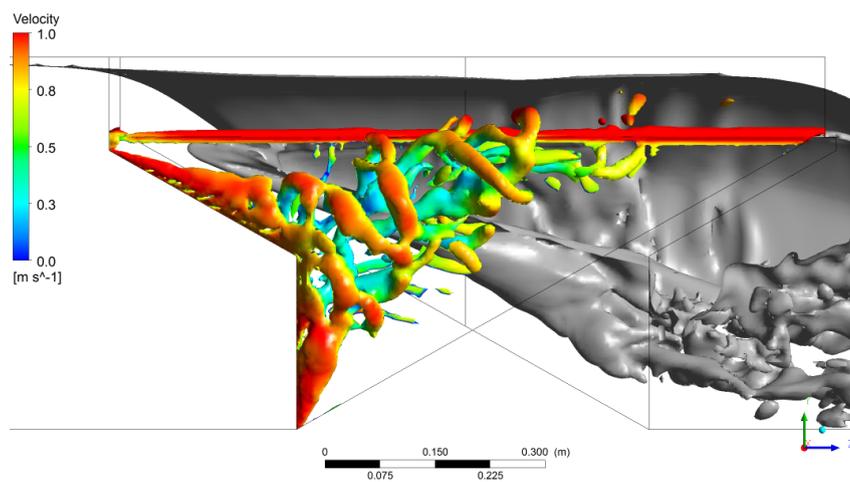
It was shown in Section 4.3.1 that the passage of a vortex in close proximity to a wall or boundary induces pressure undulations on that boundary. When a vortex causes flow to be pulled away from the boundary it causes lower pressures and when it causes flow toward the boundary it causes higher pressures. Furthermore, the vortices can form a train of counter-cyclical cores which reinforce flow toward and away from the wall as they pass. Bear in mind that the vortex cores are themselves zones of lower pressure and will thus also induce lower pressures on the boundary if close enough.

To illustrate this argument, consider the sequence of images in Figure 7.42. The figures show a clipped horizontal plane near the top and middle of the sidewall with a range of instantaneous flow field variables. Flow is from left to right and the top edge of the plot is the sidewall. Figure 7.42a depicts the  $Q$ -criterion along this plane with the red zones representing the vortex cores. The horizontal plane intersects a region where the core-axes are largely vertical hence the cores or rolls are being viewed side-on. Figure 7.42c reveals the curl (or rotation) of the flow, and that of the vortex cores, in the vertical direction. The red zones represent counter-clockwise flow and the blue zones clockwise flow. It can be seen that the system of cores nearest the wall change their direction of rotation thus successively pulling flow away from and pushing flow toward the wall. This is supported by Figure 7.42b which illustrates the transverse velocity in the inlet key. Blue zones indicate flow away from the wall and red zones flow toward the wall. The effect this has on the local pressure field and the pressures on the sidewall is set out in Figure 7.42d. This figure shows that the cores themselves are locations of low pressure and that those lengths of wall which have flow toward it have higher pressure than those where flow is moving away.

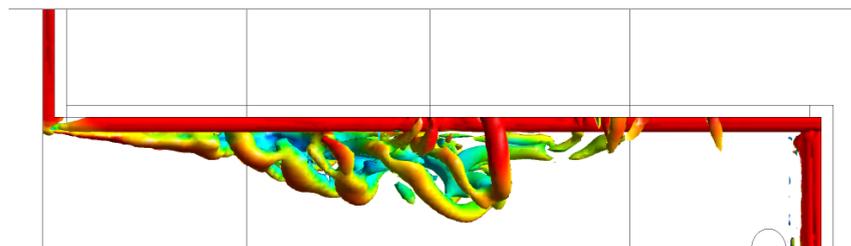
When this concept is expanded to the inlet key sidewall as a whole, the result is the instantaneous pressure field on the wall. However, since the pressure is still dominated by the far-field



(a) 3 dimensional view of Q-criterion with contour plot along inlet (flow is up and to the right)



(b) Side view of Q-criterion vortices with water level



(c) Top view of Q-criterion vortices

Figure 7.41: Q-criterion vortices

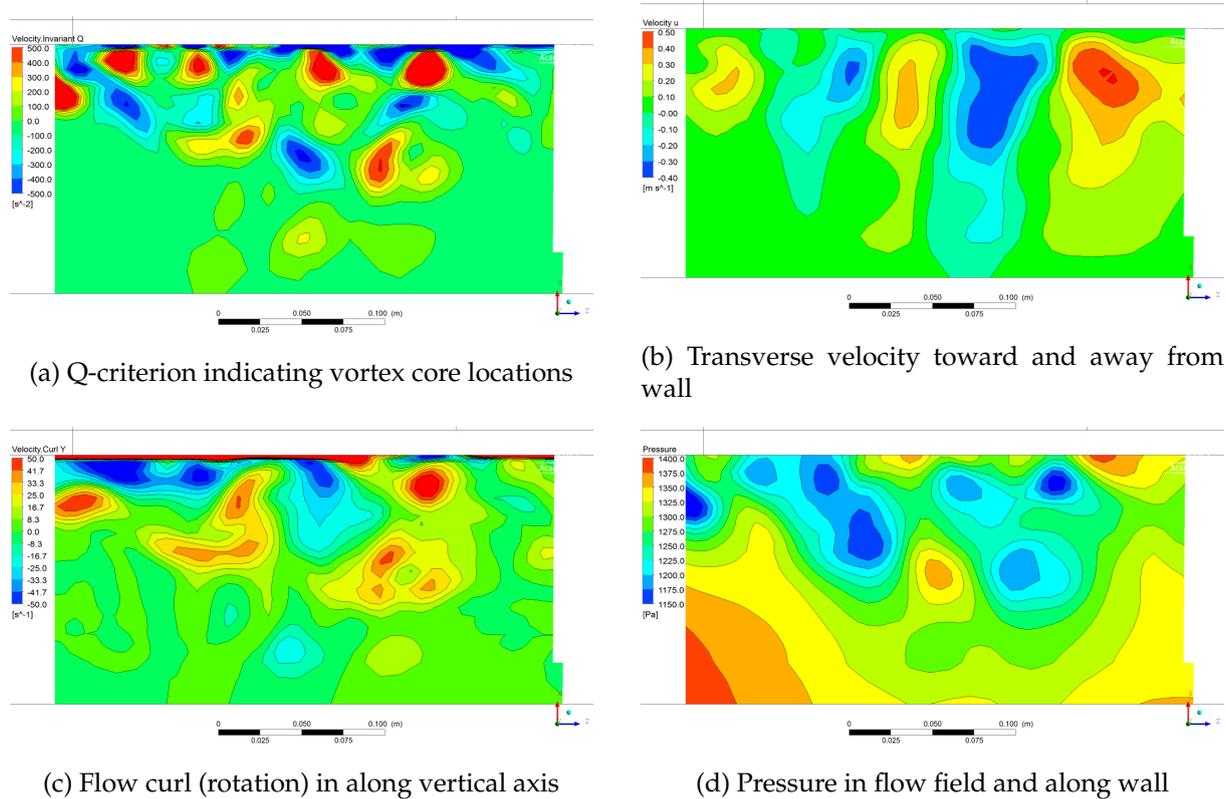


Figure 7.42: Near inlet key wall horizontal flow field generating pressure fluctuations

static pressures, the time-average pressure should be removed in order to visualise the effect. The resultant instantaneous pressure fluctuations from the mean are depicted in Figure 7.43. The fluctuations are zero or near zero over much of the upstream face of the sidewall but there are stronger fluctuations, both positive and negative, in the region of highest vortex activity. It is interesting to note that the fluctuations on the upper side of the flow tend to be vertically orientated and that those on the lower side are more horizontal. This provides further evidence that the pressure fluctuations are caused by the vortices as these are aligned in the same way.

An additional metric highlighted by Figure 7.43 is that of the wavelength of the pressure fluctuations. If a flow line through the system of vortices, parallel with the sloping floor, is imagined the fluctuations can be seen as a wave. Observing this wave, the distance from crest to crest, i.e. its wavelength, can be estimated as in the order of 0.15 to 0.20 m. This can be mathematically substantiated by calculating the cross-correlation function between two sets of points along this imaginary flow line. The distance between these two points is increased until the two pressure signals are highly correlated. Due to limited data sampling, this procedure is not exact, but the data can be interpreted to imply a wavelength of between 0.134 to 0.179 m, which fits in well with Figure 7.43.

The size and extent of the pressure fluctuations over time is summarised in the RMS value which is computed from the fluctuating pressure time sequence. This is illustrated in Figure 7.44. The average size of the total pressure fluctuation on the upstream face can reach up to 200 Pa, which, when compared to the mean total pressure in Figure 7.30c, equates to roughly

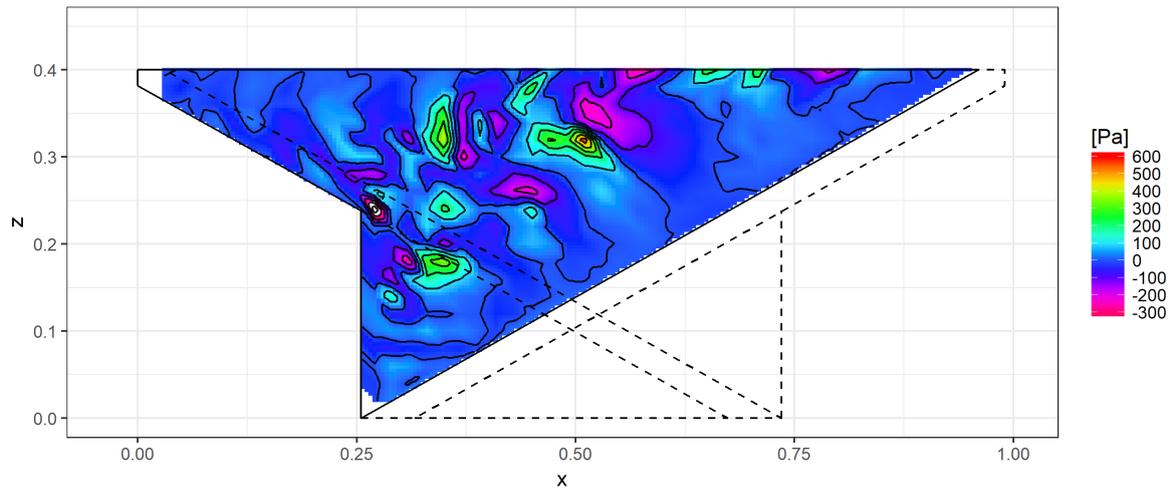


Figure 7.43: Instantaneous pressure fluctuations on upstream face of sidewall

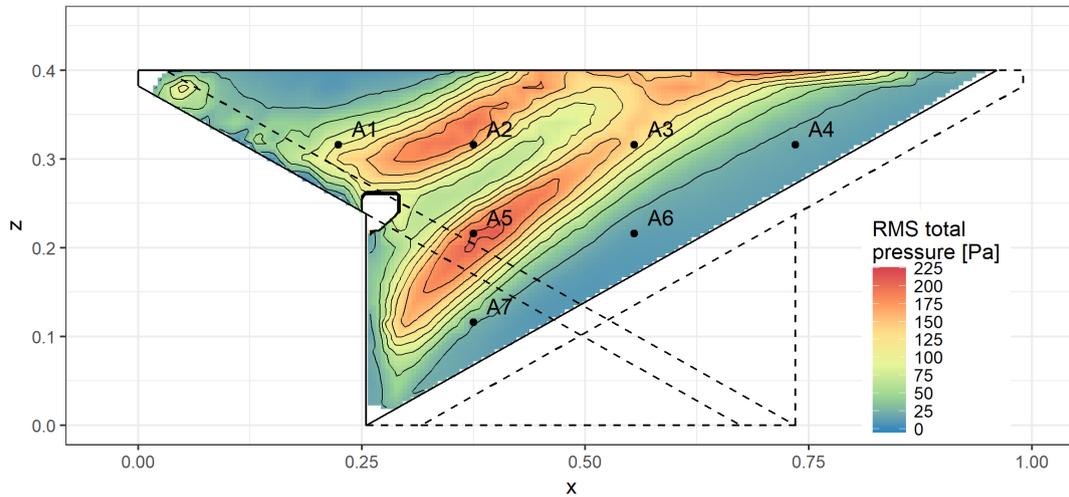
10% depending on the location and depth of the point in question.

In terms of the surface extent of the fluctuations on the face, it is immediately clear that the RMS values occur in two bands separated by a still zone. This still zone coincides with the low-velocity and low-pressure zone identified previously. This means that the vortices generated by the uppermost recirculation zone follow the path of the upper band and those vortices from the lowermost recirculation zone follow the lower band. This was previously indicated in Figures 7.9a and 7.16b where no large-scale mixing of these two flows was noted. This is especially important when considering strategies to limit the onset of these vortices as discussed in Section 7.5.7.

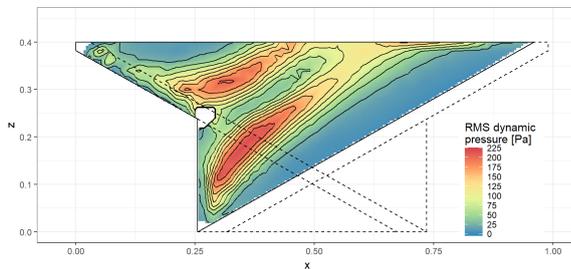
Another aspect demonstrated in Figure 7.44 is the split between the dynamic and static components making up the total fluctuation. It is evident that the bands noted in the total pressure graph are almost entirely due to the dynamics of the flow. There is a zone near the middle of the crest where there are large static pressure induced fluctuations. It is surmised that these are caused by local changes in the water level created by the periodic, vortex induced, undulations which were observed to occur at this location. This is described further in the next section.

### Pressure frequency

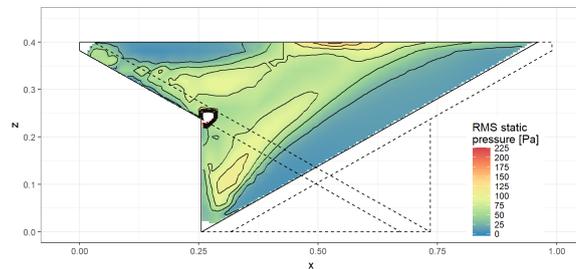
The transient nature of the fluctuations is of key importance in the current study. To this end, the pressure fluctuations were measured at a set of points along the inlet key wall as described in Chapter 5. The locations of the points, shown in Figure 5.10, have been superimposed on Figure 7.44a to indicate which of the pressure data sequences is likely to exhibit the largest activity. A snapshot of the data in the time-space is presented in Figure 7.45a. It is indeed found that the pressure signals at locations A2 and A5 have the largest and strongest fluctuations as they are located in the zone with the largest RMS values. The signals at A1, A3 and A7 also exhibit undulations but with lower amplitudes, as do A4 and A6 but at even lower amplitudes. The numerically calculated pressure oscillations at these same locations are included in the plot



(a) RMS of total pressure fluctuations



(b) Dynamic component of pressure RMS



(c) Static component of pressure RMS

Figure 7.44: RMS of pressure fluctuations on upstream sidewall

to illustrate that they have the same character, both in terms of regularity as well as amplitude.

This transient data was converted to the frequency domain to extract the power spectral densities of the signals. This is presented in Figure 7.45b. It is immediately clear that the various signals have a strong frequency peak of between 3 to 6 Hz. All the signals present this peak although the strongest peaks (represented by the area under each line) are again ascribed to locations A2 and A5 as well as A3. In addition to the main peak, point A2 also displays a secondary peak at approximately 15 to 20 Hz. All the signals portray elevated activity or energy at or below 10 to 20 Hz showcased by the broad raised PSD below these frequencies. Above these frequencies all the signals reach a noise floor which display only minor undulations. The peak frequency for each point is presented in Table 7.4 on page 146.

The data also exhibit a low frequency bulge on the left of the graph. This could be caused either by a long wave undulation that was present in the physical model flume or is related to a mathematical consequence of the FFT process trying to detrend a signal that was not 100% stationary. It is surmised that the mathematical construct is the more likely cause as this bulge is also present in the numerical model data. In any case, the bulge is of such a low frequency that it is not deemed of significance to the present study. It was not filtered out of the data as this process may have unduly affected the nearby frequency peaks.

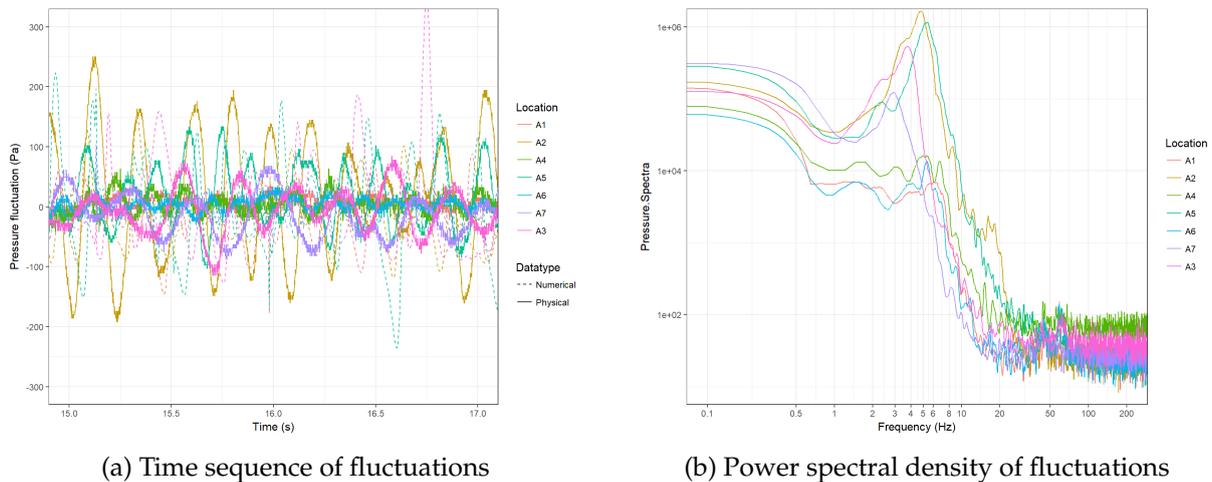


Figure 7.45: Pressure fluctuations in the time and frequency space

Studying the two graphs in Figure 7.45 the conclusion can be reached that the large peak frequency can only be caused by the regular undulations witnessed in the time plot. The amplitudes of the periodic undulations are of a similar magnitude as those illustrated in Figure 7.43 which are directly linked to the passage of the vortices. Hence this points to the physical undulations being created by the vortices which pass over the wall.

The peak frequency of the oscillations can be multiplied by the oscillation wavelength to arrive at the phase velocity. This velocity dictates the speed at which the fluctuations occur, which in the present case would also implicate the travel speed of the vortices themselves. This should not be confused with the particle speed, which may be much larger than the phase velocity (see Section 7.5.3). Considering a peak frequency in the order of 5 Hz at point A2, this equates to a phase velocity of between 0.67 to 0.89 m/s.

A representative set of the calibration results for the pressure fluctuation frequency is portrayed in Figure 7.46. The graphs depict the physical and numerical data in the frequency space at the three most active points: A2, A3 and A5. The two data sets demonstrate good agreement, as they both peak at roughly the same frequency and show a similar downward trend towards the noise floor on the right of the graphs. That said, the numerical data peak is not as defined as the physical data one. Furthermore, the numerical peak tends to be broader.

The numerical model thus simulated a wider range of frequencies than the focussed band that was recorded in the physical model. The reason for this is unclear, but it may be related to the length of the data set. The physical data set was typically 300 s long whereas the numerical data set was limited to 20 s (imposed by computational time constraints). Longer data sets of regular oscillations do reinforce a peak frequency. Another possible reason for the discrepancy is the general lower quality agreement in the near wall velocity flow field in the upper middle portion of the inlet key. Since the flow dynamics here are the direct cause of the pressure undulations on the wall, discrepancies in the velocity field would lead to discrepancies in the pressures.

The entire set of pressure frequency calibration plots is presented in Appendix D. The difficulties in calibration should not negate the results as being non-physical. The vortices are

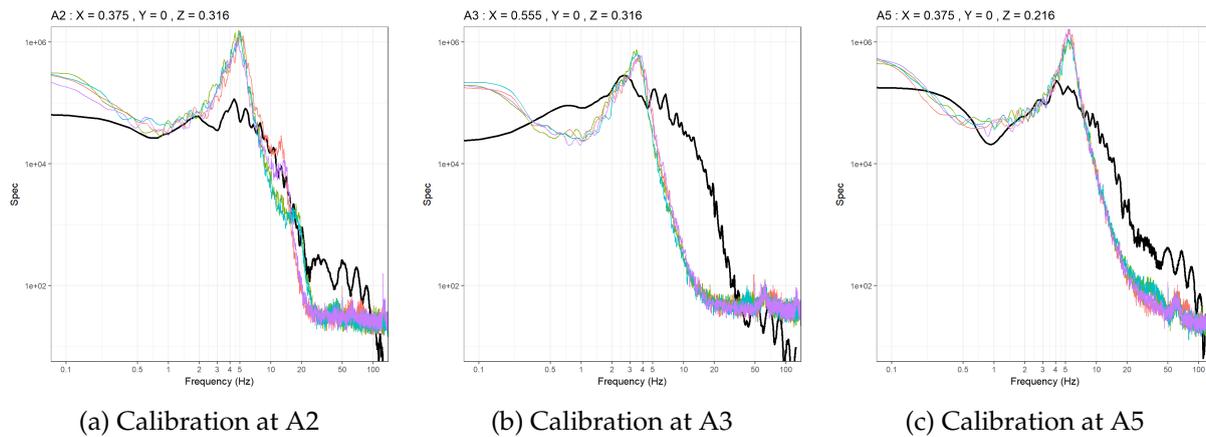


Figure 7.46: Pressure PSD calibration results between physical (coloured) and numerical data (shown in black)

present and do cause pressure fluctuations. However, the numerical model predicts these to occur over a much broader band of frequencies than those measured in the physical model.

The downstream face of the sidewall is also subjected to transient pressure fluctuations. The most significant of these occur when the nappe cavity apex becomes detached and finds an equilibrium near the middle of the sidewall. These pressures are discussed in greater detail in Section 7.4.5 where this phenomenon is explored.

#### 7.4.4 Nappe undulations

Undulations in the nappe have been noted to occur at the middle third of the sidewall. They presented in the physical model as a small localised wave comprising of a depression and a bulge directly above the crest, which then moved along the crest for a short distance before disappearing. This transient behaviour is depicted as a time sequence in Figures 7.47 and 7.48 in both the smaller physical model A ( $P = 0.4$  m) and at the larger scale model B ( $P = 1.1$  m). Each of the image frames is approximately 0.1 s long with the sequence reading from left to right per row. The sequences describe how the undulation starts off as a small depression which becomes deeper as a bulge starts growing behind it. This single wave crest and trough move downstream together, decrease in size, then vanish.

The wave is then followed by the next wave at more or less the same starting point. There seemed to be no set regularity at which undulations would appear nor were there any noticeable relation between the occurrence of an undulation and other undulations at the opposite sidewall across the inlet key nor the sidewall on the other side of the outlet key.

It was noted that at low discharges only a singular undulation would arise infrequently with long intervals of smoothness. At higher discharges, undulations occurred more frequently until several waves were present simultaneously at various stages of development. At even higher discharges, the flow becomes too rough and possibly the overflow depth too large, for the undulations to develop.

The undulations had a clear effect on the downstream nappe. The nappe extending from the bulging portion of the undulation was markedly thicker, whereas the nappe flowing from

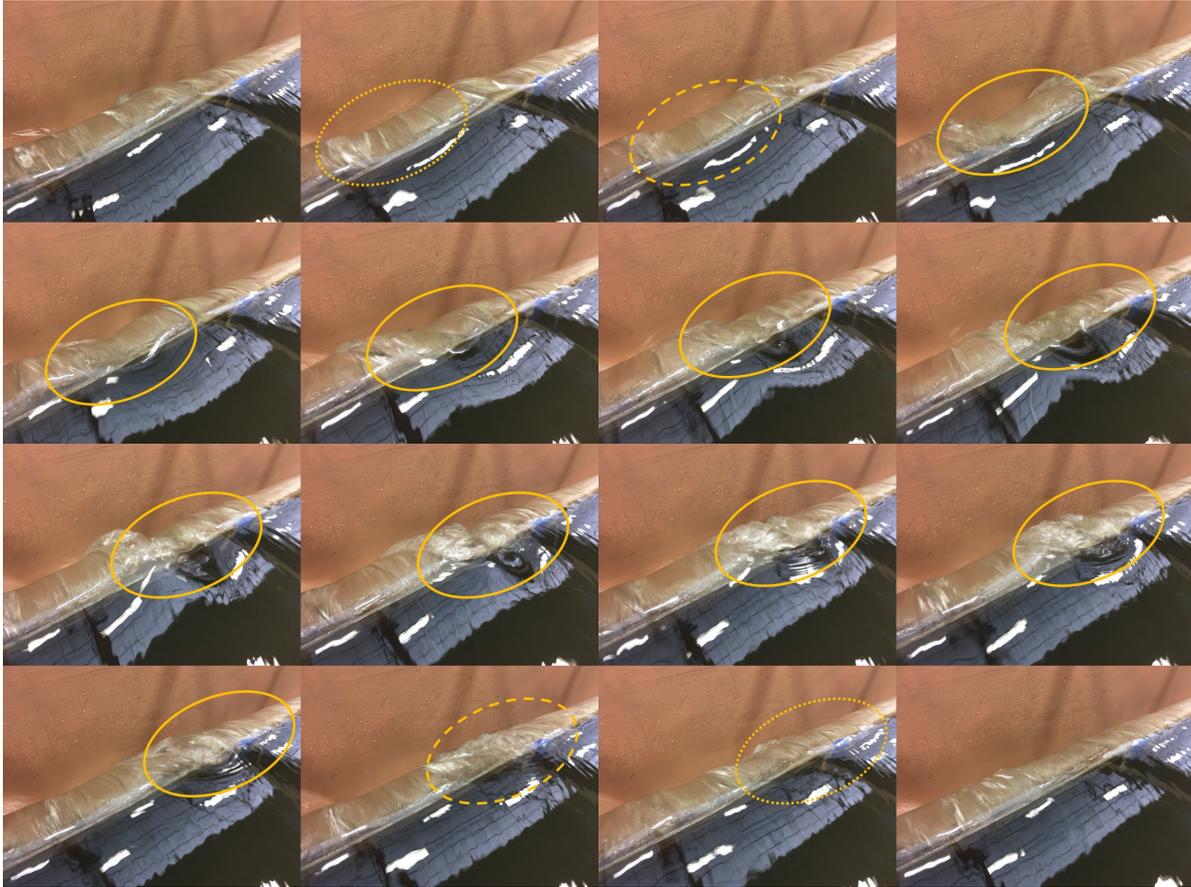


Figure 7.47: Sequence of crest undulations - Model B (viewed from upstream - flow left to right)

the trough of the wave was noticeably thinner. It was, however, never so thin such that the nappe would split or open up the nappe cavity to the atmosphere.

It was surmised from Figure 7.41b that the localised undulations are related to the presence of the vortex rolls at the crest. This is substantiated by Figure 7.49a, which presents the longitudinal velocity magnitude along a vertical, longitudinal plane on top of the crest. It thus represents the crosswise flow potential of the nappe. The majority of the flow over the sidewall crest has a slight downstream longitudinal velocity component (to the left in the figure) as well as a high transverse velocity component (not shown). In the presence of a vortex, the strong rotational currents are able to overcome the average longitudinal flow and reverse it (blue). Simultaneously, the longitudinal flows on the opposite side of the vortex are increased (red). In so doing flow at the base of the water column is retarded causing flow behind it to bulk together. At the same time, the higher discharge at the top of the water column causes a net removal of mass leading to a local depression.

Figure 7.49b illustrates what effect the crest vortex has on the downstream nappe. The flow in the bulge and at the base of the water column has a lack of longitudinal velocity hence it discharges over the sidewall at an almost perpendicular angle. Flow at the top of the column, in the depression, has excess longitudinal velocity hence it discharges at a greater angle than the remainder of the flow. This causes bulking of the nappe on both sides of the undulation but leads to almost no flow at the undulation itself. As observed in the physical model, this never

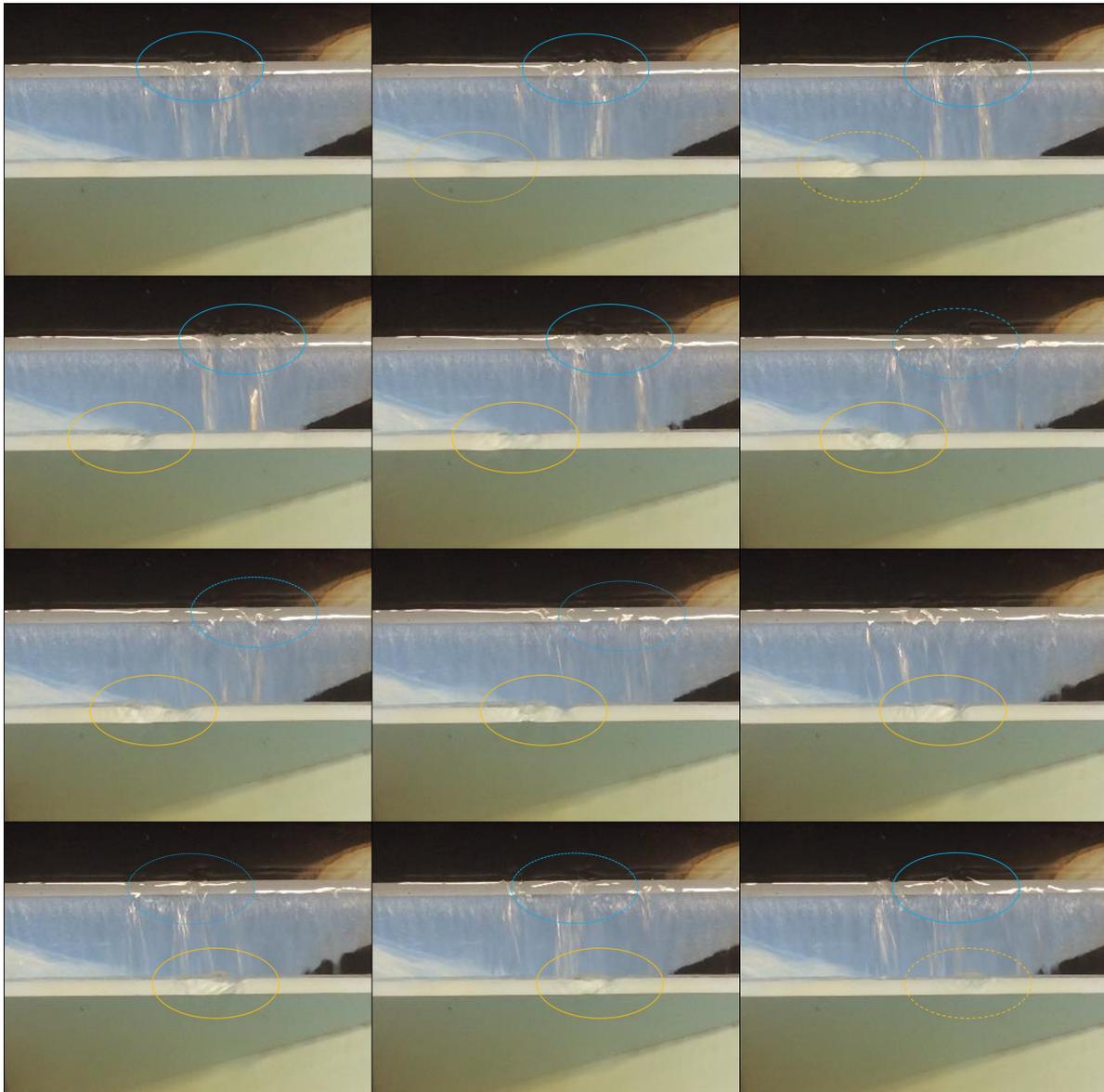


Figure 7.48: Sequence of crest undulations - Model A (view over outlet key - flow left to right)

lead to an opening of the nappe. However, due to the cell size limitation, the numerical model is not able to emulate the thin nappe in these areas hence it appears as an opening.

The periodic increase and decrease in water level as the undulation passes causes localised static pressure fluctuations over the entire water column. These can extend to the water column on the upstream face of the sidewall. These are presumably the static pressure fluctuations noted near the crest in Figure 7.44c.

#### 7.4.5 Nappe cavity apex

The underside of the nappe cavity in the outlet key was identified as a potential source of pressure oscillations on the downstream face of the sidewall. Under low flow conditions the nappe leaps or springs from the crest over the entire length of the sidewall as it would a normal linear weir under aerated conditions. At higher flow conditions, the higher overflow head

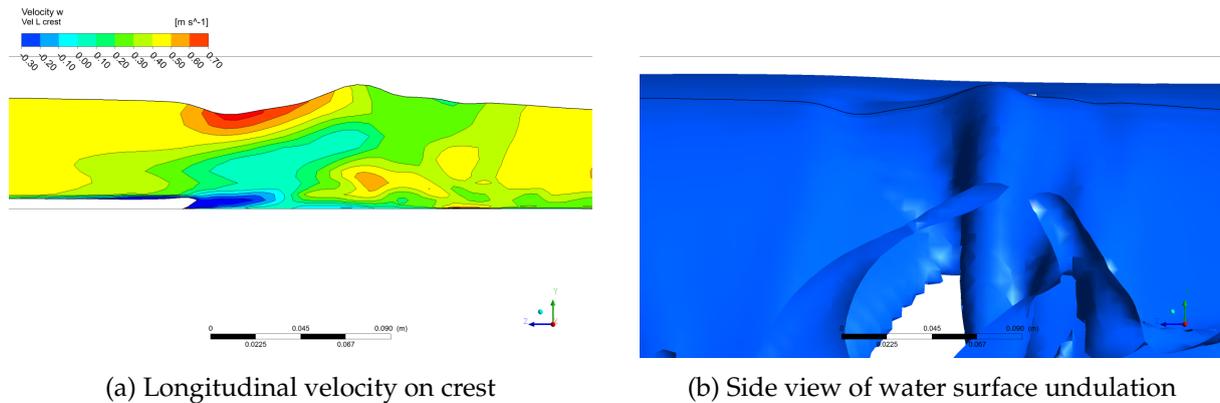


Figure 7.49: Side view of surface undulation on crest (flow is right to left)

on the crest combined with the limited discharge capacity of the upper portions of the outlet key, lead to localised submergence at the upstream edges of the sidewall. The nappe cavity thus reduces in length and forms a detached apex on its upstream side. This is portrayed in Figure 7.50. As indicated, the attached apexes extend over the whole length of the crest whereas the detached apex has withdrawn from the upstream extent of the sidewall. This image also demonstrates that the apex may not be detached or attached at all the sidewalls at the same time. It was often observed that one sidewall would exhibit a detached apex at discharges well below its occurrence at other sidewalls. The sidewalls appear to be identical, however, there may be small geometric differences in terms of the longitudinal orientation of the sidewall or the upstream overhang crest which induces earlier detachment of the cavity apex.

The nappe cavity instability and its oscillation were found to be a difficult scenario to study. The highly turbulent environment makes the collection of physical data a challenge. Despite this, it was surmised that the location of the cavity apex appears to be determined by an equilibrium of three main forces. These are the downstream momentum of the flow in the upper portions of the outlet key; the transverse (and rotational) momentum of the flow over the crest which also induces a zone of negative pressure underneath the nappe; and the air in the cavity under the nappe moving upstream to relieve this negative pressure. This interplay of forces is demonstrated in Figure 7.51 which depicts four cross sections of an instantaneous snapshot of the cavity that intersect at a point near the cavity apex.

The grey zone on the upstream side of the image represents the water pressure below the surface. The coloured portion shows the air velocity magnitude. The image reveals the presence of a zone of strong negative pressure in the drowned portion of the outlet key, directly alongside the sidewall. It appears as if this zone develops at the rough position of where the water level in the outlet key would be if it were not submerged in this location. This low-pressure zone is the centre of a region of rotational flow generated by, and located under, the falling nappe (see cross section Transverse-2). The water level in the outlet key in this vicinity is unable to subdue this negative pressure due to the strong rotational flow from the sidewalls as well as the high longitudinal velocity of the remainder of the flow.

The upwelling against the sidewall caused by the rotational flow can extend upward until

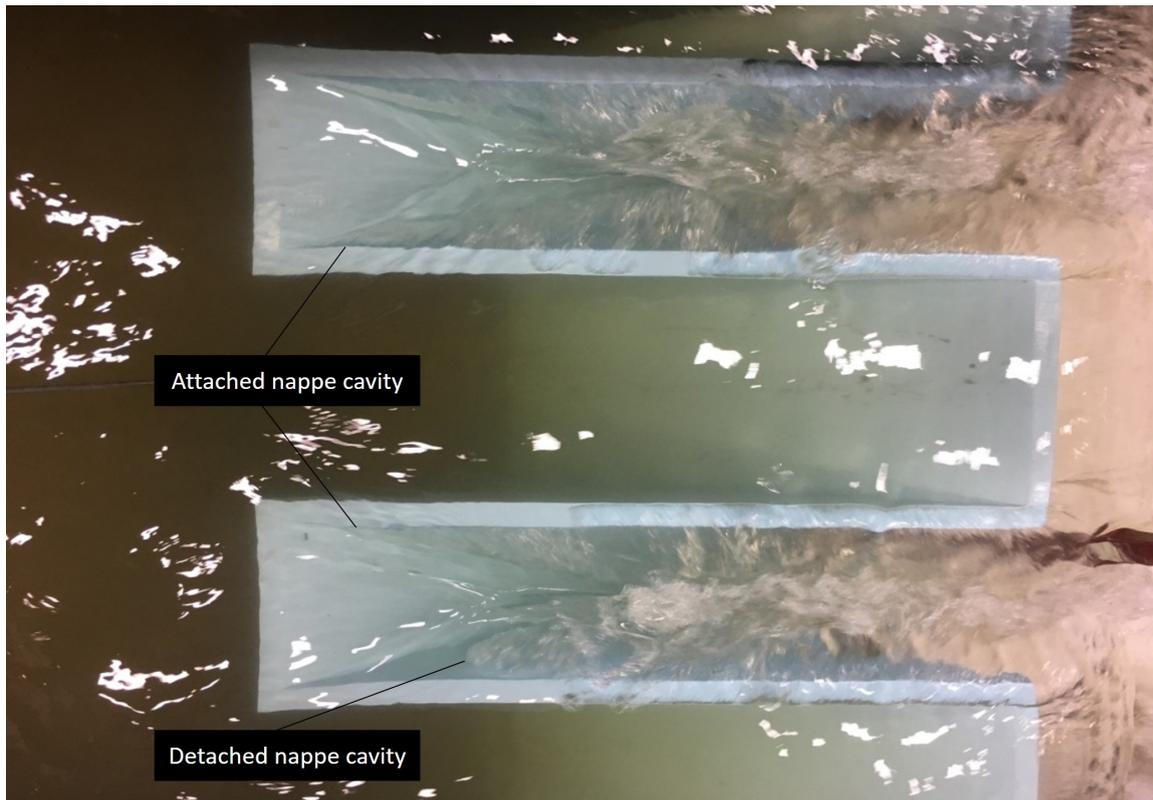


Figure 7.50: Attached and detached nappe cavity apices

it collides with the underside of the nappe. Where this occurs the nappe becomes fully drowned. At sections farther downstream in the outlet, the upwelling is either not strong enough to reach up to the crest or, from time to time, abates temporarily, forming an opening for air to rush in (red velocity magnitude in Figure 7.51). The air cavity is defined by the underside of the overflow nappe and by the upwelling of the flow at the base of the outlet key. Where these two meet, the nappe apex forms.

#### Physical model observations

Observations in the physical model revealed that, for the majority of the time, the apex was located near the crest. There were moments, however, when the air cavity obtained access to the zone of negative pressure thus causing the apex to rapidly move upstream at a location well below the crest of the sidewall. This is demonstrated in the latter images in Figure 7.52. The figure presents the cavity apex over a sequence of discharges. Note that, especially at higher discharges, the location of the nappe oscillates over a large distance. The locations set out in the figure approximate their farthest upstream reach.

The first image in Figure 7.52 shows that the cavity apex is detached by only a small distance. At discharges even lower than those shown, the nappe is fully attached, similar to that illustrated in Figure 7.50. As the discharge increases, the location of the maximum upstream reach of the apex is pushed farther and farther downstream. Furthermore, as discussed, the apex at higher discharges is located some distance below the crest whereas it is located at the crest at lower discharges.

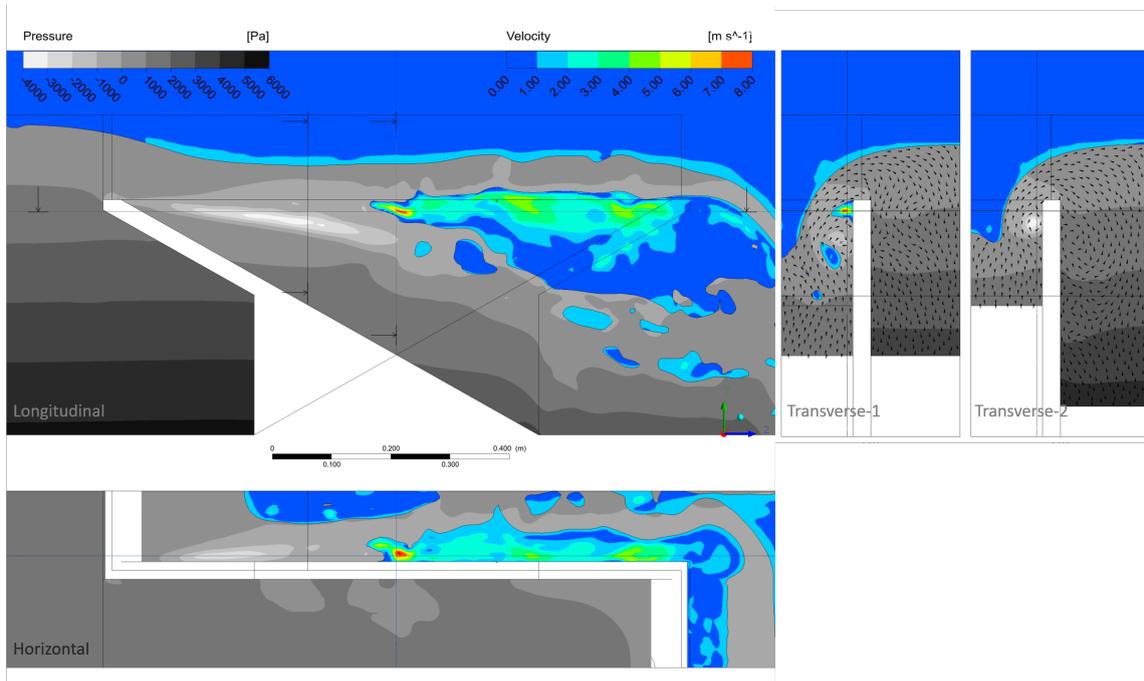


Figure 7.51: Balance between water pressure and air velocity under the nappe

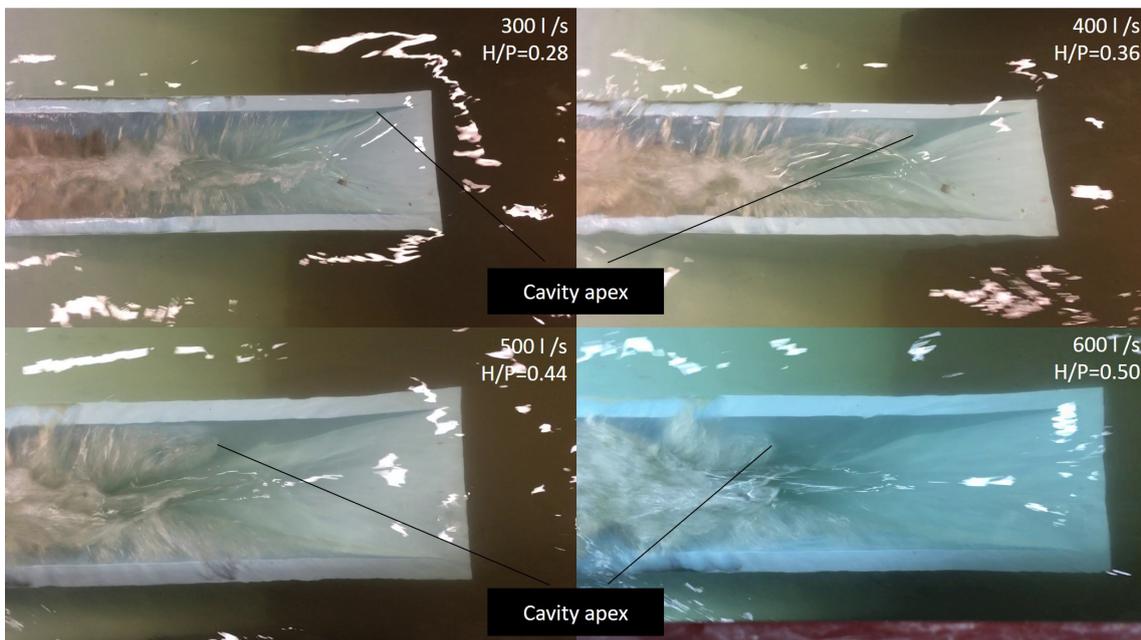


Figure 7.52: Nappe cavity apexes at different discharges (flow is right to left)

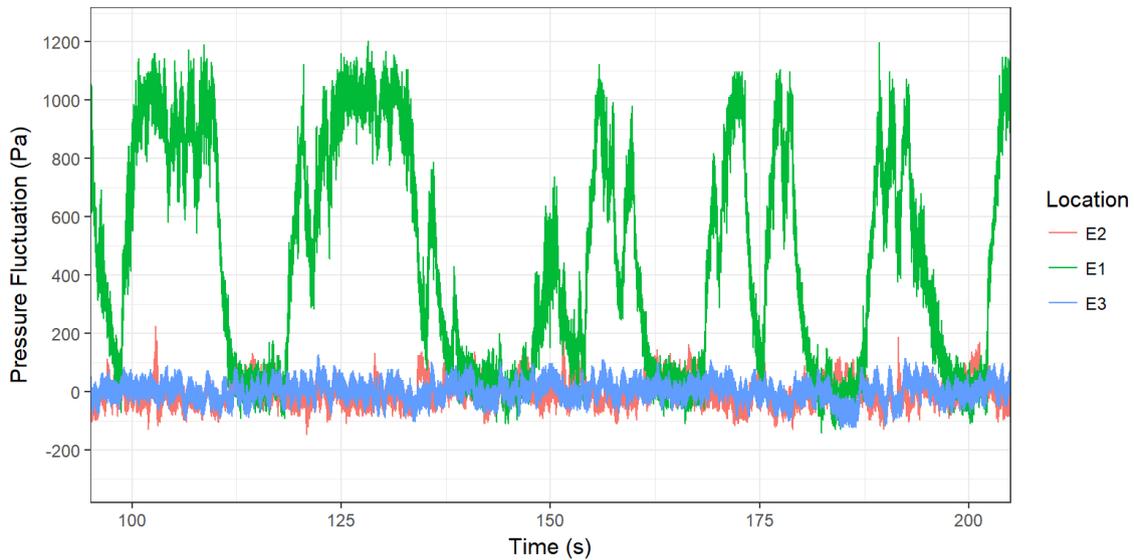


Figure 7.53: Oscillation time sequence of air cavity over pressure sensors

The apex location was fairly stable or static at lower discharges but oscillated over a wide distance at higher discharges. Figure 7.53 demonstrates the effect this oscillation has on the pressures on the downstream face of the sidewall. It presents data obtained from the three pressure sensors located on this face. Their locations are presented in Appendix B. The data demonstrate that when the apex transitions over the most upstream sensor (E1) there is a marked increase in pressure on the wall. In the flow scenario presented ( $6001/s$ ,  $H/P = 0.5$ ), the apex did not transition over the two downstream sensors, hence these continued to register the air pressure under the nappe. The data reveal that the transition between the air and water pressure state was fairly rapid. Its occurrence is however infrequent with only roughly 20 transitions being counted in the 100 s time period presented.

Bear in mind that the data presented are unreferenced pressure fluctuations and not absolute pressure. It is possible that the pressure being recorded was negative (i.e. below atmospheric), however as stated in Chapter 5, the measurement methodology did not enable these negative values to be identified in the data sequence. The fluctuation magnitudes themselves remain fully valid however.

Regarding the air pressure readings (at points E2 and E3), the fluctuations indicate that there is a fair amount of pressure variation taking place under the nappe. It was thought that these may be caused by high sound levels ( $>80$  dB) or high air velocities. Sound is however not capable of inducing such large pressure fluctuations, and the air velocities needed to register these fluctuations are much larger than those modelled in the numerical model. Another potential source of these fluctuations is, again, the vortices present in the inlet key which are being discharged over the crest of the weir. The rotational energy of the vortices remains present in the nappe as evidenced by the nappe undulations discussed above. It is likely that these vortices are also causing sufficient disturbances to the underside of the nappe in order for the pressure under the nappe to oscillate. Though not shown here, the oscillations in the air pressure have an identical peak to those observed by the upstream wall pressures (see Figure 7.45b).

### Numerical model

The numerical model results presented in Figure 7.51 are those for a discharge of 400 l/s,  $H/P = 0.36$ . The photograph of this same scenario (Figure 7.52) indicates that the nappe is not nearly so far withdrawn. The numerical model thus overestimates the ability of the upstream flow momentum to push the apex away downstream. Furthermore, all numerical flow scenarios larger than this discharge showcase a fully drowned nappe with no air cavity at all, even when fully aerated by a piped supply of air. It is possible that the numerical models used a too high downstream water level which would indeed induce earlier and farther detachments of the cavity apex. However, the physical model, even at very high water levels still exhibited some form of air cavity even if it was small. This brings into question the confidence of the numerical results and casts doubt on its ability to model the highly dynamic interplay between velocity, flow momentum and pressure at the unstable interface of the two-phase flow. It can thus be stated that, although the numerical model can be used to build an approximate understanding of the dynamics of the air cavity it could not be relied upon to be a physically representative model of the cavity for use in the vibration model.

Although the noted phenomenon is of interest the instability only arose during unusual flow conditions comprising of very high tailwater levels and large discharges over the weir. In most other flow scenarios, although the cavity apex would indeed become separated from its upstream anchor, it would not pull away far enough downstream in order for it to have a significant effect on the pressures on the sidewall. This means that the majority of the flow scenarios which are due to occur at PKWs are well below the limits needed for this instability to arise. Hence its occurrence can be neglected in PKW design, if it can be shown that large flows or high tail water levels would not occur regularly.

#### 7.4.6 Nappe oscillations

The steel model was run through a series of low flow discharges to examine the possibility of the concave sections of the nappe developing instabilities (see Section 7.3.5). These tests involved overflow depths over the crest that are very small, in the order of a few millimetres at the lowest flows, hence forces such as surface tension start to play a larger role than for deeper flows. As reported on in the scaling exercise (see Section 5.2.5), literature studies report that flows lower than about 3 cm in depth are prone to scaling effects. However, since the steel model, with a height of 1.1 m, is tall enough to be considered as a prototype in its own right, this limit should not be applied here.

The test was initiated at a flow of 5 l/s, steadily increased to 30 l/s and then reduced again to 5 l/s to control for any hysteresis effects. A number of observations relating to the behaviour of the nappe flow over a range of discharges is described below.

At low discharges of 5 to 6 l/s, the nappe exhibited clinging behaviour for much of its length along the sidewall and formed a broken nappe at the overhang and downstream crest as shown in the first photo of Figure 7.54. From 7 l/s upward, the nappe formed a continuous curtain enclosing an air pocket underneath the overhang and alongside the sidewall, although initially the nappe still clung to the most upstream parts of the crest length. The nappe did

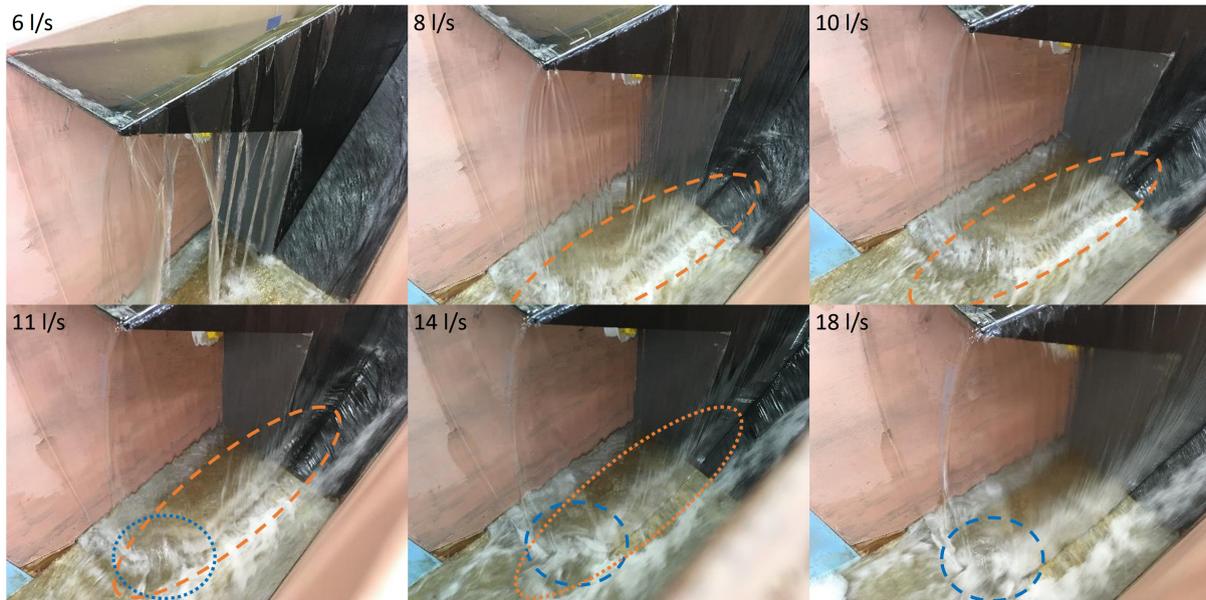


Figure 7.54: Sequence of photos of vibrating nappe at a range of discharges

break open from time to time. The nappe under the corner of the overhang was visibly pulled back toward its upstream side but did not yet form a concave indentation.

Increasing the discharge to 8 l/s up to 12 l/s resulted in the nappe underneath the corner of the PKW to start undulating at its lowermost extremities. This began with a slow inward-and-outward movement of the corner nappe. Over time this undulation increased in speed and its frequency eventually stabilized as measured by an air pressure sensor under the nappe. Once stabilized, the oscillation occurred over the full length of the nappe and was clearly audible and visible over this flow range. At higher flows than 12 l/s, the oscillations weakened, however they were still visible but were no longer audible. At 16 l/s the nappe oscillations ceased. It is possible that the thickness of the nappe had increased to a sufficient degree to limit the development of the oscillation. It is surmised that if the fall height were greater, the oscillation would still have occurred at this discharge. At this same discharge the corner nappe had formed a noticeable concavity and its vertical profile was noticeably pulled back at its lower extremity. The development of this concavity is displayed in the last few photos of Figure 7.54. At 25 l/s the first vortex water surface undulations appeared just upstream of the sidewall crest roughly  $\frac{1}{3}$  of the way from the crest's upstream corner.

During oscillation, the nappe as a whole, even those parts distant from the corner, visibly expanded and contracted in tandem with the oscillations at the corner. The profile of the nappe was fairly smooth near the crest but as it fell it developed a long wave undulation. This undulation increased in amplitude until near the floor of the flume it resulted in rapid fluctuations. This formed horizontal bands in the nappe which are made visible due to the refraction of light in Figure 7.54. The photos for 8 l/s, 10 l/s and 11 l/s show these bands in the nappe close to the floor of the flume. The photo for 14 l/s also exhibits a horizontal band but it is weaker than for the previous flows. The last photo in the sequence indicates that at higher flows, the horizontal bands stop, and the nappe forms a stable profile.

Table 7.2: Frequency and signal strength of nappe vibration

Discharge [l/s]	6	7	8	9	10	11	12	13	14	16
	Frequency [Hz]									
Increasing discharge	-	14.02	14.11	14.15	16.55	18.97	16.56	16.57	16.56	-
Decreasing discharge	-	14.11	16.48	16.48	18.96	18.99	-	-	-	-
	Sound signal strength [dB]									
Increasing discharge	-	91.4	90.8	95.7	97.1	101.9	72.2	66.3	61.8	-
Decreasing discharge	-	97.9	100.0	99.0	104.8	104.5	-	-	-	-

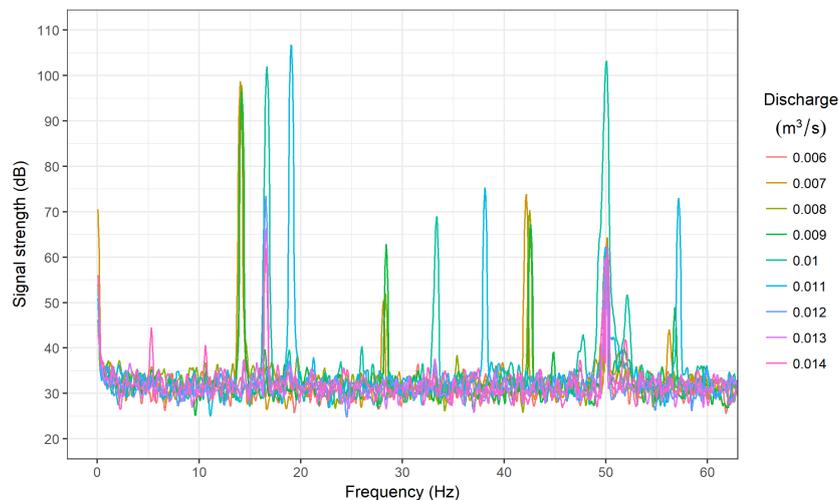


Figure 7.55: Frequency PSD plots of vibrating nappe at various discharges

The frequency of the nappe vibration was recorded with a pressure sensor located underneath the nappe. The results are presented in Table 7.2 and Figure 7.55. The PSD plot illustrates that the air pressure signal is characterised by a noise floor or base reference signal together with a number of frequency peaks. The strongest peaks are those which are generated by the oscillating nappe, which range from approximately 14 to 19 Hz depending on the discharge. The remaining peaks are either harmonic multiples of the initial frequency or interference from the electrical grid (50 Hz). The data reveal that the frequency occurs at one of three distinct values, 14.1 Hz, 16.6 Hz or 19.0 Hz. It is not entirely clear why the numerous recorded values are limited to these three frequencies, but this is probably related to the harmonics of the nappe as well as the fall height. This trend is more visible in Figure 7.56a which depicts the frequency values at one of three distinct levels. The frequency starts off at the first level, grows with discharge up the highest level and then drops down to the middle level.

The effects of hysteresis were tested by repeating the sequence of discharges mentioned above in a reverse order, from large to small. It was found that the nappe fluctuations occurred over the same range of discharges, namely 7 to 14 l/s. However, there were differences in behaviour, in that at 7, 8 and 9 l/s, where previously strong fluctuations were noted, their presence was now unstable. Strong fluctuations appeared but then developed a longer wavelength

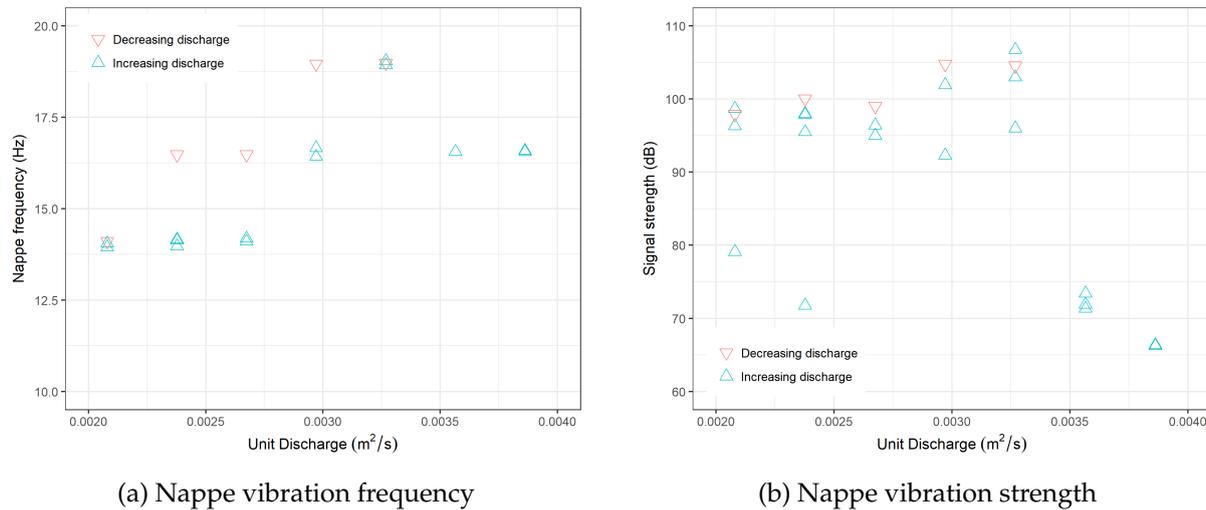


Figure 7.56: Nappe vibration change with discharge and hysteresis

thus reducing their frequency, before becoming stronger again. It was also noted that the hysteresis frequencies at each overflow discharge were also one level higher than those measured previously, although they follow the same increasing trend with discharge. This is set out in Figure 7.56a. Note that the discharge values in the graph have been reduced to their unit discharge equivalent using the overflow length of 3.366 m. It is noted that similar hysteretic effects have been surmised in other studies [94].

The adjacent graph, Figure 7.56b, describes how the strength of the pressure signal changes with discharge. This metric was found by other studies to follow a growing, plateauing and then decreasing trend [93; 94]. This trend is not precisely witnessed in the current data, however, the other studies reported constant nappe oscillation frequencies which are not the case here. The change in frequency may thus explain why the signal or oscillation strength does not follow the expected pattern.

The source or causative effect of the nappe vibration was investigated by disturbing its behaviour and examining its sensitivity to these disturbances. When the nappe was interrupted or opened in the vicinity of the corner, the nappe oscillations ceased altogether. When this disturbance was removed, the oscillations rapidly re-established. When the nappe was opened at locations farther away from the corner such that the corner nappe was not disturbed in any way, the oscillations did not cease, although they did reduce in strength and amplitude. The corner portion of the nappe thus appears to be a driver of the nappe vibration as a whole. Furthermore, it is clear that providing air to the underside of the nappe did not appear to alleviate the nappe oscillations, but directly disturbing it did.

The underside of the nappe was aerated via an open ended pipe with access to the atmosphere to test if full aeration had an effect on the oscillation behaviour. It was found that the fluctuations occurred as in the scenario without aeration. This implies that the vibration of the nappe is not related to the differential pressure which develops between the underside of the nappe and the atmosphere. Furthermore, the frequency content of the fluctuations was also unaffected. This supports the findings of recent studies which also found that the presence of

confined air behind the nappe does not affect the onset of these fluctuations but that it does affect their strength (see Section 4.3.3).

The nappe vibrations were shown to only occur at very low flows and only in a very narrow range of flows. Their lack of sensitivity to air pressure implies that their causative factor lies in the upstream water body. It is surmised that the vibration may be related to the transition of the upstream flow from laminar to turbulent flow. As the flow velocity increases in the upstream water body, the development of Tollmien-Schlichting (TS) waves along the upstream and sloping floor of the PKW may induce the nappe to vibrate in this way. It is surmised that the fixed frequency levels that the vibration attains are related to the harmonics of the falling nappe which is related to the fall height. The reason why the whole nappe stops vibrating when the corner is disturbed but not otherwise is unknown.

Despite being a clear source of vibration at the PKW, the nappe oscillations are not considered in the coupled numerical model of the vibration of the sidewall. This is because the behaviour would be very difficult to model accurately. Furthermore, the very low discharges needed to activate this vibration would mean the event would occur exclusively from all other vibrations sources. Nonetheless, the behaviour is worthy of further study, especially at thin walled PKWs whose natural frequencies may be close to that of the nappe vibration.

## 7.5 Observations and results

The previous sections described a variety of flow related static and transient phenomena which occur at PKWs. The present section aims to describe how these phenomena behave or change over a range of discharges, inlet key widths, weir heights and PKW types.

### 7.5.1 Discharge effect on velocity and turbulence

Section 7.4.1 explained how the velocity of the flow changes as it approaches and encounters a PKW using a set of graphs along a number of lines along and across the inlet key. These are aligned to the Cartesian X-Y-Z (longitudinal-transverse-vertical) directions. The lines all intersect at locations above the pressure sensor points (see Figure 7.10 and Appendix D.2). The graphs in this section (Figures 7.57 to 7.60) showcase this same behaviour but also reflect on how it changes at different discharges. These discharges are identified by their correlating  $H/P$  values as summarised in Table 7.3 for ease of reference.

The data indicate that there is no significant change in behaviour as the discharge increases. The velocities do increase in a stepwise fashion, however, their relative velocities at the same discharge follow the same trend regardless of the discharge. It is interesting to note that even though the velocities increase, the size of the near-stagnant zone representing the effect of the separation bubble remains more or less the same size. It was expected that the upstream edge of the bubble would remain in the same location, but that the downstream and transverse extent could have grown or shrunk as the external velocities changed. This turned out not to be the case.

This means that the velocity gradient between the external velocity and the recirculating

Table 7.3: Overflow ratios and discharge at model A scale

$H/P$	Discharge [l/s]
0.11	100
0.19	200
0.28	300
0.36	400
0.44	500
0.50	600

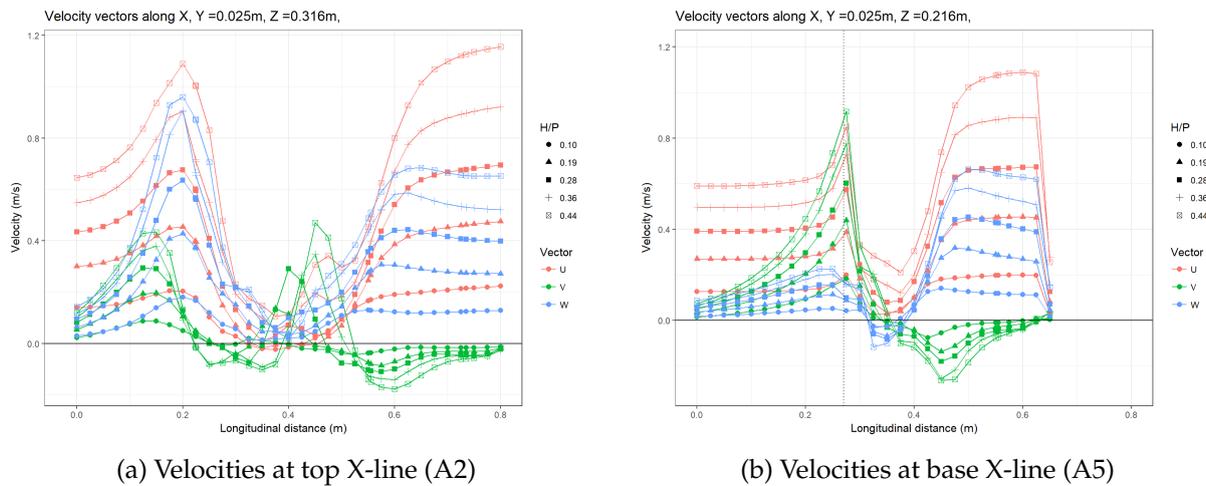


Figure 7.57: Velocity vector magnitudes at horizontal X-lines at various discharges

bubble becomes larger as the discharge increases. This leads to a much sharper shear zone which directly affects the vortices that are shed from this layer. This is detailed in Section 7.5.2.

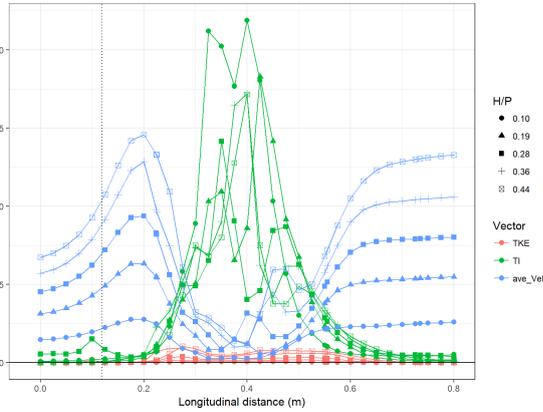
Despite the sharper velocity gradient, the internal velocities inside the stagnant zone continue to be very low. They do increase marginally, but only by a small degree. This is also reflected in the very similar levels of turbulence inside this zone (Figure 7.58) at various discharges.

This steady size of the stagnation zone has also been depicted in Figures 7.61 and 7.62 on a longitudinal and horizontal plane. These figures make it clear that the overall size of the stagnant zone is fairly constant even when the velocities become very large. They also describe how the velocity gradient grows with discharge mostly due to the increase in external velocity seeing as the internal velocity (inside the bubble) remains close to zero. It is noted that all these graphs and figures present numerical data, but it can be seen from Appendix D that the behaviour is also emulated by the physical model data.

## 7.5.2 Discharge effect on vortices

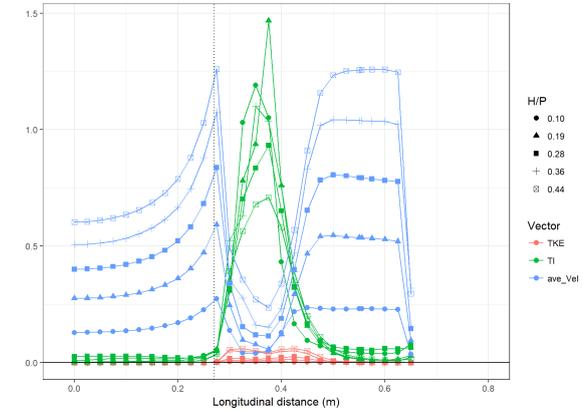
The increase in the velocity gradient with an increase in discharge is evident from the velocity data above. This implies a much stronger shear layer which would have an effect on the vortic-

X line, turbulence properties, Y = 0.025m, Z = 0.316m



(a) Turbulence at top X-line (A2)

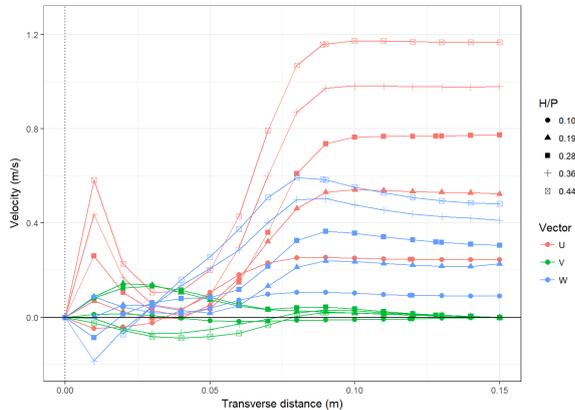
X line, turbulence properties, Y = 0.025m, Z = 0.216m



(b) Turbulence at base X-line (A5)

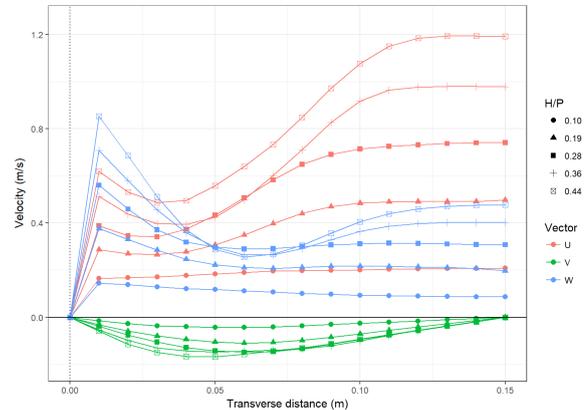
Figure 7.58: Turbulence properties at horizontal X-lines at various discharges

Y line, flow vectors at A2, X = 0.375m, Z = 0.316m



(a) Velocities at upstream Y-line (A2)

Y line, flow vectors at A3, X = 0.555m, Z = 0.316m



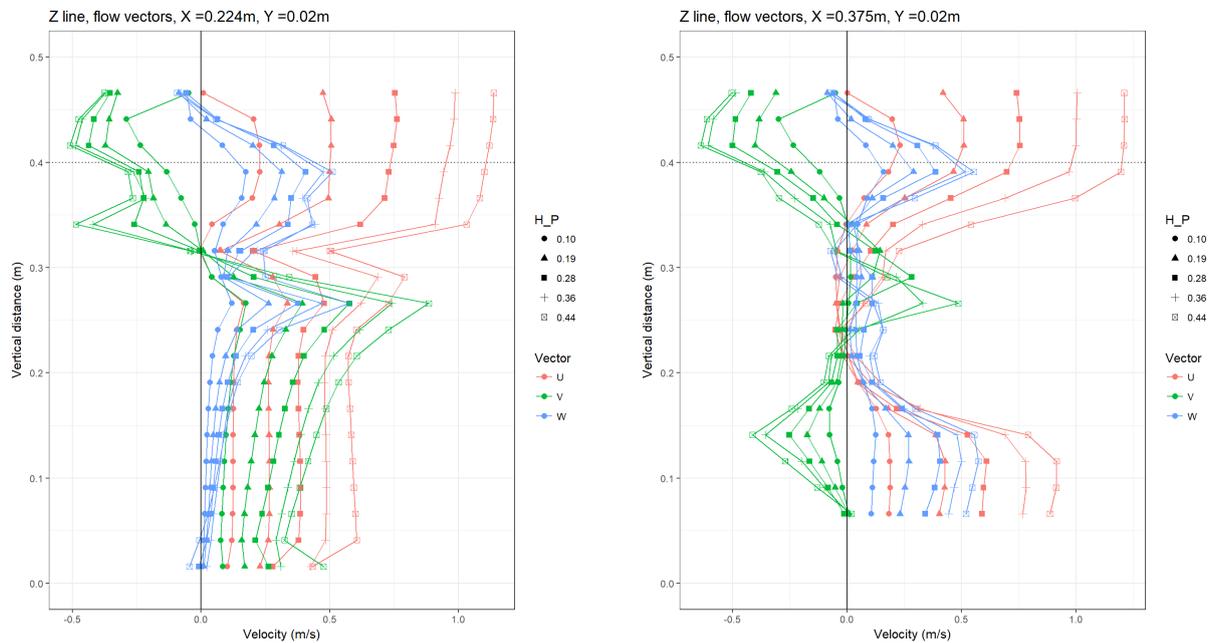
(b) Velocities at downstream Y-line (A3)

Figure 7.59: Velocity vector magnitudes at horizontal Y-lines at various discharges

ity and vortices in the inlet key. This is detailed in Figures 7.63 and 7.64. These plots illustrate that the zone of flow which is affected by the vortices remains more or less the same size. That said, the vortices do increase in strength (not shown here) and those cores farthest from the sidewall increase in speed as indicated by their change in colour in the plots.

The internal regions of the zone remain at fairly low velocities, and as it is these vortices which influence the pressures on the sidewall the most, the regularity of the pressures fluctuations (i.e. their frequency) is not greatly affected (see next section). The stronger rotational energy of the cores as discharge increases does increase the strength of the pressure fluctuations however.

Another interesting aspect to note is the location where the vortex cores overtop the crest. At low discharges (and overflow heads) the vortices cause surface undulations at a distance about a third of the length from the upstream corner of the sidewall. The size of the vortices is fairly large in relation to the water depth over the crest in these scenarios. This means that their effect is clearly noticeable both in the numerical and physical models. The undulations at



(a) Velocities at upstream Z-line (A1)

(b) Velocities at downstream Z-line (A2)

Figure 7.60: Velocity vector magnitudes at vertical Z-lines at various discharges

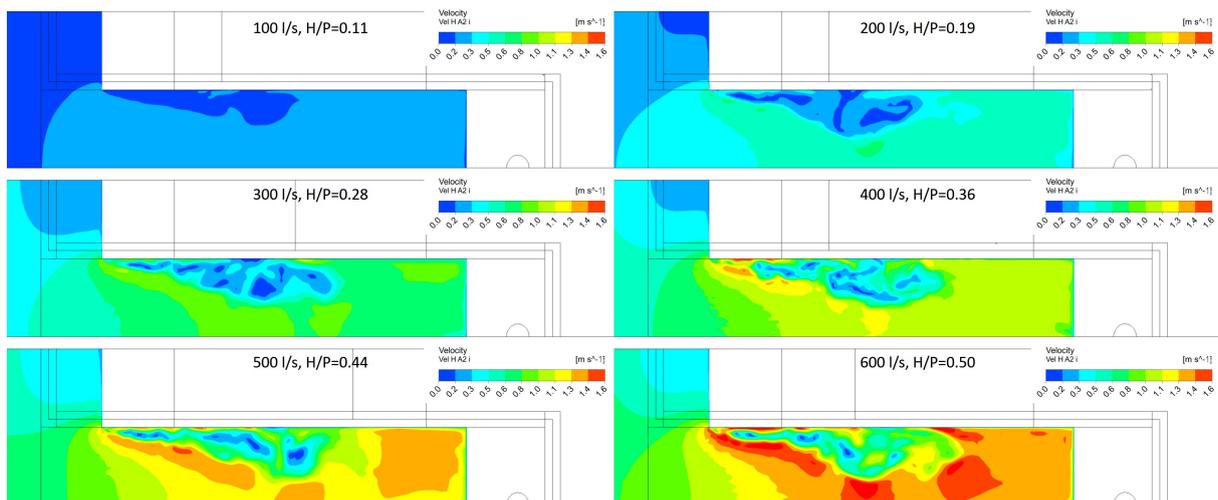


Figure 7.61: Variation in velocity magnitude on a horizontal plane over a range of discharges

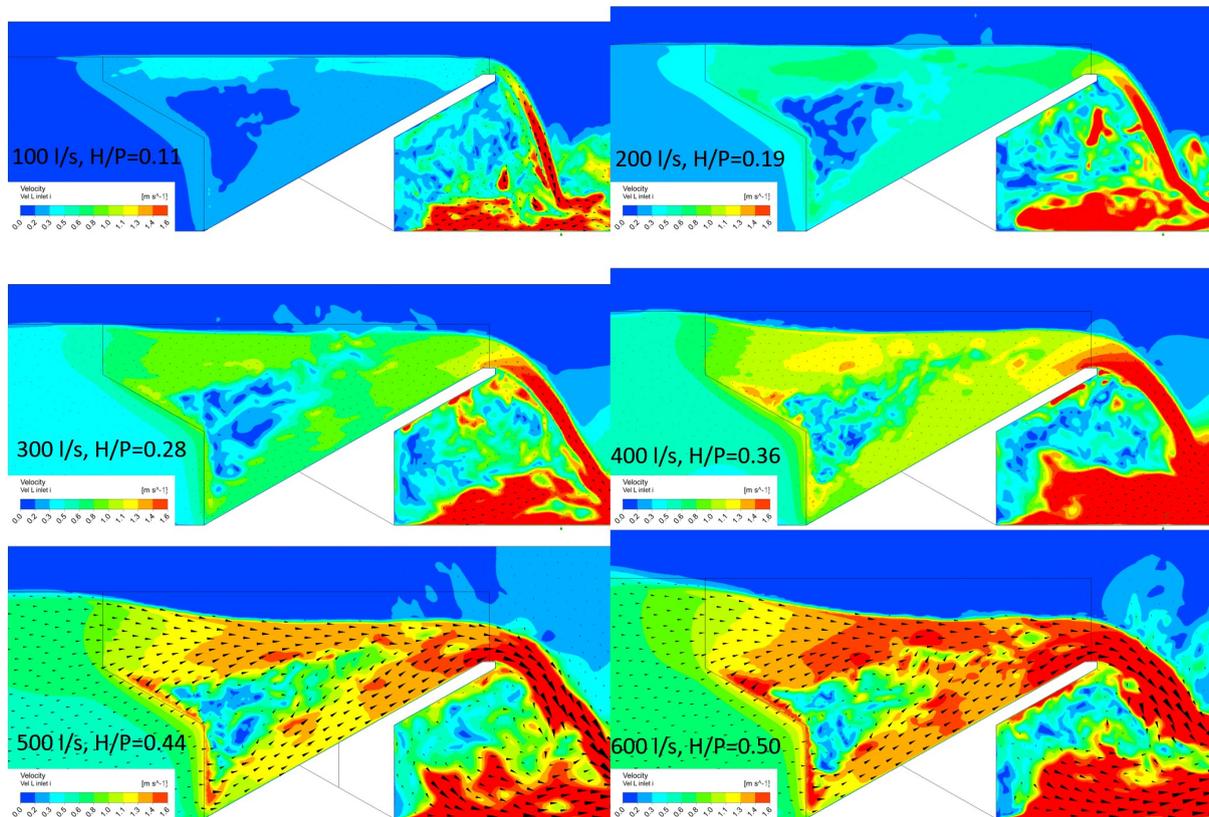


Figure 7.62: Variation in velocity magnitude on a longitudinal plane over a range of discharges

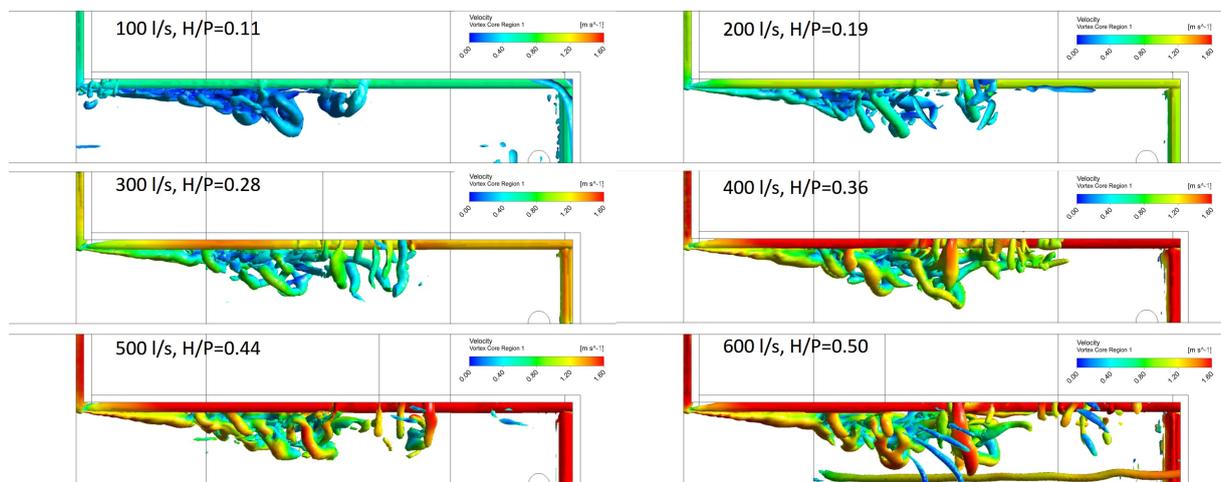


Figure 7.63: Plan view of inlet key vortices over range of discharges

the crest and the runnels they cause in the nappe curtain are clearly visible in Figure 7.64.

At larger discharges the vortices overtop the crest farther downstream, as also observed in the physical model. The larger water depth in relation to the size of the vortex often masks their presence and at the largest discharges the nappe and outlet key flow are so turbulent that the undulations are no longer discernible from the remainder of the flow.

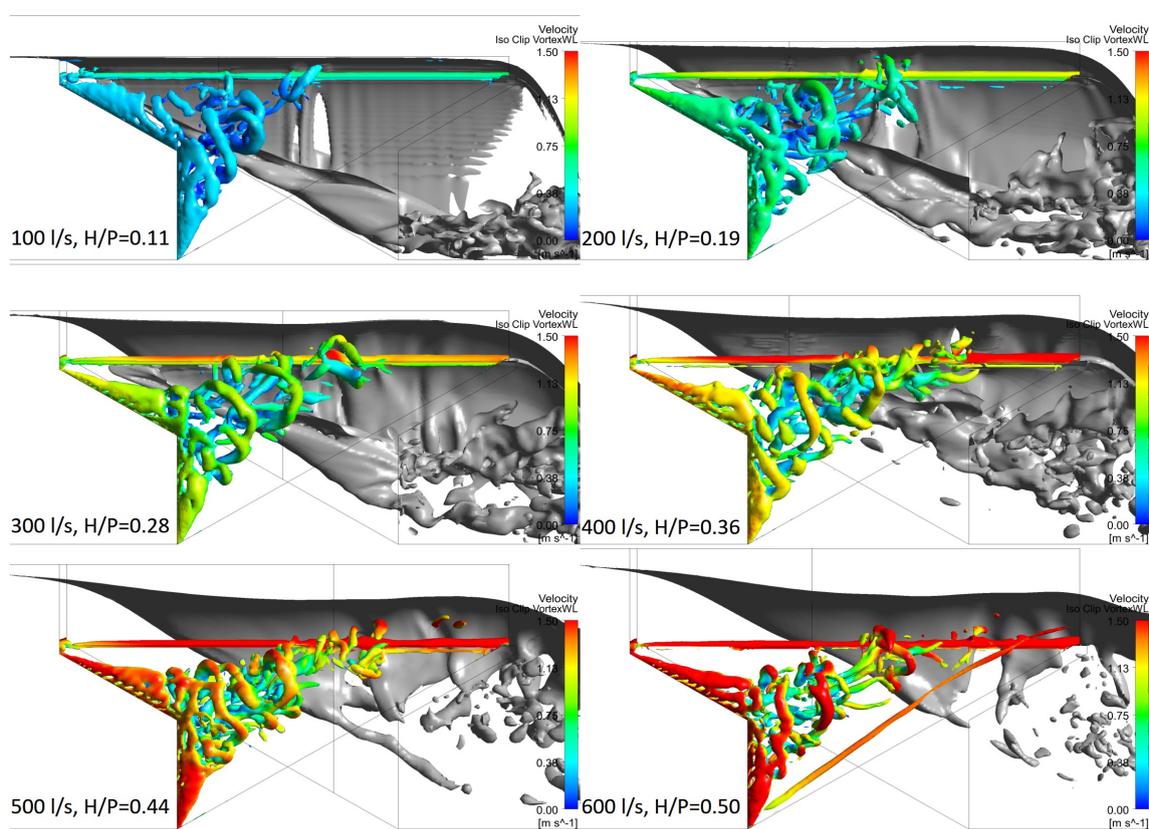


Figure 7.64: Side view of inlet key vortices over range of discharges

### 7.5.3 Discharge effect on pressure

It was noted in the previous section that the near-wall vortices which are the primary cause of the pressure fluctuations, gain in strength but not in regularity as the discharge over the weir increases. This is substantiated by the sequence of images in Figure 7.65. The plots indicate that as the discharge increases, the strength of the fluctuation (represented by the areas under the graph) increases in kind. The largest incremental increases in strength occur at the lower discharge values.

It is also strongly evident from all the graphs that even though the fluctuation strength increase, their frequency is constant (see Table 7.4). This frequency is driven by the magnitude of the phase velocity which dictates at what speed the vortices travel. Here this phase velocity is presumably controlled by the overall flow velocity in the immediate vicinity of the wall. However, this cannot be the case as, even though the increase in the near-wall velocities is relatively small, there is still an increase (see Figure 7.59). One would expect the increase in velocity to lead to an increase in the frequency as more vortices are convected in a given time period. That this is not the case can be explained by the likelihood that the large mean velocities being recorded are just the particle velocities with their large but short-lived instantaneous velocities increasing the mean value. These are caused by the much stronger vorticity in the vortices, whose convective velocity remains largely the same. This phase velocity is thus masked by the much stronger flow velocities. This is substantiated when examining the autocorrelation and

Table 7.4: Peak vortex frequencies at each pressure point for a range of discharges

Discharge [m <sup>3</sup> /s]	H/P [-]	A1 [Hz]	A2 [Hz]	A3 [Hz]	A4 [Hz]	A5 [Hz]	A6 [Hz]	A7 [Hz]
0.1	0.11	5.7	4.7	3.4	5.9	5.4	5.4	2.9
0.2	0.19	6.6	5.1	3.3	6.2	5.0	5.6	3.1
0.3	0.28	6.7	4.9	3.4	5.9	5.2	5.5	3.2
0.4	0.36	6.8	4.7	3.5	6.0	5.2	5.5	2.8
0.5	0.44	6.3	5.0	3.5	5.8	5.0	5.6	3.0
0.6	0.50	6.3	5.0	3.6	6.0	5.4	5.5	3.0
0.7	0.62	6.0	4.8	3.9	6.2	5.5	5.2	3.0

cross-correlation functions of the various data streams.

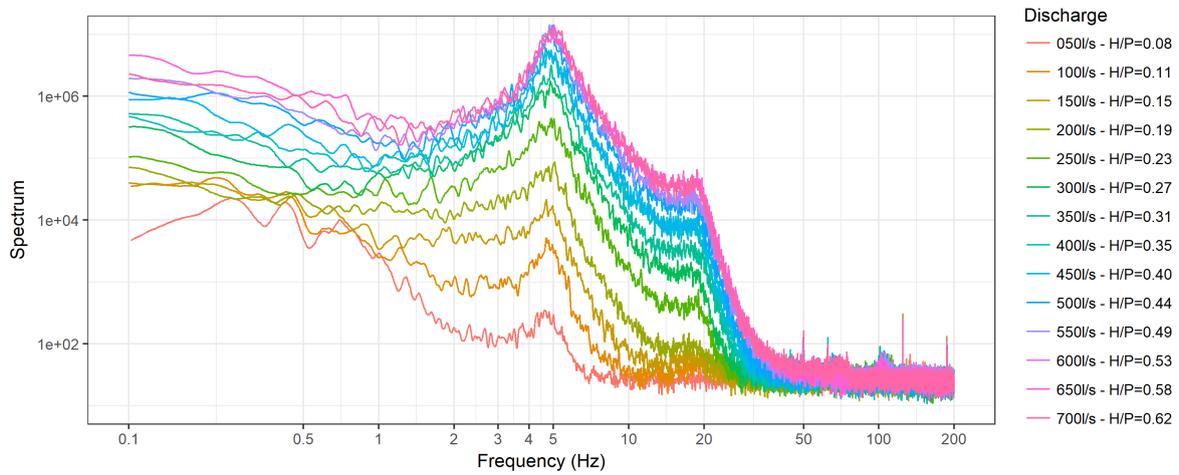
The frequency in the graphs was not non-dimensionalised to the Strouhal number, as this requires a relevant, preferably geometric, characteristic length and characteristic velocity. Neither of these could be determined. The pressure signals were found to be independent of the upstream flow velocity, the velocities in the inlet key, the inlet key width and the various size metrics of the separation bubble. The Strouhal numbers determined using these values would thus not be useful in examining the control they exercise on the frequency.

It should be noted that the numerical model results of the pressure frequencies do showcase an increasing trend as discharge increases. This behaviour is however limited to low discharges where the numerically determined frequencies are lower than the physically measured ones. These grow asymptotically until around 3001/s at which point the numerical and physical frequency data show better agreement. It is not clear why the numerical model underestimates the pressure fluctuating frequencies at low discharges but not at high discharges. The limiting factor placed on the vortex size imposed by the grid may play a role.

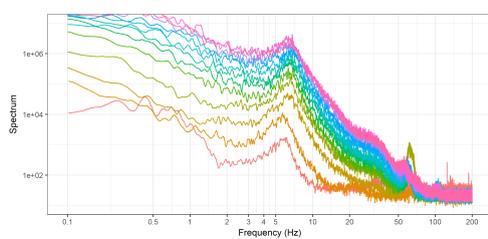
#### 7.5.4 Discharge effect on nappe trajectory

The nappe profile as it overtops the sidewall and downstream crest was recorded in the physical model to ascertain the effect of any sub-atmospheric pressures under the nappe. The two graphs pictured in Figure 7.66 reveal that when the nappe is aerated it pushes farther outward compared to when it is unaerated. This suction indicates that sub-atmospheric conditions are present under the nappe, although this data does not allow the magnitude of this pressure to be estimated.

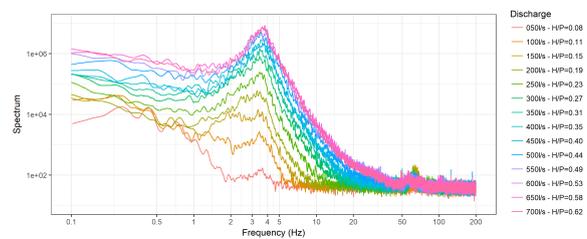
The effect of discharge shows that the water level increases, however, there appears to be no direct effect on the magnitude of the contraction caused by the lack of aeration. This implies that the nappe curtain, once established, quickly reaches a stable negative pressure equilibrium which is maintained over all discharges.



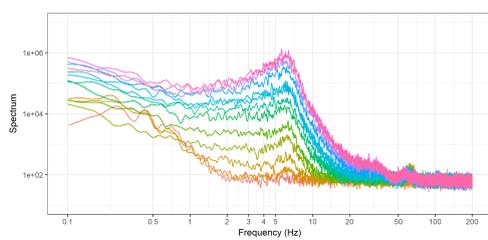
(a) Pressure spectra at point A2



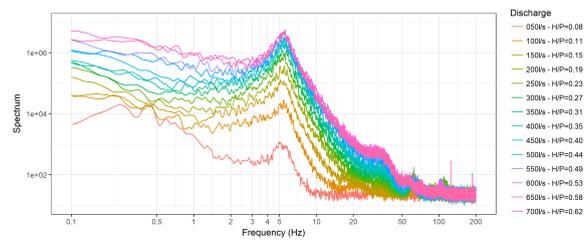
(b) Pressure spectra at point A1



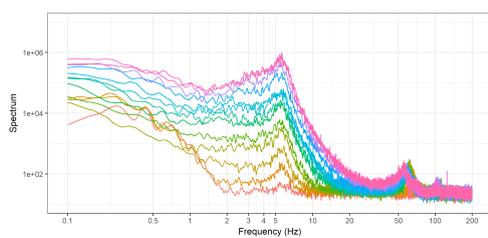
(c) Pressure spectra at point A3



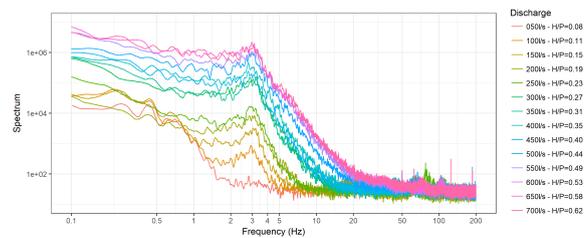
(d) Pressure spectra at point A4



(e) Pressure spectra at point A5



(f) Pressure spectra at point A6



(g) Pressure spectra at point A7

Figure 7.65: Physical model pressure spectra over a range of discharges

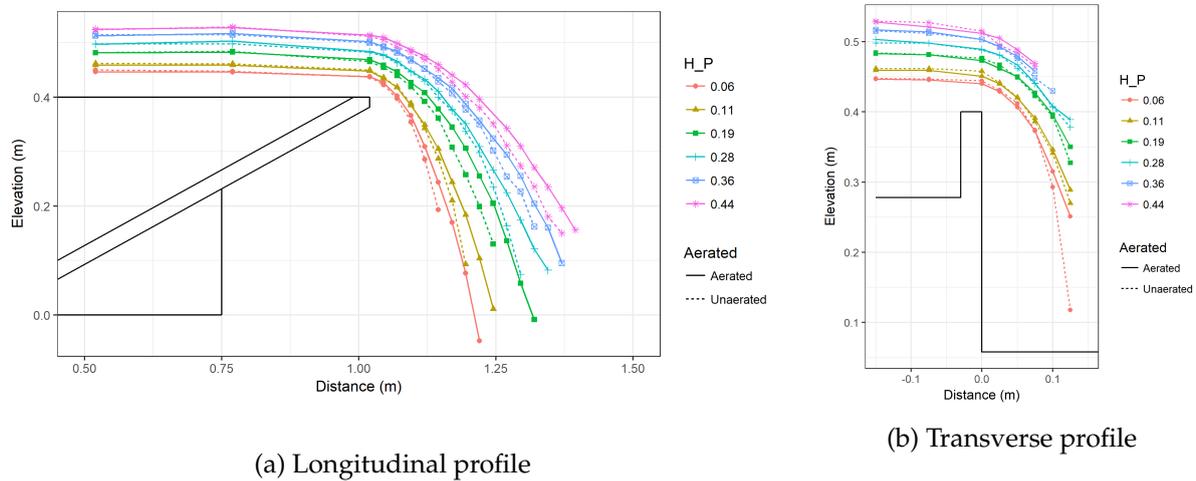


Figure 7.66: Water level profiles under aerated and unaerated conditions

Table 7.5: Numerical model discharge with changing PKW scales

$W_i$ [m]	$W_o$ [m]	$W_i/W_o$ [-]	$W_u$ [m]	$P$ [m]	$H$ [m]	$H/P$ [-]	$T_s$ [m]	$Q_{1unit}$ [m <sup>3</sup> /s]	$C_{dW}$ [-]	$Q_{Scaled}$ [m <sup>3</sup> /s]
0.30	0.24	1.25	0.30	0.40	0.144	0.36	0.030	0.083	1.71	0.083
0.60	0.48	1.25	0.60	0.80	0.288	0.36	0.060	0.468	1.71	0.468
0.90	0.72	1.25	0.90	1.20	0.431	0.36	0.090	1.293	1.72	1.289
1.50	1.20	1.25	1.50	2.00	0.719	0.36	0.150	4.636	1.72	4.623
2.25	1.80	1.25	2.25	3.00	1.079	0.36	0.225	12.769	1.71	12.740

(1unit) - 1 PKW unit with one half inlet key and one half outlet key

### 7.5.5 Scale

The change in behaviour of the hydrodynamics of the inlet key with a change in the scale of the PKW was examined in the numerical model. The geometry was scaled upwards from model A using the scaling factors in Table 5.3. The discharges determined in the model are presented in Table 7.5. This table indicates that the scaled discharges are almost exactly as expected if the scaling factor ( $\lambda^{5/2}$ ) was applied to the scaled model discharges. The same can be said for the peak pressure fluctuation frequencies, which are presented in Table 7.6 and Figure 7.67 with a scaling factor of  $\frac{1}{\sqrt{\lambda}}$ . The values shown in parenthesis are the upscaled values from the smallest model and show good agreement with the modelled values. Note that one of the models produced erroneous results but still follows the trend to some degree.

Figure 7.68 emphasises this scaling behaviour by revealing almost no difference in the character of the vortices which are shed from the upstream edges. Also recall Figure 7.19 which suggested that the relative size of the separation bubble does not change. This data demonstrates that the vortex shedding phenomenon is present at all scales and that small scale models can be utilised to model this behaviour.

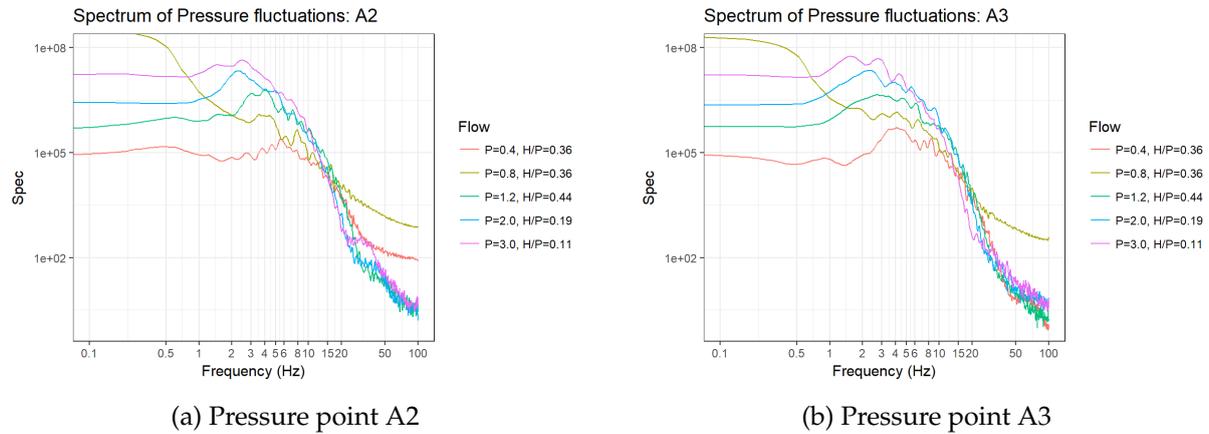


Figure 7.67: Frequency PSD at various scales

Table 7.6: Numerical model frequency with changing PKW scales

P [m]	A1 [Hz]	A2 [Hz]	A3 [Hz]	A4 [Hz]	A5 [Hz]	A6 [Hz]	A7 [Hz]
0.4	6.1 (-)	5.5 (-)	4.0 (-)	3.1 (-)	6.0 (-)	6.5 (-)	4.8 (-)
0.8	- (4.3)	3.5 (3.9)	4.2 (2.9)	2.5 (2.2)	3.8 (4.2)	- (4.6)	- (3.4)
1.2	3.1 (3.5)	4.1 (3.2)	2.6 (2.3)	1.8 (1.8)	3.7 (3.5)	4.6 (3.8)	4.7 (2.8)
2	2.6 (2.7)	2.2 (2.4)	2.2 (1.8)	1.6 (1.4)	2.8 (2.7)	3.3 (2.9)	3.6 (2.2)
3	2.4 (2.2)	2.4 (2.0)	1.5 (1.5)	1.4 (1.1)	1.9 (2.2)	3.1 (2.4)	3.2 (1.8)

### 7.5.6 Inlet key width

The manner in which the vortex sheet emanating from the upstream edges of the PKW inlet key spreads out into the inlet key suggests that there may be potential for interference with the vortex sheet from the opposite sidewall. This was explored by a series of numerical simulations at prototype scale with 2 units (one full inlet key) where the inlet key width was adjusted in relation to the width of the outlet key. It is known that adjusting this  $W_i/W_o$  ratio affects the discharge over the weir. This was confirmed by the simulations as set out in Table 7.7. Larger inlet keys lead to a larger discharge, although the increase is marginal.

A series of time sequences were processed to assess their frequency content and also whether there were any positive or negative correlations between the two separation zones on either side of the inlet key. The frequency PSD of the pressure fluctuations at point A5 is pictured in Figure 7.69. It, as well as the other pressure measuring points sampled, indicated that there is no marked shift or change in the peak frequency of the PSD as the width of the inlet key is adjusted. This again, supports the finding that the pressure fluctuations on the wall appear to be largely independent of the macro-scale hydrodynamics of the inlet key.

Figure 7.70 illustrates a related result in that the relative separation bubble size metrics showcase no increasing or decreasing trend as the inlet/outlet key ratio changes. This graph is supported by viewing Figure 7.71 which depicts the average longitudinal velocity in the inlet key. Note that as the inlet key width reduces the negative zone of flow along both sides of the

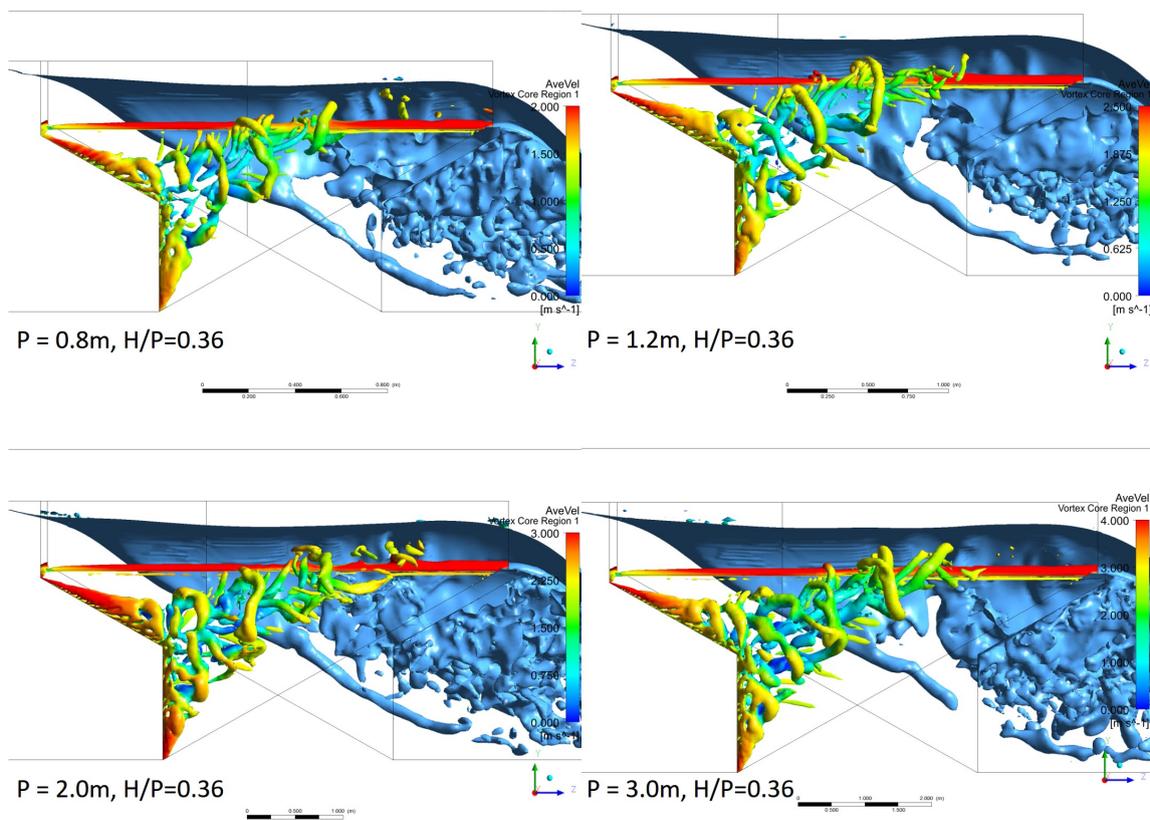


Figure 7.68: Side view of inlet key vortices over range of weir heights

Table 7.7: Numerical model discharge with changing inlet key widths

$W_i$ [m]	$W_o$ [m]	$W_i/W_o$ [-]	$W_u$ [m]	$P$ [m]	$H$ [m]	$H/P$ [-]	$T_s$ [m]	$Q$ (1unit) [m <sup>3</sup> /s]	$C_{dW}$ [-]
2.475	1.575	1.57	2.25	3.0	0.60	0.20	0.225	6.596	2.14
2.250	1.800	1.25	2.25	3.0	0.60	0.20	0.225	6.435	2.08
2.025	2.025	1.00	2.25	3.0	0.60	0.20	0.225	6.250	2.02
1.800	2.250	0.80	2.25	3.0	0.60	0.20	0.225	6.021	1.95
1.575	2.475	0.64	2.25	3.0	0.60	0.20	0.225	5.752	1.86

(1unit) - 1 PKW unit with one half inlet key and one half outlet key

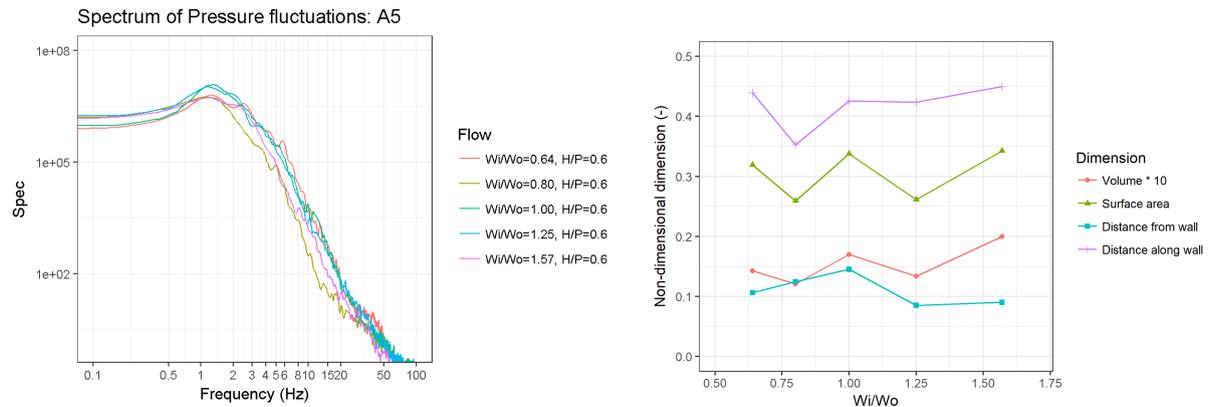


Figure 7.69: Frequency PSD of pressure fluctuation at point A5 with a variety of key width ratios

Figure 7.70: Separation bubble size metric for a range of inlet key width ratios

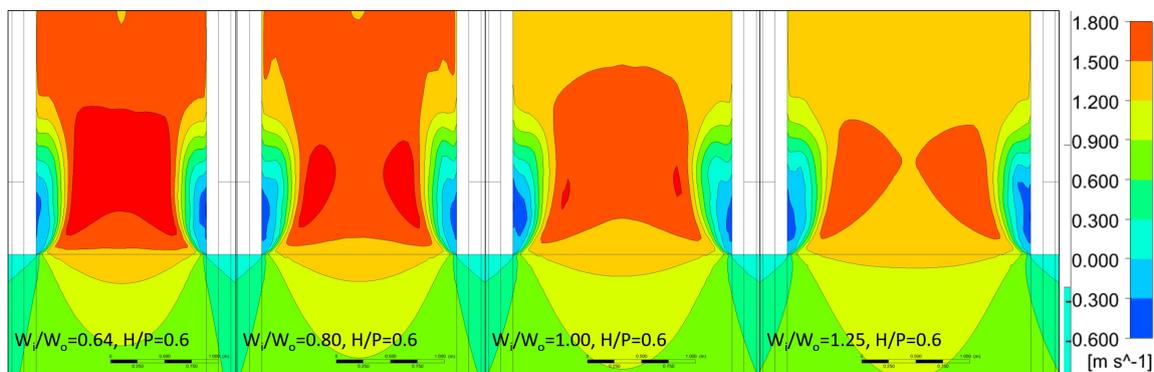


Figure 7.71: Plan view of longitudinal velocity in inlet key as inlet key width reduces (flow is up)

inlet key remains the same size. There is a significant increase in velocity as the key width gets smaller as more flow has to pass through a smaller area, but this has little effect on the size of the separation bubble.

The vortices which are generated by the unchanging separation zone are presented in plan view in Figure 7.72. It is clear that the vortices mostly remain separate and only at values of  $W_i/W_o < 1$  do the vortices on either side of the key start interfering with one another. Again, note that even though the vortices are weaving into each other, this has no effect on the pressure fluctuation frequencies on the wall. This is supported by examining the cross-correlation functions of two time series on either side of the key (not shown here). There is no direct correlation between the pressure or velocity data on either side of the key near the walls, other than the fact that they share the same oscillating behaviour. Only when the two points being compared are closer to the middle of the inlet key do stronger negative correlations start to manifest, however, even these were not that strong. This reflects the periodic crossing of the longitudinal middle line by one of the vortex cores.

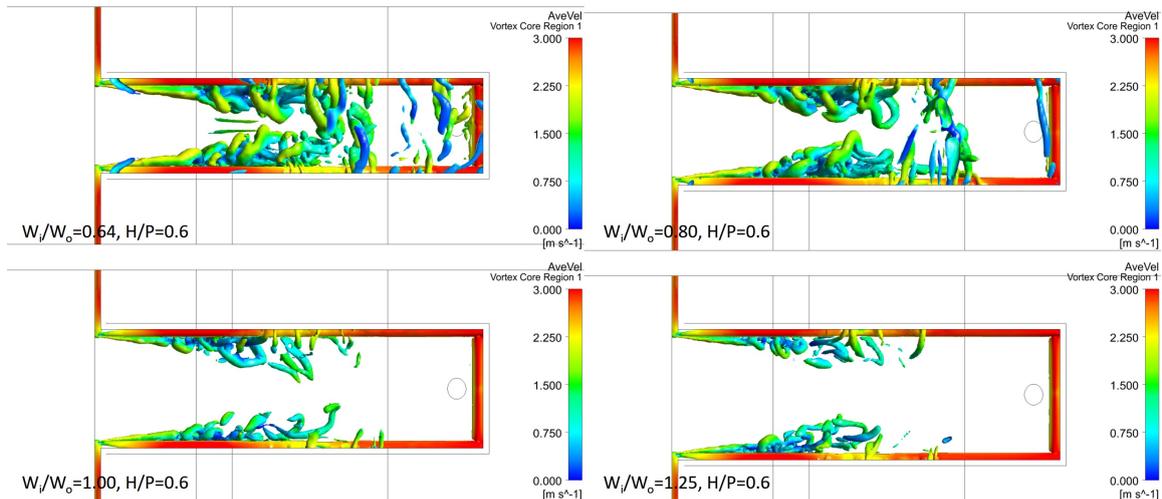


Figure 7.72: Plan view of vortices in inlet key as inlet key width reduces (flow is left to right)

### 7.5.7 PKW nose

Several prototype PKWs have been installed with upstream noses to limit the generation of vortices from the upstream edge (see Section 2.5.3). This concept was tested both in the physical model as well as the numerical model. Photos of the nose in the physical model are presented in Figures 5.6 and 5.7 as well as Appendix B. The triangular nose was fitted to the underside of the upstream overhang at an angle of 45 degrees. Similarly, the circular nose was fitted with a diameter equal to the outlet key width including the walls (0.3 m).

The effect that the upstream nose had was to generate a smoother flow profile into the inlet key. The success of this strategy is presented in Figure 7.73 which depicts the longitudinal flow velocity on a horizontal plane at the lower end of the PKW. The images clearly illustrate that both the triangular and circular noses attain a much smoother inlet profile. That said, the triangular profile still generates a separation zone, albeit a much smaller one than that for the rectangular case. No separated shear boundary can be seen for the circular profile which indicates a perfectly smooth transition.

The effect this has on the generation of vortices is detailed in Figure 7.74. Comparing the three images it is evident that the triangular nose has only a minor effect on the generated vortices. The extent of the vortex sheet is indeed smaller but is still spread out over much of the sidewall. The circular nose on the other hand appears to cancel out all vortices from the lower separation zone, or at least reduce their strength such that they are no longer identified by the Q-criterion. The upper separation zone still generates vortices like it does for the other nose types, however they appear less defined. It should be noted that this upper zone of vortices is the zone which causes the largest fluctuations on the centre portion of the upstream face. The circular nose alone is thus not able to cancel out all fluctuations.

An alternative design to limit vortices from this upper section might involve shortening the upstream edge of this overhang. The overhang length would have to be reduced to achieve this, which could then be balanced by a longer overhang length on the downstream side. This then stops being a standard type A piano key weir and starts taking on characteristics of a type

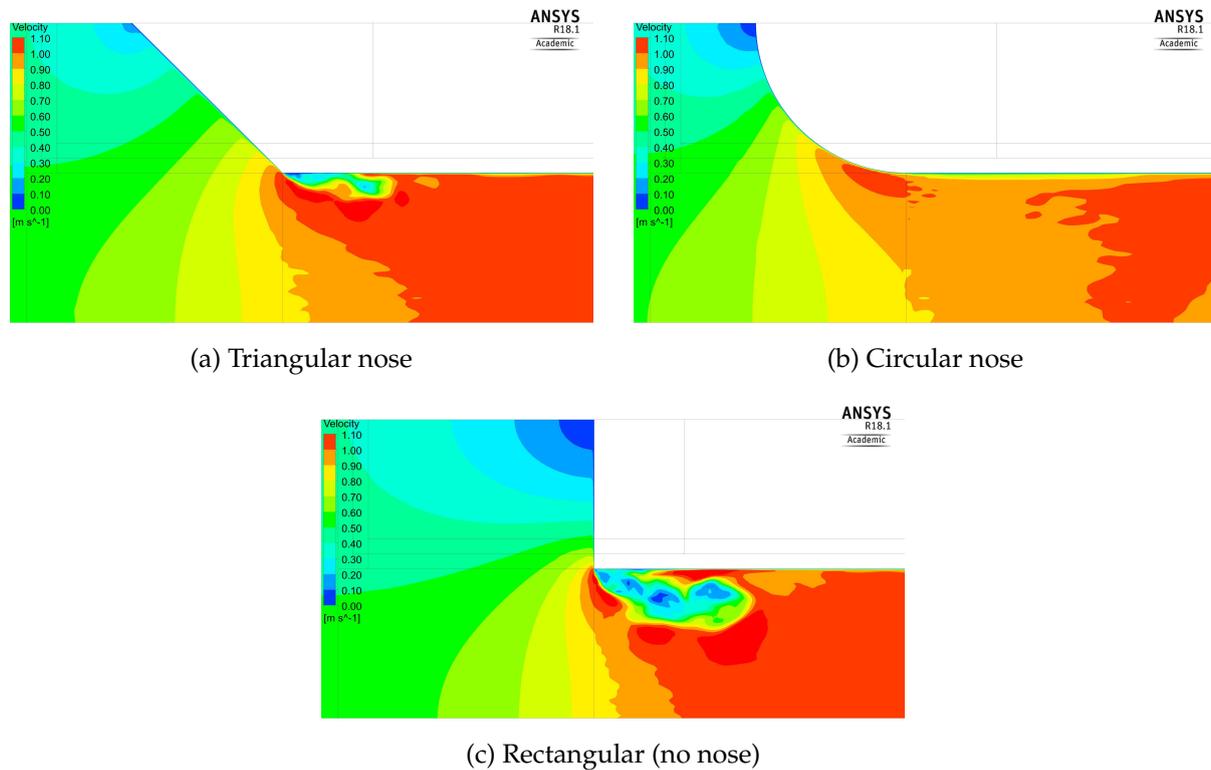


Figure 7.73: Horizontal view of longitudinal velocity at three nose types (flow is left to right)

C PKW. Different types of PKW and their effects on the vortices are briefly discussed in the next section.

The pressure fluctuations for the nose types were recorded in the physical model. The entire set is included in Appendix D, but Figure 7.75 presents a summary. The images indicate that, as expected, in the upper separation zone (A2) there is almost no difference in the strength or the frequency of the vortices between the two nose types, although both are marginally weaker than for the rectangular (no nose) case. In the lower separation zone (A5), even though no vortices are visible for the circular nose the figure illustrates that the fluctuations are still present, though only at very weak levels. The triangular nose exhibits stronger fluctuations, but not as strong as the rectangular (no nose) case. There is no difference in the fluctuation frequencies between any of the noses. This finding is in contrast to that reported in literature (see Section 4.3.1). That said, the increased frequencies noted in previous studies were linked to higher phase or vortex convection velocities caused by increased flow velocities in the main body of the flow. Since it has been determined that the phase velocity of the pressure educing vortices at PKWs is not sensitive to the velocity in the middle of the key, it is to be expected that the pressure frequencies would remain unchanged.

This demonstrates that the use of an upstream nose under the overhang is a useful design element to reduce the generation of vortices in the inlet key. However, the vortices cannot be relegated entirely, and some form of vorticity remains which will induce pressure fluctuations at unchanged frequencies albeit at much lower amplitudes.

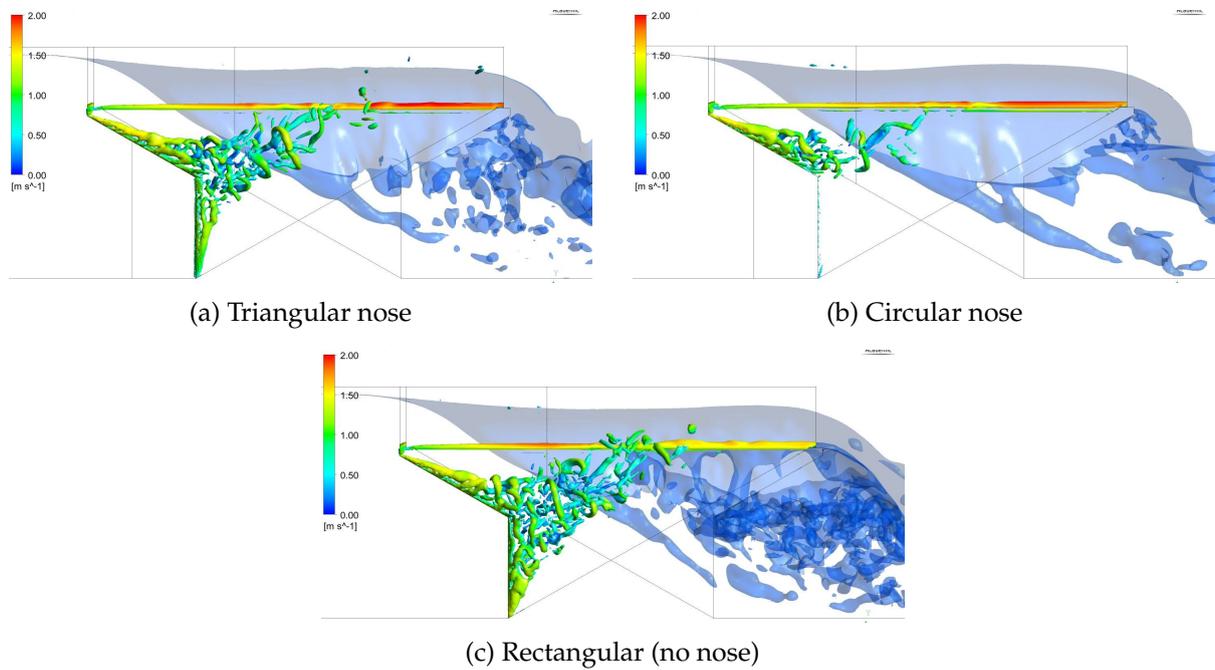


Figure 7.74: Side view of the vortices emanating from three nose types (flow is left to right)

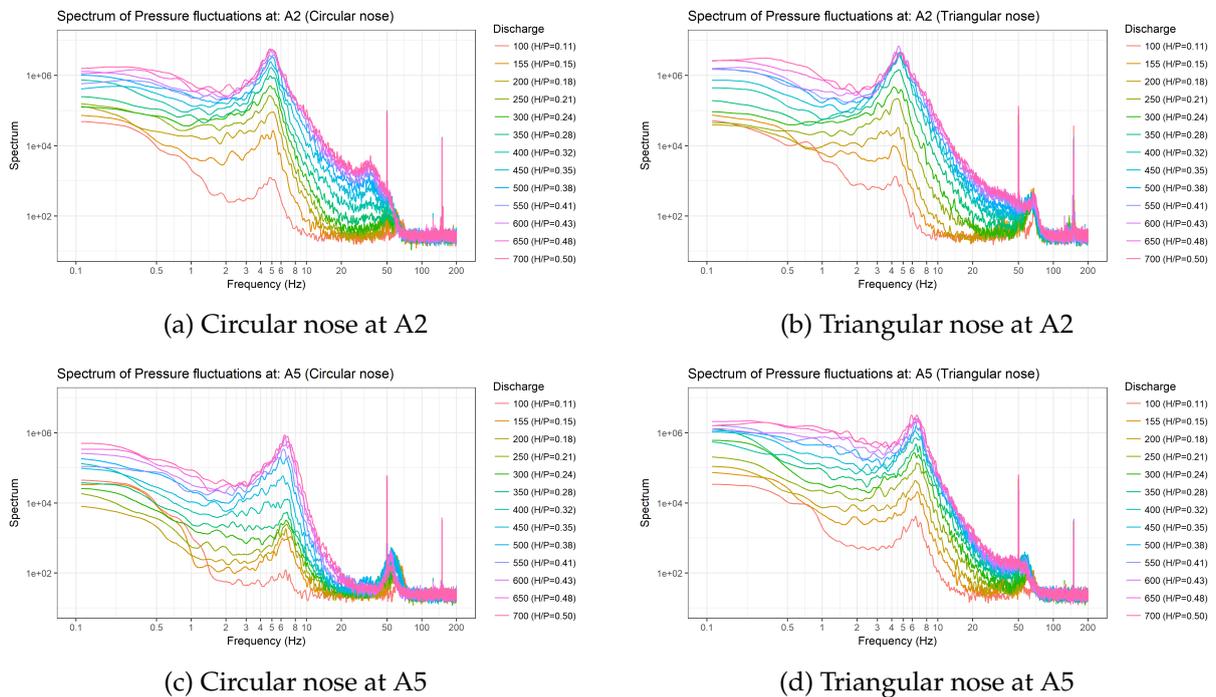


Figure 7.75: Frequency content of pressure fluctuations with two nose types

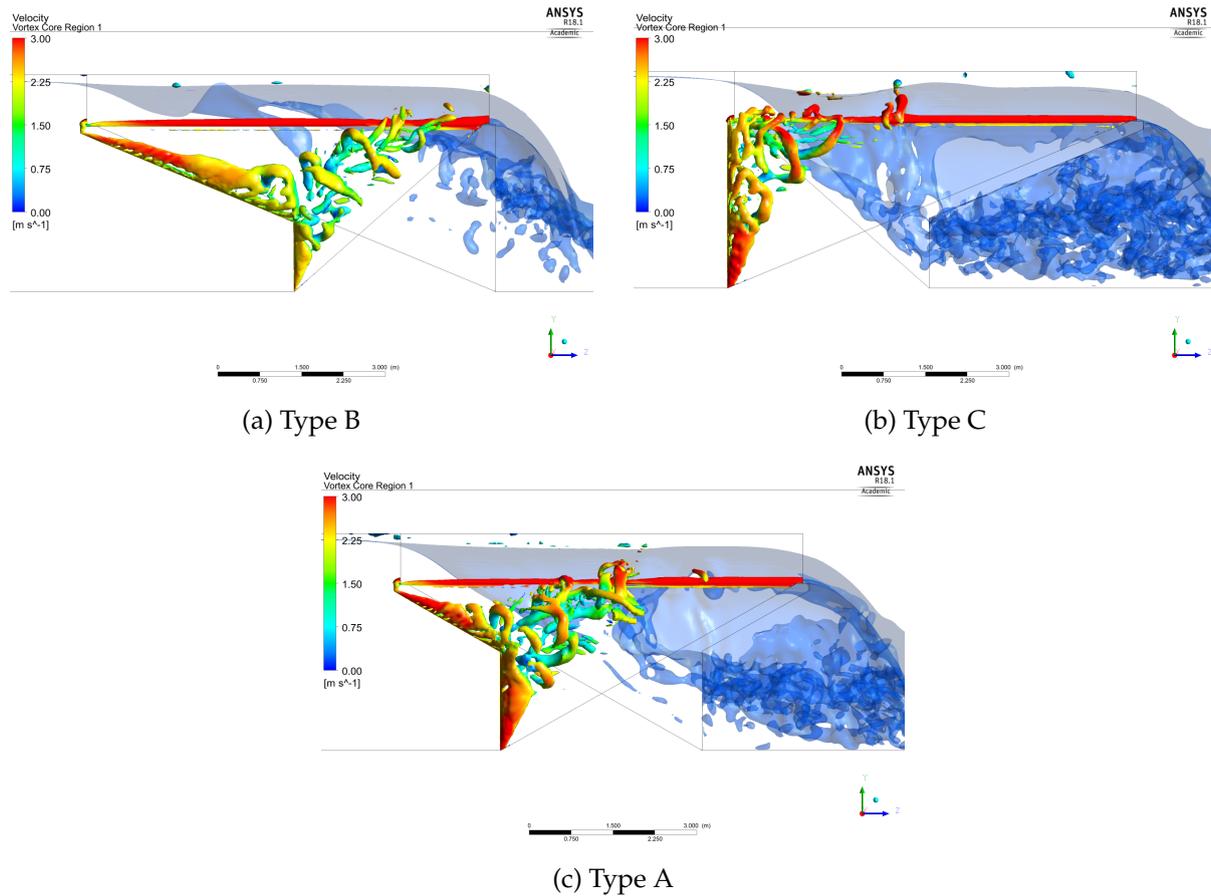


Figure 7.76: Side view of vortices for different types of PKW

### 7.5.8 PKW type

The present study focusses exclusively on type-A PKWs with both upstream and downstream overhangs. However, indicative simulations were conducted to explore the impact of type-B (upstream overhang only) and type-C (downstream overhang only) PKWs. Figure 7.76 outlines the effect that the different shapes have on the vortices entering the inlet key. The type-B PKW has a similar set of vortices as type-A and it appears that the sidewall would be exposed to pressure fluctuations over a similar areal extent. Type-C PKWs on the other hand have only a small zone of vortices limited to its upstream edge. The maximum pressure fluctuations are expected to occur at locations where the structure is braced and would thus be most able to resist excessive deflections there.

### 7.5.9 Other observations

There are a large number of additional visual observations from both the physical and numerical model. These may, or may not, be of relevance to the study of the PKW vibrations, however, they still lead to a better understanding of the hydrodynamics of the flow around a PKW. They are listed below:

- It was observed that the nappe undulations are not that noticeable at large discharges

( $H/P > 0.36$ ). This may be because the level of turbulence both in the inlet key and in the nappe itself is so high that the water level is no longer smooth enough to note individual fluctuations. On top of this, as the discharge increases the vortices become smaller relative to the water depth over the crest. They then reach a point where their size is too small in relation to the overflow depth to have any noticeable effect on the water surface. Another factor which may be at play is that the vortices are passed over the weir near to the base of the water column thus hiding the undulations from view.

- The velocities and the pressure fluctuations were not subject to hysteresis as was tested in the physical model.
- It was examined what effect turbulence in the approach flow has on the results. This would reflect on a PKW in a reservoir setting where the upstream water body is largely still. When a very low turbulence value of 0.1 % was set as the upstream boundary condition in the numerical model, there was no change in the simulated pressure fluctuation frequencies at points A2, A3 and A5.
- A set of pressure measurement points in the adjacent key were installed to check whether there was a link between the pressures in two adjacent inlet keys. Such a link would imply that pressures on their respective sidewalls were in some shape or form linked or caused by a flow phenomenon either underneath the upstream overhang or in the approach flow. The pressure measurement points locations are shown in Appendix B (labelled B1, B2 and B3), and are located in symmetry with points A1, A5 and A7 on the main sidewall.

Cross-correlation analysis revealed that there is no correlation between A5 and B2, but that there is some broad-scale, though very weak, correlation between A1-B1 and A7-B3. The link between A1 and B1 is positive, meaning that when one experiences higher pressures so does the other. This implies that there is some sort of shedding event that occurs from underneath the overhang where a stagnation bubble may have grown too large and spilled over the edges into the inlet key (see Section 4.3.1). The link between A7 and B3 is negative on the other hand. This could be caused by a large vortex in the approaching flow which induces lower pressures in one key and higher pressures in the adjacent key. In both cases however, the correlation is very weak (much lower than between points in the same inlet key) though occur over a large lag-time.

- The nappe concavity at the corners of the nappe in model A only occurred at lower discharges (up to 100l/s). Furthermore, the concavity disappeared when the nappe was opened to allow air underneath and alleviate the negative pressures there.
- After completion of the first round of experiments, model A was removed to make way for the installation of model B. It was later reinstalled in the flume for a second round of tests. When the tests were repeated it was found that the pressure fluctuation frequencies were lower than the first round of tests. It is noted that the pressure fluctuation measuring methodology was adjusted to an open ended pipe system compared to a closed end

system previously. This is the most likely cause of the reduced peak values as the frequencies could have experienced damping inside the open ended pipe as water/mass entered and exited the pipe as the pressure changed. In the closed pipe system, such mass transfers and hence damping thereof would not have occurred, and the pressure would have instead transferred as small changes to the water's density. Another possibility is that in the second round of tests model A was installed at a slightly higher elevation (0.15 m instead of 0.05 m previously). It is doubtful that such a small increase in upstream depth was the causative factor for these lower frequencies.

## 7.6 Discussion

The static and dynamic behaviour of PKWs was investigated using both physical and numerical models. The numerical model was calibrated using data collected from the physical model and then used to explore trends in the data beyond the scope of the physical model. There was fairly good agreement between the two model types although some differences remain especially in the velocity vectors and pressure fluctuation spectra near the middle of the crest. These differences can mostly be ascribed to the turbulence modelling methodologies of the numerical model. Observations from the physical model, which were not used in the calibration process, visually validated the capabilities of the numerical model to emulate the flow successfully.

It is clear from the collected data that the hydrodynamics of the flow as it interacts with the PKW structure generates fluctuating forces which are imposed on the PKW's sidewall. The global and local flowlines revealed that there were a pair of separation zones which form at the edges of the inlet key. These regions of flow shed vortices which in turn cause periodic flow patterns near the sidewall that induce fluctuating pressures on the wall.

The data illustrated that the fluctuations were strongest in an area along an imaginary line between the point where the upstream overhang starts and the centre of the sidewall crest. The strongest fluctuations occurred at the centre of the sidewall where the wall is also most susceptible to transverse forces.

The separation zone, the vortices and the pressures were found to be very stable features of the flow field. Even when upstream noses were installed to limit the generation of vortices from the upstream edge, the pressure fluctuations continue, although at reduced strength. Another interesting stable feature is the fact that both the numerical and physical model measured unchanging pressure fluctuation frequencies. These remained constant all through a range of discharges or inlet key widths or when upstream noses were added. Even when the scale was increased the resultant frequencies only changed in accordance with their scaling ratio. Another interpretation of the data is that the vortex phase velocity, which cause the regular frequencies, are unchanged through all these scenarios.

It was surmised that the fixed frequencies or phase velocities were related to the size of the separation bubble which forms at the edge of the inlet key. This feature remained roughly the same size through most of the tests and, since the bubble is the primary generator of the vortices, it could be the cause of the constant frequency. The addition of a round or triangular nose, did however drastically reduce the size of the lowermost separation bubble (see Figure 7.73)

but this also did not result in a change in the frequency (Figure 7.75).

This implies that the phase velocity or frequency is an inherent feature of the PKW. It was surmised that it may possibly also be influenced by turbulence in the approach flow. PKWs in reservoir settings, with their much deeper approach flow, would not be as exposed to large turbulence values. This was modelled in the numerical model, which found that approach turbulence had little effect on the pressures on the upstream face of the PKW sidewall.

The fairly constant pressure fluctuations found at PKWs across a range of scenarios is in contrast with what was reported in literature. Previous studies of two-dimensional separation bubbles show that the *Strouhal* number remains unchanged across a large range of *Reynolds* numbers. This means that as the velocity increases so too does the frequency. This makes sense physically as the faster flows would convect vortices at a faster rate thus increasing the frequency of their occurrence. That this does not occur at the sidewall of a PKW implies that these vortices are somehow shielded from the increasing velocity. It is clear that the outer set of vortices (those farthest from the wall) does increase in speed, but it appears that their additional energy does not get transferred to the smaller vortices underneath them. It is possible that this transfer would have occurred but is prevented from doing so because the vortices are discharged over the crest before this can happen.

This supposition implies that the main flow lines, which follow the edge of the separation bubble and are then directed back toward the crest, isolate a zone of flow directly along the wall. This separation zone does receive some transfer of energy from the vortices above it, so it doesn't become entirely stagnant but is still flowing at much lower velocities than it would be at normal 2D separation bubbles. This pattern is thus unique to PKWs and can even be considered characteristic.

Lastly it is worthwhile considering that the vortex induced vibrations are an instability induced excitation (IIE, see Section 4.2.2). This infers that they may be controlled by altering the presence of the shear layer. This can best be achieved by making changes to the geometry of the system such as the inclusion of flow guides or stiffer structural members. It was seen that upstream noses have some effect on reducing the strength of the vortices at the lower end of the PKW but were not able to eliminate the vortices entirely. Rounding of the upstream overhang edges may also have similar effects on the upper portions of the PKW.

## 8 PKW behaviour: Vibration analysis

### 8.1 Introduction

Vibration in a system is caused by some form of disturbance or excitation and the cyclic response of the system, as explained in Chapters 3 and 4. The structural modal parameters and behaviour of a PKW with a height of 1.1 m were explored in Chapter 6. It revealed that the mode of vibration associated with the lowest levels of energy exchange, where the nodes of the mode shape are located at either end of the sidewall, has a natural frequency of 20.8 Hz. This frequency reduced however when the damping effect of the upstream water body was taken into account. The damped frequency with a water level at the crest was equal to 13.2 Hz. This reduced further to 7.1 Hz when a higher water level (at 20 % above the crest) was imposed. It is noted that the vibration mode and frequency of the structure may have been influenced by the stiffening effect of the PVC wall on top of the crest. This implies that, although the stiffening effect is expected to be small, it reduced the natural frequency slightly.

The frequency of the fluid induced excitations that were recorded at the PKW were not far removed from the lowest natural frequency value of the structure. At roughly the same scale as model B, the numerical model estimated a peak pressure fluctuation in the order of 1.2 Hz. However, recall that the oscillations occurred over a band of frequencies, up to approximately 20 Hz in this case, which does extend over the structural response frequency. There thus appears to be some potential for the establishment of resonant vibration in the steel model due to the fluid induced vibrations.

It is worthwhile mentioning that the steel model that was selected for the physical tests was purposefully chosen precisely because it was anticipated that it may be susceptible to vibrations. Although it should also be borne in mind that its dimensions, including its thickness, are representative of a prototype-scale steel PKW, meaning that the model was not artificially weakened in any way. However, it is noted that almost all PKWs that have been installed to date are constructed from reinforced concrete with wall thicknesses ranging from 0.2 to 0.45 m [122]. This means that their stiffness and mass should lead to natural vibration frequencies which are outside the excitation frequencies induced by the flow. This implies that most PKW designs could safely disregard the occurrence of vibration. That said, the dynamic response of the structure including the stress levels caused by the fluid induced vibration will need to be evaluated such that interactions with other forces may be assessed.

The fluid induced vibrations on a steel PKW were explored in both the physical and numerical model. The results of both models are presented below. The problem is approached first from an excitation perspective and then from a structural response perspective. The response of the physical model was analysed via the deflections of the central point of the crest. The numerical model, however, also allowed for additional data points to be monitored. These included the stress state of the sidewall of the PKW.

## 8.2 Excitation

Operational vibrations on a steel PKW sidewall at low or medium discharges, with low tail-water levels are mainly excited by the pressure fluctuations which occur on its upstream face. Their source was explored in the previous chapter but here they will be characterised in more detail in light of the modal parameters of the sidewall (also see Section 4.2.1).

This analysis was conducted using data from the numerical model only since, as discussed in Chapter 5, obtaining suitable quality data at sufficiently detailed spatial and temporal scales from the physical model was not possible. Nonetheless, the numerical model was shown to be a suitable and representative tool for this purpose.

The upstream face of the sidewall is exposed to hydrostatic pressure forces as presented in Figure 7.30. These are largely static in nature but do showcase lower pressures in places due to the dynamics of the flow. The sidewall responds to this upstream pressure by deflecting outward as was described in Figures 6.1 and 6.2, with the largest deflection occurring in the centre and top of the sidewall crest.

In addition to these time-mean pressures, the wall is also exposed to fluctuating pressures as shown in Figure 7.43. It is notable that the pressure fluctuations are very localised and can range from positive to negative values over very short distances. Since the wall is free to move in all its degrees of freedom, each of these fluctuations will cause a small localised deformation on the sidewall. These local deformations are however vanishingly small relative to the deflection of the entire wall and can be ignored. The overall effect that the fluctuations, as a whole, have on the sidewall face will have to be accounted for however.

By definition the nett time-average effect of the fluctuations from the mean will be close to zero as the majority of the face experiences close to no fluctuations. Furthermore, those strong positive values which do occur are often negated by strong negative values nearby. That said, the temporal variation above and below the nett zero fluctuation pressure is of importance as is their spatial distribution on the face. It may occur that their distribution may activate one of the modes of vibration of the sidewall.

This concept was explored in a similar manner as that described by Pavic and Willford [131]. They employed the unity scaled mode shape together with information regarding the natural frequency and the applied excitation allows for the amplitude of the response and any resonance it may exhibit to be estimated. In this study the pressure fluctuation on the sidewall at each time step were multiplied with a weighting factor equivalent to the unity scale mode shape amplitude for a given mode number. The weighted fluctuations on the sidewall were then multiplied by their incremental area and summed to produce an effective transverse force on the sidewall. This force can be seen as a spatial correlation factor that would active a particular mode shape. The time sequence of this factor was then transformed into the frequency space to determine to what degree the mode in question was being activated. This process is described pictorially in Figure 8.1. Recall that only the upper portion of the sidewall was modelled in vibration, hence only its forces are presented.

The second image shows the pressure fluctuations on the sidewall in a particular timestep, similar to that shown in Figure 7.43. The red and blue zone represent increases and decreases

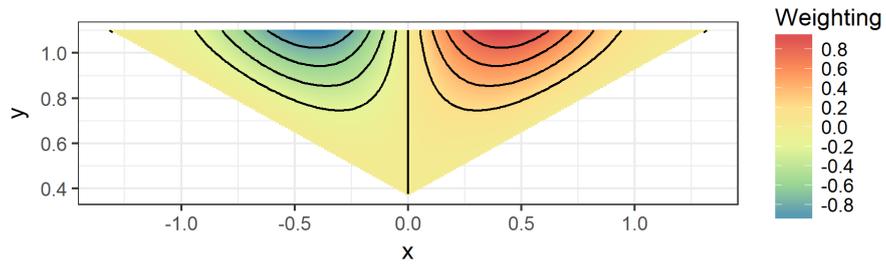
in local pressure from the mean. Most of these occur in a band from the lower left side up to the centre of the crest. The remainder of the pressure field is near zero. Note the horizontal nature of the lower set of vortices. The figure also shows the black contour lines of the weighting factor which is colourised in Figure 8.1a. The mode shape being presented here is mode 2. It can be seen from Figure 6.9 that the mode makes an S-shape with half of the wall having positive displacement and the other negative displacement. The weighting factors range from -1 to 1 to showcase this deflection profile. The displacement is thus used as an indicator to divulge whether or not the pressure fluctuation profile would excite this mode or not.

When the pressure fluctuations are multiplied by the weighting factor, the pressure plot in Figure 8.1c is obtained. Notice how much of the pressure activity at the lower end of the wall as well as that near the centre has been negated. The strong positive pressure on the right-hand side remains. It represents a pushing force on the wall on the half of the mode shape being pushed downstream. This is partially supported by a pulling force on the other half thus there may be potential for this mode to be activated in the vibration if the frequency is right to support it. There are also some strong opposing forces in the left half which may counterbalance this however. Note that the colours on the left half of the image have switched from positive to negative and vice versa in comparison to the pressure fluctuation plot. This is indicative of the negative weighting factor on the left where it is opposite to the positive values on the right. The actual value, whether positive or negative is not of concern, so long as a negative value in one zone is supported by an equally negative value in the other. Then there is potential for resonant behaviour to arise.

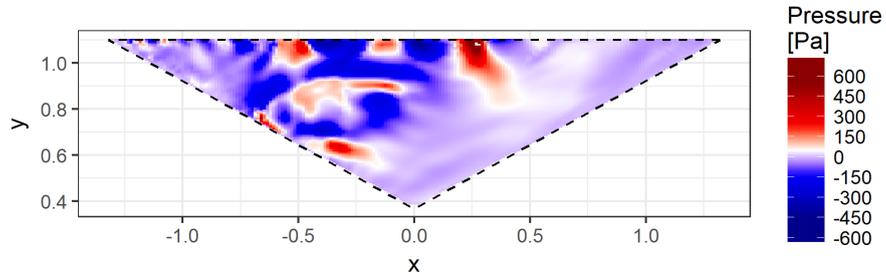
These dual negative or dual positive values allow for the fluctuating pressure and its potential to activate a mode to be summarised into a single value. The weighted pressure fluctuations are each multiplied by their incremental area and summed into a force value. Bear in mind that this is not a real force but a merely a representation of the fluctuating pressure field on the sidewall to activate a particular mode in the sidewall. The fluctuations are summed in this way for each time step and can then be plotted as set out in Figure 8.2a. This sequence reveals that there is oscillatory behaviour present in the pressure fluctuations that can cause the sidewall to vibrate in mode shape 2. That said, the amplitude of this oscillation is very low, meaning that the forces may likely be countermanded by other, stronger, influences. The frequency content of this time signal can then be extracted which, if sufficiently strong and near to the natural frequency of this mode, may induce resonance behaviour or lock-in as described in Sections 4.2.2 and 4.3.1.

This procedure was applied to each of the first six mode shapes of the sidewall. Figure 8.3 details how the same pressure fluctuation timestep has been weighted by each of these. The figure reveals that there is no single mode with all blue or all red areas, which would be indicative of strong excitation at this particular timestep. Wherever there are red areas they are generally counterbalanced by blue areas in the opposing direction. That said, the excitations in modes 1 and 2 do show an overall activation trend by being largely blue and red respectively.

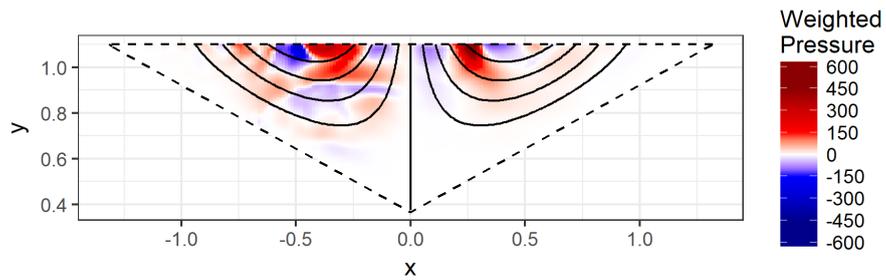
The resultant time sequence of each mode was transformed to frequency space as depicted in Figure 8.2b. The results demonstrate that none of the modes are directly activated by the spatial and temporal correlation of the pressure fluctuations. There is a strong peak at approxi-



(a) Mode shape weighting factor (Mode 2)

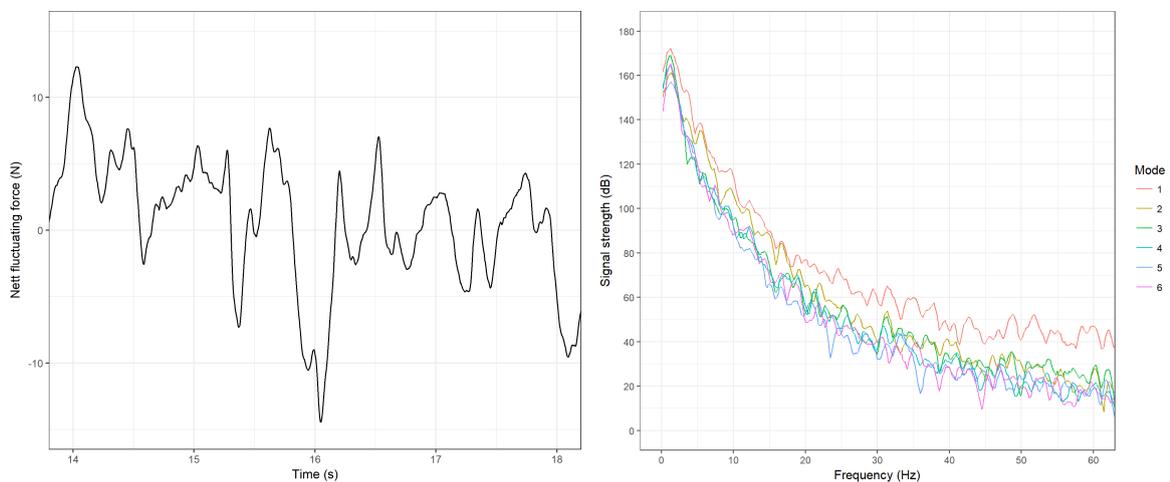


(b) Instantaneous pressure fluctuations



(c) Weighted pressure fluctuations

Figure 8.1: Weighting procedure for fluctuating pressure



(a) Time sequence of weighted force (mode 2)

(b) Frequency PSD of weighted wall force

Figure 8.2: Resultant weighted wall forces

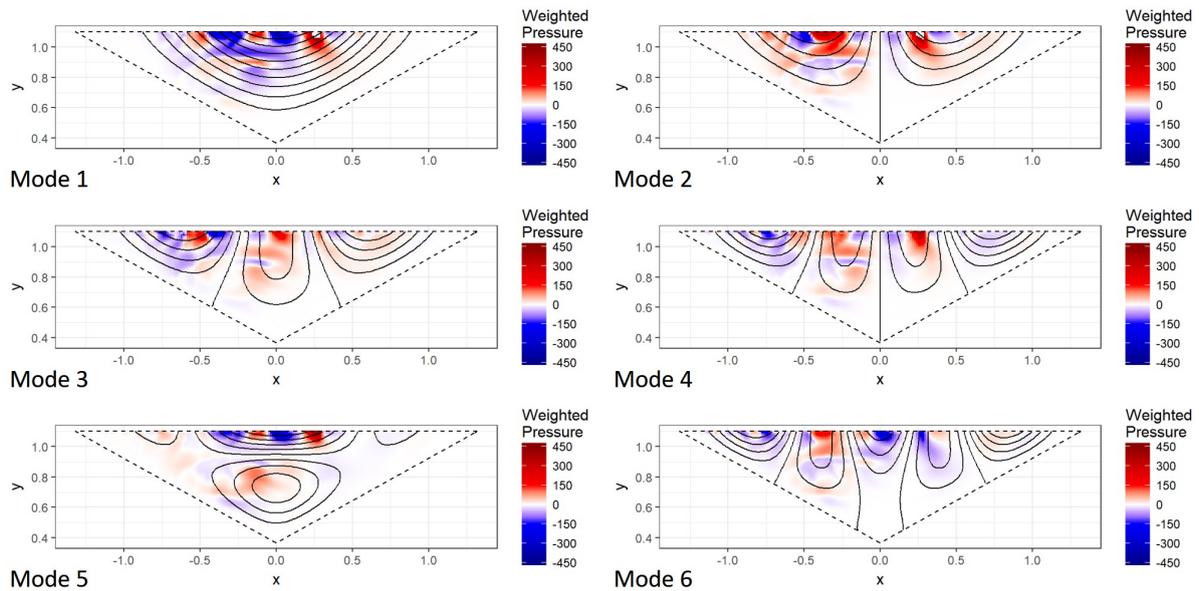


Figure 8.3: Weighted fluctuation pressures for each of the modes

mately 1.2 Hz which is presumably the inherent oscillation of the system of vortices as a whole. There is a slight peak at approximately 32 Hz in the second mode line which is close to the natural frequency of the second mode. Hence there may be a degree of excitation of mode 2 by the system of vortices. Furthermore, although the mode 1 line exhibits no strong peak at its natural frequency ( $\sim 7$  Hz), the entire line does reflect strong excitations in the mode compared to that of the others.

### 8.3 Vibration response: Physical model

Chapter 5 detailed how the steel model and the flume were designed to allow for relatively free vibration of the sidewall but at the same time model the discharge head correctly. The specifications of this physical model were presented in Table 5.1. For ease of reference, the key parameters are a weir height,  $P$ , of 1.1 m, an equal inlet,  $W_i$ , and outlet width,  $W_o$ , of 0.72 m and a thickness,  $T_s$ , of 6 mm. Bear in mind that the flume width was halved to 0.75 m for the flow tests to correctly emulate the head-discharge relationship. This means that only one PKW unit was incorporated.

A series of photos is presented in Figure 8.4. These indicate the flow over the weir for a number of different discharges. Note that both the approaching flow and nappe are very smooth at low flows but get more disturbed at higher flows. It can also be seen how the nappe trajectory extends further from the crest as flows increase. Lastly, as noted in Chapter 7, the corner of the nappe is visibly withdrawn under low flow conditions but not under high flow conditions. The extent of the inward withdrawal grows as the nappe reaches the downstream floor. This was discussed in more detail in Section 7.4.6. The low flow photo also shows the (closed) aeration pipe which could be used to feed air to the underside of the nappe.

The half-bridge strain gauge that was fitted near to the centre of the crest of the sidewall

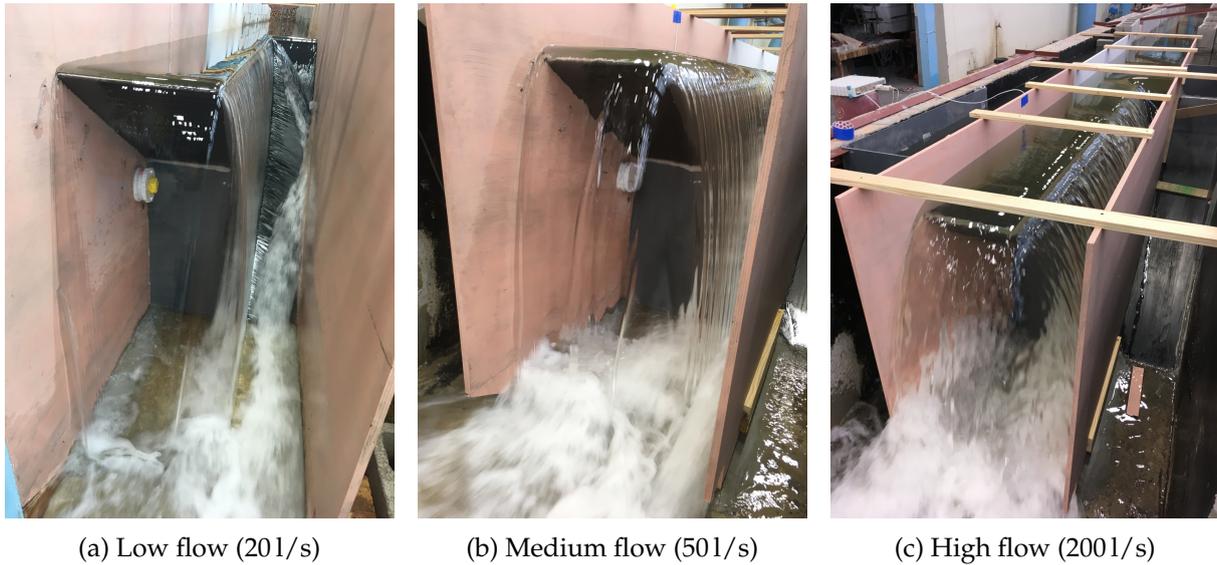


Figure 8.4: Photos of flows for physical model B

(see Figure 5.11) was used to record the vibrations of the wall under flow conditions. A number of scenarios were examined, including a range of discharges as well as aerated and unaerated conditions under the nappe. Figure 8.5 illustrates the Power Spectral Density of the vibration recordings analysis. Table 8.1 summarises these graphs by listing the peak frequency values of the first five peaks noted in the data. There are additional peaks at larger frequencies but these not only become less distinct, they are also often simply harmonic multiples of the lower frequencies. Also note that not every scenario showcased peaks at each of the expected locations.

The graphs depict a noise floor with several sharp as well as broad peaks. The sharp peaks occur at regular intervals of 10 Hz and are likely related to electronic interference from power supply earthing issues at the recorder and can thus be disregarded. The broader signals on the other hand point to a much more variable signal and can thus be considered to suitably represent the strain at the sidewall.

The vibrations of the sidewall are characterised by two wide and well defined peaks above the noise floor. These are located at just below 10 Hz and just above 30 Hz. The analysis also identified peaks at around 18 Hz and 24 Hz, however, these appear to be harmonics of the first fundamental peak. A large peak at 60 Hz is likewise likely to be the second harmonic of the 30 Hz peak. Furthermore, the table also notes a fairly consistent peak in the region of 1.5 to 3.0 Hz. Due to the large low frequency trend in the data, these low but consistent peaks are sometimes difficult to discern but appear to be present in most of the scenarios.

The two main frequencies agree well with the results of the modal analysis (see Table 6.1) which estimated a damped natural frequency of between 7.1 Hz and 12.4 Hz for the first mode and between 32.0 Hz and 39.5 Hz for the second mode. These frequency ranges are controlled by the upstream water depth which dictates the amount of added mass that is imposed on the structure. It can thus be stated that the PKW sidewall is exhibiting vibration at its first two modes.

The vibration frequencies measured at the sidewall under flow should also be seen in light

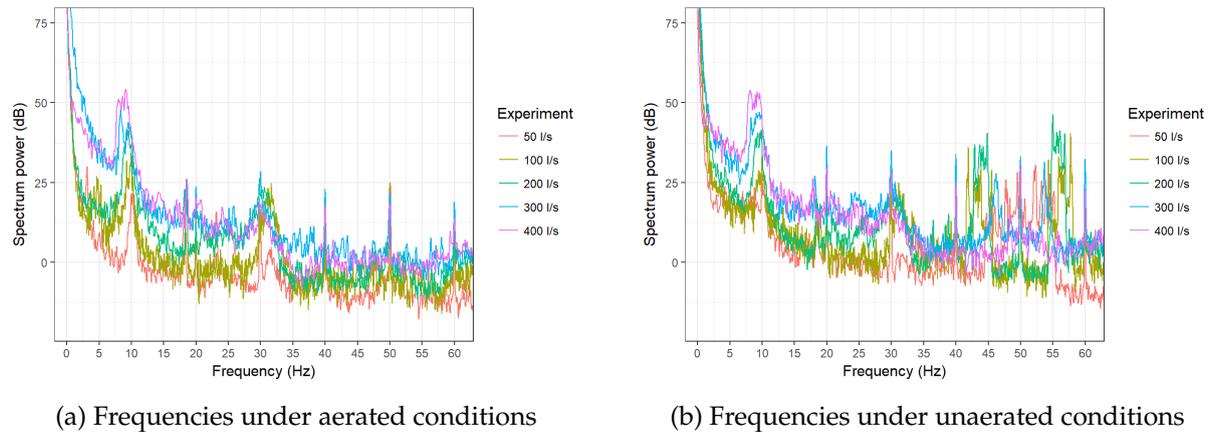


Figure 8.5: Power Spectral Density of model B sidewall vibration

of the excitation pressures on its upstream face. Pressures could not be measured on the vibrating model but if the pressures from the smaller, static, model A are scaled upward to that of model B, it can be estimated that a broad range of frequencies ranging from 1 to 20 Hz can be expected to occur. Furthermore, the peak frequency of excitation would range from 1.8 to 3.6 Hz depending on the location on the wall. The lowermost frequency peaks in the vibration signal were noted to be in this same range and are thus likely caused by the peak pressure excitations upstream of the wall.

The vibration data thus exhibits evidence of the wall being excited by the upstream system of vortices. The peak frequency of this vortex behaviour is present, albeit weakly, in the vibration of the wall. Furthermore, the spectral band of the vortices appears to be strong and wide enough to excite both the first and second modes of the sidewall.

Examining the effect that discharge has on the vibration reveals that for the lower flow scenarios only weak vibrations are evident such that few peaks above the noise floor could be reliably discerned. The signal, and thus the strain value, increased in strength as discharge increased as evidenced by both graphs in Figure 8.5. Table 8.1 also shows that as the discharge increases there is slight decreasing trend in the frequency of the peak. That said, the trend is minor, and is often a result of the peak becoming fatter, thus reflecting a lower overall average peak rather than a change in frequency.

The data table also reveals that there are only minor differences in the vibration behaviour between the aerated and unaerated scenarios. There are small differences in the frequency values but these are well within the expected random measurement error of the peak identification methodology. There also appears to be no notable difference in the strength of the signals between Figure 8.5a and Figure 8.5b. It is expected that the oscillating subatmospheric pressure conditions that develop underneath the nappe would marginally alter the deflection behaviour of the sidewall. However, considering that the subatmospheric pressure is very small (in the order of a few Pa), this change in behaviour would not be observable in a data signal that is dominated by the main vibration.

Table 8.1: Recorded strain gauge vibration frequency peaks at various discharges

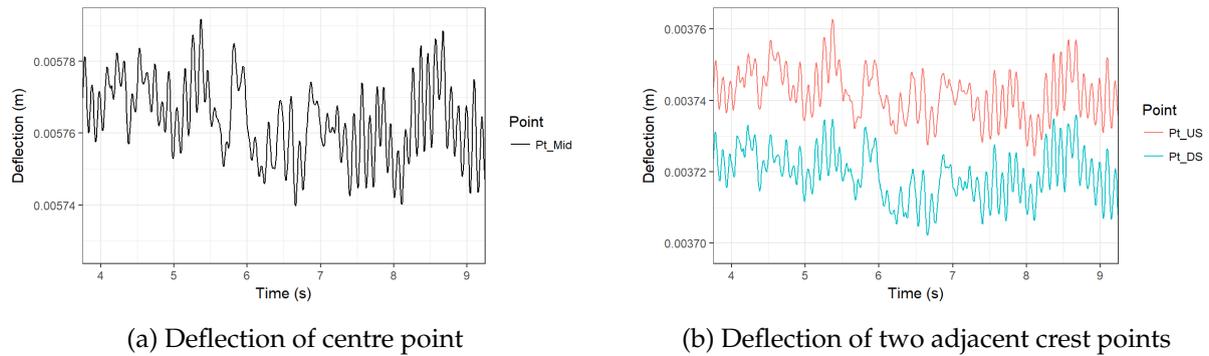
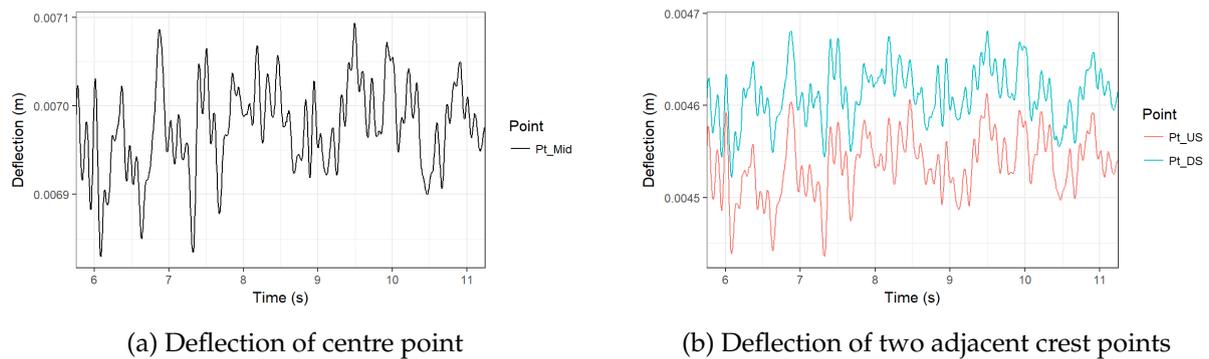
Discharge	Aeration	1	2	3	4	5
501/s	Yes	2.3	10.1	18.6	23.2	31.4
	No	2.1	10.6	18.5		
1001/s	Yes	1.7	9.6	18.5		31.7
	No	1.7	9.7	18.7		31.1
1501/s	Yes	1.5	9.8	14.6		31.0
	No	3.0	9.5			31.1
2001/s	Yes	1.6	9.4	17.7		30.5
	No	1.4	9.5	18.5		30.9
2501/s	Yes	1.8	9.5			30.8
	No	1.5	9.5			30.9
3001/s	Yes	1.5	9.3	18.5		30.6
	No	1.6	9.4	18.3		30.4
3501/s	Yes	1.7	9.2		25.0	30.9
	No	1.4	9.3		25.0	30.5
4001/s	Yes	1.4	9.1	16.7	24.3	30.0
	No	1.6	8.5	20.7	24.6	30.0

## 8.4 Vibration response: Numerical model

The physical model was emulated in the numerical model using the coupling between the Fluent and Mechanical modules. Due to the lengthy time requirements to successfully complete a simulation, only two scenarios were tested. These are a flow of 2001/s and a flow of 4001/s. These were selected to coincide with the flows of the physical model such that their results could be compared. The PKW was modelled at the same scale as the physical model. The first flow scenario thus represented  $H/P = 0.1$  and the second  $H/P = 0.2$ .

The data obtained from the three crest points and the maximum stress location were analysed for their spectral content in a similar fashion to the physical data. The results are presented in the graphs below.

The deflections of the three crest points for the first scenario are presented in Figure 8.6 and those for the second scenario in Figure 8.7. Recall that the three points are located along the sidewall crest, one at the centre and one point to either side of it at a distance of one sixth of the sidewall length (0.44 m). The deflection data illustrates that the nett deflection for  $H/P = 0.1$  is in the order of 5.7 mm for the centre point and 3.7 mm for the two adjacent points. The shape thus conforms to the convex profile presented in Figure 6.2. These values increase by approximately 1 mm for the  $H/P = 0.2$  scenario. The values are similar to those values obtained from a static structural analysis of the sidewall under hydrostatic load conducted in ANSYS Mechanical. The time signals reveal that the crest deflections vary by about 0.02 mm in both flow scenarios.

Figure 8.6: Power Spectral Density of model B sidewall vibration ( $H/P = 0.1$ )Figure 8.7: Power Spectral Density of model B sidewall vibration ( $H/P = 0.2$ )

It is interesting to note that all three deflections follow the same broad path or trend. This implies that the first mode of vibration, where the crest moves as a single flexing bulge, is dominant. However, comparing the two adjacent points to each other does reveal that the correlation is not exact. There are times ( $\sim 4.6$  s in Figure 8.6b) when the deflections on either side of the sidewall centre are not in sync. This indicates that other modes are also active.

The deflection time sequences also showcase clear periodic behaviour whose spectral content is explored in Figure 8.8. The solid green line represents the central crest point and reflects a strong peak at just under 10 Hz, which is approximately equal to the sidewall's first natural frequency. In addition to this there is also the peak at  $\sim 2$  Hz which is presumably caused by the pressure excitations on the wall. There is also a significant peak at 44 Hz. It is not entirely clear what this peak represents as it is likely not one of the natural frequencies nor does this frequency feature strongly in the vortex pressure excitations. It is possible that it could be caused by some form of subatmospheric pressure oscillation or an instability in the overflow nappe. The physical results, which have also been plotted on this graph as a dashed line, showcase no peak at this frequency in either of the scenarios. This implies that this peak results from a convergence error in the numerical model, where the model, in trying to converge upon an oscillating solution continuously overshoots that solution thus adding a phantom oscillation. This highlights that the small timestep chosen in the numerical model may not have been small enough.

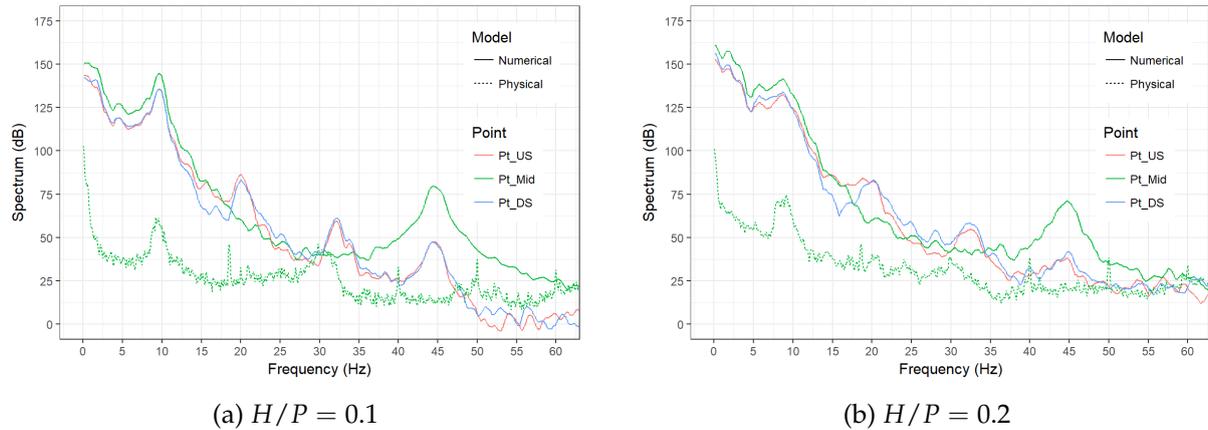


Figure 8.8: Crest point deflection PSD showing numerical and physical results

The points adjacent to the mid-point likewise exhibit this peak, although to a much smaller degree. They also detail three other peaks including the main first mode oscillation. The other two peaks are not reflected at all in the centre crest point PSD which implies that these frequencies involve modes shapes which have a node at the centre of the sidewall. This is indeed the case for the peak at 32 Hz which is the natural frequency of mode 2, and is also noted in the physical data. The peak at 20 Hz is another peak that was noted in the physical data (at 18 Hz). That peak was surmised to be a harmonic of the main physical peak at 9 Hz. The numerical data appears to support this premise.

The maximum von Mises stress data collected at the base of the sidewall was analysed in a similar manner to the deflection data. The time sequence, presented in Figure 8.9, reveals that maximum stress on the upstream face of the sidewall is, as expected, in tension. An average stress of approximately 113.6 MPa and 144.0 MPa occurs at an overflow depth of  $H/P = 0.1$  and  $H/P = 0.2$  respectively, in a very localised region in a similar zone as indicated in Figure 6.4. The time signal exhibits regular fluctuations from the mean, with stress reversals ranging from 0.01 to 1.14 MPa in the first scenario and 0.01 to 5.18 MPa in the second. These amount to roughly 1 to 3.5% of the mean.

This relatively small scale fluctuation was analysed in the frequency space as illustrated in Figure 8.10. The spectral densities are consistent with those of the deflections. It is interesting to note that the spectra more closely follow those of the two non-central crest points rather than the middle crest point. This may just be due to their closer proximity. However, this does imply, that if the wall were to be stiffened in some way to limit excessive stress fluctuations such stiffening should focus more on the sides of the crest and less on the centre of the sidewall.

## 8.5 Fluid structure interaction

It was surmised in Section 4.4 that the movement of the wall could have an effect on the flow dynamics of the inlet key. Of specific concern was the possibility that the oscillation of the wall may alter the frequency at which the vortices are shed from the free shear layer emanating from the upstream edge of the inlet key.

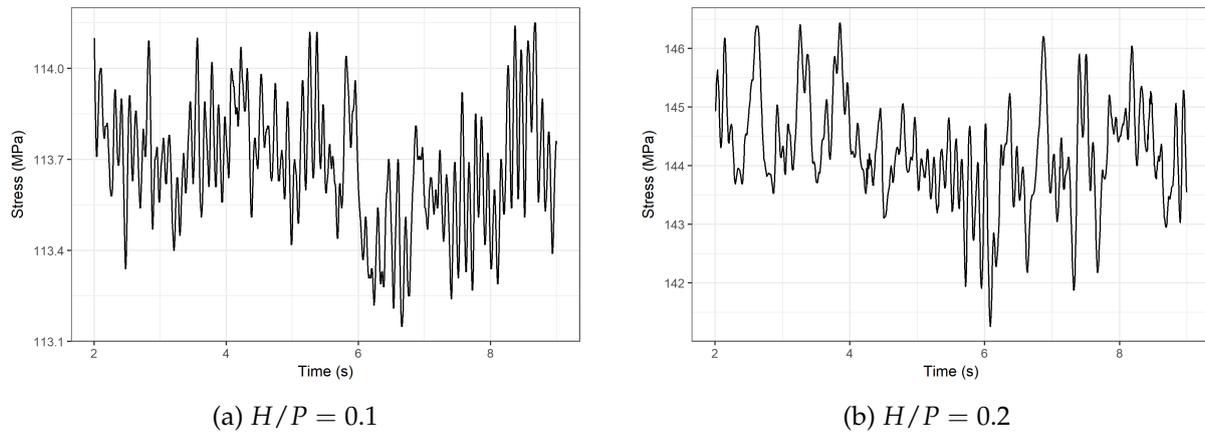


Figure 8.9: Time sequence of maximum stress

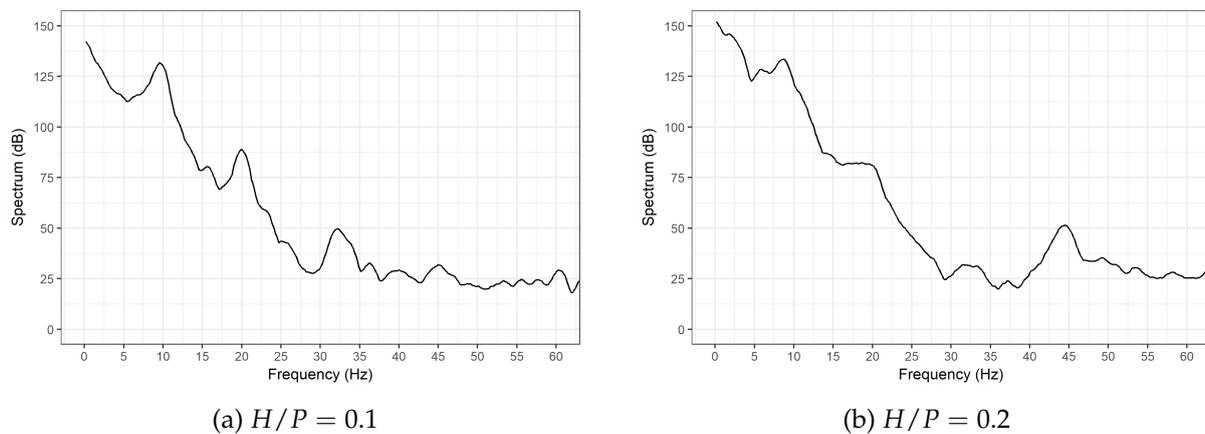


Figure 8.10: Maximum stress spectral density

It has however been determined in the hydrodynamic analysis that the system of vortices as well as the phase velocity and frequencies which dictate their behaviour are very stable properties of the flow. Changes to the discharge, the velocity, the inlet key width and upstream turbulence all had no effect on this phenomenon. It is thus considered unlikely that the small transverse movements of the sidewall would affect them either.

That said, the moving wall will certainly have an effect on the local flow dynamics in the near vicinity of the wall. This effect is detailed in Figure 8.11. The graph portrays the result of two numerical model scenarios, one being a Fluent (CFD) only simulation with a rigid sidewall and the second simulation also incorporating the Mechanical module thus allowing the wall to move (FSI). The three lines represent the PSD of pressure at three locations just upstream of the sidewall. Two of these are at points A2 and A3 (their equivalent at this scale) and the third line is the average pressure over the deformable portion of the upstream face (the triangular face shown in Figure 8.2).

The CFD only lines demonstrate the large low-frequency behaviour of the vortices upstream of the sidewall, which taper down to the noise floor without any other significant peaks. The FSI simulation (dashed line) showcases this same large low-frequency peak which evis-

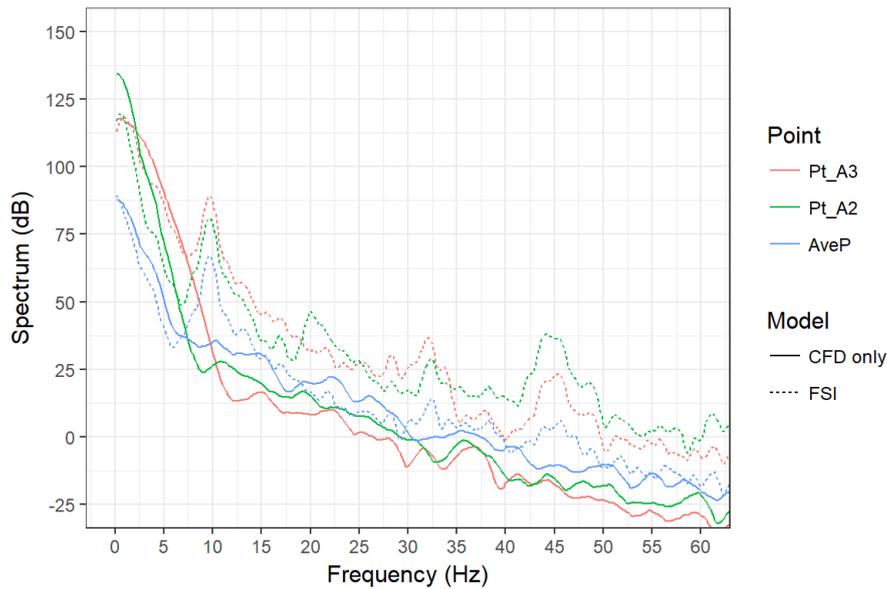


Figure 8.11: Upstream wall pressure PSD ( $H/P = 0.1$ )

dences that there is no change in this behaviour due to the wall's movement. The PSD also displays the peaks of the moving wall at the same frequencies as those presented in Figure 8.8. The difference between the solid and its corresponding dashed line reveals that the pressures in the upstream water body are being influenced by the movement of the wall.

These regular pressure pulses that the flow receives from the oscillating wall dissipate into the surrounding water body. The strength of the pulsation as well as the distance from the wall dictates the rate at which this pressure dissipates. It is conceivable that the sidewall on the opposite side of the inlet key may be near enough to be impacted upon by these pressure waves. Bear in mind that it has its own set of vortices and that it too would be oscillating and generating a set of pressure waves. As these pressure waves interact there is potential for sloshing or bulging to occur in the inlet key, both of which would have an effect on the discharge capacity of the weir. The fluid in the key may thus begin oscillating at its own modal frequencies.

It may also occur that the two vibrating walls and their sets of pressure waves eventually come into phase with one another or with only a small lag between them. It could then occur that, when a positive pressure wave from one wall arrives at the opposing wall when it is on the outward portion of its trajectory. This would reinforce this movement and cause larger deflections, higher stresses and thus more fatigue damage. Bear in mind that it was shown that the vortex induced pressures on opposing sides of the inlet key are not correlated (see Section 7.5.6) hence such synchronisation is likely to occur randomly. Data from the FSI numerical model confirmed that the vibrating sidewall did indeed generate parallel pressure waves as indicated in Figure 8.12. This graph presents the pressure signal from two points located at different longitudinal positions in the centre of the inlet key superimposed with the movement oscillations of the sidewall. There is a very clear correlation between the movement of the wall and the pressure in the middle of the key. Furthermore, since the two pressure points experi-

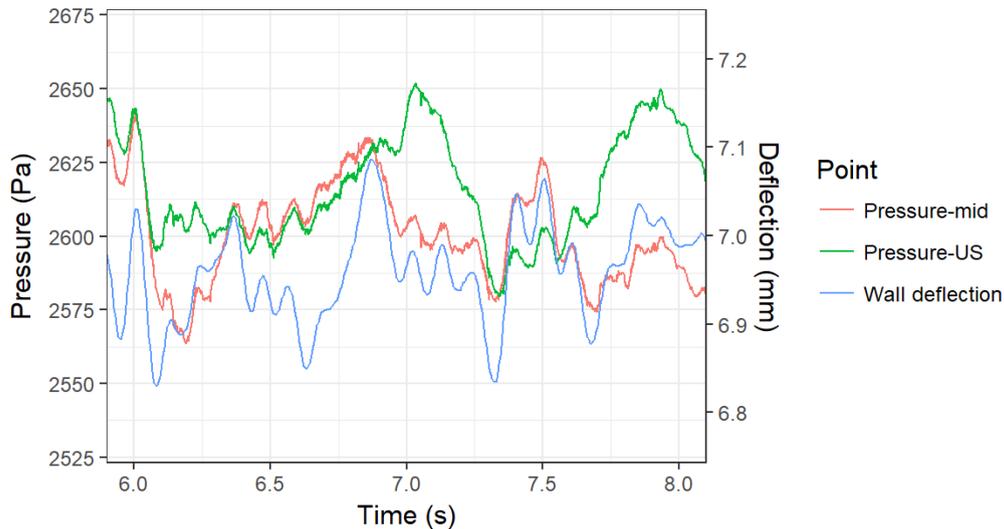


Figure 8.12: Correlation between pressure in inlet key and wall movement ( $H/P = 0.2$ )

ence the pressure wave nearly simultaneously it can be deduced that it is running parallel to the sidewall in the direction of the opposite sidewall. Despite their presence, it should be noted that the pressure waves are small in magnitude ( $\sim 2$  Pa) and that they would likely dissipate further as they travel toward the opposite sidewall. That said, the link they create between the opposing sidewalls is certainly worthy of further study as is the effect that harmonics have on this vibration.

Another FSI component that occurs at the fluctuating sidewall is the effect it has on the overflow nappe. This effect is showcased in Figure 8.13. As the wall moves downstream, or outward, the nappe thickens slightly as the wall pulls away from the flow behind it. When the wall moves upstream against the flow, the flow lines get directed upward by the moving wall causing the underside of the nappe to deflect upward. The figure reveals the difference in the trajectory of the nappe over a time step of 0.1 s where the wall has moved 1 mm to the upstream side. It also reflects on how the maximum apex of the underside of the nappe has moved upward due to the change in its trajectory. It is expected that these changes add an additional oscillation to the nappe and the air pressure underneath it. However, it should be noted that this behaviour is minor and the nappe is far more affected by the vortex induced undulations which affect it from time to time.

## 8.6 Fatigue

Vibrations at a PKW are of concern as they may lead to the development of cracks and other fatigue related failures. The main focus of the present thesis is on the vibrations themselves and their possible causes, however, a brief scoping level assessment of the fatigue potential of the generated data was undertaken.

It was described in the previous section that the oscillations in the wall are expected to result in relatively small alternating stress ranges. However, these small ranges are superimposed on a fairly large mean stress state of tension. The ability of the material to resist fatigue damage is

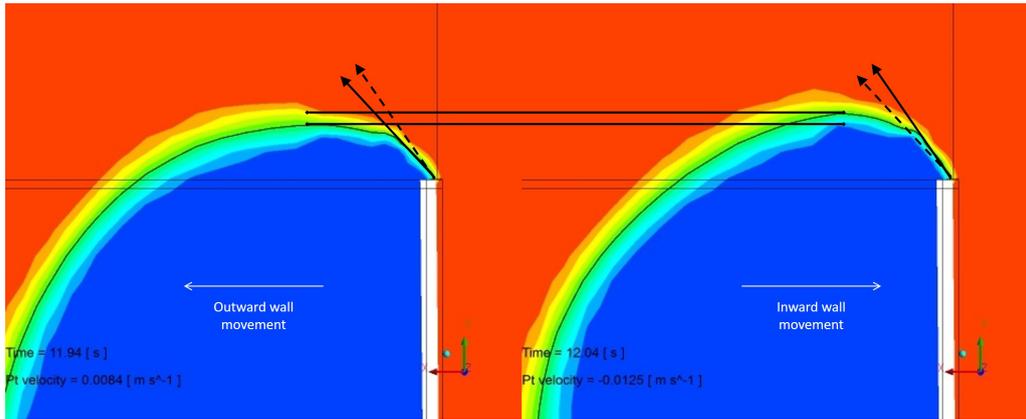
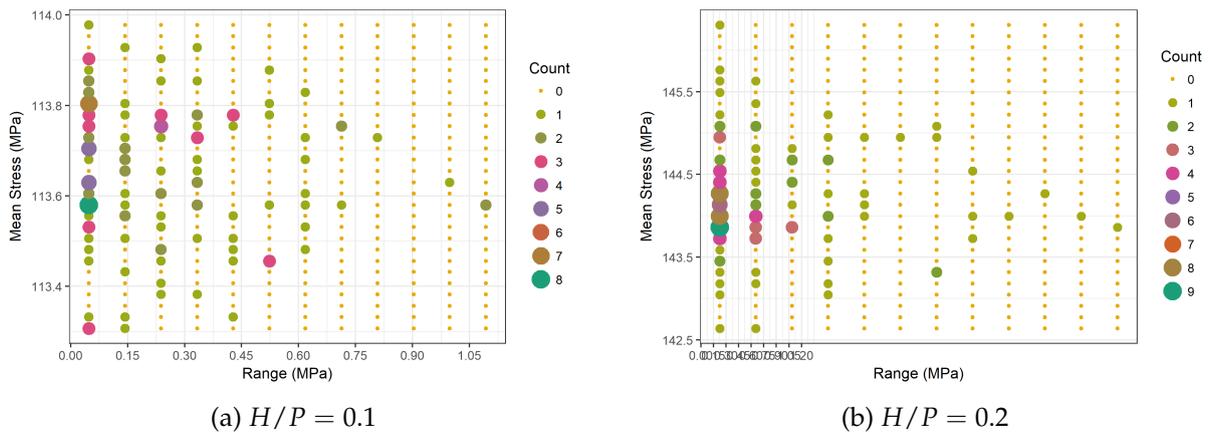
Figure 8.13: Nappe adjustment due to wall movement of 1mm ( $H/P = 0.1$ )

Figure 8.14: Stress variation rainfall counting results

thus reduced. This effect and the impact of the alternating stresses was assessed using the tools described in Section 3.4 and considering the cyclic elastoplastic and fatigue material properties published in de Jesus *et al.* [132].

The time signals presented in Figure 8.9 were processed to exclude all data except its peaks and valleys. The reversals they represented were then passed through the rainfall counting procedure which resulted in the data shown in Figure 8.14. The data reveals that most of the stress reversals are small in range and centred around the mean stress. There are a few larger alternating stresses (nearer the right of the graphs) which would cause more fatigue damage than the cumulative damage caused by those small reversals on the left of the graph. As per the Palmgren-Miner rule each of their contributions to the total number of cycles can be accumulated. The cumulative relative fatigue damage of all the reversals on this short time series amounted to  $2 \times 10^{-34}$  for  $H/P = 0.1$  and  $1 \times 10^{-26}$  for  $H/P = 0.2$ . This equates to  $5.3 \times 10^{33}$  and  $7.9 \times 10^{25}$  repeats of this short 10 s time signal to achieve fatigue failure. This far exceeds the expected 50 year design life of most hydraulic structures, hence the structure can be considered safe from fatigue failure based on the assumption of only these loading cycles occurring on a continuous basis.

When considering higher flow scenarios, the mean stress on the sidewall will increase. The

fluctuating pressures are however expected to remain of the same order of magnitude. This means that the ratio between the alternating stress and the mean stress gets smaller as the water head upstream increases. This implies that if the yield criterion is utilised in the design of these walls to cater for the largest mean stress states then fatigue related damage should not be a major design concern.

It is worth reiterating the fact that the mean stress state at the PKW is also transient albeit at a much larger time scale. Aspects such as waves and changes in the upstream water level and daily temperature fluctuations will cause the mean stress state mentioned above to fluctuate over time. These alternating stress ranges will be much larger than those caused by the fluid induced vibrations. The large periods of these repeating cycles will not lead to the early onset of fatigue cracking. However, this is not entirely true of wave loading, which may cause a high number of cyclical repetitions in short time periods. These loading conditions are outside the scope of this study but should be investigated further.

## 8.7 Discussion

Prior to the vibration analysis each component of the vibrating system was examined individually. This data inferred that, due to a general overlap between the excitation frequencies and the modal frequencies of the structure, there was potential for significant vibration to occur. Not only would the sidewall vibrate over the entire excitation spectrum, those vibrations occurring at the natural frequencies of the wall would be reinforced. This is indeed what was found in both the physical and numerical modelling that was undertaken.

That said, when the spatial and temporal characteristics of the upstream pressure fluctuations were examined, no clear evidence for the activation of any mode was found. It was found that the energy of the excitation was evenly spread out over all the modes without favouring any one of them. The modal vibrations in the sidewall that were recorded are thus a response by the sidewall to the overall fluid induced excitation spectrum and not specific excitation of those modes by the upstream pressures.

The numerical model consisted of a coupling between a fluid (CFD) and a structural (FEM) module. Both of these were calibrated separately as described in previous chapters. Without any additional adjustments, the coupling of the two calibrated modules were successfully able to emulate the vibration behaviour of the PKW sidewall measured in the physical model. The lack of any additional tweaking supports the premise that the numerical model is a valid representation of the physical vibration phenomena.

The very large computational cost of the model precludes its use in general practice but it remains highly beneficial in academic work. The data generated by the model proved that the system of vortices in the upstream inlet key cause the sidewall to vibrate and create fluctuating stresses at the base of the sidewall.

It was seen in Figure 8.9 that the stress reversals are relatively small. They are thus unlikely to cause fatigue related problems. However, considering the mean stress state itself, should rapid oscillations in the water level occur, either due to the incidence of waves or operations in the water body upstream of the weir, these may lead to cracking at the high stress zone. This is

however beyond the scope of this study.

Another aspect which could not be explored further in this study is the potential for fluid structure interaction between two opposing sidewalls on either side on an inlet key and the water body between them. It was surmised that the vibrations in both these walls, via the pressure pulsations they create and the harmonics of the vibration displacement might come into phase with one another. This could lead to additional stresses in the walls as well as sloshing in the inlet key.

## 9 Validation and verification

### 9.1 Introduction

The validation and verification of any study are important factors to consider in order for its results to attain accuracy and credibility. As with most, if not all, numerical and physical models the results should be viewed in light of their source. The question must be asked whether or not the model was implemented correctly with the correct underlying assumptions and whether or not the models are accurately representing the physical phenomena [126]. Furthermore, the inherent modelling and measurement errors must be addressed.

In the context of the present study, it is understood that verification refers to the assertion that the models and its associated measuring instruments are correctly modelling or observing the physical phenomena being investigated. Verification should ensure that there are no extraneous influences that would affect the behaviour of the phenomena or that these would be interpreted as being characteristic of that behaviour. It thus assesses the accuracy of a solution and its reliability for use as a decision making tool. Validation on the other hand deals with the external legitimacy of the model by comparing the modelled results with experimental data. It can thus be used to assess the numerical or modelling errors [126; 133].

It should be borne in mind that calibration is separate from validation. Calibration uses preferential adjustments to make the numerical model fit the experimental data meaning that it demonstrates the capability of the model of reproducing the calibrated-against data. This does not equate to evidencing the model's predictive capability. Validation compares data from external sources to that generated by the unadjusted model thus establishing empirical validity [126; 134].

### 9.2 Physical model

The physical model and the experiments on it were designed with a number of features to ensure that it could emulate the desired behaviour and thus be considered a verified representation of the phenomena.

The main design element was its scale. Due to the rigid geometry of the PKW no geometric inadequacies are present as the shape can be accurately emulated at almost any scale. However, the scale had to be large enough such that the relative fluid viscosity would be low enough to allow the model to emulate the vortex shedding behaviour from the inlet key edge. Research literature suggested that high frequency vortices would not be correctly modelled at too small scales [5; 4]. The scale of the smallest model (mode A) was set at 7.5 which results in a model that is much larger than those generally used in parametric hydraulic models with typical scales of 20 to 50. The larger model (model B) was built at a scale of 2.73 to ensure that its vibrations would be strong enough to be picked by the installed instruments. The physical size

of the model is large enough to be considered a prototype in its own right. Another benefit of these large scales is the both models are large enough to limit the onset of significant scale effects such as those caused by surface tension and viscosity [110; 112].

Another potential design flaw was the flume within which the PKWs were installed. It was constructed with sufficient length (20 m) such that the flow disturbance at the inlet arrangement would dissipate and stabilise by the time it arrived at the model PKW. This distance was estimated by a simple mathematical model prior to the construction of the flume. The width of the flume was also adjusted between model A and B to ensure that the correct approach conditions prevailed during those two model tests.

Besides the geometry of the model being emulated correctly, the instrumentation used to record the behaviour also needs to be verified. The sensors which were used to record the studied behaviour each had their own level of accuracy (see Section 5.2.3 and Appendix B.4.1). These accuracies were well within the limits needed to describe the flow and emulate it in the numerical model. The most important factor for the vibration analysis was the frequency behaviour of the various structural and fluid elements. This meant that sufficient quantities of high quality data had to be collected for long enough periods of time. The lowest frequency of all the sensors was the ADV at 200 Hz. This means that, in accordance with the Nyquist theorem, only oscillating behaviour under 100 Hz could be sufficiently refined. The most important sensors, the pressure transmitters, the accelerometers and the strain gauge, each logged data at 1 kHz or more and were thus able to define observed frequencies to a high degree of accuracy.

Errors in the measured data were minimised by the development of a suitable data collection methodology. This methodology was compiled with the understanding that all data collected is subject to random measurement errors and that no reading will ever represent the absolute truth. However, this absolute correctness is not required from an engineering perspective so long as the results are statistically representative [126]. To this end, a minimum of 20% of the tests were repeated or their values remeasured. Certain of the more important measurements, such as the pressure oscillations and the wall vibration were repeated up to 5 times. Statistical randomness was also catered for by allowing sufficient time for a time variant signal recording. Research literature suggests that for oscillating behaviour at least 400 dimensionless time units (about 120 s) should be included in the time signal in order for it to be statistically significant. Most of the time records extended well beyond this duration.

Other data gathering and processing error reduction techniques included testing for hysteresis, discarding data which was clearly contaminated by external factors (nearby machinery) and allowing the flow to stabilise before collecting any data.

### 9.3 Numerical model

The numerical model consisted of a fluid CFD component (ANSYS Fluent) and a structural FEM component (ANSYS Mechanical). These were first run separately and later coupled to simulate the vibrations at the sidewall of a PKW.

The CFD component was based on the same geometry and the same scale as physical model A. The model was set up with the published recommendations concerning boundary

conditions and turbulence models for a free-shear problem. It was noted that with these initial conditions the model was readily capable of emulating the overall flow behaviour of the weir, including the discharge coefficient of the weir, without any calibration. This validates the use of these model parameters in simulating the overall flow dynamics around the PKW.

The pressure data collected from the physical model was used to calibrate the transient features of the numerical model. Parameters subjected to sensitivity analyses included different numerical solvers, discretization schemes, turbulence generation and mesh size. The most sensitive of these parameters appeared to be the mesh size which implicates the ability of the model to represent the sheet of vortices in the inlet key. The band of pressure fluctuation frequencies was used as a calibration parameter in the CFD model and yet a wide variety of other unrelated physical phenomena witnessed in the physical model realised in the numerical model as a result. These include the water surface undulations at the crest, the discharge profile, the velocity field, the nappe cavity shape and the nappe corner indentation. There is thus an acceptable level of confidence in the ability of the CFD model.

The FEM component of the numerical model was built to emulate model B with its geometry and scale. When the initial results of the modal analysis were compared to the physically measured modal results there was general good agreement. However, if the wall of the model were thickened slightly the results did compare much better. The thickening of the walls was smaller than the manufacturer's tolerance for the supplied sheets of steel from which the physical model was built. This means that it is likely that the physical model was indeed thicker as implied by the numerical model. It can thus be stated that once the actual physical geometry was emulated in the model, the structural behaviour was well simulated without the need for calibration.

The overall PKW structure was simplified for inclusion in the vibration model such that it would reduce the computation cost of running this model. This simplification required the modal parameters of the reduced sidewall to be calibrated against the physical data. This was achieved via specifying flexible attachment points instead of fixed points as the boundary condition.

The calibrated CFD and FEM models were combined in a coupled system to allow them to share data between each other. The results of this unadjusted coupled simulation present acceptable agreement between it and the physically measured data. It is acknowledged that some errors have been identified but these have been ascribed to numerical errors mostly caused by the model's poor convergence toward an oscillating solution. They are deemed acceptable. Despite these errors the simulation correctly identified every frequency peak which presented in the physical data. This supports the statement that the uncalibrated coupled simulation of the verified CFD and FEM components is validated to the degree that it is able to emulate the observed experimental frequency data. The model was however not able to accurately replicate the vibration strengths.

## 9.4 External validation

During the planning stages of the study it was hoped that the vibration model was to be validated against an external data set. It was reported in literature that the Malarce Dam PKW, designed and operated by Électricité de France (EDF) was fitted with a number of instruments including an accelerometer. Personal communication with the team from EDF revealed that this accelerometer was damaged during the construction of the PKW and was not generating any data. It could thus not be used as hoped to externally validate the model.

## 10 Design guidelines

The investigation into the potential for fluid or flow induced vibrations at piano key weirs, identified certain problem areas or weaknesses in their design. It was outlined that these kinds of vibrations may readily occur in PKWs but that they would not cause problems in most cases as the construction materials used in their construction are readily capable of preventing fatigue induced failure. That said, very thin weirs constructed from metal and which are exposed to long durations of high discharge may be prone to such damage. A number of tactics or elements could be used in their design to either limit the generation of the vortices responsible for these vibrations or to resist the effect of the vibrations. These are described below:

- Should structural vibration of a PKW sidewall be of concern in the design process, it could be addressed by adding mass to the structure by making the sidewall thicker. This thickness should be enough increase the natural frequencies of the sidewall. An alternative would be to add stiffness elements which would also increase the natural frequencies. These could consist of shaped steel profiles installed on the upstream or downstream face of the sidewall. It was found in Chapter 8 that the maximum stresses at the base of the sidewall were most closely correlated with vibrations in the second mode of vibration. These stiffness elements should thus be placed in relevant locations where they could best resist movement in this S-form modal shape.
- The model B PKW with a fall height of  $P = 1.1$  m exhibited strong nappe oscillations at very low discharge. It was found that providing aeration to the underside of the nappe reduced the severity of these oscillations but did not eliminate them. A disturbance to the corner of the nappe, i.e. creating an opening in the nappe at this location, caused all nappe oscillation (even those along the sidewall) to cease. A small protuberance or tooth placed at the downstream corners of the PKW underneath the crest large enough to break the nappe at very low overflow depths should, according to the physical model, limit the onset of these vibrations.
- The installation of rounded or shaped noses did result in reducing the occurrence or severity of the upstream system of vortices and the pressure fluctuations they cause, but did not cancel them altogether. The data showed that the vortices generated at the lowermost portion of the wall (the area with the nose) were much reduced. However, those generated at the upper portion of the wall along the overhang continued at more or less the same strength. Rounding this upper overhang edge may reduce these vortices too.
- The physical model was constructed from S355 structural steel, which was chosen for its strength. In practice however, it is expected that PKWs, should they be built out of metal, would likely use stainless steel 316 or stainless steel 2205 for its corrosion resistive properties.

Stainless steel 316 has a lower yield strength than structural steel hence, if it is designed using the yield limit state criterion, it would need to be made thicker than the physical model of the present study (which was also designed to the yield limit criterion). This added thickness will assist in increasing the natural frequencies and thus lead to less overlap with the upstream pressure excitation resulting in less vibration.

Stainless steel 2205 on the other hand has a much higher yield strength than S355 which would allow it to be specified to a lower thickness. This would increase its exposure to the occurrence of vibrations, hence it is recommended that if this type of steel is used, that vibrations be accounted for in its design and the wall be made thicker than strictly required by the yield limit state criterion.

- Special attention should be given to the quality of the welding. Consideration should be given to welding the various steel sheets in factory controlled conditions instead of in the field. At the various T and corner joints the entire width of the steel sheet should be welded and not just with fillets. This should prevent or limit the development of stress concentrations especially at the base of the sidewall and the overhangs where the highest stresses are expected.
- When constructed from steel plates, it is recommended that the open space formed underneath the sloping floors is filled with concrete. This will add weight to the structure and so increase its overall stability. Furthermore, the bracing action of this mass against the vertical sheets of metal will stiffen the structure and so increase its natural frequencies, which will in turn limit the occurrence of vibrations.
- The application of a protective coating or water repelling sealant in the general area at the base of the sidewall may be advantageous to prevent the onset of corrosion in this higher stress zone.
- The maintenance manual which is compiled for the structure should highlight the requirement that the joints along the base of the sidewall on both the upstream and downstream sides be regularly inspected. The inspection should pay careful attention to the development of cracks in the steel itself or in any of the corrosion protection coatings that cover it.
- The placement of instruments, such as strain gauges, at the base of the sidewall and under the overhangs, would be advantageous in monitoring crack development.

## 11 Conclusions

### 11.1 Overview

Piano Key Weirs (PKW) are a novel development in the field of hydraulic structures which aim to attain a larger discharge capacity than linear weirs. Their geometry makes them very stiff and rigid structures, however, there are thinner components of a PKW which may be prone to the onset of vibrations, specifically fluid or flow induced vibrations (FIV).

Their purpose may require them to operate under low head conditions for long periods of time. This exposes them to the long term effects that these flow induced vibrations may have. These effects may include material fatigue, which could lead to cracking, induce corrosion and ultimately contribute to the failure of the structure.

The overall goal of research into PKW vibrations is to scientifically examine the cause, nature and prevention of fluid induced vibrations at PKWs. The main aim of this investigation was thus to develop a better understanding of these vibrations and to quantify their effect. The study's objectives were to examine these fluid induced vibrations by characterising their nature and their source, characterising the nature of the vibrations of a thin-walled PKW and combining these two aspects to quantify the response of the structure.

Bear in mind that the scope of the study did not allow it to conduct an exhaustive assessment of the vibration phenomena nor provide a prescriptive characterisation of all potential PKW vibrations. It was limited to describing the most common causes that were observed and highlighting the potential for their occurrence.

The study was apportioned into three main parts: an investigation into the hydrodynamic sources of the excitations, an investigation into the modal characteristics of thin-walled PKWs and an investigation into the vibration response of the structure. Each of these investigations comprised both physical and numerical modelling which were used to generate data and make observations.

### 11.2 Findings

The study determined that the most sensitive portions of the structure which would be susceptible to vibrations are the lateral sidewall as well as the upstream and downstream overhangs. The analysis focussed on the sidewall as it would be the most exposed to Flow- or Fluid-Induced Vibrations (FIV).

#### 11.2.1 Structural analysis

The structural response under normal hydrostatic loads involves the thin walls deforming outward with the largest deflections occurring at the centre of the sidewall crest. The largest stresses occur at the base of the sidewall close to the start of the overhangs. These are indicated

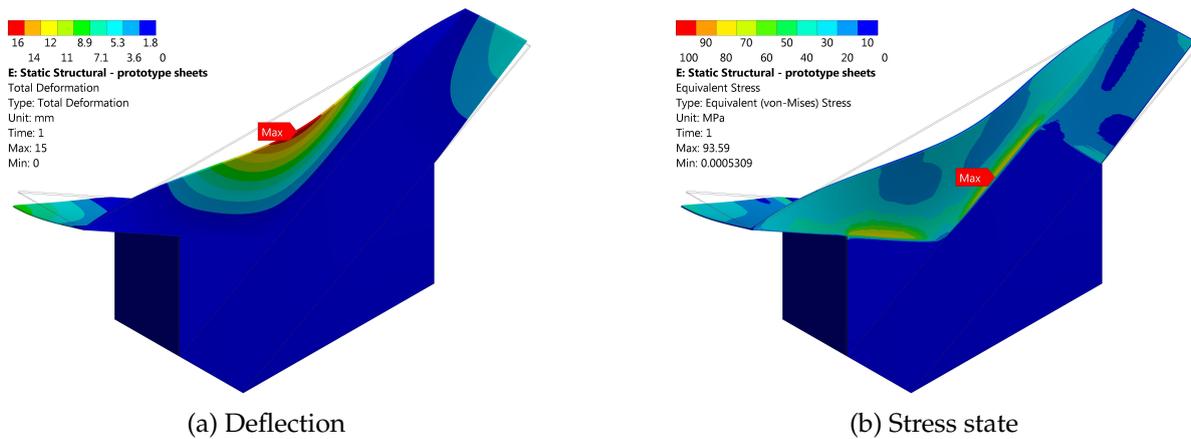


Figure 11.1: Structural response to hydrostatic load

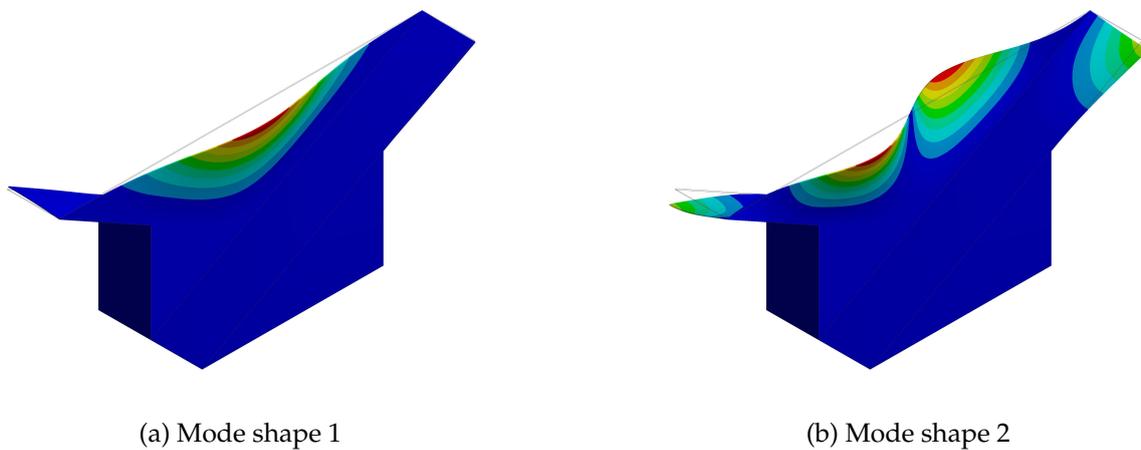


Figure 11.2: Mode shapes of sidewall

in Figure 11.1. When the sidewall vibrates it is these stress locations which will undergo the largest stress fluctuations and are thus the most susceptible to crack development and fatigue.

The modal characteristics of the most susceptible portion of the structure, the sidewall, were analysed in both the physical and numerical models. The data obtained from the physical model was closely emulated by the results of the numerical model. Almost no calibration was needed to achieve this. The numerical model only needed to simulate the exact geometrical parameters of the physical model in order to accurately simulate its behaviour. The model can thus be considered a validated tool as practically no calibration was necessary.

The first two mode shapes of the sidewall are presented in Figure 11.2. It reveals how the sidewall is flexed into the typical S-shapes of simply supported beams. Note that there are additional modes which incorporate the overhangs to a larger degree but are not considered here. These shapes were measured in the physical model using accelerometers and were easily replicated in the numerical model.

The natural frequencies at which these two mode shapes occur are 20.3 Hz and 41.5 Hz respectively, as determined by the physical model. As stated above, the numerical model was

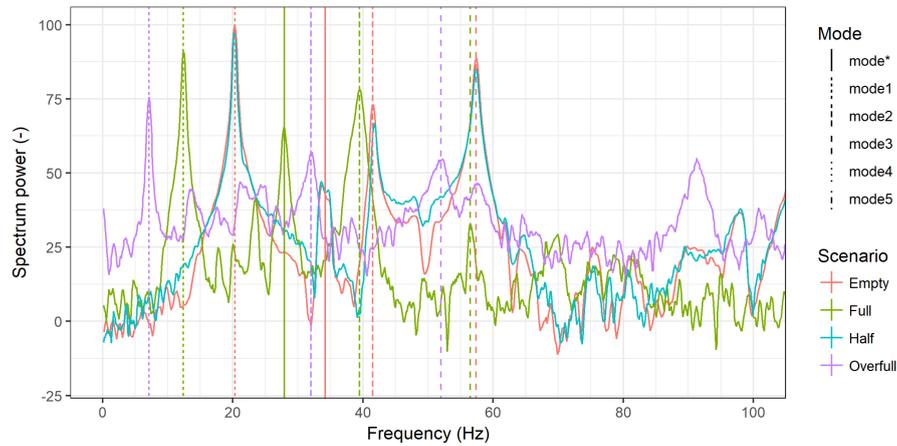


Figure 11.3: Strain gauge FRF showing natural frequencies for four scenarios

able to closely emulate these (21.1 Hz and 41.3 Hz). The natural frequencies experienced significant reductions when exposed to the added mass of the water body. The magnitude of this decrease is depicted in Figure 11.3, which presents the results of the spectral analysis of the physical model strain gauge data. It reveals how the first mode frequency of 20.3 Hz reduces to 12.4 and then 7.1 Hz when exposed to increasing water depths. This added mass brings the natural frequencies well within the range of the excitations as seen in the next section.

### 11.2.2 Hydraulic analysis

The hydraulics of the flow around a PKW is fairly well understood but has mainly been studied from a steady state perspective. Vibrations on the other hand are inherently variable over time and so the present study explored to phenomena using transient models and temporal data analyses.

The scaled physical model was constructed to observe the flow under a range of conditions and to collect velocity and pressure data. This data was used to calibrate a transient, three-dimensional, dual-phase numerical model. The turbulence module selected for this model is the Large Eddy Simulation (LES) methodology as the Reynolds Averaged Navier-Stokes (RANS) based turbulence tools were incapable of emulating the witnessed pressure fluctuations in the flow. The numerical model allowed for the dynamics of the flow to be inspected in a much greater level of detail than the physical model.

### Vortex shedding

Observing the global trends of the flow around a PKW reveals a good deal of information about the dynamics which dictate its behaviour. The vast majority of the flow approaching a PKW enters the inlet key. This means that flow under the outlet key overhang gets diverted toward the inlet key alongside it. As it does so, it builds up transverse momentum which needs to merge with the longitudinal momentum of the flow directly approaching the inlet key. This is depicted in Figure 11.4. It reveals how the merging flows lead to the development of a free shear layer which starts at the upstream edge of the inlet key. This shear layer denotes a

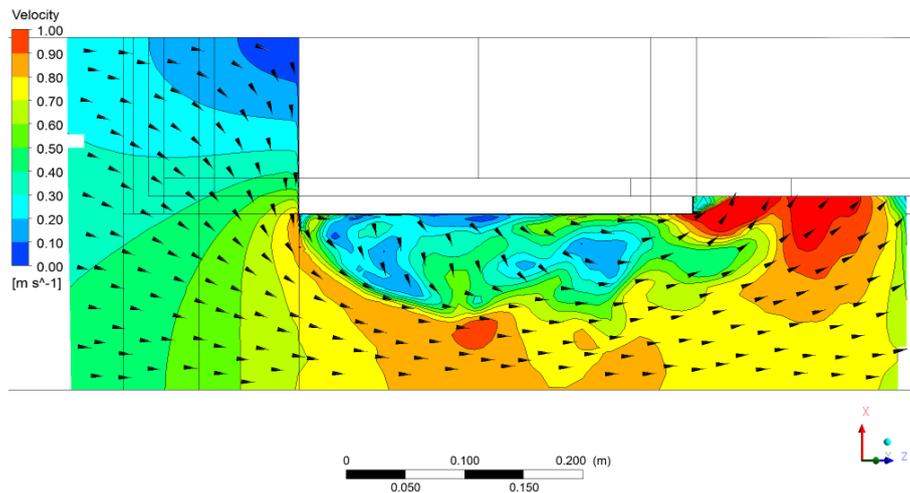


Figure 11.4: Instantaneous velocity magnitude (m/s) on plane L along the inlet key

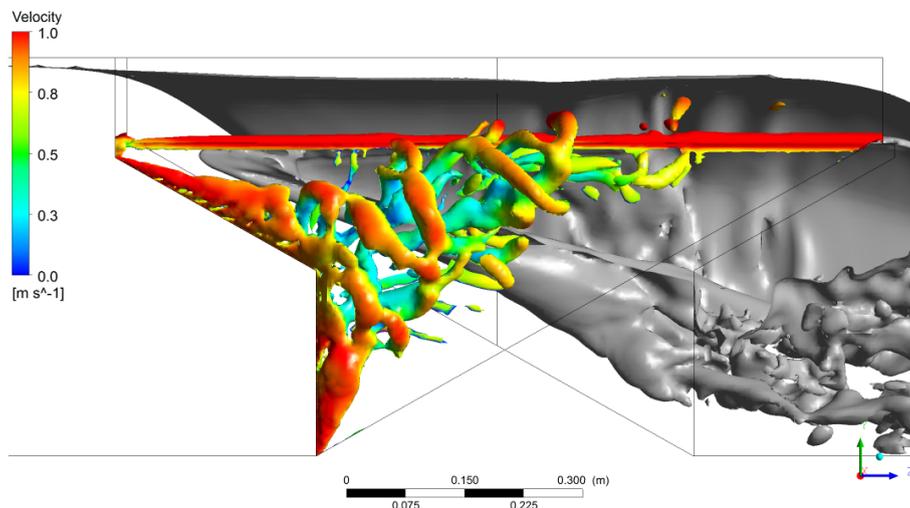


Figure 11.5: Side view of Q-criterion vortices with water level

boundary for a zone of near stagnant flow which forms behind it.

The shear layer is inherently unstable and starts to decay by forming a regular set of vortices which are shed downstream. These vortices are shown in a side view in Figure 11.5. It can be seen that they are formed by the free shear layer which forms along the entire upstream edge of the inlet key. They then roll up and get convected downstream and are eventually discharged over the crest.

Vortices near to walls or boundaries are known to create pressure fluctuations on this boundary. The vortices are rotational zones of flow which induce large velocity gradients in their vicinity. At any given location in the vortex zone, flow is directed toward or away from the wall, generating positive and negative pressure fluctuations on the wall. The vortices themselves are also zones of lower pressure so can also induce lower pressures directly. These fluctuating pressures are the first source of excitations which cause the sidewall to vibrate. It

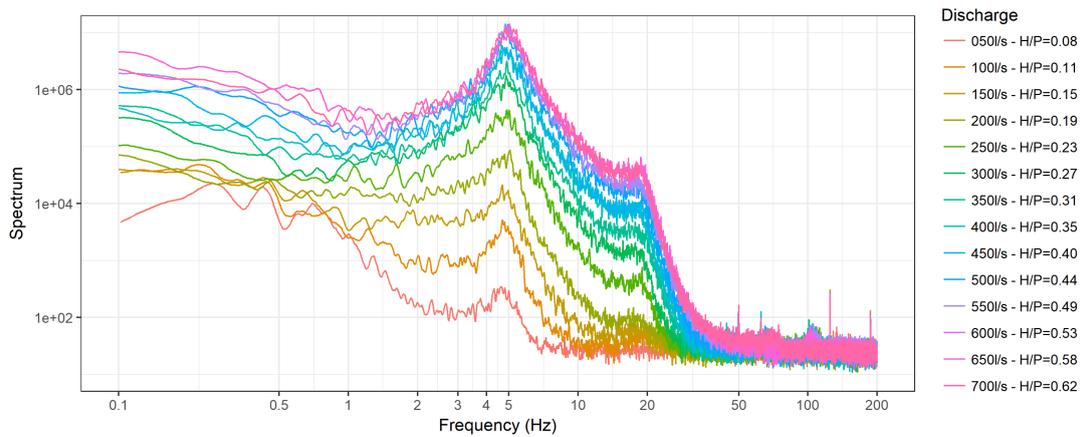


Figure 11.6: Pressure spectra at point A2

is noted that the strongest fluctuations occur near the middle portions of the sidewall and its crest, where the sidewall is most susceptible to them.

The pressure fluctuations were analysed for their frequency content at a range of discharges. In the scaled physical model, it was found that the frequencies varied depending on the location on the sidewall but were all located in a frequency band from 1 to 20 Hz. Each frequency band was focussed at a well defined peak frequency of between 3 Hz and 6 Hz. The numerical model could emulate this frequency band and its strength fairly well but could not reproduce the peak at its same strength.

The sensitivity of these pressure fluctuations and their spectral content was examined by testing a range of discharges. As can be seen in Figure 11.6, which shows the spectral content of one of the pressure measurement points of the physical model, the frequencies showed very little sensitivity to the increased flows. The fluctuations do increase in strength, meaning that the alternating forces on the wall do increase in magnitude, but there is no change in their frequency. This unintuitive result stems from the apparently unchanged phase velocity of the vortices which are the cause of the fluctuations. It would be expected that as the discharge and the velocities in the inlet key increase they would increase the convection speed of the vortices which are shed from the free shear layer. Such an increased vortex convection speed would reflect as an increase in frequency. That this is not the case proves that the vortices which cause the pressure fluctuations are separated from the main body of the flow. They do indeed reflect larger fluctuations which implies that they do receive additional energy as discharge increases but this separated zone remains near stagnant.

Similar behaviour was noted in the numerical model when the width of the inlet key was adjusted. It was thought that as the width was increased it would allow the free shear layer to create a larger separation bubble behind it thus affecting the vortices which are shed by it. This turned out not to be the case. The frequencies across all the tested inlet/outlet width ratios were the same. This shows that this parameter can't be used as a control mechanism. It is interesting to note, that even with very narrow inlet widths and clear integration of the vortex sheets from the opposite inlet key walls there was little to no correlation between the fluctuating pressures on the opposing walls. This again, points to the isolation of the stagnant zone along each wall.

Another control alternative was the incorporation of an upstream nose under the outlet key overhang. Such flow guides have been installed at a number of PKW prototypes to limit the onset of vortices from the inlet key edge. These were tested in both the physical and numerical model which determined that both triangular and circular noses do lead to a decrease in the strength of the vortices being shed. The circular nose achieved the greatest reduction, however, upon examination of the spectral content of the pressure fluctuations on the wall, it was clear that even though the vortices are difficult to visualise due to their weak strength, their effect on the fluctuations was still evident. The noses were thus able to significantly reduce the strength of the vortices, but not cancel them outright. It should be noted that the noses only affect the vortices which stem from the lower end of the PKW. Those vortices which are shed from the upper portion continue unabated. It is feasible to consider rounding off the edge of this overhang to limit these too.

A last geometric control mechanism on the vortex shedding is to consider the different types of PKWs. It was shown above that the onset of the vortices appears to be characteristic of PKWs in general and that only their strength can be controlled and not their occurrence. On the other hand, different PKW types can be used to control where these vortices are shed toward. Standard type A PKWs direct vortices (and their pressure fluctuations) to the central portion of the sidewall precisely where the sidewall is most susceptible to their influence. PKW type B and C direct flow either toward the lower end of the crest or toward the upper portion of the crest. It appears that PKW type C would be the most efficient as it would experience its pressure fluctuations in a location where the structure is relatively well braced.

### **Air cavity fluctuation**

The dynamics of the outlet key are also a potential cause for excitations on the sidewall. Under most design flow scenarios for the operation of PKWs ( $H/P < 0.3$ ), the nappe exhibits springing or leaping behaviour along most of the crest length thus forming an enclosed, elongated, conically shaped and air-filled cavity underneath it. It was shown that although the air pressure under the nappe is marginally below atmospheric pressure, it can be considered that the nappe is largely self-aerating. The turbulent flow from the colliding nappes on both sides of the outlet key entrain sufficient amounts of air to counter the air that is lost via the entrainment of bubbles in the hydraulic jump downstream of the PKW. Although many prototype PKWs have aeration systems to supply air to the underside of the nappe, the study found that nappe aeration had little significant effect on the nappe's vibration or its behaviour.

The air pressure under the nappe was found to oscillate at more or less the same frequencies as those of the vortices in the upstream water body. This implied that these vortices extended their influence to the outlet key. It was seen in both the physical and the numerical model that as the vortices reached the crest of the sidewall, their rotational nature would cause undulations in the water level at the crest. This affected the behaviour of the nappe by attempting to create an opening in the nappe curtain. The nappe was never observed to open fully in the physical model as there was always a thin sheet of water even in these gaps. It remains feasible however that these opening may assist in the alleviation of negative pressures under the nappe.

These water surface disturbances only occurred when the water depth over the crest was relatively shallow. At higher depths, the scale of the vortices become smaller relative to the water column and could thus not induce as great an effect. Their presence still affected the underside of the nappe such that it fluctuated at the same rate as the vortices themselves. These fluctuations then directly lead to the small oscillations in the air pressure under the nappe that were noted.

When the upper portions of the outlet key start to drown at much larger discharges, the behaviour of the air-cavity takes on another dimension. The apex of the conical cavity is ordinarily attached to, or close to, the upstream corner of the sidewall crest. Flow discharging over the upstream crest of the outlet key gets pushed sideways by the transverse flow from the sidewall crest, thus forming a gap for the air cavity to form. As discharge rises and the longitudinal flow momentum from the upstream crest increases it begins to drown out or dominate the transverse momentum of the flow over the sidewall. This localised drowning causes the air cavity's apex to become detached and move downstream. Without a fixed anchor the apex is highly unstable and thus its location fluctuates as the balance of flows between the longitudinal and transverse flows changes.

The transverse flow in the drowned out portions of the outlet key, still lead to the formation of a rotational zone of flow. Similar to a vortex core in the inlet key, this rotation leads to the development of a zone of negative pressure along a strip of the wall in roughly the same location where the nappe cavity would have been were it not drowned. At times, the balance of flows causes the air cavity to relieve this negative pressure with a rush of air causing the nappe apex to spring upstream at large velocity. This sudden change leads to large pressure fluctuations on the downstream face of the sidewall, although they are infrequent. Under the right flow conditions, the apex may traverse the middle portions of the sidewall where it is most sensitive to such large fluctuations in pressure.

The nature of the fluctuations in the outlet key are such that they are not a major cause for concern for the vibrations of the sidewall. The air pressure fluctuations are by their nature of low intensity and were thus not assessed further. The air-cavity apex oscillation is of larger intensity. However, the conditions needed for its onset are sufficiently beyond the range of normal operations at a PKW ( $H/P \approx 0.5$ ) that they were not deemed a danger to the long term viability of the structure.

### **Nappe oscillation**

Oscillations of the overflow nappe have been surmised to occur at PKWs, although have not been observed directly until this study. The larger of the two physical models was large enough for it to be considered a prototype in its own right. At very low flows ( $H/P = 0.006$  to  $0.01$ ) the lower most portions of the overflow nappe, near to where it struck the floor of the flume were found to oscillate at one of three distinct frequencies, namely 14.1 Hz, 16.6 Hz or 19.0 Hz, depending on the discharge. It was also noted that hysteresis played a role in which frequency occurred at which discharge. These three frequencies are thought to be related to the harmonics of the wavelength of the nappe in relation to the fall height. These values are in close proximity

to the damped natural frequencies of the sidewall hence resonance is a possibility. However, as with the oscillating air pressures, the energy of the oscillation is transported via sound waves which have low strength and are thus not considered likely to be a danger to the safety of the structure. That said, sound waves generated by the oscillation are loud ( $>90$  dB), hence they are undesirable from a noise disturbance perspective.

Their exact cause remains unknown, however, the phenomenon was surmised to be related to the transition from laminar flow to turbulent flow in the upstream water body. This implies that aeration, or lack thereof, would not affect the oscillation, which was indeed the case. Providing aeration to the underside of the nappe or breaking the nappe did not halt the oscillation but it did significantly affect their strength. The air pressure behind the nappe thus amplifies the oscillation effect as confirmed by other studies. It was interesting to note that if the nappe was broken at the corner of the PKW, where the nappe is thinnest and the oscillation strongest, the oscillations over the whole nappe ceased altogether. The fluctuation of this limited zone of the nappe thus appears to be a driver of the oscillation as a whole. Combating such fluctuations is thus straightforward with the provision of some form of protrusion at the corner large enough to break open the nappe under very low flow conditions.

### 11.2.3 Vibration

The modal behaviour of the structure and the excitations determined from the hydrodynamics of the flow were combined in a vibration model. The vibrations were measured in the physical model and compared to those of a coupled numerical fluid-structure interaction model.

The modelled fluctuating excitation forces on the upstream face of the sidewall were analysed for their spectral content and their spatial correlation to assess their potential in activating any of the modal shapes of the sidewall. Although it was found that the fluctuations were at times able to active a mode shape, it only occurred infrequently. It can thus be stated that, even though the pressure fluctuations oscillate at frequencies equal to some of the natural frequencies of the sidewall, they are not inducing resonant behaviour since their spatial correlations are not activating the modes at the right frequencies.

Considering that the excitation frequencies are constant across a range of discharges, it can be stated that the PKW sidewall is safe from experiencing resonant behaviour caused by the upstream vortex induced pressure fluctuations under most flow conditions. The wall would still vibrate at its natural frequencies and at all the excitation frequencies but would do so at limited amplitudes.

This was supported by the data collected from the physical model as well as the numerical model. The physical data, presented as the spectral content of a strain gauge located at the centre of the crest in Figure 11.7, reveals that the wall vibrates at its first two natural frequencies, near 10 Hz and 31 Hz. There is also a peak near 1.5 Hz which reflects the peak excitation frequency at the scale of this PKW model. The data also showcase how the strength of the vibrations increases with discharge, but that, again, there is very little change in their frequency. The minor change in frequency that is noted may be ascribed to the increasing water depth's effect on the added mass of the vibration system. Aeration of the nappe had little to no effect

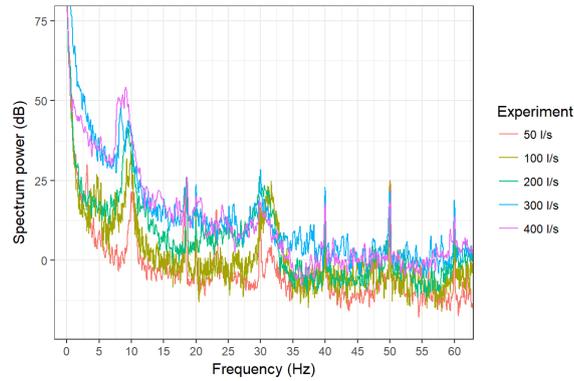


Figure 11.7: Physical model frequencies

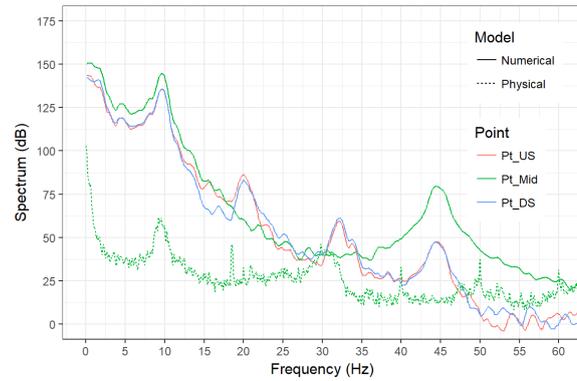


Figure 11.8: Numerical model frequencies

on the vibrations.

The numerical model coupled the calibrated fluid and the calibrated structural model into a fluid-structure interaction (FSI) model. The model was set up in staggered fashion such that the two models remained separate but could communicate their force and displacement data to each other at each iteration. This allowed the two existing models with their capable numerical algorithms to be used in an FSI scheme without additional adjustments. This methodology is however prone to poor convergence and thus requires very small time steps, each with numerous iterations, to achieve stable results. The high computational cost meant that only a limited number of simulations could be run.

The numerical results showed acceptable agreement with the physical model when the crest movement data was analysed. This is portrayed in Figure 11.8. The peaks at the natural frequencies are well emulated. There are however a number of other peaks, some of which are simple harmonics of the modal frequencies but others are likely non-physical and caused by numerical errors due to the difficulties inherent in converging toward an oscillating solution.

The numerical model allowed for the collection of data from other parts of the PKW not monitored in the physical model. This included the alternating tension stresses at the base of the sidewall. This data sequence was processed using rainflow counting to assess its potential for the development of material fatigue. The data proved that the stress fluctuations are small in comparison to the mean stress state as well as the typical ultimate and yield strengths of steel. The structure is thus considered safe against fatigue if the design of the structure adheres to the yield limit criterion. That said, larger excitations such as waves and changes in the upstream water level would engender much larger fluctuations albeit at much larger time scales. This aspect was not directly addressed in this study.

Another aspect which should be examined in greater detail is the potential for fluid structure interaction between the sidewall vibration and the fluid upstream of it which excited this vibration. Analysis of the vibration model data showed that the upstream fluid field was indeed affected by the vibration of the wall. It is considered feasible that the pressure waves caused by the vibrating wall would transfer to the sidewall on the opposite side of the inlet key. The manner in which this wall, which is also vibrating, responds to these pressure waves may lead to them falling into phase with each other. This could have some interesting effects

on the weir's discharge capacity and its behaviour as a whole.

### 11.3 Contributions to engineering science

The aim of the study was to shed light on the phenomena of vibration at PKWs. The conducted research expanded on the scope of the available knowledge in regards to the occurrence, cause and possible control of PKW vibrations.

The main objectives of the study were to conduct a scientific assessment of PKWs by characterizing the vibrations that may occur at PKWs from the perspective of their excitations, the PKW's modal parameters, and the structure's vibration response. The modal characteristics of the PKW, in the form of its natural frequencies and mode shapes, were described in Chapter 6. Chapter 7 detailed the characteristics of three potential excitation sources of fluid induced vibrations at PKWs. These are a system of vortices in the inlet key which induce fluctuating pressures on the sidewall, the unstable location of the air cavity's apex underneath the nappe and oscillations of the nappe itself. The data and models compiled in these two chapters were combined into a coupled fluid-structure interaction model to emulate and quantify the structure's vibration response, as presented in Chapter 8. A number of relevant design guidelines pertaining to the onset and control of these vibrations was outlined in Chapter 10.

Specific contributions which are novel to science that were made by the study include:

- Physical testing and data collection to determine the modal characteristics of a PKW as well as measure the effect of the water body's added mass
- Characterisation of the formation of a free shear layer and its separation zone at the upstream edge of the inlet key
- Characterisation of a system of vortices which are shed from this free shear layer, and the pressure fluctuations they cause, using both physical and numerical modelling
- Proved that the pressure fluctuations on the upstream face of the sidewall remain constant in their spectral content across a range of discharges in contrast to what was portrayed in literature
- Identified the source of the water surface undulations at the crest and the associated nappe disturbances as being the vortices which reach the crest and affect its flow field
- Described the effectiveness of proposed vortex shedding limitation strategies such as upstream noses, aeration and different PKW types
- Identified the air cavity apex's fluctuation as a potential source of vibration excitation
- Direct observation of nappe oscillations at a PKW proving that they can occur as surmised by other studies
- Physical testing for the measurement of the vibration behaviour of a PKW
- Emulated the sustained vibrations at a PKW using a coupled fluid-structure interaction numerical model

## 11.4 Further research

This study of vibrations at PKWs highlighted a number of areas of future research that would shed extra light on aspects not explored in this research. These are summarised below:

- Characterisation of the upstream vortices, their velocities and the pressures they induce on the sidewall using the Proper Orthogonal Decomposition (POD)
- Numerical modelling of mode frequencies with water damping at various depths and by how much this changes from the undamped case.
- Effect of downstream water level and submergence on the vibrations
- Improved simulation of the air-cavity underneath the overflow nappe
- Effect of a parapet wall on the separation bubble and on the nappe air-cavity
- Rounding of the upstream overhang edges to reduce the shedding of vortices from this edge similar to the inclusion of a nose at the lower portions of the PKW
- Structural vibration sensitivity of thicker or thinner PKW sidewalls
- Exploration of the separation bubble, the vortices and the pressure fluctuations for a range of upstream depths and upstream turbulence conditions
- More detailed investigation of the vibration of the nappe at the corner of the PKW. This would include the effect of the varying fall depth of the outlet key
- Effect of low frequency high amplitude fluctuations such as waves and changes in water level or temperature on the fatigue state of the material of the wall
- Investigate the FSI and phasing or synchronisation of the two sidewalls on either side of an inlet key
- The vibration characteristics of PKWs constructed from different materials such as PVC
- Frequency, modal or acoustic based solver for the fluid structure interaction of the PKW
- How does cracking, say caused by the thermal imbalance across the wall, cause changes in damping and thus the natural frequencies and their mode shapes

## 11.5 Closing comments

The findings from this dissertation reveal that Piano Key Weirs are indeed prone to fluid induced vibrations due to their geometry and the slender nature of their structural components. However, good design should be able to limit the negative effect these vibrations have on the operations and longevity of the structure.

This page is intentionally left blank.

## Bibliography

- [1] Labyrinth and Piano Key Weirs II - PKW 2013. In: Erpicum, S., Laugier, F., Pfister, M., Piroton, M., Cicero, G.-M. and Schleiss, A.J. (eds.), *Proceedings of the 2nd International Workshop on Labyrinth and Piano Key Weirs - PKW2013*, p. 291. CRC Press, Taylor & Francis Group, Chatou, Paris, France, 2013. ISBN 978-1-138-00085-8.
- [2] Hydropower & Dams: New developments and international experience with Piano Key Weirs. *The International Journal on Hydropower and Dams*, vol. 2014, no. 1, pp. 113–124, 2014.
- [3] Pfister, M. and Schleiss, A.J.: Estimation of A-type Piano Key weir rating curve. In: *Proceedings of the 2nd International Workshop on Labyrinth and Piano Key Weirs - PKW2013*, pp. 139–147. CRC Press, Taylor & Francis Group, 2013.
- [4] Ettema, R. (ed.): *Hydraulic modelling: Concepts and Practices*. ASCE, 2000.
- [5] Philips, M.A. and Lesleighter, E.J.: Piano Key Weir spillway: Upgrade option for a major dam. In: *Proceedings of the 2nd International Workshop on Labyrinth and Piano Key Weirs - PKW2013*, pp. 159–168. CRC Press, Taylor & Francis Group, 2013.
- [6] Lempérière, F. and Ouamane, A.: The Piano Keys Weir: a new cost-effective solution for spillways. *The International Journal on Hydropower and Dams*, vol. 10, no. 5, pp. 144–149, 2003. Available at: <http://www.hydrocoop.org/piano-keys-weir-a-new-cost-effective-solution-for-spillways/>
- [7] Crookston, B.M. and Tullis, B.P.: Hydraulic characteristics of labyrinth weirs. In: *Proceedings of the International Conference on Labyrinth and Piano Key Weirs - PKW2011*. CRC Press, Taylor & Francis Group, 2011.
- [8] Machiels, O., Piroton, M., Archambeau, P., Dewals, B.J. and Erpicum, S.: Experimental parametric study and design of Piano Key Weirs. *Journal of Hydraulic Research*, vol. 52, no. 3, pp. 326–335, mar 2014. ISSN 0022-1686.
- [9] Kabiri-Samani, A. and Javaheri, A.: Discharge coefficients for free and submerged flow over Piano Key weirs. *Journal of Hydraulic Research*, vol. 50, no. 1, pp. 114–120, feb 2012. ISSN 0022-1686.
- [10] Hydrocoop, Lempérière, F., Ouamane, A. and Vigny, J.P.: Piano Keys Weirs (PK weirs) could be used for most African spillways. 2013. Available at: <http://www.hydrocoop.org/piano-keys-weirs-could-be-used-for-most-african-spillways/>
- [11] Schleiss, A.J.: From Labyrinth to Piano Key Weirs - A historical review. In: *Proceedings of the International Conference on Labyrinth and Piano Key Weirs - PKW2011*, pp. 3–15. CRC Press, Taylor & Francis Group, 2011. ISBN 9780415682824.
- [12] Botha, A.J., Fitz, I.P., Moore, A.J., Mulder, F.E. and Van Deventer, N.J.: Application of the Piano Key Weir spillway in the Republic of South Africa. In: *Proceedings of the 2nd International Workshop on Labyrinth and Piano Key Weirs - PKW2013*, pp. 185–194. 2013.
- [13] Labyrinth and Piano Key Weirs - PKW 2011. In: Erpicum, S., Laugier, F., Boillat, J.-L., Piroton, M., Reverchon, B. and Schleiss, A.J. (eds.), *Proceedings of the International Conference on Labyrinth and Piano Key Weirs - PKW2011*, p. 297. CRC Press/Balkema, Liège, Belgium, 2011. ISBN 978-0-415-68282-4.
- [14] Paxson, G., Tullis, B.P. and Hertel, D.J.: Comparison of Piano Key Weirs with labyrinth and gates spillways: Hydraulics, cost constructability and operations. In: *Proceedings of the 2nd International Workshop on Labyrinth and Piano Key Weirs - PKW2013*, pp. 123–130. CRC Press, Taylor & Francis Group, 2013.

- [15] Laugier, F., Vermeulen, J. and Lefebvre, V.: Overview of Piano Key Weirs experience developed at EDF during the past few years. In: *Proceedings of the 2nd International Workshop on Labyrinth and Piano Key Weirs - PKW2013*, pp. 213–226. CRC Press, Taylor & Francis Group, 2013.
- [16] Belaabed, F. and Ouamane, A.: Submerged flow regimes of Piano Key Weir. In: *Proceedings of the 2nd International Workshop on Labyrinth and Piano Key Weirs - PKW2013*, pp. 85–92. CRC Press, Taylor & Francis Group, 2013.
- [17] Cicero, G.-M. and Delisle, J.R.: Discharge characteristics of Piano Key weirs under submerged flow. In: *Proceedings of the 2nd International Workshop on Labyrinth and Piano Key Weirs - PKW2013*, pp. 101–109. CRC Press, Taylor & Francis Group, 2013.
- [18] Pfister, M., Schleiss, A.J. and Tullis, B.P.: Effect of driftwood on hydraulic head on Piano Key Weirs. In: *Proceedings of the 2nd International Workshop on Labyrinth and Piano Key Weirs - PKW2013*, pp. 255–264. CRC Press, Taylor & Francis Group, 2013.
- [19] Pfister, M. and Schleiss, A.J.: Discharge capacity of PK-Weirs considering floating wooden debris. In: *Proceedings of the 25th Int. congress on large dams, ICOLD, EPFL-CONF-210189*, pp. 52–53. 2015.
- [20] Ackers, J.C., Bennett, F.C.J., Scott, T.A. and Karunaratne, G.: Raising the bellmouth spillway at Black Esk reservoir using Piano Key Weirs. In: *Proceedings of the 2nd International Workshop on Labyrinth and Piano Key Weirs - PKW2013*, pp. 235–242. 2013.
- [21] Pralong, J., Vermeulen, J., Blancher, B., Laugier, F., Erpicum, S., Machiels, O., Pirotton, M., Boillat, J.-L., Leite Ribeiro, M. and Schleiss, A.J.: A naming convention for the Piano Key Weirs geometrical parameters. In: *Proceedings of the International Conference on Labyrinth and Piano Key Weirs - PKW2011*, pp. 271–278. CRC Press, Taylor & Francis Group, 2011. ISBN 978-0-415-68282-4.
- [22] Leite Ribeiro, M., Pfister, M. and Schleiss, A.J.: Overview of Piano Key weir prototypes and scientific model investigations. In: *Proceedings of the 2nd International Workshop on Labyrinth and Piano Key Weirs - PKW2013*, pp. 273–281. CRC Press, Taylor & Francis Group, 2013.
- [23] Lefebvre, V., Vermeulen, J. and Blancher, B.: Influence of geometrical parameters on PK-weirs discharge with 3D numerical analysis. In: *Proceedings of the 2nd International Workshop on Labyrinth and Piano Key Weirs - PKW2013*, pp. 49–56. CRC Press, Taylor & Francis Group, 2013.
- [24] Machiels, O.: *Experimental study of the hydraulic behaviour of Piano Key Weirs*. PhD dissertation, University of Liège, 2012.
- [25] ICOLD: *Cost Savings in Dams*. ICOLD Bulletin 144. 2010.
- [26] Lempérière, F., Vigny, J.P. and Ouamane, A.: General comments on labyrinths and piano key weirs - the past and present. In: *Proceedings of the International Conference on Labyrinth and Piano Key Weirs - PKW2011*, pp. 17–24. CRC Press, Taylor & Francis Group, 2011.
- [27] Erpicum, S., Archambeau, P., Pirotton, M. and Dewals, B.J.: Geometric parameters influence on Piano Key Weir hydraulic performances. In: *5th Int. Symp. on Hydraulic Structures*. The University of Queensland, 2014.
- [28] Leite Ribeiro, M., Bieri, M., Boillat, J.-L., Schleiss, A.J., Singhal, G. and Sharma, N.: Discharge Capacity of Piano Key Weirs. *Journal of Hydraulic Engineering*, vol. 138, no. 2, pp. 199–203, feb 2012. ISSN 0733-9429.
- [29] Ribeiro, M.L., Pfister, M., Schleiss, A.J. and Boillat, J.-L.: Hydraulic design of A-type Piano Key Weirs. *Journal of Hydraulic Research*, vol. 50, no. 4, pp. 400–408, aug 2012. ISSN 0022-1686.
- [30] Pfister, M. and Schleiss, A.J.: Comparison of hydraulic design equations for A-Type Piano Key Weirs. In: *Proceedings of the International Conference on Water Storage and Hydropower Development for Africa (AFRICA 2013)*, pp. 1–8. Addis Ababa, Ethiopia, 2013.

- [31] Hager, W.H. and Schleiss, A.J.: *Constructions Hydrauliques - Ecoulements stationnaires [Hydraulic structures - steady flow]*. Press Polytechniques et Universitaires Romandes, Lausanne, Switzerland, 2009. ISBN 978-2-88074-746-6.
- [32] Blancher, B., Montarros, F. and Laugier, F.: Hydraulic Comparison Between Piano Key Weirs and Labyrinth Spillways. In: *Proceedings of the International Conference on Labyrinth and Piano Key Weirs - PKW2011*, pp. 141–150. CRC Press, Taylor & Francis Group, 2011.
- [33] Anderson, R.M. and Tullis, B.P.: Piano Key Weir hydraulics and labyrinth weir comparison. *Journal of Irrigation and Drainage Engineering*, vol. 139, no. 3, pp. 246–253, 2013.
- [34] Cicero, G.-M., Delisle, J.R., Lefebvre, V. and Vermeulen, J.: Experimental and numerical study of the hydraulic performance of a trapezoidal Piano Key Weir. In: *Proceedings of the 2nd International Workshop on Labyrinth and Piano Key Weirs - PKW2013*, pp. 265–272. CRC Press, Taylor & Francis Group, 2013.
- [35] Mehboudi, A., Attari, J. and Hosseini, S.A.: Flow regimes over trapezoidal Piano Key Weirs. In: *Labyrinth and Piano Key Weirs III: Proceedings of the 3rd International Workshop on Labyrinth and Piano Key Weirs (PKW 2017), February 22-24, 2017, Qui Nhon, Vietnam*, p. 65. CRC Press, 2017.
- [36] Safarzadeh, A. and Noroozi, B.: 3D Hydrodynamics of Trapezoidal Piano Key Spillways. *International Journal of Civil Engineering*, vol. 15, no. 1, pp. 89–101, jan 2017. ISSN 2383-3874.
- [37] Machiels, O., Erpicum, S., Dewals, B.J., Archambeau, P. and Pirotton, M.: Experimental observation of flow characteristics over a Piano Key Weir. *Journal of Hydraulic Research*, vol. 49, no. 3, pp. 359–366, jun 2011. ISSN 0022-1686.
- [38] Aelbrecht, D.: Innovation and Research serving an industrial Hydraulic Safety Project: upgrading spillway systems at EDF dams. 2014.
- [39] Pralong, J., Montarros, F., Blancher, B. and Laugier, F.: A sensitivity analysis of Piano Key Weirs geometrical parameters based on 3D numerical modeling. In: *Proceedings of the International Conference on Labyrinth and Piano Key Weirs - PKW2011*, pp. 133–139. CRC Press, Taylor & Francis Group, 2011.
- [40] Machiels, O., Erpicum, S., Archambeau, P., Dewals, B.J. and Pirotton, M.: Parapet Wall Effect on Piano Key Weir Efficiency. *Journal of Irrigation and Drainage Engineering*, vol. 139, no. 6, pp. 506–511, jun 2013. ISSN 0733-9437.
- [41] Anderson, R.M.: *Piano key weir head discharge relationships*. Master's Thesis, Utah State University, 2011.
- [42] Leite Ribeiro, M., Boillat, J.-L., Schleiss, A.J., Le Doucen, O. and Laugier, F.: Experimental parametric study for hydraulic design of PKWs. In: *Proceedings of the International Conference on Labyrinth and Piano Key Weirs - PKW2011*, pp. 183–190. CRC Press, Taylor & Francis Group, 2011. ISBN ISBN 978-0-415-68228-4.
- [43] Vermeulen, J., Laugier, F., Faramond, L. and Gille, C.: Lessons learnt from design and construction of EDF first Piano Key Weirs. In: *Proceedings of the International Conference on Labyrinth and Piano Key Weirs - PKW2011*, pp. 215–224. CRC Press, Taylor & Francis Group, 2011.
- [44] Taylor, Z.J., Gurka, R. and Kopp, G.A.: Effects of leading edge geometry on the vortex shedding frequency of an elongated bluff body at high Reynolds numbers. *Journal of Wind Engineering and Industrial Aerodynamics*, vol. 128, pp. 66–75, may 2014. ISSN 01676105.
- [45] Ribeiro, M.L., Boillat, J.-L., Schleiss, A.J. and Laugier, F.: Coupled spillway devices and energy dissipation system at St-Marc Dam (France). In: *Proceedings of the International Conference on Labyrinth and Piano Key Weirs - PKW2011*, pp. 113–121. CRC Press, Taylor & Francis Group, 2011.
- [46] Bieri, M. and Jenzer, J.: Large scale particle image velocimetry applications for complex free surface flows in river and dam engineering. In: *Proceedings of 33rd IAHR Congress, Vancouver, Canada*, pp. 604–611. 2009.

- [47] Anderson, R.M. and Tullis, B.P.: Piano Key Weir: Reservoir versus Channel Application. *Journal of Irrigation and Drainage Engineering*, vol. 138, no. 8, pp. 773–776, aug 2012. ISSN 0733-9437.
- [48] Cicero, G.-M. and Delisle, J.R.: Effects of the crest shape on the discharge efficiency of a Type A Piano Key weir. In: *Proceedings of the 2nd International Workshop on Labyrinth and Piano Key Weirs - PKW2013*, pp. 41–48. CRC Press, Taylor & Francis Group, 2013.
- [49] Erpicum, S. and Daux, C.: Energy dissipation on a stepped spillway downstream of a Piano Key Weir - Experimental study. In: *Proceedings of the International Conference on Labyrinth and Piano Key Weirs - PKW2011*. CRC Press, Taylor & Francis Group, 2011.
- [50] Machiels, O., Erpicum, S., Archambeau, P., Dewals, B.J. and Piroton, M.: Piano Key Weir preliminary design method - application to a new dam project. In: *Proceedings of the International Conference on Labyrinth and Piano Key Weirs - PKW2011*, pp. 199–206. CRC Press, Taylor & Francis Group, 2011.
- [51] Bishop, R.E.D.: *Vibration*. 1st edn. CUP Archive, 1965. ISBN 0521296390.
- [52] Naudascher, E. and Rockwell, D.: *Flow-Induced Vibrations: An Engineering Guide*. Courier Corporation, 2012. ISBN 0486136132.
- [53] Chakrabarti, S.K.: *The Theory and Practice of Hydrodynamics and Vibration*. World Scientific, 2002. ISBN 9810249225.
- [54] Mercer, C., Davies, D., Mason, C., Wren, J., Lincoln, A. and Donegan, M.: *PROSIG: Noise & Vibration Measurement Handbook*. 2016.
- [55] ASTM E1049-85: Standard Practices for Cycle Counting in Fatigue Analysis. Tech. Rep., ASTM, 2017.
- [56] Papadimitriou, C., Fritzen, C.-P., Kraemer, P. and Ntotsios, E.: Fatigue predictions in entire body of metallic structures from a limited number of vibration sensors using Kalman filtering. *Structural Control and Health Monitoring*, vol. 18, no. 5, pp. 554–573, aug 2011. ISSN 15452255.
- [57] Stotera, D.: STOFLO. 2015.  
Available at: <http://stotera.com/stoflo/>
- [58] Dowling, N.E.: Mean stress effects in stress-life and strain-life fatigue. Tech. Rep., SAE Technical Paper, 2004.
- [59] Hiatt, J.: What is a SN-Curve? 2016.  
Available at: <https://community.plm.automation.siemens.com/t5/Testing-Knowledge-Base/What-is-a-SN-Curve/ta-p/355935>
- [60] Fujita, K., Ito, T., Kodama, T., Eguchi, Y. and Yamamoto, K.: Flow-Induced Vibration of a Flexible Weir Due to Fluid Discharge; Effect of Weir Stiffness. *Journal of Fluids and Structures*, vol. 10, no. 1, pp. 79–98, jan 1996. ISSN 08899746.
- [61] Anami, K., Ishii, N. and Knisely, C.W.: Pressure induced by vertical planar and inclined curved weir-plates undergoing streamwise rotational vibration. *Journal of Fluids and Structures*, vol. 29, pp. 35–49, feb 2012. ISSN 08899746.
- [62] Crookston, B.M., Anderson, A., Shearin-Feimster, L. and Tullis, B.P.: Mitigation investigation of flow-induced vibrations at a rehabilitated spillway. *5th IAHR International Symposium on Hydraulic Structures*, pp. 1–8, 2014.
- [63] Naudascher, E.: On identification and preliminary assessment of sources of flow-induced vibrations. In: Naudascher, E. and Rockwell, D. (eds.), *Practical experiences with flow-induced vibrations*, pp. 520–522. Springer, Karlsruhe, Germany, 1980.
- [64] Cebeci, T.: *Analysis of turbulent flows*. Elsevier, 2004. ISBN 9780080443508.

- [65] Koziół, A.P.: Three-Dimensional Turbulence Intensity in a Compound Channel. *Journal of Hydraulic Engineering*, vol. 139, no. 8, pp. 852–864, aug 2013.
- [66] Munson, B.R., Rothmayer, A.P. and Okiishi, T.H.: *Fundamentals of Fluid Mechanics, 7th Edition*. John Wiley & Sons, Incorporated, 2012. ISBN 1118214595.
- [67] Falvey, H.T.: Bureau of Reclamation experience with flow-induced vibrations. In: Naudascher, E. and Rockwell, D. (eds.), *IAHR Symposium on Practical Experiences with Flow-Induced Vibrations*, pp. 386–398. Springer, Karlsruhe, Germany, 1980.
- [68] Denys, F.J.M. and Basson, G.R.: Transient Hydrodynamics of Piano Key Weirs. In: *7th International Symposium on Hydraulic Structures*. IAHR, 2018.
- [69] Tenaud, C., Podvin, B., Fraigneau, Y. and Daru, V.: On wall pressure fluctuations and their coupling with vortex dynamics in a separated-reattached turbulent flow over a blunt flat plate. *International Journal of Heat and Fluid Flow*, vol. 61, no. Part B, pp. 730–748, 2016. ISSN 0142-727X.
- [70] Langari, M. and Yang, Z.: Numerical study of the primary instability in a separated boundary layer transition under elevated free-stream turbulence. *Physics of Fluids*, vol. 25, no. 7, p. 74106, 2013.
- [71] Bruno, L., Fransos, D., Coste, N. and Bosco, A.: 3D flow around a rectangular cylinder: A computational study. *Journal of Wind Engineering and Industrial Aerodynamics*, vol. 98, no. 6-7, pp. 263–276, jun 2010. ISSN 01676105.
- [72] Kiya, M. and Sasaki, K.: Structure of a turbulent separation bubble. *Journal of Fluid Mechanics*, vol. 137, pp. 83–113, apr 1983. ISSN 0022-1120.
- [73] Langari, M.: *Large eddy simulation of separated boundary layer transition under free-stream turbulence*. Ph.D. thesis, University of Sussex, 2014.
- [74] Hillier, R. and Cherry, N.: The effects of stream turbulence on separation bubbles. *Journal of Wind Engineering and Industrial Aerodynamics*, vol. 8, no. 1-2, pp. 49–58, jul 1981. ISSN 01676105.
- [75] Kiya, M. and Sasaki, K.: Free-stream turbulence effects on a separation bubble. *Journal of Wind Engineering and Industrial Aerodynamics*, vol. 14, no. 1-3, pp. 375–386, 1983. ISSN 0167-6105.
- [76] Cherry, N., Hillier, R. and Latour, M.: The unsteady structure of two-dimensional separated-and-reattaching flows. *Journal of Wind Engineering and Industrial Aerodynamics*, vol. 11, no. 1-3, pp. 95–105, may 1983. ISSN 01676105.
- [77] Tafti, D.K. and Vanka, S.P.: A numerical study of flow separation and reattachment on a blunt plate. *Physics of Fluids A*, vol. 3, no. 7, p. 1749, 1991. ISSN 08998213.
- [78] Tafti, D.K. and Vanka, S.P.: A three-dimensional numerical study of flow separation and reattachment on a blunt plate. *Physics of Fluids A*, vol. 3, no. 12, p. 2887, 1991. ISSN 08998213.
- [79] Yang, Z. and Abdalla, I.E.: On coherent structures in a separated/reattached flow. *WSEAS Transactions on Fluid Mechanics*, vol. 3, no. 2, pp. 143–153, 2008.
- [80] Yang, Z. and Abdalla, I.E.: Effects of free-stream turbulence on a transitional separated-reattached flow over a flat plate with a sharp leading edge. *International Journal of Heat and Fluid Flow*, vol. 30, no. 5, pp. 1026–1035, 2009. ISSN 0142-727X.
- [81] Sicot, C., Perrin, R., Tran, T.T. and Borée, J.: Wall pressure and conditional flow structures downstream of a reattaching flow region. *International Journal of Heat and Fluid Flow*, vol. 35, no. Supplement C, pp. 119–129, 2012. ISSN 0142-727X.
- [82] Pearson, D.S., Goulart, P.J. and Ganapathisubramani, B.: Turbulent separation upstream of a forward-facing step. *Journal of Fluid Mechanics*, vol. 724, pp. 284–304, 2013.
- [83] Lamballais, E., Silvestrini, J. and Laizet, S.: Influence of Rounded Leading Edge on the Flow Separation BY DNS. In: *20th International Congress of Mechanical Engineering COBEM*. 2009.

- [84] Kiya, M. and Sasaki, K.: Structure of large-scale vortices and unsteady reverse flow in the reattaching zone of a turbulent separation bubble. *Journal of Fluid Mechanics*, vol. 154, pp. 463–491, apr 1985. ISSN 0022-1120.
- [85] Castro, I.P. and Epik, E.: Boundary layer development after a separated region. *Journal of Fluid Mechanics*, vol. 374, pp. 91–116, 1998.
- [86] Hoarau, C., Borée, J., Laumonier, J. and Gervais, Y.: Analysis of the wall pressure trace downstream of a separated region using extended proper orthogonal decomposition. *Physics of Fluids*, vol. 18, no. 5, pp. 55107–1–12, 2006.
- [87] Saathoff, P.J. and Melbourne, W.H.: Effects of free-stream turbulence on surface pressure fluctuations in a separation bubble. *Journal of Fluid Mechanics*, vol. 337, pp. 1–24, 1997.
- [88] Tran, T.T., Perrin, R., Manceau, R., Boree, J. and Jordan, P.: Flow sources of wall pressure fluctuations resolved by DDES in a reattaching flow region. 2013.
- [89] Suksangpanomrung, A., Djalali, N. and Moinat, P.: Large-eddy simulation of separated flow over a bluff rectangular plate. *International Journal of Heat and Fluid Flow*, vol. 21, no. 5, pp. 655–663, oct 2000. ISSN 0142727X.
- [90] Dabling, M.R.: *Nonlinear Weir Hydraulics*. Master's thesis, Utah State University, 2014.
- [91] Crookston, B.M. and Tullis, B.P.: Hydraulic Design and Analysis of Labyrinth Weirs. II: Nappe Aeration, Instability, and Vibration. *Journal of Irrigation and Drainage Engineering*, vol. 139, no. 5, pp. 371–377, oct 2012.
- [92] Vermeulen, J., Lassus, C. and Pinchard, T.: Design of a Piano Key Weir aeration network. In: *Labyrinth and Piano Key Weirs III: Proceedings of the 3rd International Workshop on Labyrinth and Piano Key Weirs (PKW 2017), February 22-24, 2017, Qui Nhon, Vietnam*, pp. 127–133. CRC Press, 2017.
- [93] Lodomez, M., Crookston, B.M., Tullis, B.P., Pirotton, M. and Erpicum, S.: Nappe Vibration Mitigation Techniques for Free-overfall Structures. In: *6th International Symposium on Hydraulic Structures*, pp. 342–349. Portland, OR, 2016.
- [94] Lodomez, M., Pirotton, M., Dewals, B., Archambeau, P. and Erpicum, S.: Nappe Oscillations on Free-Overfall Structures: Experimental Analysis. *Journal of Hydraulic Engineering*, vol. 144, no. 3, 2018.
- [95] Anderson, A.: *Causes and Countermeasures for Nappe Oscillation: An Experimental Approach*. Master of Science, Utah State University, 2014.
- [96] El Hami, A. and Radi, B.: *Fluid-Structure Interactions and Uncertainties*. John Wiley and Sons, Inc., Hoboken, NJ, USA, feb 2017. ISBN 9781119388937.
- [97] Bazilevs, Y., Takizawa, K. and Tezduyar, T.E.: Challenges and directions in computational fluid structure interaction. *Mathematical Models and Methods in Applied Sciences*, vol. 23, no. 2, pp. 215–221, 2013.
- [98] Parker, R. and Welsh, M.C.: Effects of sound on flow separation from blunt flat plates. *International Journal of Heat and Fluid Flow*, vol. 4, no. 2, pp. 113–127, 1983. ISSN 0142-727X.
- [99] Lu, D., Takizawa, A. and Kondo, S.: Overflow-Induced Vibration of a Weir Coupled with Sloshing in a Downstream Tank. *Journal of Fluids and Structures*, vol. 11, no. 4, pp. 367–393, may 1997. ISSN 08899746.
- [100] Machiels, O., Dewals, B.J., Archambeau, P., Pirotton, M. and Erpicum, S.: An analytical approach for Piano Key Weir hydraulic design. In: *Proceedings of the 2nd International Workshop on Labyrinth and Piano Key Weirs - PKW2013*, pp. 131–138. CRC Press, Taylor & Francis Group, 2013.
- [101] Ho Ta Khanh, M.: The Piano Key Weirs: 15 years of Research and Development - Prospect. In: *Proceedings of the 2nd International Workshop on Labyrinth and Piano Key Weirs - PKW2013*, pp. 3–14. CRC Press, Taylor & Francis Group, 2013.

- [102] ICOLD: Technical Advancements in Spillway Design, 2017.
- [103] Martins, R.: *Recent advances in hydraulic physical modelling*, vol. 165. Springer Science & Business Media, 2012.
- [104] Goring, D.G. and Nikora, V.I.: Despiking Acoustic Doppler Velocimeter Data. *Journal of Hydraulic Engineering*, vol. 128, no. 1, pp. 117–126, jan 2002. ISSN 0733-9429.
- [105] Lodomez, M., Piroton, M., Dewals, B., Archambeau, P. and Erpicum, S.: Frequencies of Nappe Vibration for Free-overfall Structures. In: *6th IAHR IJREWHS*. 2016.
- [106] Lombaard, J.: *Piano Key Weirs: The effect of aeration on the discharge capacity and flow induced vibrations*. Ph.D. thesis, Stellenbosch University, 2019.
- [107] Heller, V.: Scale effects in physical hydraulic engineering models. *Journal of Hydraulic Research*, vol. 49, no. 3, pp. 293–306, jun 2011. ISSN 0022-1686.
- [108] Pfister, M. and Chanson, H.: Scale effects in physical hydraulic engineering models By VALENTIN HELLER, *Journal of Hydraulic Research*, Vol. 49, No. 3 (2011), pp. 293 - 306. *Journal of Hydraulic Research*, vol. 50, no. 2, pp. 244–246, apr 2012. ISSN 0022-1686.
- [109] Ettema, R., Kirkil, G. and Muste, M.: Similitude of large-scale turbulence in experiments on local scour at cylinders. *Journal of Hydraulic Engineering*, vol. 132, no. 1, pp. 33–40, 2006.
- [110] Erpicum, S., Tullis, B.P., Lodomez, M., Archambeau, P., Dewals, B.J. and Piroton, M.: Scale effects in physical piano key weirs models. *Journal of Hydraulic Research*, vol. 54, no. 6, pp. 692–698, nov 2016. ISSN 0022-1686.
- [111] Pfister, M., Erpicum, S., Machiels, O., Schleiss, A.J. and Piroton, M.: Discussion of "Discharge coefficient for free and submerged flow over Piano Key weirs". *Journal of Hydraulic Research*, vol. 50, no. 6, pp. 642–643, dec 2012. ISSN 0022-1686.
- [112] Tullis, B.P., Young, N. and Crookston, B.M.: Physical modeling size-scale effects for labyrinth weirs with half-round crests. In: *Labyrinth and Piano Key Weirs III: Proceedings of the 3rd International Workshop on Labyrinth and Piano Key Weirs (PKW 2017), February 22-24, 2017, Qui Nhon, Vietnam*, p. 185. CRC Press, 2017.
- [113] Novak, P., Guinot, V., Jeffrey, A. and Reeve, D.E.: *Hydraulic modelling: An introduction: Principles, methods and applications*. CRC Press, 2010.
- [114] Geng, B., Zheng, B., Zhang, H. and Liu, H.: Elastic model scale and material for underwater structure of cross-sea bridge. In: *7th International Conference on Asian and Pacific Coasts*, pp. 470–473. Hasanuddin University Press, Bali, Indonesia, 2013. ISBN 978-979-530-125-7.
- [115] Laugier, F., Pralong, J. and Blancher, B.: Influence of structural thickness of sidewalls on PKW spillway discharge capacity. In: *Proceedings of the International Conference on Labyrinth and Piano Key Weirs - PKW2011*, pp. 159–165. CRC Press, Taylor & Francis Group, 2011.
- [116] Wescott, T.: Sampling: what Nyquist didn't say, and what to do about it. *Wescott Design Services, Oregon City, OR*, 2016.
- [117] Parsheh, M., Sotiropoulos, F. and Porté-Agel, F.: Estimation of Power Spectra of Acoustic-Doppler Velocimetry Data Contaminated with Intermittent Spikes. *Journal of Hydraulic Engineering*, vol. 136, no. 6, pp. 368–378, jun 2010. ISSN 0733-9429.
- [118] Welch, P.: The use of fast Fourier transform for the estimation of power spectra: A method based on time averaging over short, modified periodograms. *IEEE Transactions on Audio and Electroacoustics*, vol. 15, no. 2, pp. 70–73, jun 1967. ISSN 0018-9278.
- [119] Nakamura, T., Kaneko, S., Inada, F., Kato, M., Ishihara, K., Nishihara, T., Mureithi, N.W. and Langthjem, M.A.: *Flow-induced vibrations: Classifications and lessons from practical experiences*. Butterworth-Heinemann, 2013.

- [120] ANSYS: ANSYS® Academic Research Fluent, Release 18.1. 2017.
- [121] ANSYS: ANSYS® Academic Research Mechanical, Release 18.1. 2017.
- [122] Labyrinth and Piano Key Weirs III - PKW 2017. In: Erpicum, S., Laugier, F., Ho Ta Khanh, M. and Pfister, M. (eds.), *Proceedings of the 3rd International Workshop on Labyrinth and Piano Key Weirs - PKW2017*. CRC Press, Taylor & Francis Group, Qui Nhon, Vietnam, 2017.
- [123] Breuer, M., Jovičić, N. and Mazaev, K.: Comparison of DES, RANS and LES for the separated flow around a flat plate at high incidence. *International Journal for Numerical Methods in Fluids*, vol. 41, no. 4, pp. 357 – 388, 2003. ISSN 0271-2091.
- [124] Davoudabadi, P.: The Most Accurate and Advanced Turbulence Capabilities. In: *Confidence by Design Workshop Chicago, IL, June*, vol. 14. 2012.
- [125] CHPC: Centre for High Performance Computing. 2016.  
Available at: <https://www.chpc.ac.za/>
- [126] Anderson, A.E., Ellis, B.J. and Weiss, J.A.: Verification, Validation and Sensitivity Studies in Computational Biomechanics. jun 2007.
- [127] Pinchard, T., Boutet, J.-M. and Cicero, G.-M.: Spillway capacity upgrade at Malarce dam: Design of an additional Piano Key Weir spillway. In: *Proceedings of the International Conference on Labyrinth and Piano Key Weirs - PKW2011*, pp. 233–240. CRC Press, Taylor & Francis Group, 2011.
- [128] Denys, F.J.M., Basson, G.R. and Strasheim, J.: Fluid structure interaction of Piano Key Weirs. In: *Labyrinth and Piano Key Weirs III: Proceedings of the 3rd International Workshop on Labyrinth and Piano Key Weirs (PKW 2017), February 22-24, 2017, Qui Nhon, Vietnam*, p. 119. CRC Press, 2017.
- [129] Cicero, G.-M., Menon, J., Luck, M. and Pinchard, T.: Experimental study of side and scale effects on hydraulic performances of a Piano Key Weir. In: *Proceedings of the International Conference on Labyrinth and Piano Key Weirs - PKW2011*, pp. 167–172. CRC Press, Taylor & Francis Group, 2011.
- [130] Machiels, O., Erpicum, S. and Piroton, M.: Experimental analysis of PKW hydraulic performance and geometric parameters optimum. In: *Proceedings of International Workshop on Piano Key Weir for In-stream Storage and Dam Safety (PKWISD-2012)*, pp. 97–114. CRC Press, Taylor & Francis Group, 2012.
- [131] Pavic, A. and Willford, M.R.: Appendix G: Vibration serviceability of post-tensioned concrete floors. *Post-Tensioned Concrete Floors Design Handbook*, Concrete Society, Slough, UK, pp. 99–107, 2005.
- [132] de Jesus, A.M.P., Matos, R., Fontoura, B.F.C., Rebelo, C., da Silva, L.S. and Veljkovic, M.: A comparison of the fatigue behavior between S355 and S690 steel grades. *Journal of Constructional Steel Research*, vol. 79, pp. 140–150, 2012. ISSN 0143-974X.
- [133] Oberkampf, W.L., Trucano, T.G. and Hirsch, C.: Verification, validation, and predictive capability in computational engineering and physics. *Applied Mechanics Reviews*, vol. 57, no. 5, pp. 345–384, dec 2004. ISSN 0003-6900.
- [134] American Society of Mechanical Engineers: Guide for verification and validation in computational solid mechanics. Tech. Rep., ASME Committee (PT60), 2006.
- [135] R Core Team: *R: A Language and Environment for Statistical Computing*. R Foundation for Statistical Computing, Vienna, Austria, 2017.
- [136] RStudio Team: *RStudio: Integrated Development Environment for R*. RStudio, Inc., Boston, MA, 2016.

# Appendices

## A Piano Key Weir discharge methodologies

The hydraulic behaviour of piano key weirs, and the large number of variables which affect it, is now reasonably well understood despite its complex nature. Several general rating curve formulas have been compiled as described in the subsections below. It should be noted that each of these equations is only applicable within the geometrical limits which were used to compile them. These limits should be respected as some of the resultant rating curves are very sensitive to them [111]. These limits are presented in Table A.1.

### A.1 Standard reference design

It should be noted that the methodologies described below are not definitive. There are a large number of parameters which they do not take into account and furthermore, when used outside realistic ranges for the various parameters their results become erratic. A good estimate of what is realistic concerning a PKW is the standard PKW weir shape which was proposed in ICOLD [25]. This shape was stated as being close to the hydraulic optimum although it probably doesn't reflect an economic optimum [26]. The reference shape is shown below in Figure A.1.

### A.2 Kabiri-Samani and Javaheri 2012

Kabiri-Samani and Javaheri [9], at the Isfahan University of Technology, Iran, conducted scaled physical model tests incorporating PKW Types A, B and C with specific discharge ranges from 25 to 1751/s/m. Both free flow and submerged flow were investigated although the equation below is only applicable to free overflow. The methodology was developed using, and is thus generally applicable to, sharp crested PK weirs. The method is based on the ogee crest overflow equation in the form of Equation (A.2.1),

$$Q_P = \frac{2}{3} C_d W \sqrt{2gH_t^3} \quad (\text{A.2.1})$$

Table A.1: Application limits for the Type-A PKW capacity equations [21]

	$L/W$	$H/P$	$W_i/W_o$	$B/P$	$B_i/B,$ $B_o/B$	$P/W_u$	$B_i/P,$ $B_o/P$
Kabiri-Samani and Javaheri [9]	2.5 – 7.0	0.1 – 0.6	0.33 – 1.22	1.0 – 2.5	0.00 – 0.26	?	?
Ribeiro <i>et al.</i> [29]	3.0 – 7.0	0.1 – 2.8	0.50 – 2.00	1.5 – 4.6	0.20 – 0.40	0.29 – 0.65	0.25 – 4.00
Machiels <i>et al.</i> [8]	4.2 – 5.0	0.1 – 5.0	0.50 – 2.00	1.0 – 6.0	?	0.33 – 2.00	0.00 – 2.67

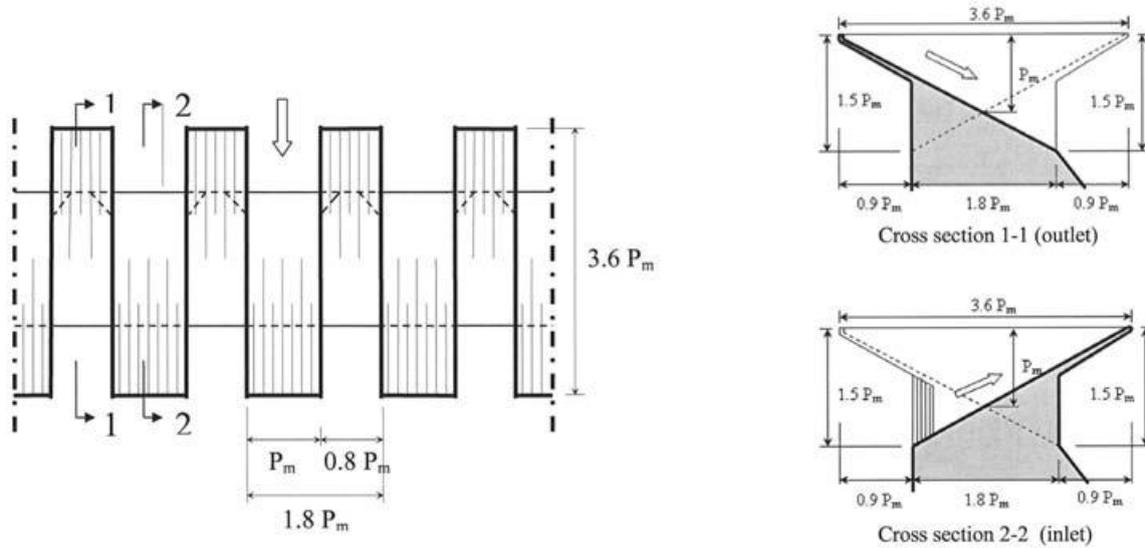


Figure A.1: Reference design of a Type A PKW [26]

with the discharge coefficient,  $C_d$ , being defined as a function of the various relevant geometrical parameters:

$$C_d = \left[ 0.212 \left( \frac{H}{P} \right)^{-0.675} \left( \frac{L}{W} \right)^{0.377} \left( \frac{W_i}{W_o} \right)^{0.426} \left( \frac{B}{P} \right)^{0.306} e^{1.504 \frac{B_o}{B} + 0.093 \frac{B_i}{B}} \right] + 0.606 \quad (\text{A.2.2})$$

### A.3 Leite Ribeiro et al. 2012

Ribeiro, Pfister, Schleiss and Boillat [29] also conducted systematic physical model tests at the Laboratory of Hydraulic Constructions, Ecole Polytechnique Fédérale de Lausanne, Switzerland. Tests were limited to PKW Type-A with free overflow conditions and ranged across specific discharges of 26 to 440 l/s/m. The methodology was developed using, and is thus generally applicable to, PK weirs with half-circular rounded crests. The resultant rating curve is expressed in terms of the discharge enhancement ratio, which is defined as the discharge of the PKW,  $Q_{PKW}$ , relative to that of a linear sharp crested weir,  $Q_s$ .

$$r = \frac{Q_{PKW}}{Q_s} = \frac{Q_{PKW}}{0.42W\sqrt{2gH_t^3}} \quad (\text{A.3.1})$$

The ratio was found to vary primarily as a function of four key parameters, namely, the overflow length,  $L$ , the weir width,  $W$ , the weir height,  $P_i$ , and the overflow depth,  $H$ . Secondary parameters were also incorporated to reflect the contributions of key widths, overhang lengths and parapet walls.

$$r = 1 + 0.24 \left( \frac{(L - W)P_i}{WH} \right)^{0.9} \text{wpba} \quad (\text{A.3.2})$$

where,

- $w = \left(\frac{W_i}{W_o}\right)^{0.05}$  is used to define the influence of the inlet and outlet key ratio,
- $p = \left(\frac{P_o}{P_i}\right)^{0.25}$  to reflect any difference in the height of the inlet and outlet keys,
- $b = \left(0.3 + \frac{B_o + B_i}{B}\right)^{-0.5}$  to specify the influence of the overhang lengths and,
- $a = 1 + \left(\frac{R_o}{P_o}\right)^2$  to stipulate the presence of any parapet walls.

#### A.4 Machiels 2012

As part of his PhD dissertation, at the University of Liège, Belgium, Machiels [24][8] conducted an extensive parametric study limited to free overflow conditions and charged with specific discharges ranging from 13 to 400 l/s/m. The methodology was developed using, and is thus generally applicable to, flat topped PK weirs. The developed analytical discharge formula is based on a summation of the calculated discharge over each of the three elements of a typical PKW, namely the downstream overhang ( $d$ ), the upstream overhang ( $u$ ) and the lateral, side crests ( $s$ ). The unit discharge is then calculated as follows:

$$q = \frac{Q_{PKW}}{W} = q_u \frac{W_o}{W_u} + q_d \frac{W_i}{W_o} + q_s \frac{2B}{W_u} \quad (\text{A.4.1})$$

with  $W_u = W_i + W_o + 2T$  being defined as the width of an individual cycle. Each of the specific discharges over each of the three PKW elements are estimated as follows:

$$q_u = 0.374 \left(1 + \frac{1}{1000H + 1.6}\right) \left[1 + 0.5 \left(\frac{H}{H + P_T}\right)^2\right] \sqrt{2gH_t^3} \quad (\text{A.4.2})$$

$$q_d = 0.445 \left(1 + \frac{1}{1000H + 1.6}\right) \left[1 + 0.5 \left(\frac{H}{H + P}\right)^2\right] \sqrt{2gH_t^3} \quad (\text{A.4.3})$$

$$q_s = 0.41 \left(1 + \frac{1}{833H + 1.6}\right) \left[1 + 0.5 \left(\frac{0.833H}{0.833H + P_e}\right)^2\right] \left(\frac{P_e^\alpha + \beta}{(0.833H + P_e)^\alpha + \beta}\right) K_{W_i} K_{W_o} \sqrt{2gH_t^3} \quad (\text{A.4.4})$$

Note that each of the above three equations defines the weir height differently.

- $P$  is the height of the weir
- $P_T$  is the total upstream height (including that of the dam the PKW is built upon),  $P_T = P + P_d$
- $P_e$  is the mean weir height along the sidewall,  $P_e = P_T \frac{B_o}{B} + \frac{P}{2} \left(1 - \frac{B_o}{B}\right)$

The Greek symbols define the influence of the inlet key slope,  $S_i = \frac{P}{B-B_o}$ , where

- $\alpha = \frac{0.7}{S_i^2} - \frac{3.58}{S_i}$  and
- $\beta = 0.029e^{-\frac{1.446}{S_i}}$

The  $K_{W_i}$  coefficient defines the influence of the variation in flow velocity along the lateral crest. The  $K_{W_o}$  parameter has been incorporated to describe how the effective overflow length over the sidewall is reduced as the overflow nappes in the outlet key interfere with one another and eventually cause local submergence effects. They were refined after the original study [8] and are defined below.

- The inlet key width parameter is equal to

$$K_{W_i} = 1 - \frac{\gamma}{\gamma + W_i^2}$$

where  $\gamma = 0.0037 \left(1 - \frac{W_i}{W_o}\right)$

- The outlet key width parameter is a stepwise function defined as

$$K_{W_o} = 1 \quad \text{for} \quad \frac{H}{W_o} \leq \delta_1$$

$$K_{W_o} = \frac{2}{(\delta_2 - \delta_1)^3} \left(\frac{H}{W_o}\right)^3 - \frac{3(\delta_2 + \delta_1)}{(\delta_2 - \delta_1)^3} \left(\frac{H}{W_o}\right)^2$$

$$+ \frac{6\delta_2\delta_1}{(\delta_2 - \delta_1)^3} \left(\frac{H}{W_o}\right) + \frac{\delta_2^2(\delta_2 - 3\delta_1)}{(\delta_2 - \delta_1)^3} \quad \text{for} \quad \delta_1 \leq \frac{H}{W_o} \leq \delta_2$$

$$K_{W_o} = 0 \quad \text{for} \quad \delta_2 \leq \frac{H}{W_o}$$

where the function's thresholds are defined by

- $\delta_1 = -0.788S_o^{-1.88} + 5$
- $\delta_2 = 0.236S_o^{-1.94} + 5$

## A.5 Comparison

Pfister and Schleiss [30] presented a comparative review of all three of the above methodologies. Careful cognisance of each method's application limitations was accounted for. The various PKW rating curves were applied to an indicative example (with  $L/W = 5$ ) and compared with those of a standard, 100 m wide, ogee and a broad crested weir. The results are shown in Figure A.2.

The comparison reveals that the models deliver similar though not identical results. It has been hypothesised that the differences in the results stem largely from the differences in the crest shape profiles used in each of the methods. The Machiels [24] methodology is the more conservative of the three in that, for a given head, it results in the smallest discharge, or, for a given discharge, it results in a larger head.

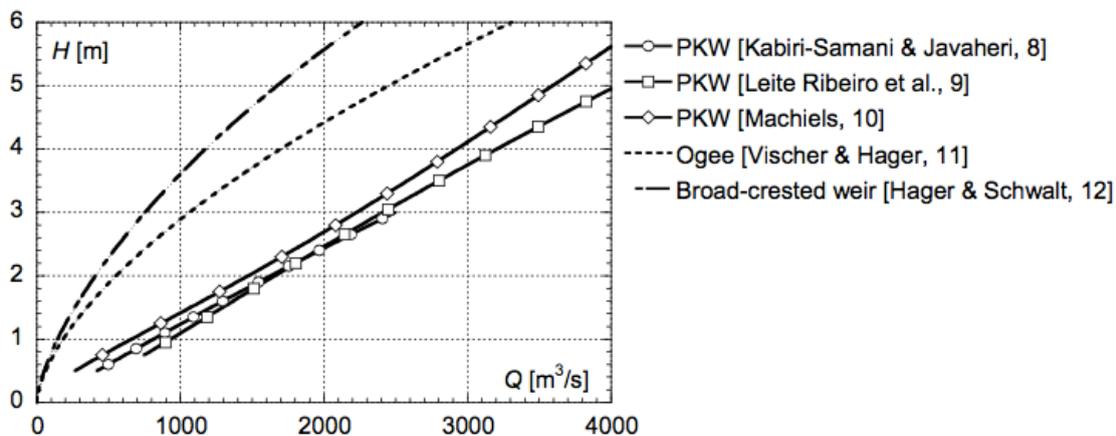


Figure A.2: Comparison of rating curves for PKW, ogee crest and broad crested weirs [30]

It should be noted that several of the above physical tests were conducted in channels and may thus not reflect the different approach flow conditions that are present in open reservoirs [30]. Furthermore, none of the equations allow for the economic optimisation of the weir dimensions, hence additional mathematical or physical modelling investigations are recommended.

## B Experimental details

### B.1 Laboratory flume photos

Photos of the flume are shown in Figures B.1 to B.4

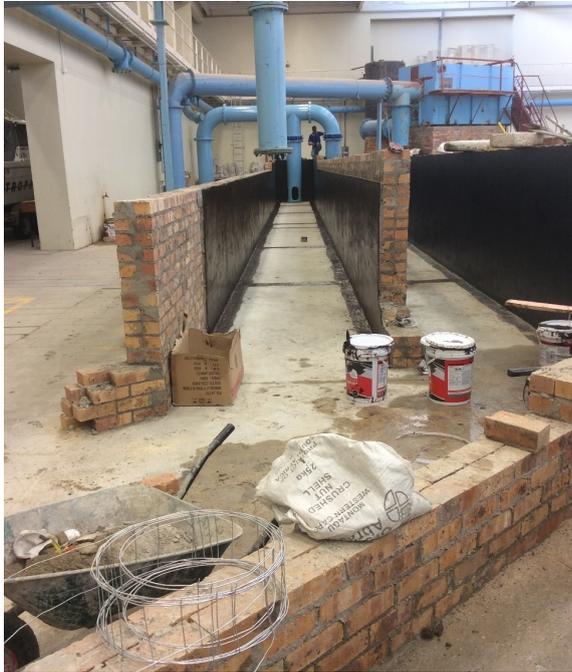


Figure B.1: Empty flume looking upstream



Figure B.2: View of flume with model A



Figure B.3: Upstream stilling basin



Figure B.4: Flume looking downstream

## B.2 Model A

### B.2.1 Testing procedures

The testing procedure which was followed in the experiments involving model A are as follows:

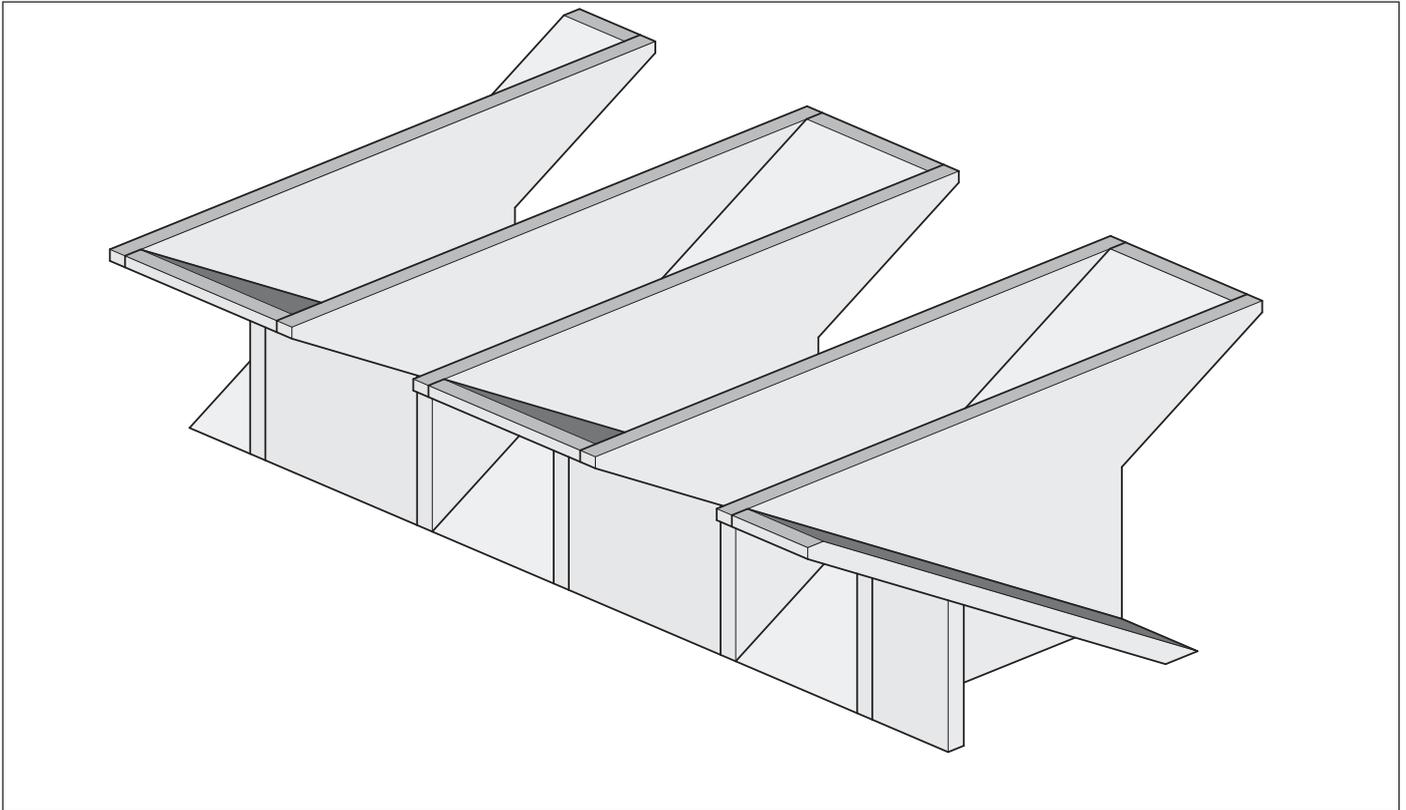
- Measure, survey and record the exact dimensions and position of the weir in the canal, the canal itself and the measurement instruments (using survey equipment).
- Fill the canal and allow the flow to reach a stable equilibrium. Then measure the flow and water level.
- Ensure that the flow upstream of the PKW is uniform and not at all affected by the discharge into the canal via visual observation
- Visually observe and record the flow patterns (using dye wands and video camera equipment)
- Measure and record the water surface elevation (as well as its profile, where relevant) upstream of the inlet key, inside the inlet key, as well midway along the flume's length
- Measure and record the pressure excitation variations on the walls of the PKW (using the installed pressure sensors)
- Measure and record the time-variant velocity field upstream of the PKW as well as in the inlet keys (using rail mounted ADV) at a set number of points which together represent one longitudinal, one transverse and two horizontal cross sections through the flow field.
- Record simultaneous recordings of the pressure undulations on the wall together with the velocity vectors using the ADV. The two data sequences are then reconciled using a strong but temporary disturbance in the flow.

The scenarios which were investigated include:

- A range of flows from 50 l/s to 750 l/s in 50 l/s increments
- Three difference nose types: rectangular (i.e. no nose), triangular (angled at 45 °), circular (with a diameter equal to the width of the upstream portion of the outlet key)
- Two upstream depths, namely the difference between the two installation instances. The first was installed on a sloped pedestal of 7 cm to make room for the foundation bracket to be bolted to the floor. The second was installed on a sloped pedestal of 15 cm to allow for the aeration pipes to extend to the side of the flume.
- The effect of an aeration pipe, to aerate the cavity under the nappe.

### B.2.2 Model A schematics

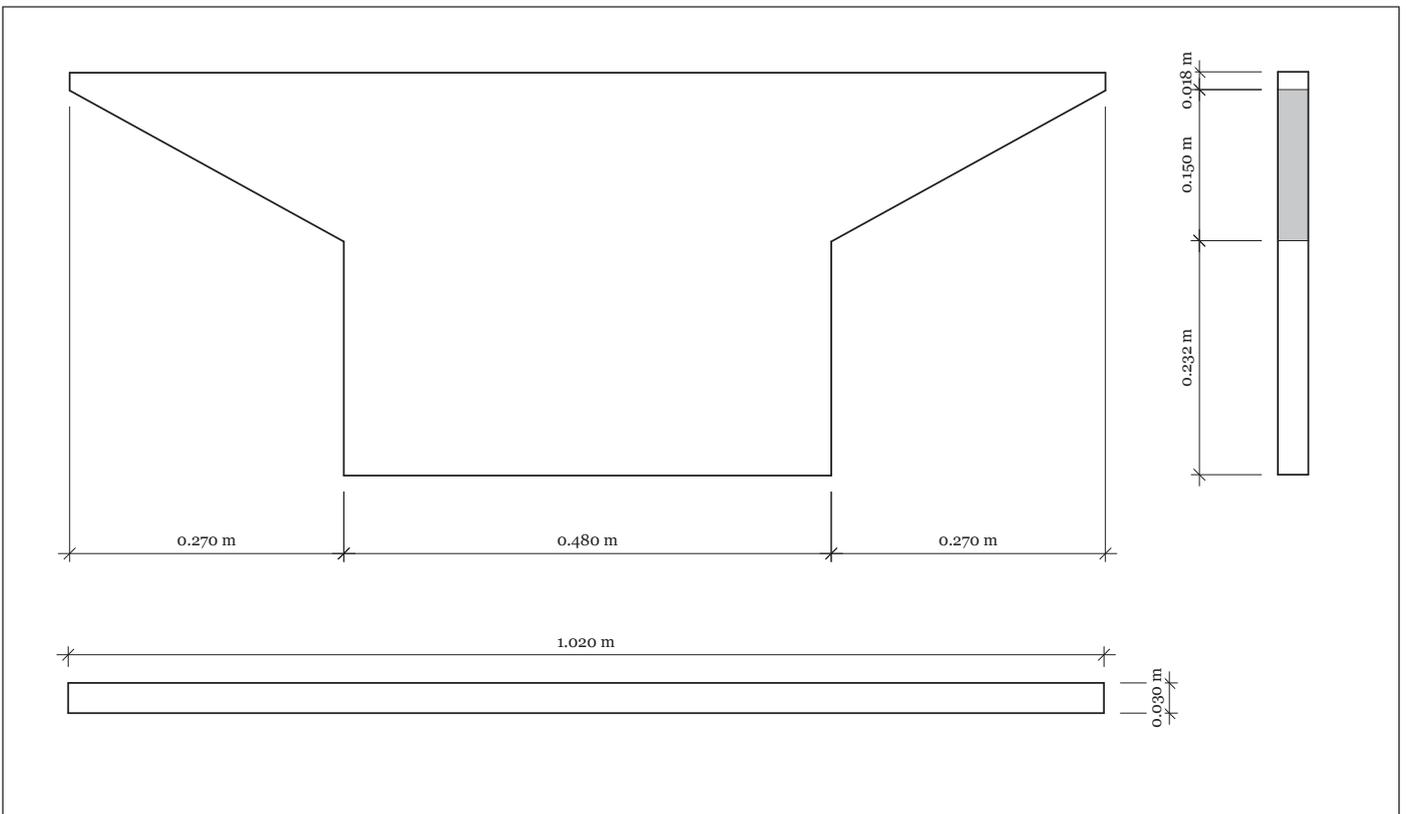
The schematics of model A follow:



Piano Key Weir: Flow-induced vibrations

Model 1

July 6, 2015



Piano Key Weir: Flow-induced vibrations

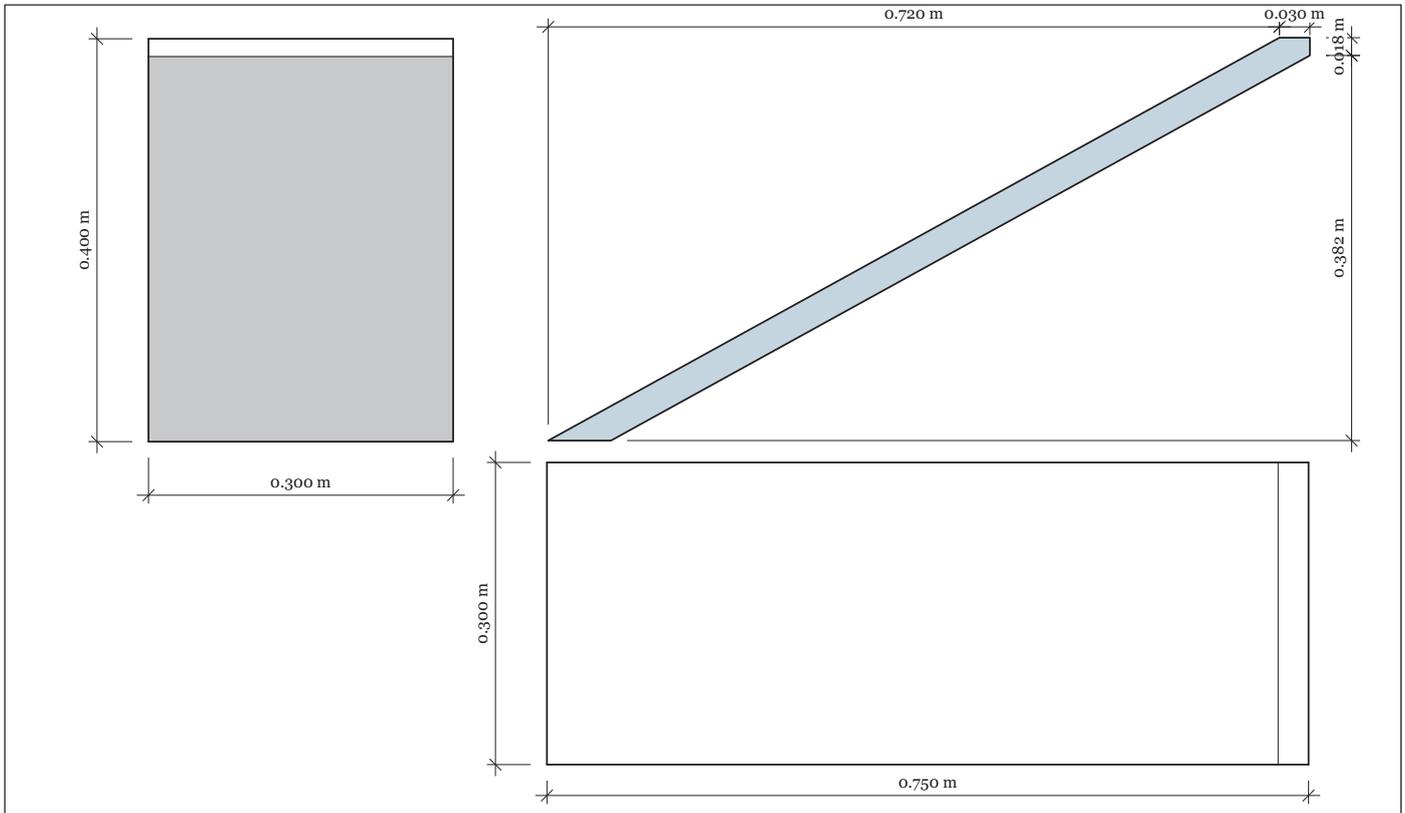
Model 1

Component: Transverse walls

REVISIONS	
DD/MM/YY	REMARKS
1 11/05/2015	For discussion
2	...
3	...
4	...
5	...

01

1A

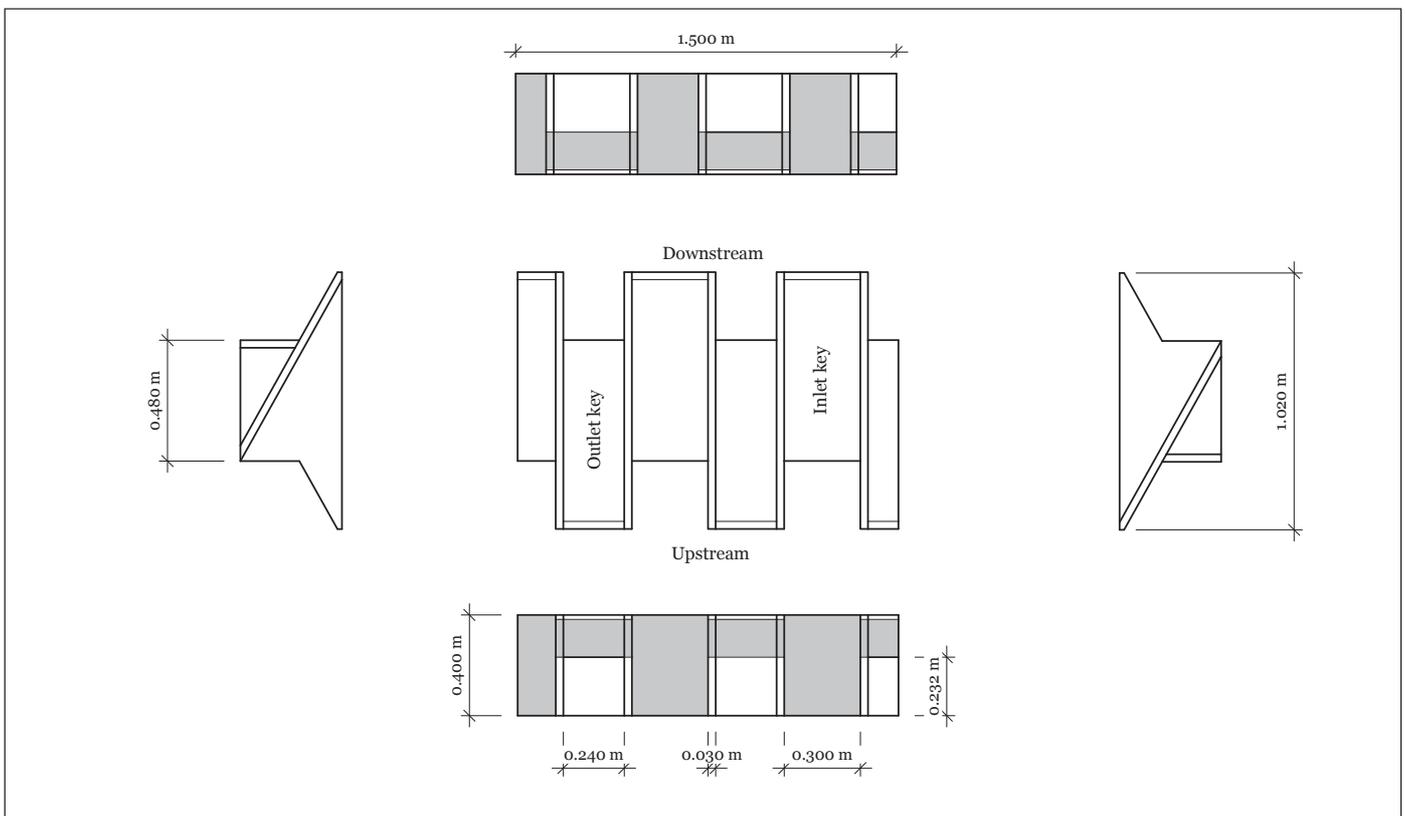


Piano Key Weir: Flow-induced vibrations

Model 1  
Component: Inlet key slope

REVISIONS		
DD/MM/YY	REMARKS	
11/05/2015	For discussion	1
...	...	2
...	...	3
...	...	4
...	...	5

1A 02

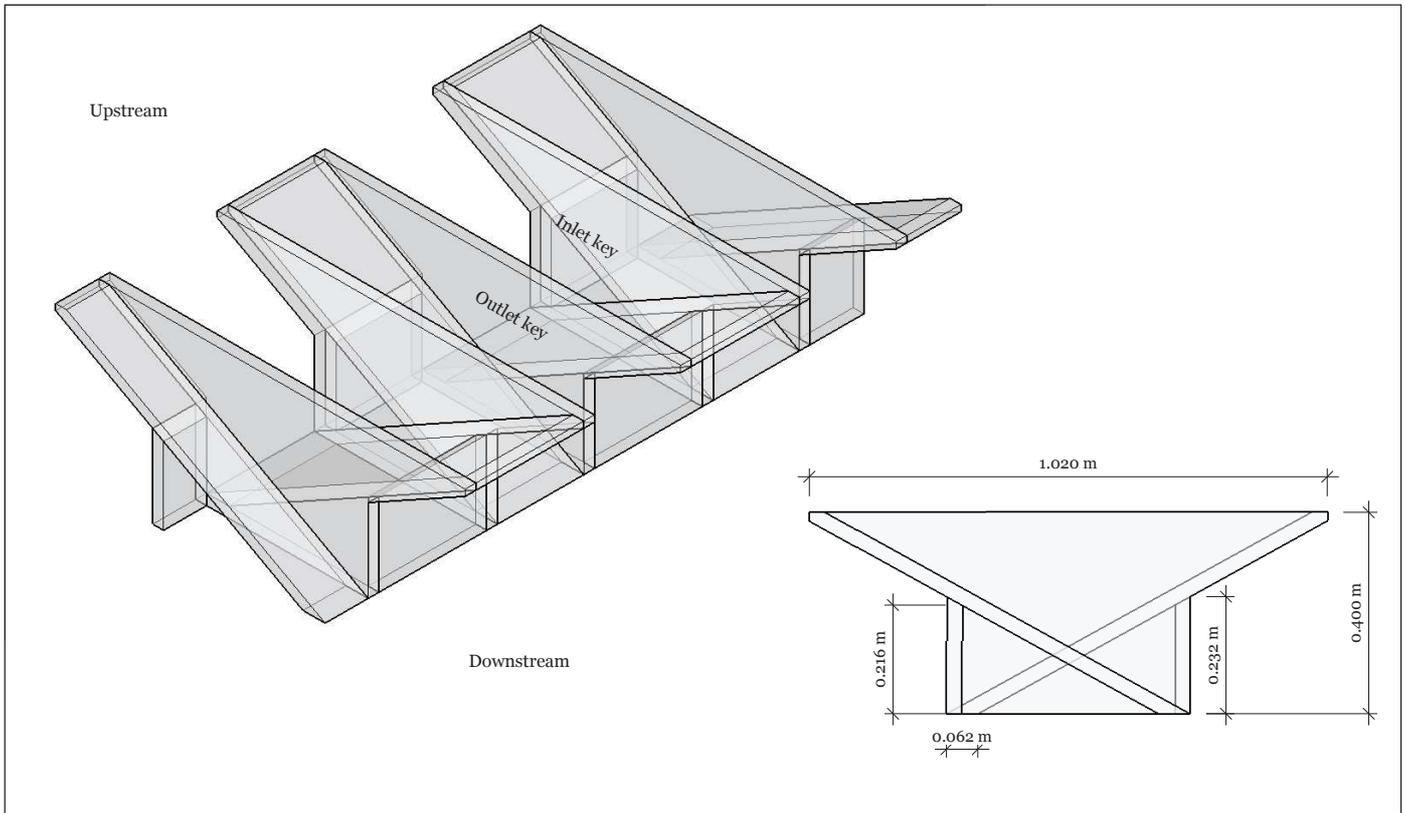


Piano Key Weir: Flow-induced vibrations

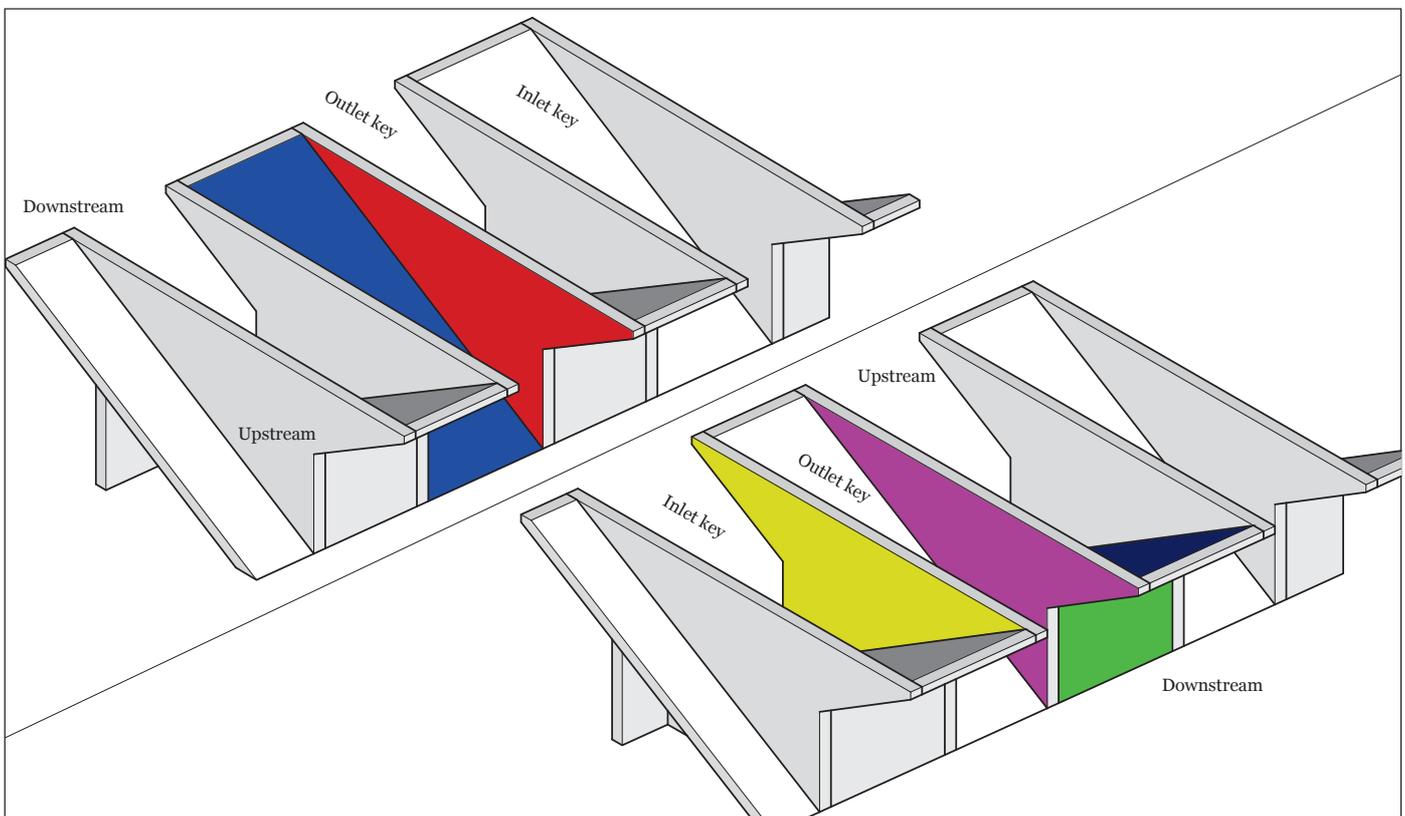
Model 1  
Completed model

REVISIONS		
DD/MM/YY	REMARKS	
11/05/2015	For discussion	1
...	...	2
...	...	3
...	...	4
...	...	5

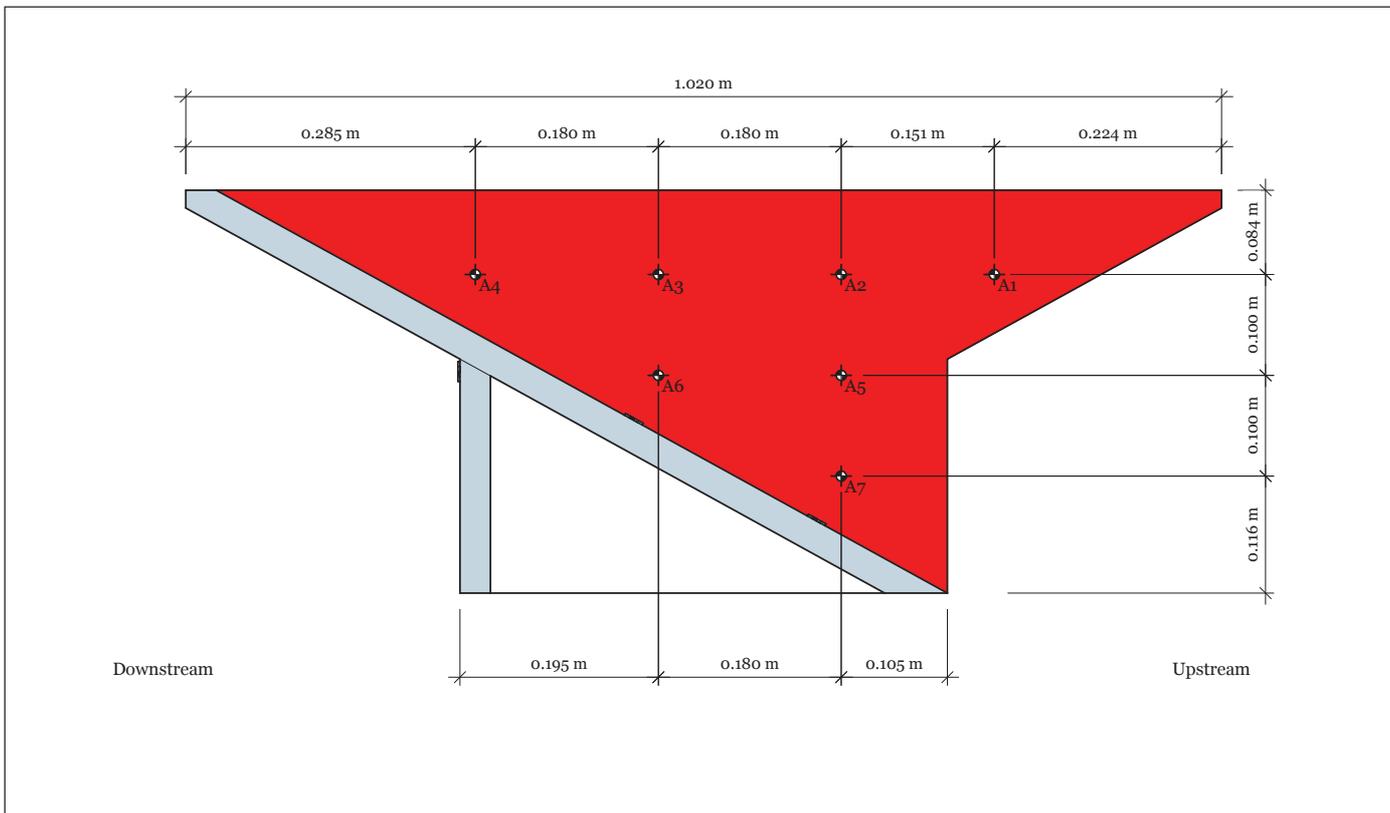
1A 05



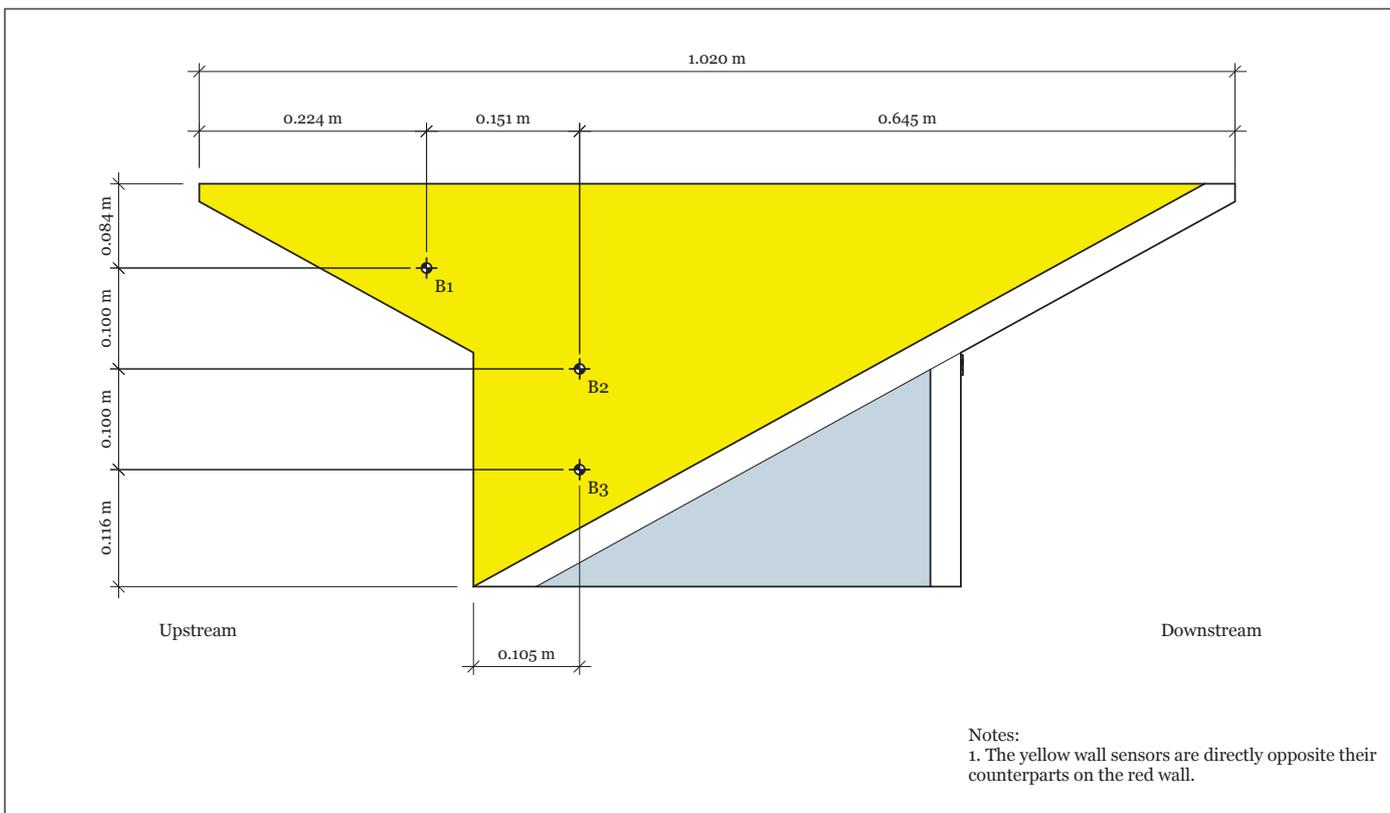
Piano Key Weir: Flow-induced vibrations	Model 1	REVISIONS		1A 07
	Completed model: components	DD/MM/YY	REMARKS	
		11/05/2015	For discussion	
		...	...	
		...	...	
		...	...	
		...	...	



Piano Key Weir: Flow-induced vibrations	Model 1	REVISIONS		1A 08
	Pressure sensor placement: key	DD/MM/YY	REMARKS	
		11/05/2015	For discussion	
		...	...	
		...	...	
		...	...	
		...	...	

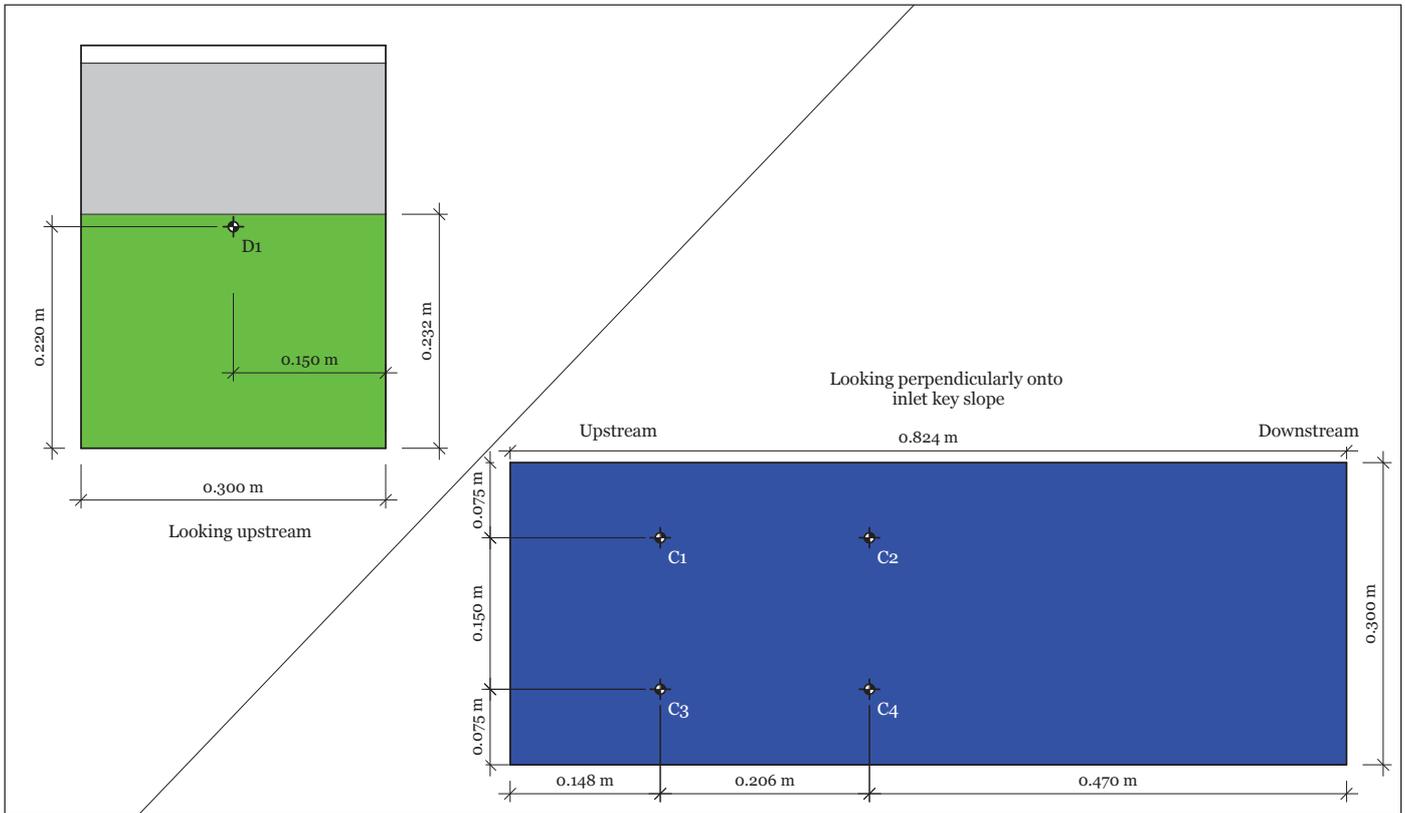


Piano Key Weir: Flow-induced vibrations	Model 1	REVISIONS		09	
		DD/MM/YY	REMARKS		
Pressure sensor placement: inlet key (red wall)		1	11/05/2015	For discussion	1A
		2	---	---	
		3	---	---	
		4	---	---	
		5	---	---	

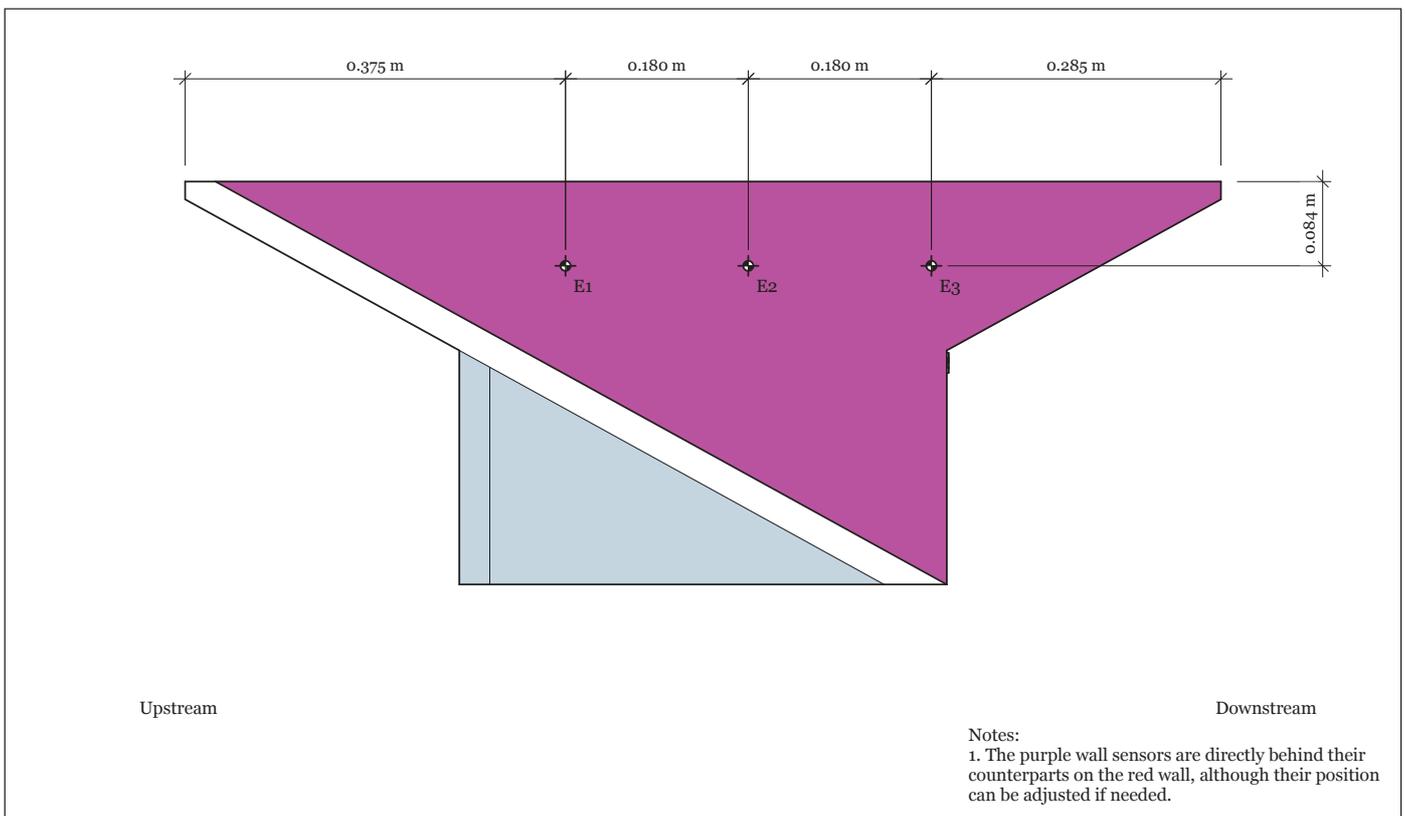


Notes:  
1. The yellow wall sensors are directly opposite their counterparts on the red wall.

Piano Key Weir: Flow-induced vibrations	Model 1	REVISIONS		10	
		DD/MM/YY	REMARKS		
Pressure sensor placement: inlet key (yellow wall)		1	11/05/2015	For discussion	1A
		2	---	---	
		3	---	---	
		4	---	---	
		5	---	---	



<b>Piano Key Weir: Flow-induced vibrations</b>	<b>Model 1</b>	REVISIONS		<b>1A 11</b>
		DD/MM/YY	REMARKS	
	Pressure sensor placement: inlet key (green and blue wall)	11/05/2015	For discussion	<b>1A</b>
		2	...	
		3	...	
		4	...	
		5	...	



<b>Piano Key Weir: Flow-induced vibrations</b>	<b>Model 1</b>	REVISIONS		<b>1A 12</b>
		DD/MM/YY	REMARKS	
	Pressure sensor placement: inlet key (purple wall)	11/05/2015	For discussion	<b>1A</b>
		2	...	
		3	...	
		4	...	
		5	...	

Notes:  
 1. The purple wall sensors are directly behind their counterparts on the red wall, although their position can be adjusted if needed.

### B.2.3 Model A photos



Figure B.5: Model A construction 1



Figure B.6: Model A construction 2



Figure B.7: Model A construction 3

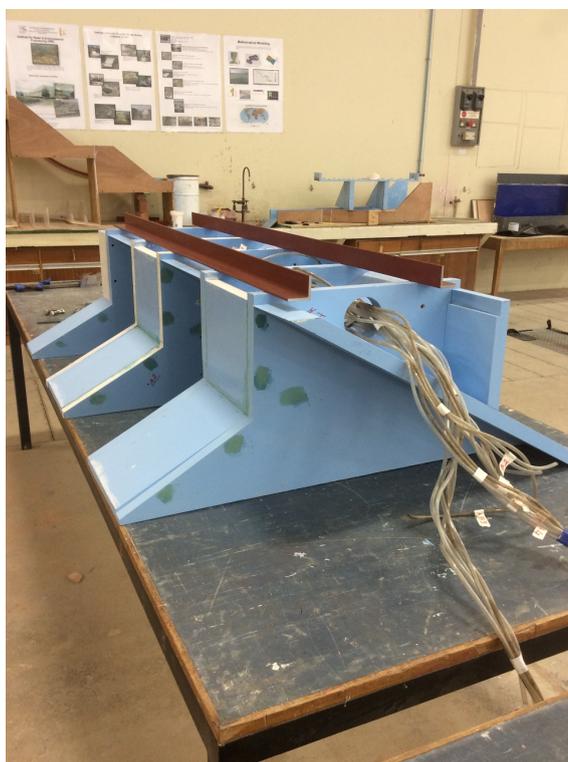


Figure B.8: Model A construction 4



Figure B.9: Model A with no upstream nose



Figure B.10: Model A with circular nose

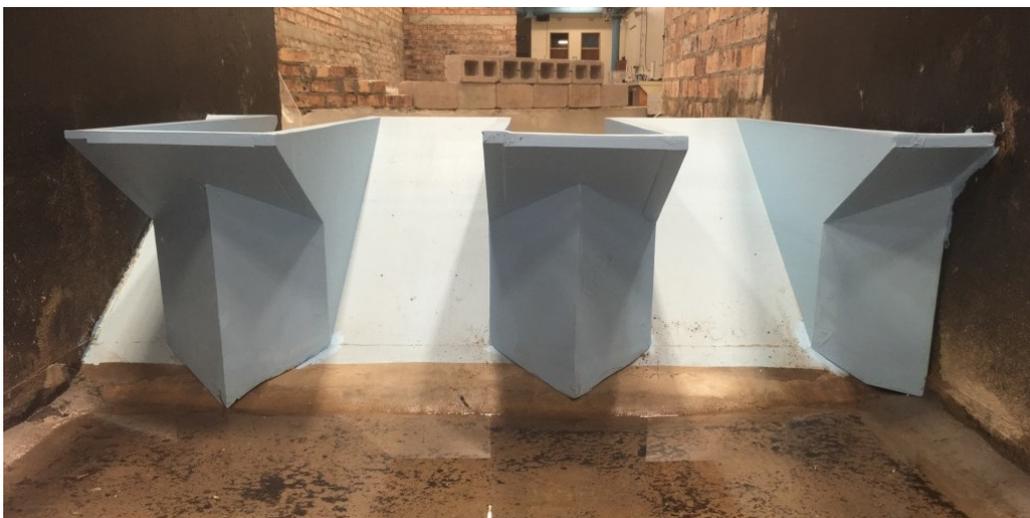


Figure B.11: Model A with triangular nose



Figure B.12: Model A circular nose



Figure B.13: Model A triangular nose



Figure B.14: Model A with aeration pipes

### B.2.4 Model A scaling

A comprehensive list of relevant dimensions, forces and scaling ratios is presented in Table B.1, based on the assumption that the same fluid is used in the prototype and the model. The main focus of model A is the hydrodynamics of the flow around a PKW. This means that there was less emphasis placed on the model's materials, beyond the requirement that it be stiff enough to withstand low frequency vibrations and possibly affect the hydrodynamic instrument readings. The table shows that the prototype being emulated is made of 0.225 m thick concrete. This is thin by typical concrete PKW standards but should still be thick and stiff enough to withstand these vibrations.

Table B.2 shows the Froude, Reynolds and Weber numbers for each of the flow scenarios. It is clear that the Reynolds number is in the turbulent range over the full range of tests and that the vortex shedding behaviour (see Section 5.2.5), which is heavily reliant on it, will not be excessively affected. The Weber number does become small for the smaller flows, but its value remains in excess of the suggested limit. Despite this, some errors related to surface tension may be noted.

## B.3 Model B

### B.3.1 Testing procedures

The testing procedure which was followed in the experiments involving model B are as follows:

- Measure, survey and record the exact dimensions and position of the weir in the canal, the canal itself and the measurement instruments (using survey equipment).
- Assuming the model is to be observed under flow:
  - Fill the canal and allow the flow to reach a stable equilibrium. Then measure the flow and water level.
  - Ensure that the flow upstream of the PKW is uniform and not at all affected by the discharge into the canal via visual observation
  - Visually observe and record the flow patterns (using dye wands and video camera equipment)
  - Measure and record the water surface elevation (as well as its profile, where relevant) upstream of the inlet key, inside the inlet and outlet keys, as well midway along the flume's length
  - Measure and record the time-variant velocity field in the inlet keys (using rail mounted ADV) at a set number of points.
  - Measure and record strain gauge
- Assuming the model is to be observed in its static state:
  - Fill the canal up to the desired level and allow the water level to stabilize

Table B.1: Model A scaling ratios and dimensions

Dimension / Ratio	Symbol	Scaling ratio	Unit	Prototype	Model (as scaled)	Model (as built)	Comment
Scale	$\lambda$	$\frac{\text{prototype}}{\text{model}}$	-	1	7.5	7.5	-
Depth	$H_t$	$\lambda$	m	1.313	0.175	0.175	-
Height	$P$	$\lambda$	m	3.000	0.400	0.400	-
Length	$B_t$	$\lambda$	m	7.500	1.000	1.000	-
Wall thickness	$T_s$	$\lambda$	m	0.225	0.030	0.030	-
Velocity	$V$	$\sqrt{\lambda}$	m/s	1.588	0.580	0.580	-
Discharge	$Q$	$\lambda^{5/3}$	$m^3/s$	77.0	0.500	0.500	-
Force	$F$	$\lambda^3$	N	421.9	1.00	1.00	-
Moment	$M$	$\lambda^4$	Nm	3164.0	1.00	1.00	-
Plate mass	$W$	$\lambda^3$	kg	4050.0	9.60	2.20	-
Acceleration	$g$	1	g	9.81	9.81	9.81	-
Pressure	$P$	$\lambda$	Pa	75.0	10.0	10.0	-
Water density	$\rho$	1	$kg/m^3$	1000	1000	1000	-
Material density	$\rho$	1	$kg/m^3$	2400	2400	550	Concrete and wood
Young's Modulus	$E$	$\lambda$	GPa	20.0	2.7	11.0	-
Moment of inertia	$I$	$\lambda^5$	$10^6 m^4$	1898	0.60	0.60	$I = \frac{1}{12} P_m T^3$
Flexural rigidity	$EI$	$\lambda^6$	$Nm^2$	37968750	1600	1600	-
Kinematic viscosity	$\nu$	1	$m^2/s$	$1 \times 10^{-6}$	$1 \times 10^{-6}$	$1 \times 10^{-6}$	-
Frequency	$\omega$	$\frac{1}{\sqrt{\lambda}}$	Hz	1.826	5.00	5.00	-
Surface tension	$\sigma$	1	N/m	0.073	0.073	0.073	-
Froude number	$Fr$	<i>gravity</i>	-	0.244	0.244	0.244	Similitude
Reynolds number	$Re$	<i>viscosity</i>	-	$6.8 \times 10^6$	$3.3 \times 10^5$	$3.3 \times 10^5$	Mismatch
Weber number	$We$	<i>surface tension</i>	-	103170	1834	1834	Mismatch
Strouhal number	$St$	<i>frequency</i>	-	1.51	1.51	1.51	Similitude
Cauchy number	$Ca$	<i>elasticity</i>	-	302.5	302.5	16.8	Mismatch
Euler number	$Eu$	<i>pressure</i>	-	0.030	0.030	0.030	Similitude

Table B.2: Model A scenarios and their force ratios

Discharge (m <sup>3</sup> /s)	Head (m)	H/P (-)	Velocity (m/s)	Froude (-)	Reynolds* (-)	Weber** (-)
0.050	0.029	0.073	0.078	0.038	$3.3 \times 10^4$	50.9
0.100	0.044	0.110	0.150	0.072	$6.7 \times 10^4$	116.1
0.150	0.059	0.148	0.218	0.103	$1.0 \times 10^5$	209.8
0.200	0.075	0.186	0.281	0.130	$1.3 \times 10^5$	333.2
0.300	0.106	0.265	0.395	0.177	$2.0 \times 10^5$	672.9
0.400	0.138	0.345	0.496	0.216	$2.7 \times 10^5$	1140.0
0.500	0.170	0.425	0.585	0.247	$3.3 \times 10^5$	1734.8
0.600	0.202	0.506	0.664	0.273	$4.0 \times 10^5$	2452.9
0.700	0.234	0.586	0.736	0.295	$4.7 \times 10^5$	3285.4

\* Reynolds number in the water body upstream of the weir

\*\* Weber number at the overflow crest

- Measure and record the vibration sensor (accelerometer and strain gauge) signal data.
- First record the background data and use these to recalibrate the signal processing unit to this background level.
- Measure and record the vibration sensor data when the structure is struck (once) by the hammer at a particular location. Repeat test three times.

The scenarios which were investigated include:

- In the dynamic scenario a range of relatively low flows from 11 l/s to 20 l/s and then a range of larger flows, from 50 l/s to 400 l/s in 50 l/s increments
- Two aeration pipe sizes, one 32 mm and the other 100 mm in diameter.
- In the static scenario, four water levels namely dry, half-full, full (at crest) and overflow (0.2 m above the crest). The overflow state was achieved via the installation of a temporary PVC wall on top of the crest.
- The effect of the narrower flank walls on the modal parameters was also explored

### B.3.2 Model B scaling

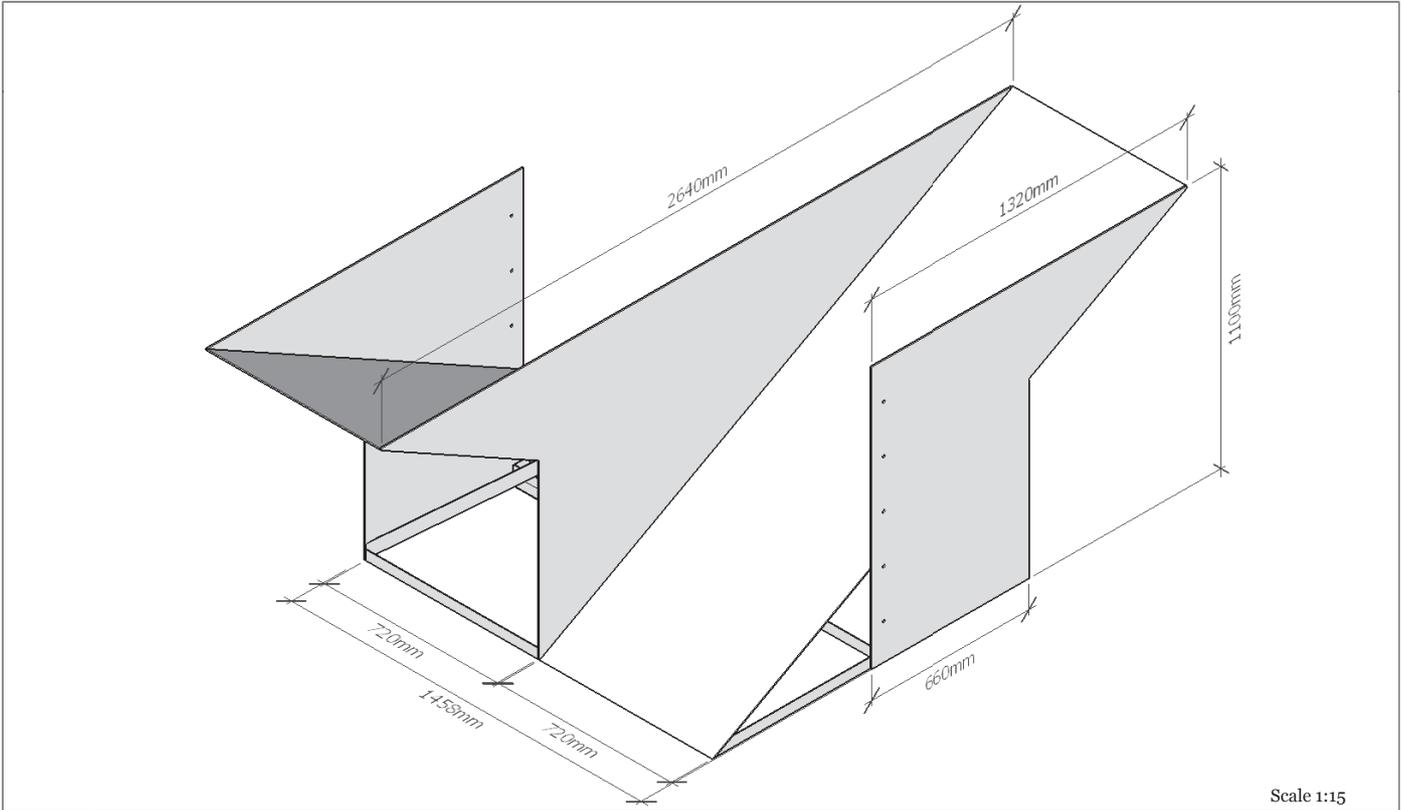
A prototype thickness of 25 mm was selected based on the serviceability limit states recommended in SANS 10160-1 for the terminal deflection of vertical members. This suggests an irreversible serviceability limit state deflection of  $L/100$  and a long term serviceability limit state deflection of  $L/250$ . Here  $L$  is the maximum length to the nearest support which is equal to 1.75 m at prototype scale and 0.64 m at the model scale.

The two serviceability states are assumed to equate to a hydrostatic load on the upstream face of the PKW of  $H/P = 0.2$  for the irreversible and  $H/P = 0$  for the long-term limit states. The prototype has a maximum deflection of 15.9 mm ( $L/\delta = 110$ ) and 6.5 mm ( $L/\delta = 269$ ) for each of these load cases. When this was geometrically scaled downward to a model with a thickness of 9 mm, but keeping the same material, these deflection  $L/\delta$  values come to 279 and 698 respectively. This is mainly because the use of the same material causes the model to act stronger than it if its elasticity was also scaled. To counter this the model thickness was then reduced such that the product  $EI$ , which determines the deflection, is the same as for the directly scaled version (see Table B.3). This results in a thickness of 6.6 mm which results in deflection  $L/\delta$  values of 113 and 279, both of which are good approximations of the prototype deflections.

As explained in the main text, steel plate of 6.6 mm is not generally available, hence the nearest available thickness was specified, namely 6.0 mm. This attained  $L/\delta$  values of 86 and 207, which is marginally lower than the limit state design values but deemed acceptable for the purposes of this study.

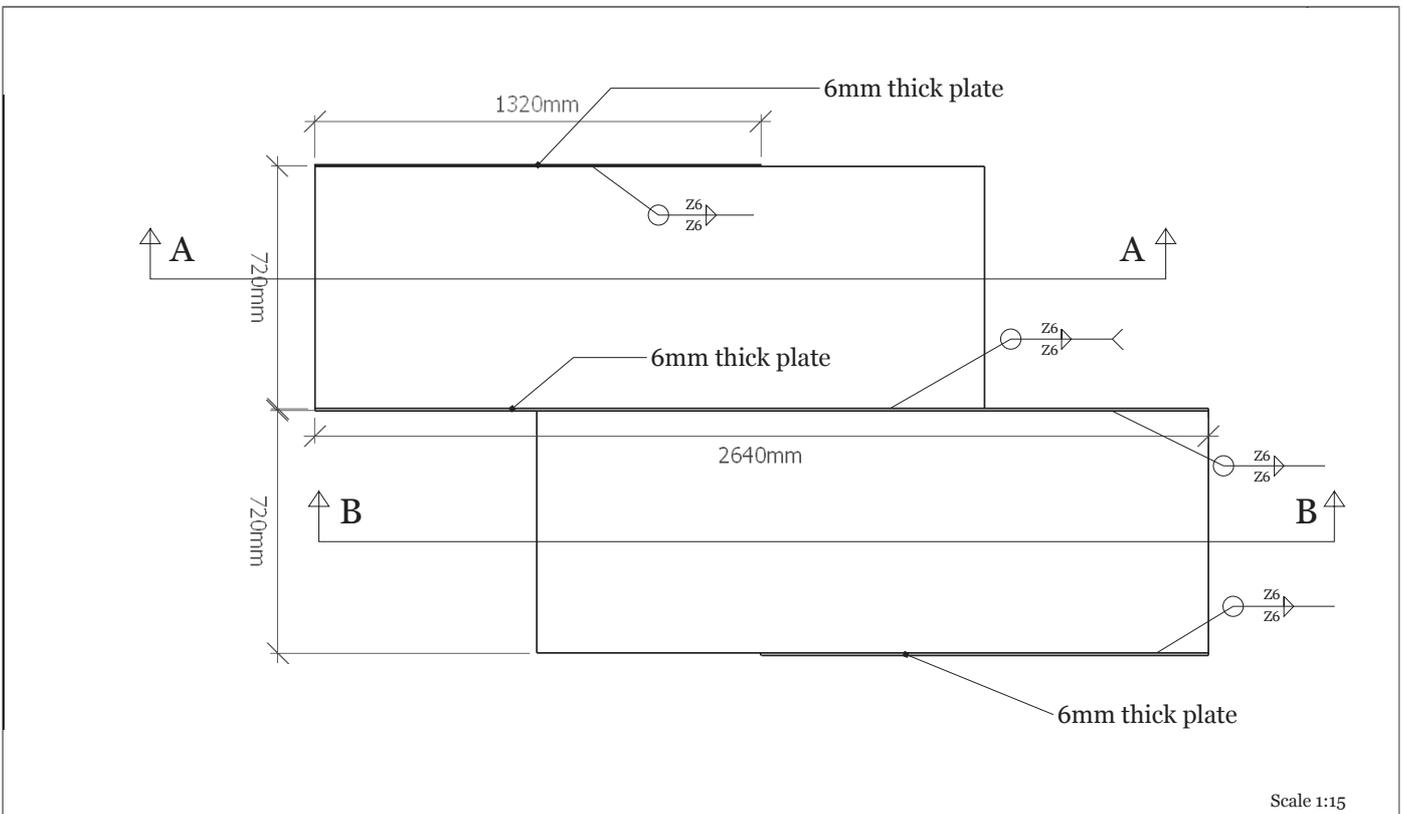
### **B.3.3 Model B schematics**

The schematics of model B follow:



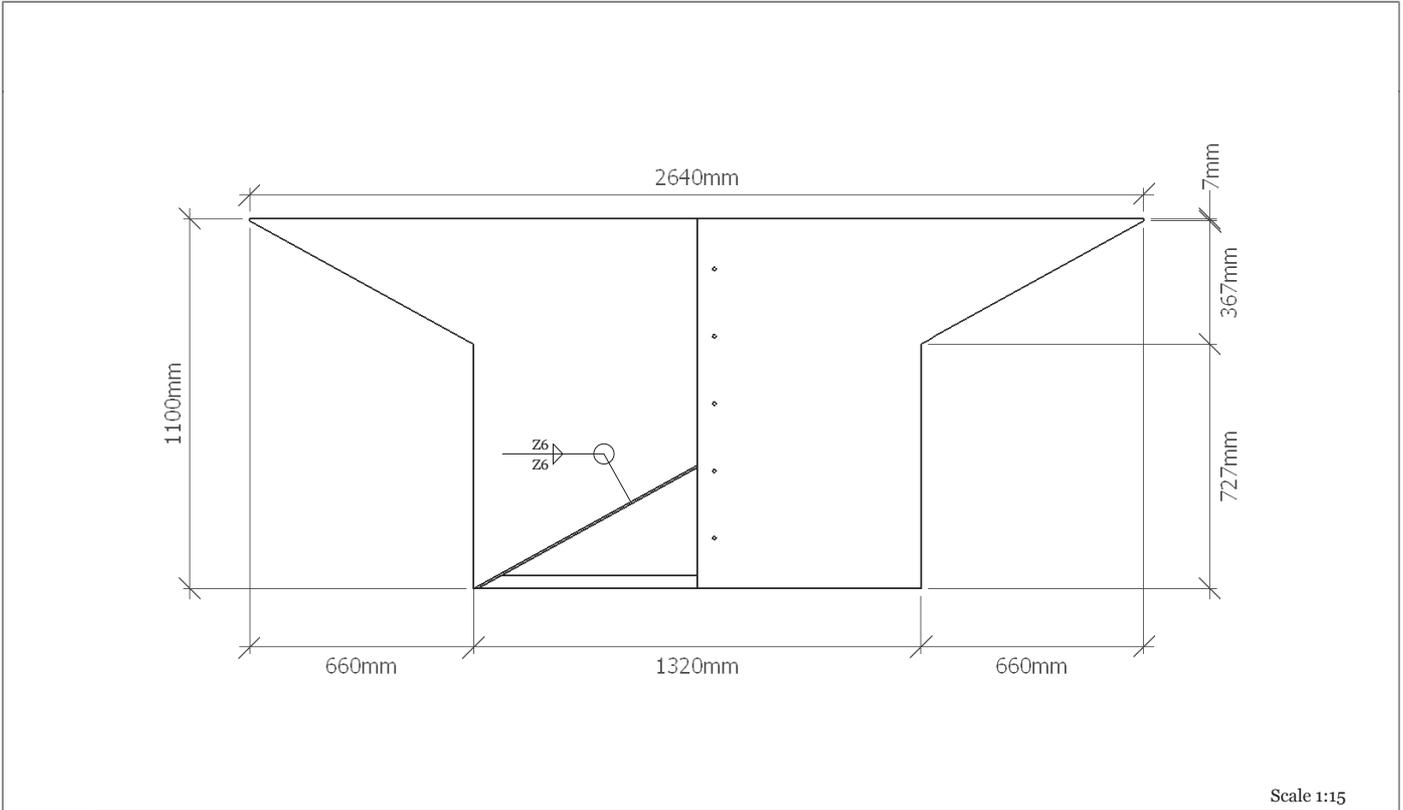
Scale 1:15

Piank Key Weir: Flow induced vibrations	Model B	REVISIONS		B 01
	Isometric view	MM/DD/YY	REMARKS	
		1 29/06/2016	Final Draft	
		2 01/07/2016	Final	
		3 --/--/--	...	
		4 --/--/--	...	
		5 --/--/--	...	



Scale 1:15

Piank Key Weir: Flow induced vibrations	Model B	REVISIONS		B 02
	Top (PLAN) view	MM/DD/YY	REMARKS	
		1 29/06/2016	Final Draft	
		2 01/07/2016	Final	
		3 --/--/--	...	
		4 --/--/--	...	
		5 --/--/--	...	

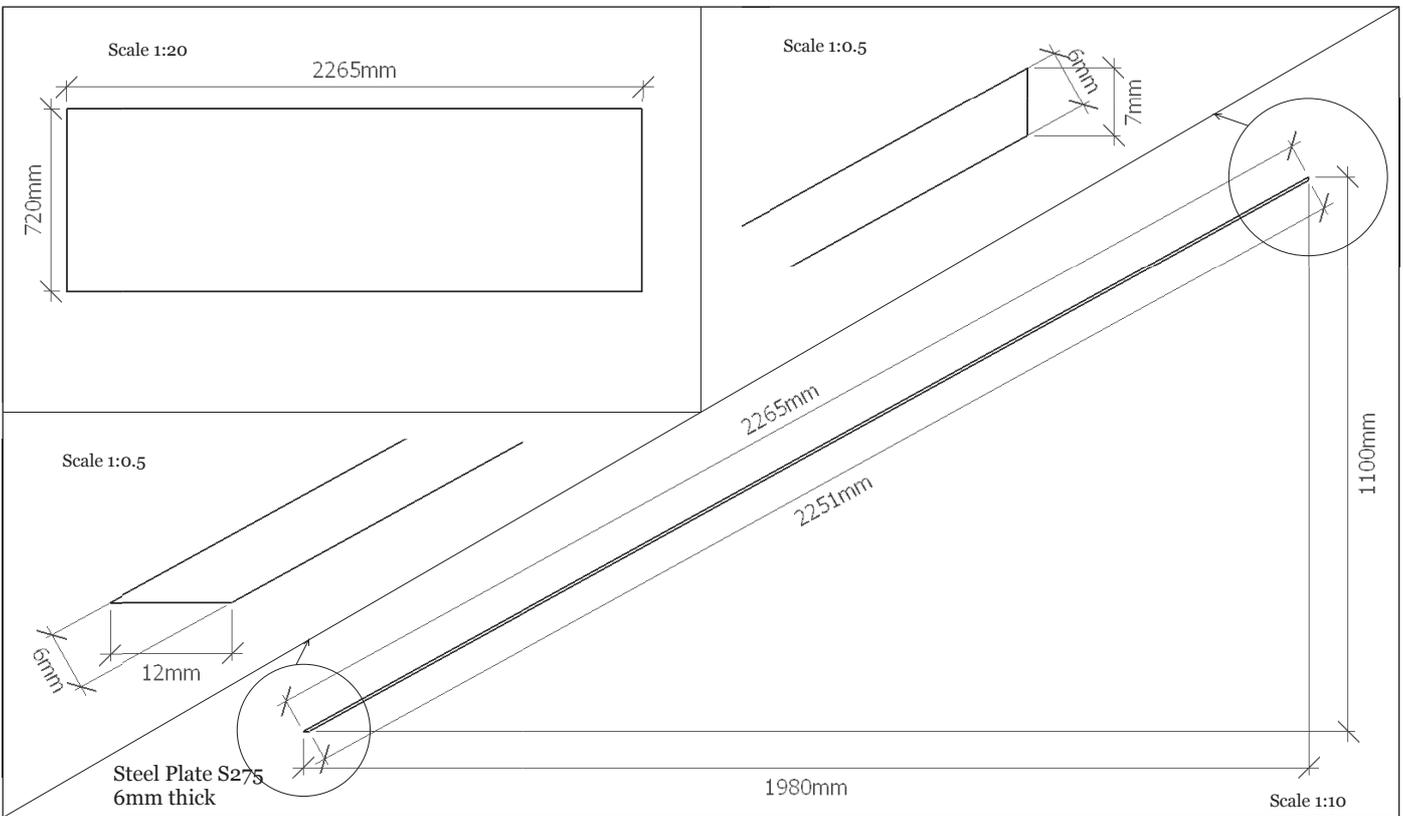


Piank Key Weir: Flow induced vibrations

Model B  
Side view

REVISIONS	
MM/DD/YY	REMARKS
1 29/06/2016	Final Draft
2 01/07/2016	Final
3	...
4	...
5	...

B 03



Piank Key Weir: Flow induced vibrations

Model B  
Part B3 (x2)

REVISIONS	
MM/DD/YY	REMARKS
1 29/06/2016	Final Draft
2 01/07/2016	Final
3	...
4	...
5	...

B 07

B.3.4 Model B photos



Figure B.15: Model B with crest parapet



Figure B.16: Model B with guide walls



Figure B.17: Model B crest detail



Figure B.18: Model B at low flow with closed air vent under inlet key

Table B.3: Model B scaling ratios and dimensions

Dimension / Ratio	Sym-bol	Scaling ratio	Unit	Proto-type	Model (as scaled)	Model (as desired)	Model (as built)	Up-scaled from as-built	Comment
Scale	$\lambda$	$\frac{\text{prototype}}{\text{model}}$	-	1	2.727	2.727	2.727	0.37	-
Depth	$H_t$	$\lambda$	m	0.464	0.170	0.170	0.170	0.464	-
Height	$P$	$\lambda$	m	3.000	1.100	1.100	1.100	3.000	-
Length	$B_t$	$\lambda$	m	7.200	2.640	2.640	2.640	7.200	-
Wall thickness	$T_s$	$\lambda$	m	0.025	0.009	0.0066	0.006	0.016	Thinner
Velocity	$V$	$\sqrt{\lambda}$	m/s	1.418	0.859	0.859	0.859	1.418	-
Discharge	$Q$	$\lambda^{5/3}$	$m^3/s$	3.684	0.300	0.300	0.300	3.684	-
Force	$F$	$\lambda^3$	N	20.3	1.00	1.00	1.00	20.3	-
Moment	$M$	$\lambda^4$	Nm	55.30	1.00	1.00	1.00	55.30	-
Plate mass	$W$	$\lambda^3$	kg	1413.0	69.7	49.9	45.6	924.8	Lighter
Acceleration	$g$	1	g	9.81	9.81	9.81	9.81	9.81	-
Pressure	$P$	$\lambda$	Pa	27.3	10.0	10.0	10.0	27.3	-
Water density	$\rho$	1	$kg/m^3$	1000	1000	1000	1000	1000	-
Material density	$\rho$	1	$kg/m^3$	7850	7850	7850	7850	7850	Steel
Young's Modulus	$E$	$\lambda$	GPa	200.0	73.3	200.0	200.0	545.4	-
Moment of inertia	$I$	$\lambda^4$	$10^6 m^4$	2.604	0.047	0.017	0.013	0.0730	$I = \frac{1}{12} P_m T^3$
Flexural rigidity	$EI$	$\lambda^4$	Nm	520833	3454	3454	2640	398174	-
Kinematic viscosity	$\nu$	1	$m^2/s$	$1 \times 10^{-6}$	$1 \times 10^{-6}$	$1 \times 10^{-6}$	$1 \times 10^{-6}$	$1 \times 10^{-6}$	-
Frequency	$\omega$	$\frac{1}{\sqrt{\lambda}}$	Hz	3.03	5.00	5.00	5.00	3.03	-
Surface tension	$\sigma$	1	N/m	0.073	0.073	0.073	0.073	0.073	-
Froude number	$Fr$	<i>gravity</i>	-	0.243	0.243	0.243	0.243	0.243	Similitude
Reynolds number	$Re$	<i>viscosity</i>	-	$4.9 \times 10^6$	$1.1 \times 10^6$	$1.1 \times 10^6$	$1.1 \times 10^6$	$4.9 \times 10^6$	Mismatch
Weber number	$We$	<i>surface tension</i>	-	12871	1731	1731	1731	12871	Mismatch
Strouhal number	$St$	<i>frequency</i>	-	1	1	1	1	1	Similitude
Cauchy number	$Ca$	<i>elasticity</i>	-	79.0	79.0	29.0	29.0	29.0	Mismatch
Euler number	$Eu$	<i>pressure</i>	-	0.014	0.014	0.014	0.014	0.014	Similitude

## B.4 Instrumentation

### B.4.1 Instrument accuracies

Table B.4: Physical model instrument accuracies

Instrument	Accuracy
SAFMAG flow meter	$\pm 0.5\%$
Water level needle gauge	0.1 mm
Pitot tube	1.0 mm
ADV	$\pm 1\%$
Pressure transmitter	$\pm 0.5\%$
Accelerometer	$\pm 100\text{ mV/g}$
Strain gauge	-

### B.4.2 Acoustic Doppler Velocimeter

The data capturing settings for the ADV were selected by testing a range of settings also using published guidelines for the collection of data in high shear flow, and selecting the most favourable ones. The main settings were as follows:

- Nominal velocity range: 1 m/s. This depended on the magnitude of the velocity being captured and had to be increased in places to prevent aliasing.
- Sampling volume (SV): 7.6 mm. Relatively large SV to limit the collection of large instantaneous velocities resulting from small energetic eddies. These small eddies can, in any event, not be modelled by the numerical model with its cell size limit of  $\sim 5.0$  mm.
- Transmit length (TL): 2.4 mm. Large transmit length to allow for larger averaging to take place across the SV, thus resulting in cleaner data.
- Power level: Low+. Used to reduce the SNR and dB output in the relatively turbid water.
- Frequency: 200 Hz. Highest setting to collect as much frequency data as possible but results in noisy data requiring data cleaning algorithms (see below).

In general, the raw beam data ( $u$ ,  $v$ ,  $w_1$ ,  $w_2$ ) was captured and used to assess the quality of the data and then manually converted to UVW data using the conversion matrix provided by Nortek.

The grid layout for the ADV sensor is as shown in Figure B.19. The sensor was adjusted such that its sampling volume was located at each of the individual grid points and data recorded for a duration of 20 s to 30 s.

At least one reading was taken in the centre of the flume as far as possible upstream of the PKW. The orientation of the vector recorded at this location was used to adjust the alignment



all the other ADV vector readings taken that day. The vector at the upstream control point was assumed to have only one vector component (i.e. U: longitudinal downstream) with the other two vector components (V and W) being zero.

The physics of the ADV's operation can lead to the collection of spurious data and outliers known as spikes. These often alter the character of the data when flow parameters such as average velocity or turbulence are calculated and should thus be removed. These spikes can be algorithmically identified through one of several techniques. The selected procedure used in the present study was as follows:

1. Visually check each beam data stream on linear (time) and density plots and reject a poor data sequence for later recollection in the physical model
2. Remove obvious spikes which lie more than 5 sigma away from the mean and replace data with the median
3. Apply the Parsheh *et al.* [117] methodology with values of  $C1 = 1.8$  and  $C2 = 1.35$ , to the highpass filtered beam data from the previous step
4. Apply the standard Phase-Space-Threshold technique from Goring and Nikora [104] together with the above step
5. Ensure that if any data point is flagged as a spike in one beam's data that the corresponding data point in the related beam also gets flagged for replacement. Note the 4 beams are not all related to each other, only U and W1 and V and W2 are directly related.
6. Replace the identified spikes with the *last observation carried forward* methodology
7. Convert the despiked and reconstructed beam data to UVW data using the published transformation matrix
8. Reorient the UVW data to counter measured misalignments in the ADV sensor
9. Visually check plots of the data
10. Generate relevant flow parameters including velocity vectors, averages, RMS values, turbulence statistics, Reynold stresses, etc.

### B.4.3 Pressure transmitters

Model A was prefitted with internal conduits for the installation of small diameter (5 mm) pneumatic tubes. The tubes were in the order of 2.5 m long and ended in a T-piece configuration as shown in Figure B.23. One end of the T was fitted with a WIKA-S10 pressure transmitter. The other leg of the T was utilised to prime the pneumatic tube with water and to remove any air in the system. After this priming the priming tube-end was closed to limit the ingress and egress of mass into the tube as the pressure changed. Such mass movement would have induced damping in the tube tainting the pressure signal.

The 4 to 20 mA signal from the pressure transmitter was then transmitted to a custom built receiver, converted to voltage and the resultant signal transmitted via USB cable to a laptop loaded with PicoLog data logging software. Two data capturing frequencies were tested, namely 10 kHz and 1000 Hz. The high frequency data collection was limited to the converter's buffer storage and was thus limited to 2 000 000 data points. Using 10 simultaneous data channels further reduced this limit to 200 000 data points per channel which equated to 20 s of data. The lower frequency data collection was not limited in this way and could collect data continuously for long periods of time. Considering that the frequencies under investigation were relatively low the high frequency data collection was not chosen due to its duration limit and its large data files.

The various tubes were labelled as were the signal data cables. These were checked before every test to ensure there was no cross-over.

#### **B.4.4 Accelerometers**

Model B was fitted with 7 three-dimensional accelerometers whose X-axis data stream was collected by an LMS SCADAS Mobile signal processor. Siemens' LMS Test.Lab was used to transform the signal data into a Frequency Response Function and then recorded the signal's frequency, its Real and Imaginary component and its coherence. The complex function can then be converted to amplitude and phase. Observing the plots of amplitude (suitably converted to dB) and the Real component of the complex FRF, allows the natural frequencies or eigenvalues of the signal to be identified. These are located where there is a zero-crossing in the Real plot or a localised peak in the amplitude plot. The Imaginary plot also shows peaks and valleys at these frequencies and can further be used to estimate the modal shape at that frequency when the geometry of the accelerometer placement is accounted for, as depicted in Figure 6.7.

#### **B.4.5 Strain gauge**

The strain gauge was fitted near the top and centre of the sidewall. This location was selected as this is where the highest deflections are expected. It is not the area with the highest expected strains but this area (at the base of the sidewall near the start of the overhang) is both very localised (and so the strain placement may miss it) and is periodically disturbed by the flow or impact of water. The crest placement is relatively still and also allows the strain gauge to be placed in a half-bridge formation, with one strain gauge on either face of the sidewall, which boosts the signal sensitivity. This could not be achieved at the area where highest strains are expected.

The strain gauge data signal was collected by a HBM Spider 8 signal processor and recorded using HBM's CatmanEasy (v4.1). The strain gauge data was checked for stationarity and processed to extract its spectral content as described in Appendix B.5.

**B.4.6 Instrumentation photos**

Figure B.20: 4-pronged down looking ADV sensor head



Figure B.21: ADV body mounted on trolley with extendible arm



Figure B.22: Pressure pipes exiting the flume wall



Figure B.23: Pressure gauge with T-piece attachment

## B.5 Statistics and data processing

Data were processed in *R* using the *RStudio* compiler [135; 136].

Each of the three main data streams (velocity, pressure, strain) were processed in a similar manner to obtain their spectral content.

1. The data sequence was plotted in time to check for stationarity, duration, spurious data and general quality. If necessary, low frequency trends were filtered out or spurious data clipped from the data record.
2. The data sequence was then centred by removing the mean from the sequence
3. The Welch method was applied which reduces the amount of noise in the resultant Power Spectral Density (PSD) plot. This entails the splitting up of the data sequence into equal and partially overlapping parts. The overlap was 25% on both ends of the sequence portion.
4. Each sequence portion was then converted to frequency space using the FFT which is encapsulated into the `spec.pgram` function which forms part of the *R* `seewave` package. A taper of 0.05 was applied together with a Daniell kernel smoothing parameter with a value of 3. This results in a PSD for each sequence portion
5. The PSD for each of the split up portions is averaged and plotted on a log-log scale.
6. The peak frequencies were read off manually.

## C Structural behaviour data

### C.1 Accelerometer results

The accelerometers and the strain gauge positions are located on the sidewall of model B as shown on Figure C.1. The vibration hammer was struck near point number 2. The response time signal from each of the points was analysed and resulted on a frequency response function (FRF) for each point. These consist of a complex number comprising both a real and an imaginary component. These values can then be transcribed into amplitude and phase values. The amplitude value was converted to decibel values, however it and the other data have no quantitative value other than their relative magnitude to each other as well as their frequency.

The data for each of the points as well as each scenario is presented in Figures C.2 to C.8 below. They are explained in the main text.

When the various components of the FRFs are plotted together the main natural frequencies or modes become evident. These are shown in Figures C.9 and C.10. Note that it is clear that the Full and Half-full scenario are identical, hence only the Full scenario is presented together with the Dry scenario.

The imaginary component of the FRF allows the mode shape for each natural frequency to be elucidated. The mode shapes are presented in Figure 6.7 and Figure C.11. Note that these shapes have been non-dimensionalized and so the magnitude of their deflections is not relevant; only their shape is of relevance.

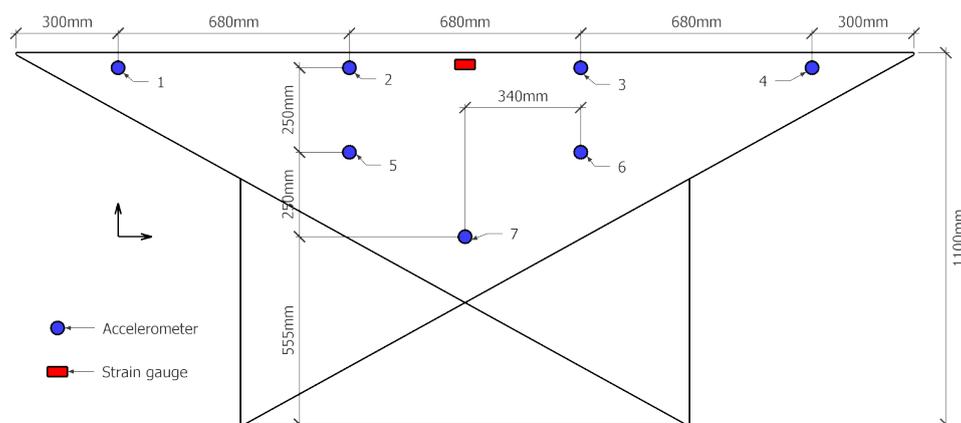


Figure C.1: Accelerometer and strain gauge positions

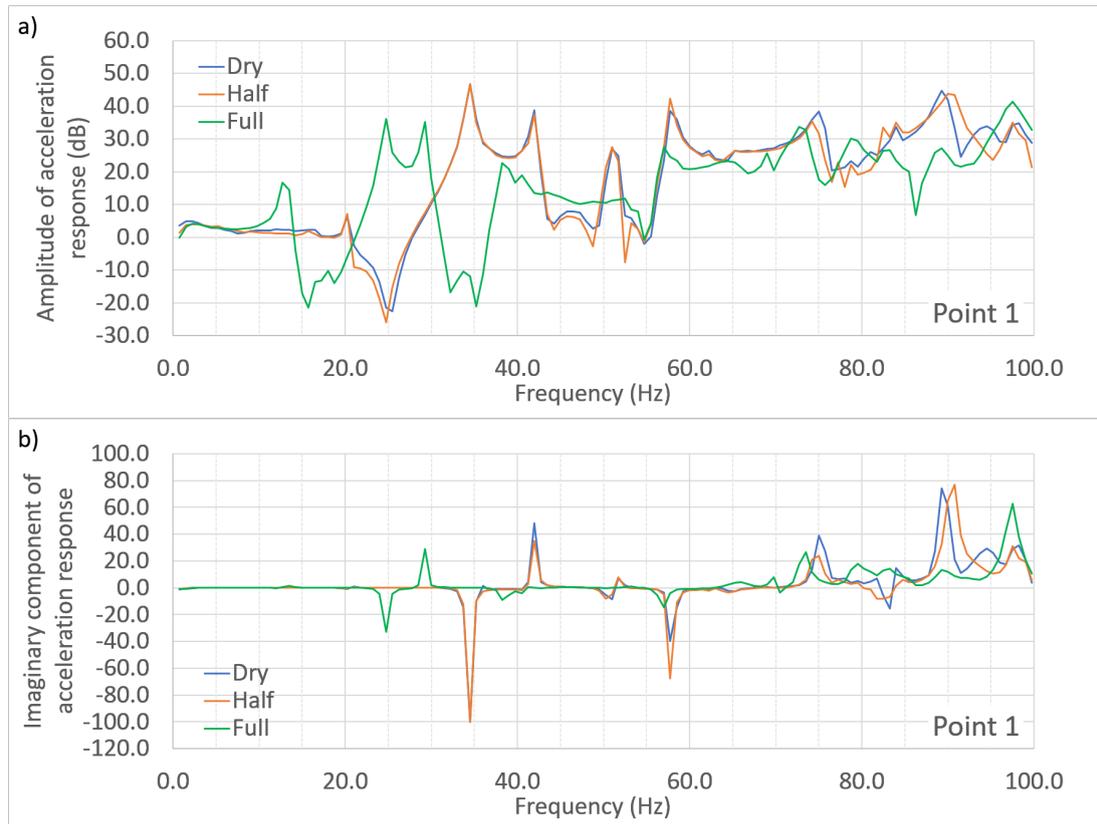


Figure C.2: Accelerometer point 1 Frequency Response Functions

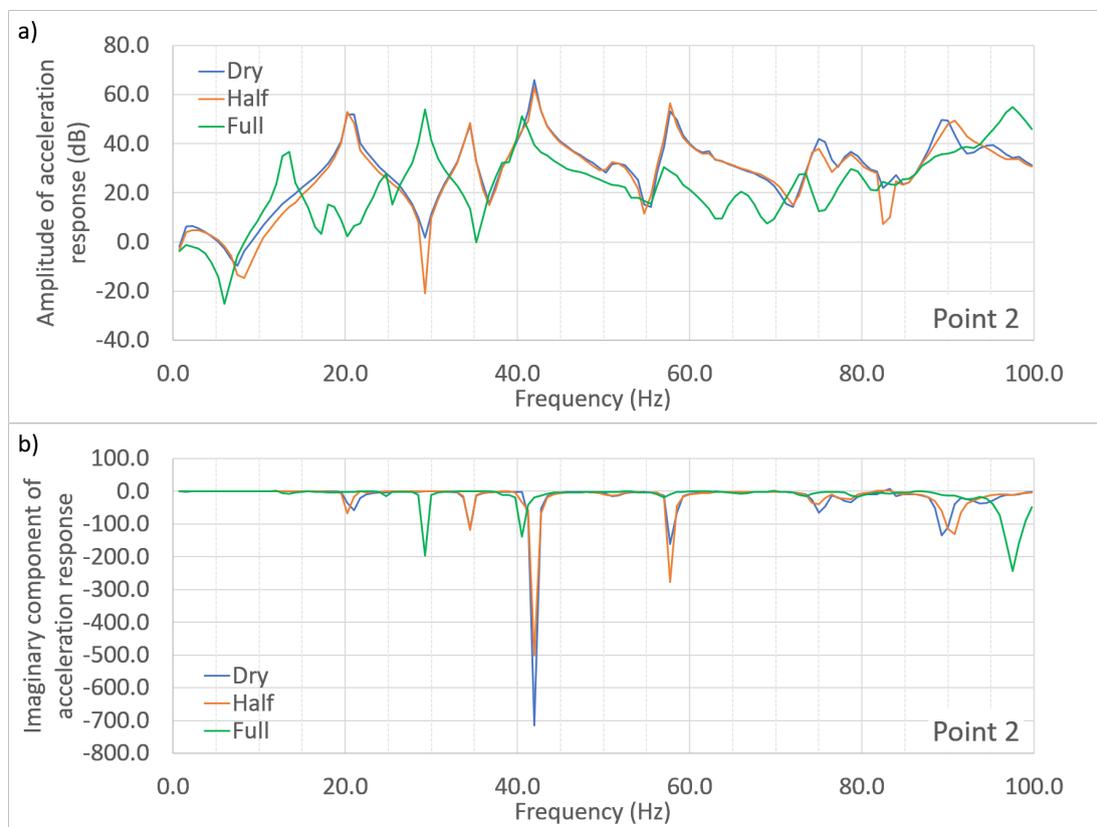


Figure C.3: Accelerometer point 2 Frequency Response Functions

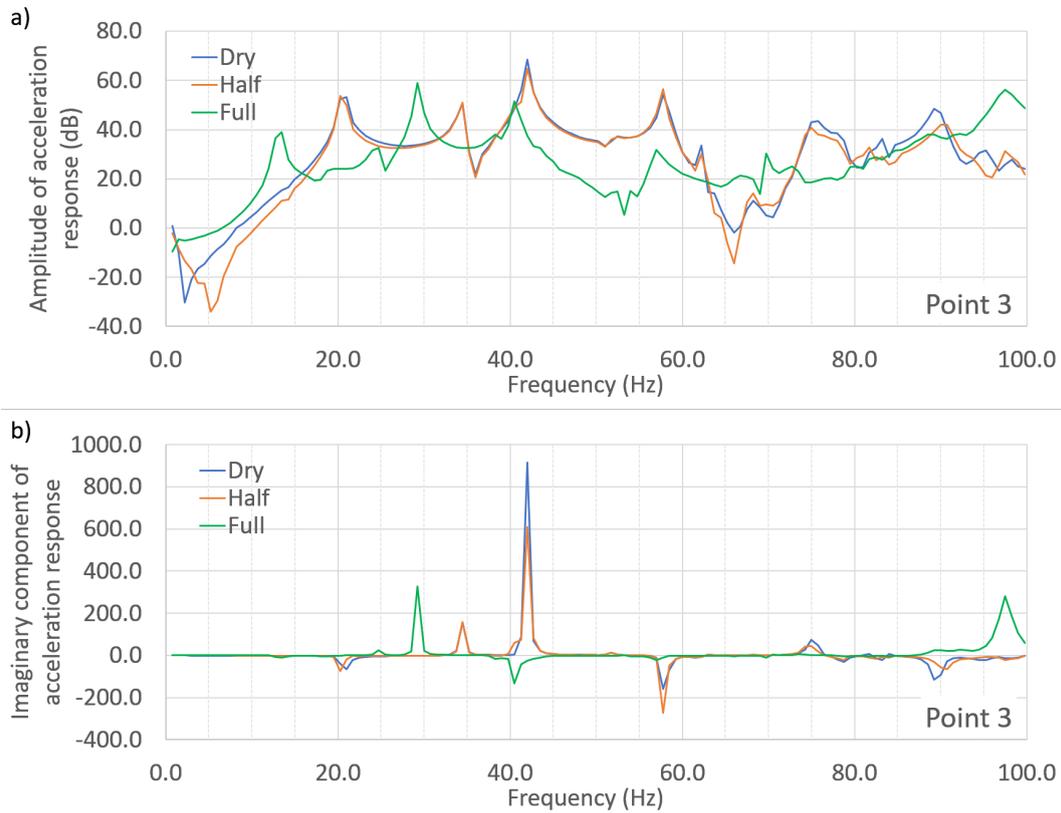


Figure C.4: Accelerometer point 3 Frequency Response Functions

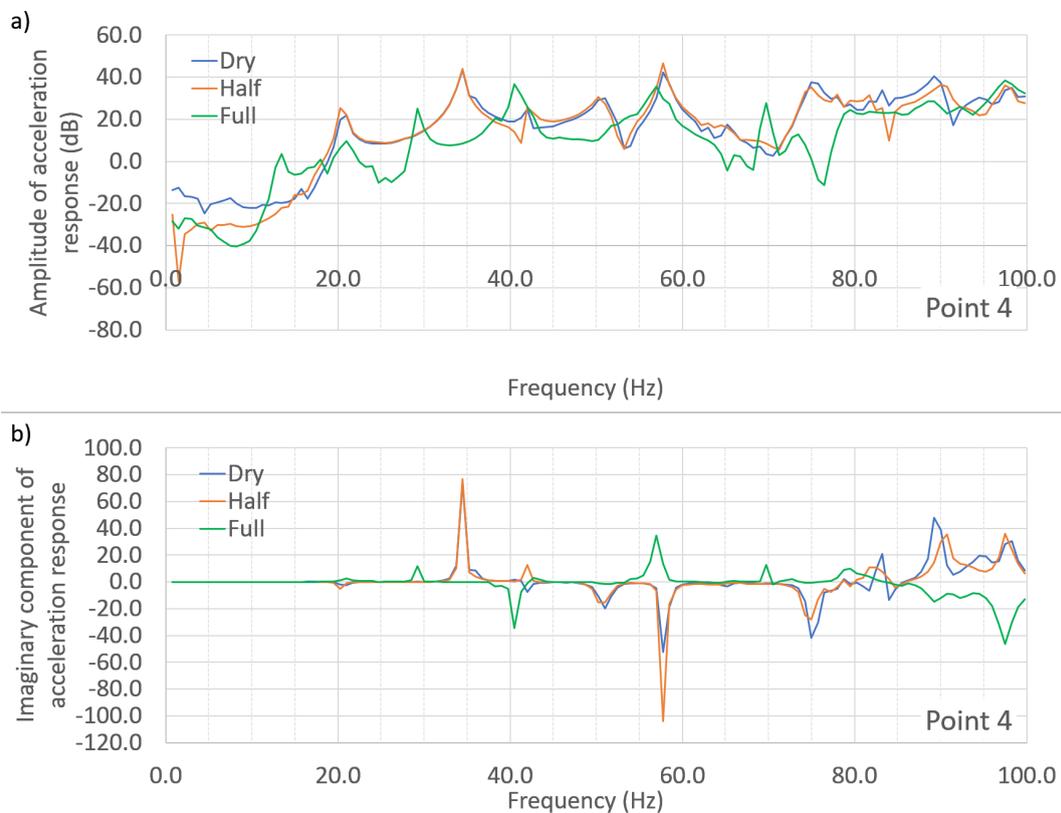


Figure C.5: Accelerometer point 4 Frequency Response Functions

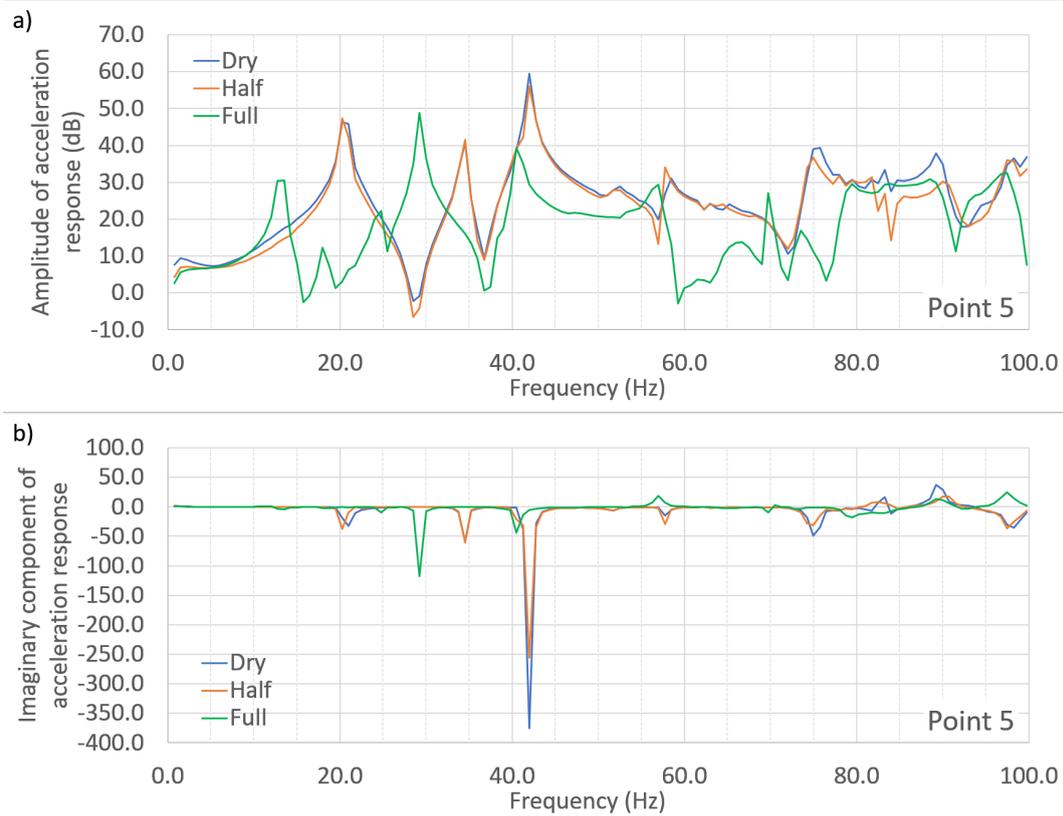


Figure C.6: Accelerometer point 5 Frequency Response Functions

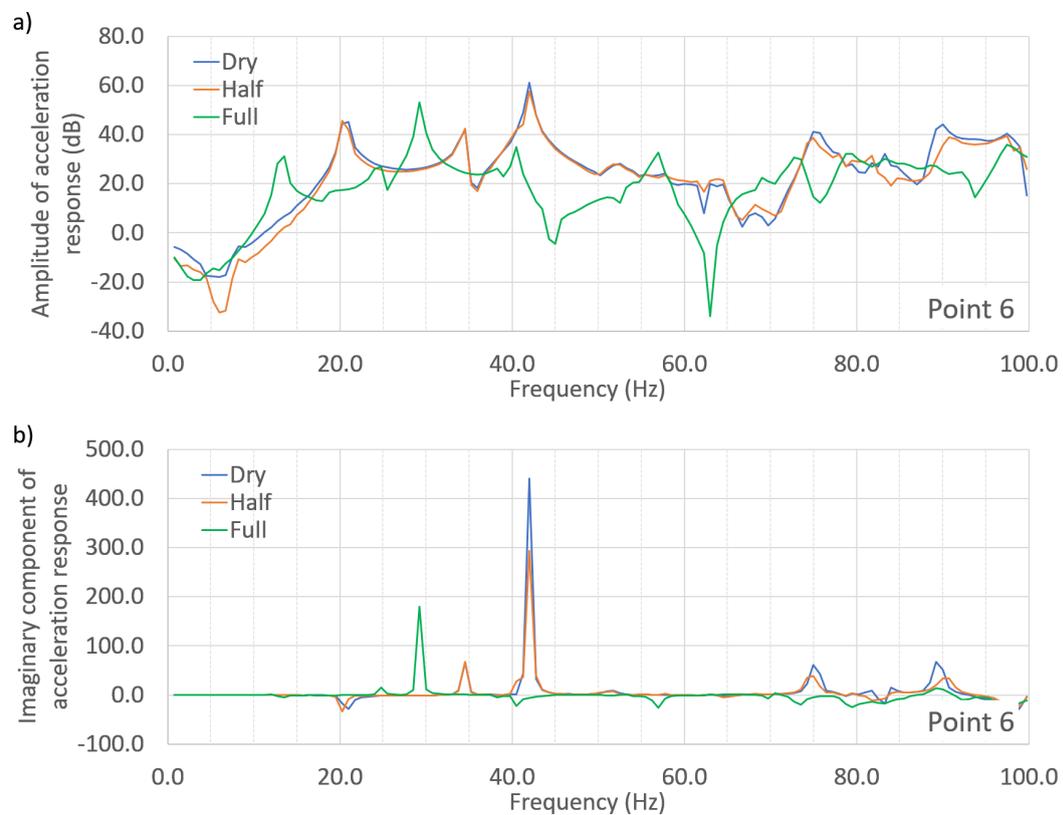


Figure C.7: Accelerometer point 6 Frequency Response Functions

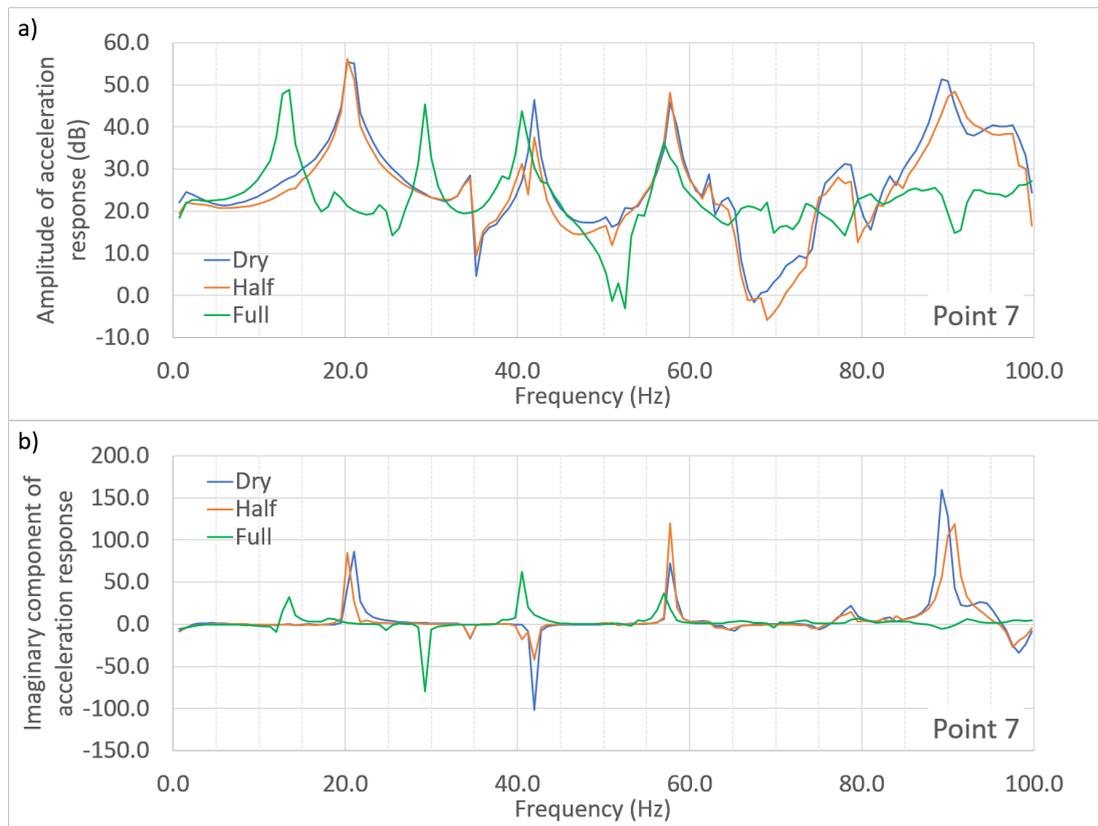


Figure C.8: Accelerometer point 7 Frequency Response Functions

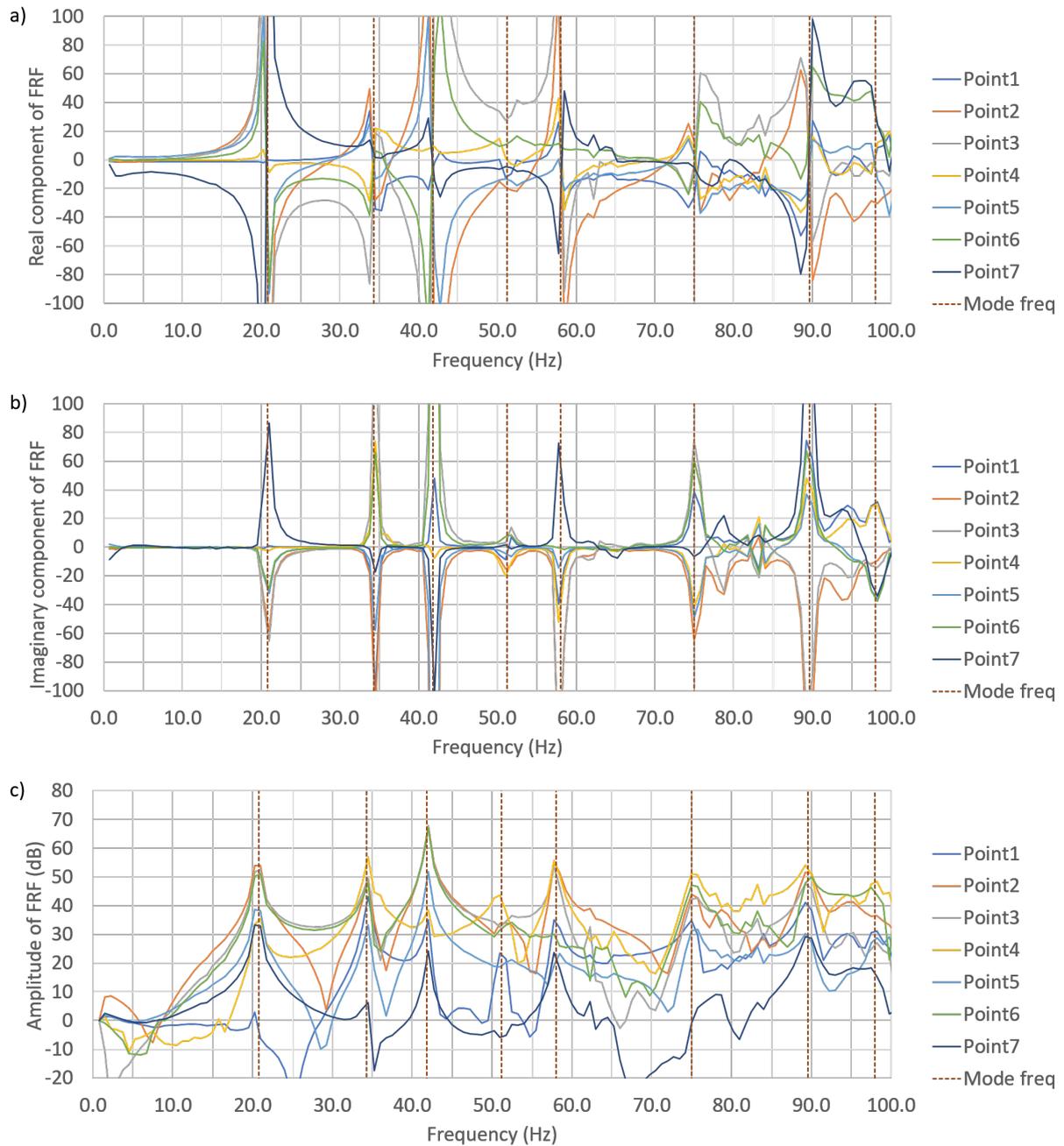


Figure C.9: Accelerometer FRF with natural frequencies - Dry scenario

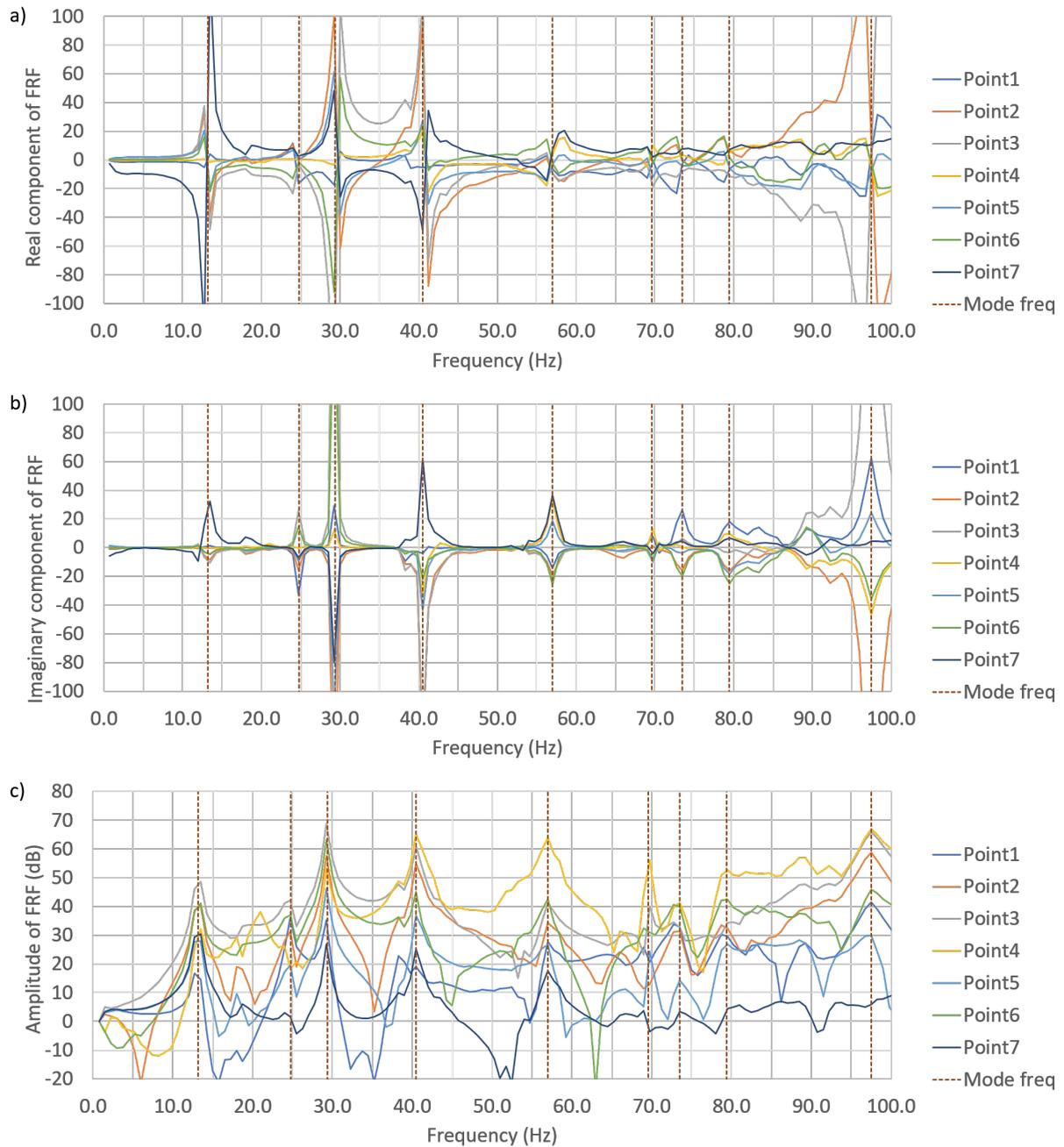


Figure C.10: Accelerometer FRF with natural frequencies - Full scenario

## C.2 Numerical model mode shapes

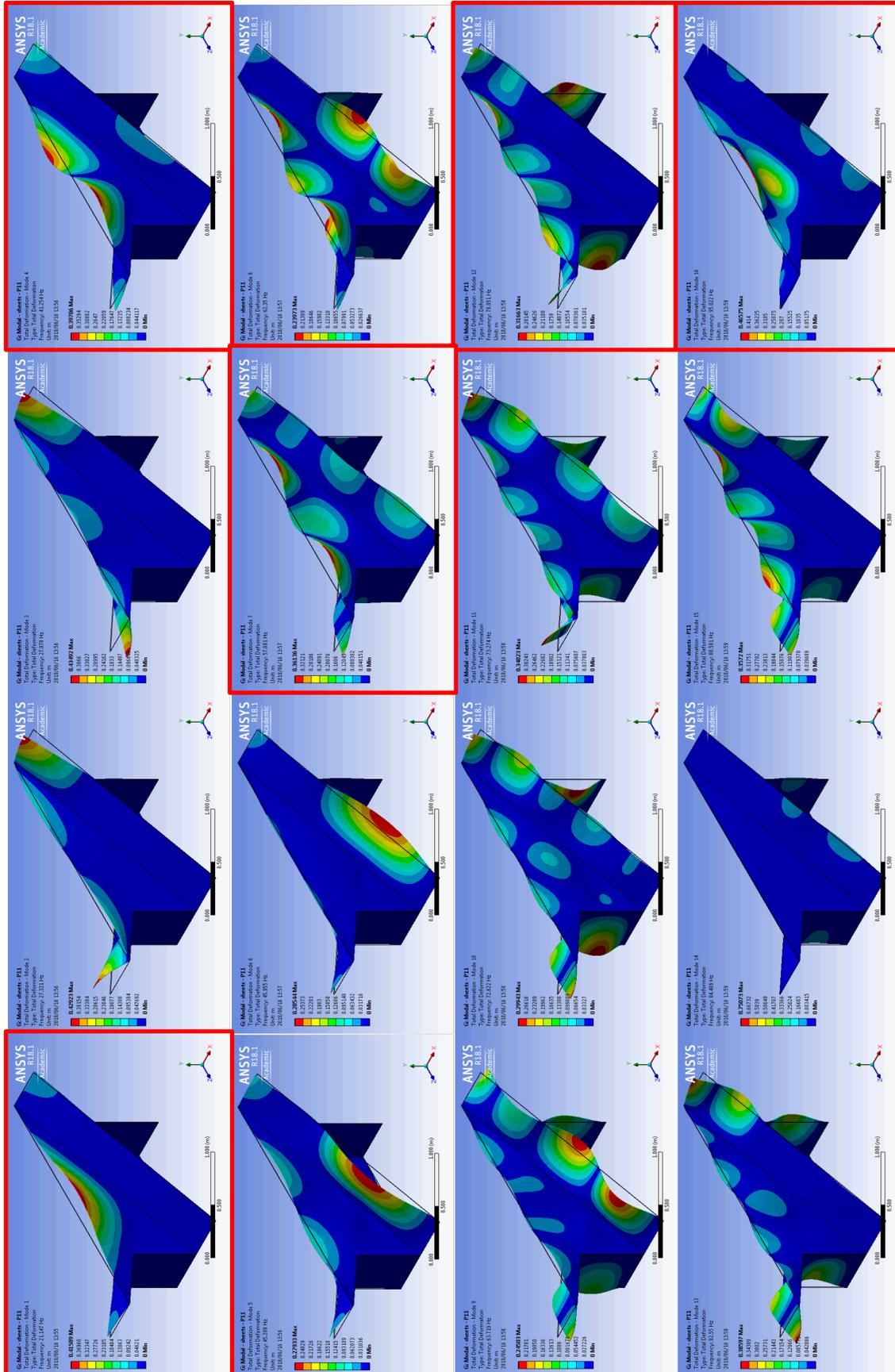


Figure C.11: Model B - numerical mode shapes 1 to 16

## D Hydraulic behaviour data

### D.1 Numerical calibration results

There were five main flow scenarios which were recorded in the physical model (model A) with the purposes of using the collected data for calibration of the numerical model. The results of this calibration are shown below for two of these flow scenarios, namely 2001/s and 4001/s. The remaining three have been excluded for brevity's sake but are similar to the two shown below.

The data at the same location was recorded in the physical model and extracted from the numerical model. These locations correspond to four planes as shown in Figure B.19. The X-axis is in the longitudinal direction, the Y-axis is the transverse direction, and the Z-axis is in the vertical direction. The two XY planes are horizontal planes at elevations of 0.216 m and 0.316 m. The XZ plane is a vertical plane in the longitudinal direction located 0.025 m from the sidewall of the inlet key. The YZ plane is a vertical plane in the transverse direction. It is located roughly in the middle of the inlet key and intersects the XY planes above the A2 and A5 pressure measurement points (see Figures 5.10 and B.19). For the XY and XZ planes flow is from left to right and for the YZ plane flow is toward the viewer.

In some of the comparison plots below, the physical data results are superimposed on top of the numerical results as grey/white contour lines.

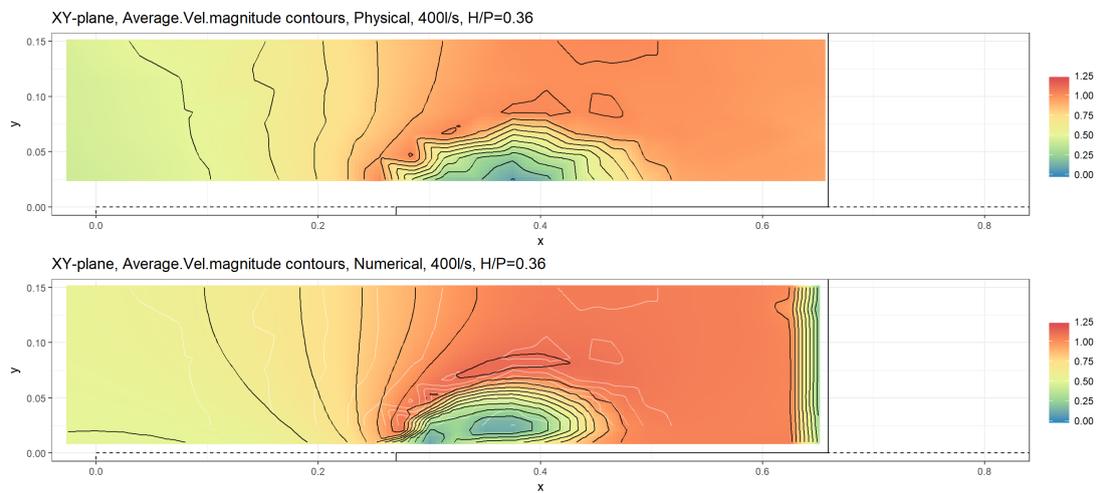
**D.1.1 Model A, Discharge 400 l/s, H/P = 0.36**

Figure D.1: Horizontal physical and numerical velocity magnitude ( $m/s$ ) at elevation of  $0.54P$ , 400l/s

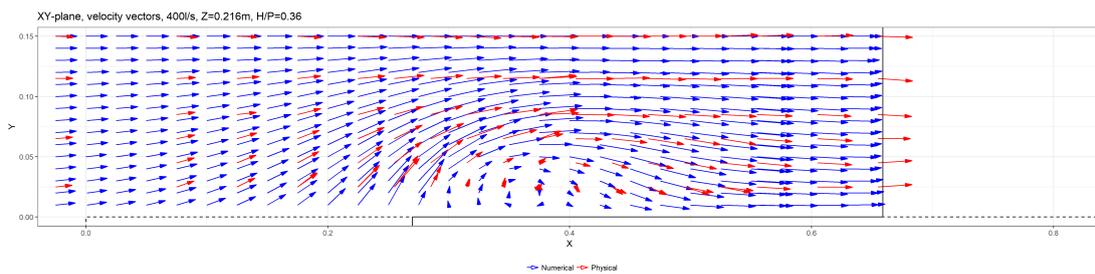


Figure D.2: Horizontal physical and numerical velocity vectors at elevation of  $0.54P$ , 400l/s

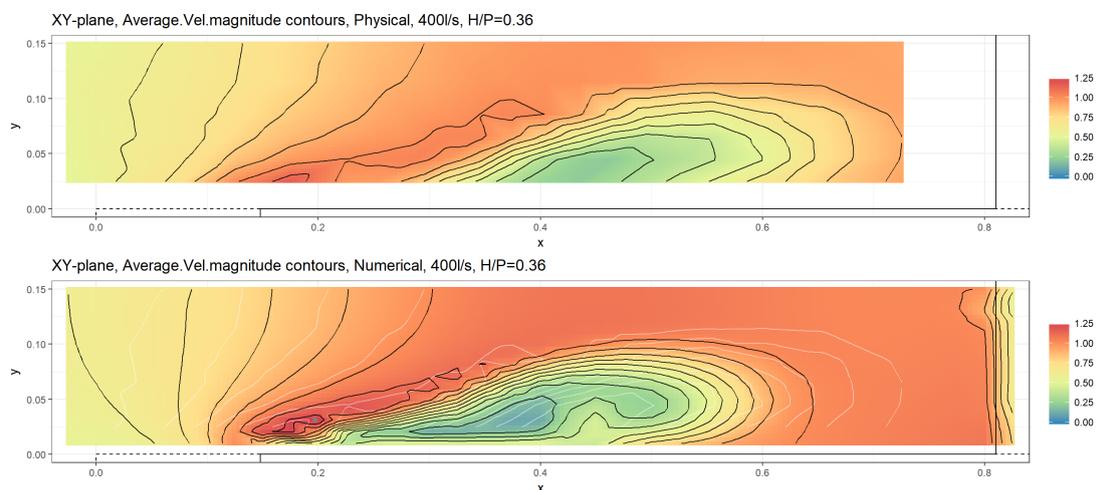


Figure D.3: Horizontal physical and numerical velocity magnitude ( $m/s$ ) at elevation of  $0.79P$ , 400l/s

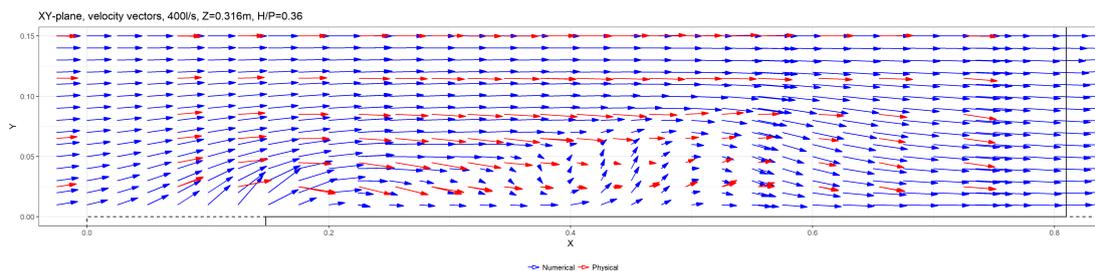


Figure D.4: Horizontal physical and numerical velocity vectors at elevation of  $0.79P$ ,  $400l/s$

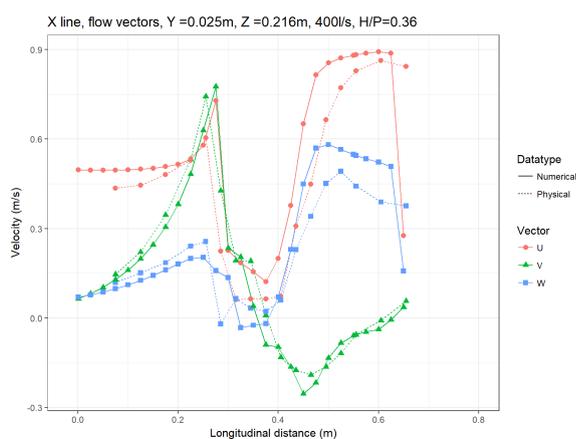


Figure D.5: Velocity vector magnitudes along the inlet key at elevation of  $0.54P$ ,  $400l/s$

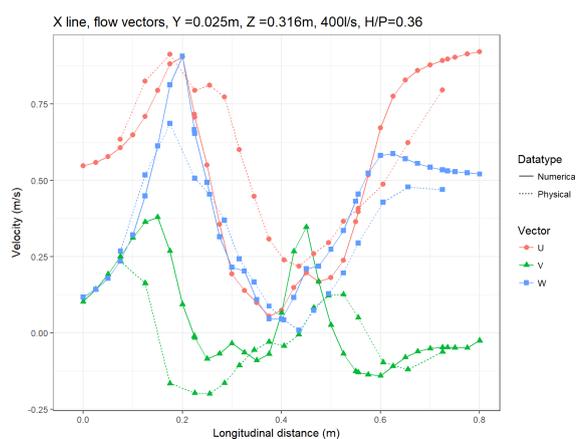


Figure D.6: Velocity vector magnitudes along the inlet key at elevation of  $0.79P$ ,  $400l/s$

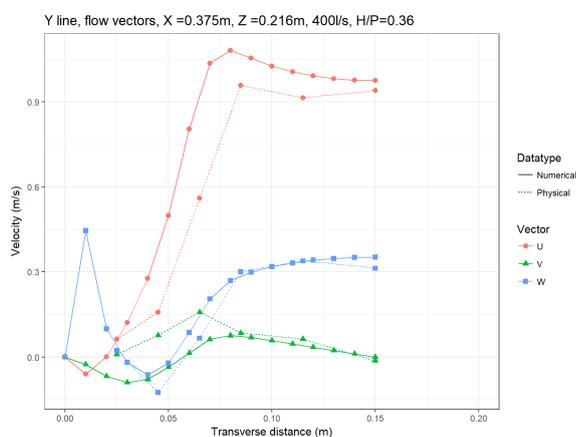


Figure D.7: Velocity vector magnitudes across the inlet key at elevation of  $0.54P$ ,  $400l/s$

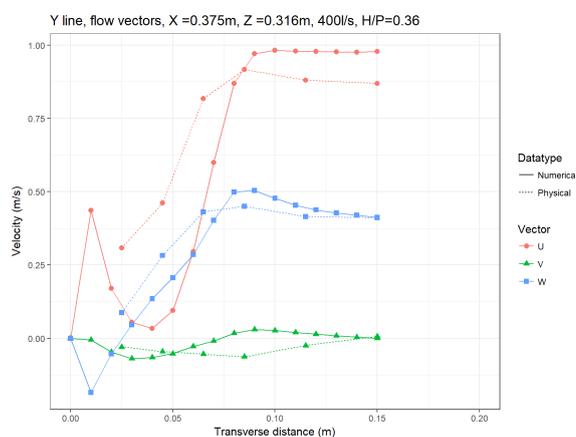


Figure D.8: Velocity vector magnitudes across the inlet key at elevation of  $0.79P$ ,  $400l/s$

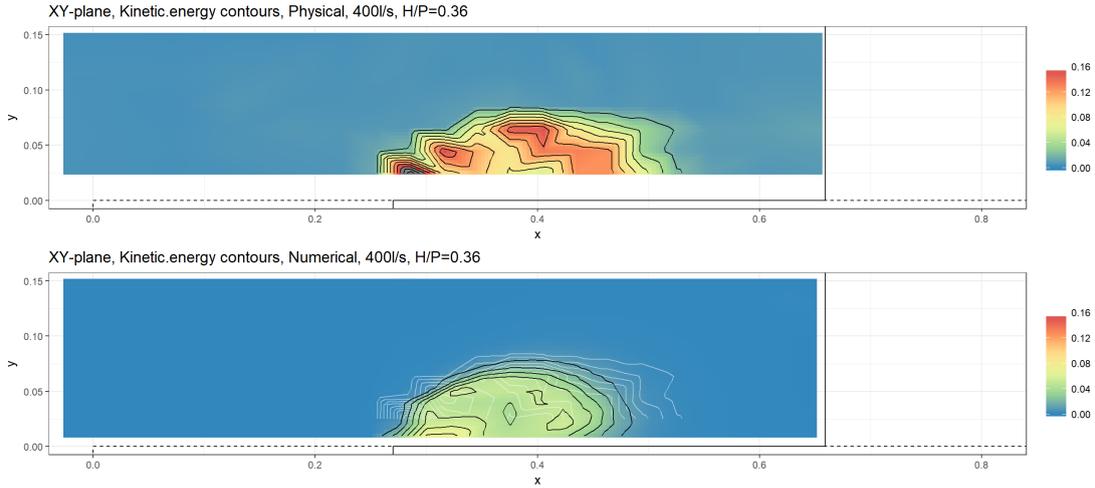


Figure D.9: Horizontal physical and numerical kinetic energy ( $m^2/s^2$ ) at elevation of  $0.54P$ ,  $400l/s$

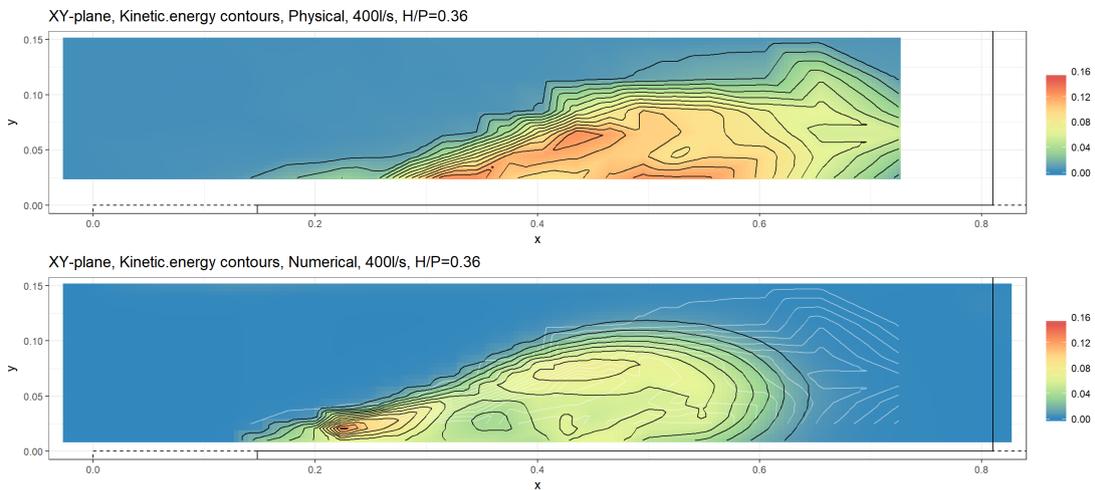


Figure D.10: Horizontal physical and numerical kinetic energy ( $m^2/s^2$ ) at elevation of  $0.79P$ ,  $400l/s$

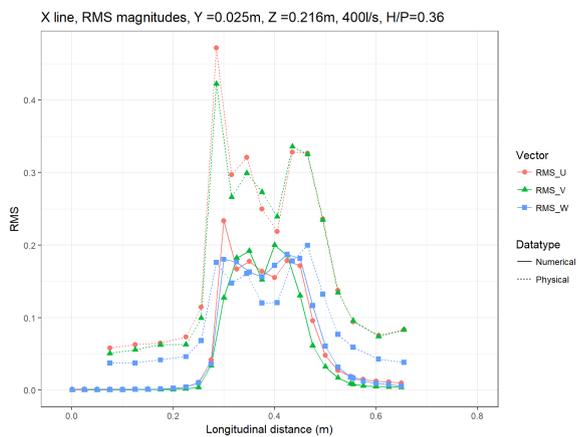


Figure D.11: Velocity RMS values along the inlet key at elevation of  $0.54P$ ,  $400l/s$

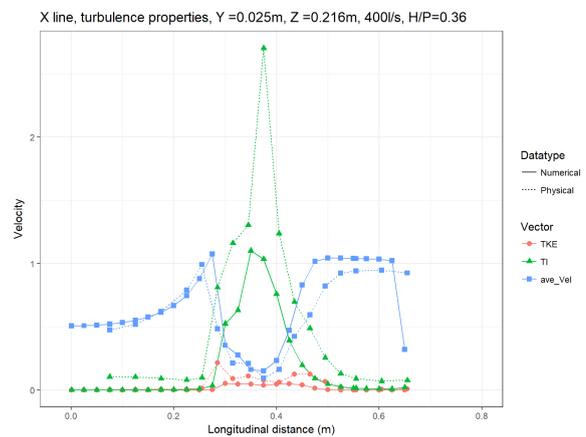


Figure D.12: Turbulence properties along the inlet key at elevation of  $0.54P$ ,  $400l/s$

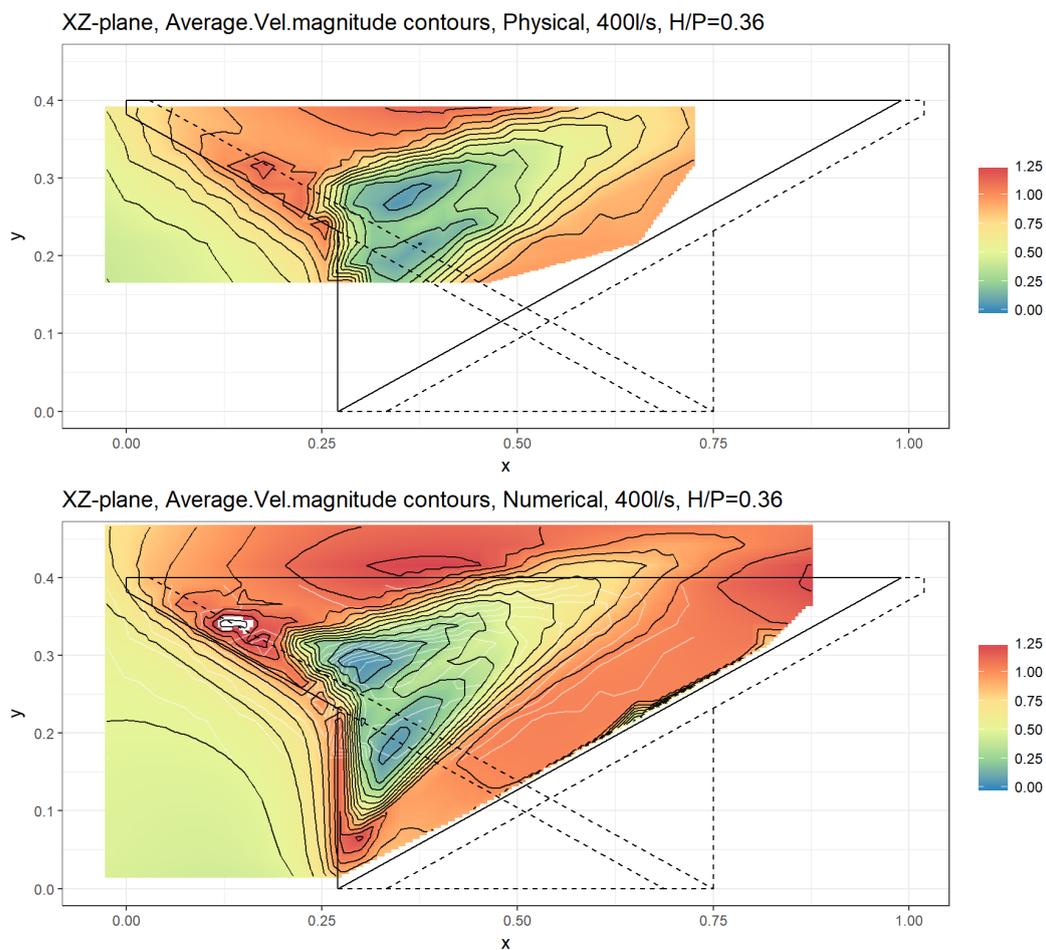


Figure D.13: Longitudinal physical and numerical velocity magnitude ( $m/s$ ), 400l/s

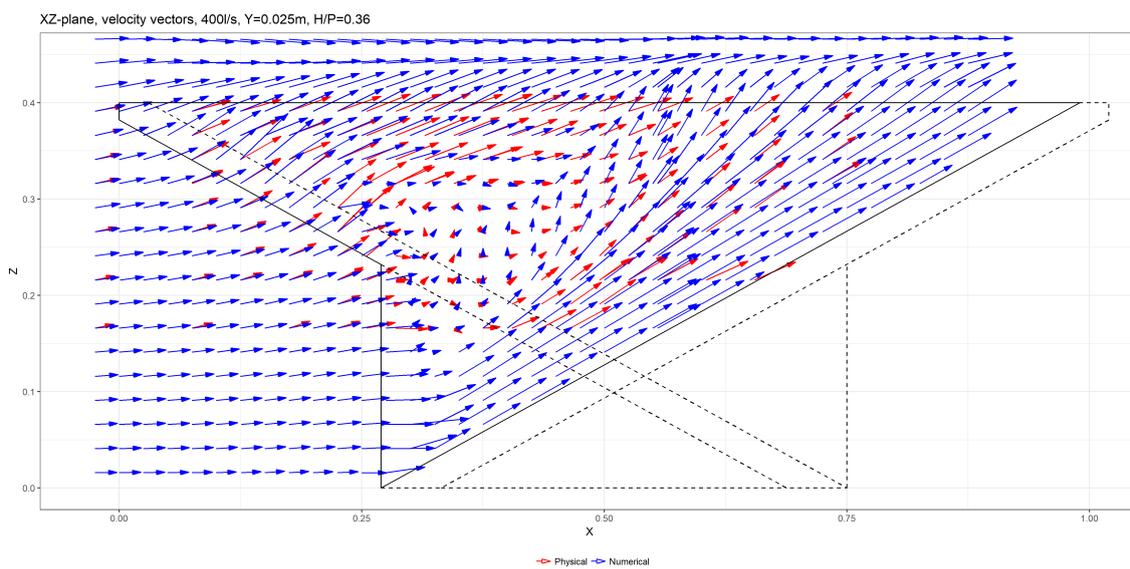


Figure D.14: Longitudinal physical and numerical velocity vectors, 400l/s

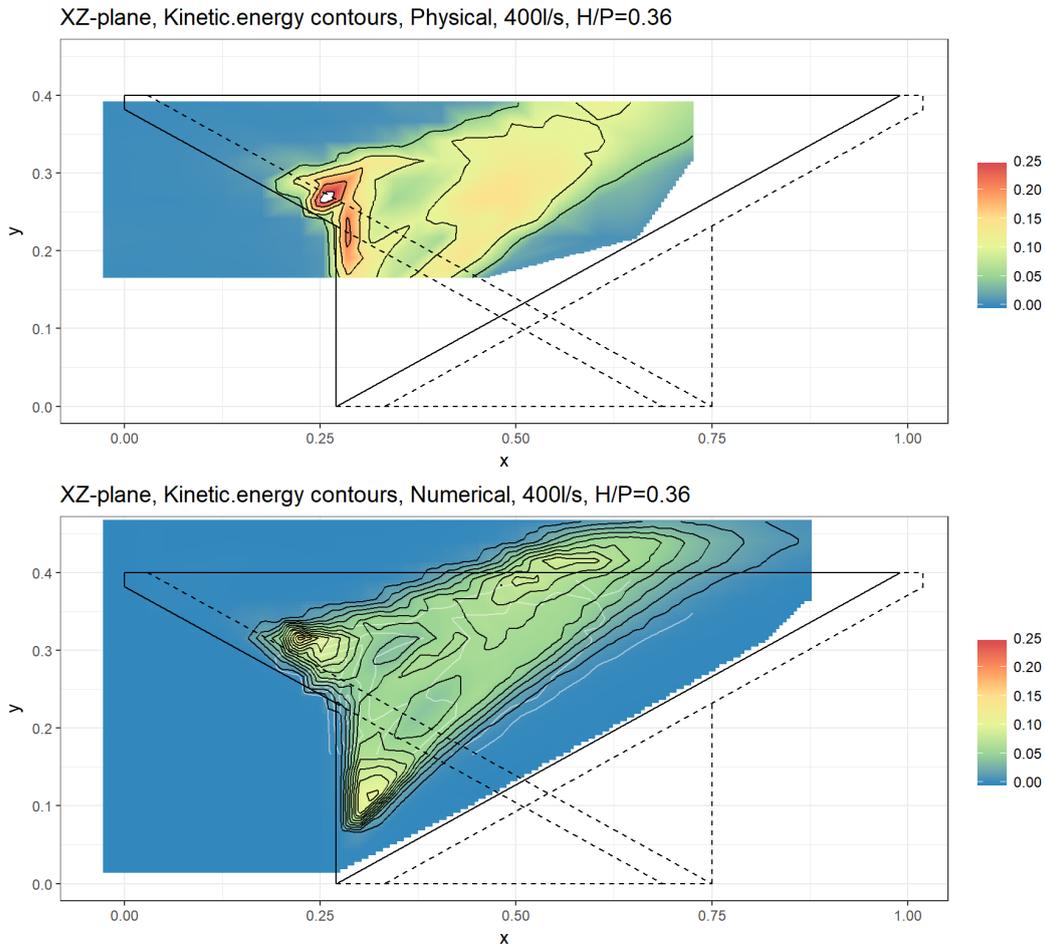


Figure D.15: Longitudinal physical and numerical kinetic energy ( $m^2/s^2$ ), 400l/s

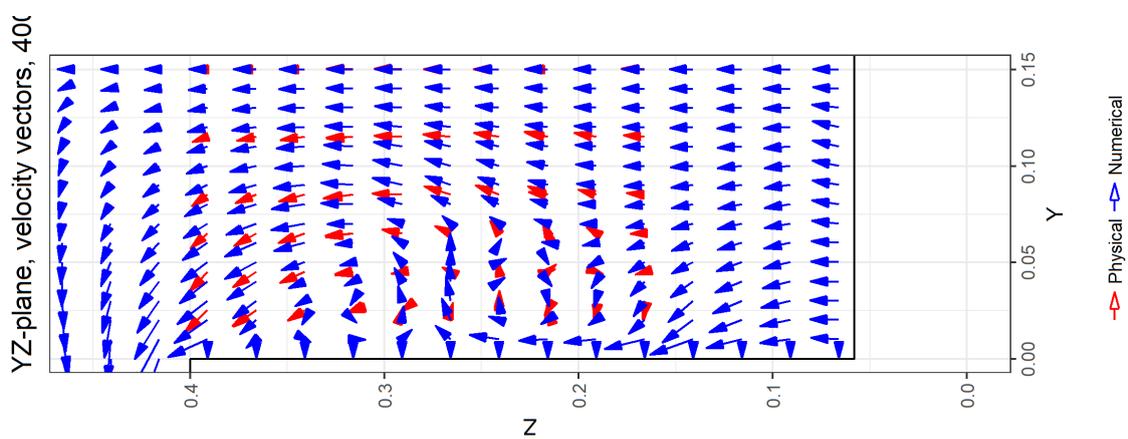


Figure D.16: Transverse physical and numerical velocity vectors, 400l/s (rotated)

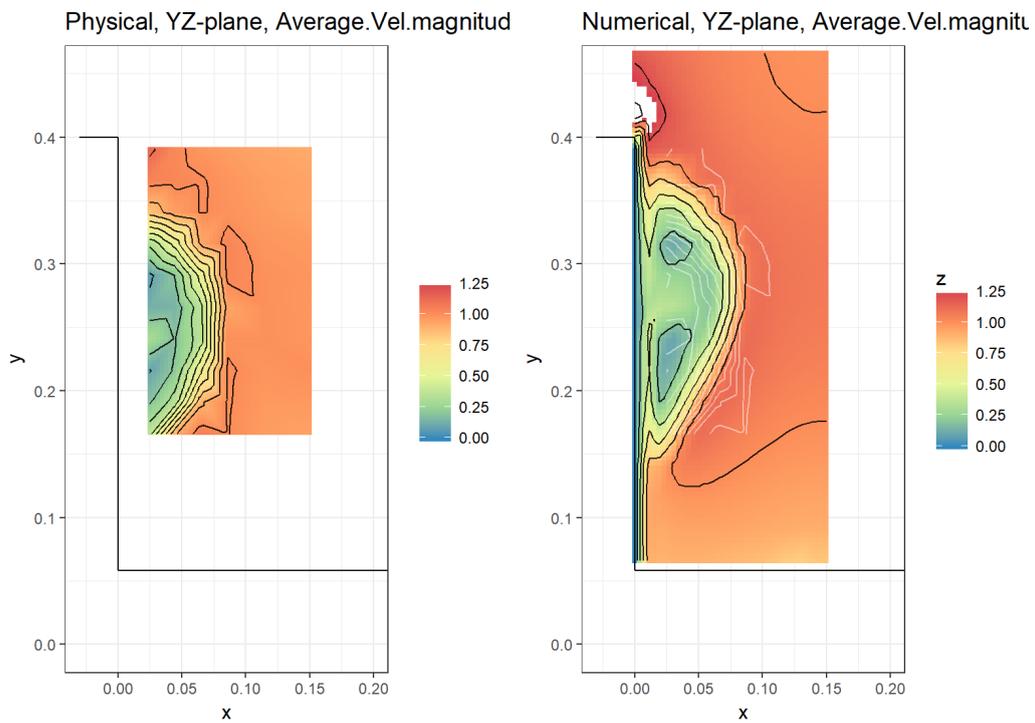


Figure D.17: Transverse physical and numerical velocity magnitude ( $m/s$ ), 4001/s

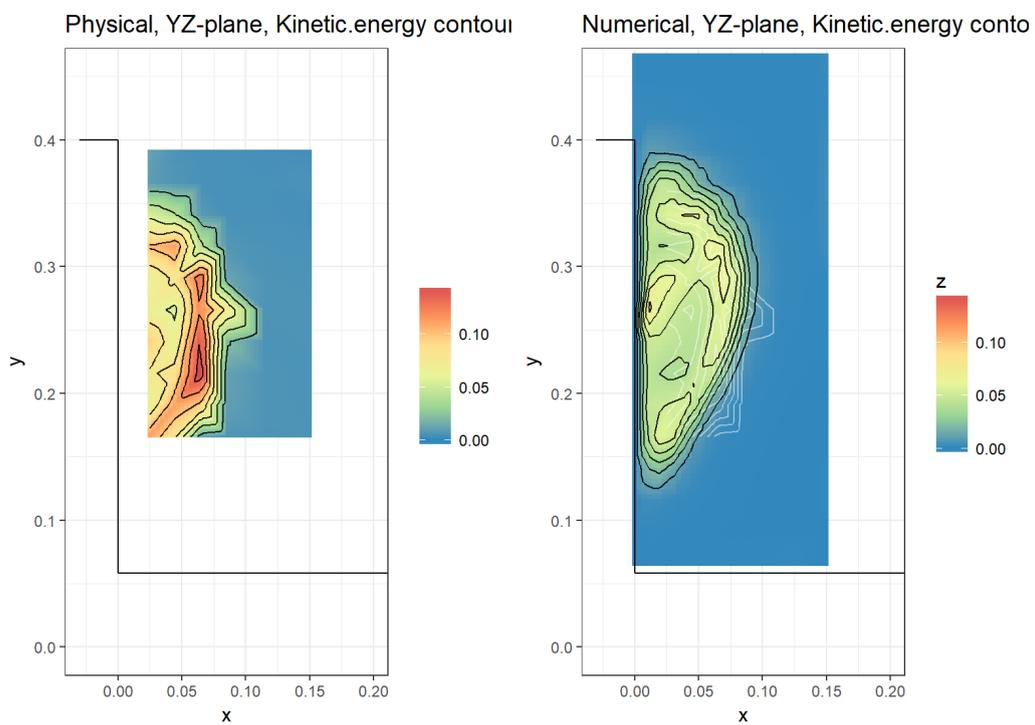


Figure D.18: Transverse physical and numerical kinetic energy ( $m^2/s^2$ ), 4001/s

D.1.2 Model A, Discharge 200 l/s, H/P = 0.19

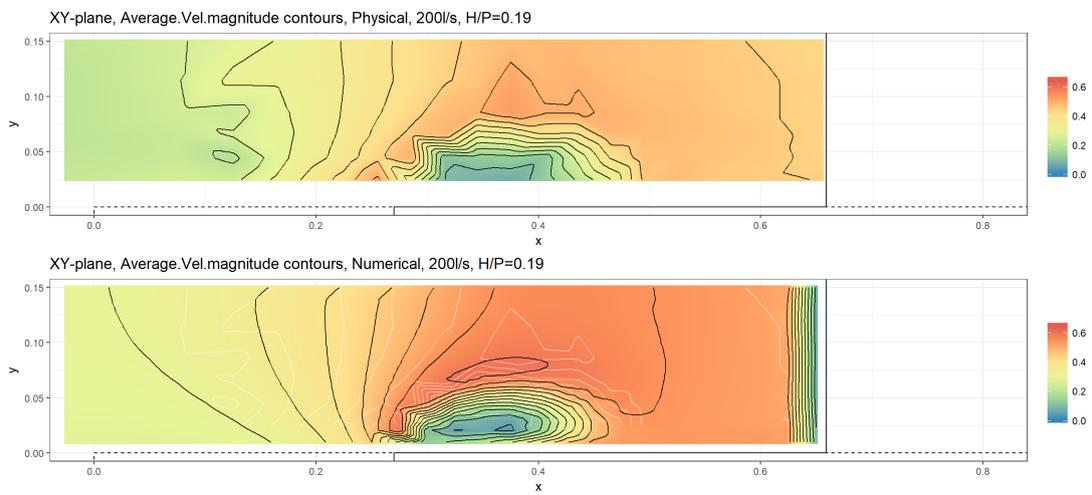


Figure D.19: Horizontal physical and numerical velocity magnitude ( $m/s$ ) at elevation of  $0.54P$ , 200l/s

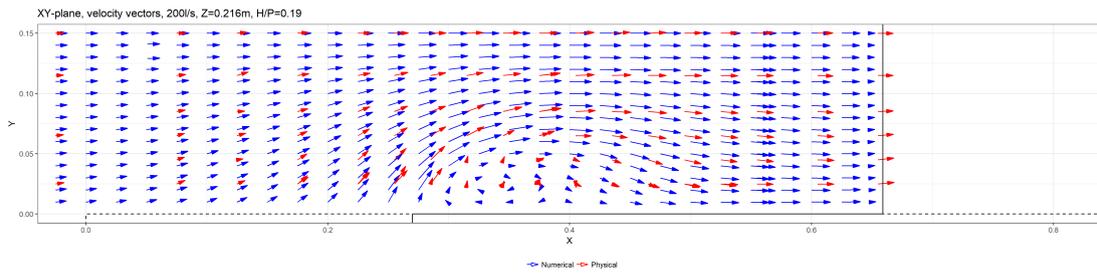


Figure D.20: Horizontal physical and numerical velocity vectors at elevation of  $0.54P$ , 200l/s

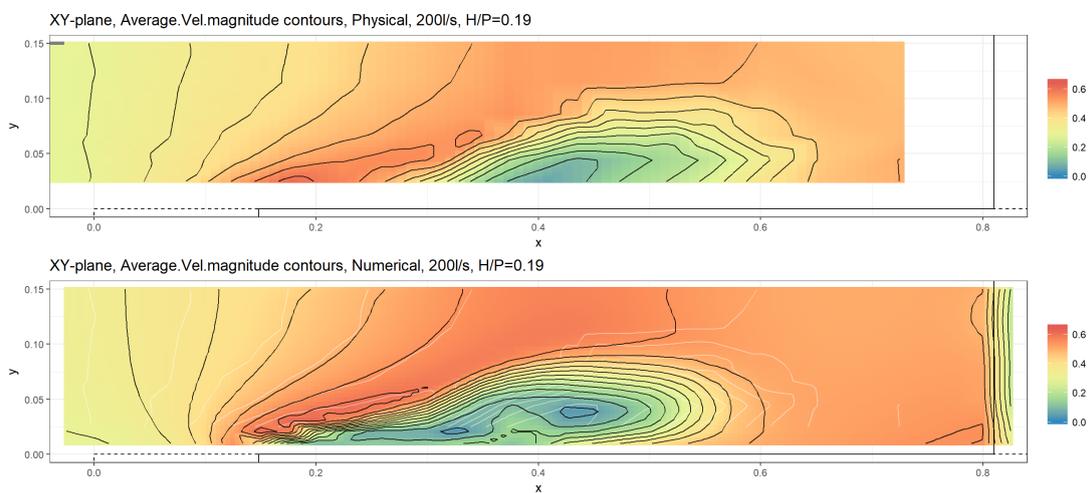


Figure D.21: Horizontal physical and numerical velocity magnitude ( $m/s$ ) at elevation of  $0.79P$ , 200l/s

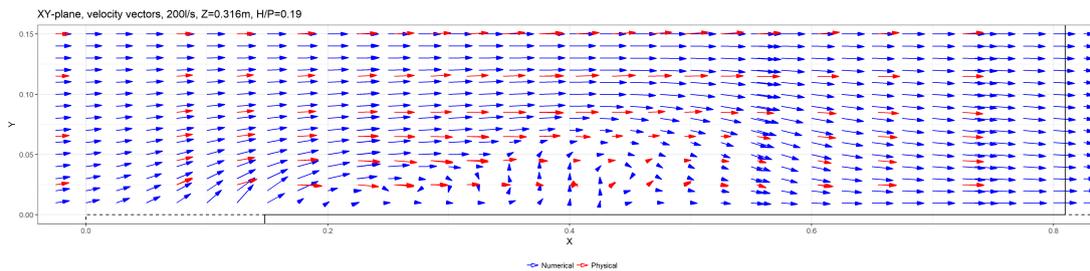


Figure D.22: Horizontal physical and numerical velocity vectors at elevation of  $0.79P$ , 200l/s

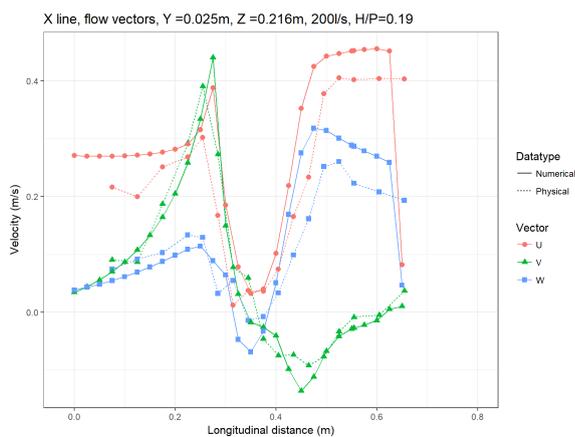


Figure D.23: Velocity vector magnitudes along the inlet key at elevation of  $0.54P$ , 200l/s

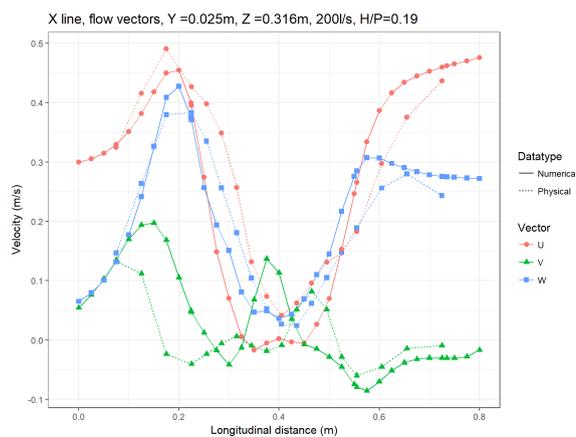


Figure D.24: Velocity vector magnitudes along the inlet key at elevation of  $0.79P$ , 200l/s

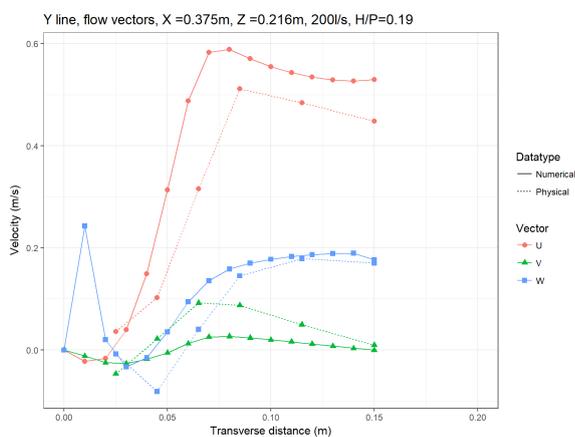


Figure D.25: Velocity vector magnitudes across the inlet key at elevation of  $0.54P$ , 200l/s

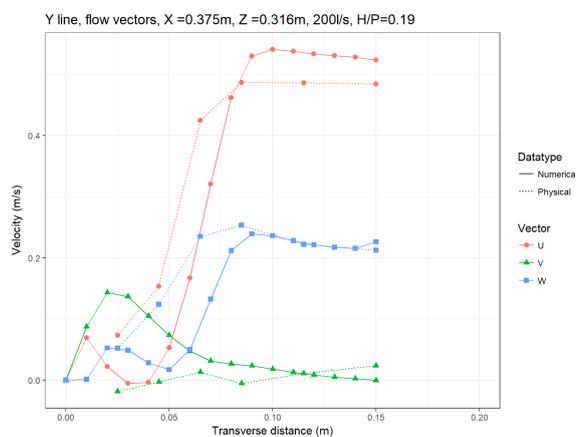


Figure D.26: Velocity vector magnitudes across the inlet key at elevation of  $0.79P$ , 200l/s

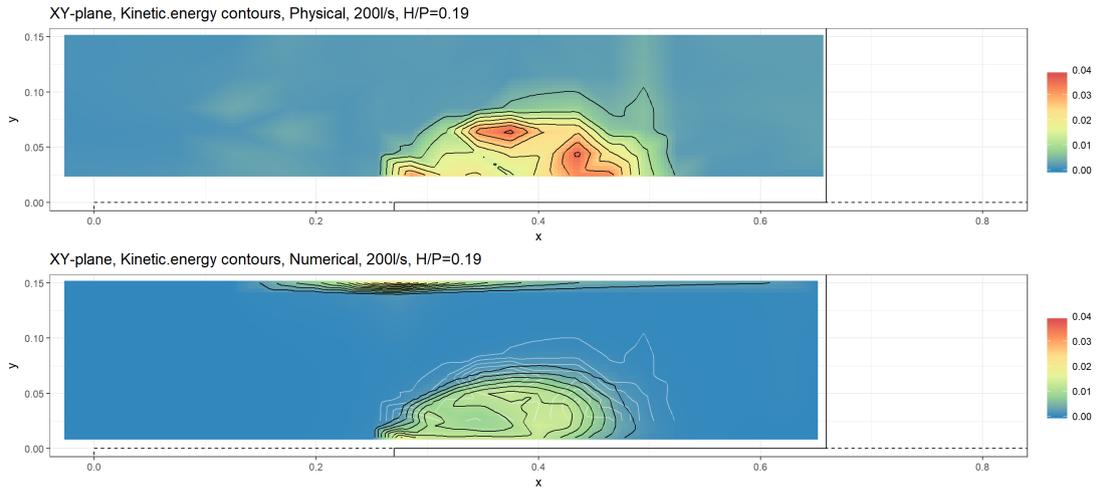


Figure D.27: Horizontal physical and numerical kinetic energy ( $m^2/s^2$ ) at elevation of  $0.54P$ , 2001/s

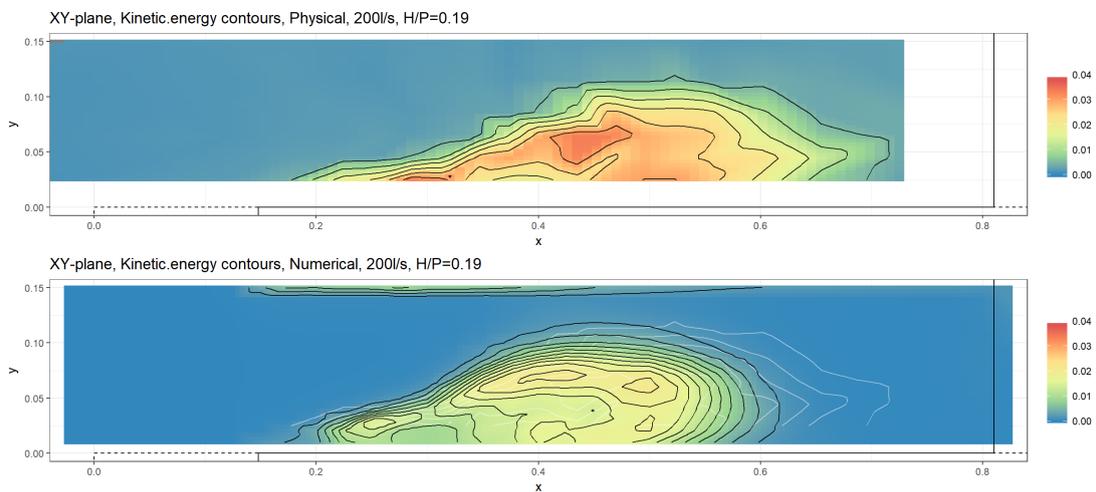


Figure D.28: Horizontal physical and numerical kinetic energy ( $m^2/s^2$ ) at elevation of  $0.79P$ , 2001/s

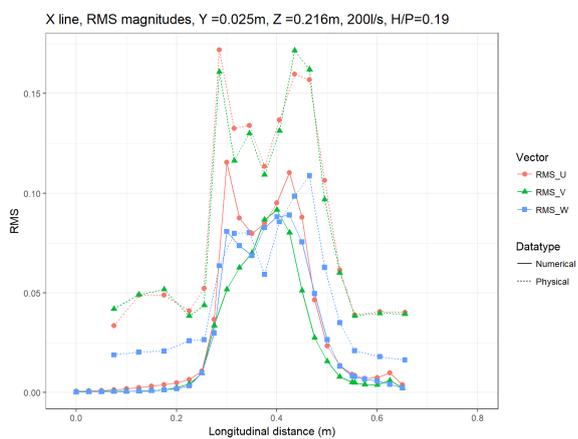


Figure D.29: Velocity RMS values along the inlet key at elevation of  $0.54P$ , 2001/s

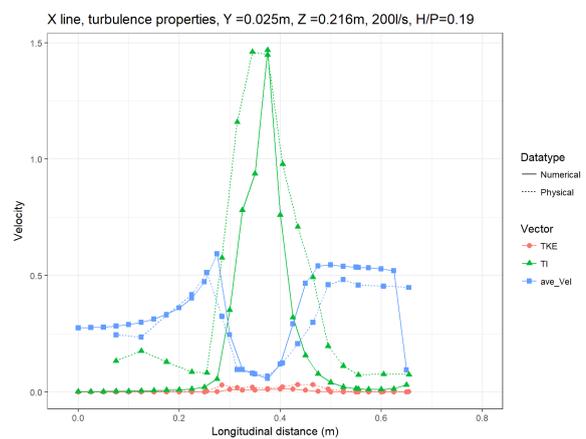


Figure D.30: Turbulence properties along the inlet key at elevation of  $0.54P$ , 2001/s

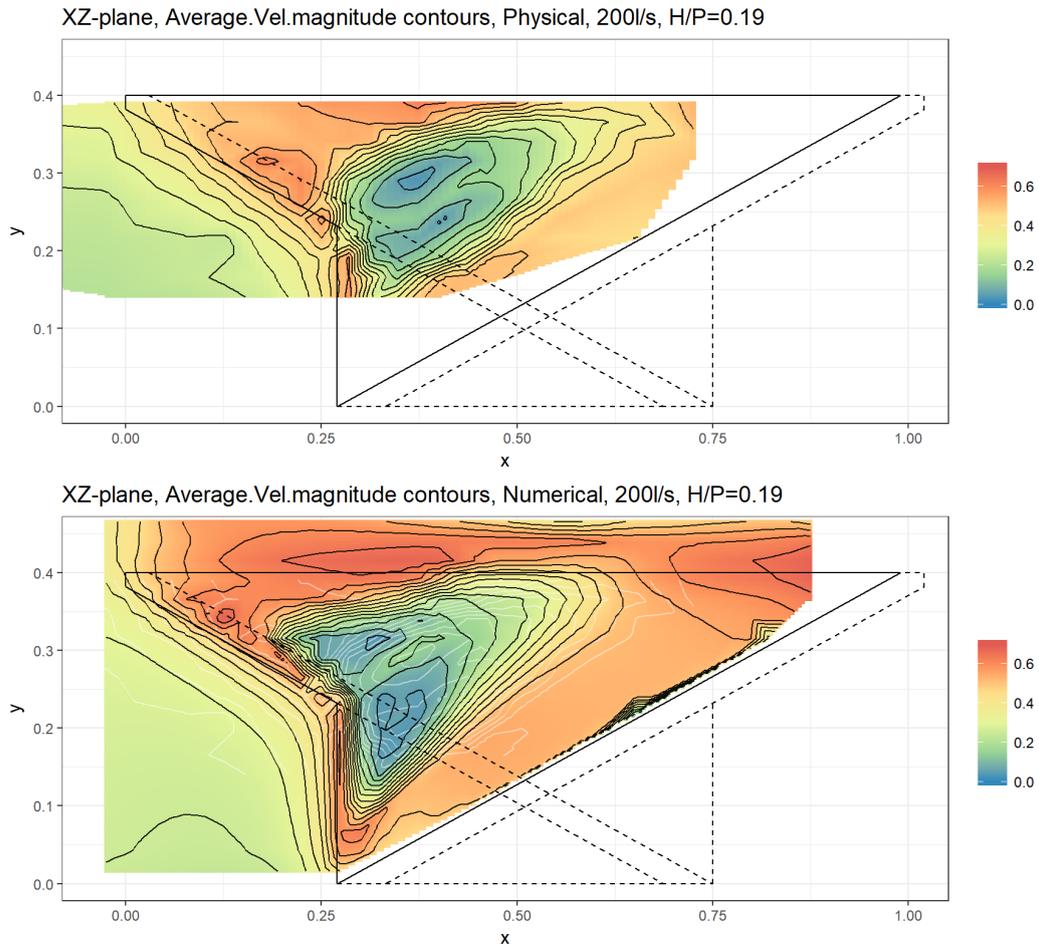


Figure D.31: Longitudinal physical and numerical velocity magnitude ( $m/s$ ), 2001/s

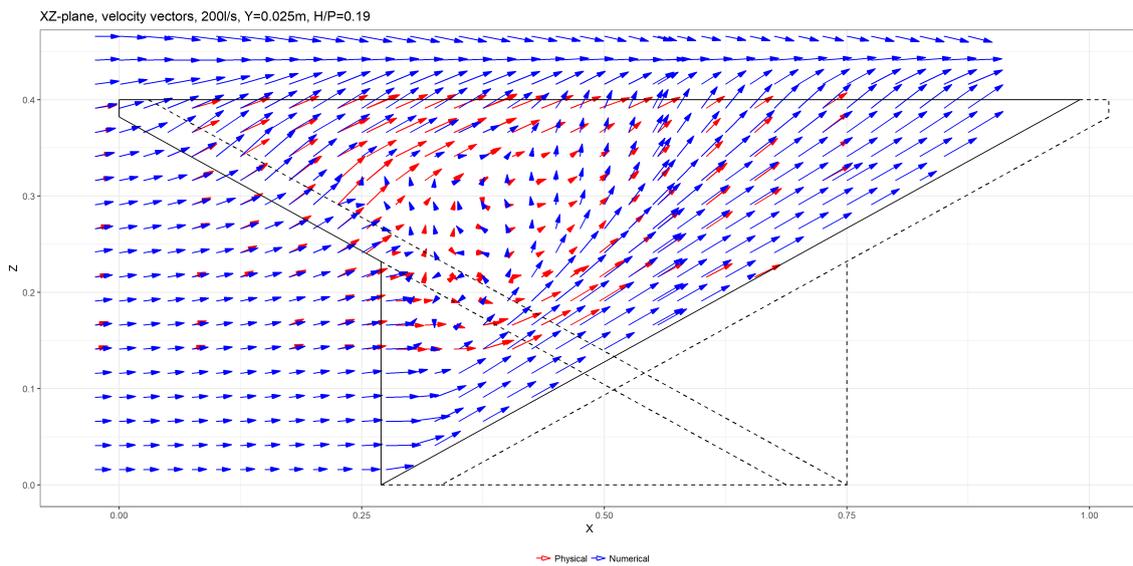


Figure D.32: Longitudinal physical and numerical velocity vectors, 2001/s

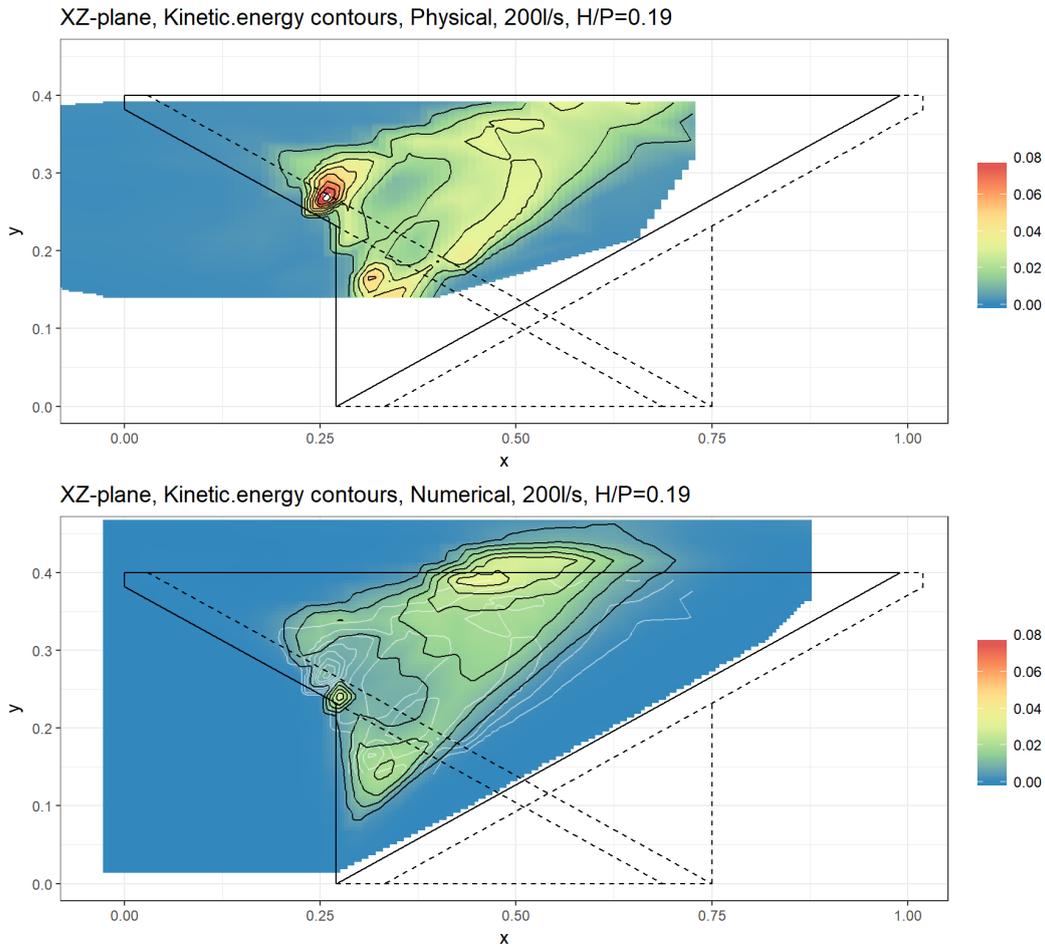
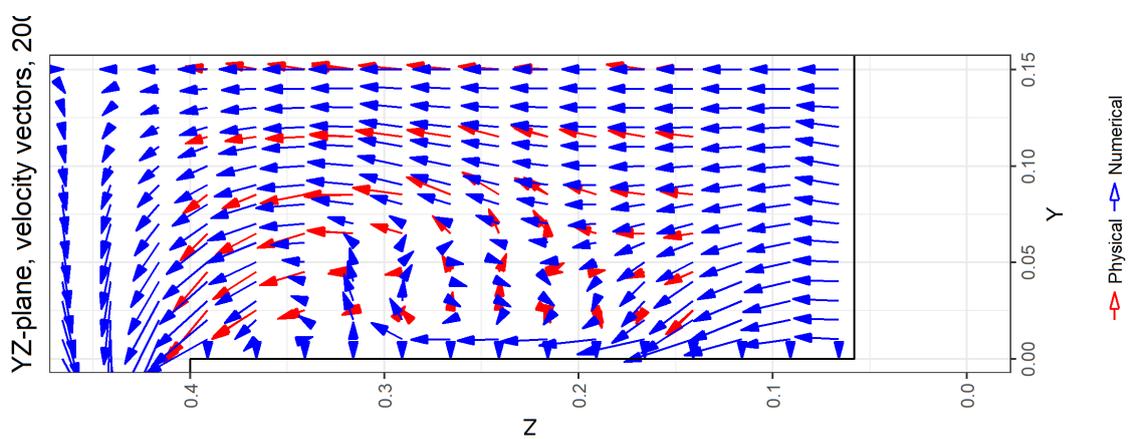
Figure D.33: Longitudinal physical and numerical kinetic energy ( $m^2/s^2$ ), 200l/s

Figure D.34: Transverse physical and numerical velocity vectors, 200l/s (rotated)

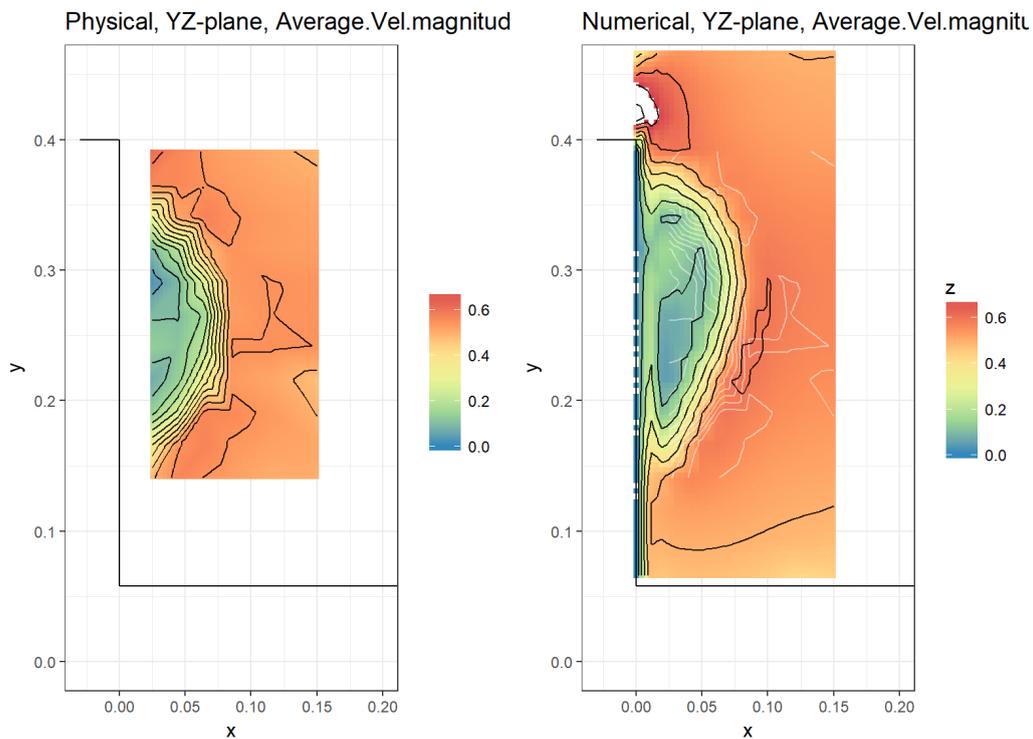


Figure D.35: Transverse physical and numerical velocity magnitude ( $m/s$ ), 2001/s

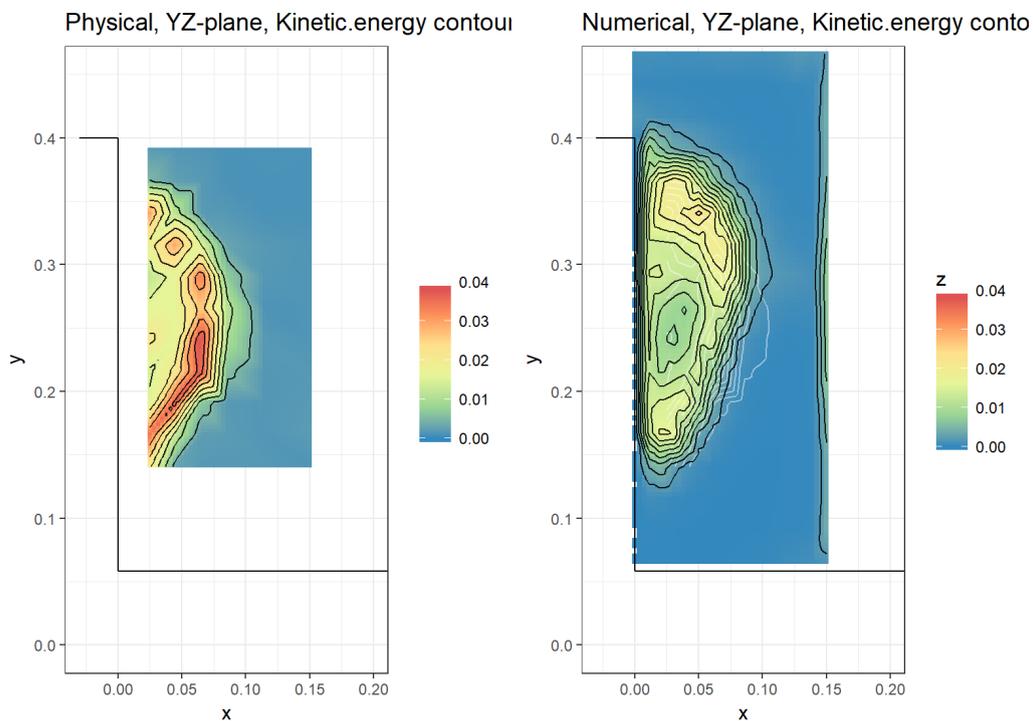


Figure D.36: Transverse physical and numerical kinetic energy ( $m^2/s^2$ ), 2001/s

## D.2 Vector and turbulence graphs

The velocity of the flow and its changes as it approaches and encounters a PKW are described using a set of graphs along a number of lines along and across the inlet key. These are aligned to the Cartesian X-Y-Z (longitudinal-transverse-vertical) directions. The lines all intersect at locations above the pressure sensor points (see Figure 7.10). In each of the graphs, a dotted line shows the location of where the flow encounters the PKW (either the upstream edge, the wall or the crest). The coordinates of the lines are as follows:

- The topmost X-line ( $Z = 0.316$ ) runs on a plane at points A1, A2, A3 and A4 at a distance of 0.025 m from the wall
- The lowermost X-line ( $Z = 0.216$ ) runs on a plane at points A5 and A6 at a distance of 0.025 m from the wall
- The transverse Y-lines run across the inlet key from the pressure point in question at an equal elevation
- The most downstream vertical line runs on a vertical plane joining points A2, A5 and A7 at a distance of 0.025 m from the wall
- The most upstream vertical line runs on a vertical plane at point A1 at a distance of 0.025 m from the wall

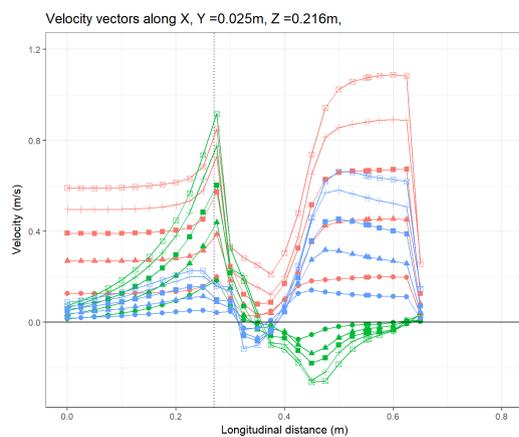


Figure D.37: X-axis vectors, base level

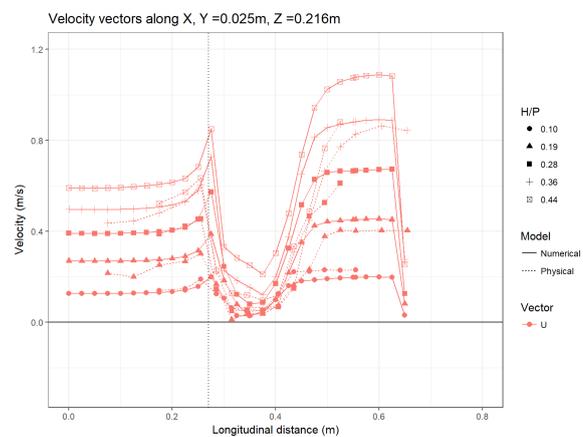


Figure D.38: X-axis U-vector, base level

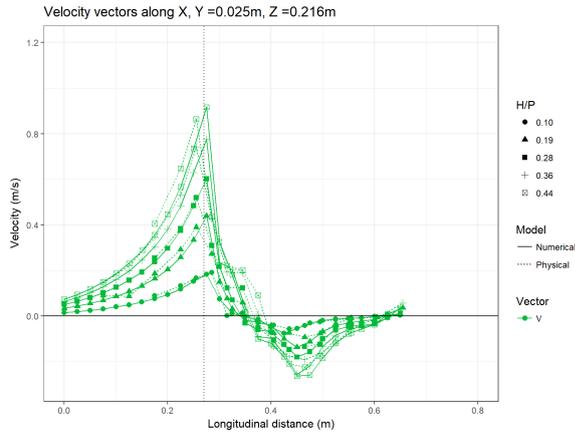


Figure D.39: X-axis V-vector, base level

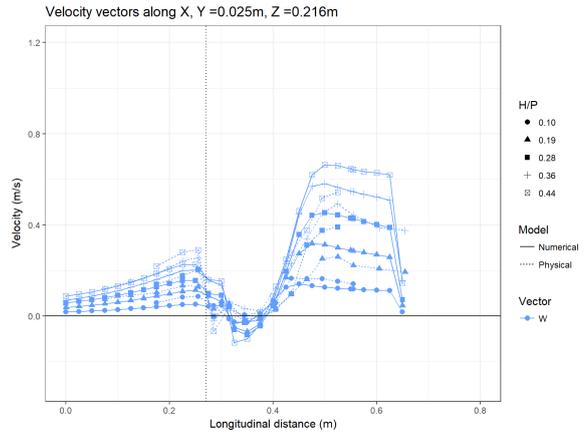


Figure D.40: X-axis W-vector, base level

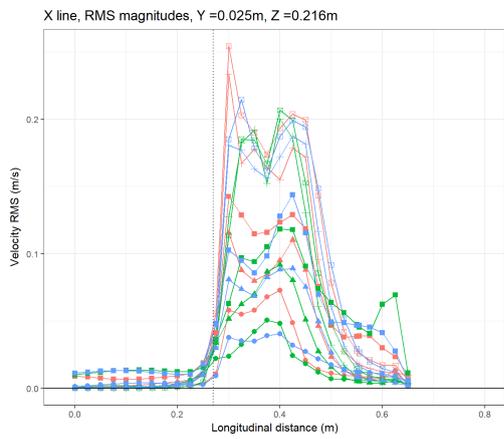


Figure D.41: X-axis RMS, base level

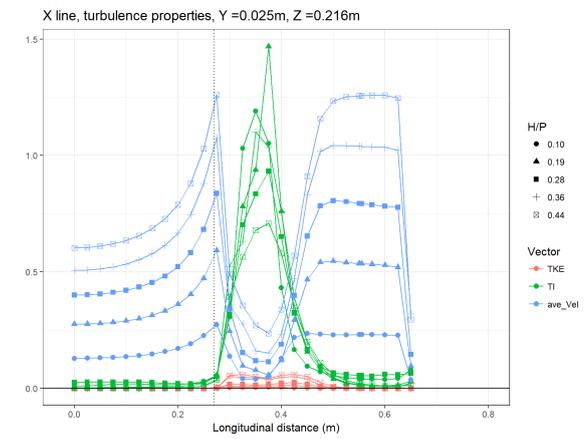


Figure D.42: X-axis turbulence, base level

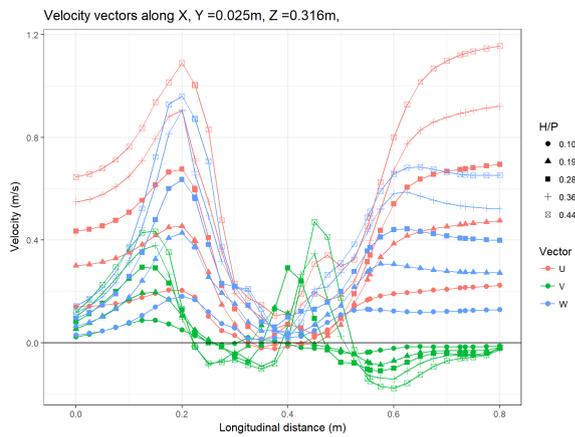


Figure D.43: X-axis vectors, top level

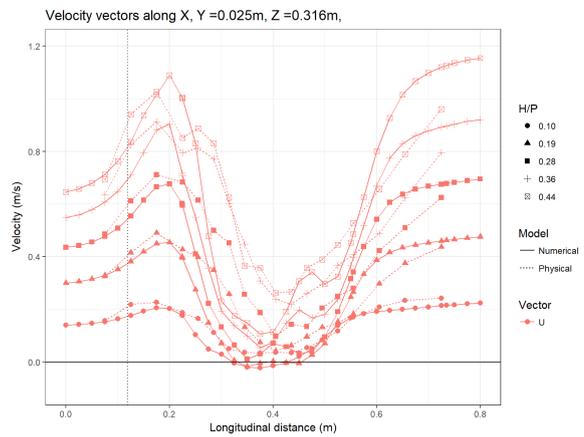


Figure D.44: X-axis U-vector, top level

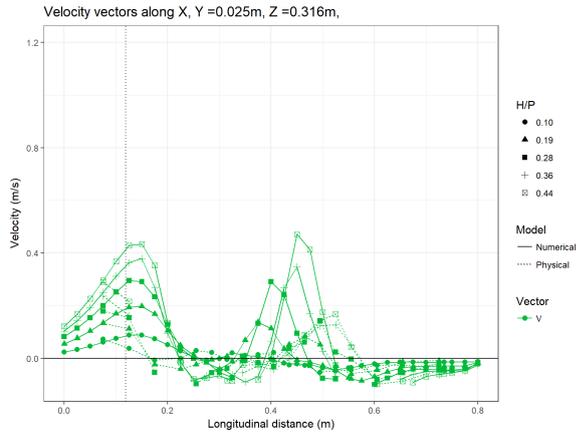


Figure D.45: X-axis V-vector, top level

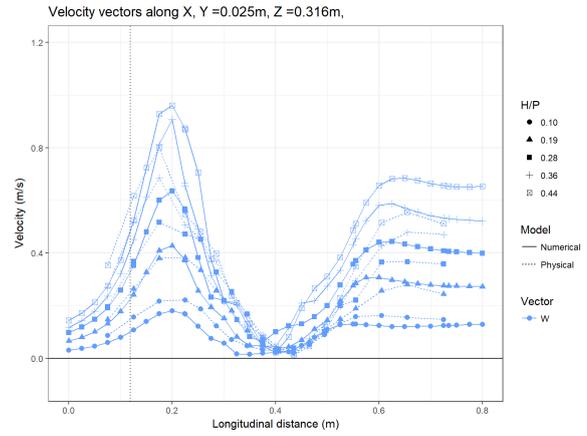


Figure D.46: X-axis W-vector, top level

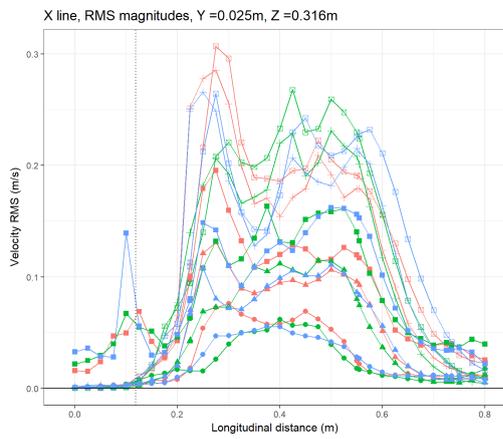


Figure D.47: X-axis RMS, top level

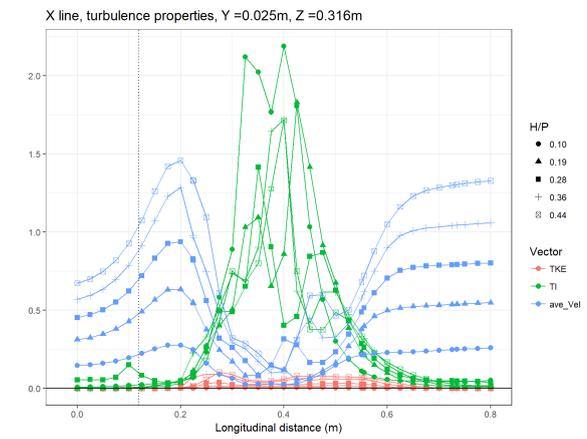


Figure D.48: X-axis turbulence, top level

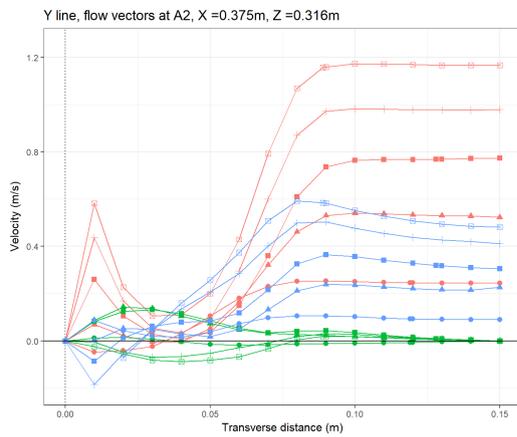


Figure D.49: Y-axis vectors, A2

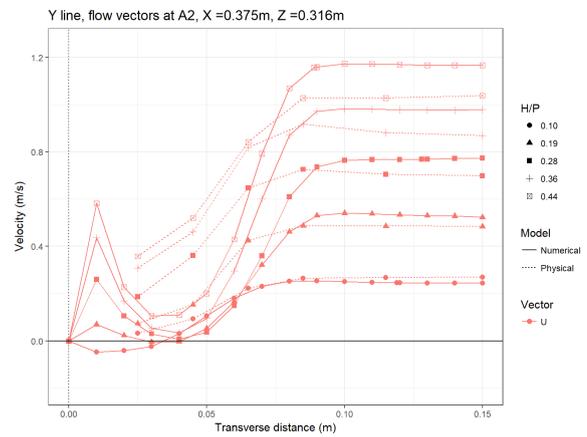


Figure D.50: Y-axis U-vector, A2

D.2. VECTOR AND TURBULENCE GRAPHS

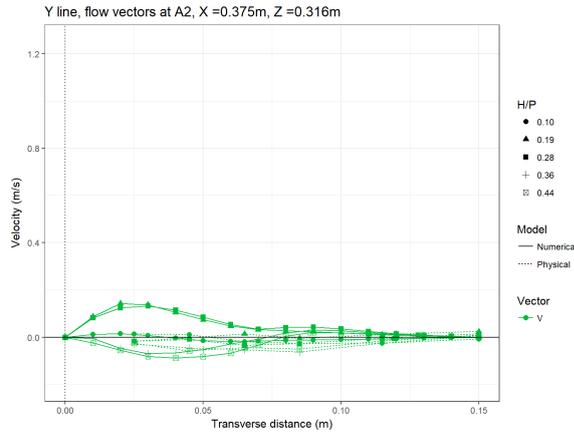


Figure D.51: Y-axis V-vector, A2

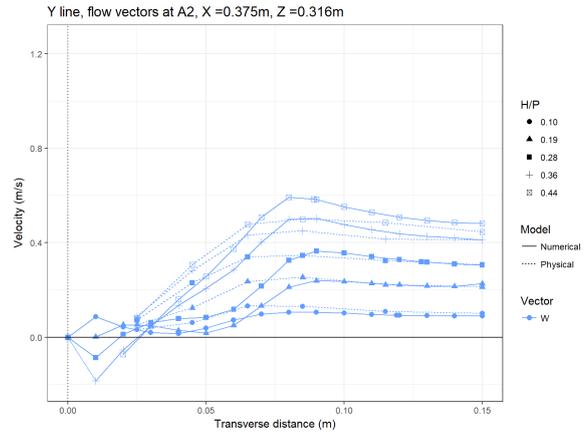


Figure D.52: Y-axis W-vector, A2

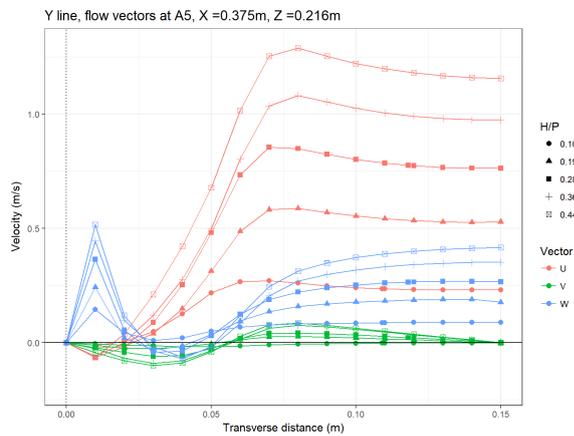


Figure D.53: Y-axis vectors, A5

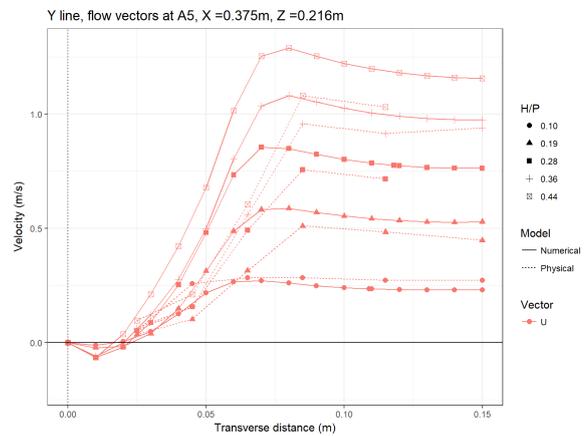


Figure D.54: Y-axis U-vector, A5

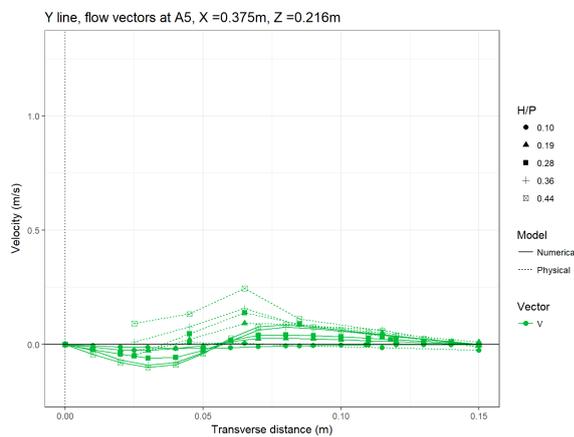


Figure D.55: Y-axis V-vector, A5

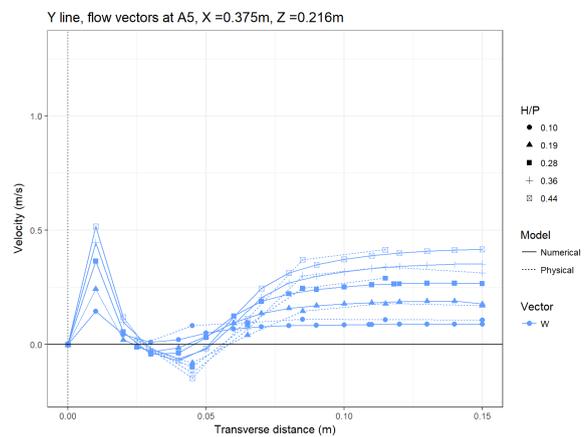


Figure D.56: Y-axis W-vector, A5

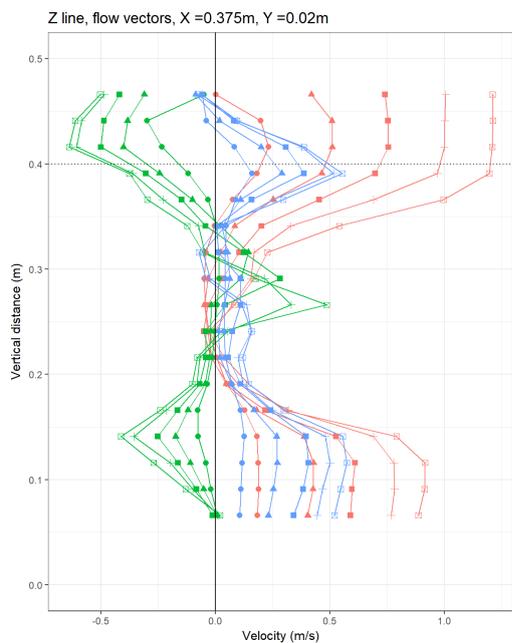


Figure D.57: Z-axis vectors, A2-A7

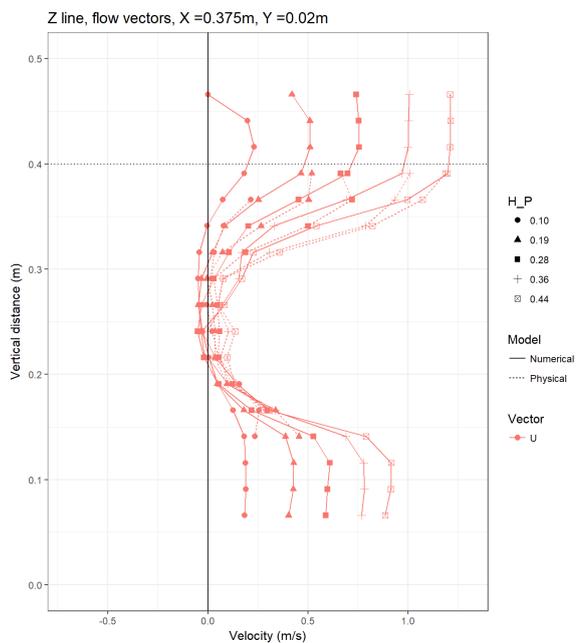


Figure D.58: Z-axis U-vector, A2-A7

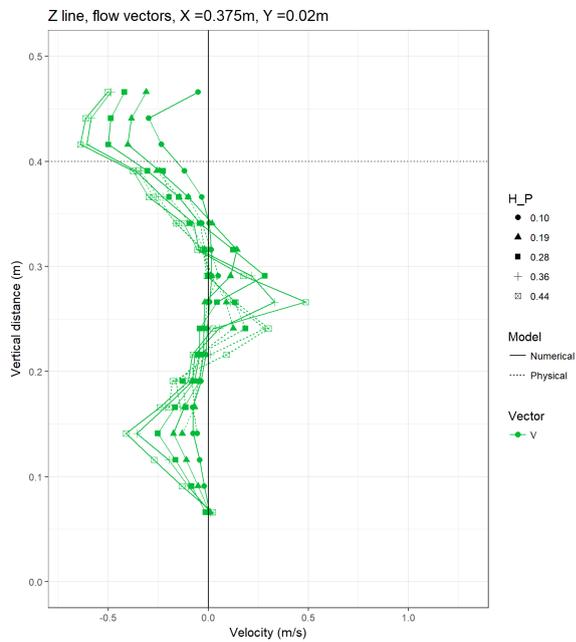


Figure D.59: Z-axis V-vector, A2-A7

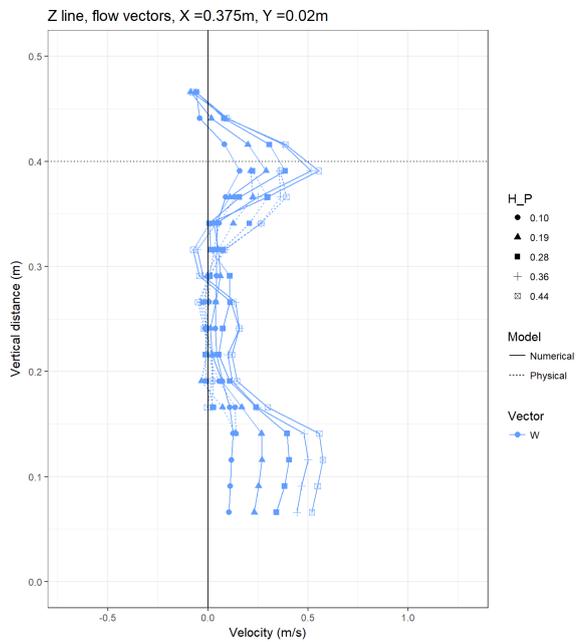


Figure D.60: Z-axis W-vector, A2-A7

### D.3 Pressure spectrum graphs

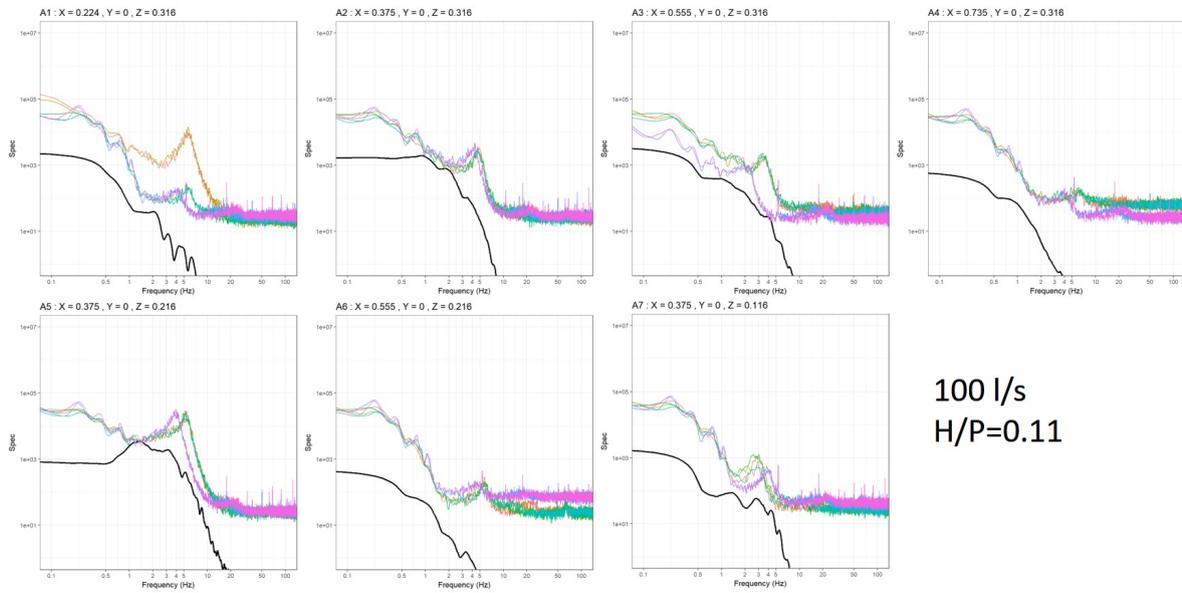


Figure D.61: Pressure spectrum calibration - 100l/s

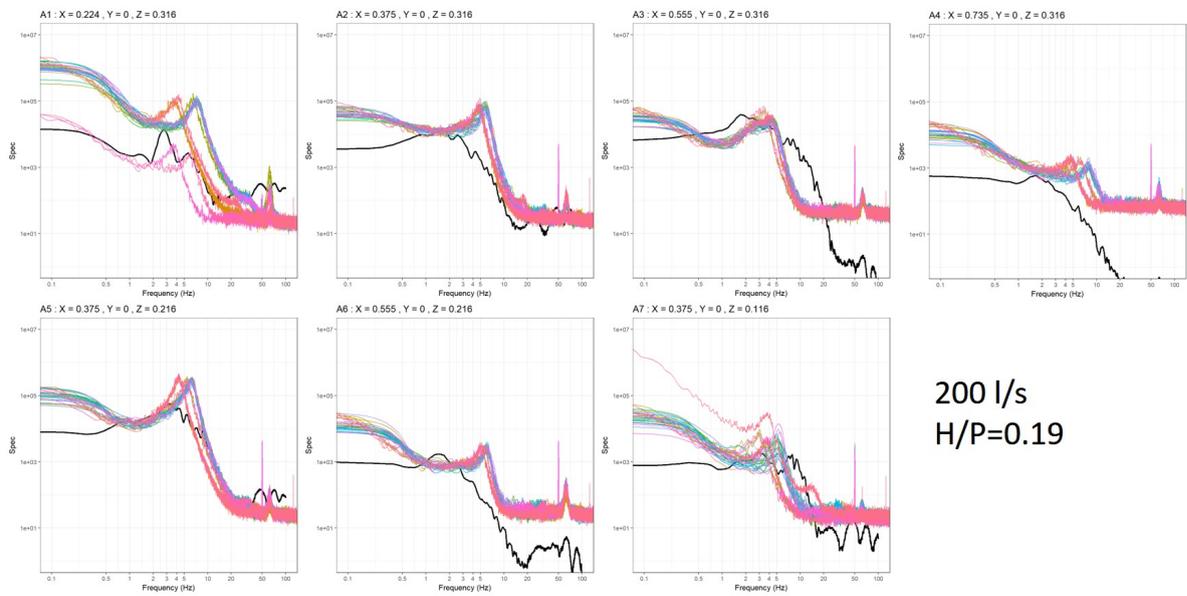


Figure D.62: Pressure spectrum calibration - 200l/s

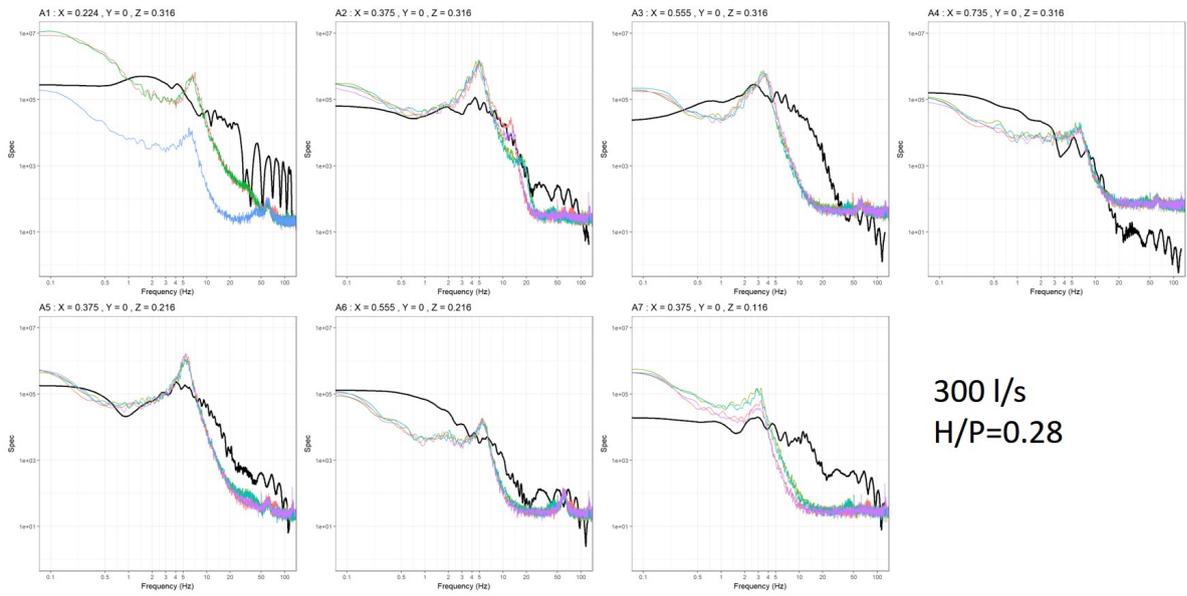


Figure D.63: Pressure spectrum calibration - 300l/s

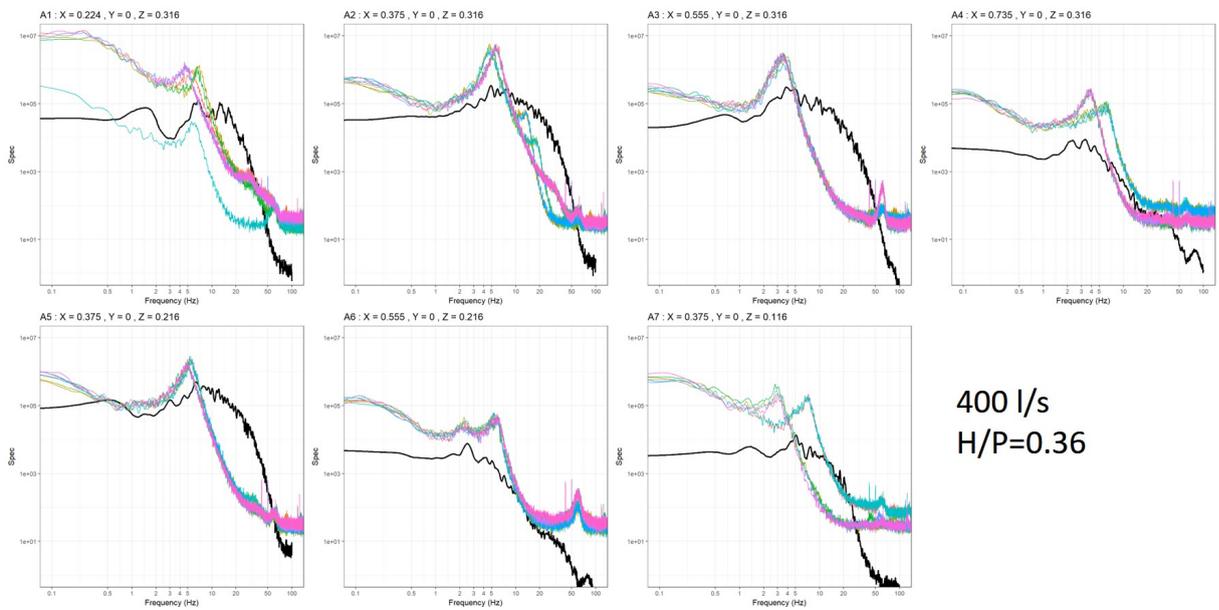


Figure D.64: Pressure spectrum calibration - 400l/s

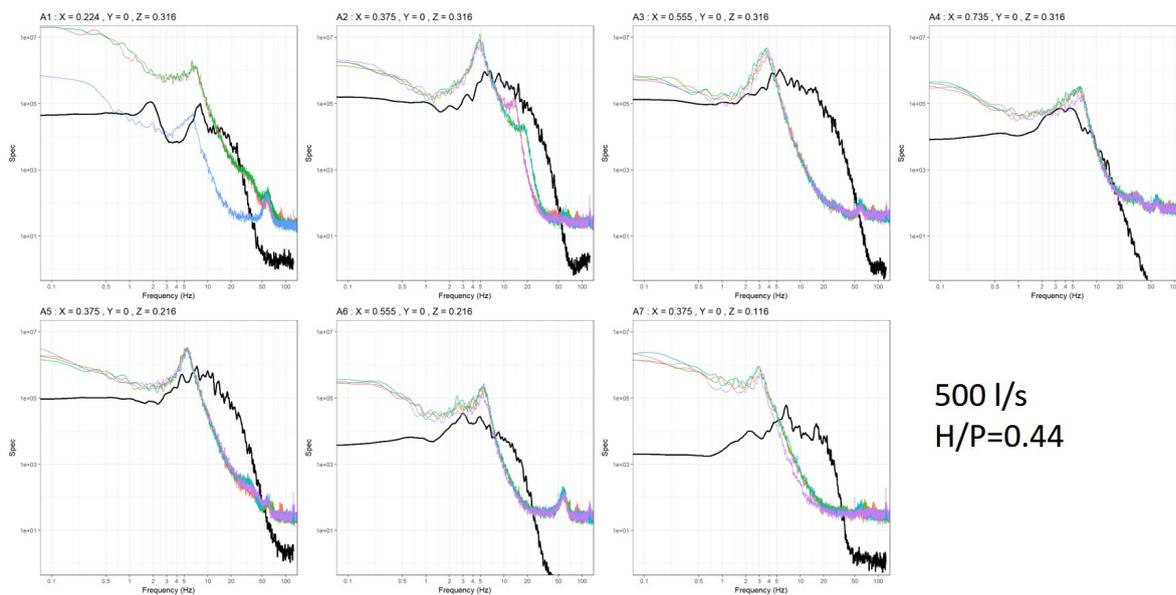


Figure D.65: Pressure spectrum calibration - 500l/s

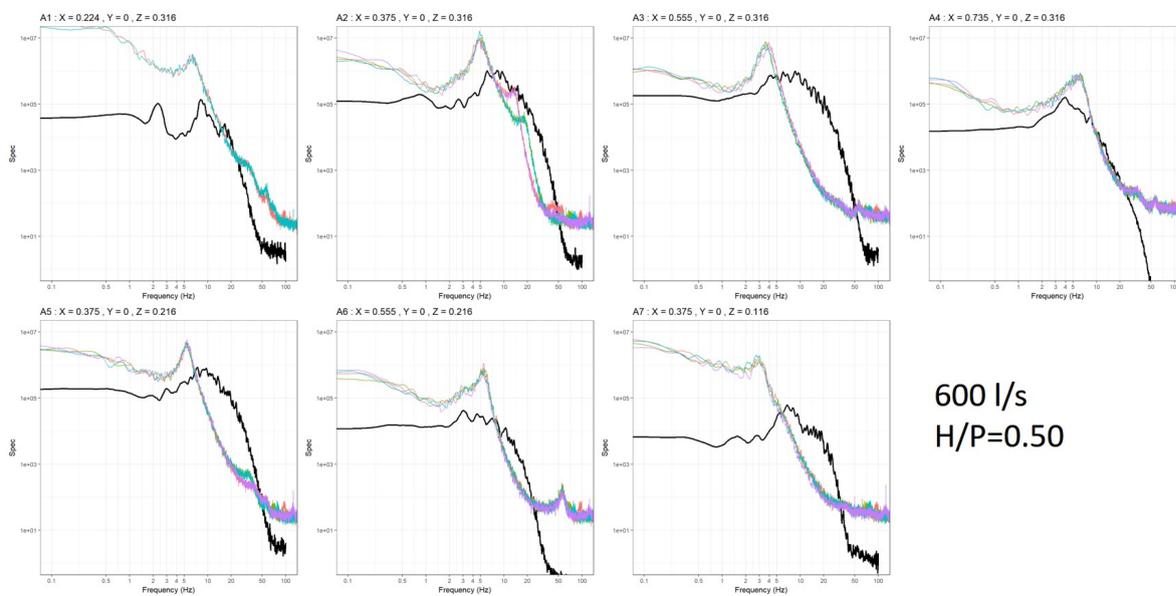
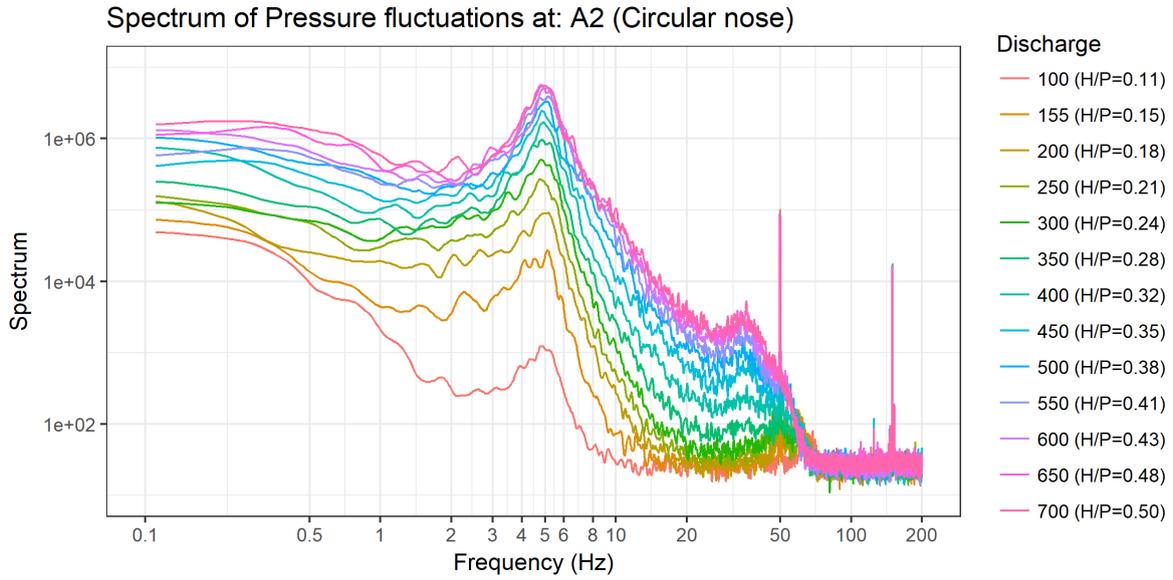
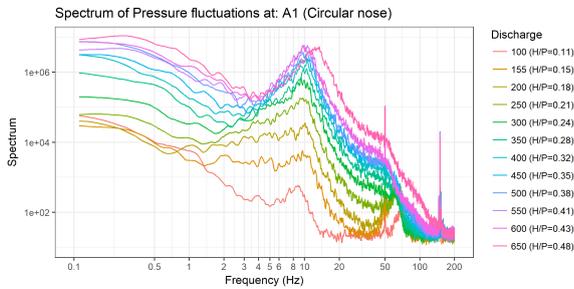


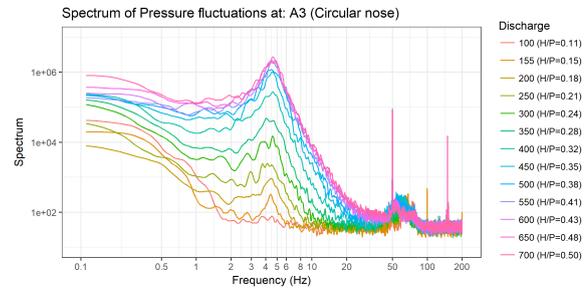
Figure D.66: Pressure spectrum calibration - 600l/s



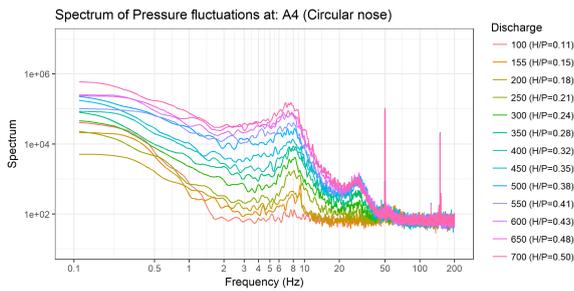
(a) Pressure spectra at point A2



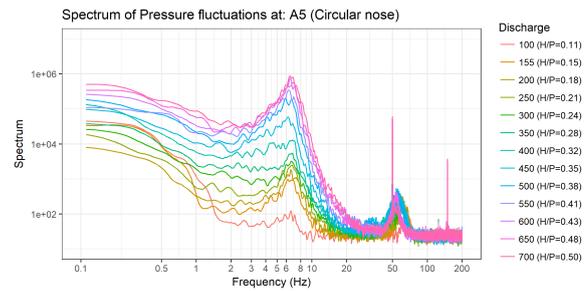
(b) Pressure spectra at point A1



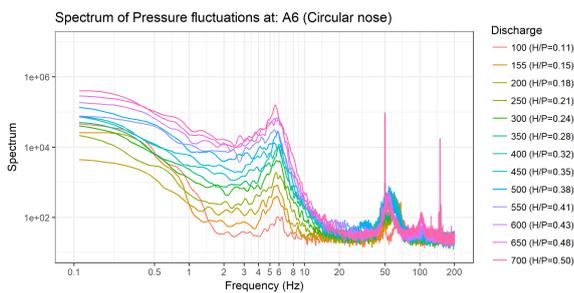
(c) Pressure spectra at point A3



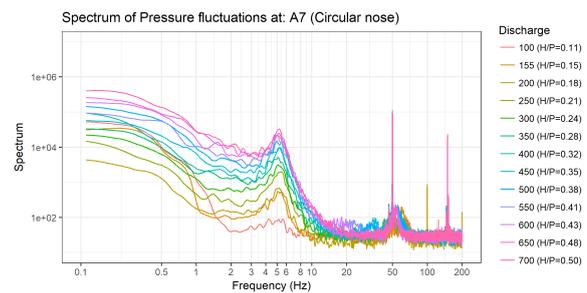
(d) Pressure spectra at point A4



(e) Pressure spectra at point A5

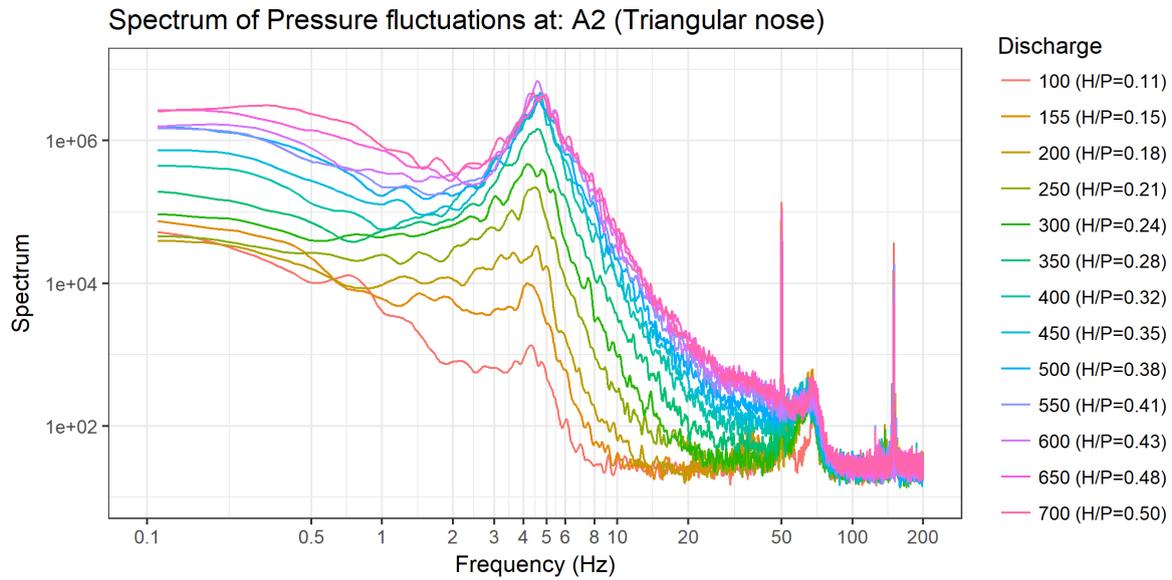


(f) Pressure spectra at point A6

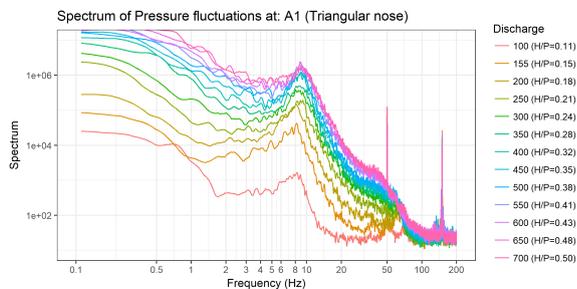


(g) Pressure spectra at point A7

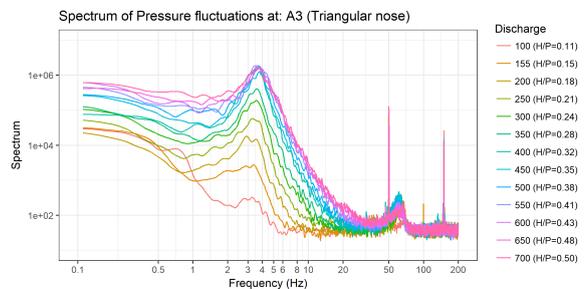
Figure D.67: Physical model pressure spectra over a range of discharges with circular nose



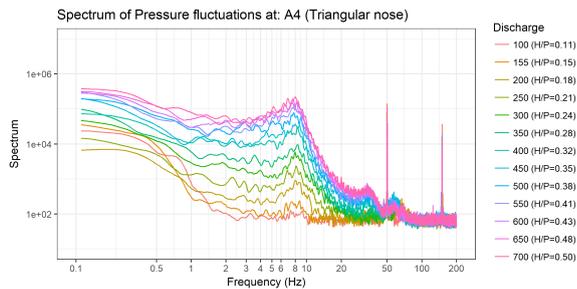
(a) Pressure spectra at point A2



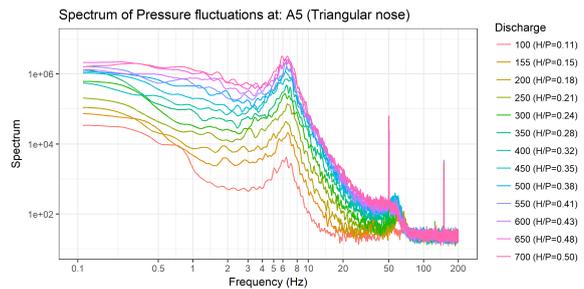
(b) Pressure spectra at point A1



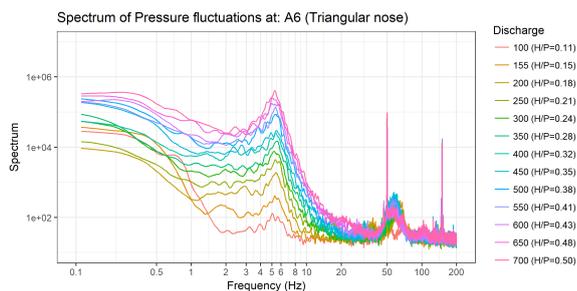
(c) Pressure spectra at point A3



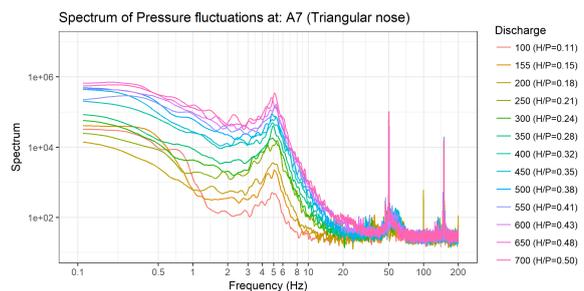
(d) Pressure spectra at point A4



(e) Pressure spectra at point A5



(f) Pressure spectra at point A6



(g) Pressure spectra at point A7

Figure D.68: Physical model pressure spectra over a range of discharges with triangular nose

## D.4 Physical model discharge data

Physical model discharge results: Stellenbosch Hydraulics Laboratory											
P (m)	0.4	W (m)	1.5	Type	A						
Wi (m)	0.3	Ts (m)	0.03	Triangular nose angle (degrees)	45						
Wo (m)	0.24	Bi=Bo (m)	0.27	Round nose diameter (m)	0.3						
P <sub>T</sub> (m)	0.45	Bb (m)	0.48								
Q(m <sup>3</sup> /s)	H(m)	H/P	CdW	Nose	Q(m <sup>3</sup> /s)	H(m)	H/P	CdW	Nose		
0.0530	0.0275	0.068	2.63	Rectangular	0.6008	0.2007	0.450	1.51	Rectangular		
0.0996	0.0470	0.115	2.21	Rectangular	0.6500	0.2196	0.492	1.43	Rectangular		
0.1028	0.0437	0.107	2.54	Rectangular	0.6506	0.2188	0.490	1.44	Rectangular		
0.1070	0.0456	0.111	2.48	Rectangular	0.6750	0.2306	0.517	1.38	Rectangular		
0.1250	0.0525	0.128	2.35	Rectangular	0.7000	0.2354	0.525	1.38	Rectangular		
0.1500	0.0596	0.144	2.33	Rectangular	0.7003	0.2326	0.517	1.41	Rectangular		
0.1505	0.0600	0.145	2.31	Rectangular	0.7300	0.2419	0.537	1.38	Rectangular		
0.2000	0.0729	0.174	2.30	Rectangular	0.7458	0.2474	0.548	1.37	Rectangular		
0.2000	0.0754	0.180	2.18	Rectangular	0.0974	0.0440	0.108	2.38	Triangular		
0.2000	0.0744	0.178	2.22	Rectangular	0.1560	0.0604	0.146	2.37	Triangular		
0.2003	0.0744	0.178	2.23	Rectangular	0.2040	0.0751	0.179	2.24	Triangular		
0.2050	0.0775	0.185	2.15	Rectangular	0.2490	0.0888	0.210	2.12	Triangular		
0.2050	0.0755	0.180	2.23	Rectangular	0.2990	0.1043	0.244	2.01	Triangular		
0.2070	0.0805	0.193	2.05	Rectangular	0.3510	0.1201	0.278	1.90	Triangular		
0.2500	0.0892	0.211	2.12	Rectangular	0.4020	0.1375	0.316	1.78	Triangular		
0.2500	0.0899	0.213	2.09	Rectangular	0.4500	0.1516	0.346	1.72	Triangular		
0.2998	0.1025	0.239	2.06	Rectangular	0.4970	0.1658	0.376	1.66	Triangular		
0.3000	0.1057	0.247	1.97	Rectangular	0.5490	0.1821	0.410	1.59	Triangular		
0.3020	0.1066	0.250	1.96	Rectangular	0.6010	0.1949	0.435	1.58	Triangular		
0.3500	0.1234	0.287	1.82	Rectangular	0.6490	0.2141	0.477	1.48	Triangular		
0.3500	0.1219	0.283	1.86	Rectangular	0.6980	0.2262	0.500	1.46	Triangular		
0.3509	0.1223	0.284	1.85	Rectangular	0.1000	0.0449	0.110	2.37	Circular		
0.3983	0.1345	0.309	1.82	Rectangular	0.1620	0.0649	0.157	2.21	Circular		
0.4005	0.1365	0.314	1.79	Rectangular	0.2000	0.0771	0.185	2.11	Circular		
0.4050	0.1425	0.329	1.70	Rectangular	0.2500	0.0915	0.217	2.04	Circular		
0.4100	0.1418	0.326	1.73	Rectangular	0.3000	0.1071	0.251	1.93	Circular		
0.4500	0.1558	0.357	1.65	Rectangular	0.3500	0.1216	0.282	1.86	Circular		
0.4500	0.1542	0.353	1.68	Rectangular	0.4000	0.1367	0.315	1.79	Circular		
0.4503	0.1533	0.350	1.69	Rectangular	0.4500	0.1534	0.351	1.69	Circular		
0.4990	0.1692	0.384	1.62	Rectangular	0.5000	0.1672	0.379	1.65	Circular		
0.5000	0.1696	0.385	1.62	Rectangular	0.5500	0.1847	0.417	1.56	Circular		
0.5500	0.1861	0.421	1.55	Rectangular	0.6000	0.1992	0.447	1.52	Circular		
0.5510	0.1858	0.420	1.55	Rectangular	0.6500	0.2145	0.478	1.48	Circular		
0.6000	0.2039	0.459	1.47	Rectangular	0.7000	0.2319	0.515	1.42	Circular		
P (m)	1.1	W (m)	0.75	Type	A						
Wi (m)	0.72	Ts (m)	0.006								
Wo (m)	0.72	Bi=Bo (m)	0.66								
P <sub>T</sub> (m)	1.1	Bb (m)	1.32								
Q(m <sup>3</sup> /s)	H(m)	H/P	CdW	Nose	Q(m <sup>3</sup> /s)	H(m)	H/P	CdW	Nose		
0.0050	0.0055	0.005	5.53	Rectangular	0.0300	0.0243	0.022	3.56	Rectangular		
0.0060	0.0063	0.006	5.41	Rectangular	0.0250	0.0205	0.019	3.83	Rectangular		
0.0070	0.0071	0.006	5.28	Rectangular	0.0200	0.0172	0.016	3.99	Rectangular		
0.0080	0.0080	0.007	5.04	Rectangular	0.0180	0.0155	0.014	4.20	Rectangular		
0.0090	0.0088	0.008	4.92	Rectangular	0.0160	0.0141	0.013	4.31	Rectangular		
0.0100	0.0100	0.009	4.51	Rectangular	0.0140	0.0126	0.011	4.46	Rectangular		
0.0110	0.0105	0.010	4.61	Rectangular	0.0130	0.0119	0.011	4.51	Rectangular		
0.0120	0.0113	0.010	4.50	Rectangular	0.0120	0.0111	0.010	4.63	Rectangular		
0.0130	0.0120	0.011	4.46	Rectangular	0.0110	0.0105	0.010	4.61	Rectangular		
0.0140	0.0126	0.011	4.46	Rectangular	0.0100	0.0099	0.009	4.58	Rectangular		
0.0160	0.0141	0.013	4.31	Rectangular	0.0090	0.0091	0.008	4.68	Rectangular		
0.0180	0.0155	0.014	4.20	Rectangular	0.0080	0.0083	0.008	4.77	Rectangular		
0.0200	0.0168	0.015	4.14	Rectangular	0.0070	0.0072	0.007	5.17	Rectangular		
0.0250	0.0208	0.019	3.75	Rectangular	0.0060	0.0065	0.006	5.17	Rectangular		